UAB
Universitat Autònoma de Barcelona

The Photothermal Effect in MOFs

Jordi Espín Martí

Tesi Doctoral

Doctorat en Química

Directors de la Tesi:

Prof. Dr. Daniel Maspoch Comamala

Dr. Inhar Imaz Gabilondo

Tutor de la Tesi:

Dr. Félix Busqué Sánchez

Institut Català de Nanociència i Nanotecnologia (ICN2)

Facultat de Ciències. Departament de Química.

2018

Memòria presentada per a aspirar al Grau de Doctor per Jordi Espín Martí.

Vist-i-plau

Prof. Dr. Daniel Maspoch Comamala

Investigador ICREA i director de grup

Supramolecular NanoChemistry and Materials Group (NanoUP)

Institut Català de Nanociència i Nanotecnologia (ICN2)

Dr. Inhar Imaz Gabilondo

Investigador sènior

Supramolecular NanoChemistry and Materials Group (NanoUP)

Institut Català de Nanociència i Nanotecnologia (ICN2)

Dr. Félix Busqué Sánchez

Professor agregat

Departament de Química

Universitat Autònoma de Barcelona (UAB)

Bellaterra, 3 de setembre de 2018

Table of contents

Abstract

This Thesis is devoted to the study of the interaction of light with Coordination Polymers (CPs) and Metal-Organic Frameworks (MOFs). Two strategies have been followed to accomplish this objective. The first approach consisted on the study of the photothermal effect observed in different subfamilies of reported MOFs, which exhibited local heating upon UV-Vis irradiation. Such temperature increase was proved useful for MOF activation and Covalent Post-Synthetic Modification (CPSM) purposes. The second strategy was based on the synthesis of CPs following a ligand design approach using light-harvesting Ru^{2+}-terpyridine complexes.

Chapter 1 encloses a general introduction to CPs and MOFs, containing a historical overview of their discoveries and evolution, as well as some of the multiple applications in which these materials are involved. In this sense, we have focused on the applications arisen from the use of light as external stimulus.

In Chapter 2, we have summarized the main objective of this Thesis and detailed the specific sub goals.

Chapter 3 introduces the fundamentals of the light-to-heat conversion in different materials. Some examples of MOFs composites, where the nanoparticles exhibit the photothermal properties are reviewed. Moreover, a summary of some of the most common methods for removing guests from MOF pores (activation) is included. In this chapter, we demonstrate that MOFs also show photothermal effect and that this effect can be used to activate them by removing the solvent molecules after their irradiation with a UV-Vis lamp for short periods.

In Chapter 4, Post-Synthetic Modification (PSM) of MOFs is reviewed based on the interactions between the framework and the desired modifying agents. To this end, some alternative strategies to perform such reactions are included. Thereafter, the use of the local heat generated upon MOF irradiation in CPSM reactions is reported. Amino-tagged MOFs with strong photothermal effects and anhydrides or aldehydes were mixed (sovent-free), and subsequent UV-Vis exposure for short times allowed the melting of the reagents and the covalent reaction.

In Chapter 5, the light-harvesting and photothermal properties of some organometallic complexes are exemplified. The beneficial strategy of confining these moieties as building units in CPs and MOFs for enhancing their performance is described. The synthesis and characterization of three new CPs build up from Ru^{2+}-terpyridine complexes is reported here. Their photothermal characterization is performed and the new CPs showed maximum temperatures in the range of the MOFs with the strongest photothermal effect. In addition, future assessment of the CPs in photocatalytic reactions might be carried out, taking advantage of the close disposition of the Ru complexes and the metal ions of the nodes.

Resum

Aquesta Tesi està dedicada a l'estudi de la interacció de la llum amb Polímers de Coordinació (CPs) i Xarxes Metalorgàniques (MOFs). S'ha seguit dos camins per aconseguir aquest objectiu; en primer lloc estudiant l'efecte fototèrmic observat en diferents subfamilies de MOFs, els quals, un cop irradiats amb llum UV-Vis, presenten un escalfament local. Aquest augment de temperatura ha resultat útil tant en processos d'activació de MOFs com en Modificacions Covalents Post-Sintètiques (CPSM). Per altra banda, sintetitzant nous CPs seguint l'estratègia de disseny de lligands fent servir complexos de coordinació de Ru^{2+}-terpiridines amb propietats de captació de llum.

El Capítol 1 inclou una introducció general als CPs i MOFs, amb una visió històrica del seu descobriment i evolució, així com algunes de les múltiples aplicacions en les que aquests materials es poden implicar. En aquest sentit, ens hem centrat en les aplicacions que aprofiten la llum com a estímul extern.

En el Capítol 2, hem resumit l'objectiu principal d'aquesta Tesi i n'hem detallat els objectius parcials.

El Capítol 3 presenta una introducció als fonaments de la conversió de llum a calor en diferents materials. Alguns exemples de composites de MOFs, on les nanopartícules demostren un comportament fototèrmic, es troben resumits. Per altra banda també s'hi expliquen alguns dels mètodes més emprats per evacuar molècules que obstrueixen els porus de MOFs (activació). En aquest capítol es demostra que els MOFs també presenten efecte fototèrmic i que aquest efecte es pot utilitzar per a activar-los eliminant les molècules de dissolvent un cop irradiats amb una làmpada UV-Vis per temps curts.

En el Capítol 4, la Modificació Post-Sintètica (PSM) de MOFs es resumeix basant-se en les interaccions entre l'esquelet del material porós i els agents modificants. També s'hi inclouen algunes estratègies alternatives per realitzar aquestes transformacions. En aquest sentit, l'ús de la calor local generada a partir de irradiar MOFs és utilitzada per aconseguir reaccions de CPSM. MOFs amb funcionalitzacions amino que presenten un fort efecte fototèrmic i anhídrids o aldehids es van mesclar (sense dissolvent) i la posterior exposició a llum UV-Vis per temps curts va afavorir la fusió dels reactius i la reacció covalent.

En el Capítol 5, les propietats d'absorció de llum i fototèrmiques d'alguns complexos organometàl·lics s'exemplifiquen. També s'hi descriu l'estratègia beneficiosa de confinar aquests grups com a unitats estructurals en CPs i MOFs per a millorar la seva activitat. La síntesi i caracterització de tres nous CPs construïts a partir de complexos de Ru^{2+}-terpiridina i ions catalítics és descrita en aquest apartat. La caracterització fototèrmica d'aquests nous CPs demostra que presenten temperatures màximes en el rang dels MOFs amb un efecte fototèrmic més elevat. També es proposa realitzar un estudi dels CPs en reaccions de fotocatàlisi aprofitant la disposició dels complexes de Ru i dels ions metàl·lics en els nodes.

Acknowledgements

En primer lloc vull donar les gràcies a l'Institut Català de Nanociència i Nanotecnologia, a la Universitat Autònoma de Barcelona i al Programa de Doctorat en Química per permetre'm realitzar un doctorat en unes condicions òptimes.

Als directors de tesi, el Prof. Daniel Maspoch i el Dr. Inhar Imaz, els hi vull agrair l'oportunitat d'haver pogut desenvolupar aquesta tesi doctoral en el seu grup d'investigació, i el seu guiatge i ajuda durant aquests anys. Al tutor de tesi, el Dr. Félix Busqué, li agraeixo també els seus consells de síntesi orgànica.

Al Servei d'Anàlisi Químic i al Servei de Ressonància Magnètica Nuclear de de la UAB per la seva ajuda en les diferents tècniques analítiques. La resolució estructural no hauria estat possible sense la col·laboració del sincrotró ALBA-CELLS, en concret al suport tècnic de la Dra. Judith Juanhuix. També vull agrair als nostres col·laboradors en treballs aliens a aquesta tesi; a la Dra. Julia Lorenzo pels assajos de citotoxicitat realitzats al IBB i al Prof. Javier Tejada per tot el que em va ensenyar sobre el magnetisme molecular del Mn12 en les reunions a la UB.

Em sento molt afortunat d'haver pogut compartir tots aquests anys amb la gent que ha anat passant per NanoUp i els que encara hi són. Als col·legues d'aventures dins i fora del lab; el Dr. Luis Carlos Garzón, el Dr. Xavi Aríñez, el Dr. Arnau Carné, el Dr. Iván Burneo, la Claudia Vignatti, el Dr. Abraham Ayala, el Heng Xu, la Marta Ruiz, la Blanca Chocarro, el Dr. Vahid Safarifard, el Civan Avci, la Ceren Avci i l'Amirali Yazdi, amb qui espero seguir compartint moments allà on sigui. Al millor Ru-terpy team; el Jorge Albalad, la Laura Hernández i la Dra. Sabina Rodríguez per la seva dedicació en aquest projecte i sobretot per la seva paciència, i al Gerard Boix per la seva ajuda. Als post-docs; Dr. Carles Carbonell, Dr. Javier Troyano, Dr. Javier Pérez, Dr. Vincent Guillerm, Dra. Thais Grancha, per tots els bons consells. A les tècnics de laboratori; Dra. Emi Evangelio i Dra. Marta Sanmartí per la paciència que han tingut amb tot el grup. A l'equip d'encapsulació, la Dra. Mary Cano, la Dra. Sonia García i la Dra. Nereida Mejías, i també a les group managers, que sempre han procurat que tingués els papers al dia; la Marta González, la Dra. Raquel Ríos i la Rosa Puga.

Als meus amics per totes les vegades que m'han preguntat de què anava la tesi i els hi acabava resumint amb onomatopeies.

A l'Ona, per tot el seu suport, paciència i ajuda durant aquesta última etapa de la tesi.

I finalment a la meva família, per ensenyar-me que l'esforç és fonamental per a aconseguir tot el que ens proposem i que sempre han estat al meu costat. A la meva germana, un exemple de força de voluntat i la veritable doctora de casa.

Glossary of acronyms

1	$[Ru(L_1\text{-}COOH)_2](PF_6)_2$
2	$[Ru(L_2)_2]$
BA	Benzoic anhydride
BDC	1,4-benzenedicarboxylic acid
BPDC	4,4'-biphenyldicarboxylic acid
Bpy	Bipyridine
Bpydc	2,2'-bipyridine-5,5'-dicarboxylic acid
BrBz-CHO	4-bromobenzaldehyde
BrBz-COOH	4-bromobenzoic acid
BTC	1,3,5-benzenetricarboxylic acid
Co-1	$[Co(1)](PF_6)_2 \cdot solv$
Co-2	$[Co_2(2)(Cl)_4]$
CP	Coordination polymer
CPSM	Covalent post-synthetic modification
Dcbpy	2,2'-bipyridine 4,4'-dicarboxylic acid
DEF	N,N'-diethylformamide
DHTA	2,5-dihydroxyterephthalic acid
DMF	N,N'-dimethylformamide
DMSO	Dimethyl sulfoxide
EA	Elemental analysis
ESI-MS	Electrospray ionization – mass spectrometry
EtOH	Ethanol
FTIR	Fourier transform infrared spectroscopy
HKUST	Hong Kong University of Science and Technology
HAcOBIP	2-((2,6-bis(3-methyl-3H-indol-2-yl)pyridin-4-yl)oxy)acetic acid
HOBIP	2,6-bis(3-methyl-3H-indol-2-yl)pyridin-4-ol
ICP-OES	Inductively coupled plasma - optical emission spectrometry
IUPAC	International Union of Pure and Applied Chemistry
$L_{1\text{-}Furyl}$	4'-(furan-2-yl)-2,2':6',2''-terpyridine

L_{1-COOH}	[2,2':6',2''-terpyridine]-4'-carboxylic acid
L_2	4'-(4-carboxyphenyl)-2,2':6',2''-terpyridine
MA	Maleic anhydride
MeCN	Acetonitrile
MeOH	Methanol
MIL	Material from Institute Lavoisier
MOF	Metal-organic framework
NH_2-BDC	2-aminoterephthalic acid
NMR	Nuclear magnetic resonance
PSM	Post-synthetic modification
RT	Room Temperature
SALE	Solvent assisted ligand exchange
SALI	Solvent assisted ligand incorporation
S_{BET}	Brunauer Emmett Teller surface area
SBU	Secondary building unit
SCSC	Single Crystal-to-Single Crystal
SCXRD	Single Crystal X-Ray Diffraction
SEM	Scanning electron microscopy
Terpy	2,2':6',2''-terpyridine
TGA	Thermogravimetric analysis
THF	Tetrahydrofuran
UiO	Universitetet i Oslo
UV-Vis	Ultraviolet-visible
XRPD	X-Ray powder diffraction
Zr-2	$[Zr(2)(HCOO)_4]$

Chapter 1

Introduction

In this chapter, coordination polymers (CPs) and metal-organic frameworks (MOFs), and some of their multiple features and applications are introduced. Then, a subclass of MOFs that are responsive to light is shown. This light-responsive MOFs include the use of MOFs for photocatalysis, the development of light-triggered delivery systems and the use of light to post-synthetically modify MOFs.

1. Coordination Polymers

CPs are a class of hybrid materials build up from organic molecules and inorganic ions or clusters assembled through coordinative interactions, which are continuously extended in one (chains), two (layers) or three (frameworks) dimensions, depending mainly on the coordination environment of both building units.[1–3] The concept "*coordination polymer*" was introduced for the first time by Bailar in 1964.[4]
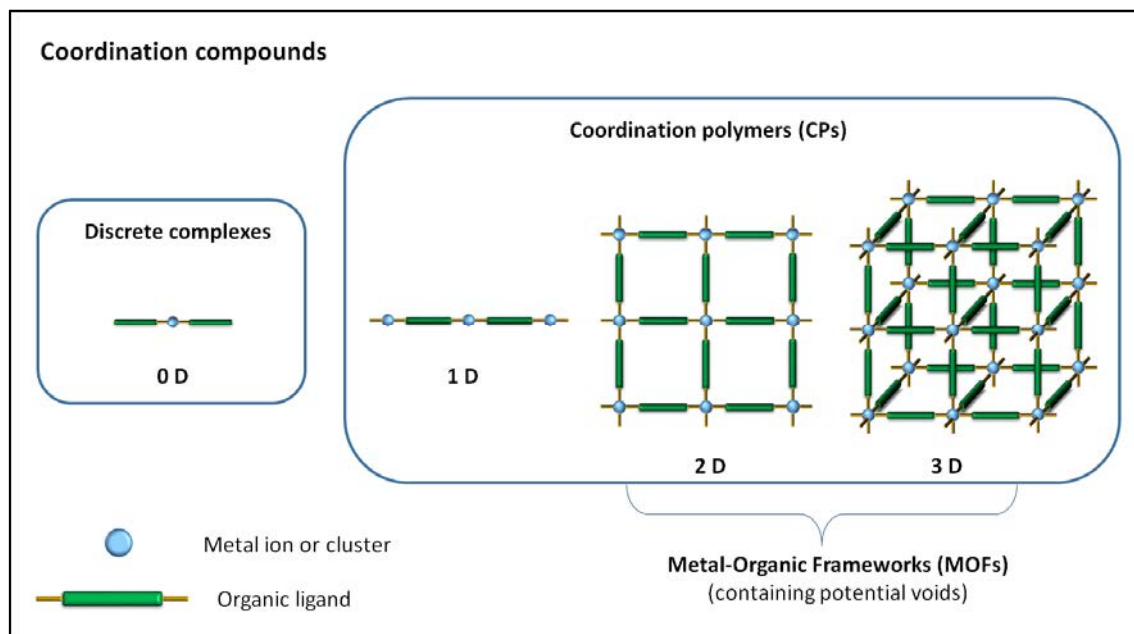
Figure 1.1. Classification of coordination compounds.

The history of CPs started back to the early 18th century in Berlin (Germany), when by serendipity Prussian Blue was first synthesised.[5] This was not the goal of Diesbach, a professional colour maker, who was looking forward to produce Florentine lake, a red pigment. The original recipe consisted on mixing carminic acid (extracted from cochineal insects), iron sulfate, potassium alum and potassium carbonate. Unfortunately, that time he ran out of potassium carbonate and decided to borrow some from his lab mate, without being aware of the contamination of this reagent with hexacyanoferrate. Instead of the expected red colour, he obtained a strong blue precipitate that was proved useful as an inexpensive pigment. However, the composition and detailed structure of Prussian Blue was not discovered until 1970s by Lundi and co-workers, who demonstrated the accepted formula $Fe[Fe(CN)_6]_3 \cdot xH_2O$ (x = 14-16) with the help of X-ray crystallography.[6] This pigment is commercialized nowadays under the name of Iron Blue. Iron Blue is today used in paints and textile dyes. In addition, it is employed as poison antidote due to the high affinity for thalium and cesium cations, in electrochromism, as the

colour changes for the different oxidation states, and as a sensor, upon the catalytic reduction of hydrogen peroxide to oxygen.

Although the first example of CP was rather serendipitous, coordination compounds started to be conceptualized and rationalized by Alfred Werner at the end of 19th century, whose research was awarded with the Nobel Prize in 1913.[7] He postulated that there is a fixed coordination number for a given metal centre with a defined arrangement of the ligands around it. Werner also showed different kinds of geometry in complexes with formula $[M(NH_3)_4Cl_2]$, taking into account the basic experimental techniques that they had to rely by that time. Werner's complexes, with formula β-$[M(PIC)_4(NCS)_2]$ (where M is Ni^{2+} and Co^{2+}; PIC is γ-picoline; and NCS is thiocyanate), were demonstrated to adsorb gases reversibly by Barrer in 1969.[8]

The first willingly synthesised coordination networks were the Hofmann clathrates, being the original one from 1897, with formula $[Ni(CN)_2(NH_3)] \cdot C_6H_6$.[9] Its structure was not elucidated until 1952 thanks to X-ray analysis. It consisted on 2D layers of octahedral and square planar Ni^{2+} connected through CN^- moieties, whereas the NH_3 was coordinated in an axial disposition generating voids able to encapsulate benzene molecules.[10] Later, Iwamoto and co-workers rationalized the synthesis of these clathrates, starting by mixing two charged complexes, $[M(NH_3)_2]^{2+}$ with $[M'(CN)_4]^{2-}$, and leading to structures with the formula $[M(NH_3)_2M'(CN)_4] \cdot$guest.[11,12] In these clathrates, ditopic ligands such as ethylenediamine or diamines with longer alkyl chains were used as bridges between the layers, proving the selective encapsulation of guests.[13]

Later, in 1959, Saito and co-workers synthesised a series of CPs of different dimensionality based on the well-known inorganic building unit $Cu(-CN)_4$ and organic moieties of different length.[14–16] They showed that succinonitrile, glutaronitrile and adiponitrile ligands gave rise to one-, two, and three-dimensional CPs, respectively (Figure 1.2).

However, it was not until 1989 when Hoskins and Robson proposed the potential synthesis of "*infinite polymeric frameworks*".[17] They synthesised an infinite framework with formula $[Cu(TCTPM)]^+$ by reacting a tetrahedral building unit $Cu(-CN)_4$ with the tetrahedral ligand 4,4',4'',4'''-tetracyanotetraphenylmethane (TCTPM). This framework was charge balanced with BF_4^- anions situated in the voids of the structure, which could be exchanged with PF_6^- anions without altering its crystallinity.[18] This principle based on tetrahedral building units led to many diamond-like frameworks with different metal ions (Zn^{2+} and Cd^{2+}) and longer ligands (1,4-dicyanobenzene, 4,4'-dipyridyl and 2,5-dimethylpyrazine). Behind their excellent experimental results, they were pioneers in predicting plausible features and applications for these solid

materials and in applying the concept introduced by Wells in 1977, who claimed that crystal structures could be reduced to networks by identifying their nodes and connectors.[19] This approach was already used for the interpretation of zeolite structures and is now considered as the foundation of today's design strategies of crystalline materials. Hoskins and Robson identified the metal ions as nodes and the organic ligands as spacers, setting the basis of the rational design of CPs.
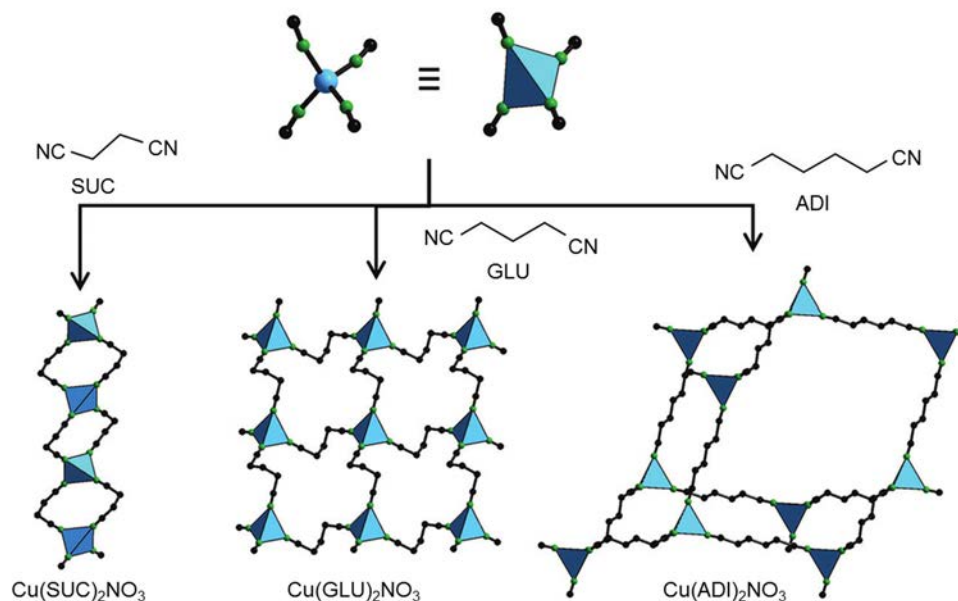
Figure 1.2. Structures of Saito's CPs.[14–16]

However, the applications of the potential voids present in the CPs were not explored until 1994, when Fujita and co-workers performed the first catalytic studies in a 2D structure with formula $Cd(4,4'-bpy)_2(NO_3)_2$, where bpy is bipyridine.[20] They reported the encapsulation of dihalobenzenes and cyanosilylation of aldehydes proving specificity depending on the size of the molecule to diffuse in the channels.

During the following years, the number of publications about CPs clearly increased (Figure 1.3) and more efforts were devoted to apply crystal engineering principles to obtain new materials with tailored applications.[1] In parallel, a new family of porous materials with outstanding performances was beginning to catch the attention of the research community: the metal-organic frameworks (MOFs).
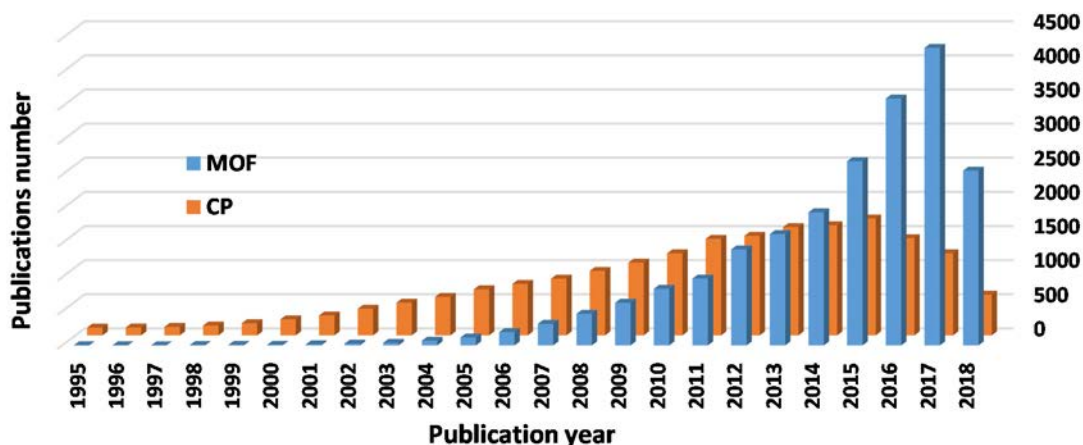
Figure 1.3. Bar chart of the number of publications including the concept "coordination polymer" or "metal-organic framework" in the last decades. SciFinder database, June 2018.

2. Metal-Organic Frameworks

The definition of MOF might cause some lack of consensus and other acronyms can be found in the literature, such as Porous Coordination Polymer (PCP). With the goal to unify and clarify the nomenclature and terminology of these materials, the International Union of Pure and Applied Chemistry (IUPAC) initiated some projects interacting with scientists of the field. Summarizing these projects, IUPAC concluded that "*MOFs are a subclass of CPs with an open framework containing potential voids*" (Figure 1.1).[2]

Although the short history of these porous crystalline materials (*ca.* two decades), MOFs have emerged as very promising materials thanks to their exceptional properties, which have proved useful in a myriad applications (*vide infra*). The term "*metal-organic framework*" was first coined by Yaghi and co-workers in 1995, when they reported the hydrothermal synthesis of a metal-organic open framework, which asymmetric unit was composed of $Cu(4,4'-bpy)_{1.5} \cdot NO_3(H_2O)_{1.25}$.[21] It consisted on a diamond-like framework with the Cu^{1+} in trigonal planar geometry, a metal coordination observed for the first time in this structure. This cationic framework was stabilized by NO_3^- anions and could perform anion exchange with SO_4^{2-} and BF_4^-. In the same year, Yaghi and co-workers studied the selective adsorption of guests in a microporous MOF with formula $Co(BTC)(pyr)_2 \cdot 2/3pyr$, where BTC is 1,3,5-benzenetricarboxylic acid and pyr is pyridine.[22] The solvating pyridine molecules were evacuated (activation process) and further soaking of the crystalline material into different solvents permitted the assessment of the selective adsorption of aromatic molecules, such as benzene, nitrobenzene, chlorobenzene and cyanobenzene, but not of acetonitrile, nitromethane and dichloroethane.

In 1997, Kitagawa and co-workers first assessed gas adsorption in a three-dimensional MOF.[23] Its unit cell consisted on $M_2(4,4'-bpy)_3(NO_3)_4 \cdot xH_2O$, where M is Co^{2+}, Ni^{2+} or Zn^{2+}. N_2, O_2 and CH_4 adsorption measurements were carried out at 298 K from 1 to 36 atm after solid dehydration, showing a type I isotherm. Remarkably, the crystalline structure remained intact upon water desolvation and gas adsorption assessment.

One year after, a MOF named MOF-2, which was composed of $Zn(BDC) \cdot (DMF)(H_2O)$ (where BDC is 1,4-benzenedicarboxylic acid) was synthesised by Yaghi and co-workers.[24] This MOF was built up from the assembly of paddlewheel secondary building units (SBUs, *vide infra*) generating 2D layers strongly packed together by hydrogen bonding between water molecules. The presence of DMF and H_2O molecules in the structure evidenced the presence of voids. After removing these solvent molecules, MOF-2 gas adsorption isotherms (N_2 and CO_2 at 77 and 198 K, respectively) showed Langmuir surface areas of 270 and 310 $m^2 \cdot g^{-1}$, respectively. Such experiment served to demonstrate permanent porosity in this activated MOF-2.

However, it was not until 1999 when the first outstanding performance in a MOF was observed. The synthesis of MOF-5 by Yaghi and co-workers was probably the beginning of a new era for these materials.[25] The formula of as-synthesised MOF-5 is $Zn_4O(BDC)_3 \cdot (DMF)_8(C_6H_5Cl)$. The coordination environment of its SBU consists on a central oxygen atom coordinated tetrahedrally to four Zn^{2+}, which are also coordinated to six carboxylates coming from the BDC moiety, presenting a **pcu** (cubic network) topology (Figure 2.1). Guest molecules occupying the voids were first exchanged with chloroform that could easily be evacuated following a mild activation step. N_2 adsorption experiments at 77 K of the evacuated MOF-5 demonstrated a Brunauer-Emmett-Teller surface area[26] (S_{BET}) of 2320 $m^2 \cdot g^{-1}$. This surface area value resulted in the highest ever reported to date for a porous material, surpassing zeolites, silicas and carbon-based materials' performance (Figure 2.4). It was not only the fact of attaining a record-high surface area porous material what made this work valuable, but also the introduction of the term "*permanent porosity*" of MOFs. Indeed, it was demonstrated that after the solvent exchange step to eliminate the as-synthesised guest molecules, MOF-5 retained the original crystallinity and the structure voids were then accessible to gas molecules. The guest removal evacuation or activation of MOFs became a field of study and optimization with the goal to reach the highest S_{BET} value for each newly synthesised MOF (see Chapter 3).
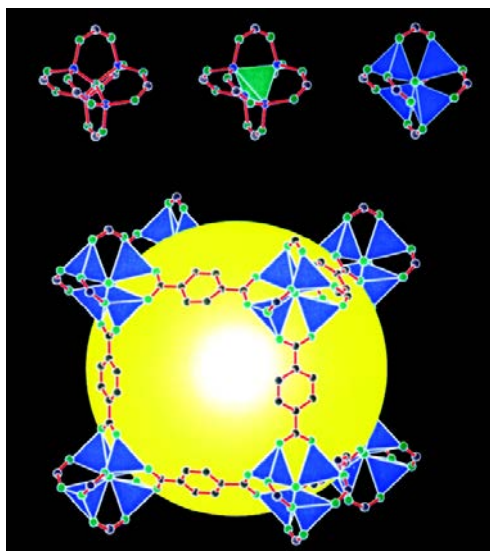
Figure 2.1. Schematic SBU and structure of MOF-5.

Noteworthy, the large number of early-synthesised MOFs required guidelines for the rationalization of such crystalline structures. The principles proposed by Wells[19] in 1977 were used for the structural description of CPs, which consisted on the abstraction of their underlying nets through the "*node and spacer*" approach. Following this concept, the metal ions were considered as nodes interconnected through the organic ligands, seen as rigid rods. However, such distinction resulted insufficient when complex building blocks were employed to construct MOFs, resulting in more elaborated final structures. To solve this, Yaghi and co-workers suggested that those crystalline materials can be assembled from molecular clusters represented as geometrical shapes, called SBUs, instead of single atoms (Figure 2.2).[27–29] Those SBUs consisted on the inorganic metal ion or cluster surrounded by the coordinating groups from the organic ligands. In this approach, the organic ligand was also observed as a geometrical shape taking into account its number of coordinating moieties. Today, the discipline devoted to understanding and predicting the final topologies obtained from mixing and linking different SBUs is called reticular chemistry.
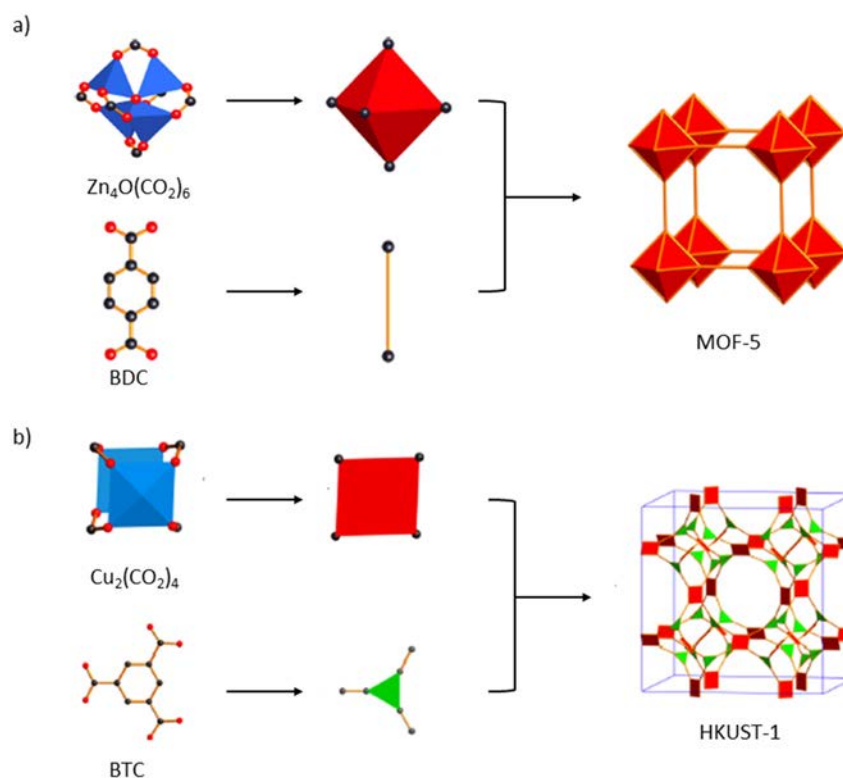
Figure 2.2. Building blocks and SBUs illustration of a) MOF-5 and b) HKUST-1.[29]

Later, in 2002, Yaghi and co-workers reported the synthesis of a series of isoreticular MOFs based on the topology of MOF-5. These materials, namely IRMOF-n (where n = 1-10, 12, 14, 16), were built by substituting the initial BDC ligand by longer aromatic dicarboxylate ligands. With these substitutions, the pore size could be increased from 3.8 to 28.8 Å, and the pore walls could be decorated with different functional groups (Figure 2.3).[30]
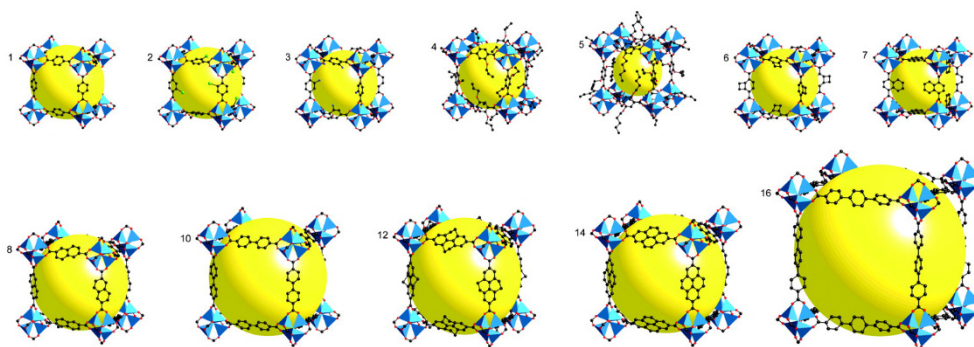
Figure 2.3. Schematic representation showing that the isoreticular synthesis of MOFs allowed the functionalization of the pore walls (top) and the enlargement of the pore size and the surface area (down).[30]

Since the synthesis of MOF-5 and IRMOF family, many efforts have been devoted in obtaining MOFs with ever-increasing surface areas. Such objective was accomplished by following the isoreticular synthetic approach and the use of longer organic ligands. In fact, in 2012, Farha, Yazaydin, Hupp and co-workers reported two MOFs (NU-109 and NU-110) with an experimental S_{BET} above 7000 $m^2 \cdot g^{-1}$,[31] which are the highest reported values up to date (Figure 2.4).
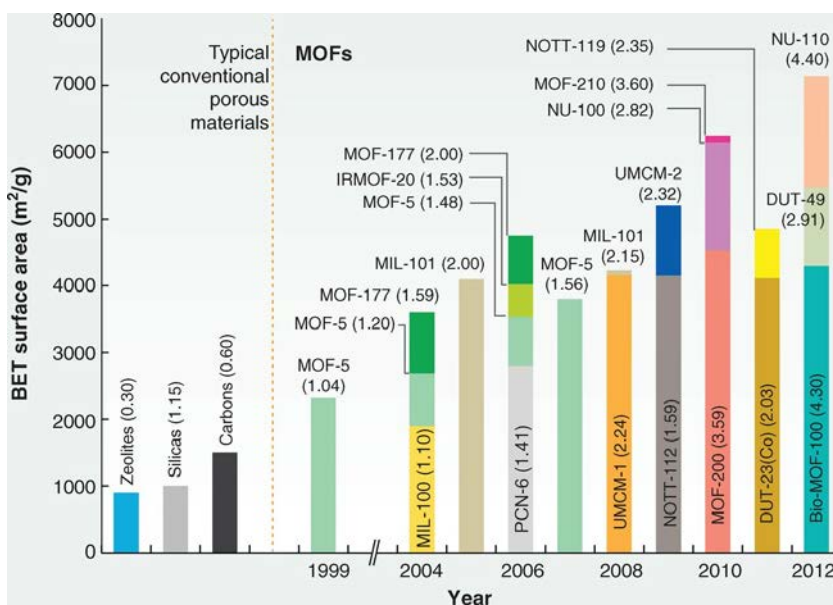
Figure 2.4. Comparison of the surface area values between conventional porous materials and MOFs along the years. The values in parentheses indicate the pore volume ($cm^3 \cdot g^{-1}$) of the material.[32]

The exceptional sorption performance of MOFs in combination with their composition tunability have made them suitable for a wide range of applications, including gas storage[33–42] and separation,[43–48] drug delivery[49–59] and catalysis,[60–72] among many others.[73–79]

2.1. Stimuli-responsive MOFs

Beyond the classical properties and applications of MOFs, **stimuli-responsive MOFs**[80,81] are starting to be considered a type of smart materials that can show a response to physical or chemical inputs. Some of the most common stimuli include pressure,[82,83] temperature,[84,85] chemicals[86,87] and light.[88,89] Among them, light presents significant advantages and versatility because it can be easily applied, and it allows spatial and temporal control over the irradiated sample. In this section, some of the most representative light-driven applications of MOFs are summarized.

2.1.1. Light as stimulus in MOF applications

As light-responsive materials, MOFs can incorporate a variety of photoactive ligands and metal clusters. The rational design and synthesis of these materials might allow the enhancement of their performance in light-driven applications or the exploration of new venues in this field.

2.1.1.1. Photocatalysis

The role of MOFs in photocatalytic processes can be diverse, depending on the properties that the material confers to the reaction medium. When MOFs act as photocatalysts, they must absorb light to produce photogenerated charge carriers that will act later in photoredox reactions. These MOFs are light-energy transducers that mediate the conversion of light into energized electrons and holes. In this sense, the organic ligands can be seen as antennas and perform a ligand to metal cluster charge transfer (LCCT), thereafter generating electrons and holes that are transferred to the crystal surface for further use in photocatalytic reactions. Thus, when constructing photocatalytic MOFs, there are at least two requirements that must be fulfilled: i) the ability to **absorb light** in order to undergo electronic excitation with the light source, which might be accomplished by selecting the appropriate organic ligand or the inorganic metal ions; and ii) to achieve a good **charge separation**, which is favourable in MOFs due to the rigid distribution of both building blocks and the close contact between them.

Some of the most studied photocatalytic processes in MOFs include organic transformations,[90,91] carbon dioxide reduction,[92,93] water splitting[94,95] (hydrogen and oxygen evolution) and artificial photosynthesis.[96] An interesting example of photocatalytic MOF was reported by Li and co-workers, who studied the use of Fe-based MOFs for CO_2 reduction (Figure 2.5).[93] In this work, they used MIL-101(Fe), MIL-53(Fe) and MIL-88B(Fe) because these MOFs exhibit visible light absorption properties due to the Fe-O cluster. They irradiated a suspension of these MOFs in MeCN degassed with CO_2 using triethanolamine (TEOA) as a sacrificial electron donor in a wavelength range of 420-800 nm using a 300 W Xe lamp for 8 hours. It was found that the best performance was achieved for MIL-101(Fe) as it contains open metal sites. In addition, as the functionalization of the organic ligands with amino groups leads to an enhanced absorption of visible light,[97] they also assessed the photocatalytic behaviour of MIL-101-NH_2(Fe), MIL-53-NH_2(Fe) and MIL-88B-NH_2(Fe). These amino-functionalised MOFs showed a better performance generating three times more formate in the case of MIL-101-NH_2(Fe) than MIL-

101(Fe). This increase was attributed to a dual excitation pathway: on one hand, to the LCCT from the BDC-NH$_2$ (2-aminoterephtalic acid) ligand to the Fe oxocluster; on the other hand, to the excitation of the Fe-O of the inorganic SBU. Both pathways accomplished the electron transfer to Fe^{3+} converting it into Fe^{2+} species ready for reducing CO$_2$. A recent review about photocatalytic CO$_2$ reduction with MOFs was published by the same group.[98]
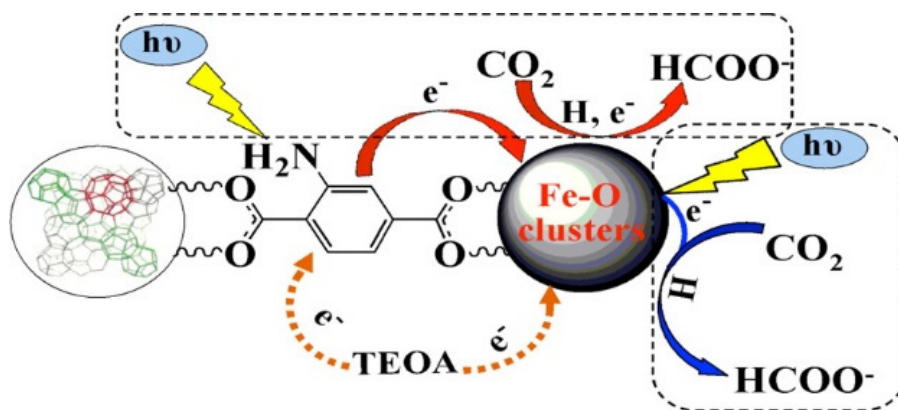
Figure 2.5. Scheme of the photocatalytic CO$_2$ reduction process taking place in Fe-based MILs.[93]

In photocatalysis, the MOF can also act as a co-catalyst. In this case, the light-harvesting function is carried out by other compounds such as dyes or semiconductors, and the MOFs are responsible of promoting kinetic processes of charge separation and catalytic reactions.

Enzymatically produced H$_2$ in nature might arise from NiFe or FeFe hydrogenases, which contain an organometallic cluster based on their respective dinuclear centers surrounded by the cysteic sulfur ligands coordinating the protein (NiFe) or by non-proteic CN$^-$, CO and thiolate binding to the protein (FeFe).[99] Incorporation of this catalytic cores in artificial materials has been pursued by many research groups.[100] However, one of the main drawbacks has beed the lack of stabilization of the active site, a role that is performed by the enzyme matrix. With the goal to attain a protective scaffold for such catalysts, Ott, Cohen and co-workers proposed the integration of a ligand modified with the Fe-Fe core in a MOF (Figure 2.6).[101] The strategy consisted on first synthesising the thermally and chemically stable UiO-66 followed by a post-synthetic exchange (PSE) (or solvent assisted ligand exchange (SALE)), with the BDC-based ligand 2,3-dimercaptoterephtalic acid coordinated to the [FeFe](CO)$_6$ cluster. With this approach, a degree of ligand integration of 14 % was achieved. In the H$_2$ evolution reaction, this MOF acted as co-catalyst, the complex Ru(2,2'-bpy)$_3$$^{2+}$ acted as the photosensitizer and ascorbic acid was used as electron donor. It was proved that, upon irradiation with a blue LED (470 nm), H$_2$ production was higher with the heterogeneous catalyst UiO-66-[FeFe](dcbdt)(CO)$_6$ (*ca.* 3-fold

enhanced) than in the homogeneous catalysis process driven by the organometallic moiety [FeFe](dcbdt)(CO)$_6$.
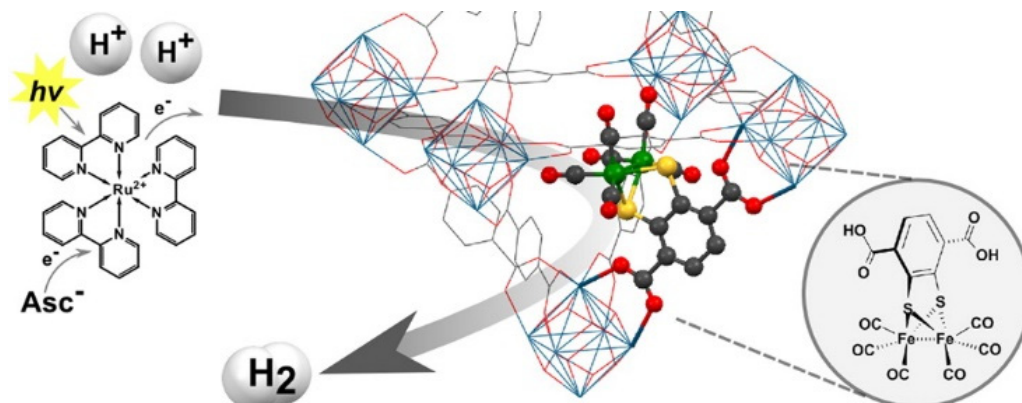
Figure 2.6. Illustration of the electron transfer from Ru(2,2'-bpy)$_3^{2+}$ dye to the FeFe cluster of the postsynthetically modified UiO-66.[101]

MOFs can also act as hosts in photocatalysis. This happens when the MOF has no catalytic activity, but light-induced reactions with enhanced performance occur in the pores or the surface of the framework. Indeed, the cavities/channels of MOFs and the ease of functionalisation of their organic ligands via direct synthesis or postsynthetic chemistry convert them in appropriate candidates for hosting photocatalytic reactions.

A very smart approach of MOF acting as a host for hydrogen evolution photocatalysis was reported by Gascón, van der Vlugt, Reek and co-workers. They encapsulated a cobaloxime derivative in MIL-125-NH$_2$(Ti) using a "*ship-in-a-bottle*" approach (Figure 2.7).[102] Due to steric hindrance, the preformed cobaloxime could not be entrapped in the pores of the MOF. Therefore, they introduced this complex in the pores by diffusing the organic moiety overnight and further reacting it with CoBr$_2$ (loadings up to 2.7 % of Co (w/w %)). The reaction setup consisted on the visible light irradiation (500 W Xe/Hg lamp) of a suspension of the composite in MeCN and H$_2$O using TEA as sacrificial electron donor for 24 hours. In this MOF, the photogenerated charge was transferred from the organic ligand to the Ti^{4+} cluster and subsequently, to the cobalt species. H$_2$ evolution of the Co@MOF was increased 20 times with respect of the parental MOF. It was also proved that the cobaloxime derivative did not show photocatalytic activity.
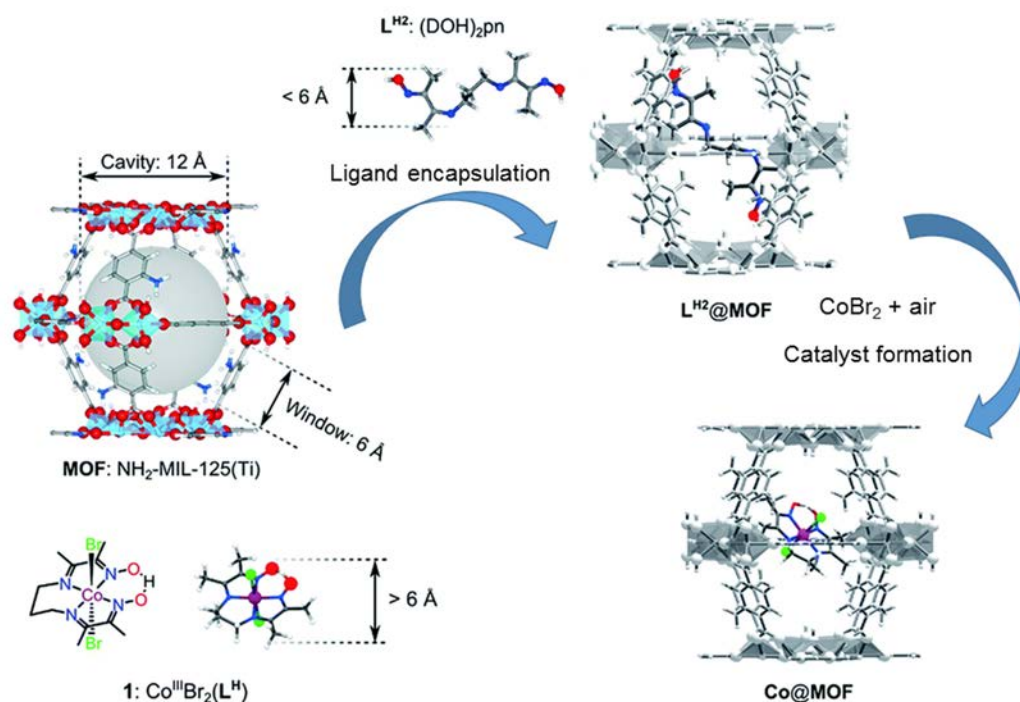
Figure 2.7. Scheme of the "*ship-in-a-bottle*" approach followed to host a Co^{3+} complex in MIL-125-NH_2(Ti).[102]

Finally, rational incorporation of both photosensitizer and catalyst in the skeleton of a MOF has been recently proposed by different research groups.[103,104] In a very recent example, the charge transfer between both sites of the MOF was experimentally verified (Figure 2.8).[105] For this work, Huang and co-workers used a material reported by Chen and co-workers,[103] who synthesised a isoreticular UiO-67 MOF using 4,4'-biphenyldicarboxylic acid, $[Ru(dcbpy)(bpy)_2]^{2+}$ and Pt(dcbpy)Cl_2, where dcbpy is 5,5'-dicarboxy-2,2'-bipyridine. The resulting Ru-Pt@UiO-67 framework contained 1.2 wt % of Ru and 2 wt % of Pt. In this MOF, the Ru moiety acts as the photosensitizer and transfers electrons to the neighbouring Pt complex, which is responsible of the catalytic activity. The authors confirmed this behaviour experimentally by studying the charge separation dynamics using optical transient absorption (OTA) and X-ray transient absorption (XTA) spectroscopy. Moreover, the hybrid material generated 34000 µmol H_2/g MOF after 30 hours of visible light exposure (λ > 420 nm) using a Xe lamp (150 W) upon dispersion of the composite in H_2O and MeCN in the presence of *N,N'*-dimethylaniline (DMA) that acted as the sacrificial electron donor.
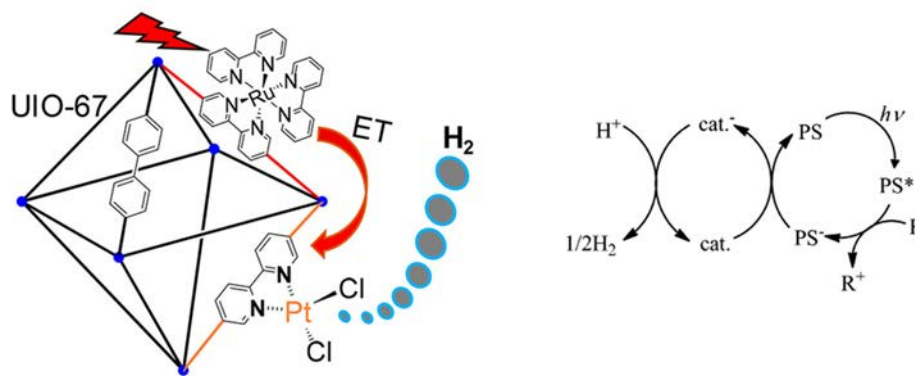
Figure 2.8. Model structure of the MOF obtained upon mixed-ligand strategy combining a Ru^{2+} photosensitizer and a Pt^{2+} catalyst for H_2 evolution, and proposed catalytic cycle.[105]

2.1.1.2. Light-triggered delivery systems

One of the first strategies used for modifying the void space in MOFs without altering their chemical composition consisted on using photoswitchable organic ligands. These ligands contain an azobenzene functional group, which is known to perform *trans*-to-*cis* isomerization upon light irradiation. The conformational modification induces changes on the channels of the MOF that can be exploited in the adsorption and desorption of molecules by opening or closing the pores. In addition, this isomerization can be reversed under irradiation at the required wavelength or under heating treatment. This approach was first reported by Stock and co-workers[88] and was further used by Zhou and co-workers to alter the CO_2 adsorption properties of a MOF.[106] Yaghi and co-workers used this strategy for controlling the pore size of azo-IRMOF-74-III.[89] Kitagawa and co-workers also employed light to control the isomerization of a guest in a flexible MOF that modified its structural conformation in order to fit the guest isomer.[107]

In 2015, Hill, Ladewig and co-workers took advantage of the conformational change in the azobenzene moiety for increasing the sorption properties of a MOF (Figure 2.9).[108] Composites of methyl red@MOF (where MOF is Mg-MOF-74 or MIL-53-(Al)) were obtained after overnight incubation of the MOFs with a dichloromethane solution of methyl red. Subsequent irradiation of the composites with visible light caused photoisomerization of the methyl red dye in the pore channels. The *trans*-to-*cis* isomerization of the azobenzene moiety gave rise to a pore-opening effect, allowing an enhancement of the CO_2 adsorption with irradiation time. In the case of Mg-MOF-74@MR with higher methyl red loading (50 %), an increase of 84 % in the CO_2 adsorption was achieved after 60 minutes of irradiation. This increase was attributed to an improvement of the dipole-quadrupole interaction between the pore walls and the CO_2 molecules.
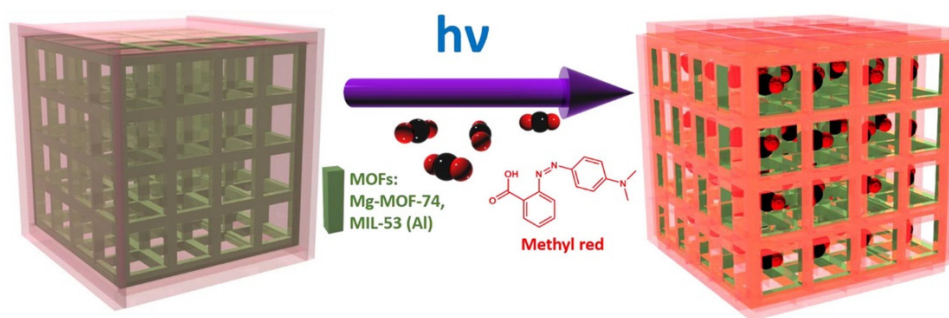
Figure 2.9. Schematic illustration of the pore-opening effect upon light irradiation.[108]

Nitric oxide (NO) is a toxic gas but also acts as a gasotransmitter and plays a number of biological roles, such as neurotransmission, immune response and vasodilation, among others.[109,110] For this reason, the design of solid hybrid materials showing NO-release properties is an excellent approach for developing new therapeutic approaches. In such context, MOFs allow the disposition of a high concentration of organic or metalorganic moieties with desired functionalities in a restricted space, converting them in proper candidates to perform local release of NO. In 2013, Kitagawa and co-workers reported the synthesis of two zeolitic imidazolate frameworks that include a NO_2 group in the organic ligand (Figure 2.10a).[111] Interestingly, the irradiation of these MOFs, named as NOF-1 and NOF-2, using a NIR laser allowed the release of NO from the skeleton of the crystals. *In vitro* tests confirmed the efficient delivery of this gas molecule from a MOF/PDMS substrate to the cell cultures of HEK293 (Figure 2.10b). Later, the same group showed the synthesis of two MOFs that include two methylamino groups in the BDC parental ligand.[112] Then, they post-synthetically modified these MOFs with $NaNO_3$ in acidic conditions allowing the formation of a bis-N-nitroso moiety.
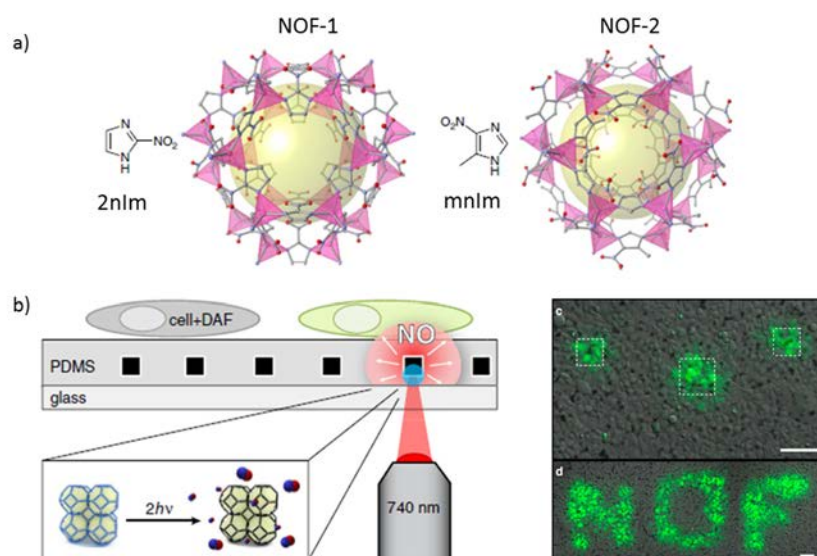
Figure 2.10. a) NOF-1 and -2 structures. b) Illustration of the irradiation experiments and release of NO over selected cells *in vitro.*[111]

Very recently, Furukawa, Kitagawa and co-workers also reported the inclusion of a manganese carbonyl complex in a UiO-67 derivative with the goal to synthesise a photoinduced CO-releasing material (Figure 2.11).[113] The strategy that they followed consisted on the post-synthetic metalation of the bipyridine moiety of each ligand using the organometallic complex MnBr(CO)$_5$. A maximum loading of 95 % of the coordination sites leading to MnBr(2,2'-bpy)(CO)$_3$ was attained by tuning the crystal size of UiO-67-bpy with the use of a modulating agent. CO release was monitored using visible light (460 nm) with an efficiency of 84 %; being one of the highest reported value for a photoinduced CO-releasing material. As CO is a gas used for biomedical purposes, they also demonstrated its *in situ* release over HeLa cells.
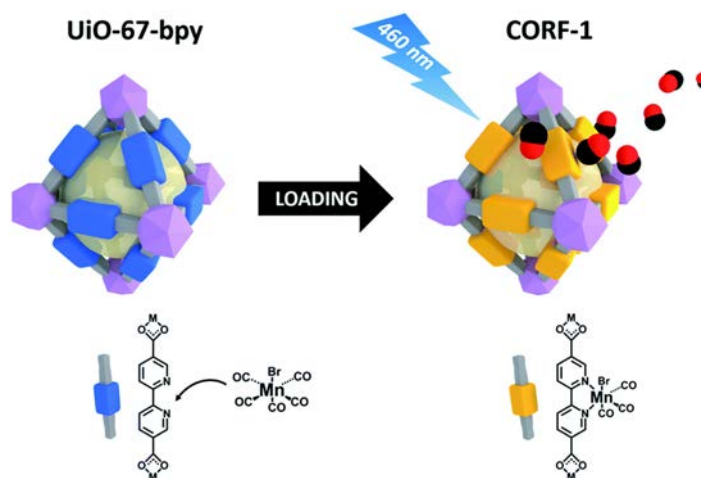
Figure 2.11. Scheme of the post-synthetic strategy followed to introduce a Mn^{1+} complex in UiO-67 scaffold for further photoinduced CO release.[113]

2.1.1.3. Light-induced post-synthetic modifications

Organic building blocks in MOFs are susceptible to be modified upon synthesis of the framework. This covalent post-synthetic modifications can also occur through light-induced covalent reactions. One of the most common reaction is the photochemical [2+2] cycloaddition to access to cyclobutane-containing structures. This reaction consists on the combination of an alkene with the excited state of an enone under light irradiation.[114–116] For example, Vittal, Zaworotko, Lee and co-workers used this reaction to make a 3D framework from 2D sheets. They first synthesised 2D Zn-based sheets with a ligand containing available C=C bonds.[117] Under UV light, reversible [2+2] cycloaddition between neighbouring ligands allowed the linkage of these sheets to form a 3D framework thanks to the formation of cyclobutane moieties (Figure 2.12).[117] By applying a heat treatment to the modified MOF, the synthesised bonds could be broken again so that the initial structure was recovered.
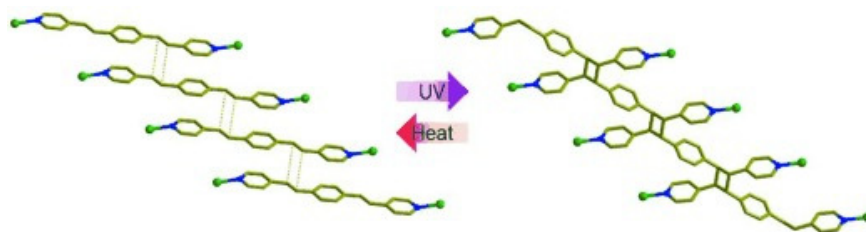
Figure 2.12. Scheme of the [2+2] reaction taking place in the framework crystals.[117]

Kitagawa, Matsuda and co-workers applied the [2+2] cycloaddition for gas separation purposes. They synthesised a mixed ligand flexible MOF using BDC and 1,2-di(4-pyridyl)ethylene. This MOF was then placed between two glass slides and irradiated with UV light (350 nm) for 24 hours/side.[118] Exposure of both materials (as-synthesised and irradiated) to mixtures of CH_2CH_2/CO_2 50:50 revealed that the as-synthesised phase showed selectivity towards CO_2, whereas the irradiated phase did not accommodate neither CO_2 nor CH_2CH_2. The explanation of this phenomenon was based on the electrostatic potential formed in the small pores, which effectively interacts with the quadruple moment of CO_2 and results repulsive to CH_2CH_2 because of the opposite quadrupole moment. The [2+2] product did not adsorb any of the gases due to electrostatic potential loss.

Another interesting application of light-induced reaction should be the post-synthetic deprotection of functional groups into MOFs. This deprotection consists on the removal of an organic moiety that is capping a desired functional group using light in order to avoid its reaction in previous synthetic steps. One of the first examples of light-induced post-synthetic

deprotection was reported by Kitagawa, Matsuda and co-workers, who obtained a Zn-based MOF build up from 5-azidoisophthalic acid and 4,4'-bipyridine.[119] The irradiation of this MOF with UV light for 24 hours yielded a conversion of 70 % of the deprotection reaction from aryl azides to singlet aryl nitrenes. This experiment was carried out in a single crystal at 77 K for 40 minutes and a conversion percentage of 31 % was calculated from the crystal data. The same photoirradiation of the MOF was done in oxygen atmosphere, generating a mixture of both nitro- and nitroso-substituted MOFs.[119]

In parallel, a light-induced post-synthetic deprotection was carried out by Cohen and co-workers, in which 2-nitrosobenzaldehyde was removed from two Zn-based MOFs upon irradiation at 365 nm for 24-48 hours.[120] After this deprotection, both hydroxyl and catechol groups were available in the MOF pore channels, whereas direct solvothermal synthesis of the MOFs with these functional groups could not be attained. Later, the same authors also reported two isoreticular MOFs with pendant nitrobenzyl groups. The irradiation of this photolabile group under near-UV light led to hydroxyl-substituted MOFs.[121]

Similarly, Telfer and co-workers proposed the synthesis of an isoreticular Zn-based MOF using a derivative of 4,4'-biphenyldicarboxylic substituted with a 2-nitrobenzyl ether, which acts both as a bulky group to avoid framework interpenetration and as a photolabile moiety.[122] Upon irradiation of the non-interpenetrated MOF in DMF or THF at 355 nm for 2-6 hours, hydroxyl groups were generated.

Very recently, Kitagawa and co-workers also proved the efficient post-synthetic deprotection of a Zn-based MOF giving rise to a free thiyl radical under UV light, which was not affordable by direct synthesis (Figure 2.13).[123] Thiyl radicals have been used by nature in a broad range of biochemical processes and attracted the attention of synthetic chemists due to their high efficiency in radical reactions and easily coupling to alkenes, alkynes and isonitriles, among other functional groups.[124] However, these radicals tend to dimerize in solution, limiting their activity. Thus, Kitagawa and co-workers showed that this radical can be stabilized by confining it in a periodic framework. To this end, crystals of the MOF with asymmetric disulphide protecting groups were dispersed in fresh DMF and irradiated at 350 nm in a quartz cuvette for 48 hours at an emission power of 8 W. The deprotection rate was estimated to be *ca.* 60 %.
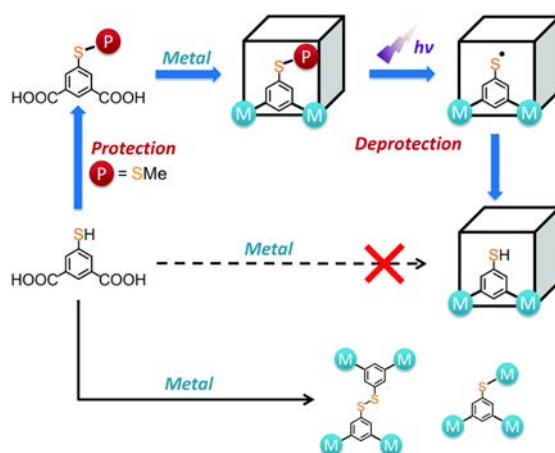
Figure 2.13. Diagram of the strategies attempted to introduce a protected thiyl group in a MOF.[123]

Taking into consideration the number of works that report the benefits of using light as an stimulus to interact with MOFs, we set our Thesis objectives with the goal to **address novel applications of light such as the exploration of the photothermal effect in MOFs**.

3.   References

1.   Janiak, C. Engineering Coordination Polymers Towards Applications. *Dalton Trans.* **0,** 2781–2804 (2003).

2.   Batten, S. R., Champness, N. R., Chen, X.-M., Garcia-Martinez, J., Kitagawa, S., Ohrstrom, L., O'Keeffe, M., Suh, M. P. & Reedijk, J. Coordination Polymers, Metal-Organic Frameworks and the Need for Terminology Guidelines. *CrystEngComm* **14,** 3001–3004 (2012).

3.   Batten, S. R., Neville, S. M. & Turner, D. R. *Coordination Polymers*. (The Royal Society of Chemistry, 2009). doi:10.1039/9781847558862

4.   Bailar, J. C. Coordination Polymers. *Prep. Inorg. React.* **1,** 1–27 (1964).

5.   Kraft, A. On the Discovery and History of Prussian Blue. *Bull. Hist. Chem.* **33,** 61–67 (2008).

6.   Buser, H. J., Schwarzenbach, D., Petter, W. & Ludi, A. The Crystal Structure of Prussian Blue: $Fe_4[Fe(CN)_6]_3.xH_2O$. *Inorg. Chem.* **16,** 2704–2710 (1977).

7.   Constable, E. C. & Housecroft, C. E. Coordination Chemistry: the Scientific Legacy of Alfred Werner. *Chem. Soc. Rev.* **42,** 1429–1439 (2013).

8.   Allison, S. A. & Barrer, R. M. Sorption in the β-Phases of Transition Metal(II) tetra-(4-methylpyridine) thiocyanates and Related Compounds. *J. Chem. Soc. A* **0,** 1717–1723 (1969).

9.   Hofmann, K. A. & Küspert, F. Verbindungen von Kohlenwasserstoffen mit Metallsalzen. *Zeitschrift für Anorg. Chemie* **15,** 204–207 (1897).

10.   Rayner, J. H. & Powell, H. M. 67. Structure of Molecular Compounds. Part X. Crystal Structure of the Compound of Benzene with an Ammonia-Nickel Cyanide Complex. *J. Chem. Soc.* **0,** 319–328 (1952).

11.   Iwamoto, T., Miyoshi, T., Miyamoto, T., Sasaki, Y. & Fujiwara, S. The Metal Ammine Cyanide Aromatics Clathrates. I. The Preparation and Stoichiometry of the Diamminemetal(II) Tetracyano-niccolate(II) Dibenzene and Dianiline. *Bull. Chem. Soc. Jpn.* **40,** 1174–1178 (1967).

12.   Iwamoto, T., Nakano, T., Morita, M., Miyoshi, T., Miyamoto, T. & Sasaki, Y. The Hofman-Type Clathrate: $M(NH_3)_2M'(CN)_4$. 2G. *Inorg. Chim. Acta* **2,** 313–316 (1968).

13.   Miyoshi, T., Iwamoto, T. & Sasaki, Y. The Structure of Catena-μ-ethylenediaminecadmium(II) tetracyanoniccolate(II) dibenzene Clathrate: $Cd(en)Ni(CN)_4.2C_6H_6$. *Inorg. Chim. Acta* **6,** 59–64 (1972).

14.   Kinoshita, Y., Matsubara, I. & Saito, Y. The Crystal Structure of Bis(succinonitrilo)copper(I) Nitrate. *Bull. Chem. Soc. Jpn.* **32,** 741–747 (1959).

15.   Kinoshita, Y., Matsubara, I. & Saito, Y. The Crystal Structure of Bis(glutaronitrilo)copper(I) Nitrate. *Bull. Chem. Soc. Jpn.* **32,** 1216–1221 (1959).

16.   Kinoshita, Y., Matsubara, I., Higuchi, T. & Saito, Y. The Crystal Structure of Bis(adiponitrilo)copper(I) Nitrate. *Bull. Chem. Soc. Jpn.* **32,** 1221–1226 (1959).

17.   Hoskins, B. F. & Robson, R. Infinite Polymeric Frameworks Consisting of Three Dimensionally Linked Rod-like Segments. *J. Am. Chem. Soc.* **111,** 5962–5964 (1989).

18.   Hoskins, B. F. & Robson, R. Design and Construction of a New Class of Scaffolding-Like Materials Comprising Infinite Polymeric Frameworks of 3D-Linked Molecular Rods. A Reappraisal of the Zinc Cyanide and Cadmium Cyanide Structures and the Synthesis and

Structure of the Diamond-Rela. *J. Am. Chem. Soc.* **112,** 1546–1554 (1990).

19. Wells, A. F. *Three-Dimensional Nets and Polyhedra*. (John Wiley & Sons, Ltd., 1977).

20. Fujita, M., Kwon, Y. J., Washizu, S. & Ogura, K. Preparation, Clathration Ability, and Catalysis of a Two-Dimensional Square Network Material Composed of Cadmium(II) and 4,4'-Bipyridine. *J. Am. Chem. Soc.* **116,** 1151–1152 (1994).

21. Yaghi, O. M. & Li, H. Hydrothermal Synthesis of a Metal-Organic Framework Containing Large Rectangular Channels. *J. Am. Chem. Soc.* **117,** 10401–10402 (1995).

22. Yaghi, O. M., Li, G. & Li, H. Selective Binding and Removal of Guests in a Microporous Metal–Organic Framework. *Nature* **378,** 703–706 (1995).

23. Kondo, M., Yoshitomi, T., Matsuzaka, H., Kitagawa, S. & Seki, K. Three-Dimensional Framework with Channeling Cavities for Small Molecules: $\{[M_2(4,4'\text{-}bpy)_3(NO_3)_4]\cdot xH_2O\}_n$ (M = Co, Ni, Zn). *Angew. Chem. Int. Ed.* **36,** 1725–1727 (1997).

24. Li, H., Eddaoudi, M., Groy, T. L. & Yaghi, O. M. Establishing Microporosity in Open Metal–Organic Frameworks: Gas Sorption Isotherms for Zn(BDC) (BDC = 1,4-Benzenedicarboxylate). *J. Am. Chem. Soc.* **120,** 8571–8572 (1998).

25. Li, H., Eddaoudi, M., O'Keeffe, M. & Yaghi, O. M. Design and Synthesis of an Exceptionally Stable and Highly Porous Metal-Organic Framework. *Nature* **402,** 276–279 (1999).

26. Brunauer, S., Emmett, P. H. & Teller, E. Adsorption of Gases in Multimolecular Layers. *J. Am. Chem. Soc.* **60,** 309–319 (1938).

27. Eddaoudi, M., Moler, D. B., Li, H., Chen, B., Reineke, T. M., O'Keeffe, M. & Yaghi, O. M. Modular Chemistry: Secondary Building Units as a Basis for the Design of Highly Porous and Robust Metal–Organic Carboxylate Frameworks. *Acc. Chem. Res.* **34,** 319–330 (2001).

28. O'Keeffe, M. & Yaghi, O. M. Deconstructing the Crystal Structures of Metal–Organic Frameworks and Related Materials into Their Underlying Nets. *Chem. Rev.* **112,** 675–702 (2012).

29. Li, M., Li, D., O'Keeffe, M. & Yaghi, O. M. Topological Analysis of Metal–Organic Frameworks with Polytopic Linkers and/or Multiple Building Units and the Minimal Transitivity Principle. *Chem. Rev.* **114,** 1343–1370 (2014).

30. Eddaoudi, M., Kim, J., Rosi, N., Vodak, D., Wachter, J., O'Keeffe, M. & Yaghi, O. M. Systematic Design of Pore Size and Functionality in Isoreticular MOFs and Their Application in Methane Storage. *Science* **295,** 469–472 (2002).

31. Farha, O. K., Eryazici, I., Jeong, N. C., Hauser, B. G., Wilmer, C. E., Sarjeant, A. A., Snurr, R. Q., Nguyen, S. T., Yazaydın, A. Ö. & Hupp, J. T. Metal–Organic Framework Materials with Ultrahigh Surface Areas: Is the Sky the Limit? *J. Am. Chem. Soc.* **134,** 15016–15021 (2012).

32. Furukawa, H., Cordova, K. E., O'Keeffe, M. & Yaghi, O. M. The Chemistry and Applications of Metal-Organic Frameworks. *Science* **341,** 974–987 (2013).

33. Murray, L. J., Dinca, M. & Long, J. R. Hydrogen Storage in Metal-Organic Frameworks. *Chem. Soc. Rev.* **38,** 1294–1314 (2009).

34. Suh, M. P., Park, H. J., Prasad, T. K. & Lim, D.-W. Hydrogen Storage in Metal–Organic Frameworks. *Chem. Rev.* **112,** 782–835 (2012).

35. Peng, Y., Krungleviciute, V., Eryazici, I., Hupp, J. T., Farha, O. K. & Yildirim, T. Methane Storage in Metal–Organic Frameworks: Current Records, Surprise Findings, and Challenges. *J. Am. Chem. Soc.* **135,** 11887–11894 (2013).

36.   He, Y., Zhou, W., Qian, G. & Chen, B. Methane Storage in Metal-Organic Frameworks. *Chem. Soc. Rev.* **43,** 5657–5678 (2014).

37.   Mason, J. A., Oktawiec, J., Taylor, M. K., Hudson, M. R., Rodriguez, J., Bachman, J. E., Gonzalez, M. I., Cervellino, A., Guagliardi, A., Brown, C. M., Llewellyn, P. L., Masciocchi, N. & Long, J. R. Methane Storage in Flexible Metal–Organic Frameworks with Intrinsic Thermal Management. *Nature* **527,** 357–361 (2015).

38.   Tian, T., Zeng, Z., Vulpe, D., Casco, M. E., Divitini, G., Midgley, P. A., Silvestre-Albero, J., Tan, J.-C., Moghadam, P. Z. & Fairen-Jimenez, D. A Sol–Gel Monolithic Metal–Organic Framework with Enhanced Methane Uptake. *Nat. Mater.* **17,** 174–179 (2017).

39.   Czaja, A. U., Trukhan, N. & Muller, U. Industrial Applications of Metal-Organic Frameworks. *Chem. Soc. Rev.* **38,** 1284–1293 (2009).

40.   Ferey, G., Serre, C., Devic, T., Maurin, G., Jobic, H., Llewellyn, P. L., De Weireld, G., Vimont, A., Daturi, M. & Chang, J.-S. Why Hybrid Porous Solids Capture Greenhouse Gases? *Chem. Soc. Rev.* **40,** 550–562 (2011).

41.   Sumida, K., Rogow, D. L., Mason, J. A., McDonald, T. M., Bloch, E. D., Herm, Z. R., Bae, T.-H. & Long, J. R. Carbon Dioxide Capture in Metal–Organic Frameworks. *Chem. Rev.* **112,** 724–781 (2012).

42.   Yichao, L., Chunglong, K., Qiuju, Z. & Liang, C. Metal-Organic Frameworks for Carbon Dioxide Capture and Methane Storage. *Adv. Energy Mater.* **7,** 1601296 (2017).

43.   Li, J.-R., Sculley, J. & Zhou, H.-C. Metal–Organic Frameworks for Separations. *Chem. Rev.* **112,** 869–932 (2012).

44.   Li, B., Wen, H.-M., Zhou, W. & Chen, B. Porous Metal–Organic Frameworks for Gas Storage and Separation: What, How, and Why? *J. Phys. Chem. Lett.* **5,** 3468–3479 (2014).

45.   Kang, Z., Fan, L. & Sun, D. Recent Advances and Challenges of Metal-Organic Framework Membranes for Gas Separation. *J. Mater. Chem. A* **5,** 10073–10091 (2017).

46.   Li, H., Wang, K., Sun, Y., Lollar, C. T., Li, J. & Zhou, H.-C. Recent Advances in Gas Storage and Separation Using Metal–Organic Frameworks. *Mater. Today* **21,** 108–121 (2018).

47.   Lin, R.-B., Xiang, S., Xing, H., Zhou, W. & Chen, B. Exploration of Porous Metal–Organic Frameworks for Gas Separation and Purification. *Coord. Chem. Rev.* (2017). doi:https://doi.org/10.1016/j.ccr.2017.09.027

48.   Zhang, J.-P. & Chen, X.-M. Optimized Acetylene/Carbon Dioxide Sorption in a Dynamic Porous Crystal. *J. Am. Chem. Soc.* **131,** 5516–5521 (2009).

49.   Horcajada, P., Serre, C., Vallet-Regí, M., Sebban, M., Taulelle, F. & Férey, G. Metal–Organic Frameworks as Efficient Materials for Drug Delivery. *Angew. Chem. Int. Ed.* **45,** 5974–5978 (2006).

50.   Peng, S., Bie, B., Sun, Y., Liu, M., Cong, H., Zhou, W., Xia, Y., Tang, H., Deng, H. & Zhou, X. Metal-Organic Frameworks for Precise Inclusion of Single-Stranded DNA and Transfection in Immune Cells. *Nat. Commun.* **9,** 1293 (2018).

51.   Wang, L., Zheng, M. & Xie, Z. Nanoscale Metal-Organic Frameworks for Drug Delivery: a Conventional Platform with New Promise. *J. Mater. Chem. B* **6,** 707–717 (2018).

52.   McKinlay, A. C., Morris, R. E., Horcajada, P., Férey, G., Gref, R., Couvreur, P. & Serre, C. BioMOFs: Metal–Organic Frameworks for Biological and Medical Applications. *Angew. Chem. Int. Ed.* **49,** 6260–6266 (2010).

53.   Imaz, I., Rubio-Martinez, M., An, J., Sole-Font, I., Rosi, N. L. & Maspoch, D. Metal-

Biomolecule Frameworks (MBioFs). *Chem. Commun.* **47,** 7287–7302 (2011).

54. Keskin, S. & Kızılel, S. Biomedical Applications of Metal Organic Frameworks. *Ind. Eng. Chem. Res.* **50,** 1799–1812 (2011).

55. Della Rocca, J., Liu, D. & Lin, W. Nanoscale Metal–Organic Frameworks for Biomedical Imaging and Drug Delivery. *Acc. Chem. Res.* **44,** 957–968 (2011).

56. Horcajada, P., Gref, R., Baati, T., Allan, P. K., Maurin, G., Couvreur, P., Férey, G., Morris, R. E. & Serre, C. Metal–Organic Frameworks in Biomedicine. *Chem. Rev.* **112,** 1232–1268 (2012).

57. Chowdhury, M. A. Metal-Organic-Frameworks for Biomedical Applications in Drug Delivery, and as MRI Contrast Agents. *J. Biomed. Mater. Res. Part A* **105,** 1184–1194 (2016).

58. Rojas, S., Devic, T. & Horcajada, P. Metal Organic Frameworks Based on Bioactive Components. *J. Mater. Chem. B* **5,** 2560–2573 (2017).

59. Chen, W. & Wu, C. Synthesis, Functionalization, and Applications of Metal-Organic Frameworks in Biomedicine. *Dalton Trans.* **47,** 2114–2133 (2018).

60. Farrusseng, D., Aguado, S. & Pinel, C. Metal–Organic Frameworks: Opportunities for Catalysis. *Angew. Chem. Int. Ed.* **48,** 7502–7513 (2009).

61. Lee, J., Farha, O. K., Roberts, J., Scheidt, K. A., Nguyen, S. T. & Hupp, J. T. Metal-Organic Framework Materials as Catalysts. *Chem. Soc. Rev.* **38,** 1450–1459 (2009).

62. Skobelev, I. Y., Sorokin, A. B., Kovalenko, K. A., Fedin, V. P. & Kholdeeva, O. A. Solvent-Free Allylic Oxidation of Alkenes with O_2 Mediated by Fe- and Cr-MIL-101. *J. Catal.* **298,** 61–69 (2013).

63. Cirujano, F. G., Llabres i Xamena, F. X. & Corma, A. MOFs as Multifunctional Catalysts: One-Pot Synthesis of Menthol from Citronellal over a Bifunctional MIL-101 Catalyst. *Dalton Trans.* **41,** 4249–4254 (2012).

64. Hwang, Y. K., Hong, D.-Y., Chang, J.-S., Seo, H., Yoon, M., Kim, J., Jhung, S. H., Serre, C. & Férey, G. Selective Sulfoxidation of Aryl Sulfides by Coordinatively Unsaturated Metal Centers in Chromium Carboxylate MIL-101. *Appl. Catal., A* **358,** 249–253 (2009).

65. Corma, A., Garcia, H. & Llabres i. Xamena, F. X. Engineering Metal Organic Frameworks for Heterogeneous Catalysis. *Chem. Rev.* **110,** 4606–4655 (2010).

66. Llabres i Xamena, F. & Gascon, J. *Metal Organic Frameworks as Heterogeneous Catalysts*. (The Royal Society of Chemistry, 2013). doi:10.1039/9781849737586

67. Gascon, J., Corma, A., Kapteijn, F. & Llabrés i Xamena, F. X. Metal Organic Framework Catalysis: Quo vadis? *ACS Catal.* **4,** 361–378 (2014).

68. Liu, J., Chen, L., Cui, H., Zhang, J., Zhang, L. & Su, C.-Y. Applications of Metal-Organic Frameworks in Heterogeneous Supramolecular Catalysis. *Chem. Soc. Rev.* **43,** 6011–6061 (2014).

69. Garcia-Garcia, P., Muller, M. & Corma, A. MOF Catalysis in Relation to Their Homogeneous Counterparts and Conventional Solid Catalysts. *Chem. Sci.* **5,** 2979–3007 (2014).

70. Huang, Y.-B., Liang, J., Wang, X.-S. & Cao, R. Multifunctional Metal-Organic Framework Catalysts: Synergistic Catalysis and Tandem Reactions. *Chem. Soc. Rev.* **46,** 126–157 (2017).

71. Rogge, S. M. J., Bavykina, A., Hajek, J., Garcia, H., Olivos-Suarez, A. I., Sepulveda-

Escribano, A., Vimont, A., Clet, G., Bazin, P., Kapteijn, F., Daturi, M., Ramos-Fernandez, E. V, Llabres i Xamena, F. X., Van Speybroeck, V. & Gascon, J. Metal-Organic and Covalent Organic Frameworks as Single-Site Catalysts. *Chem. Soc. Rev.* **46,** 3134–3184 (2017).

72. Vermoortele, F., Ameloot, R., Alaerts, L., Matthessen, R., Carlier, B., Fernandez, E. V. R., Gascon, J., Kapteijn, F. & De Vos, D. E. Tuning the Catalytic Performance of Metal-Organic Frameworks in Fine Chemistry by Active Site Engineering. *J. Mater. Chem.* **22,** 10313–10321 (2012).

73. Lustig, W. P., Mukherjee, S., Rudd, N. D., Desai, A. V, Li, J. & Ghosh, S. K. Metal-Organic Frameworks: Functional Luminescent and Photonic Materials for Sensing Applications. *Chem. Soc. Rev.* **46,** 3242–3285 (2017).

74. Lantao, L., Yanli, Z., Shuang, L. & Maotian, X. The Applications of Metal–Organic Frameworks in Electrochemical Sensors. *ChemElectroChem* **5,** 6–19 (2017).

75. Kurmoo, M. Magnetic Metal-Organic Frameworks. *Chem. Soc. Rev.* **38,** 1353–1379 (2009).

76. Shimizu, G. K. H., Taylor, J. M. & Kim, S. Proton Conduction with Metal-Organic Frameworks. *Science* **341,** 354–355 (2013).

77. Shalini, S., Dhavale, V. M., Eldho, K. M., Kurungot, S., Ajithkumar, T. G. & Vaidhyanathan, R. 1000-Fold Enhancement in Proton Conductivity of a MOF Using Post-Synthetically Anchored Proton Transporters. *Sci. Rep.* **6,** 32489 (2016).

78. Mingabudinova, L. R., Vinogradov, V. V, Milichko, V. A., Hey-Hawkins, E. & Vinogradov, A. V. Metal-Organic Frameworks as Competitive Materials for Non-Linear Optics. *Chem. Soc. Rev.* **45,** 5408–5431 (2016).

79. Stavila, V., Talin, A. A. & Allendorf, M. D. MOF-Based Electronic and Opto-Electronic Devices. *Chem. Soc. Rev.* **43,** 5994–6010 (2014).

80. Coudert, F.-X. Responsive Metal–Organic Frameworks and Framework Materials: Under Pressure, Taking the Heat, in the Spotlight, with Friends. *Chem. Mater.* **27,** 1905–1916 (2015).

81. Nagarkar, S. S., Desai, A. V. & Ghosh, S. K. Stimulus-Responsive Metal–Organic Frameworks. *Chem. – Asian J.* **9,** 2358–2376 (2014).

82. Chapman, K. W., Sava, D. F., Halder, G. J., Chupas, P. J. & Nenoff, T. M. Trapping Guests within a Nanoporous Metal–Organic Framework through Pressure-Induced Amorphization. *J. Am. Chem. Soc.* **133,** 18583–18585 (2011).

83. Tan, J. C. & Cheetham, A. K. Mechanical Properties of Hybrid Inorganic-Organic Framework Materials: Establishing Fundamental Structure-Property Relationships. *Chem. Soc. Rev.* **40,** 1059–1080 (2011).

84. Liu, Y., Her, J.-H., Dailly, A., Ramirez-Cuesta, A. J., Neumann, D. A. & Brown, C. M. Reversible Structural Transition in MIL-53 with Large Temperature Hysteresis. *J. Am. Chem. Soc.* **130,** 11813–11818 (2008).

85. Deshpande, R. K., Minnaar, J. L. & Telfer, S. G. Thermolabile Groups in Metal–Organic Frameworks: Suppression of Network Interpenetration, Post-Synthetic Cavity Expansion, and Protection of Reactive Functional Groups. *Angew. Chem. Int. Ed.* **49,** 4598–4602 (2010).

86. Razavi, S. A. A., Masoomi, M. Y. & Morsali, A. Stimuli-Responsive Metal–Organic Framework (MOF) with Chemo-Switchable Properties for Colorimetric Detection of $CHCl_3$. *Chem. – Eur. J.* **23,** 12559–12564 (2017).

87. Chen, W.-H., Yu, X., Cecconello, A., Sohn, Y. S., Nechushtai, R. & Willner, I. Stimuli-Responsive Nucleic Acid-Functionalized Metal-Organic Framework Nanoparticles Using pH- and Metal-Ion-Dependent DNAzymes as Locks. *Chem. Sci.* **8,** 5769–5780 (2017).

88. Modrow, A., Zargarani, D., Herges, R. & Stock, N. The First Porous MOF with Photoswitchable Linker Molecules. *Dalton Trans.* **40,** 4217–4222 (2011).

89. Brown, J. W., Henderson, B. L., Kiesz, M. D., Whalley, A. C., Morris, W., Grunder, S., Deng, H., Furukawa, H., Zink, J. I., Stoddart, J. F. & Yaghi, O. M. Photophysical Pore Control in an Azobenzene-Containing Metal-Organic Framework. *Chem. Sci.* **4,** 2858–2864 (2013).

90. Dan-Hardi, M., Serre, C., Frot, T., Rozes, L., Maurin, G., Sanchez, C. & Férey, G. A New Photoactive Crystalline Highly Porous Titanium(IV) Dicarboxylate. *J. Am. Chem. Soc.* **131,** 10857–10859 (2009).

91. Yu, X., Wang, L. & Cohen, S. M. Photocatalytic Metal-Organic Frameworks for Organic Transformations. *CrystEngComm* **19,** 4126–4136 (2017).

92. Dengrong, S., Yanghe, F., Wenjun, L., Lin, Y., Dengke, W., Lin, Y., Xianzhi, F. & Zhaohui, L. Studies on Photocatalytic CO_2 Reduction over NH_2-Uio-66(Zr) and Its Derivatives: Towards a Better Understanding of Photocatalysis on Metal–Organic Frameworks. *Chem. – Eur. J.* **19,** 14279–14285 (2013).

93. Wang, D., Huang, R., Liu, W., Sun, D. & Li, Z. Fe-Based MOFs for Photocatalytic CO_2 Reduction: Role of Coordination Unsaturated Sites and Dual Excitation Pathways. *ACS Catal.* **4,** 4254–4260 (2014).

94. Meyer, K., Ranocchiari, M. & van Bokhoven, J. A. Metal Organic Frameworks for Photo-Catalytic Water Splitting. *Energy Environ. Sci.* **8,** 1923–1937 (2015).

95. Wang, W., Xu, X., Zhou, W. & Shao, Z. Recent Progress in Metal-Organic Frameworks for Applications in Electrocatalytic and Photocatalytic Water Splitting. *Adv. Sci.* **4,** 1600371 (2017).

96. Zhang, T. & Lin, W. Metal-Organic Frameworks for Artificial Photosynthesis and Photocatalysis. *Chem. Soc. Rev.* **43,** 5982–5993 (2014).

97. Nasalevich, M. A., Goesten, M. G., Savenije, T. J., Kapteijn, F. & Gascon, J. Enhancing Optical Absorption of Metal-Organic Frameworks for Improved Visible Light Photocatalysis. *Chem. Commun.* **49,** 10575–10577 (2013).

98. Chen, Y., Wang, D., Deng, X. & Li, Z. Metal-Organic Frameworks (MOFs) for Photocatalytic CO2 Reduction. *Catal. Sci. Technol.* **7,** 4893–4904 (2017).

99. Michel, F. Hydrogenases: Hydrogen-Activating Enzymes. *ChemBioChem* **3,** 153–160 (2002).

100. Tard, C. & Pickett, C. J. Structural and Functional Analogues of the Active Sites of the [Fe]-, [NiFe]-, and [FeFe]-Hydrogenases. *Chem. Rev.* **109,** 2245–2274 (2009).

101. Pullen, S., Fei, H., Orthaber, A., Cohen, S. M. & Ott, S. Enhanced Photochemical Hydrogen Production by a Molecular Diiron Catalyst Incorporated into a Metal–Organic Framework. *J. Am. Chem. Soc.* **135,** 16997–17003 (2013).

102. Nasalevich, M. A., Becker, R., Ramos-Fernandez, E. V, Castellanos, S., Veber, S. L., Fedin, M. V, Kapteijn, F., Reek, J. N. H., van der Vlugt, J. I. & Gascon, J. Co@NH_2-MIL-125(Ti): Cobaloxime-Derived Metal-Organic Framework-Based Composite for Light-Driven H2 Production. *Energy Environ. Sci.* **8,** 364–375 (2015).

103. Hou, C.-C., Li, T.-T., Cao, S., Chen, Y. & Fu, W.-F. Incorporation of a [Ru(dcbpy)(bpy)$_2$]$^{2+}$

Photosensitizer and a Pt(dcbpy)Cl$_2$ Catalyst into Metal-Organic Frameworks for Photocatalytic Hydrogen Evolution from Aqueous Solution. *J. Mater. Chem. A* **3,** 10386–10394 (2015).

104. Kim, D., Whang, D. R. & Park, S. Y. Self-Healing of Molecular Catalyst and Photosensitizer on Metal–Organic Framework: Robust Molecular System for Photocatalytic H$_2$ Evolution from Water. *J. Am. Chem. Soc.* **138,** 8698–8701 (2016).

105. Yang, S., Fan, D., Hu, W., Pattengale, B., Liu, C., Zhang, X. & Huang, J. Elucidating Charge Separation Dynamics in a Hybrid Metal–Organic Framework Photocatalyst for Light-Driven H$_2$ Evolution. *J. Phys. Chem. C* **122,** 3305–3311 (2018).

106. Park, J., Yuan, D., Pham, K. T., Li, J.-R., Yakovenko, A. & Zhou, H.-C. Reversible Alteration of CO$_2$ Adsorption upon Photochemical or Thermal Treatment in a Metal–Organic Framework. *J. Am. Chem. Soc.* **134,** 99–102 (2012).

107. Yanai, N., Uemura, T., Inoue, M., Matsuda, R., Fukushima, T., Tsujimoto, M., Isoda, S. & Kitagawa, S. Guest-to-Host Transmission of Structural Changes for Stimuli-Responsive Adsorption Property. *J. Am. Chem. Soc.* **134,** 4501–4504 (2012).

108. Lyndon, R., Konstas, K., Thornton, A. W., Seeber, A. J., Ladewig, B. P. & Hill, M. R. Visible Light-Triggered Capture and Release of CO$_2$ from Stable Metal Organic Frameworks. *Chem. Mater.* **27,** 7882–7888 (2015).

109. Murad, F. Discovery of Some of the Biological Effects of Nitric Oxide and its Role in Cell Signaling. *Biosci. Rep.* **24,** 452–474 (2004).

110. Fukumura, D., Kashiwagi, S. & Jain, R. K. The Role of Nitric Oxide in Tumour Progression. *Nat. Rev. Cancer* **6,** 521 (2006).

111. Diring, S., Wang, D. O., Kim, C., Kondo, M., Chen, Y., Kitagawa, S., Kamei, K. & Furukawa, S. Localized Cell Stimulation by Nitric Oxide Using a Photoactive Porous Coordination Polymer Platform. *Nat. Commun.* **4,** 2684 (2013).

112. Kim, C., Diring, S., Furukawa, S. & Kitagawa, S. Light-Induced Nitric Oxide Release from Physiologically Stable Porous Coordination Polymers. *Dalton Trans.* **44,** 15324–15333 (2015).

113. Diring, S., Carne-Sanchez, A., Zhang, J., Ikemura, S., Kim, C., Inaba, H., Kitagawa, S. & Furukawa, S. Light Responsive Metal-Organic Frameworks as Controllable CO-Releasing Cell Culture Substrates. *Chem. Sci.* **8,** 2381–2386 (2017).

114. Raghavender, M., Rika, T., Lin, K. L. & Vittal, J. J. Assembly of 3D Coordination Polymers from 2D Sheets by [2+2] Cycloaddition Reaction. *Chem. – Eur. J.* **20,** 1231–1236 (2014).

115. Lee, J. H., Park, S., Jeoung, S. & Moon, H. R. Single-Crystal-to-Single-Crystal Transformation of a Coordination Polymer from 2D to 3D by [2 + 2] Photodimerization Assisted by a Coexisting Flexible Ligand. *CrystEngComm* **19,** 3719–3722 (2017).

116. Park, I.-H., Mulijanto, C. E., Lee, H.-H., Kang, Y., Lee, E., Chanthapally, A., Lee, S. S. & Vittal, J. J. Influence of Interpenetration in Diamondoid Metal–Organic Frameworks on the Photoreactivity and Sensing Properties. *Cryst. Growth Des.* **16,** 2504–2508 (2016).

117. In-Hyeok, P., Anjana, C., Zhenjie, Z., Sung, L. S., Zaworotko, M. J. & Vittal, J. J. Metal–Organic Organopolymeric Hybrid Framework by Reversible [2+2] Cycloaddition Reaction. *Angew. Chem. Int. Ed.* **53,** 414–419 (2013).

118. Foo, M. L., Matsuda, R., Hijikata, Y., Krishna, R., Sato, H., Horike, S., Hori, A., Duan, J., Sato, Y., Kubota, Y., Takata, M. & Kitagawa, S. An Adsorbate Discriminatory Gate Effect in a Flexible Porous Coordination Polymer for Selective Adsorption of CO$_2$ over C$_2$H$_2$. *J. Am.*

Chem. Soc. **138,** 3022–3030 (2016).

119. Sato, H., Matsuda, R., Sugimoto, K., Takata, M. & Kitagawa, S. Photoactivation of a Nanoporous Crystal for On-Demand Guest Trapping and Conversion. *Nat. Mater.* **9,** 661–666 (2010).

120. Tanabe, K. K., Allen, A. C. & Cohen, S. M. Photochemical Activation of a Metal–Organic Framework to Reveal Functionality. *Angew. Chem. Int. Ed.* **49,** 9730–9733 (2010).

121. Allen, C. A. & Cohen, S. M. Near-UV Photo-Induced Modification in Isoreticular Metal-Organic Frameworks. *J. Mater. Chem.* **22,** 10188–10194 (2012).

122. Deshpande, R. K., Waterhouse, G. I. N., Jameson, G. B. & Telfer, S. G. Photolabile Protecting Groups in Metal-Organic Frameworks: Preventing Interpenetration and Masking Functional Groups. *Chem. Commun.* **48,** 1574–1576 (2012).

123. Kusaka, S., Matsuda, R. & Kitagawa, S. Generation of Thiyl Radicals in a Zinc(II) Porous Coordination Polymer by Light-Induced Post-Synthetic Deprotection. *Chem. Commun.* **54,** 4782–4785 (2018).

124. Dénès, F., Pichowicz, M., Povie, G. & Renaud, P. Thiyl Radicals in Organic Synthesis. *Chem. Rev.* **114,** 2587–2693 (2014).

Chapter 2

Objectives

The main goal of this Thesis is to **evaluate and exploit the interaction between light and metal-organic frameworks**. More specifically, we aim on evaluating the light-to-heat conversion (photothermal effect) of several subfamilies of MOFs using an external UV-Vis light source, and using this effect to discover new properties/applications of these materials. This objective will involve:

1. Design a setup to assess the photothermal effect of MOFs and test the versatility of this phenomenon with a number of MOFs.

2. Develop an **activation method** based on the photothermal effect. For this, we will need to demonstrate if the generated local heat is sufficient to remove entrapped solvent molecules, thus leading to MOFs with permanent porosity (Figure 1.1).
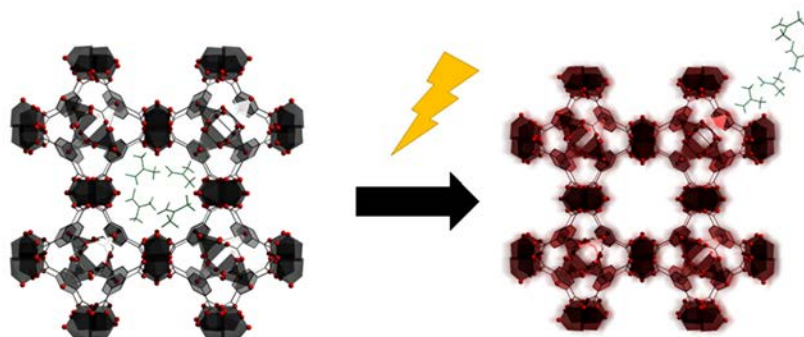
Figure 1.1. Scheme of the photothermal activation process.

3. Implement the photothermal effect in a solvent-free **covalent post-synthetic modification** (CPSM) process. This strategy will consist on exploiting the photothermal effect of the studied MOFs to convert them into local "heaters" for performing organic reactions on their frameworks (Figure 1.2).
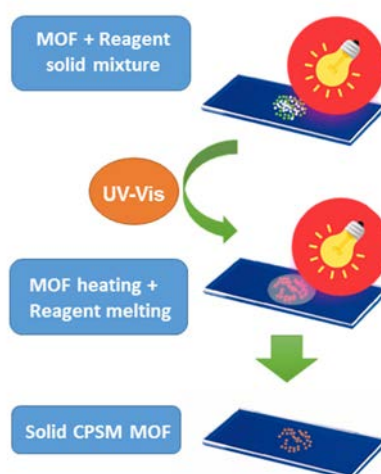
Figure 1.2. Scheme of the UV-Vis mediated CPSM of MOFs.

In a second part of this Thesis, we also aim on starting a new research line based on the design and synthesis of new photoactive MOFs based on metalloligands containing the organic core 2,6-bis(1'-methylbenzimidazolyl)pyridine (MeBIP) or dicarboxylic Ru^{2+}-terpyridine complexes as light-harvesting building blocks. More specifically, the subgoals of this part will be:

1. Synthesis and characterization of the MeBIP-containing and terpyridinic organic ligands. Terpyridinic ligands will be subsequently complexated with Ru^{2+} (Figure 1.3).

2. Develop the synthetic approach to connect these ligands and metalloligands to form MOFs.

3. Assessment of the photothermal properties of the resulting MOFs.
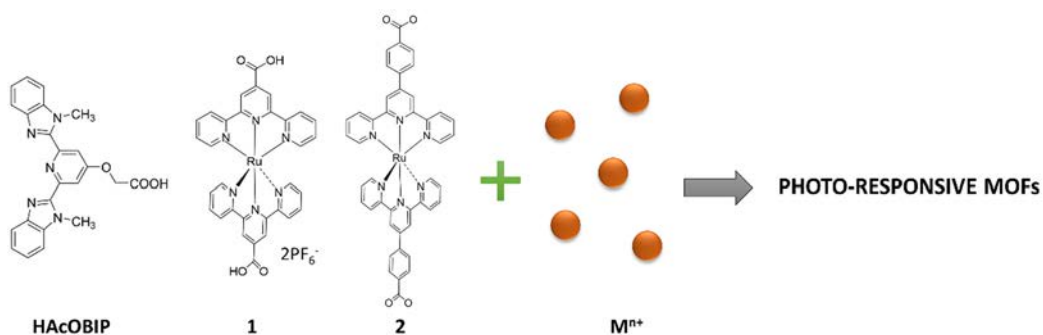
Figure 1.3. Selected ligands and metalloligands used in this Thesis.

Chapter 3

Photothermal activation of MOFs using a UV-Vis light source

In this chapter, a one-step method for activating MOFs based on the photothermal effect induced by directly irradiating them with a UV-Vis lamp is developed. The localized light-to-heat conversion produced in the MOF crystals upon irradiation enables a very fast solvent removal, thereby significantly reducing the activation time to as low as 30 minutes and supressing the need for time-consuming solvent-exchange procedures and vacuum conditions. This approach is successful for a broad range of MOFs, including HKUST-1, UiO-66-NH$_2$, ZIF-67, CPO-27-M (M = Zn, Ni, and Mg), Fe-MIL-101-NH$_2$, and IRMOF-3, all of which exhibit absorption bands in the light emission range. Moreover, this photothermal activation can also be used to activate covalent-organic frameworks (COFs).

1. The photothermal effect

Light is able to interact with matter in different manners depending on the wavelength and the type of matter that encounters. These interactions include transmission, reflexion, refraction, diffraction, scattering and **absorption**. The absorption phenomenon occurs when the frequency of the incoming light matches the frequency of the atoms that constitute the irradiated matter, thereby promoting electronic vibration. These excited electrons collide with the neighbouring atoms converting such vibrational energy into thermal energy. Photothermal science is devoted to the study of the phenomena by which materials, including solids, liquids and gases, absorb radiant energy and convert it into heat (**photothermal effect**) employing a wide range of techniques.[1,2] The radiation exciting the sample can be in the optical range or in other ranges, such as ultraviolet (UV), infrared (IR), microwaves, etc. The initial absorption process might be very selective depending on the nature of the material. For instance, photoexcitation through surface plasmon resonance in nanoparticles allows subsequent heat release. In macroscopic bulk materials, electronic excitation from the ground to the excited states of atoms or molecules, followed by energy loss, leads to material heating. Hereafter, these two photoexcitation phenomena are described and exemplified.

1.1. Surface plasmon resonance-driven photothermal effect

The plasmon-driven photothermal effect is based on the surface plasmon resonance phenomenon. Surface plasmon resonance was first observed in noble metal nanoparticles[3] when the cloud of conduction electrons generated on the surface of such nanoparticles led to a collective coherent oscillation in resonance with the frequency of the applied electromagnetic field (light). This oscillation induces a charge separation between free electrons and the metal core, which in turn exhibits a restoring Coloumb force to make the electrons oscillate back and forth on the particle surface resulting in a dipole oscillation (Figure 1.1a). Absorption of light due to surface plasmon resonance is dependent on the particle size, shape, structure, dielectric properties of the metal and the medium, which affect the electron charge density of the particle surface.[4] By modifying the mentioned parameters, the absorption can be tuned from the visible to the infrared regions (Figure 1.2).[5,6]

Enhancing light absorption also means an increase in the yield of conduction electrons promoted from the ground state to an excited state, known as "hot electrons".[6–8] The energy of the absorbed photon decays both through radiative or nonradiative damping. The radiative damping corresponds to enhanced elastic scattering, while the nonradiative results in a complete loss of coherence to the exciting light field. The temperature of the lattice is elevated

within several picoseconds when the hot electrons and the phonons of the metal lattice are coupled (Figure 1.1b). Then, the energy is transferred to the environment due to the decay of the oscillations in the nanoparticle.[9–12] The dynamics of the heating and cooling of the nanoparticles are extremely fast because of the small volume heated, as it was demonstrated by a gold nanoparticle in water that was thermally equilibrated in few nanoseconds.[13]
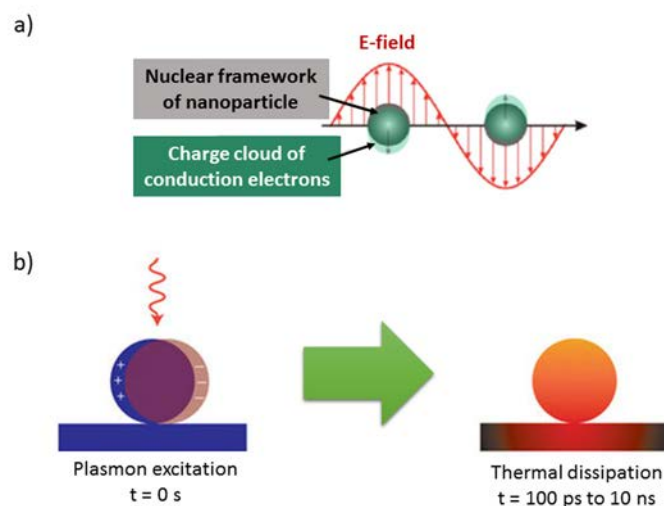
Figure 1.1. a) Scheme showing the interaction of the electric field with an spherical metallic nanoparticle acting as a dipole. b) Time scale of the photothermal effect in nanoparticles. Adapted from references.[6,7]
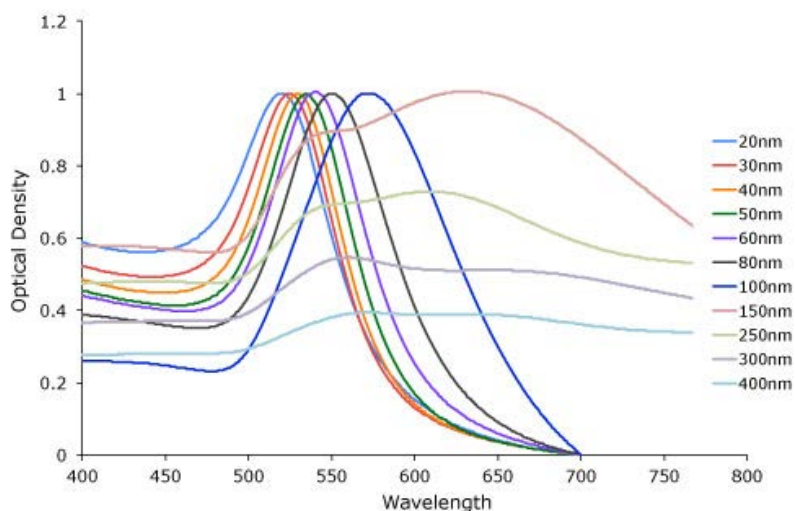
Figure 1.2. Size-depending gold nanoparticles absorption.[14]

Extensive work has been carried out in order to exploit the applications of these photothermal materials (mainly, being noble metal nanoparticles). Some of the most relevant applications include the photothermal therapy for cancer,[15–22] water evaporation,[23–26] sterilization[27] and desalination[28,29] devices, drug delivery,[30] sensing,[31–34] heterogenous catalysis[35] and chemical separation.[36]

1.2. Electron excitation from the valence to the excited state

Although plasmon-driven photothermal effect has proved to be a versatile phenomenon with myriad potential applications, the materials studied in this Thesis behave as macroscopic materials. Therefore, their photoexcitation is based on the electron promotion from the ground to the excited state. This section includes a detailed description of the fundamentals of this effect.

When the energy of an irradiated photon matches the quantum of energy between the valence and excited states of the molecules building a material, an electron is promoted to this state. In the excited state, the electron is not stabilized. Thus, it is subsequently relaxed leading to different phenomena (Figure 1.3). When an electron from an excited vibrational state decays to a vibrational state of lower energy, conversion of vibrational energy excess to thermal energy occurs (Figure 1.4). The generated heat is then released to the surrounding molecules, which permits an increase of the **local temperature**.
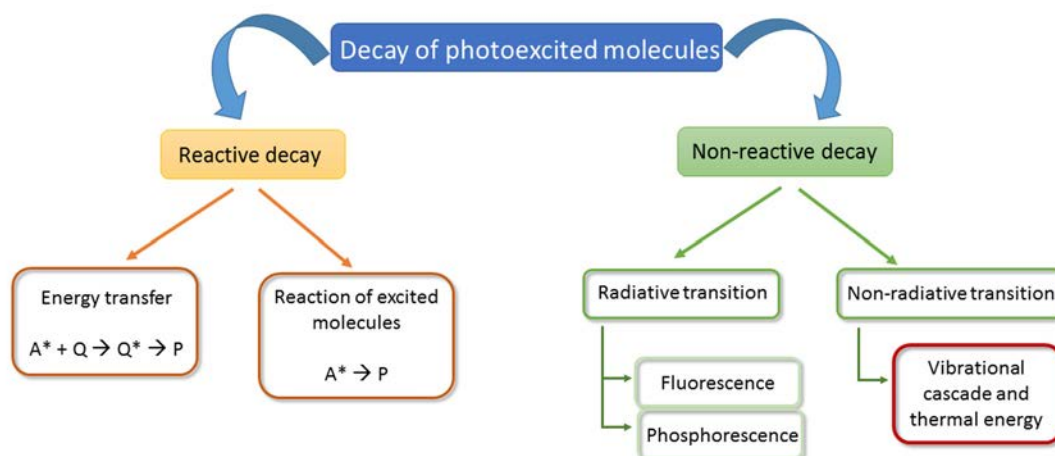
Figure 1.3. Scheme of the possible phenomena occurring in electron decay.

Consequently, the material is homogeneously heated minimizing thermal diffusion. Therefore, it consists on a more efficient heating process than the conventional external heating (*e.g.* heating mantle and oven), where the thermal energy must diffuse from the surroundings of the sample to the material core to reach the set temperature.
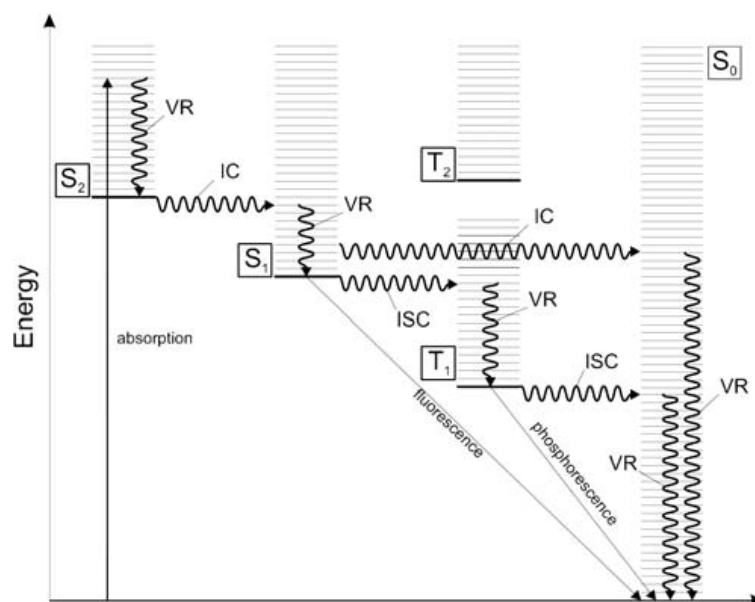
Figure 1.4. Jablonski diagram of the primary photophysical processes. The ordinate indicates increasing energies of the electronic states. On the abscissa, the latter are grouped by spin multiplicity. IC: internal conversion, ISC: intersystem crossing, S_x: singlet states, T_x: triplet states, VR: vibrational relaxation.[37,38]

The main requirement that should be satisfied by a photothermal material is the efficient absorption of optical radiation. An overall high absorbance is essential to reach a high **light-to-heat conversion**. In addition, the performance of these materials is also determined by the reflectance, which should be minimized in order to enhance energy capture and the efficiency of the conversion from light into thermal energy. Among photothermal materials, the carbon-based materials are excellent photothermal candidates because they show high absorbance and are selective solar absorbers. Moreover, they can be easily engineered to attain different size, shape and porosity aggregates. Some carbon-based photothermal materials are amorphous carbon, graphene, carbon nanotubes, graphite and carbon black.[39–48] Among them, carbon black is an excellent photothermal material, as it presents a broadband absorption in the UV-Vis-NIR (250-2500 nm) range (Figure 1.5). This material is widely used in industries to convert sunlight into heat, and it has proved to exhibit high photothermal conversion.[49] Other excellent photothermal materials are semiconductors,[38] conjugated polymers[50–52] and organometallic complexes.[53]
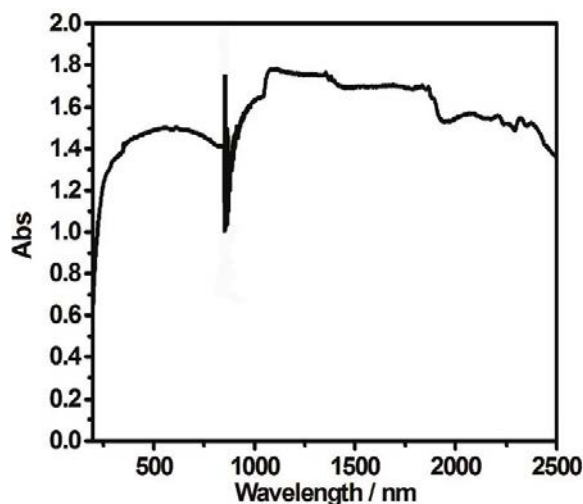
Figure 1.5. Solid-state UV-Vis-NIR absorption spectrum of carbon black powder.[54]

Nowadays, many efforts are devoted to the development of devices able to efficiently harvest solar energy aiming for steam generation, which might afford engaging applications including power generation, desalination, purification of drinking water and sterilization. The two following contributions exemplify the advantages of light-to-heat conversion in water evaporation devices based on graphite and graphene oxide, respectively. Chen and co-workers reported an example of a steam generating device taking advantage of the photothermal effect given by a carbon foam that supports a graphite layer (Figure 1.6).[47] When this porous layer was irradiated using a solar simulator, the carbon-based material was heated until reaching a steady state, allowing water evaporation. In this device, thermal losses are minimized as the thermal energy is localized in the material, allowing a fast temperature increase of the surrounding water molecules. The solar thermal efficiency achieved was up to 85 % by irradiating the sample at 1000 mW·cm^{-2}, which afforded temperatures higher than 100 °C.
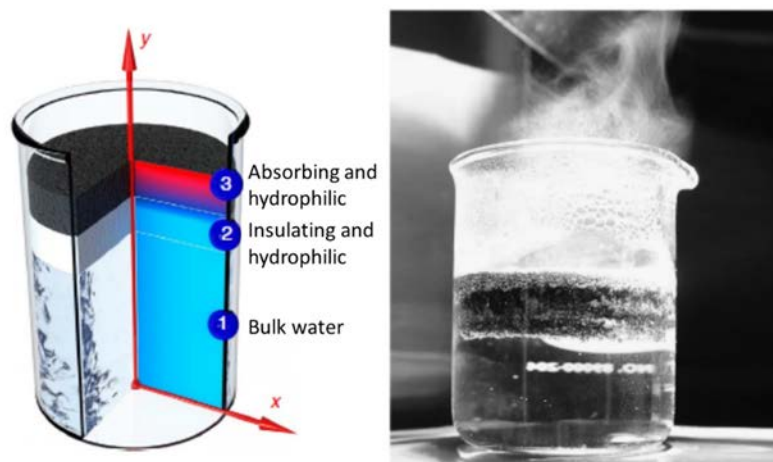
Figure 1.6. Scheme and picture of a carbon-based material exhibiting photothermal behaviour for steam generation.[47]

In a different example, Zhu and co-workers proposed the use of a graphene oxide layer to promote seawater desalination (Figure 1.7).[40] In this device, the light absorber stands over a piece of polystyrene acting as a thermal insulator with the aim to supress heat diffusion in that dimension. Seawater is conducted to the surface of the graphene oxide layer by capillarity using a cellulose coating. One sun (100 mW·cm^{-2}) of light was irradiated over the absorbing material, leading to a maximum temperature of 39 °C after 45 minutes of exposure. The collected water upon evaporation, which lowered its salinity levels 4 orders of magnitude, confirmed the efficiency of this device.
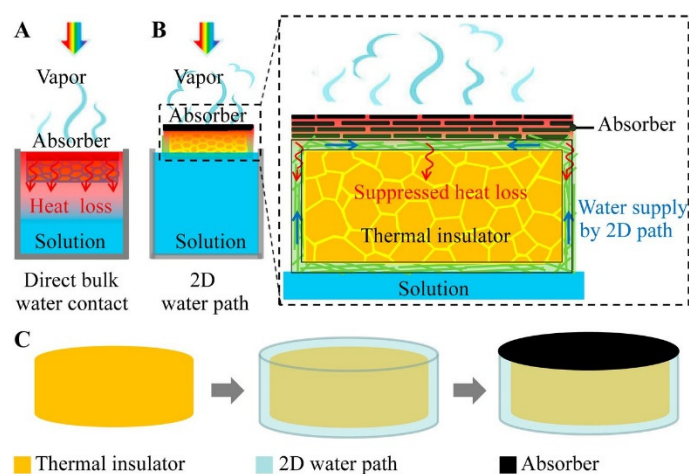
Figure 1.7. Scheme of the desalination device based on the photothermal effect of graphene oxide.[40]

2. Photothermal effect in MOFs

Research about the photothermal effect in MOFs is very recent and, in fact, all the reported studies up to date are based on MOF-based composites. In most of these composites, nanoparticles with light absorption abilities are confined in the pores of MOFs in order to avoid nanoparticle aggregation and grant reusability to the composites. In addition, the importance of the porous matrix strongly relies on the possibility to create synergistic effects between the secondary building units (SBUs) of the MOF and the nanoparticle, and/or the heat generated upon light absorption. Embedding MOF nanocrystals in a polymer matrix that exhibits improved light absorption is another useful approach to make photothermally active materials. It is noteworthy that the photothermal effect in MOF composites has been mainly applied in catalysis and photothermal therapy.

One of the first reports on these MOF-based composites dates from 2016, when Xu and co-workers encapsulated nanoparticles of Cu_7S_4, a semiconductor material, in a ZIF-8 scaffold.[55] When this composite was irradiated using NIR laser irradiation (1450 nm) at 500 mW·cm^{-2}, a mild heating of the suspension was observed ($T_{max} \approx 43$ °C). The generated heat was due to the light irradiation of the nanoparticles, which combined with the acid-base catalytic sites of ZIF-8 (Zn^{2+} and imidazolate groups), created a synergistic catalytic system. In this case, they studied the reaction of a heat-driven cyclocondensation. To do so, they first mixed a suspension of the composite Cu_7S_4@ZIF-8 with the reagents 1,3-cyclohexanedione and 3-methyl-2-butenal. Then, the conversion of the photothermally and thermally (43 °C) driven reactions (97 and 55 %, respectively) was calculated. Remarkably, with these results, it was demonstrated that the composite heated through local light-to-heat conversion was more efficient than the one heated using an external heating source.

Jiang *and* co-workers contributed with another example that consisted on the synthesis of the composite Pd nanocubes@ZIF-8, which allowed the selective hydrogenation of olefins through plasmonic photothermal effect (Figure 2.1).[56] The irradiation of the sample with visible light at 100 mW·cm^{-2} led to a 100 % of conversion in the hydrogenation reaction of 1-hexene in 90 minutes. Furthermore, it was proved that the MOF could act as a sieve, according to the conversion rates of 1-octene (37 %) and cyclohexene (27 %). When using bulkier reagents, such as cyclooctene, conversion was negligible. In all these cases, the reaction yields were lower when an external thermal source was used.

Figure 2.1. Synthesis scheme of the Pd nanocubes@ZIF-8 and the plasmon-driven photothermal effect used in hydrogenation reactions.[56]

The strong extinction coefficient presented by some polymers such as polyaniline (PAN) has also been used to design photothermal MOF-based composites. Jing and co-workers took advantage of the NIR absorption of PAN to make the composite UiO-66@PAN and used it in cancer photothermal therapy (Figure 2.2).[57] This therapy is a local minimally invasive treatment that uses photoabsorbers placed in tumours, which are able to convert light energy into heat. The main goal of the generated heat in the targeted zone, also known as hyperthermia, is to damage irreversibly cancer cells. A temperature increase to 41-47 °C selectively destroys tumours thanks to their lack of heat resistance compared to normal tissue. In this composite, the growth of PAN on the surface of nanoUiO-66 led to a maximum absorbance around 800 nm. Irradiation of a water suspension of the composite (200 µg·mL^{-1}) at 808 nm and an irradiance of 1500 mW·cm^{-2} for 10 minutes provoked a heating of the mixture up to 57.2 °C. *In vitro* assays were performed with murine (CT26) and human (HCT116) colon cancer cells under the same conditions and showed that 70 % of the cells were dead after irradiation. In this study, the *in vivo* assessment in subcutaneous colon cancer of mice was also carried out. By injecting 0.1 mL of UiO-66@PAN (1 mg·mL^{-1}) and irradiating (808 nm and 700 mW·cm^{-2}) the tumour zone, the maximum temperature reached was around 45 °C. This localized increase of temperature confirmed a regression of the tumour after 10 days with a 93 % of tumour suppression efficiency in comparison with the control mice, in which the tumour volume increased.
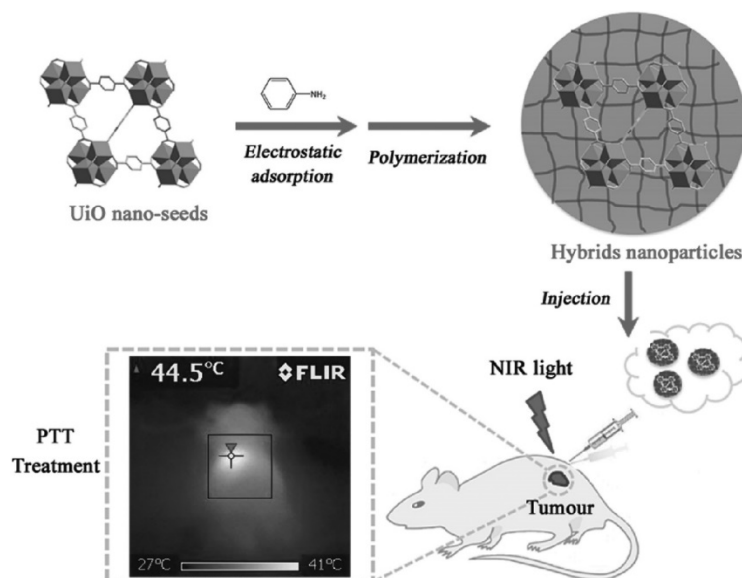
Figure 2.2. Scheme of the synthesis of hybrid nanoparticles based on PAN@UiO-66 for further evaluation of *in vivo* photothermal therapy.[57]

In 2017, Zhu and co-workers prepared a composite consisting of doxorubicin, a model anticancer drug, encapsulated into ZIF-8 and graphene quantum dot nanoparticles (DOX-ZIF-8/GQD).[58] In this composite, graphene quantum dots were the responsible of the photothermal effect once it was irradiated with a NIR laser (808 nm). For example, when a suspension of 20 mg/mL of DOX-ZIF-8/GQD was irradiated at 1500 mW·cm^{-2} for 10 minutes, the temperature increased from 30 to 50 °C. This temperature increase is high enough to be used in cancer thermal treatment, which was confirmed after the *in vitro* assessment of the composite with the breast cancer cell line 4T1. A synergistic effect between the release of doxorubicin and the *in situ* heat generation due to the exposure of NIR for 3 minutes led to 18 % of cell viability.

Even though in the previous examples the encapsulated nanoparticles played the role of light-to-heat converters, a work evidencing photothermal effect by both the nanoparticle and the MOF scaffold was recently published by Jiang and co-workers. These authors synthesised composites based on Pt nanocrystals and the MOF PCN-224(M) (M = Zn, Ni, Co, Mn) (Figure 2.3).[59] When these composites suspended in water were irradiated under a wavelength range higher than 400 nm (visible light) with irradiances lower than 100 mW·cm^{-2}, a synergistic effect was observed between the MOF scaffold and the Pt nanocrystals. Indeed, both components exhibited photothermal effect, leading to the production of singlet oxygen ($^1O_2$). These reactive oxygen species act as oxidants, which were proved useful in the conversion of alcohol to aldehyde. In fact, with the use of MOF PCN-224(Zn), several substituted benzyl and

heteroaromatic alcohols were oxidized with conversions higher than 99 % and a selectivity of 100 %.
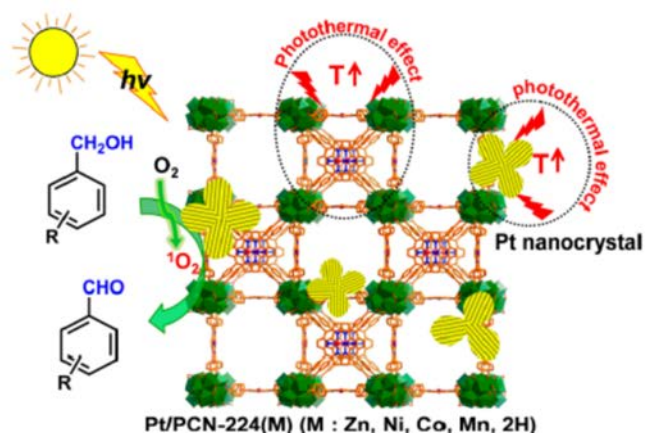
Figure 2.3. Illustration of the PCN-224 composite with Pt nanocrystals and scheme of the photothermal effect and singlet oxygen obtaining.[59]

3. Photothermal effect for MOF activation

Despite the fact that MOFs might be built up from organic molecules and inorganic ions or clusters having light-absorbing abilities, their photothermal effect has not been deeply studied. Herein, we report experimental evidences of this effect in several well-known MOFs and its use to evacuate entrapped solvent molecules, namely **activation process**. The activation of MOFs has been a very important process since the first synthesised porous materials were assessed for gas storage or capture. **Removal of solvent** molecules entrapped in MOF channels is a crucial process prior to access to the porosity of these materials. To date, different processes have been developed to activate MOFs, including thermal activation, solvent exchange, supercritical CO_2 drying and freeze-drying.[60–62]

3.1. Thermal activation

Activation of MOFs by applying heat consists on heating a solid sample of the MOF while applying vacuum for several hours. Some MOFs that can be fully activated using only a thermal activation process are ZIF-8[63] and MIL-101(Cr).[64]

3.2. Solvent Exchange

The harsh conditions of the thermal activation make this process a non-suitable strategy for all synthesised MOFs. For this reason, a prior solvent exchange step is usually required to

exchange the residual guest solvent molecules from the synthesis (*e.g.* DMF and H_2O) for low-boiling point solvents (*e.g.* $CHCl_3$ and CH_2Cl_2). This solvent exchange method is done by soaking the MOF crystals in these solvents. As a consequence, milder activation conditions are required. In addition, the weaker intermolecular interactions of the low-boiling point solvents in comparison to the ones with high-boiling point reduce the surface tension and capillary forces when being evacuated from the pores. This solvent exchange procedure can last from hours to days and solvent should be usually replaced by fresh one from time to time.

Yaghi and co-workers initially introduced the solvent exchange approach. They found that a series of Zn^{2+}-carboxylate MOFs[65,66] (MOF-2,-3,-4,-5) and the later expanded IRMOF subfamily[67] suffered from partially or even full loss of porosity (structural collapse) once thermally activated. To solve this problem, they immersed the MOF crystals in $CHCl_3$ and found that the solvent molecules used in the synthesis were exchanged by $CHCl_3$ molecules, which could then be easily removed under milder conditions. With this method, it was reported an increase of the S_{BET} of the well known IRMOF-3 and IRMOF-16 when solvent exchange was applied instead of the conventional thermal treatment.

In these two MOFs, the original activation method consisted on heating them at 110 °C for 12 hours under vacuum, and the solvent exchange process implied a chloroform solvent exchange for 18 hours and evacuation at room temperature. IRMOF-3 presented S_{BET} values of 10 $m^2 \cdot g^{-1}$ (thermal treatment) and of 1800 $m^2 \cdot g^{-1}$ (solvent exchange). IRMOF-16, which thermal treatment led to a non-porous material, presented a S_{BET} of 470 $m^2 \cdot g^{-1}$ upon solvent exchange.[68]

Some materials (*e.g.* CPO-27-M *a.k.a.* MOF-74-M) need to be solvent-exchanged for long periods in order to favour the removal of the strongly coordinated water molecules in the coordination vacancies of the inorganic cluster. One week of solvent exchange in MeOH is required in the cases of M = Ni^{2+}, Zn^{2+}, Co^{2+} and 12 days for M = Mg^{2+}. In such cases, the combination of the solvent exchange step with a thermal treatment (T > 200 °C) under vacuum is required to ensure the removal of all guest species.[69,70]

The solvent exchange mechanism in the case of HKUST-1 has been stepwise characterized using spectroscopic methods (Figure 3.1). The open metal sites of the as-synthesised MOF (Cu^{2+} paddlewheel) were initially coordinating water molecules. CH_2Cl_2 was used as low-boiling point solvent in order to exchange water molecules. Interestingly, subsequent spontaneous decoordination of CH_2Cl_2 was proved by comparing Raman shifts, demonstrating the route employed to attain evacuated HKUST-1 in very soft conditions.[71]

Figure 3.1. Schematic representation of the solvent exchange procedure in HKUST-1.[71]

3.3. Supercritical CO_2 drying

Supercritical CO_2 drying, which was already used in the synthesis and processing of polymers[72] and preparation of nanoporous organosilicates,[73] is an alternative strategy to improve the stability of MOFs containing large ligands that tend to collapse during the guest removal step. The use of supercritical CO_2 in MOF activation was developed by Hupp's group.[68] This strategy consists on a first solvent exchange step with EtOH (72 hours) and a second with liquid CO_2 (6 hours). At this point, the CO_2 molecules entrapped in the MOF cavities are the responsible to avoid structural disintegration. Afterwards, the temperature and pressure of the sample are set above the CO_2 critical point (31 °C and 73 atm) and left for 1 hour. Finally, the chamber is slowly vented for 18 hours. The key point of this strategy is the supressing of surface tension and capillary forces, which is attained thanks to the supercritical conditions of CO_2 (Figure 3.2).

This method was tested with Zn^{2+}-carboxylate MOFs, from which a comparative study between thermally activated, solvent-exchanged and the supercritical CO_2 dried samples confirmed the advantages of the new method. For instance, the already reported IRMOF-3 and IRMOF-16 were assessed using this method, increasing their S_{BET} from 1800 to 2850 $m^2 \cdot g^{-1}$ and 470 to 1910 $m^2 \cdot g^{-1}$, respectively.[68] With this method, Hupp and co-workers activated two of the MOFs with the highest S_{BET} values in 2012 (*ca*. 7000 $m^2 \cdot g^{-1}$), namely NU-109 and NU-110.[74] Moreover, Kaskel and co-workers used this activation method in a series of robust MOFs (DUT-23,-24,-33,-34) that required this type of activation to fully remove the entrapped solvent molecules.[75]
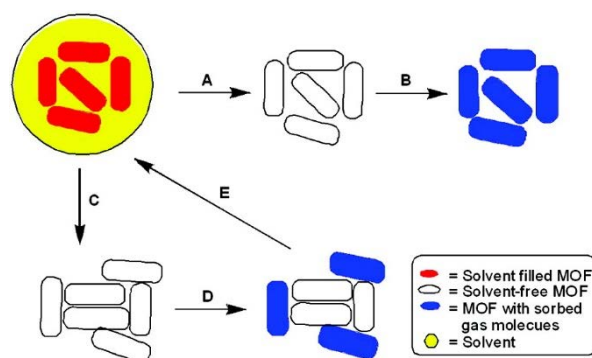
Figure 3.2. Schematic representation of the supercritical CO_2 drying activation (A->B) process in comparison to the thermal activation (C->D) process.[68]

3.4. Freeze-drying

Lin and co-workers first tested the use of the freeze-drying method, already used in the stabilization of biological samples,[76] for MOF activation.[77] They hypothesized that a solid-gas transition (sublimation) of the guest molecules in the framework would avoid the liquid phase surface tension generated when being evacuated. The proof of concept MOFs consisted on two Cu^{2+}-carboxylate MOFs (tetracarboxylic acid ligands), which were previously solvent exchanged using benzene. The solids were evacuated under vacuum at 0 °C for 24 hours, at room temperature for 24 hours more and finally, heated to 60 °C for 16 hours. N_2 adsorption isotherms confirmed an enhanced porosity compared to the conventional thermal activation (60 °C under vacuum overnight), with a S_{BET} increase from 520 to 1560 $m^2 \cdot g^{-1}$ for $[Cu_2(\mathbf{L^1})(H_2O)_2] \cdot 6DEF \cdot 2H_2O$, where L^1 is methanetetra(p-benzoic acid), and from 724 to 1020 $m^2 \cdot g^{-1}$ for $[Cu_2(\mathbf{L^2})(H_2O)_2] \cdot 14DMF \cdot 5H_2O$, where L^2 is methanetetra(biphenyl-p-carboxylic acid). Higher H_2 storage capacities were also reached, almost doubling the thermally activated materials.

4.   Results and discussion

Most of the above-mentioned activation methods are time-consuming, energy demanding, suffer from extensive use of solvent and/or require expensive equipment. Although many efforts have been devoted to green synthesis and industrial scalability MOFs, there is still a lack of research on how to simplify activation methods, as for example, convert them in one-step procedures. As presented in Chapter 2, the goal of this project is firstly to assess the photothermal effect of a series of representative MOF subfamilies and secondly, to observe if the released heat is sufficient to fully activate these materials. In this section, we will introduce a new activation method that shortens time avoiding solvent exchange steps by only irradiating MOF powders with a UV-Vis light source.

4.1.   HKUST-1 as the proof-of-concept MOF

HKUST-1 was selected as the proof of concept MOF to test the feasibility of the UV-Vis activation method. The facile synthesis of this material (Section 5) and the well-standardized activation protocol, made it a proper candidate to compare the reported data with our first results. Indeed, HKUST-1 is usually activated using several solvent-exchange steps (*e.g.* with CH_2Cl_2 or MeOH) followed by a thermal treatment (from 80 to 170 °C) under vacuum. It usually shows S_{BET} values ranging from 1450 to 1800 $m^2 \cdot g^{-1}$.[71,78]

4.1.1.   Photothermal characterization setup

In order to study the photothermal properties of HKUST-1, a setup consisting of the following elements was first designed and constructed as shown in Figure 4.1.

The **UV-Vis light source** was a high-intensity spot lamp without filter (300-650 nm) Bluepoint 4 Ecocure (Hönle UV Technology) with a 1 m long light guide and 1 cm of diameter. It was used at a 100 % power and its irradiance was modified by varying the light guide-to-sample distance. Light filters, which are able to irradiate only the selected region, UV (320-390 nm) and visible (390-500 nm), were applied when necessary. The end of light guide pointed the powder sample directly. Irradiation time was mainly set to 30 minutes. The **IR camera** was a PI 450 (Optris), which was used to record the real-time temperature during the experiment. The working temperature range was 0-250 °C, and data were obtained using the PI Connect software. The **sample amount** was normalized to 100 mg in all photothermal experiments, and it was spread over a quartz slide using a spatula in a circular shape of the highest diameter possible (2.5-3.5 cm). The whole setup was covered to avoid UV light damage while the experiments were running.
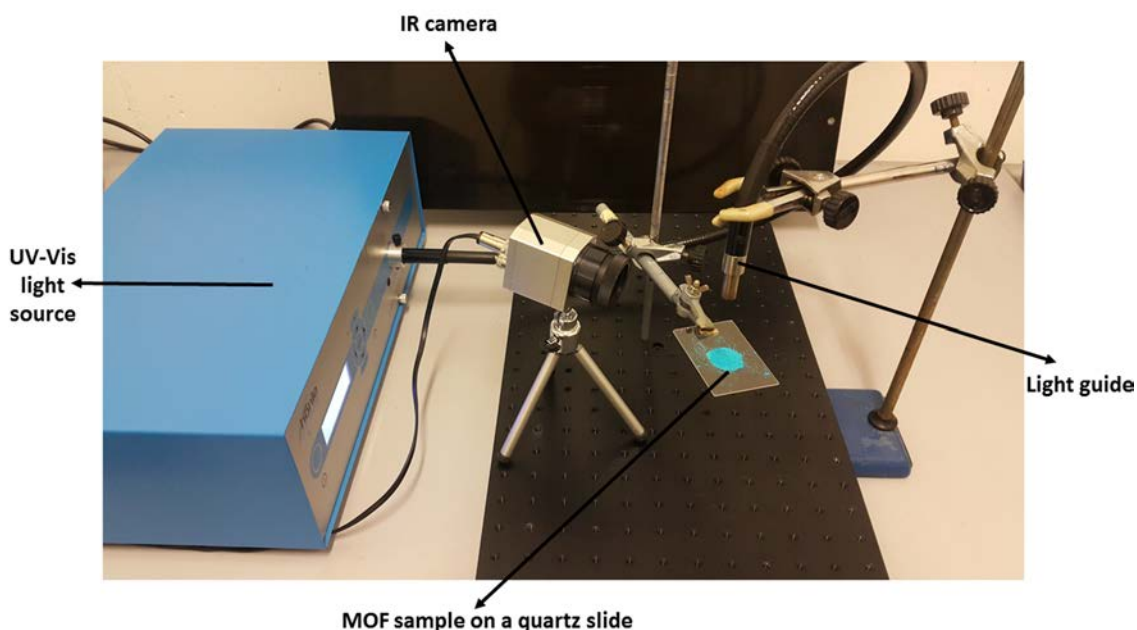
Figure 4.1. Picture of the setup used to study the photothermal properties of MOFs.

4.1.2. Light guide-to-sample distance effect

The distance between the light guide and the sample is a key factor that determines the irradiance (mW·cm^{-2}) received by the MOF sample. For this reason, we initially conducted a study to elucidate the irradiance received by the samples depending on the light guide-to-sample distance. To this end, the power meter (Newport 1918-C) was placed at different distances (3, 4, 5, 6, 7, 8 and 9 cm) from the light source and setting the UV-Vis lamp power to 100 %. The irradiance value was obtained by triplicate for each distance (Table 4.1). As expected, the irradiance readings for each distance followed the inverse-square law of light, which states that intensity of light is proportional to the inverse of the squared distance between the source and the irradiated object (I α 1 / r^2).[79,80] Figure 4.2 confirms the linear fitting (R^2 = 0.99938) of our results with the stated physical law.

Table 4. 1. Summary of the calibration experiments of the distance between the light guide and the sample.

Distance (cm)	Irradiance average ± SD (mW·cm^{-2})
3	2880.0 ± 28.3
4	1520.0 ± 35.4
5	1001.0 ± 19.8
6	680.5 ± 16.3
7	499.5 ± 17.7
8	358.0 ± 11.3
9	265.5 ± 3.5
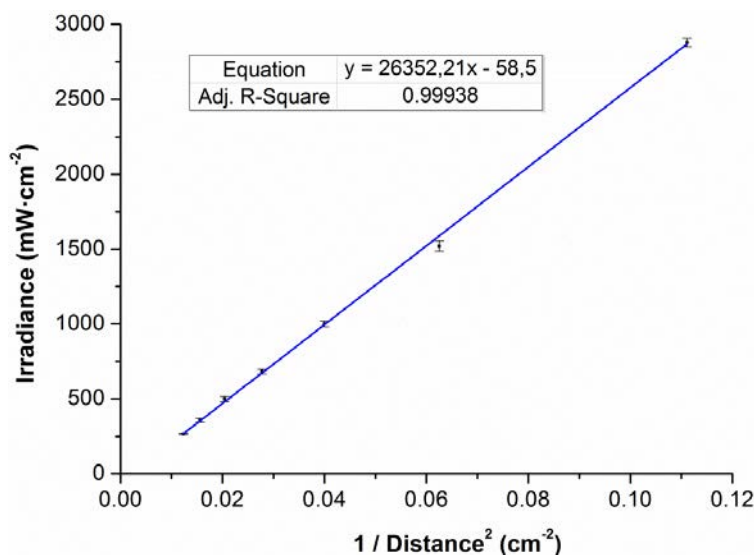
Figure 4.2. Plot of UV-Vis irradiance of the lamp as a function of the inverse squared light guide to sample distance.

4.1.3. Photothermal effect characterization

Then, a blank experiment was performed in order to prove that the sample holder (quartz slide) was not affected by the UV-Vis irradiation and therefore, that is not implying any temperature change in the MOF. For this purpose, the quartz slide was placed at a distance of 7 cm from the light guide (500 mW·cm^{-2}). This irradiance was chosen as an intermediate value from the calibration experiments. The IR camera did not detect any temperature change during the irradiation at 500 mW·cm^{-2} for 30 minutes, confirming that there is not thermal influence due to the sample holder employed.

Thereafter, 100 mg of HKUST-1 spread over a quartz slide forming a thin round layer with the largest possible area was situated at a distance of 7 cm from the light guide (Figure 4.1). UV-Vis light was then applied to the MOF sample for 30 minutes, while the infrared camera recorded the temperature variation of the material. Figure 4.3a shows the temperature *vs*. time diagram that was plotted from the video data.
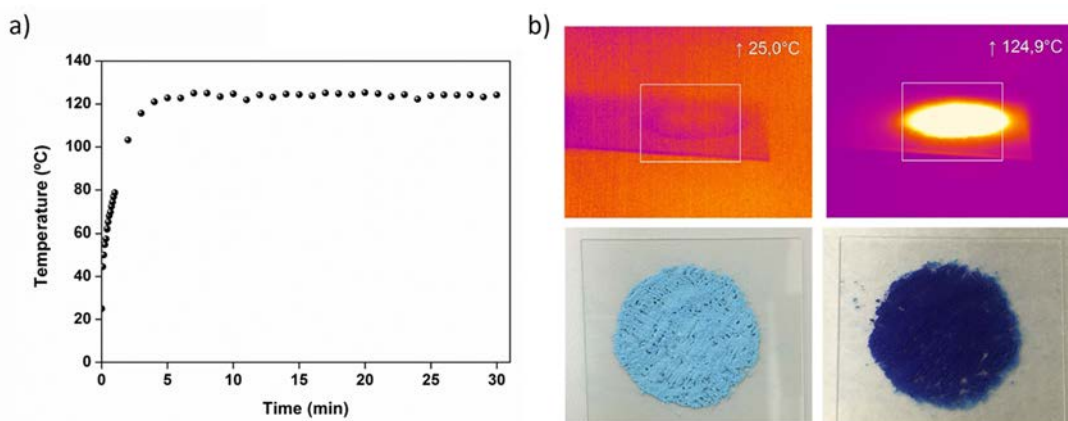
Figure 4.3. a) HKUST-1 photothermal plot at 500 mW·cm^{-2}. b) IR camera snapshots and pictures of HKUST-1 before and after UV-Vis irradiation.

This plot shows that a fast temperature increase (120 °C) was observed during the first 5 minutes. After that, the temperature reached a plateau and it was stabilized for the following 25 minutes. Once the lamp was turned off, a clear colour change from sky blue (as-synthesised) to navy blue (after UV-Vis exposure) was detected (Figure 4.3b). This colour change was attributed to the release of the initially coordinated solvent molecules (H_2O) in the Cu^{2+} paddle-wheel cluster. With these first results and evidences, we evaluated the crystallinity of the HKUST-1 sample after 5 and 30 minutes of irradiation. We concluded that the crystallinity was retained in both cases (Figure 4.4). In order to understand the light absorption abilities of HKUST-1, a solid-state UV-Vis spectrum was recorded showing an absorption band centred at 720 nm, which is attributed to d-d transitions in the Cu^{2+} paddle-wheel clusters of the MOF. This band might be the responsible for the strong photothermal effect (Figure 4.5).
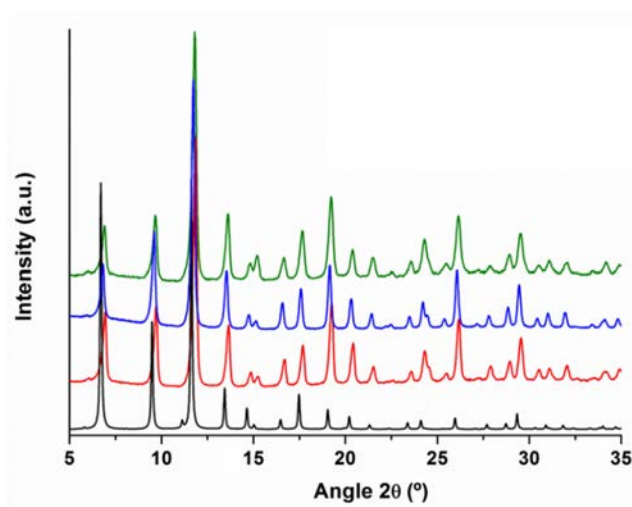
Figure 4.4. XRPD of simulated (black) and as-synthesised (red) HKUST-1, and after 5 minutes (blue) and 30 minutes (green) of irradiation.
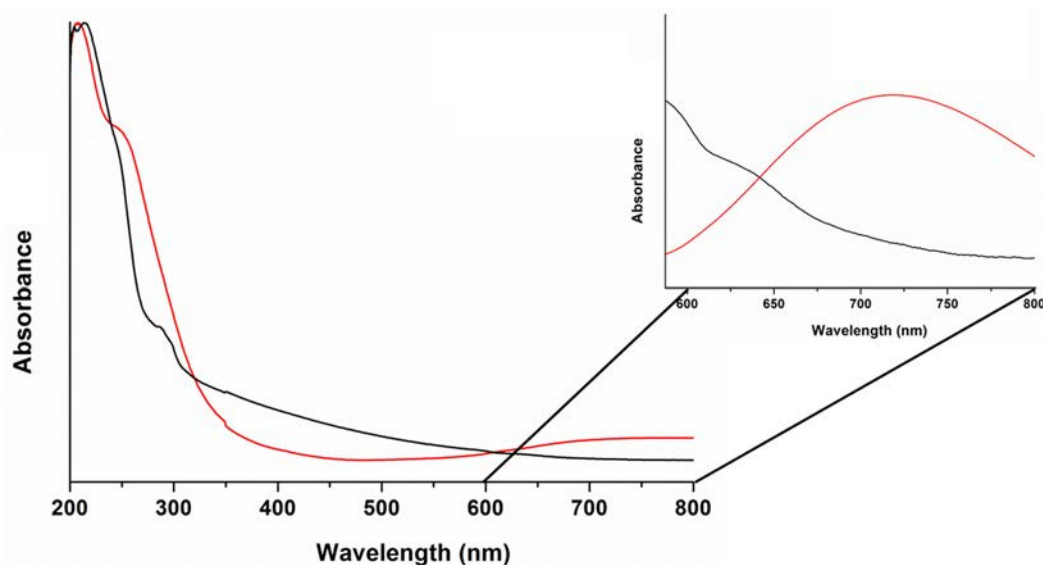
Figure 4.5. Solid-state UV-Vis spectrum of HKUST-1 (red) and BTC ligand (black) in the range of 200-800 nm. Zoom shows the 600-800 nm range of the same spectrum.

The influence of the irradiated light regions on the temperature increase was studied by using filters (Figure 4.6). The default irradiation wavelength range was from 300 to 650 nm, but the use of UV and visible filters allowed to only irradiate at the specific ranges of 320-390 nm and 390-500 nm, respectively. Thereafter, experiments were repeated under the original conditions (500 mW·cm^{-2} for 30 minutes) using these two filters. From these experiments, it was found that the UV light contributed with a temperature rise up to 40 °C, whereas it reached 65 °C with the visible irradiation. Thus, noting that the temperature without filters was of 120 °C, we hypothesize that the region 500-650 nm has the most important influence in the photothermal effect of HKUST-1.
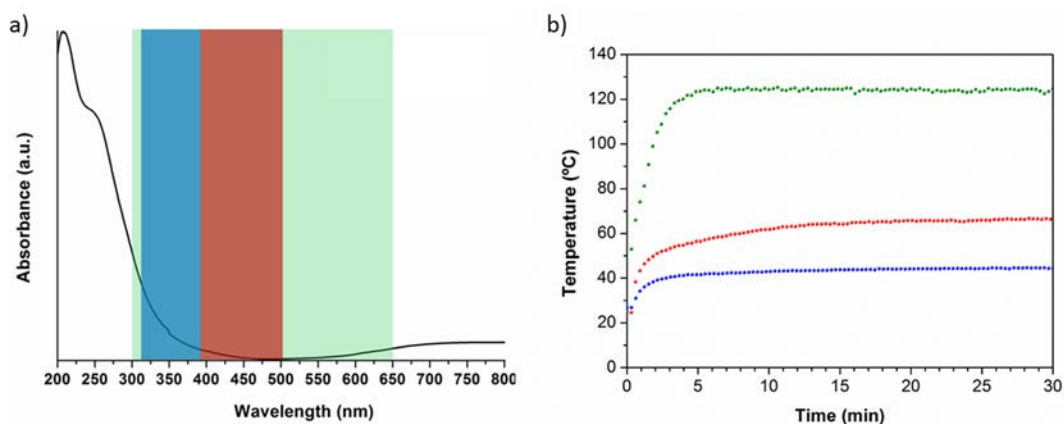
Figure 4.6. Irradiation experiment concerning the different wavelength ranges, without filters (300-650 nm, green), UV filter (320-390 nm, blue) and visible (390-500 nm, red).

4.1.4. Photothermal activation setup

The next step was to prove the efficiency of this localized heating in terms of guest evacuation in HKUST-1. The setup employed to assess the photothermal activation of MOFs consists on a UV-Vis light source connected to a light guide, which is fixed using parafilm in the central neck of a three-neck round-bottom flask containing the MOF sample (Figure 4.7).
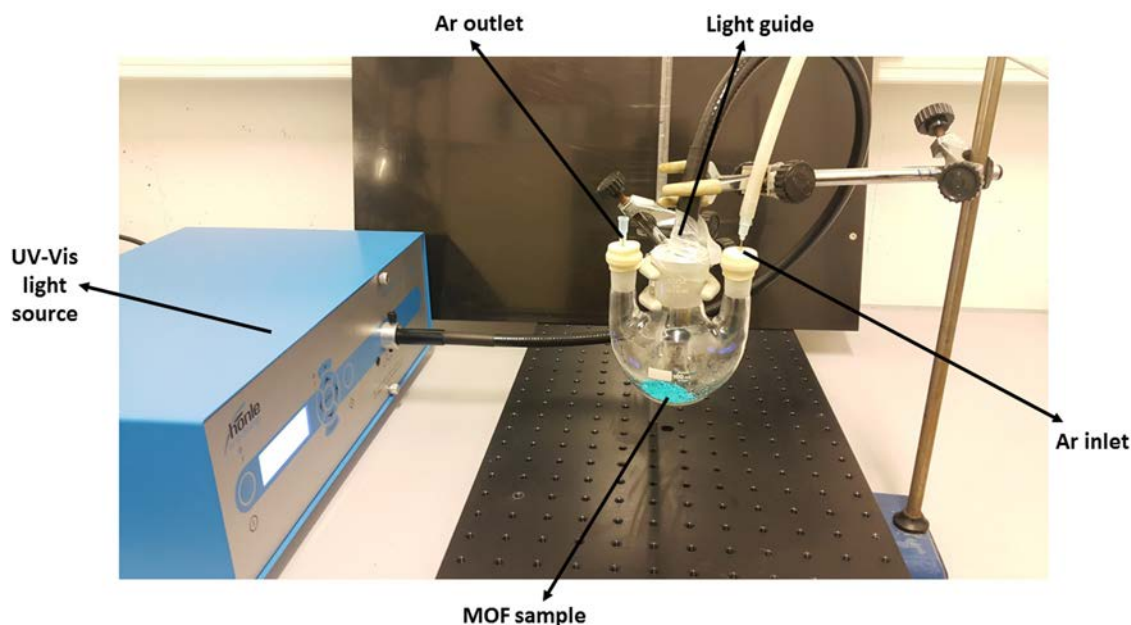
Figure 4.7. Picture showing the setup used for the photothermal activation.

The side necks are then capped using septa, and poked needles serve as inlet and outlet of inert gas flow (8 Normal Liter Per Minute (NL·min^{-1})) in the flask in order to facilitate the removal of evaporated solvent. The MOF temperature during irradiation was considered the same as in the photothermal effect characterization because the sample amount and light guide-to-MOF sample parameters were unmodified. It is important to highlight that this setup was covered to avoid UV light damage while the experiments were running.

4.1.5. HKUST-1 photothermal activation

To prove that HKUST-1 is photothermally activated, 100 mg of MOF were placed in the three-neck round-bottomed flask of the above mentioned setup. The light guide was then set at a distance of 7 cm from the material (500 mW·cm^{-2}), reproducing the conditions of the photothermal characterization. The UV-Vis lamp was turned on, and the sample was irradiated at 100 % intensity for 30 minutes. In order to avoid moisture adsorption once the experiment was finished, the light guide was removed from the central neck, which was rapidly capped using a septum and subsequently introduced in a glovebox. The MOF was weighed in a gas sorption

cell under argon atmosphere and transferred to the gas sorption equipment, where the N_2 isotherm at 77 K was measured for further S_{BET} calculation. The N_2 isotherm (Figure 4.8) revealed a S_{BET} value of 1583 $m^2 \cdot g^{-1}$, which is in the range of the highest S_{BET} reported values for HKUST-1. This result was quite remarkable as HKUST-1 was activated after only 30 minutes of irradiation without the need of any solvent exchange step.
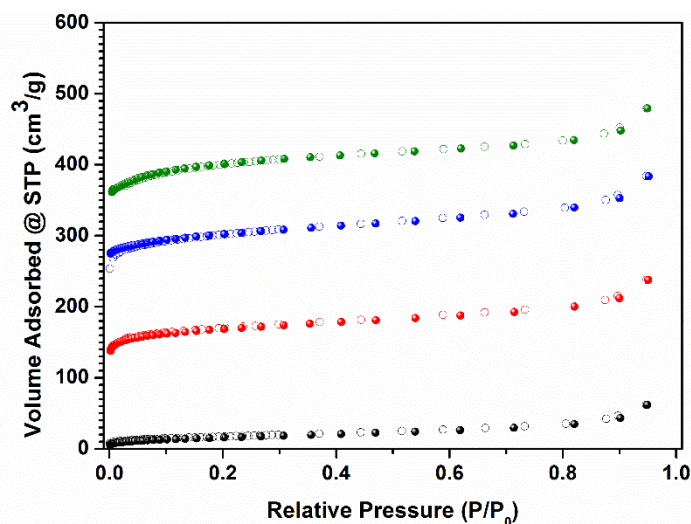
Figure 4.8. N_2 adsorption isotherms for HKUST-1 after 30 minutes of heat treatment (red) and after 5 (blue) and 30 minutes (green) of irradiation at 500 $mW \cdot cm^{-2}$, in comparison to the as-synthesised sample (black).

Irradiation time was shortened to 5 minutes with the goal to test if the required time to activate the sample could be minimized. We selected this time because it is necessary to reach the plateau at *ca*. 120 °C. N_2 sorption isotherm of this activated sample revealed a S_{BET} value of 1208 $m^2 \cdot g^{-1}$. This value is lower than that obtained when activated for 30 minutes, but it is surprisingly high taking into account the low irradiation time. This result evidences that the fast local heating of HKUST-1 achieved through light-to-heat conversion is very effective for evaporating the solvent from the MOF pores.

In order to compare the heating rate of the sample, a conventional thermal treatment was also performed by heating the same amount of MOF sample in a round-bottom flask under vacuum, using an oil bath at 120 °C for 30 minutes. By doing this, the temperature conditions obtained during the UV-Vis irradiation experiment were reproduced using an external heating device and vacuum to favour the solvent molecules removal. The main difference in this experiment relies on the temperature diffusion, which, in this case, goes from the oil in the bath to all the interior of the flask until reaching the entire sample. The S_{BET} value calculated after the N_2 sorption isotherm of the thermally activated sample was of 656 $m^2 \cdot g^{-1}$ (Figure 4.8). This lower

value proves that the localized nature of the UV-Vis irradiation minimizes heat loss and therefore, it becomes a more effective strategy to evacuate guest molecules than the conventional activation method.

Another key parameter that should be also assessed is the light guide-to-sample distance, which determines the light power that the MOF sample receives. Such influence was studied by irradiating HKUST-1 at shorter distances, 5 and 3 cm, resulting in irradiance values of 900 and 2650 mW·cm^{-2}, respectively. This decrease in the distance between light guide and MOF implied a temperature increase of the sample, reaching 187 °C when irradiated at 5 cm (Figure 4.9b) and higher than 250 °C, out of the IR camera range, for the experiment at 3 cm. In the sample irradiated at 900 mW·cm^{-2}, it was found that it remained crystalline and showed a S_{BET} of 1819 m^2·g^{-1}. However, the one irradiated at 2650 mW·cm^{-2} was amorphous and non-porous to N_2 (Figure 4.9a,c). These experiments demonstrated the importance of the light guide-to-sample distance and that HKUST-1 could be fully activated by tuning this parameter, reaching one of the highest S_{BET} values ever reported for this MOF.
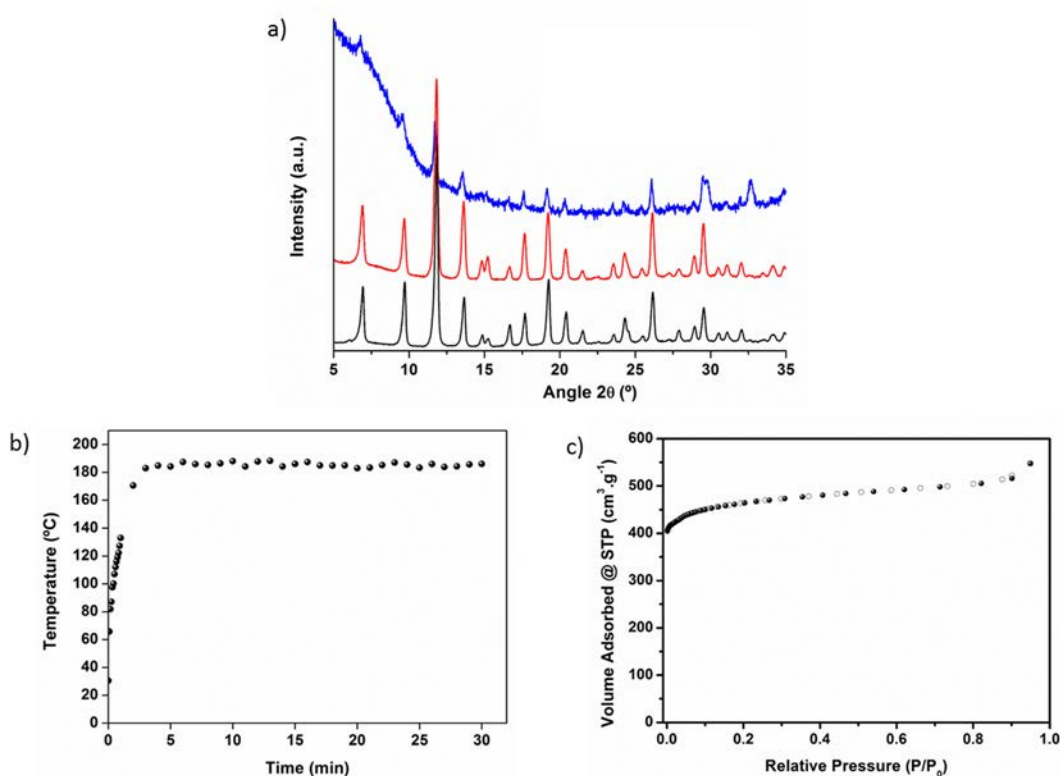
Figure 4.9. a) XRPD patterns of as-synthesised HKUST-1 (black), and after UV-Vis irradiation for 30 minutes at 900 mW·cm^{-2} (red) and at 2650 mW·cm^{-2} (blue). b) Photothermal plot of HKUST-1 irradiated at 900 mW·cm^{-2} for 30 minutes. c) N_2 adsorption isotherm.

To further prove that the photothermal effect occurs purely due to the framework of HKUST-1 and there is no absorbing effect by the entrapped solvent molecules, two continuous

irradiation cycles of 30 minutes each were applied, allowing the sample to cool down between both cycles (Figure 4.10). In the first cycle, HKUST-1 reached a temperature of ≈ 120 °C and the solvent molecules were evacuated (activated HKUST-1). Interestingly, the temperature evolution during the second irradiation cycle matched the first one, also reaching a temperature of ≈ 120 °C. Since there were no solvent molecules in this second irradiation cycle, it was concluded that the photothermal effect is mainly due to the UV-Vis absorption of the MOF.
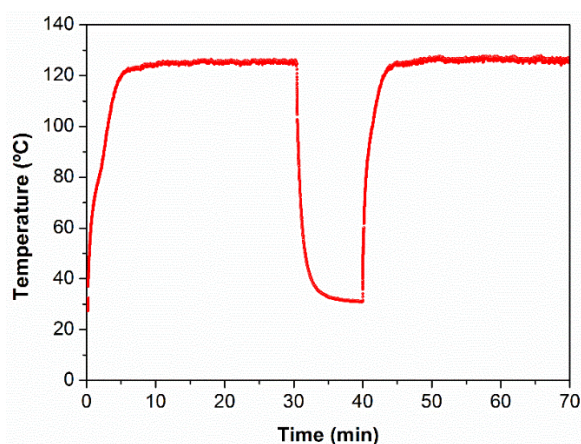
Figure 4.10. Temperature profile as a function of time from the two irradiation experiments of HKUST-1 at 7 cm (500 mW·cm^{-2}) for 30 minutes each.

4.2. Versatility of the photothermal activation method

After testing the light-induced activation of HKUST-1, the scope of this new method was evaluated with a series of the most representative MOF subfamilies, including UiO-66, UiO-66-NH$_2$, ZIF-8, ZIF-67, CPO-27-M (where M is Zn^{2+}, Ni^{2+} and Mg^{2+}), MIL-101-NH$_2$(Fe), and IRMOF-3. The activation method was also studied for a COF, the COF-TAPB-BTCA. The synthetic procedures for these materials are included in Section 5.

4.2.1. Photothermal effect characterization

The same procedure as per HKUST-1 was followed for the new candidates (100 mg of sample for 30 minutes at an irradiance of 500 mW·cm^{-2}). Temperature *vs*. time diagram plots were arranged by subfamily with the aim to extract proper conclusions (Figure 4.11). Figure 4.12 encloses pictures of the samples before and after irradiation and IR pictures of the temperature changes.

UiO-66 and ZIF families showed two marked different behaviours. While UiO-66 and ZIF-8 reached a maximum temperature of 57 and 70 °C, respectively, UiO-66-NH$_2$ and ZIF-67 were heated up to 149 and 127 °C. In order to rationalize these results, solid-state UV-Vis spectra of

the as-synthesised MOFs were recorded (Figure 4.13). Mild-heated MOFs showed no absorption band in the irradiation range (300-650 nm), whereas UiO-66-NH$_2$ had an absorption maximum around 375 nm and ZIF-67 at 600 nm; both wavelengths falling in the UV-Vis lamp irradiation range. These absorption characteristics resulted critical to determine the presence of photothermal effect of the following studied MOFs. The IRMOF-3 and MIL-101-NH$_2$(Fe) candidates also showed an elbow at 350 nm in the UV-Vis spectra and reached temperatures of 119 and 143 °C, respectively. In the case of the CPO-27-M subfamily, the three synthesised compounds showed strong photothermal conversion, CPO-27-Mg (136 °C), CPO-27-Zn (145 °C) and CPO-27-Ni (167 °C), as all these materials presented a significant absorption band centred around 400 nm. The COF example (COF-TAPB-BTCA) had an absorption band at 425 nm and performed a significant light-to-heat conversion, reaching 136 °C. Moreover, the photothermal transduction efficiency (PTE) of all the synthesised materials was calculated (*vide infra*). CPO-27-Ni (94 %) and MIL-101-NH$_2$(Fe) (87 %) were the materials with higher PTE, whereas ZIF-8 (0.3 %) and UiO-66 (5 %) were the ones with lower values (Table 4.2). The crystallinity of all the studied materials was maintained after irradiation experiments, as it was proved by XRPD (Figure 4.14).
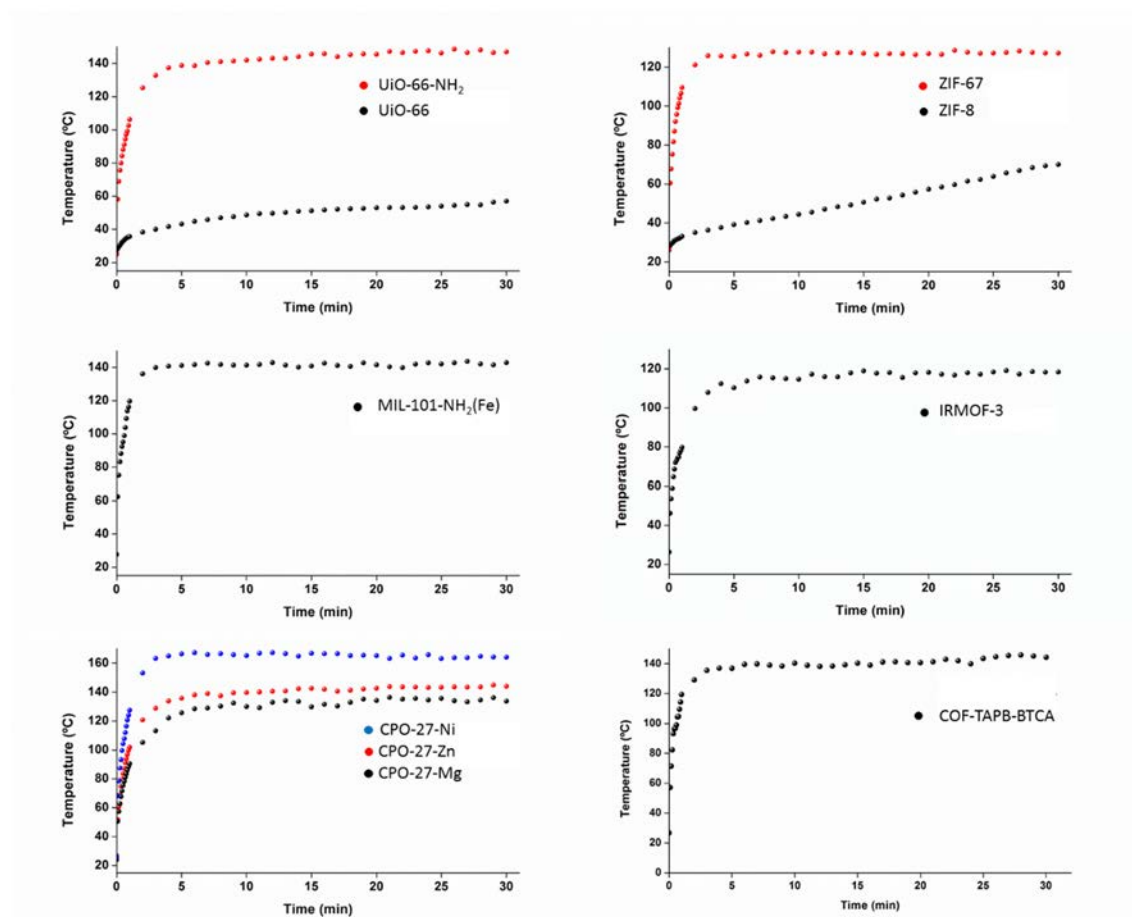
Figure 4.11. Photothermal plots (temperature vs. time) of all the studied MOFs and COF irradiated for 30 minutes at 500 mW·cm^{-2}.
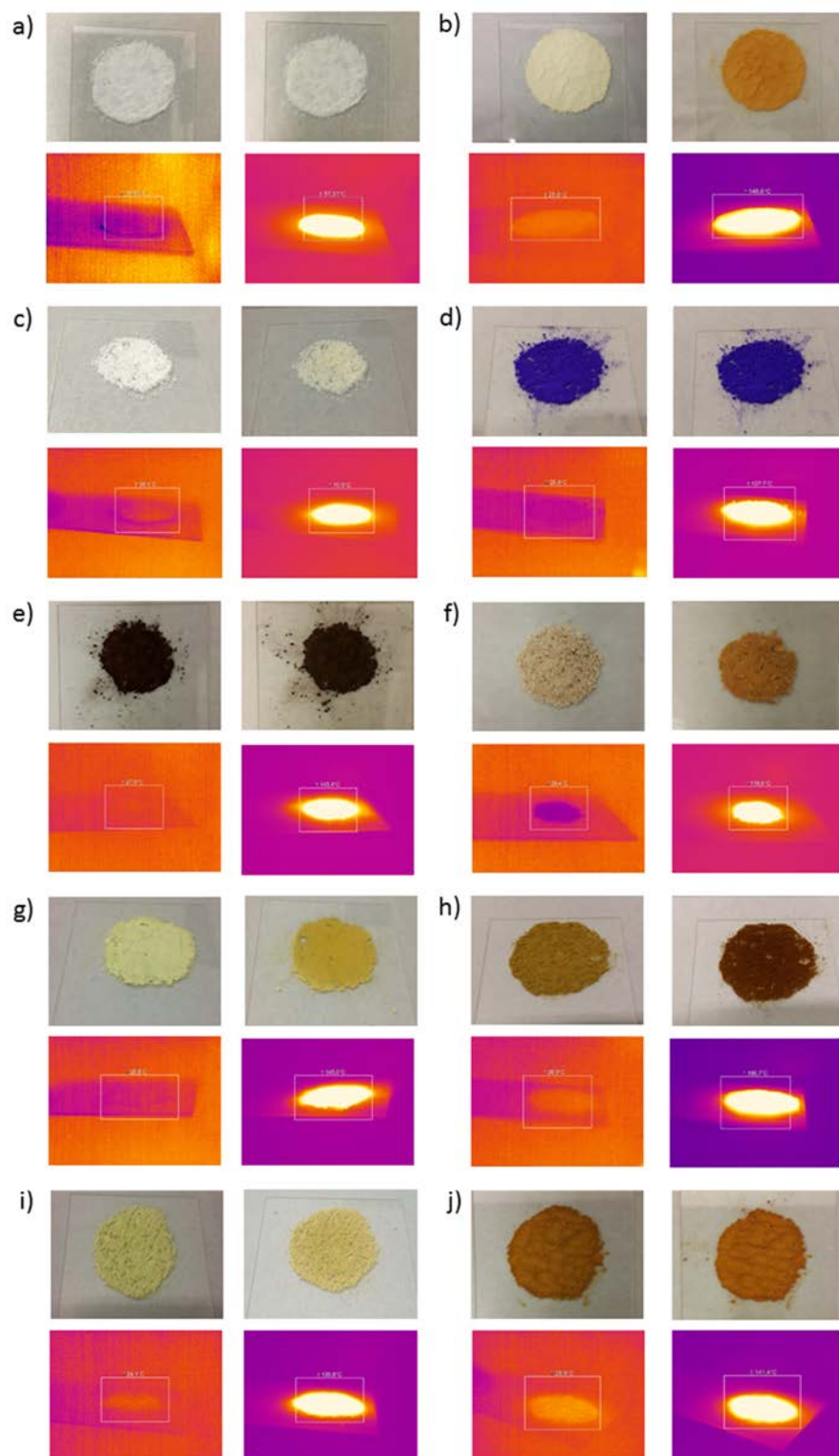
Figure 4.12. Pictures of UiO-66 (a), UiO-66-NH$_2$ (b), ZIF-8 (c), ZIF-67 (d), MIL-101-NH$_2$(Fe) (e), IRMOF-3 (f), CPO-27-Zn (g), CPO-27-Ni (h), CPO-27-Mg (i) and COF-TAPB-BTCA (j) before (top left) and after (top right) irradiation for 30 minutes at 500 mW·cm^{-2}. Infrared camera snaphots before (bottom left) and at the maximum temperature (bottom right).
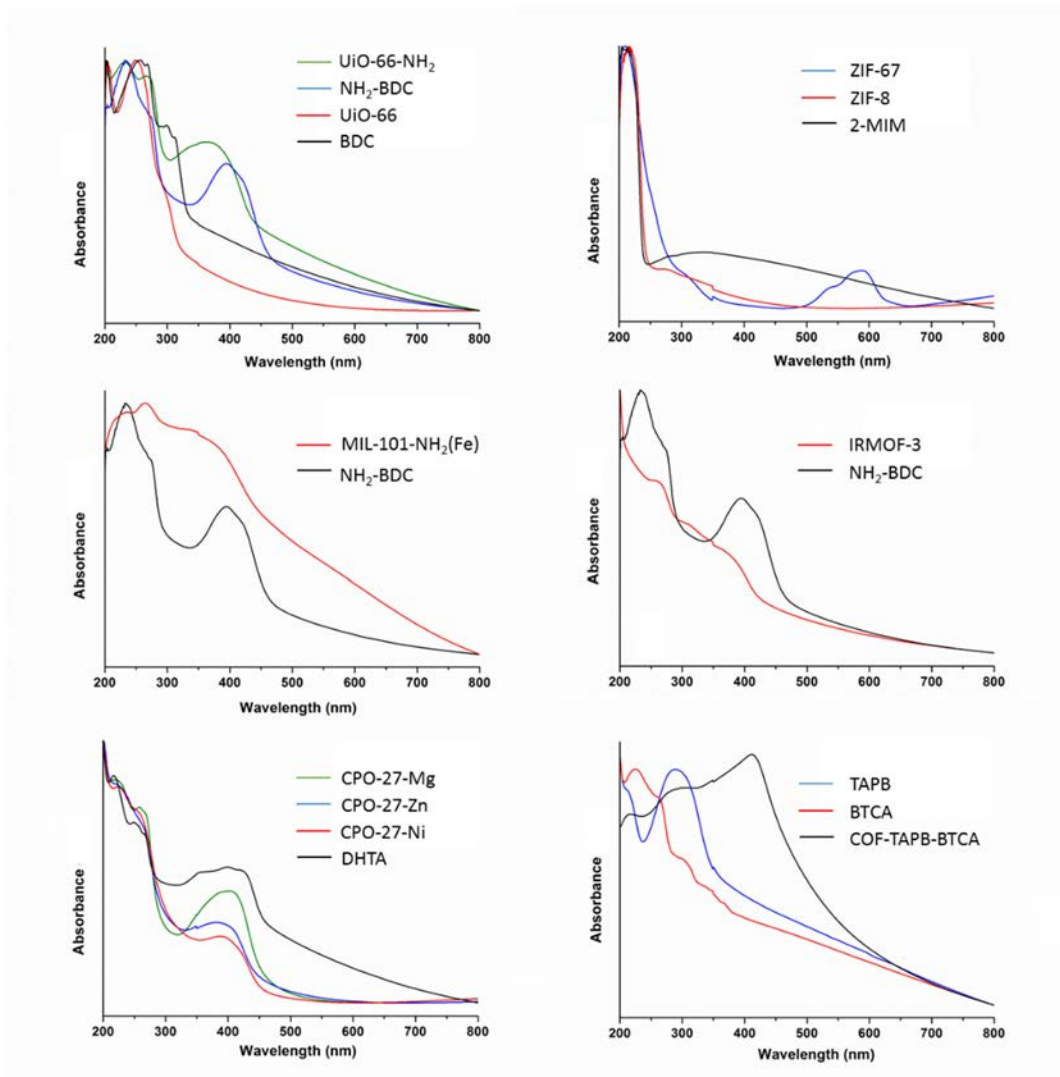
Figure 4.13. Solid-state UV-Vis spectra of all studied MOFs and COF in comparison with their organic ligands.

Table 4.2. Summary of the main parameters of the photothermally activated materials.

Material	Phothermal Temperature (°C)[*]	Photothermal Transduction Efficiency η (%)	S_{BET} (m² g⁻¹) This work	S_{BET} (m² g⁻¹) Reported	Residual solvent (%)[**]
HKUST-1	125	33.6	1583	1740[71]	5.1[a]
UiO-66	57	5.0	424	1580[81]	11.2[b]
UiO-66-NH₂	149	59.3	1098	1200[81]	3.4[b]
ZIF-8	70	0.3	1130	1079[82]	-[c]
ZIF-67	127	50.0	1666	1319[83]	-[c]
CPO-27-Zn	145	23.8	932	1154[69]	1.7[d]
CPO-27-Ni	167	93.6	922	1351[69]	0.4[d]
CPO-27-Mg	136	21.6	1630[***]	1603[69]	2.0[d]
MIL-101-NH₂(Fe)	143	86.6	1506	2436[84]	1.8[a]
IRMOF-3	119	25.8	2556	2850[68]	3.6[b]
COF-TAPB-BTCA	136	55.4	1185	1120[85]	3.0[e]

[*]Irradiating the MOFs for 30 minutes at 500 mW·cm⁻².

[**]Calculated from the residual [a]DMF and EtOH, [b]DMF, [d]MeOH, and [e]acetone. [c]Note than H_2O could not be determined by ^{1}H-NMR.

[***]S_{BET} value obtained upon irradiation at 2650 mW·cm⁻² (T_{max} = 250 °C).
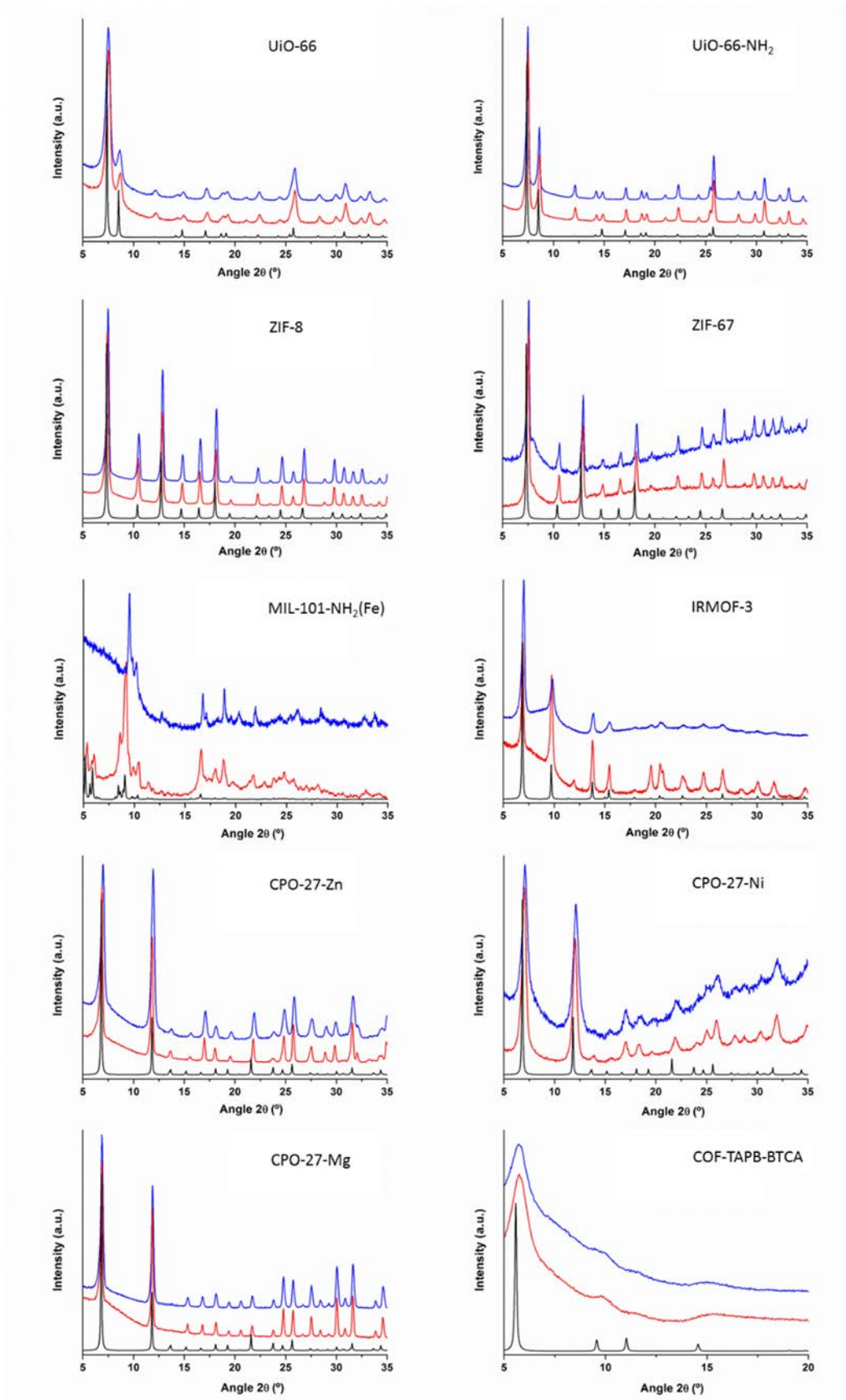
Figure 4.14. XRPD of all studied MOFs and COF: simulated (black), as-synthesised (red) and after photothermal effect characterization (blue).

4.2.2. Photothermal activation characterization

Upon photothermal characterization of all synthesised materials, the next task was to assess their photothermal activation. Once the setup was adjusted for this purpose (round-bottom flask, Ar flow and 500 mW·cm^{-2}), the as-synthesised MOFs and COF were irradiated for 30 minutes without performing any prior solvent exchange step.

Some differences between the S_{BET} values of the UiO-66 and ZIF families were identified. The UiO-66 family was synthesised using DMF, a solvent that is difficult to remove because of its high boiling point. The conventional activation of these MOFs usually requires 2-3 days of solvent exchange step (MeOH or EtOH) and overnight evacuation at 120 °C.[81] With the presented method, UiO-66-NH$_2$ showed a S_{BET} of 1098 m^2·g^{-1} only after 30 minutes of irradiation (close to the highest reported value).[81] However, UiO-66 presented only a S_{BET} of 424 m^2·g^{-1}. This result is in accordance with the previous photothermal characterization, in which the effect exhibited by UiO-66 was much weaker than that exhibited by UiO-66-NH$_2$. In these MOFs, the solvent removal was followed by ^{1}H-NMR spectroscopy upon digestion of the MOFs (Figure 4.15b and c). The as-synthesised and the UV-Vis irradiated samples of the UiO-66 family were digested with HF 5 % (120 µL) and DMSO-d_6 (500 µL) and the DMF signal at 7.90 ppm was compared with the ligand shifts 8.02 and 7.78 ppm for BDC and NH$_2$-BDC, respectively. The residual solvent amount of each sample was quantified, showing a reduction of DMF molecules of 55 % and 94 % for UiO-66 and UiO-66-NH$_2$, respectively. This test confirmed that there was still a number of occluded DMF molecules in the pores of UiO-66, thereby leading to a lower S_{BET} value. Nevertheless, the fact that only 30 minutes were needed to activate UiO-66-NH$_2$ is an exceptional result, which not only shortens the required time for this purpose but also makes it a greener process, as solvent exchange is not required.

The conventional activation of the synthesised ZIF family members does not require such strong conditions as for the UiO-66, as water and MeOH are used for the synthesis and washing step, respectively. In this case, both ZIF-8 and ZIF-67 can be fully activated suppressing the solvent exchange step and only using a thermal treatment of 120 °C under vacuum for 1 hour.[86]
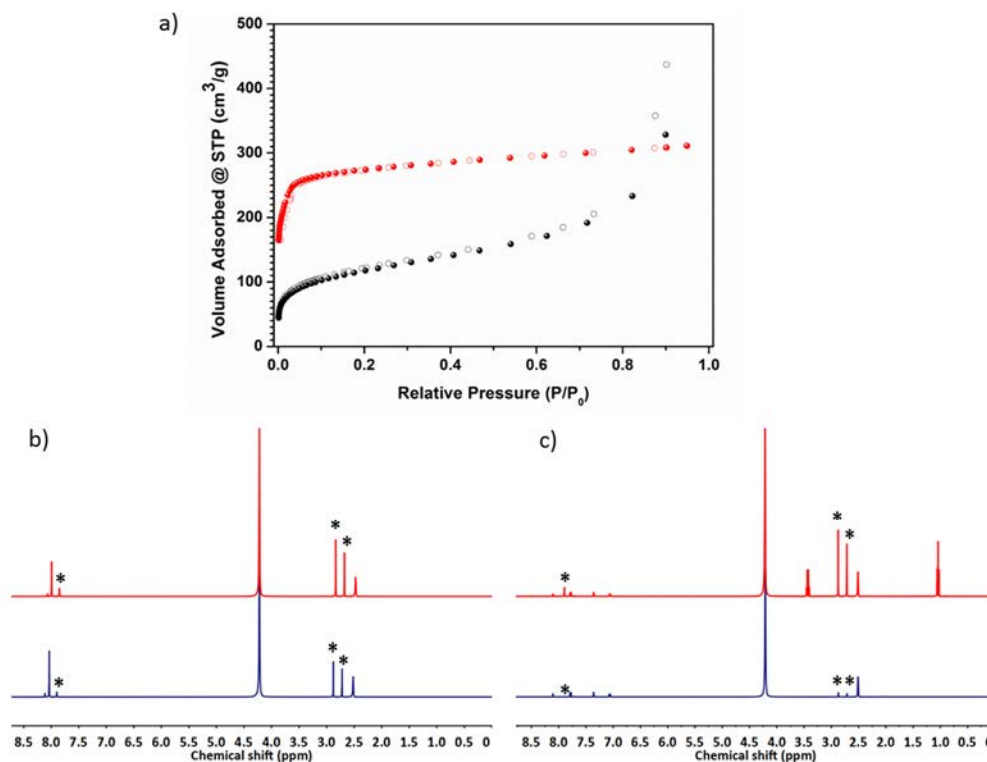
Figure 4.15. a) N_2 adsorption isotherms for UiO-66 (black) and UiO-66-NH$_2$ (red) after photothermal activation. b) ^{1}H-NMR spectra of as-synthesised UiO-66 (red) and after photothermal activation (blue). c) ^{1}H-NMR spectra of as-synthesised UiO-66-NH$_2$ (red) and after photothermal activation (blue). DMF peaks are highlighted with an asterisk (*).

UV-Vis photothermal activation of the ZIFs lead to a similar behaviour as for the UiO-66 family. ZIF-67, which reached around 120 °C, showed a S_{BET} value of 1666 $m^2 \cdot g^{-1}$ (calculated from the second step of the isotherm between 0.01-0.2 P/P$_0$), in accordance with the highest reported values for this MOF (Figure 4.16).[83] In the case of ZIF-8 (T$_{max}$ = 70 °C), the S_{BET} value was of 1130 $m^2 \cdot g^{-1}$ (calculated from the second step of the isotherm between 0.01-0.2 P/P$_0$; Figure 4.16). Although it is a quite high value, it is still lower than the usually reported value for this material, ranging from 1400 to 1500 $m^2 \cdot g^{-1}$.[82,86] These results mean that the milder photothermal effect in ZIF-8 compared with ZIF-67 did not allow to fully activate it. However, the relatively high S_{BET} value for ZIF-8 can be explained by the lower energy required to evaporate the lower boiling point solvent used in the synthesis of the ZIF-8 (water) compared to DMF used for the UiO-66 family.
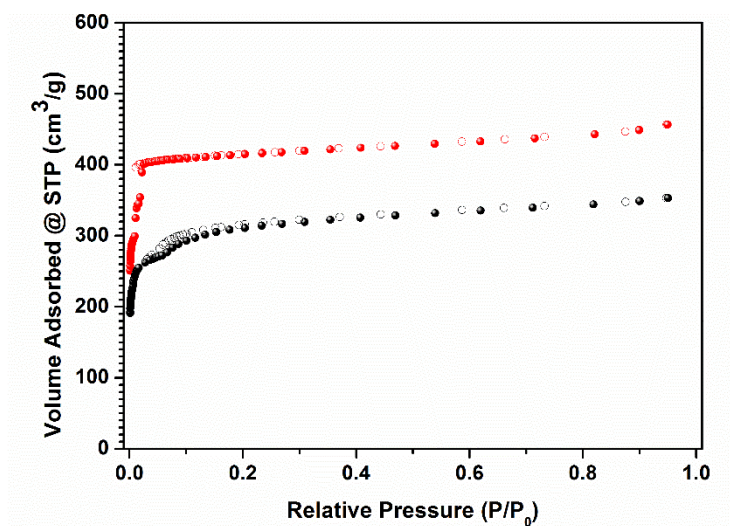
Figure 4.16. N_2 adsorption isotherms for ZIF-8 (black) and ZIF-67 (red) after photothermal activation.

Other NH_2-BDC-containing MOFs from two subfamilies were also synthesised, containing different metal ions and features: MIL-101-NH_2(Fe) and IRMOF-3. Both MOFs require specific solvent exchange steps before measuring their N_2 adsorption isotherms. In the case of MIL-101-NH_2(Fe), the common activation procedure consists on the overnight heating of the sample at 150 °C under vacuum. However, with the photothermal activation method, we only needed 30 minutes of UV-Vis irradiation to achieve an S_{BET} value of 1506 $m^2 \cdot g^{-1}$ (Figure 4.17). Although this value is not the highest reported, it proves its effective activation that is consistent with its strong photothermal effect.
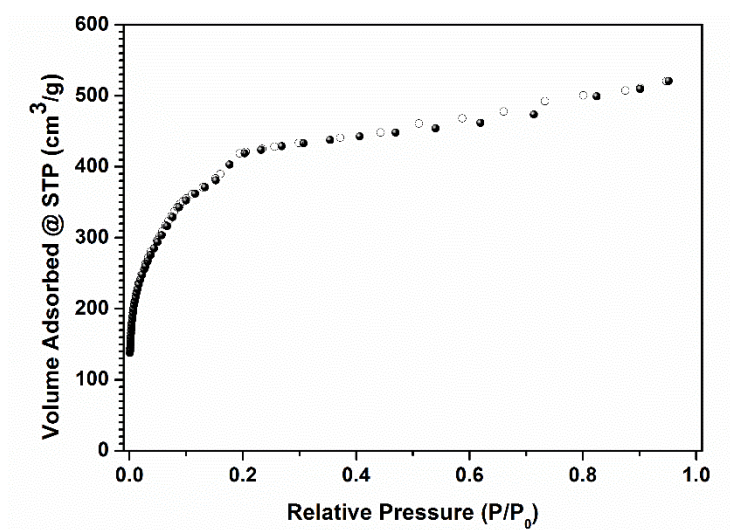
Figure 4.17. N_2 adsorption isotherm of MIL-101-NH_2(Fe) activated for 30 minutes under UV-Vis irradiation (500 $mW \cdot cm^{-2}$).

IRMOF-3 was chosen as a challenging-to-activate MOF because its degradation and loss of porosity on exposing it to air moisture is well known. To overcome this drawback, an alternative activation method using supercritical CO_2 was required (*vide supra*). As demonstrated by Hupp and co-workers, this activation procedure allows reaching the permanent porosity of the more sensitive MOFs.[68] However, this method is instrument-demanding and time-consuming. For this reason, we tested our photothermal activation approach to this MOF. Remarkably, XRPD confirmed the crystallinity of the material upon irradiation (Figure 4.14), and the N_2 adsorption isotherm showed an S_{BET} value of 2556 $m^2 \cdot g^{-1}$ (Figure 4.18). These results demonstrated the full activation of IRMOF-3, confirming that the photothermal method is also respectful with less robust MOFs, and that the localized heat generated is very effective.
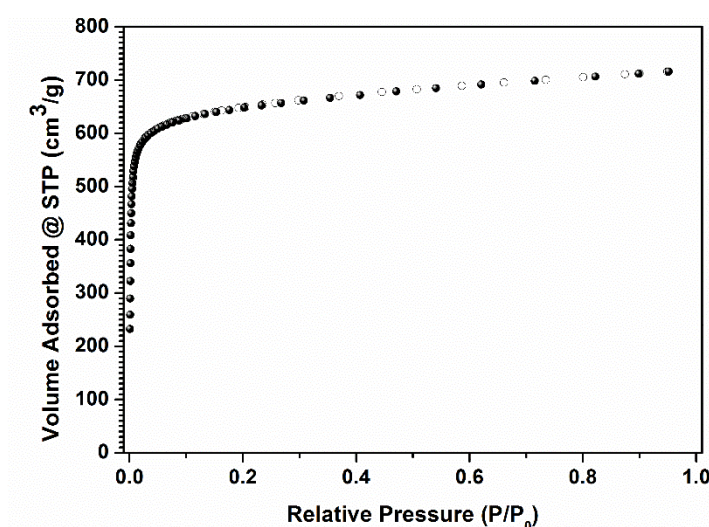
Figure 4.18. N_2 adsorption isotherm of IRMOF-3 activated for 30 minutes under UV-Vis irradiation (500 $mW \cdot cm^{-2}$).

MOFs that require time-consuming activation steps, such as the CPO-27-M (M = Zn, Ni, Mg) subfamily, were also challenged using the photothermal activation method. These MOFs contain open metal sites that can strongly coordinate water molecules. This fact makes quite difficult to access to their permanent porosity. Typical activation protocols for this subfamily consist on long solvent exchange steps, from 7 to 12 days in MeOH (refreshing the solvent every day), and subsequent application of vacuum at very high temperatures (over 180 °C).[69] After applying the UV-Vis light (500 $mW \cdot cm^{-2}$) for 30 minutes to the three as-synthesised MOFs and measuring the N_2 adsorption isotherms, we found that only CPO-27-Zn and CPO-27-Ni were successfully activated, with S_{BET} values of 932 $m^2 \cdot g^{-1}$ and 922 $m^2 \cdot g^{-1}$, respectively (Figure 4.19a). These values were not far from the highest reported ones for both MOFs,[69] considering that only 30 minutes of activation treatment were applied. The same conditions did not lead to a fully activated CPO-

27-Mg, which N_2 adsorption isotherm showed a S_{BET} value of 416 $m^2 \cdot g^{-1}$. However, higher irradiance was applied in order to evaluate if coordinated water molecules could be removed. By shortening the light guide-to-sample distance to 5 and 3 cm, the irradiance was modified to 900 and 2650 $mW \cdot cm^{-2}$, respectively. The photothermal effect characterization was previously assessed for both experiments, and gave rise to maximum temperatures of 184 °C (5 cm) and 250 °C (3 cm). In these cases, the crystallinity was also retained. Finally, N_2 adsorption measurements showed S_{BET} values of 1062 and 1630 $m^2 \cdot g^{-1}$, respectively, the latter value being close to the highest ever reported for CPO-27-Mg[69] (Figure 4.19b). With this experiment, we proved that by varying the irradiance, robust MOFs can also be activated in short times.
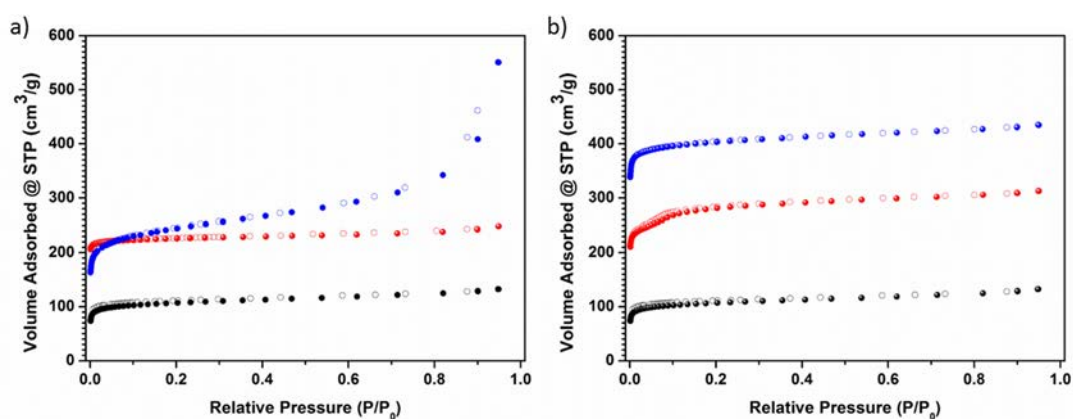
Figure 4.19. a) N_2 adsorption isotherms of CPO-27-Mg (black), - Zn (red) and -Ni (blue) after irradiated at 500 $mW \cdot cm^{-2}$. b) N_2 adsorption isotherms of CPO-27-Mg after irradiated at 500 (black), 900 (red) and 2650 $mW \cdot cm^{-2}$ (blue).

COF-TAPB-BTCA was synthesised with the aim to explore the photothermal activation method for other porous materials such as COFs. The N_2 adsorption isotherm for COF-BTCA-TAPB upon irradiation at 500 $mW \cdot cm^{-2}$ for 30 minutes showed an S_{BET} value of 1185 $m^2 \cdot g^{-1}$ (Figure 4.20). This value is in accordance with the reported one in the literature. Remarkably, this photothermal process simplifies the activation of this COF as the common activation process entails a thermal treatment of 150 °C under vacuum for 12 hour.[85]
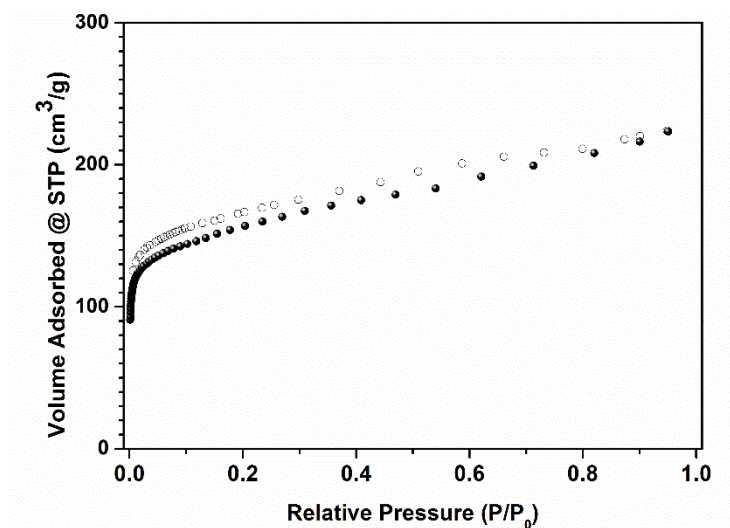
Figure 4.20. N_2 adsorption isotherm of COF-TAPB-BTCA activated for 30 minutes under UV-Vis irradiation (500 mW·cm^{-2}).

Table 4.2 (*vide supra*) includes a summary of the results obtained along this project, showing the maximum temperatures reached during the photothermal characterization of the MOFs, their photothermal transduction efficiency (PTE), the comparative S_{BET} values after photothermal activation and the conventional reported methods, and the residual solvent percentage after being activated with the new proposed method. Figures containing ^{1}H-NMR spectra and S_{BET} linear fittings can be found in the Appendix.

5. Experimental section

5.1. Synthetic procedures

Synthesis of HKUST-1

The spray-drying methodology was used in order to obtain HKSUT-1 in short times and good yields.[87] In a typical synthesis, a solution of 2.00 g (8.60 mmol) of $Cu(NO_3)_2$·$2.5H_2O$ and 1.20 g (5.71 mmol) of 1,3,5-benzenetricarboxylic acid (BTC) in 50 mL of a mixture of dimethylformamide (DMF), ethanol and water (1:1:1) was spray-dried in a B-290 Mini Spray-dryer (BÜCHI Labortechnik) at a feed rate of 4.5 mL·min^{-1}, a flow rate of 336 mL·min^{-1} and an inlet temperature of 180 °C, using a spray-cap with a 0.5 mm-diameter hole. After 12 minutes, 2.13 g of blue powder were collected. This powder was washed several times with 40 mL of methanol and recovered by centrifugation. The final product was air-dried and no further solvent exchange was applied.

Synthesis of UiO-66

In a typical synthesis,[88] 0.68 g (2.92 mmol) of $ZrCl_4$ in 15 mL of a mixture of DMF and water (5.48:1 v/v) was added to a solution of 0.48 g (2.90 mmol) of benzene-1,4-dicarboxylic acid (BDC) in 15 mL of DMF. The resulting mixture was heated at 120 °C under stirring for 2 hours. The solid obtained was collected by centrifugation, washed twice with 20 mL of DMF and twice with 20 mL of absolute ethanol, and finally air-dried overnight.

Synthesis of UiO-66-NH$_2$

In a typical synthesis,[88] 3.5 mL of 37% HCl was added to a solution of 1.17 g (5.02 mmol) of $ZrCl_4$ and 0.91 g (5.02 mmol) of 2-aminoterephthalic acid (NH_2-BDC) in 50 mL of DMF. The resulting mixture was heated at 120 °C under stirring for 2 hours. The solid obtained was collected by centrifugation, washed twice with 20 mL of DMF and twice with 20 mL of absolute ethanol, and finally air-dried overnight.

Synthesis of ZIF-8

In a typical synthesis,[86] a solution of 0.30 g (1.37 mmol) of $Zn(OAc)_2 \cdot 2H_2O$ in 5 mL of deionized (DI) water was added to a solution of 1.12 g (13.64 mmol) of 2-methylimidazole (2-MIM) in 5 mL of DI water. The resulting mixture was homogenised by stirring for a few seconds. Then, the mixture was left to stand at room temperature for 6 hours. White crystals were recovered by centrifugation, washed three times with 20 mL of methanol, and finally air-dried.

Synthesis of ZIF-67

In a typical synthesis,[86] a solution of 0.60 g (2.41 mmol) of $Co(OAc)_2 \cdot 4H_2O$ in 5 mL of DI water was added to a solution of 2.24 g (27.28 mmol) of 2-MIM in 5 mL of DI water. The resulting mixture was homogenised by stirring for a few seconds. Then, the mixture was left to stand for 2 hours at room temperature. Purple crystals were collected by centrifugation, washed three times with 20 mL of methanol, and finally air-dried.

Synthesis of CPO-27-Zn

In a typical synthesis,[69] a solution of 0.36 g (1.82 mmol) of 2,5-dihydroxyterephthalic acid (DHTA) in 5.0 mL of sodium hydroxide solution (0.29 g, 7.30 mmol) was added to a solution of 0.79 g (3.60 mmol) of $Zn(OAc)_2 \cdot 2H_2O$ in 5.0 mL of DI water. The resulting yellow suspension was stirred for 1 hour at room temperature. The product was collected by centrifugation, washed twice with DI water (30 mL) and twice with 30 mL of methanol, and finally air-dried overnight.

Synthesis of CPO-27-Ni

In a typical synthesis,[69] a solution of 0.09 g (0.45 mmol) of DHTA in 10.0 mL of sodium hydroxide solution (0.07 g, 1.75 mmol) was added to a solution of 0.22 g (0.88 mmol) of $Ni(OAc)_2 \cdot 4H_2O$ in 10.0 mL of DI water. The resulting green solution was stirred at room temperature for 24 hours. The product was collected by centrifugation, washed three times with 30 mL of DI water and three times with 30 mL of methanol, and finally air-dried overnight.

Synthesis of CPO-27-Mg

In a typical synthesis,[69] a solution of 0.18 g (0.91 mmol) of DHTA in 5.0 mL of sodium hydroxide solution (0.15 g, 3.75 mmol) was added to a solution of 0.48 g (2.24 mmol) of $Mg(OAc)_2 \cdot 4H_2O$ in 5.0 mL of DI water. The resulting green suspension was stirred for 6 hours at room temperature. The product was collected by centrifugation, washed three times with 30 mL of DI water and three times with 30 mL of methanol, and finally air-dried overnight.

Synthesis of MIL-101-NH$_2$(Fe)

The synthesis was adapted from reported procedures.[89] 0.68 g (2.52 mmol) of $FeCl_3 \cdot 6H_2O$ in 7.5 mL of DMF was added to a solution of 0.23 g (1.27 mmol) of NH_2-BDC in 7.5 mL of DMF, and the resulting mixture was heated at 120 °C for 24 hours. The solid obtained was collected by centrifugation, washed three times with 20 mL of DMF and twice with 20 mL of absolute ethanol. The resulting powder was air-dried overnight. To eliminate most of the free NH_2-BDC, the product was dispersed in DMF at 110 °C under stirring for 8 hours and precipitated by centrifugation. This process was repeated three times.

Synthesis of IRMOF-3

The synthesis was adapted from reported procedures.[90] 1.20 g (4.03 mmol) of $Zn(NO_3)_2 \cdot 6H_2O$ and 0.30 g (1.66 mmol) of NH_2-BDC were dissolved in 40 mL of DMF. The solution was divided into 8 scintillation vials and heated at 100 °C for 24 hours in an oven. Crystals were harvested from the bottom of these vial, then washed twice with 10 mL of DMF and 10 mL of chloroform. Dried crystals were kept under an argon atmosphere.

Synthesis of COF-TAPB-BTCA

COF-TAPB-BTCA was synthesised following a previously reported method.[85] 0.03 g (0.19 mmol) of 1,3,5-benzenetricarbaldehyde (BTCA) in 12.5 mL of acetone and 2.5 mL of acetic acid was added to a solution of 0.06 g (0.17 mmol) of 1,3,5-tris-(4-aminophenyl)benzene (TAPB) in 12.5 mL of acetone. The resulting mixture was stirred for 1 hour. The obtained yellow solid was

collected by centrifugation, washed twice with 20 mL of acetone and twice with 20 mL of THF. After that, the solid was dispersed in a mixture of 1,4-dioxane and mesitylene (9:1 v/v), adding 1.75 mL of water and 2.60 mL of acetic acid under continuous stirring at room temperature. The resulting mixture was heated at 80 °C under stirring for 8 days. The obtained solid was collected by centrifugation at 9000 rpm for 4 minutes, washed three times with 10 mL of toluene, and finally air-dried.
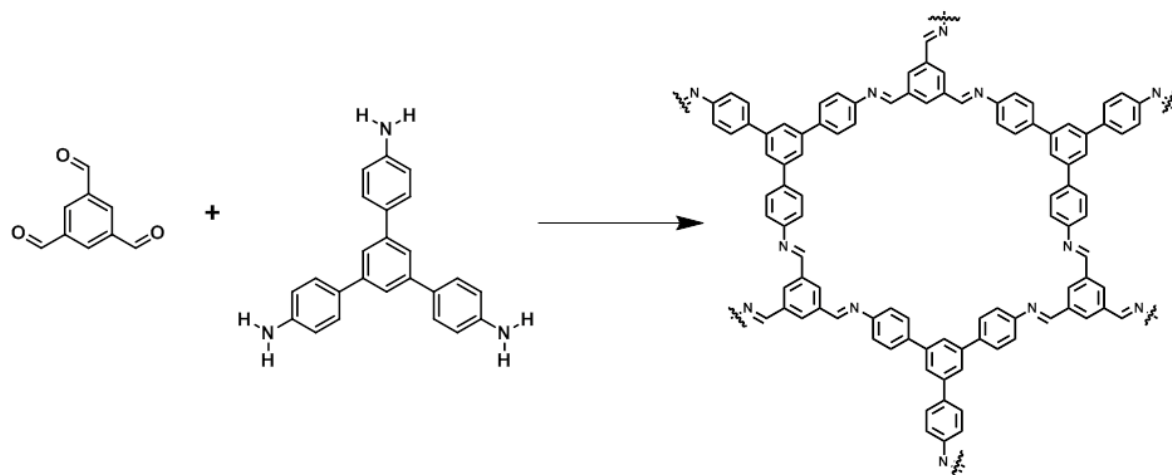
Figure 5.1. Schematic representation of the synthesis of COF-TAPB-BTCA.

5.2. Photothermal transduction efficiency calculations

The photothermal transduction efficiency (η) is a calculated value that determines the efficacy in which a certain material or particle converts light into heat. The photothermal transduction efficiency of all the studied materials in this chapter was calculated following the reported procedures in the literature.[55,91]

The system energy balance consists on:

$$\sum_i m_i \, C_{p,i} \frac{dT}{dt} = Q_{in,MOF} + Q_{in,surr} - Q_{out} \qquad (1)$$

, where m_i and $C_{p,i}$ are the mass and heat capacity of the system components.

$Q_{in,MOF}$ is the heat input from the MOFs due to the photothermal effect according to Equation (2):

$$Q_{in,MOF} = I(1 - 10^{-A_\lambda})\eta \qquad (2)$$

, where I is the light power, A_λ is the absorbance of the material at a certain wavelength, and η is the photothermal transduction efficiency. The light power was measured using the power-

meter. At a distance of 7 cm, the light power was 500 mW. The term 10^{-A_λ} tends to 0 due to the high A_λ value of 100 mg used in our experimental setup.

$Q_{in,surr}$ is the heat input from the photothermal effect of the surroundings. In our case, there is only air between the light guide and the sample, which is not heated by the light source, thus not affecting the energy balance.

Q_{out} is the heat loss of the material to the surroundings, as defined by Equation (3):

$$Q_{out} = hA(T - T_{surr}) \quad (3)$$

, where T_{surr} is the room temperature, h is the heat-transfer coefficient, and A is the surface of the irradiated powder.

At the maximum temperature (T_{max}), the heat flux reaches a steady state, which allows balancing the energy input with energy output:

$$Q_{in,MOF} = Q_{out} \quad (4)$$

Substituting Equation 2 and 3 into Equation 4, Equation 5 is obtained:

$$\eta = \frac{hA(T_{max} - T_{surr})}{I} \quad (5)$$

The temperature increase as a function of time during light irradiation follows the expression:

$$\frac{T_{amb} - T}{T_{amb} - T_{max}} = 1 - e^{(-t/\tau_s)} \quad (6)$$

, where τ_s is a time constant:

$$\tau_s = \frac{\sum_i m_i C_{p,i}}{hA} \quad (7)$$

Fitting the data (Equation (8)) of each material to a linear trend, we calculated τ_s:

$$\ln\left(1 - \frac{T_{amb} - T}{T_{amb} - T_{max}}\right) = -t/\tau_s \quad (8)$$

Then, the heat transfer coefficient of each material was calculated using Equation (9):

$$hA = \frac{\sum_i m_i C_{p,i}}{\tau_s} \quad (9)$$

Finally, we substituted these values in Equation (10) to calculate each photothermal transduction efficiency (Table 4.3):

$$\eta = \frac{hA(T_{max} - T_{surr})}{I} \quad (10)$$

Table 4.3. Summary of the η for all studied MOFs.

Material	τ_s (sec)	Cp*	hA (mW/K)	$T_{max}-T_{surr}$	η (%)
HKUST-1	71.8	1.225	1.7	98.5	33.6
UiO-66	123.6	1.750	1.4	17.8	5.0
UiO-66-NH$_2$	60.9	1.607	2.6	112.5	59.3
ZIF-8	123.8	0.124	0.1	12.8	0.3
ZIF-67	43.4	1.084	2.5	100.1	50.0
IRMOF-3	71.0	1.062	1.5	86.1	25.8
MIL-101-NH$_2$(Fe)	41.3	1.578	3.8	113.2	86.6
CPO-27-Zn	69.8	0.766	1.1	108.2	23.8
CPO-27-Ni	49.9	1.670	3.4	139.7	93.6
CPO-27-Mg	97.7	1.050	1.1	100.5	21.6
COF-TAPB-BTCA	47.2	1.185	2.5	110.4	55.4

* Cp values were determined from Differential Scanning Calorimetry (DSC) analysis.

6.   Conclusions

This chapter reports for the first time the photothermal effect in MOFs and its use for their activation. This light-to-heat conversion is observed in MOFs that present an absorption maximum in the UV-Vis range (300-650 nm), which is the emitting wavelength range of the used lamp. These MOFs could reach temperatures as high as 120-250 °C after only 5 minutes of irradiation. The strong photothermal effect exhibited allowed to use this thermal energy to activate MOFs, removing the entrapped solvent molecules from their pores. Using the proposed activation method, we attained fully activated MOFs in only 30 minutes in a single step and avoiding previous solvent exchange procedures. This method was tested for a series of the most representative MOF subfamilies: HKUST-1, UiO-66, UiO-66-NH$_2$, ZIF-8, ZIF-67, MIL-101-NH$_2$(Fe), IRMOF-3 and CPO-27-M (M = Zn, Ni, Mg). The variety of selected MOFs allowed us to confirm that the photothermal activation method was useful for MOFs containing open metal sites, for the removal of high-boiling point solvents and for the less robust MOFs. The activated MOFs reached S$_{BET}$ values comparable to the highest reported ones in the literature. In addition, the method was also tested for a COF, the COF-TAPB-BTCA, demonstrating the utility of the photothermal activation method in other porous materials.

This single step method might be useful in continuous large-scale manufacturing of MOFs, where a conveyor belt transporting the as-synthesised material pass through a chamber with several light guides irradiating the powder surface. In addition, other applications behind the activation process could be addressed with the photothermal effect, such as triggering guest release from the MOF pores or confining organic reactions and polymerizations in the channels of the framework.

7.   References

1.   Almond, D. P. & Patel, P. M. *Photothermal Science and Techniques*. (Springer Science & Business Media, 1996).

2.   Sell, J. A. *Photothermal Investigations of Solids and Fluids*. (Academic Press, Inc., 1989).

3.   Kreibig, U. & Vollmer, M. *Optical Properties of Metal Clusters*. (Springer-Verlag, 1995).

4.   Link, S. & El-Sayed, M. A. Size and Temperature Dependence of the Plasmon Absorption of Colloidal Gold Nanoparticles. *J. Phys. Chem. B* **103,** 4212–4217 (1999).

5.   Ni, W., Kou, X., Yang, Z. & Wang, J. Tailoring Longitudinal Surface Plasmon Wavelengths, Scattering and Absorption Cross Sections of Gold Nanorods. *ACS Nano* **2,** 677–686 (2008).

6.   Brongersma, M. L., Halas, N. J. & Nordlander, P. Plasmon-Induced Hot Carrier Science and Technology. *Nat. Nanotechnol.* **10,** 25–34 (2015).

7.   Qiu, J. & Wei, W. D. Surface Plasmon-Mediated Photothermal Chemistry. *J. Phys. Chem. C* **118,** 20735–20749 (2014).

8.   Hartland, G. V. Optical Studies of Dynamics in Noble Metal Nanostructures. *Chem. Rev.* **111,** 3858–3887 (2011).

9.   Boyer, D., Tamarat, P., Maali, A., Lounis, B. & Orrit, M. Photothermal Imaging of Nanometer-Sized Metal Particles Among Scatterers. *Science* **297,** 1160–1163 (2002).

10.   Baffou, G., Kreuzer, M. P., Kulzer, F. & Quidant, R. Temperature Mapping Near Plasmonic Nanostructures Using Fluorescence Polarization Anisotropy. *Opt. Express* **17,** 3291–3298 (2009).

11.   Baffou, G., Quidant, R. & Girard, C. Heat Generation in Plasmonic Nanostructures: Influence of Morphology. *Appl. Phys. Lett.* **94,** 153109 (2009).

12.   Baffou, G., Quidant, R. & García de Abajo, F. J. Nanoscale Control of Optical Heating in Complex Plasmonic Systems. *ACS Nano* **4,** 709–716 (2010).

13.   Chen, X., Chen, Y., Yan, M. & Qiu, M. Nanosecond Photothermal Effects in Plasmonic Nanostructures. *ACS Nano* **6,** 2550–2557 (2012).

14.   Huang, X. & El-Sayed, M. A. Gold nanoparticles: Optical properties and implementations in cancer diagnosis and photothermal therapy. *J. Adv. Res.* **1,** 13–28 (2010).

15.   Huang, X., El-Sayed, I. H., Qian, W. & El-Sayed, M. A. Cancer Cell Imaging and Photothermal Therapy in the Near-Infrared Region by Using Gold Nanorods. *J. Am. Chem. Soc.* **128,** (2006).

16.   El-Sayed, I. H., Huang, X. & El-Sayed, M. A. Selective Laser Photo-Thermal Therapy of Epithelial Carcinoma Using anti-EGFR Antibody Conjugated Gold Nanoparticles. *Cancer Lett.* **239,** 129–135 (2006).

17.   Huang, X., Jain, P. K., El-Sayed, I. H. & El-Sayed, M. A. Plasmonic Photothermal Therapy (PPTT) Using Gold Nanoparticles. *Lasers Med. Sci.* **23,** 217 (2007).

18.   Huang, X., Neretina, S. & El-Sayed, M. A. Gold Nanorods: From Synthesis and Properties to Biological and Biomedical Applications. *Adv. Mater.* **21,** 4880–4910 (2009).

19.   Hessel, C. M., Pattani, V. P., Rasch, M., Panthani, M. G., Koo, B., Tunnell, J. W. & Korgel, B. A. Copper Selenide Nanocrystals for Photothermal Therapy. *Nano Lett.* **11,** 2560–2566 (2011).

20.   Jaque, D., Martinez Maestro, L., del Rosal, B., Haro-Gonzalez, P., Benayas, A., Plaza, J. L.,

Martin Rodriguez, E. & Garcia Sole, J. Nanoparticles for Photothermal Therapies. *Nanoscale* **6,** 9494–9530 (2014).

21. El-Hussein, A., Mfouo-Tynga, I., Abdel-Harith, M. & Abrahamse, H. Comparative Study Between the Photodynamic Ability of Gold and Silver Nanoparticles in Mediating Cell Death in Breast and Lung Cancer Cell Lines. *J. Photochem. Photobiol. B Biol.* **153,** 67–75 (2015).

22. Huang, X., Zhang, W., Guan, G., Song, G., Zou, R. & Hu, J. Design and Functionalization of the NIR-Responsive Photothermal Semiconductor Nanomaterials for Cancer Theranostics. *Acc. Chem. Res.* **50,** 2529–2538 (2017).

23. Neumann, O., Urban, A. S., Day, J., Lal, S., Nordlander, P. & Halas, N. J. Solar Vapor Generation Enabled by Nanoparticles. *ACS Nano* **7,** 42–49 (2013).

24. Liu, Y., Yu, S., Feng, R., Bernard, A., Liu, Y., Zhang, Y., Duan, H., Shang, W., Tao, P., Song, C. & Deng, T. A Bioinspired, Reusable, Paper-Based System for High-Performance Large-Scale Evaporation. *Adv. Mater.* **27,** 2768–2774 (2015).

25. Wang, Z., Liu, Y., Tao, P., Shen, Q., Yi, N., Zhang, F., Liu, Q., Song, C., Zhang, D., Shang, W. & Deng, T. Bio-Inspired Evaporation Through Plasmonic Film of Nanoparticles at the Air–Water Interface. *Small* **10,** 3234–3239 (2014).

26. Deng, Z., Zhou, J., Miao, L., Liu, C., Peng, Y., Sun, L. & Tanemura, S. The Emergence of Solar Thermal Utilization: Solar-Driven Steam Generation. *J. Mater. Chem. A* **5,** 7691–7709 (2017).

27. Neumann, O., Feronti, C., Neumann, A. D., Dong, A., Schell, K., Lu, B., Kim, E., Quinn, M., Thompson, S., Grady, N., Nordlander, P., Oden, M. & Halas, N. J. Compact Solar Autoclave Based on Steam Generation Using Broadband Light-Harvesting Nanoparticles. *Proc. Natl. Acad. Sci.* **110,** 11677–11681 (2013).

28. Zhou, L., Tan, Y., Wang, J., Xu, W., Yuan, Y., Cai, W., Zhu, S. & Zhu, J. 3D Self-Assembly of Aluminium Nanoparticles for Plasmon-Enhanced Solar Desalination. *Nat. Photonics* **10,** 393–398 (2016).

29. Yi, L., Ci, S., Luo, S., Shao, P., Hou, Y. & Wen, Z. Scalable and Low-Cost Synthesis of Black Amorphous Al-Ti-O Nanostructure for High-Efficient Photothermal Desalination. *Nano Energy* **41,** 600–608 (2017).

30. Sershen, S., Westcott, S., Halas, N. & West, J. Temperature-Sensitive Polymer-Nanoshell Composites for Photothermally Modulated Drug Delivery. *J. Biomed. Mater. Res.* **51,** 293–298 (2000).

31. Jain, P. K., Huang, X., El-Sayed, I. H. & El-Sayed, M. A. Noble Metals on the Nanoscale: Optical and Photothermal Properties and Some Applications in Imaging, Sensing, Biology, and Medicine. *Acc. Chem. Res.* **41,** 1578–1586 (2008).

32. Tseng, S.-C., Yu, C.-C., Wan, D., Chen, H.-L., Wang, L. A., Wu, M.-C., Su, W.-F., Han, H.-C. & Chen, L.-C. Eco-Friendly Plasmonic Sensors: Using the Photothermal Effect to Prepare Metal Nanoparticle-Containing Test Papers for Highly Sensitive Colorimetric Detection. *Anal. Chem.* **84,** 5140–5145 (2012).

33. Lee, S. H., Choi, S., Kwon, K., Bae, N.-H., Kwak, B. S., Cho, W. C., Lee, S. J. & Jung, H.-I. A Photothermal Biosensor for Detection of C-Reactive Protein in Human Saliva. *Sens. Actuators, B.* **246,** 471–476 (2017).

34. Xu, S., Bai, X. & Wang, L. Exploration of Photothermal Sensors Based on Photothermally Responsive Materials: a Brief Review. *Inorg. Chem. Front.* **5,** 751–759 (2018).

35. Adleman, J. R., Boyd, D. A., Goodwin, D. G. & Psaltis, D. Heterogenous Catalysis Mediated by Plasmon Heating. *Nano Lett.* **9,** 4417–4423 (2009).

36. Boyd, D. A., Adleman, J. R., Goodwin, D. G. & Psaltis, D. Chemical Separations by Bubble-Assisted Interphase Mass-Transfer. *Anal. Chem.* **80,** 2452–2456 (2008).

37. Plaetzer, K., Krammer, B., Berlanda, J., Berr, F. & Kiesslich, T. Photophysics and Photochemistry of Photodynamic Therapy: Fundamental Aspects. *Lasers Med. Sci.* **24,** 259–268 (2009).

38. Hua, Z., Li, B., Li, L., Yin, X., Chen, K. & Wang, W. Designing a Novel Photothermal Material of Hierarchical Microstructured Copper Phosphate for Solar Evaporation Enhancement. *J. Phys. Chem. C* **121,** 60–69 (2017).

39. Zeng, Y., Yao, J., Horri, B. A., Wang, K., Wu, Y., Li, D. & Wang, H. Solar Evaporation Enhancement Using Floating Light-Absorbing Magnetic Particles. *Energy Environ. Sci.* **4,** 4074–4078 (2011).

40. Li, X., Xu, W., Tang, M., Zhou, L., Zhu, B., Zhu, S. & Zhu, J. Graphene Oxide-Based Efficient and Scalable Solar Desalination Under One Sun With a Confined 2D Water Path. *Proc. Natl. Acad. Sci.* **113,** 13953–13958 (2016).

41. Jiang, Q., Tian, L., Liu, K.-K., Tadepalli, S., Raliya, R., Biswas, P., Naik, R. R. & Singamaneni, S. Bilayered Biofoam for Highly Efficient Solar Steam Generation. *Adv. Mater.* **28,** 9400–9407 (2016).

42. Ren, H., Tang, M., Guan, B., Wang, K., Yang, J., Wang, F., Wang, M., Shan, J., Chen, Z., Wei, D., Peng, H. & Liu, Z. Hierarchical Graphene Foam for Efficient Omnidirectional Solar–Thermal Energy Conversion. *Adv. Mater.* **29,** 1702590 (2017).

43. Hu, X., Xu, W., Zhou, L., Tan, Y., Wang, Y., Zhu, S. & Zhu, J. Tailoring Graphene Oxide-Based Aerogels for Efficient Solar Steam Generation under One Sun. *Adv. Mater.* **29,** 1604031 (2017).

44. Yang, K., Feng, L., Shi, X. & Liu, Z. Nano-graphene in biomedicine: theranostic applications. *Chem. Soc. Rev.* **42,** 530–547 (2013).

45. Yang, K., Zhang, S., Zhang, G., Sun, X., Lee, S.-T. & Liu, Z. Graphene in Mice: Ultrahigh In Vivo Tumor Uptake and Efficient Photothermal Therapy. *Nano Lett.* **10,** 3318–3323 (2010).

46. Wang, Y., Zhang, L. & Wang, P. Self-Floating Carbon Nanotube Membrane on Macroporous Silica Substrate for Highly Efficient Solar-Driven Interfacial Water Evaporation. *ACS Sustain. Chem. Eng.* **4,** 1223–1230 (2016).

47. Ghasemi, H., Ni, G., Marconnet, A. M., Loomis, J., Yerci, S., Miljkovic, N. & Chen, G. Solar Steam Generation by Heat Localization. *Nat. Commun.* **5,** 406–412 (2014).

48. Sahadev, N. & Anappara, A. A. Enhanced Photothermal Effect in Reduced Graphene Oxide in Solid-State. *J. Appl. Phys.* **122,** 1–6 (2017).

49. Jiang, R., Cheng, S., Shao, L., Ruan, Q. & Wang, J. Mass-Based Photothermal Comparison Among Gold Nanocrystals, PbS Nanocrystals, Organic Dyes, and Carbon Black. *J. Phys. Chem. C* **117,** 8909–8915 (2013).

50. Xu, L., Cheng, L., Wang, C., Peng, R. & Liu, Z. Conjugated Polymers for Photothermal Therapy of Cancer. *Polym. Chem.* **5,** 1573–1580 (2014).

51. Yang, K., Xu, H., Cheng, L., Sun, C., Wang, J. & Liu, Z. In Vitro and In Vivo Near-Infrared Photothermal Therapy of Cancer Using Polypyrrole Organic Nanoparticles. *Adv. Mater.*

24, 5586–5592 (2012).

52.   Li, S., Wang, X., Hu, R., Chen, H., Li, M., Wang, J., Wang, Y., Liu, L., Lv, F., Liang, X.-J. & Wang, S. Near-Infrared (NIR)-Absorbing Conjugated Polymer Dots as Highly Effective Photothermal Materials for In Vivo Cancer Therapy. *Chem. Mater.* **28,** 8669–8675 (2016).

53.   He, X., He, X., Li, S., Zhuo, K., Qin, W., Dong, S., Chen, J., Ren, L., Liu, G. & Xia, H. Amphipathic Metal-Containing Macromolecules with Photothermal Properties. *Polym. Chem.* **8,** 3674–3678 (2017).

54.   Han, D., Meng, Z., Wu, D., Zhang, C. & Zhu, H. Thermal Properties of Carbon Black Aqueous Nanofluids for Solar Absorption. *Nanoscale Res. Lett.* **6,** 1–7 (2011).

55.   Wang, F., Huang, Y., Chai, Z., Zeng, M., Li, Q., Wang, Y. & Xu, D. Photothermal-Enhanced Catalysis in Core-Shell Plasmonic Hierarchical Cu_7S_4 Microsphere@Zeolitic Imidazole Framework-8. *Chem. Sci.* **7,** 6887–6893 (2016).

56.   Yang, Q., Xu, Q., Yu, S.-H. & Jiang, H.-L. Pd Nanocubes@ZIF-8: Integration of Plasmon-Driven Photothermal Conversion with a Metal–Organic Framework for Efficient and Selective Catalysis. *Angew. Chem. Int. Ed.* **55,** 3685–3689 (2016).

57.   Wang, W., Wang, L., Li, Y., Liu, S., Xie, Z. & Jing, X. Nanoscale Polymer Metal–Organic Framework Hybrids for Effective Photothermal Therapy of Colon Cancers. *Adv. Mater.* **28,** 9320–9325 (2016).

58.   Tian, Z., Yao, X., Ma, K., Niu, X., Grothe, J., Xu, Q., Liu, L., Kaskel, S. & Zhu, Y. Metal–Organic Framework/Graphene Quantum Dot Nanoparticles Used for Synergistic Chemo- and Photothermal Therapy. *ACS Omega* **2,** 1249–1258 (2017).

59.   Chen, Y.-Z., Wang, Z. U., Wang, H., Lu, J., Yu, S.-H. & Jiang, H.-L. Singlet Oxygen-Engaged Selective Photo-Oxidation over Pt Nanocrystals/Porphyrinic MOF: The Roles of Photothermal Effect and Pt Electronic State. *J. Am. Chem. Soc.* **139,** 2035–2044 (2017).

60.   Farha, O. K. & Hupp, J. T. Rational Design, Synthesis, Purification, and Activation of Metal–Organic Framework Materials. *Acc. Chem. Res.* **43,** 1166–1175 (2010).

61.   Mondloch, J. E., Karagiaridi, O., Farha, O. K. & Hupp, J. T. Activation of Metal–Organic Framework Materials. *CrystEngComm* **15,** 9258 (2013).

62.   Howarth, A. J., Peters, A. W., Vermeulen, N. A., Wang, T. C., Hupp, J. T. & Farha, O. K. Best Practices for the Synthesis, Activation, and Characterization of Metal–Organic Frameworks. *Chem. Mater.* **29,** 26–39 (2017).

63.   Park, K. S., Ni, Z., Côté, A. P., Choi, J. Y., Huang, R., Uribe-Romo, F. J., Chae, H. K., O'Keeffe, M. & Yaghi, O. M. Exceptional Chemical and Thermal Stability of Zeolitic Imidazolate Frameworks. *Proc. Natl. Acad. Sci.* **103,** 10186–10191 (2006).

64.   Férey, G., Mellot-Draznieks, C., Serre, C., Millange, F., Dutour, J., Surblé, S. & Margiolaki, I. A Chromium Terephthalate-Based Solid with Unusually Large Pore Volumes and Surface Area. *Science* **309,** 2040–2042 (2005).

65.   Eddaoudi, M., Li, H. & Yaghi, O. M. Highly Porous and Stable Metal–Organic Frameworks: Structure Design and Sorption Properties. *J. Am. Chem. Soc.* **122,** 1391–1397 (2000).

66.   Li, H., Eddaoudi, M., O'Keeffe, M. & Yaghi, O. M. Design and Synthesis of an Exceptionally Stable and Highly Porous Metal-Organic Framework. *Nature* **402,** 276–279 (1999).

67.   Eddaoudi, M., Kim, J., Rosi, N., Vodak, D., Wachter, J., O'Keeffe, M. & Yaghi, O. M. Systematic Design of Pore Size and Functionality in Isoreticular MOFs and Their Application in Methane Storage. *Science* **295,** 469–472 (2002).

68. Nelson, A. P., Farha, O. K., Mulfort, K. L. & Hupp, J. T. Supercritical Processing as a Route to High Internal Surface Areas and Permanent Microporosity in Metal–Organic Framework Materials. *J. Am. Chem. Soc.* **131,** 458–460 (2009).

69. Garzon-Tovar, L., Carne-Sanchez, A., Carbonell, C., Imaz, I. & Maspoch, D. Optimised Room Temperature, Water-Based Synthesis of CPO-27-M Metal-Organic Frameworks with High Space-Time Yields. *J. Mater. Chem. A* **3,** 20819–20826 (2015).

70. Wang, L. J., Deng, H., Furukawa, H., Gándara, F., Cordova, K. E., Peri, D. & Yaghi, O. M. Synthesis and Characterization of Metal–Organic Framework-74 Containing 2, 4, 6, 8, and 10 Different Metals. *Inorg. Chem.* **53,** 5881–5883 (2014).

71. Kim, H. K., Yun, W. S., Kim, M.-B., Kim, J. Y., Bae, Y.-S., Lee, J. & Jeong, N. C. A Chemical Route to Activation of Open Metal Sites in the Copper-Based Metal–Organic Framework Materials HKUST-1 and Cu-MOF-2. *J. Am. Chem. Soc.* **137,** 10009–10015 (2015).

72. Cooper, A. I. Polymer Synthesis and Processing Using Supercritical Carbon Dioxide. *J. Mater. Chem.* **10,** 207–234 (2000).

73. Lubguban, J. A., Gangopadhyay, S., Lahlouh, B., Rajagopalan, T., Biswas, N., Sun, J., Huang, D. H., Simon, S. L., Mallikarjunan, A., Kim, H.-C., Hedstrom, J., Volksen, W., Miller, R. D. & Toney, M. F. Supercritical CO_2 Extraction of Porogen Phase: An Alternative Route to Nanoporous Dielectrics. *J. Mater. Res.* **19,** 3224–3233 (2004).

74. Farha, O. K., Eryazici, I., Jeong, N. C., Hauser, B. G., Wilmer, C. E., Sarjeant, A. A., Snurr, R. Q., Nguyen, S. T., Yazaydın, A. Ö. & Hupp, J. T. Metal–Organic Framework Materials with Ultrahigh Surface Areas: Is the Sky the Limit? *J. Am. Chem. Soc.* **134,** 15016–15021 (2012).

75. Klein, N., Senkovska, I., Baburin, I. A., Grünker, R., Stoeck, U., Schlichtenmayer, M., Streppel, B., Mueller, U., Leoni, S., Hirscher, M. & Kaskel, S. Route to a Family of Robust, Non-interpenetrated Metal–Organic Frameworks with pto-like Topology. *Chem. – Eur. J.* **17,** 13007–13016 (2011).

76. Rey, L. New Ventures in Freeze Drying. *Nature* **345,** 185–186 (1990).

77. Ma, L., Jin, A., Xie, Z. & Lin, W. Freeze Drying Significantly Increases Permanent Porosity and Hydrogen Uptake in 4,4-Connected Metal–Organic Frameworks. *Angew. Chem. Int. Ed.* **48,** 9905–9908 (2009).

78. Song, X., Jeong, S., Kim, D. & Lah, M. S. Transmetalations in Two Metal-Organic Frameworks with Different Framework Flexibilities: Kinetics and Core-Shell Heterostructure. *CrystEngComm* **14,** 5753–5756 (2012).

79. Born, M. & Wolf, E. *Principles of Optics: Electromagnetic Theory of Propagation, Interference and Diffraction of Light*. (Elsevier Science, 2013).

80. McCluney, W. R. *Introduction to Radiometry and Photometry*. (Artech House Publishers, 2014).

81. Katz, M. J., Brown, Z. J., Colon, Y. J., Siu, P. W., Scheidt, K. A., Snurr, R. Q., Hupp, J. T. & Farha, O. K. A Facile Synthesis of UiO-66, UiO-67 and Their Derivatives. *Chem. Commun.* **49,** 9449–9451 (2013).

82. Pan, Y., Liu, Y., Zeng, G., Zhao, L. & Lai, Z. Rapid Synthesis of Zeolitic Imidazolate Framework-8 (ZIF-8) Nanocrystals in an Aqueous System. *Chem. Commun.* **47,** 2071–2073 (2011).

83. Shi, Q., Chen, Z., Song, Z., Li, J. & Dong, J. Synthesis of ZIF-8 and ZIF-67 by Steam-Assisted Conversion and an Investigation of Their Tribological Behaviors. *Angew. Chem. Int. Ed.* **50,** 672–675 (2011).

84. Savonnet, M., Kockrick, E., Camarata, A., Bazer-Bachi, D., Bats, N., Lecocq, V., Pinel, C. & Farrusseng, D. Combinatorial Synthesis of Metal-Organic Frameworks Libraries by Click-Chemistry. *New J. Chem.* **35,** 1892–1897 (2011).

85. Rodríguez-San-Miguel, D., Yazdi, A., Guillerm, V., Pérez-Carvajal, J., Puntes, V., Maspoch, D. & Zamora, F. Confining Functional Nanoparticles into Colloidal Imine-Based COF Spheres by a Sequential Encapsulation–Crystallization Method. *Chem. – Eur. J.* **23,** 8623–8627 (2017).

86. Avci, C., Ariñez-Soriano, J., Carné-Sánchez, A., Guillerm, V., Carbonell, C., Imaz, I. & Maspoch, D. Post-Synthetic Anisotropic Wet-Chemical Etching of Colloidal Sodalite ZIF Crystals. *Angew. Chem. Int. Ed.* **54,** 14417–14421 (2015).

87. Carné-Sánchez, A., Imaz, I., Cano-Sarabia, M. & Maspoch, D. A Spray-Drying Strategy for Synthesis of Nanoscale Metal–Organic Frameworks and Their Assembly into Hollow Superstructures. *Nat. Chem.* **5,** 203–211 (2013).

88. Ragon, F., Horcajada, P., Chevreau, H., Hwang, Y. K., Lee, U.-H., Miller, S. R., Devic, T., Chang, J.-S. & Serre, C. In Situ Energy-Dispersive X-ray Diffraction for the Synthesis Optimization and Scale-up of the Porous Zirconium Terephthalate UiO-66. *Inorg. Chem.* **53,** 2491–2500 (2014).

89. Bauer, S., Serre, C., Devic, T., Horcajada, P., Marrot, J., Férey, G. & Stock, N. High-Throughput Assisted Rationalization of the Formation of Metal Organic Frameworks in the Iron(III) Aminoterephthalate Solvothermal System. *Inorg. Chem.* **47,** 7568–7576 (2008).

90. Tanabe, K. K., Wang, Z. & Cohen, S. M. Systematic Functionalization of a Metal–Organic Framework via a Postsynthetic Modification Approach. *J. Am. Chem. Soc.* **130,** 8508–8517 (2008).

91. Roper, D. K., Ahn, W. & Hoepfner, M. Microscale Heat Transfer Transduced by Surface Plasmon Resonant Gold Nanoparticles. *J. Phys. Chem. C* **111,** 3636–3641 (2007).

Chapter 4

Covalent Post-Synthetic Modification of MOFs Mediated by UV-Vis Light under Solvent-Free Conditions

The local nature of the heat generated when MOFs are irradiated with a UV-Vis light opens up novel opportunities. In this chapter, we show that this photothermal effect can be used for the covalent post-synthetic modification (CPSM) of MOFs. In this case, the thermal energy released by the MOF once irradiated is used to melt the selected reagent, which then reacts with the pendant functional groups in the MOF channels. The proof of concept study was performed by reacting either UiO-66-NH$_2$ or MIL-101-NH$_2$(Al) with maleic anhydride or benzoic anhydride, leading to the formation of amide bonds. The versatility of the PSM method was confirmed by demonstrating a photoinduced cascade reaction between 4-bromobenzaldehyde and UiO-66-NH$_2$, giving rise to the formation of an amide bond instead of the expected imine. This new PSM method is performed under solvent-free conditions and in short irradiation times, attaining considerably high conversion rates.

1.   Post-synthetic modification of MOFs

The classical route to introduce functionalities on the pores of MOFs consisted on tagging the organic ligands with functional groups (-NH$_2$, -Br, -CH$_3$, free radicals) (Figure 1.1).[1–5] However, the use of this strategy is limited by the reaction conditions or due to undesired coordination to metal ions. It was in 2007 when the term "**post-synthetic modification of MOFs**" (PSM) was coined by Cohen and co-workers, with the aim to obtain a more varied spectrum of functionalized porous materials.[6] The post-synthetic approach consists on the heterogeneous modification of previously formed MOFs independently to their synthetic conditions. In this sense, PSM allowed the construction of new MOFs integrating more complex functionalities that could not be attained in one-pot synthesis. To date, the most common PSM approaches for MOFs[7–9] can be classified depending on the presence of non-covalent or covalent interactions between the framework and the newly introduced species.
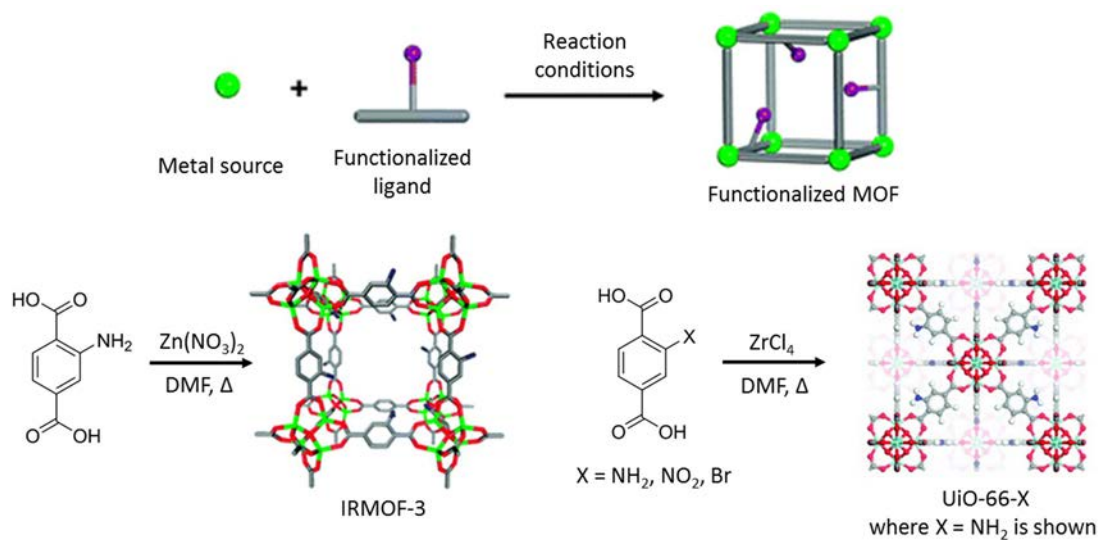

Figure 1.1. Scheme of the classical route to introduce functionalities on the pores of MOFs.[4,8]

1.1. Non-covalent interactions

1.1.1.   Guest molecules adsorption and exchange

The most studied PSM processes in MOFs are the ones related to non-covalent interactions between the framework and neutral molecules or ions. These PSMs include guest removal/adsorption and ion exchange (in charged frameworks). One of the original examples of removal and adsorption of neutral molecules was carried out by Yaghi and co-workers in 1995. They showed that uncoordinated pyridine molecules could be removed from the as-synthesised Co(BTC)(pyr)$_3$·(pyr)$_{0.66}$, and that the activated form could selectively adsorb aromatic molecules

by π-π stacking interactions.[10] In order to unambiguously proof the adsorption and desorption of molecules in MOFs, Rosseinsky and co-workers characterized this process by single crystal X-ray diffraction.[11] Through this technique, they observed that EtOH solvent molecules from the as-synthesised material ($Ni(bipy)_{2/3}(NO_3)_2 \cdot EtOH$) were reversibly removed and adsorbed (Figure 1.2). In addition to the retention of the initial cell parameters, the activated form of the structure could also adsorb N_2, H_2O, EtOH, MeOH and ^iPrOH.

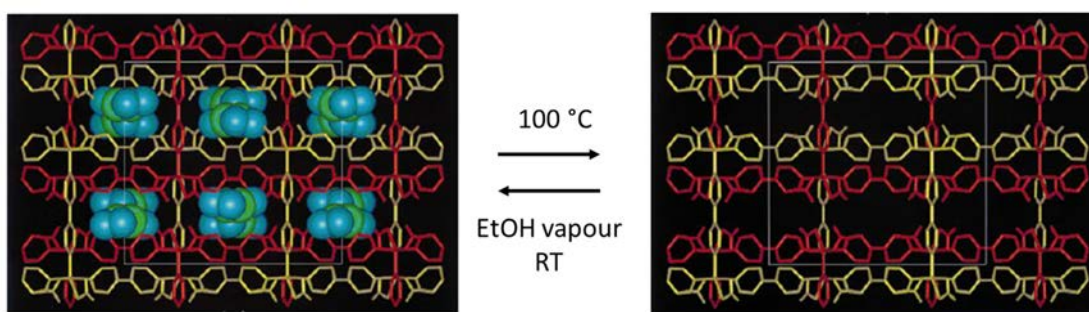**Figure 1.2**. Crystalline structure of $Ni(bipy)_{2/3}(NO_3)_2 \cdot EtOH$ in the as-synthesised (left) and activated form (right).[11]

As demonstrated by Cui and co-workers, positively charged ions can also be exchanged in MOFs.[12] They demonstrated that $H_2NMe_2^+$ cations of $(H_2NMe_2)_2Cd_3(C_2O_4)_4 \cdot MeOH \cdot 2H_2O$ could be fully replaced by NH_4^+, Na^+ or K^+ upon suspension in saturated solutions of NH_4Cl, NaCl or KCl. In this sense, Rosi and co-workers depicted interesting applications arising from ion exchange procedures in the anionic bio-MOF-1 ($Zn_8(ad)_4(BPDC)_6O \cdot 2Me_2NH_2$), where ad is adenine and BPDC is biphenyl-4,4'-dicarboxylic acid.[13,14] Dimethylammonium (DMA) cations, which balance the negative charge of the framework, could be exchanged with tetramethylammonium (TMA), tetraethylammonium (TEA) and tetrabutylammonium (TBA) via post-synthetic ion exchange. Although the bulkier anions led to lower S_{BET} values when assessed for N_2 sorption, bio-MOF-1 exchanged with TMA and TEA showed increasing adsorption of CO_2.[13] This MOF was also proved useful for sensing a series of lanthanide cations when DMA was exchanged with Sm^{3+}, Tb^{3+}, Yb^{3+} and Eu^{3+}(Figure 1.3). These visible and NIR-emitting cations could be protected from water quenching, making them useful for biological applications.[14]
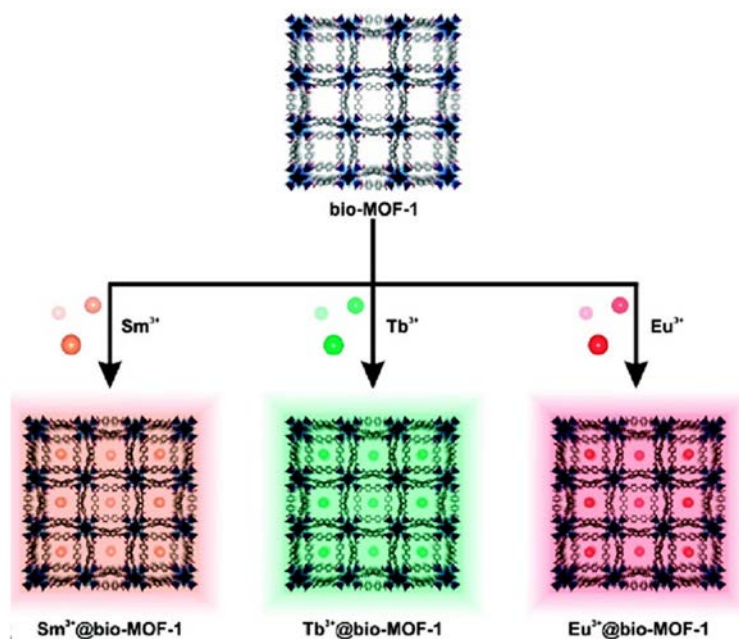
Figure 1.3. Scheme of lanthanide ions exchange in a negatively charged MOF (bio-MOF-1) for sensing applications.[14]

1.1.2. Coordinative interactions

PSMs that involve coordinative interactions between the MOF scaffold and the desired coordinating species might implicate either open metal sites in the inorganic SBU, free coordinating groups in the organic building blocks or exchange of ligands or metal ions.

The strategy based on open metal sites uses these positions to coordinate new molecules. In this approach, solvent molecules are first removed during the activation process. Then, new coordinating molecules are coordinated to these metal sites. This method is also known as dative PSM. The first example of PSM using this strategy was carried out in the well-known HKUST-1. This MOF is built up from the assembly of Cu^{2+} ions and the organic ligand BTC, leading to a unit cell with formula $Cu_3(BTC)_2(H_2O)_3$. The water molecules coordinating the dicopper (II) tetracarboxylate building block can be removed under heating. The exposure of the dehydrated MOF to pyridine leads to coordination of this molecule to the Cu paddlewheel, fully replacing the initial water-coordinated sites.[15] Later, Farha and co-workers coined the term solvent assisted ligand incorporation (SALI) when they functionalized the Zr_6 oxocluster of NU-1000 via charge compensation and strong bonding of perfluoroalkane carboxylates (Figure 1.4).[16]
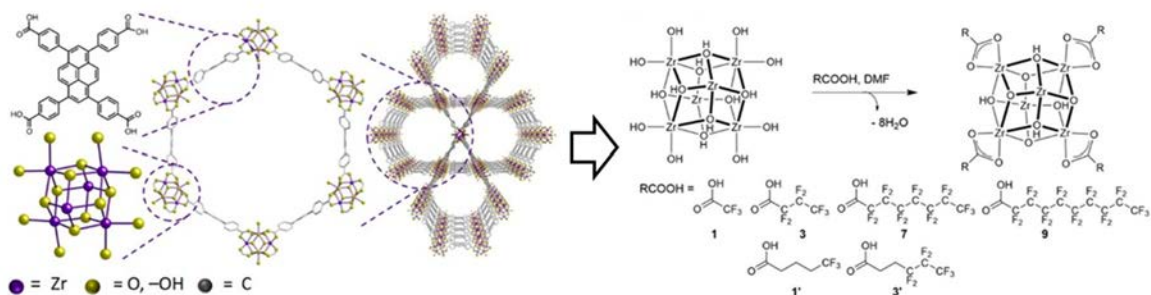
Figure 1.4. SALI process scheme in NU-1000.[16]

A second PSM strategy that uses coordinative interactions is based on using free functional groups of the organic building blocks that are able to coordinate metallic ions or organometallic complexes. This approach is also known as post-synthetic metalation.[17] In one of the first examples, Lin and co-workers showed that a homochiral MOF made of (*R*)-6,6'-dichloro-2,2'-dihydroxy-1,1'-binaphthyl-4,4'-bipyridine[18] can use the pyridine moiety of this ligand to coordinate with Cd^{2+} ions extending the structure. Then, these uncoordinated -OH groups were further reacted with $Ti(O^iPr)_4$ leading to a functionalization of one third of the ligands due to strong π-π stacking between the other organic units.

Later, in 2010, Yaghi and co-workers first synthesised a MOF with uncoordinated bipyridine moieties using the ligand 2,2'-bipyridine-5,5'-dicarboxylic acid (Figure 1.5).[19] In order to avoid coordination of the bipyridine group during solvothermal synthesis, the authors took advantage of the hard-soft acid-base theory of coordination chemistry. In this ligand, a different behaviour between the carboxylic acid and the bipyridine groups is evidenced. The bipyridine chelator is a soft ligand as it is mainly a π-acceptor, whereas the carboxylate is considered a hard ligand due to its σ-donating ability. With this knowledge in mind, the selection of an oxophilic metallic ion such as Al^{3+} directed the coordination of the carboxylic groups and left free 2,2'-bipyridine groups in MOF-253 [Al(OH)(bpydc), where bpydc is 2,2'-bipyridine-5,5'-dicarboxylic acid]. This scenario allowed $PdCl_2$ and $Cu(BF_4)_2$ to be incorporated through coordination with the bipyridine groups into this MOF by soaking them separately in acetonitrile.
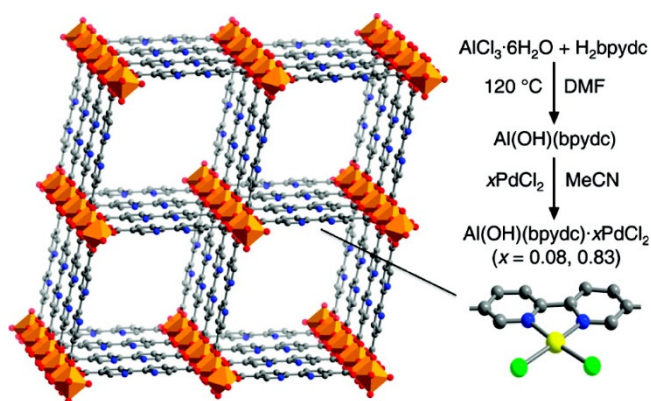
Figure 1.5. Structure of MOF-253 and subsequent metalation.[19]

Moreover, coordinative interactions in organic building units without available functional groups have also been reported. As an example, IRMOF-1 was metalated by Long and co-workers using $Cr(CO)_6$.[20] This MOF is build up from 1,4-benzenedicarboxylic acid (BDC) coordinated to Zn^{2+} ions ($Zn_4O(BDC)_3$). Therefore, the complexation with Cr^0 was carried out in the aromatic ring, leading to a piano stool complex (Figure 1.6).
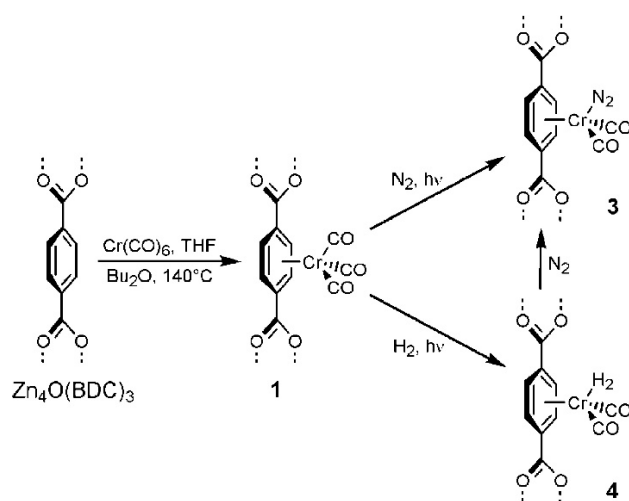

Figure 1.6. Scheme of the reactions followed to coordinate $Cr(CO)_6$ in the tag-less IRMOF-1.[20]

In addition to the coordination-based PSMs above exemplified, a strategy that was also implemented was the solvent assisted linker exchange (SALE). This method consists on suspending a synthesised MOF in a concentrated solution of an organic ligand containing the same number of coordinating sites and applying thermal energy when necessary. The final MOF undergoes the exchange of the initial ligand by the new organic molecule retaining the topology of the parental material (Figure 1.7).[21] This method for obtaining MOFs that cannot be synthesised *de novo* was proved useful for many subfamilies; even for the most "inert" frameworks such as UiO-66.[22]
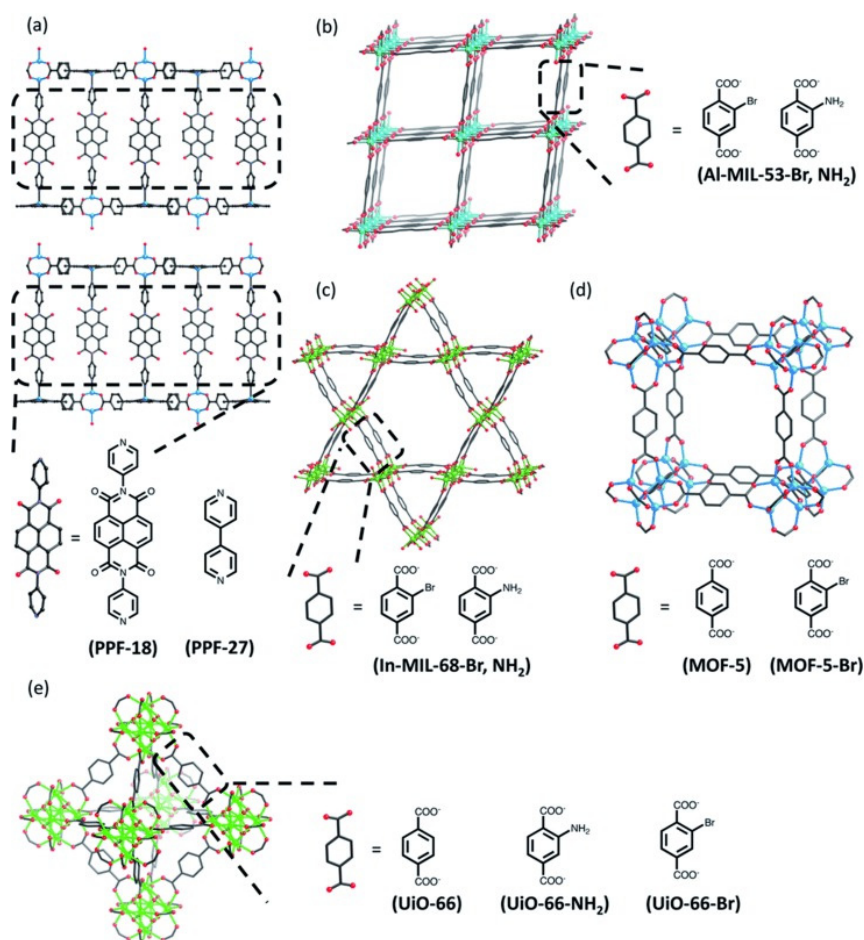
Figure 1.7. Examples of MOFs that have been successfully modified using the SALE approach.[21]

Such dynamic behaviour of MOFs was also confirmed by Kim and co-workers, who proved the metathesis of metallic ions in the SBU.[23] A Cd^{2+}-based MOF was subjected to immersion in a Pb^{2+} solution, and *in situ* single crystal X-ray diffraction (SCXRD) confirmed the decrease in occupancy of the Cd^{2+} ions, which underwent complete and reversible exchange with Pb^{2+} ions. This exchange could also be done with the lanthanide Dy^{3+} and Nd^{3+} ions (Figure 1.8).

Figure 1.8. Scheme of the metathesis between Pb^{2+} and Cd^{2+} in the MOF scaffold.[23]

1.2. Covalent interactions

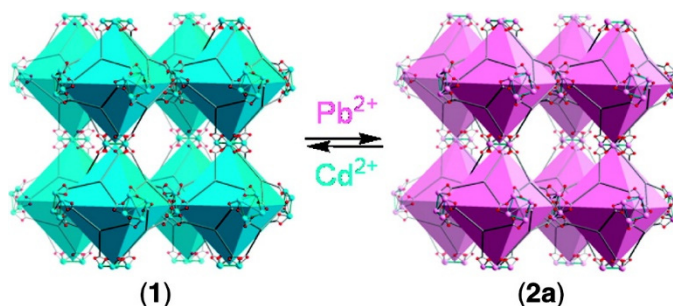Although non-covalent PSM of MOFs has been demonstrated to be an appealing strategy, as briefly summarized here, the strength of such interactions might somehow limit the performance of the new materials in some applications. In this sense, covalent interactions allow the inclusion of strongly attached organic moieties in the framework.

Covalent post-synthetic modification (CPSM) of MOFs is a very attractive and useful tool to introduce functional groups on the pore walls through organic reactions between the pendant functional groups located on the MOF pores and the selected reagents. By anchoring larger and more complex organic moieties in the channels and/or surface of the MOFs, a wider spectrum of materials that could not be synthesised using direct methods can be obtained. The most exploited MOFs for covalent derivatisation include the amino-tagged, aldehyde-tagged and the ones able to perform "click" chemistry (azide- or alkyne-tagged) (Figure 1.9). Other less common functionalities include thioethers, halides and alkenes.
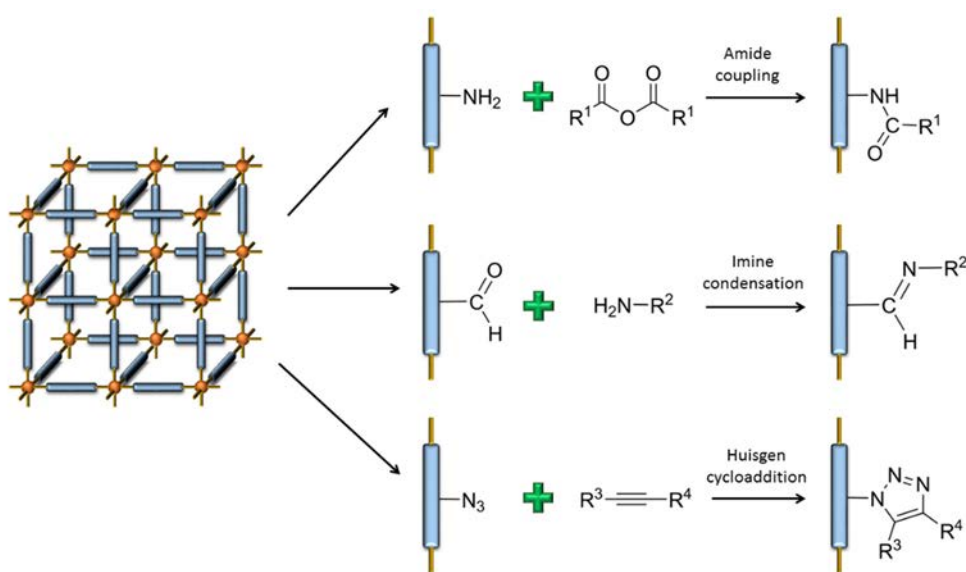
Figure 1.9. Scheme of some of the most representative CPSM reactions.

The first reported example of CPSM dates from 1999, when Lee and co-workers synthesised a series of MOFs based on the assembly of 1,3,5-tris(4-ethynylbenzonitrile)benzene derivatives with silver(I) trifluoromethanesulfonate (AgOTf).[24] In this work, they included pendant hydroxyl functional groups in the central benzene ring that were reacted with trifluoroacetic anhydride forming an ester (Figure 1.10). This quantitative reaction, which was the first proof that covalent reactions can be done on the MOF pore walls without affecting the framework integrity, was performed by exposing the MOF to vapours of the anhydride.

Figure 1.10. Reaction scheme of the first CPSM of a MOF.[24]

In 2000, Kim and co-workers showed the CPSM of a chiral MOF named POST-1.[25] The enantiopure chiral building block used in the synthesis of t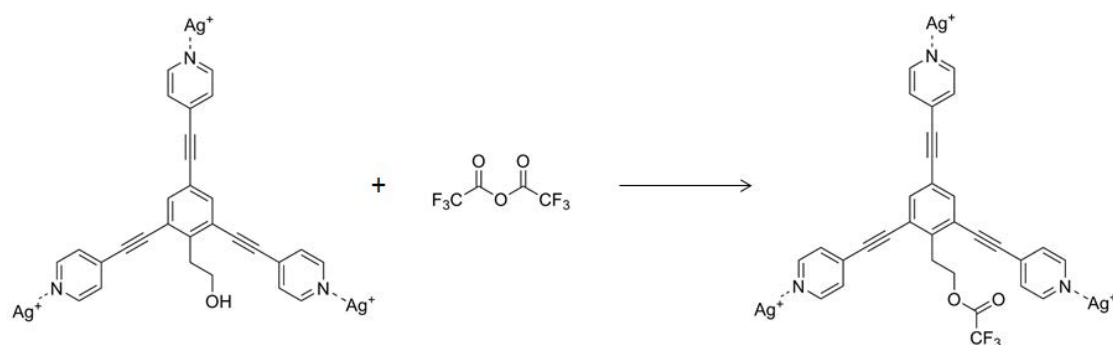his MOF presented pyridyl groups that are available on the pore walls. *N*-alkylation of the pyridyl groups was successfully achieved by suspending the MOF in a DMF solution of iodomethane. After 2 hours of exposure, the original pyridyl groups were quantitatively converted into *N*-methyl pyridinium ions and the overall charge of POST-1 changed from negative to positive. However, it was not until 2007 when Cohen and colleagues published the first work that set the basis for upcoming studies of CPSM of MOFs.[6] The organic reaction of an amine-tagged MOF (IRMOF-3) with acetic anhydride was monitored over time by simply suspending the MOF with the anhydride in CH_2Cl_2. ^{1}H-NMR spectroscopy of the digested sample served to confirm the formation of the amide bond, and ESI-MS analysis was used as an additional proof of the correct CPSM. Moreover, the XRPD pattern of the modified IRMOF-3 matched the as-synthesised one. The following year, Cohen's group subjected IRMOF-3 to systematic CPSMs using 10 more alkyl anhydrides (Figure 1.11).[26] This publication reported the protocol that is needed for demonstrating the CPSM of MOFs, which usually includes the digestion of the MOF for ^{1}H-NMR and ESI-MS analyses and study of the MOFs using TGA, XRPD and gas sorption (S_{BET}). In addition, they used single-crystal X-ray diffraction to show further evidence of covalent attachment.

However, IRMOF-3 might not be stable enough when subjecting it to harsh reaction conditions. In order to explore different organic reactions, robust amino-tagged MOFs such as MIL-53-NH$_2$(Al), MIL-101-NH$_2$(X), where X is Fe and Al, and UiO-66-NH$_2$[27–29] have been studied (Table 1.1). For instance, Férey, Stock and co-workers generated the formylated MIL-53-NH$_2$(Al) by reacting the as-synthesised MOF with formic acid at 70 °C for 3 hours.[30]
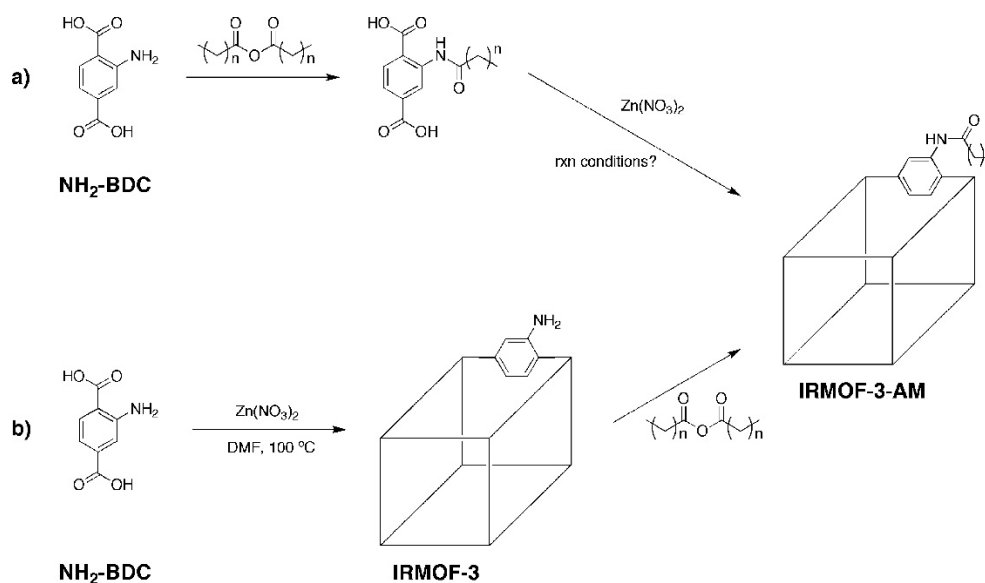
Figure 1.11. Illustration of two possible approaches to obtain a modified MOF: a) by previous reaction of the ligand with the desired organic compound and subsequent synthesis of MOF; and b) by pre-synthesising a tagged MOF and further reacting its pendant group with the reagent.[26]

Finally, "click chemistry" that classically consists on the Huisgen cycloaddition,[31] a copper (I)-catalyzed reaction between an azide and an alkyne, has also been exploited for CPSM of MOFs (Figure 1.12). Both approaches, tagging the MOF with an azide[32,33] or an alkyne,[34] have been demonstrated.
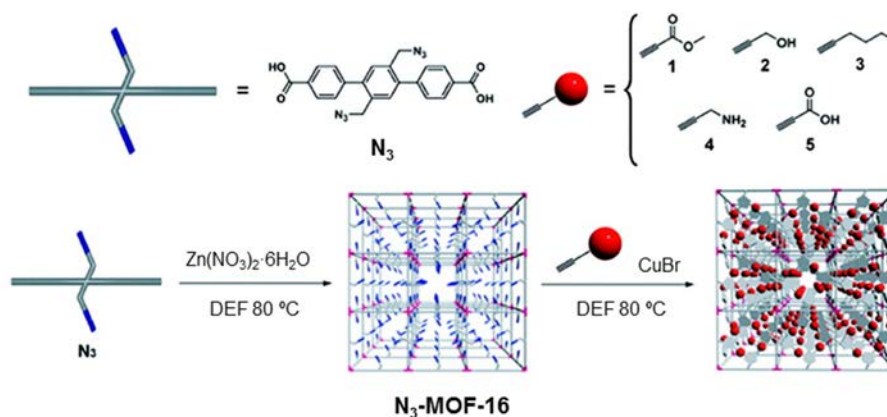
Figure 1.12. Synthesis of an azide-tagged MOF and subsequent click CPSM reaction using an organic molecule with an alkyne group.[32]

1.3. Synthetic strategies for the CPSM of MOFs

Once classified the different CPSM of MOFs based on the nature of the interaction with the modifying agent (ionic species, organometallic complexes and organic molecules), this section is dedicated to summarize the experimental protocols used so far to conduct CPSMs of MOFs.

1.3.1. Solvent immersion

The vast majority of the CPSM performed in MOFs are based on soaking the desired crystalline material in a solution containing the organic reagent and usually applying temperature with time in order to exceed the reaction energy barrier while retaining the crystallinity of the MOF. This strategy was proved useful in the first examples of CPSMs of IRMOF-3,[6,35] and it was extended to the efficient CPSM of other MOFs, such as UMCM-1-NH$_2$,[36] DMOF-1-NH$_2$,[36] UiO-66-NH$_2$[28] and MIL-53-NH$_2$(Al), among many others.[30] Table 1.1 summarizes some of the reactions performed on MOFs using this approach.

Table 1.1. Summary of some of the most representative CPSM examples.

MOF	Reagent	Reaction name	Formed group	Solvent	Temperature and time	Ref.
IRMOF-3 DMOF-1-NH$_2$ UMCM-1-NH$_2$ UiO-66-NH$_2$	Alkyl anhydrides	Amide coupling	Amide	Chloroform	RT (3 days) or 55 °C (1 day)	26,27,36
UiO-66-NH$_2$	Acetic anhydride	Amide coupling	Amide	DCM	RT (14 days)	28
MIL-53-NH$_2$(Al)	Formic acid	Amide coupling	Amide	-	70 °C (3 hours)	30
MOF-LIC-1	Acetic acid	Amide coupling	Amide	DMF (wet crystals)	120 °C (1 hour)	37
MOF-LIC-1	Ethylisocyanate	Ethylurea coupling and hydrolysis	Urethane	DMF (wet crystals)	120 °C (1 hour)	37
MIL-53-NH$_2$(Al)	Diphosgene	Isocyanate coupling	Isocyanate	THF	RT (18 hours)	38
MIL-53-NH$_2$(Al)	Thiophosgene	Isothiocyanate coupling	Isothiocyanate	THF	55 °C (18 hours)	38
1*	2,4-dinitrophenyl-hydrazine	Carbonyl addition	Hidrazone	DMF	RT (7 days)	39
ZIF-90	NaBH$_4$	Oxidation	Alcohol	MeOH	60 °C (24 hours)	40
ZIF-90	Ethanolamine	Imine condensation	Imine	MeOH	60 °C (3 hours)	40
IRMOF-3	Salicylaldehyde	Imine condensation	Imine	Toluene	RT (7 days)	35
UMCM-1-NH$_2$	2-pyridine-carboxaldehyde	Imine condensation	Imine	Toluene	RT (5 days)	41

SIM-1	Docecylamine	Imine condensation	Imine	MeOH	RT (1 day)	42
2*	Ethidium bromide monoazide	Huisgen cycloaddition	Triazole	DMF	RT (12 hours)	34
N_3-MOF-16	Azide ligand (Figure 1.12)	Huisgen cycloaddition	Triazole	DEF	80 °C (1 day)	32
DMOF-N_3 MIL-68-N_3(In)	Phenylacetylene	Huisgen cycloaddition	Triazole	THF	RT (1 day)	43
UiO-68-alkyne	Azides	Huisgen cycloaddition	Triazole	DMF	60 °C (1 day)	44
UiO-68-allyl	Ethanethiol	Thiol-ene reaction	Thioether	THF	RT (14 hours + UV light)	45
PEPEP-PIZOF-15 PEPEP-PIZOF-19	Nitrile oxides	Nitrile oxide-alkyne cycloaddition	Isoxazole	MeOH/H_2O	RT (71 hours)	46

*1: [$Zn_4O(L^1)_3(OH_2)_2$]·4 DMF, built up from $Zn(NO_3)_2$·6H_2O, and 2-formyl-biphenyl-4,4'-dicarboxylic acid (L1).

*2: $C_{26}H_{16}O_4N_2Zn$, built up from $Zn(NO_3)_2$·6H_2O, 2,6-naphthalenedicarboxylic acid (NDC) and 3-[(trimethylsilyl)ethynyl]-4-[2-(4-pyridinyl)ethenyl]pyridine (L1).

1.3.2. Continuous flow CPSM

Continuous flow approach consists on performing a desired transformation in a dynamic system where the involved species react in short times once they get in contact. In 2016, Nune and co-workers showed the PSM of UiO-66-NH_2 using microfluidics devices.[47] They synthesised the MOF *in situ* and subsequently mixed it with acetic acid or fluorescein isothiocyanate. The mixture was allowed to pass through an oven at 120 °C, which permitted the crystallization of the MOF inside the droplets. Using this continuous manufacturing method, it was demonstrated that the PSM reaction can take place in 1 hour, whereas the batch process might last from 6 to 20 days. In addition, this method allowed a production rate of 5 mg·h^{-1} and a space-time yield of 0.5-1 kg·m^{-3}·day^{-1}.

1.3.3. Spray-drying CPSM

The use of spray-drying equipment, also known for the scalable synthesis of MOFs,[48] was used by Maspoch and co-workers with the aim to confine CPSM organic reactions at the droplet scale (Figure 1.13).[49] The selected reaction was the Schiff-base condensation reaction between amide and aldehyde groups. Amino- and aldehyde-tagged MOFs (UiO-66-NH_2 and ZIF-90) were suspended in ethanol and mixed with aromatic aldehydes or alkyl amines, respectively. This

mixture was sprayed at 130 °C leading to the formation of imine bonds in times as short as few seconds. Maximum conversion rates of 20 % (UiO-66-NH$_2$ with 2-pyridinecarboxyaldehyde) and 42 % (ZIF-90 with butylamine) were attained.
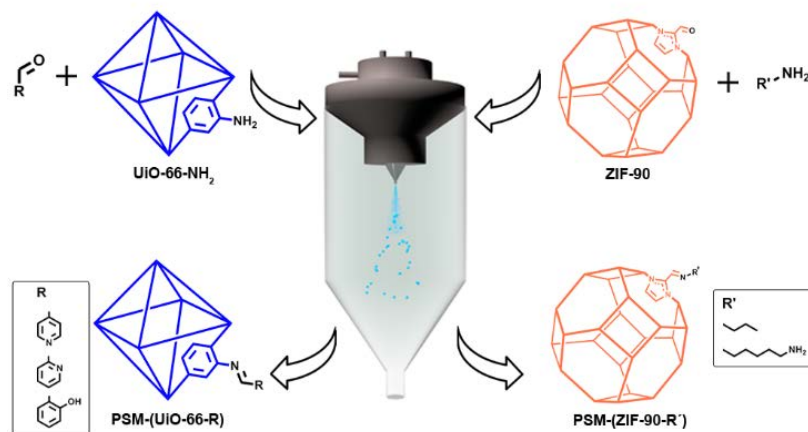

Figure 1.13. Scheme of the tested reactions for CPSM of UiO-66-NH$_2$ and ZIF-90 using the spray-drying technique.[49]

1.3.4. Solvent-free CPSM

Decreasing the amount of solvent not only in organic reactions but also in other chemistry processes (*e.g*. washing steps) is of main importance when concerning scaling up reactions for safety reasons and environmental issues. To date, several strategies have been developed for the solvent-free (or with little amount of it) CPSM of MOFs.

MOF-LIC-1, built up from Gd^{3+} ions and NH$_2$-BDC, was subjected to (almost) solvent-free CPSM by Gamez and co-workers.[37] The reaction of the amino pendant groups of the MOF with either acetic acid or ethylisocyanate led to the formation of an amide or an urethane bond, respectively. Wet crystals (DMF) were placed in a test tube that was introduced in a Pyrex tube containing the reagent and subsequently sealed. One hour at 120 °C led to evaporation of the reagent and diffusion to the MOF cavities where the reaction took place.

Based on a solvent-free CPSM approach, Telfer and co-workers synthesised a Zn-based MOF with a modified 4,4'-biphenyldicarboxylate ligand containing the thermolabile *tert*-butylcarbamate (NHBoc) group.[50] Thermolysis of the final solid (microwave, 150 °C/4hours) or a suspension in DMF/DEF (oven, 200 °C/2hours) allowed the deprotection of the amino group upon decomposition of Boc in CO$_2$ and isobutylene. The initial Boc cleavage supressed MOF interpenetration due to steric hindrance. Thus, its decomposition not only unmasked reactive amino groups, but also enlarged the voids of the MOF.

Remarkably, Ranocchiari, Van Bokhoven and co-workers developed a solvent-free CPSM by mixing solid MOFs with vapours of the desired organic reagent, also known as vapor-phase post-synthetic modification (VP-PSM) (Figure 1.14).[51] The authors performed Schiff-base condensations between a series of amino-tagged MOFs [IRMOF-3, MIXMOF-5, UiO-66-NH$_2$] and aldehydes. The heating (100-120 °C) of the MOF with 1.5 equivalents of the reagents in a Schlenk tube under vacuum led to the formation of imine bonds. Moreover, they could prove the formation of amide bonds by mixing UiO-66-NH$_2$ with vapours of different anhydrides. This reaction did not occur in the less robust MOFs, as the carboxylic acid by-product affected the integrity of the crystals. Using this method, the authors reduced the reaction time from 1-5 days (conventional solvent methods) to 16 hours (Figure 1.14).
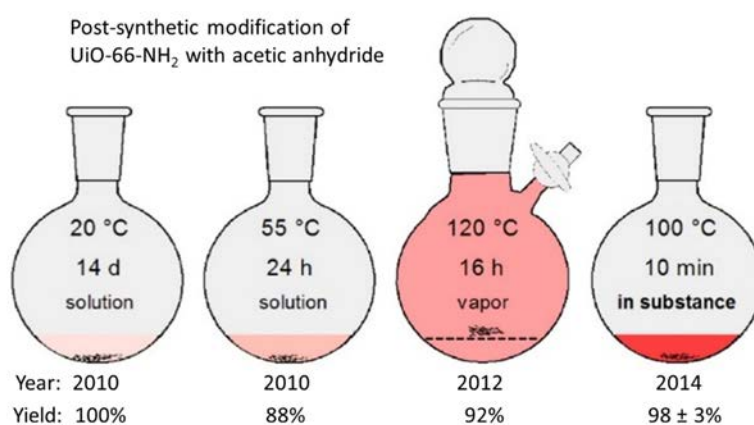

Figure 1.14. Illustration of the evolution of CPSM methods using different conditions of solvent, temperature and time.[52]

In order to reduce the time employed in post-synthetic reactions, Wuttke and co-workers performed solvent-free CPSM by heating solid mixtures of MOF and organic reagents (Figure 1.14).[52] Three amino-tagged MOFs [MIL-53-NH$_2$(Al), MIL-101-NH$_2$(Al) and UiO-66-NH$_2$] were reacted with several carboxylic acids, acid chlorides and acid anhydrides, leading to amide moieties. The temperature applied (60-120 °C) allowed the reagents to fully melt, thus acting as solvent while reacting with the functionalities of the MOFs in 10 minutes. Also, Richardson and co-workers recently proved a solvent-free PSM in a IRMOF-9-like MOF with pendant dimethylthiocarbamate moieties (WUF-1) (Figure 1.15).[53] Newmann-Kwart rearrangement, consisting on a position exchange between the sulphur and the oxygen in the thiocarbamate group, was achieved by applying 285 °C to the solid MOF. The reaction took place quantitatively.
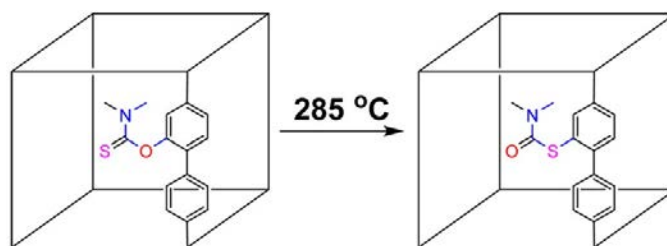
Figure 1.15. Scheme of the Newmann-Kwart rearrangement occurring in a solid MOF under heating.

2. Results and discussion

As reported in Chapter 3, the photothermal effect exhibited by MOFs was proved efficient for their activation. In this chapter, the use of this light-to-heat conversion process for the post-synthetic covalent functionalization of MOFs is evaluated.

2.1. CPSM of UiO-66-NH$_2$

UiO-66-NH$_2$ was selected to test the UV-Vis light mediated CPSM as it is known to exhibit a strong photothermal behaviour (Chapter 3), and also contains pendant amino groups in the channels that are available for organic reactions once properly activated. These amino groups are able to react with organic acid anhydrides leading to the formation of amide moieties. Maleic (MA) and benzoic (BA) anhydrides were chosen as they are found in solid state but present moderately low melting points, 51-56 °C and 38-42 °C, respectively.

2.1.1. CPSM setup and procedure

In a typical CPSM experiment, 25 mg of MOF (in this case, UiO-66-NH$_2$) and a predetermined number of molar equivalents of the anhydride (relative to the amino group of the unit cell) were gently ground in a mortar for 5 minutes to create a homogeneous solid mixture. The sample was then spread between two quartz slides and the light guide was placed at a distance of 7 cm (500 mW·cm^{-2}). The setup used for these experiments was identical to that used in the previous chapter (Figure 2.1). Irradiation was applied during 15 minutes in each side of the quartz sandwich and the resulting solid was washed with DMF (2 x 10 mL), soaked in DMF for 24 hours, and then washed with acetone (4 x 10 mL). The washed material was digested in 120 μL of 5% HF in D$_2$O and 500 μL of DMSO-d_6 for further ^{1}H-NMR analysis.
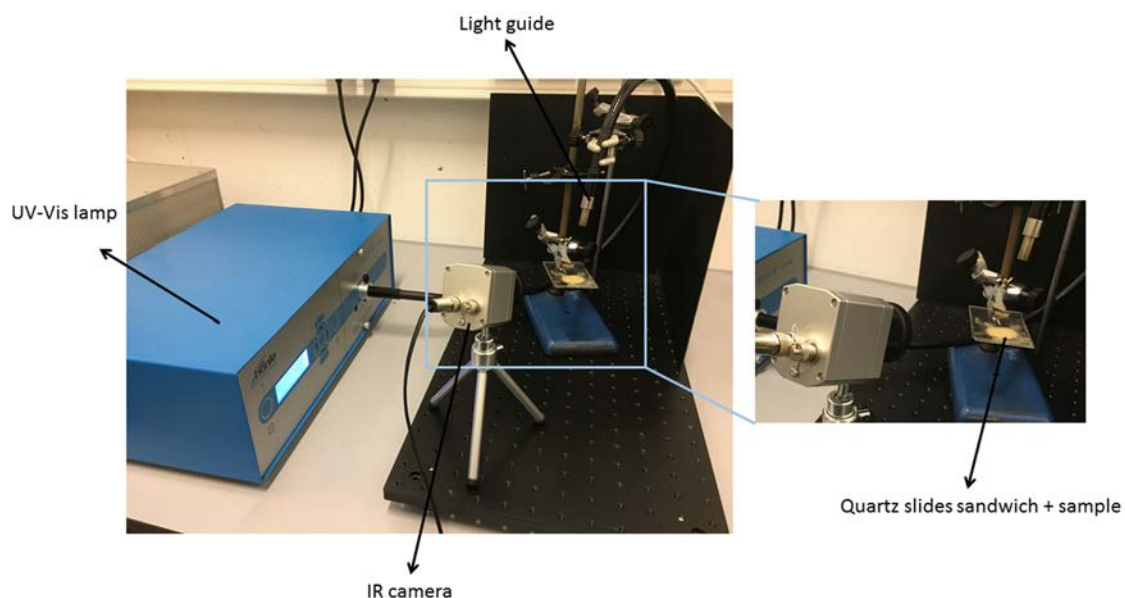
Figure 2.1. Setup employed for the light-induced CPSM of MOFs.

2.1.2. UiO-66-NH$_2$ synthesis and activation

UiO-66-NH$_2$ was synthesised following a previously reported method (Section 3.1).[54] This synthesised MOF was then activated as reported in Chapter 3. This activation process was done by irradiating (300-650 nm at 500 mW·cm^{-2}) 100 mg of UiO-66-NH$_2$ for 30 minutes. The S$_{BET}$ value after this photothermal activation was of 936 m^2·g^{-1} (Figure 2.2). Also, its stability after activation was confirmed by XRPD (Figure 2.3).
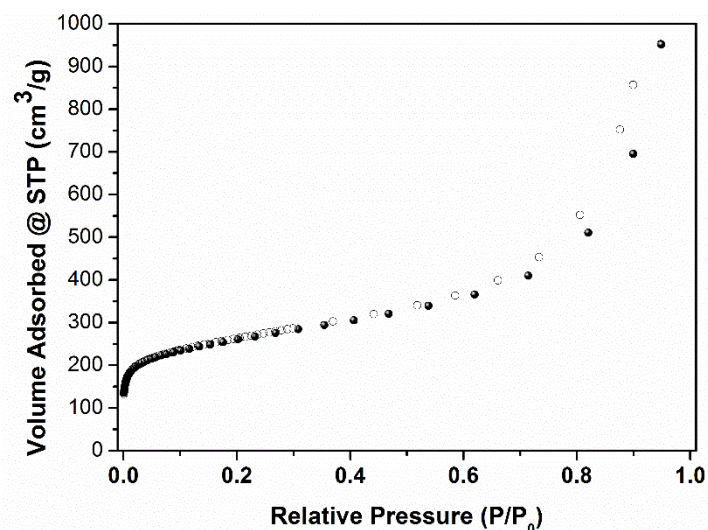

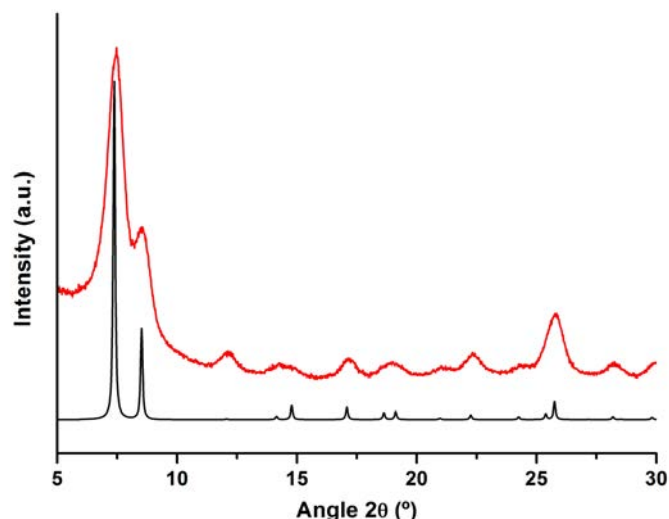**Figure 2.2.** N$_2$ adsorption isotherm of the photothermally activated UiO-66-NH$_2$.

Figure 2.3. XRPD patterns of the simulated UiO-66-NH$_2$ (black) and activated (red) UiO-66-NH$_2$.

2.1.3. Photothermal effect of UiO-66-NH$_2$ and anhydrides under CPSM conditions

In an initial step, the light-to-heat conversion of the amount of MOF used (25 mg) was assessed in order to identify the maximum temperature that it can reach. In this case, 25 mg of UiO-66-NH$_2$ irradiated with a UV-Vis lamp at 500 mW·cm^{-2} for 30 minutes reached a temperature of 78 °C. This temperature is lower than that reached when using 100 mg (140 °C), thus confirming the dependence between the exhibited photothermal effect and the amount of irradiated sample (Figure 2.4).
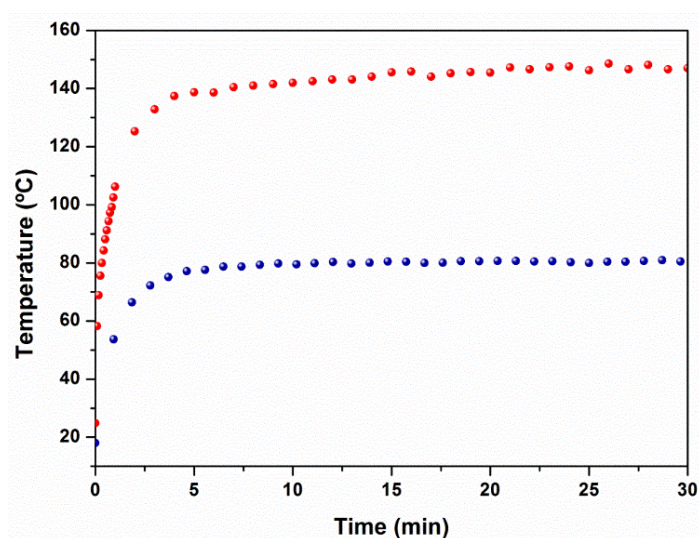

Figure 2.4. Change in temperature over time for 100 mg (red) and 25 mg (blue) of UiO-66-NH$_2$ irradiated at 500 mW·cm^{-2} (light guide-to-sample distance: 7 cm) for 30 minutes.

Also as a control experiment, and to demonstrate that anhydrides are not exhibiting photothermal effect, three equivalents (relative to the amino group of the unit cell) of MA and BA were placed in a quartz slide and irradiated alone under the same conditions (500 mW·cm^{-2} for 30 minutes). Both MA and BA reached only 27 °C and 30 °C, respectively, thus confirming that these organic molecules do not exhibit photothermal effect.

2.1.4. CPSM optimization of UiO-66-NH$_2$ with maleic anhydride

The first tests of light-induced CPSM were carried out by mixing UiO-66-NH$_2$ with MA (m.p. 51-56 °C). The pendant amino groups in the MOF scaffold might react with this anhydride forming amide moieties, as shown in Figure 2.5a. In order to prove the feasibility of the proposed strategy, the initial CPSM tests were performed using 1, 3 and 6 equivalents of MA, namely (UiO-66-MA)$_x$, being x the number of equivalents. It should be mentioned that all the experiments were carried out by triplicate. Following the designed protocol, the three mixtures were irradiated for 30 minutes (15 minutes each side) at 7 cm of light guide-to-sample distance (500 mW·cm^{-2}). The maximum temperatures attained were similar for each experiment (78-82 °C) (Figure 2.6a). A clear colour change was noticed after UV-Vis irradiation (Figure 2.5b). Also, melted reagent was still observed in the quartz slides sandwich before the washing step. This observation permitted to conclude that the temperature reached by the MOF was high enough to melt the MA along the 30 minutes of irradiation. Once irradiated, the mixture was washed with DMF and acetone. XRPD of the resulting solids confirmed that all of them retain the crystallinity (Figure 2.6b).

^{1}H-NMR characterization (Figure 2.7) confirmed the CPSM of the MOF and allowed the calculation of the conversion rate (*vide infra*). By comparing the peak at 7.34 ppm from the unreacted 2-aminoterephthalic (NH$_2$-BDC) with the one at 6.58 ppm corresponding to the alkenyl hydrogens due to the CPSM with MA, we could demonstrate that the reaction takes place. The conversion rates were calculated to be 70.0 ± 0.4 % for (UiO-66-MA)$_1$, 85.0 ± 1.0 % for (UiO-66-MA)$_3$ and 83.0 ± 0.3 % for (UiO-66-MA)$_6$. These conversion rate values indicated that there is a clear influence when using one or three equivalents of MA, while there is no significant increase when using six equivalents. In addition, the standard deviations resulting from the triplicate reactions revealed homogeneity of the conversion rates among the repeated experiments.
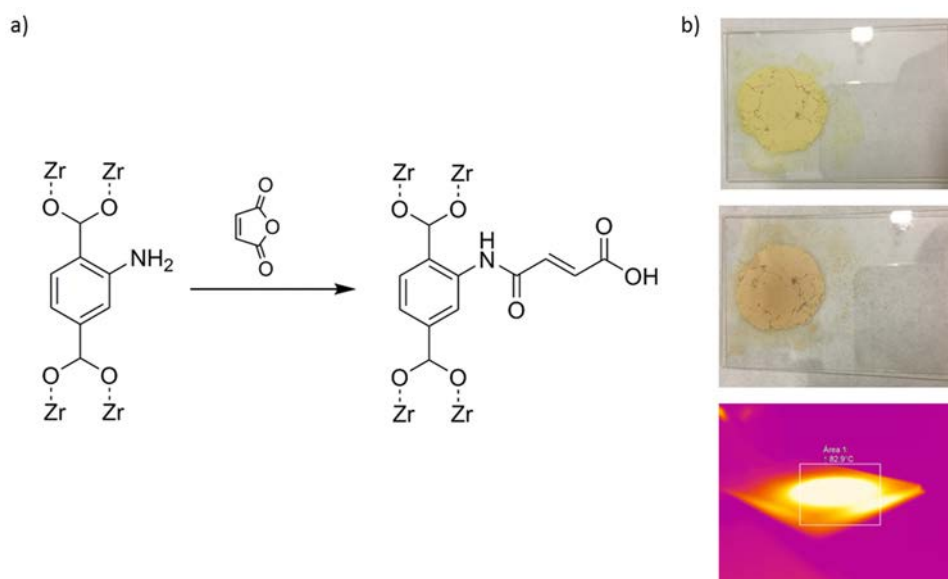
Figure 2.5. a) Scheme of the reaction between the amino moiety of UiO-66-NH$_2$ and MA. b) Photos of the formation of (UiO-66-MA)$_3$ upon UV-Vis irradiation (500 mW·cm^{-2}) of UiO-66-NH$_2$ and MA: before (top), after (middle) and infrared camera image during irradiation (down).
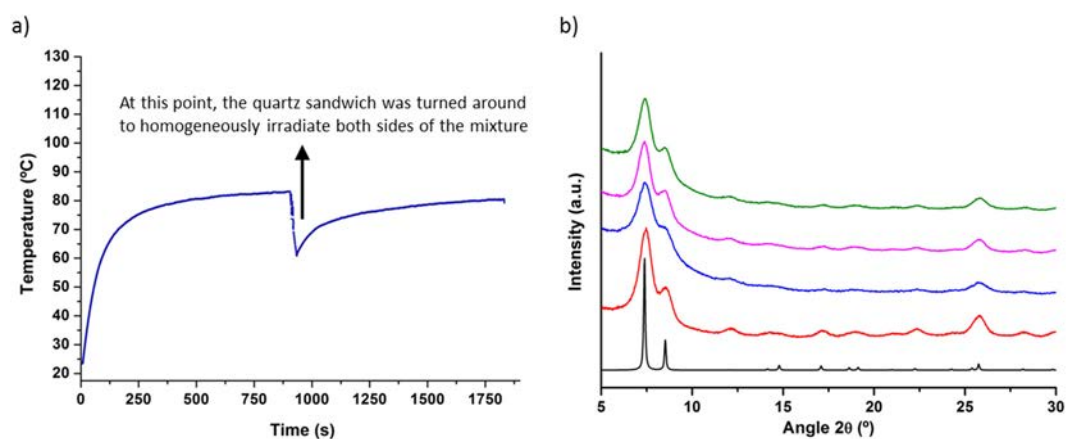
Figure 2.6. a) Photothermal plot of the formation of (UiO-66-MA)$_3$ upon UV-Vis irradiation of UiO-66-NH$_2$ and MA at 500 mW·cm^{-2}. b) XRPD patterns for synthesised (UiO-66-MA)$_x$ (blue: x = 1; pink: x = 3; green: x = 6), activated UiO-66-NH$_2$ (red) and simulated UiO-66-NH$_2$ (black).
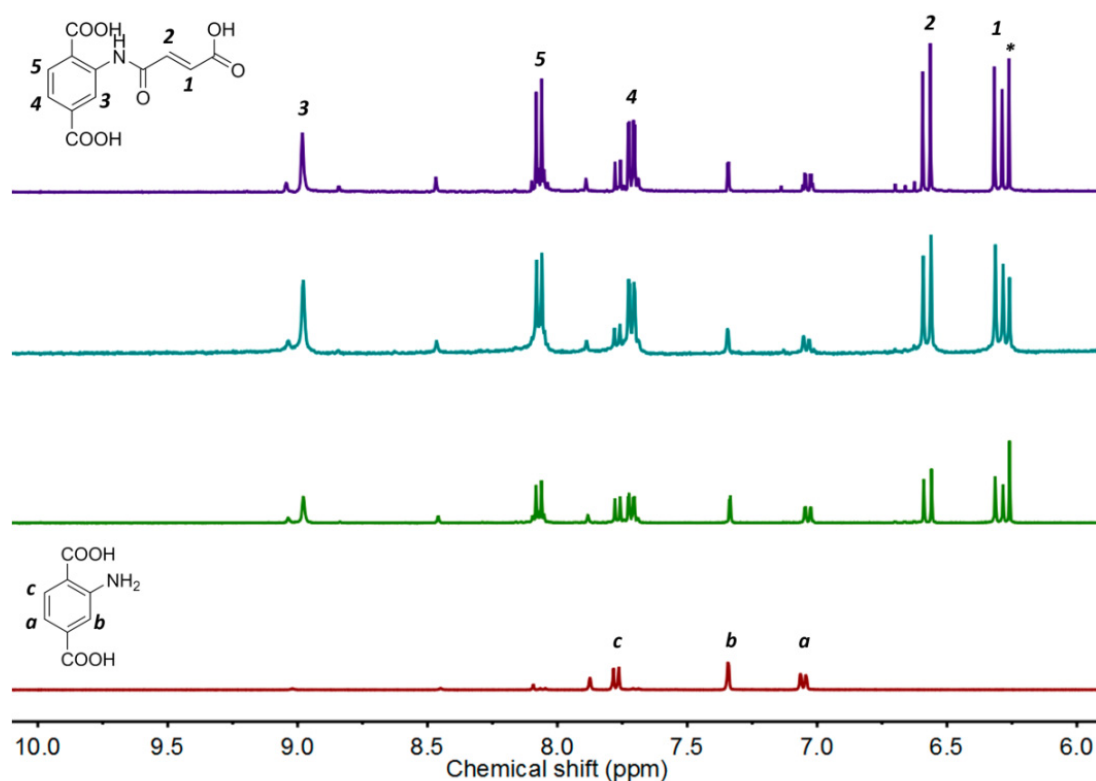
Figure 2.7. ^{1}H-NMR spectra of digested (UiO-66-MA)$_x$ at molar ratios (NH$_2$-BDC:MA) of 1:1 (green; x = 1), 1:3 (blue; x = 3) or 1:6 (purple; x = 6), as compared to the spectrum of activated UiO-66-NH$_2$ (red). *Peak attributed to maleic acid. NMR solvent: DMSO-d_6/HF.

Moreover, the formation of the amide bond was further proved through electrospray-ionization mass spectrometry (ESI-MS) analysis. The digestion of the sample (UiO-66-MA)$_3$ using 120 μL of 5% HF in D$_2$O allowed to break the Zr-O coordination bonds of the MOF generating the corresponding zirconium fluoride salt (ZrF$_4$). After evaporation of the excess acid under a N$_2$ gas flow overnight, the organic building blocks were ready to be solubilized in EtOH and be analysed. The peak at m/z = 278.0 matched the molecular formula of the desired amide product [C$_{12}$H$_8$NO$_7$]$^-$ (*m/z* = 278.0) (Figure 2.8).

Figure 2.8. ESI-MS spectrum of digested (UiO-66-MA)$_3$.

At this point, the N$_2$ adsorption isotherm of (UiO-66-MA)$_3$ was measured at 77 K and showed a S$_{BET}$ value of 699 m^2·g^{-1} (Figur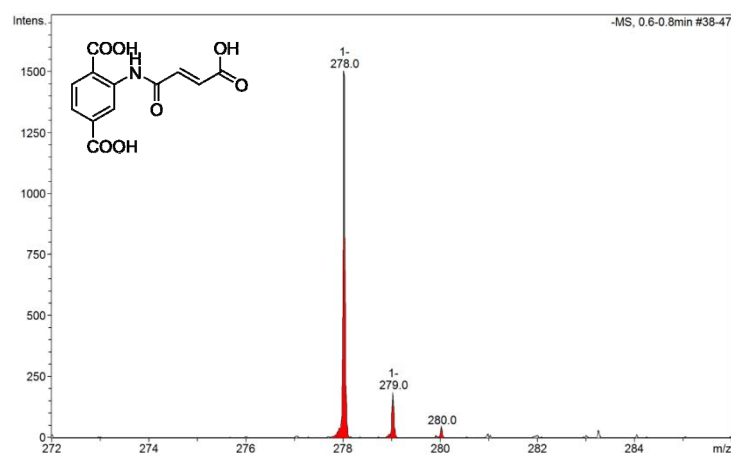e 2.9), which is a smaller value compared with the as-synthesised UiO-66-NH$_2$ (936 m^2·g^{-1}). This result is in agreement with the CPSM of the MOF as the formation of the amide groups leads to sterically bulkier substituents than the original amino groups.
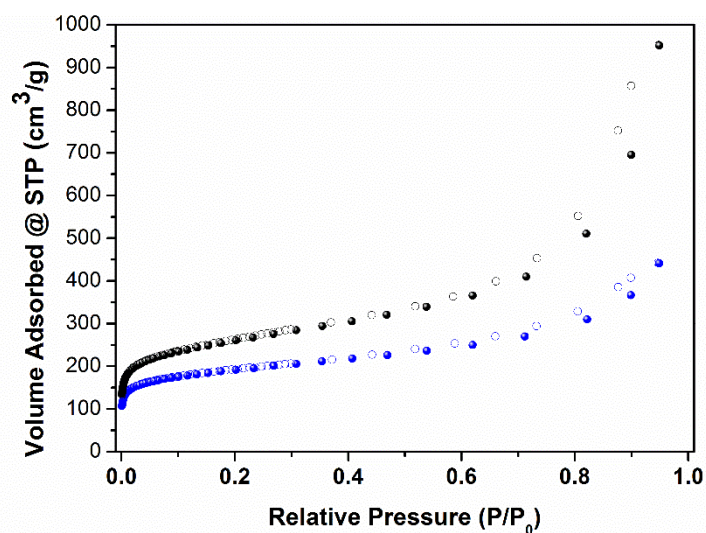
Figure 2.9. N$_2$ sorption isotherm of the photothermally activated UiO-66-NH$_2$ (black) and (UiO-66-MA)$_3$ (blue).

Consequently, we set the optimal molar ratio of NH$_2$-BDC:MA to be 1:3. The next step was to determine the influence of the irradiance on the (UiO-66-MA)$_3$ mixture. In order to characterize the influence of the distance between the light guide and the sample, we irradiated the mixture at 5 cm (900 mW·cm^{-2}) instead of 7 cm (500 mW·cm^{-2}) for 30 minutes. Although such conditions were more aggressive and the maximum temperature reached was of 118-120 °C, the crystalline integrity of the MOF was maintained, as confirmed by XRPD (Figure 2.10a). The conversion rate

of this experiment was of 79 ± 1.5 %, slightly less than the reaction performed at 500 mW·cm^{-2}, revealing that the irradiance did not influence the post-synthetic conversion rate.

Irradiation time was another parameter that should be optimized. Upon melting of MA, the required time to diffuse into the pores of the solid UiO-66-NH$_2$ might have an impact in the conversion rate. The assessment of time as an experimental variable was carried out by irradiating the UiO-66-NH$_2$ and MA mixture at 500 mW·cm^{-2} for 60 minutes instead of the original 30 minutes. The initial UV-Vis irradiance was kept constant as it was proved to be the optimum for the reaction rate of (UiO-66-MA)$_3$, which led to a maximum temperature of 78-80 °C. Even though the time exposure was doubled, the crystallinity of the sample was retained (Figure 2.10b). Here, the conversion rate was of 83 ± 4.9 %; almost the same value than the CPSM experiment for 30 minutes (Figure 2.11).

Thus, it was concluded that the optimum conditions for the UV-Vis mediated CPSM of UiO-66-NH$_2$ with MA were using a ratio of 1:3 (NH$_2$-BDC:MA), an irradiance of 500 mW·cm^{-2} and 30 minutes of exposure (15 each side). Table 2.1 summarizes the results of the described experiments.
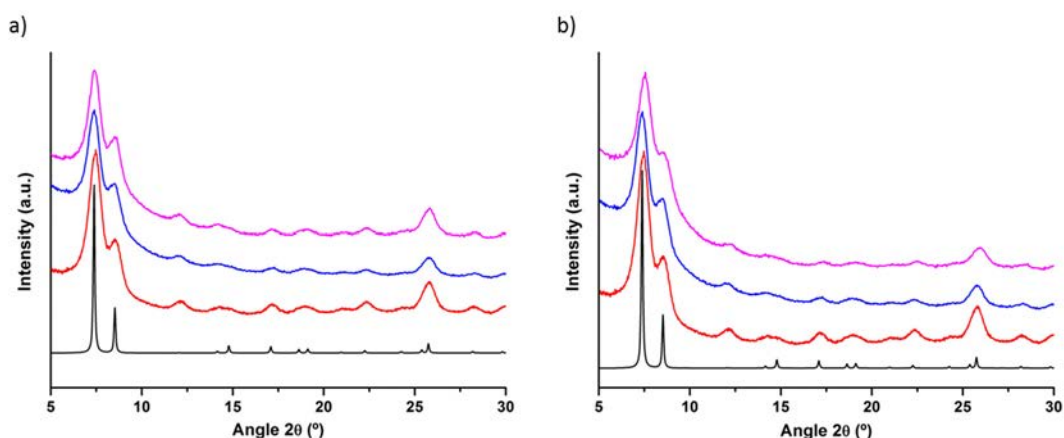
Figure 2.10. a) XRPD patterns for synthesised (UiO-66-MA)$_3$ irradiated at either 500 mW·cm^{-2} (blue) or 900 mW·cm^{-2} (pink), as compared to those for activated UiO-66-NH$_2$ (red) and simulated UiO-66-NH$_2$ (black). b) XRPD patterns for (UiO-66-MA)$_3$ irradiated for 30 minutes (blue) or 60 minutes (pink), as compared to those for activated UiO-66-NH$_2$ (red) and simulated UiO-66-NH$_2$ (black).
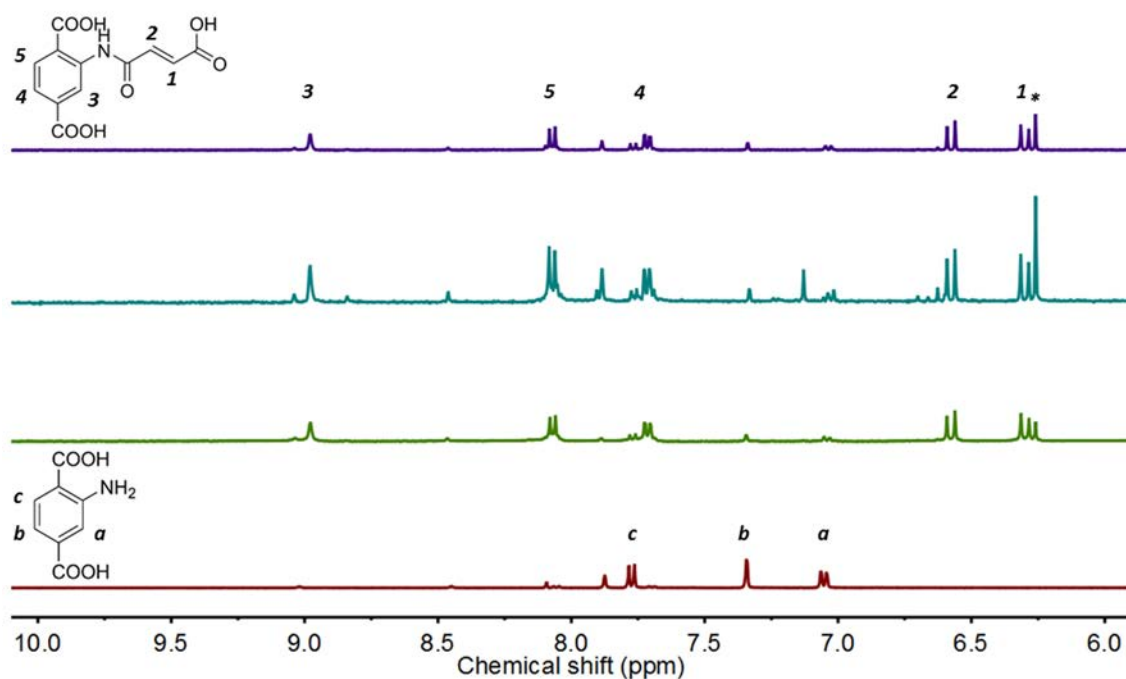
Figure 2.11. ^{1}H-NMR spectra of digested (UiO-66-MA)$_3$, irradiated at either 500 mW·cm^{-2} (green) or 900 mW·cm^{-2} (blue) for 30 minutes, and irradiated at 500 mW·cm^{-2} for 60 minutes (purple), as compared to the spectrum of activated UiO-66-NH$_2$ (red). *Peak attributed to maleic acid. NMR solvent: DMSO-d_6/HF.

Table 2.1. Summary of the optimization experiments for UiO-66-NH$_2$ with MA.

Equivalents	Irradiance (mW·cm^{-2})	Time (minutes)	Temperature reached (°C)	Conversion rate (%)
1	500	30	78 - 82	70 ± 0.4
3	500	30	78 - 82	85 ± 1.0
6	500	30	78 - 82	83 ± 0.3
3	900	30	118 - 120	79 ± 1.5
3	500	60	78 - 80	83 ± 4.9

2.1.5. CPSM of UiO-66-NH$_2$ with benzoic anhydride

Having proved the feasibility of the photothermally mediated CPSM between UiO-66-NH$_2$ and MA, which was subsequently optimized, the use of other organic acid anhydrides for the CPSM of the UiO-66-NH$_2$ was explored. To this end, BA was selected as the second acid anhydride (Figure 2.12a). BA has a melting point of 38-42 °C. Therefore, the thermal energy released during UV-Vis irradiation of the MOF should be enough to melt it. The optimised conditions for the previous example were also used to conduct this reaction. Thus, a solid

mixture of 25 mg of UiO-66-NH$_2$ and BA (NH$_2$-BDC:BA 1:3 molar ratio) was irradiated at 500 mW·cm^{-2} for 30 minutes. The maximum temperature reached during the UV-Vis irradiation of (UiO-66-BA)$_3$ was of 78-82 °C (Figure 2.13a). Noteworthy, the aspect of the resulting mixture was found as a slurry after light exposure instead of being a solid (Figure 2.12b). As above, XRPD analysis proved that the crystallinity of the MOF was retained (Figure 2.13b). In this case, the comparison between the integration of the unreacted NH$_2$-BDC peak (7.34 ppm) and one hydrogen of the amide moiety (8.14 ppm) revealed a conversion rate of 49.0 ± 1.0 % (Figure 2.14).
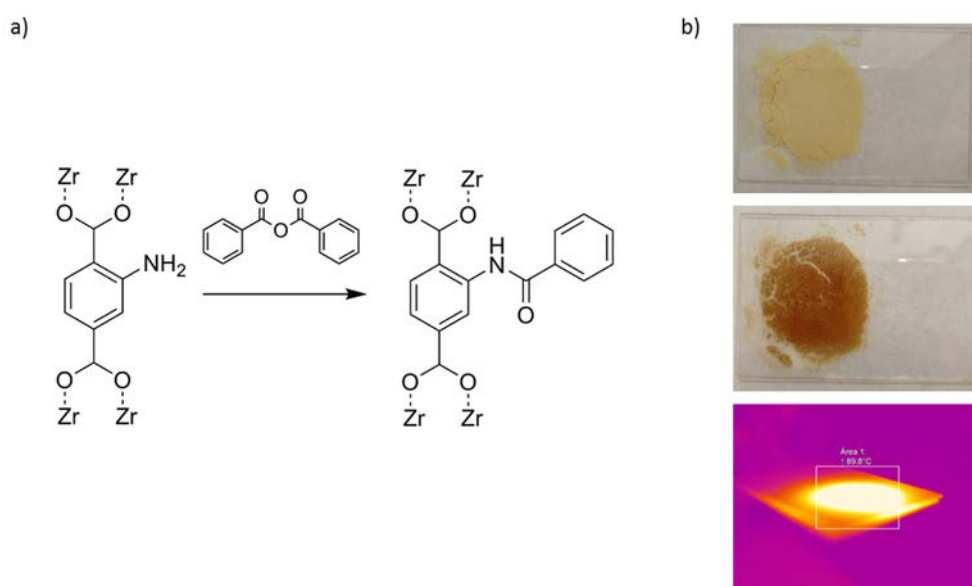
Figure 2.12. a) Scheme of the reaction between UiO-66-NH$_2$ and benzoic anhydride. b) Photos of the formation of (UiO-66-BA)$_3$ upon UV-Vis irradiation (500 mW·cm^{-2}) of UiO-66-NH$_2$ and BA: before (top), after (middle) and infrared camera image during irradiation (down).
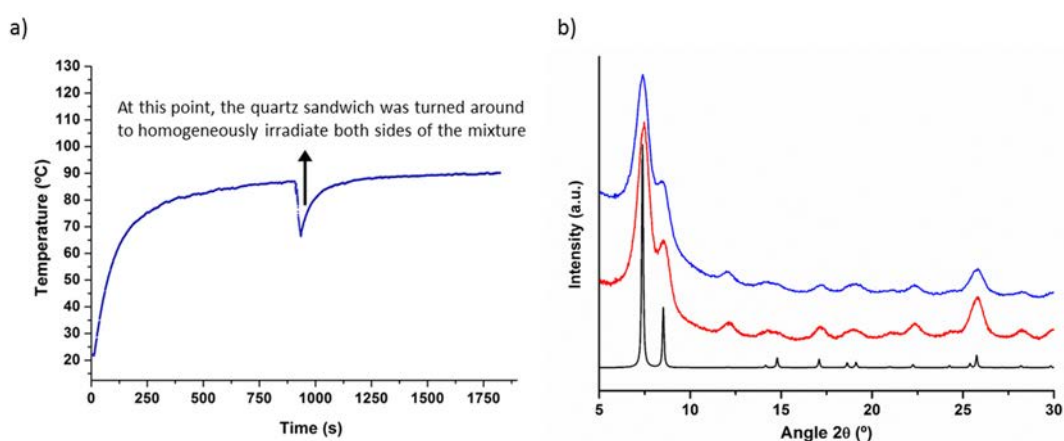
Figure 2.13. a) Photothermal plot of the formation of (UiO-66-BA)$_3$ upon UV-Vis irradiation of UiO-66-NH$_2$ and BA at 500 mW·cm^{-2}. b) XRPD patterns for synthesised (UiO-66-BA)$_3$ (blue), activated UiO-66-NH$_2$ (red) and simulated UiO-66-NH$_2$ (black).
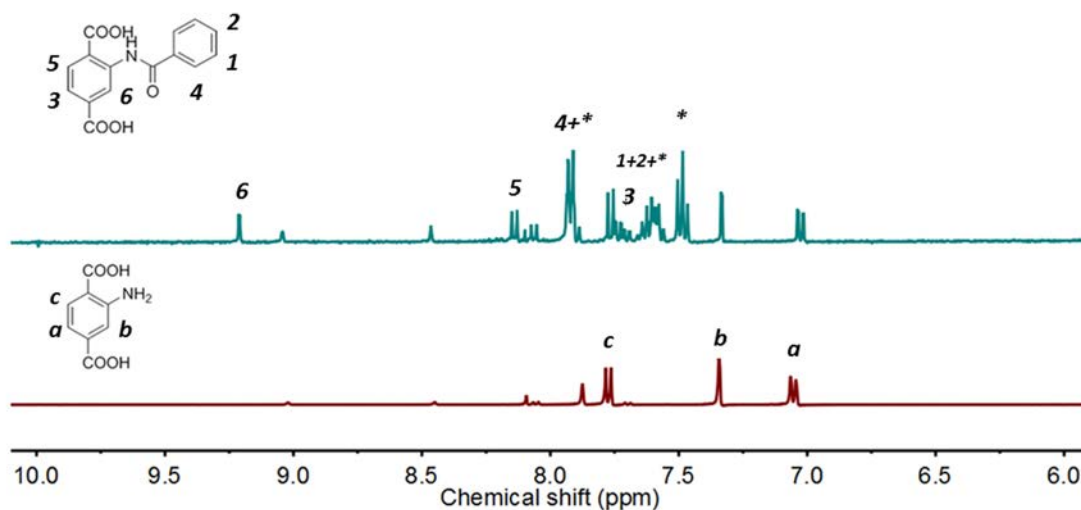
Figure 2.14. ^{1}H-NMR spectrum of digested (UiO-66-BA)$_3$ (blue) as compared to the spectrum of activated UiO-66-NH$_2$ (red). * Peaks attributed to benzoic acid. NMR solvent: DMSO-d_6/HF.

In order to complete the characterization of (UiO-66-BA)$_3$ and confirm the reaction between the amino group of the MOF and the BA, ESI-MS analysis after digestion of the mixture was also performed. The peak at m/z = 284.1 matched the molecular formula of the expected product [C$_{15}$H$_{10}$NO$_5$]$^-$ (*m/z* = 284.1) (Figure 2.15). Also, as expected, the CPSM of UiO-66-NH$_2$ led to a smaller surface area (S$_{BET}$ = 621 m$^2 \cdot$g^{-1}) (Figure 2.16).
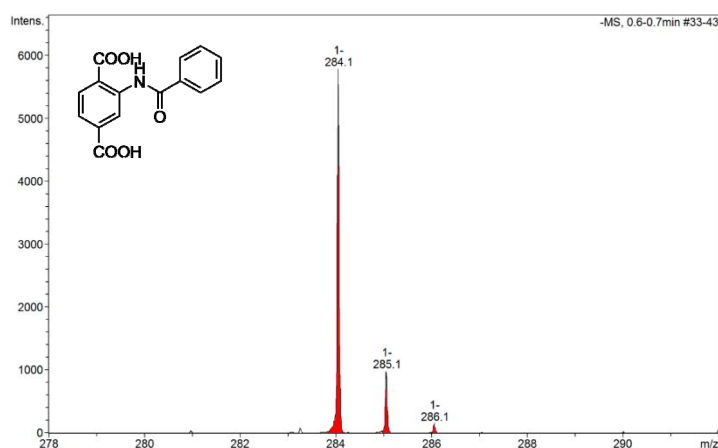
Figure 2.15. ESI-MS spectrum of digested (UiO-66-BA)$_3$.
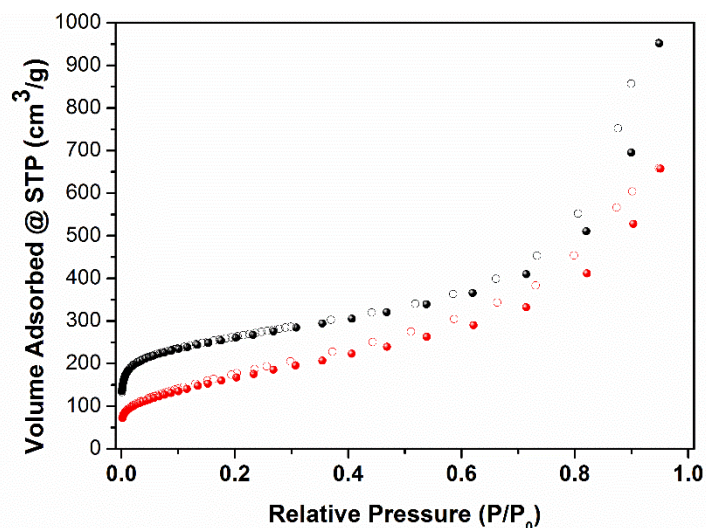
Figure 2.16. N$_2$ sorption isotherm of the photothermally activated UiO-66-NH$_2$ (black) and (UiO-66-BA)$_3$ (red).

2.2. CPSM of MIL-101-NH$_2$(Al)

Once the applicability of the photothermal CPSM was demonstrated with UiO-66-NH$_2$ for both MA and BA, this method was extended to other MOFs, such as MIL-101-NH$_2$(Al). This MOF presents bigger pore size than UiO-66-NH$_2$ and also shows photothermal effect when being irradiated with a UV-Vis lamp (300-650 nm) at 500 mW·cm^{-2} for 30 minutes.

2.2.1. Synthesis and activation of MIL-101-NH$_2$(Al)

MIL-101-NH$_2$-(Al) was synthesised following a previously reported method (Section 3.1).[52] Then, it was photothermally activated by spreading 100 mg of as-synthesised MIL-101-NH$_2$(Al) over a quartz slide and irradiating (300-650 nm) it at 500 mW·cm^{-2} for 30 minutes. Under these conditions, MIL-101-NH$_2$(Al) reached a maximum temperature of 165 °C (Figure 2.17a). Such behaviour was attributed to the strong absorption band centred at 360 nm in the solid-state UV-Vis spectrum (Figure 2.17b). After the UV-Vis light irradiation, XRPD studies confirmed that the crystallinity of the MOF was retained (Figure 2.17c) Also, its successful activation was corroborated by N$_2$ adsorption measurements at 77 K, from which a S$_{BET}$ of 2702 m^2·g^{-1} was found (Figure 2.17d).
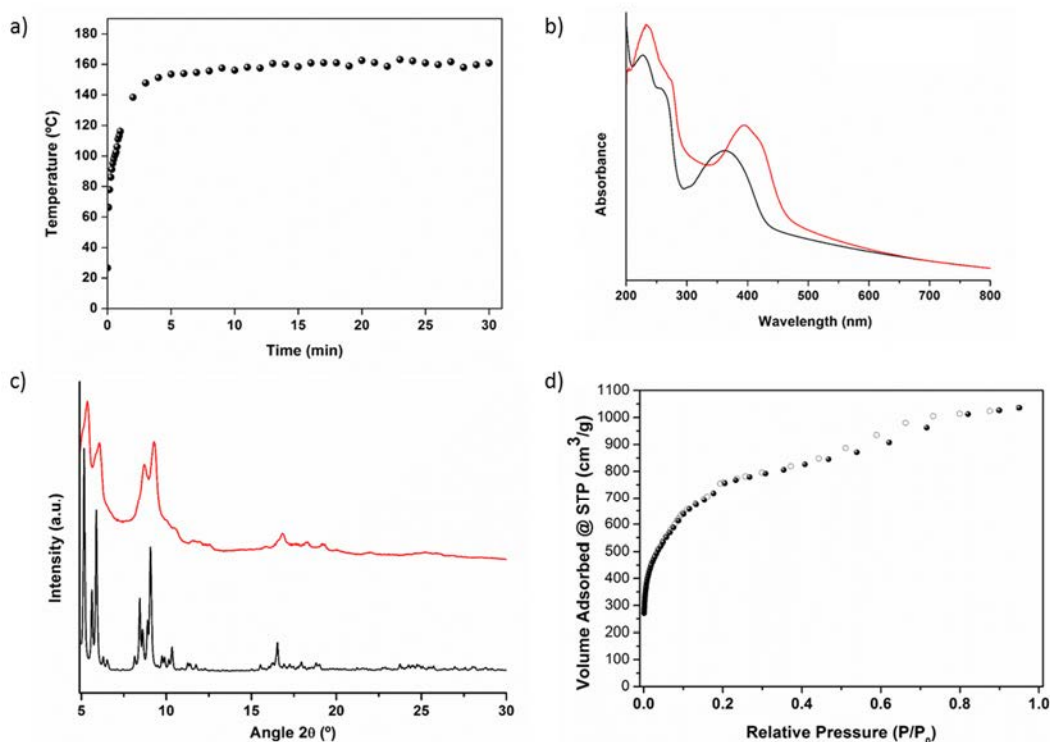
Figure 2.17. a) Photothermal plot of MIL-101-NH$_2$(Al) upon irradiation of 100 mg of sample at 500 mW·cm^{-2} for 30 minutes. b) UV-Vis solid-state spectra of MIL-101-NH$_2$(Al) (black) and NH$_2$-BDC (red). c) XRPD patterns of simulated MIL-101-NH$_2$(Al) (black) and synthesised MIL-101-NH$_2$(Al) (red). d) N$_2$ adsorption isotherm of synthesised MIL-101-NH$_2$(Al).

2.2.2. CPSM of MIL-101-NH$_2$(Al) with maleic and benzoic anhydride

With the goal to demonstrate the photothermal CPSM of MIL-101-NH$_2$(Al), the same reagents (MA and BA) were tested as per the UiO-66-NH$_2$ experiments. For this, we applied the same conditions optimized for (UiO-66-MA)$_3$. A solid mixture of 25 mg of MIL-101-NH$_2$(Al) with a 1:3 molar ratio (NH$_2$-BDC:MA) was placed in a quartz slides sandwich and irradiated at 500 mW·cm^{-2} for 30 minutes (15 minutes each side) (Figure 2.18). A maximum temperature of 80-82 °C was reached under these conditions (Figure 2.19a).

Once the resulting mixture was washed and dried, the solid was analysed by XRPD confirming that the post-functionalized MIL-101-NH$_2$(Al) retains the crystallinity of the parent MIL-101-NH$_2$(Al) (Figure 2.19b). The conversion rates were then calculated by performing ^{1}H-NMR of (MIL-101-(Al)-MA)$_3$ digested with 5 % HF (Figure 2.20). The integrated peaks in the ^{1}H-NMR spectra consisted on the unreacted NH$_2$-BDC (7.34 ppm) and the amide moiety formed after covalent reaction (6.58 ppm). Thus, upon calculation, it resulted in a conversion of 79.0 ± 1.4 %. In addition, the post-synthetic modification of MIL-101-NH$_2$(Al) was studied by mass spectrometry analysis of a digested sample. The peak at *m/z* = 278.0 matched with the expected

$[C_{12}H_8NO_7]^-$, also confirming the amide formation (Figure 2.21). Moreover, N_2 adsorption isotherm evidenced a high degree of reaction by showing a much lower S_{BET} value (549 $m^2 \cdot g^{-1}$) (Figure 2.22).
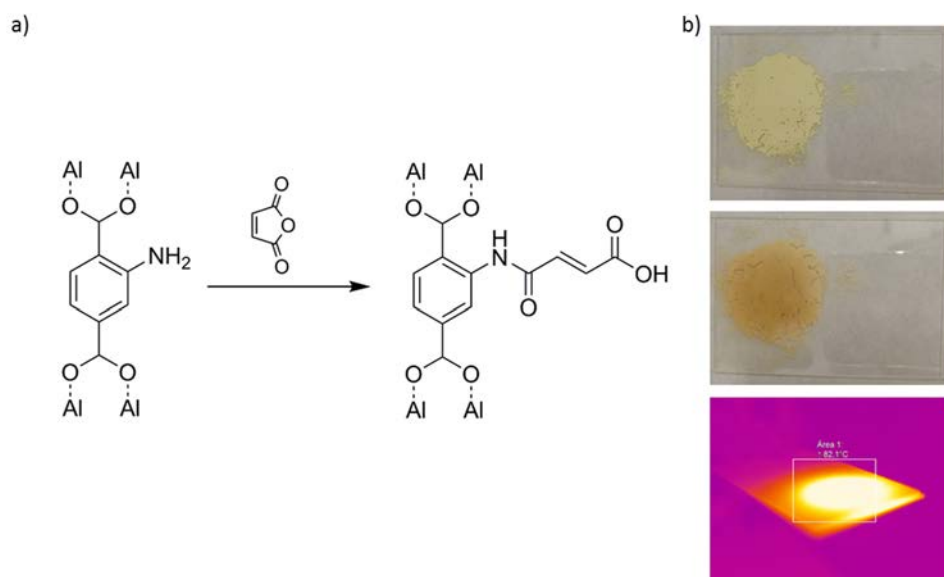
Figure 2.18. a) Scheme of the reaction between MIL-101-NH$_2$(Al) and MA. b) Photos of the formation of (MIL-101-(Al)-MA)$_3$ upon UV-Vis irradiation (500 mW·cm^{-2}) of MIL-101-NH$_2$(Al) and MA: before (top), after (middle) and infrared camera image during irradiation (down).

Figure 2.19. a) Photothermal plot of the formation of (MIL-101-(Al)-MA)$_3$ upon UV-Vis irradiation of MIL-101-NH$_2$(Al) and MA at 500 mW·cm^{-2}. b) XRPD patterns for synthesised (MIL-101-(Al)-MA)$_3$ (blue), as compared to those for activated MIL-101-NH$_2$(Al) (red) and simulated MIL-101-NH$_2$(Al) (black).
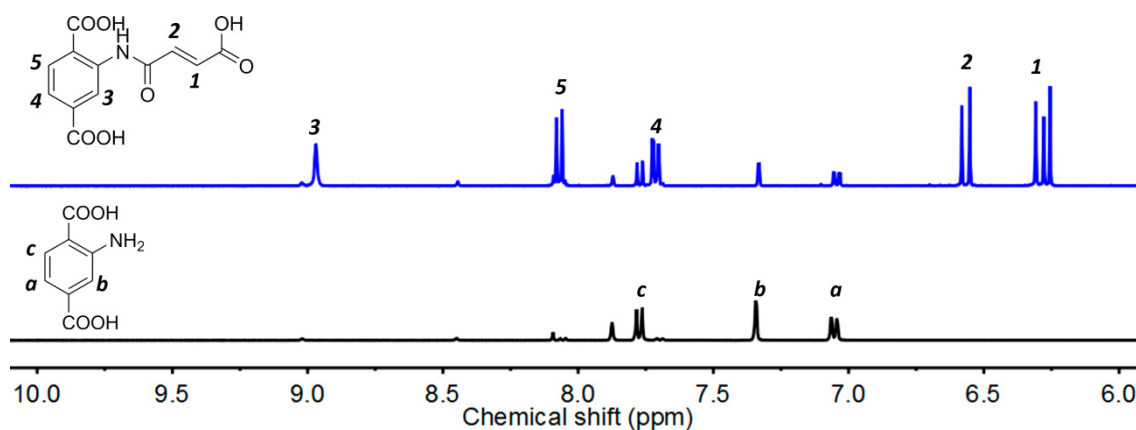
Figure 2.20. ^{1}H-NMR spectrum of digested (MIL-101-(Al)-MA)$_3$ (blue), as compared to that of activated MIL-101-NH$_2$(Al) (black). NMR solvent: DMSO-d_6/HF.
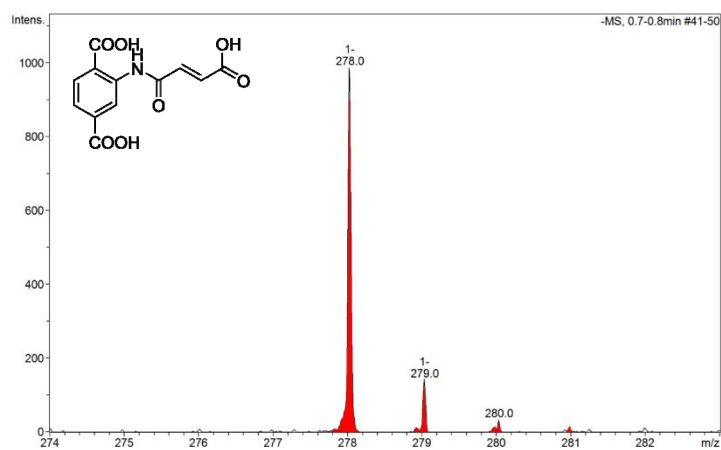
Figure 2.21. ESI-MS spectrum of digested (MIL-101-(Al)-MA)$_3$.
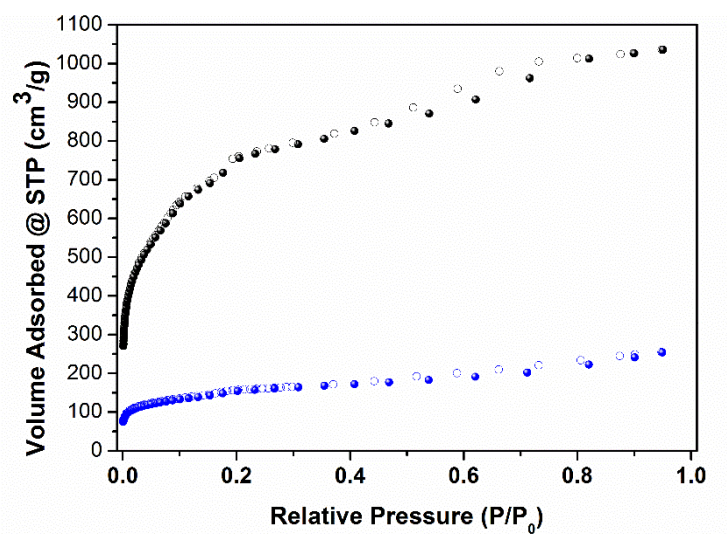
Figure 2.22. N$_2$ sorption isotherm of the photothermally activated MIL-101-NH$_2$(Al) (black) and (MIL-101-(Al)-MA)$_3$ (blue).

Finally, the CPSM using BA as the reagent was also assessed ((MIL-101-(Al)-BA)$_3$). In this experiment, the solid mixture ratio was kept constant (25 mg of MOF and 1:3 NH$_2$-BDC:BA ratio) as per the optimized reaction. However, the irradiation conditions could not be maintained because of the loss of crystallinity of the mixture when being irradiated with the UV-Vis lamp at 500 mw·cm^{-2} (light guide-to-sample distance = 7 cm) (Figure 2.23). We hypothesised that this loss of crystallinity was due to a network collapse induced by the metal clusters disconnection during a post-synthetic ligand exchange process between NH$_2$-BDC and benzoic acid (by-product during the amide formation). To further confirm this hypothesis, the ^{1}H-NMR spectrum of the digested powder was analysed indicating that 62.9 ± 1.8 % of the NH$_2$-BDC ligand was replaced by benzoic acid (Figure 2.24). Similar results were observed by Wuttke and co-workers,[52] where an amorphous solid was obtained after the CPSM of MIL-101-NH$_2$(Al) with benzoic acid.

For this reason, the CPSM of MIL-101-NH$_2$(Al) with BA was carried out at an irradiance of 265 mW·cm^{-2} (light guide distance of 9 cm). Under these new conditions, even though a ligand exchange of 32.5 ± 1.1 % was found, the resulting (MIL-101-(Al)-BA)$_3$ retained the crystallinity of the parent MOF (Figure 2.26b). This post-synthetic ligand exchange was also observed by Wuttke and co-workers.[52] during the amide formation. The maximum temperature reached by (MIL-101-(Al)-BA)$_3$ after 30 minutes of irradiation was of 68 °C, which was sufficiently high to fully melt BA (Figure 2.26a). After 30 minutes, the colour of the mixture changed forming a slurry (Figure 2.25), as also observed in (UiO-66-BA)$_3$.
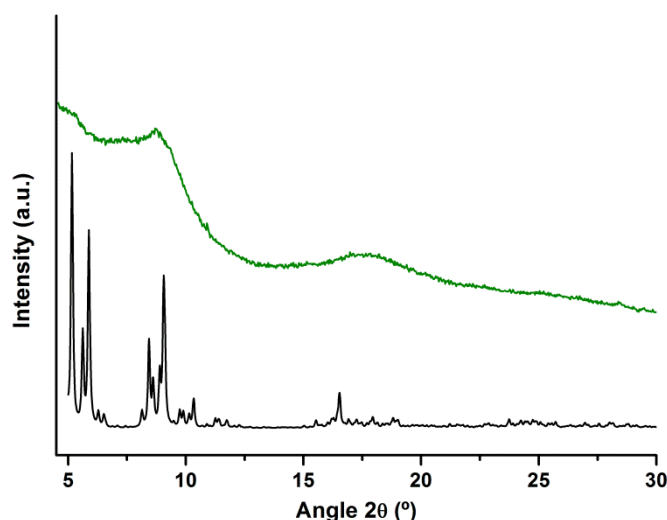
Figure 2.23. XRPD patterns for simulated MIL-101-NH$_2$(Al) (black) and synthesised (MIL-101-(Al)-BA)$_3$ (green) upon UV-Vis irradiation at 500 mW·cm^{-2} for 30 minutes.
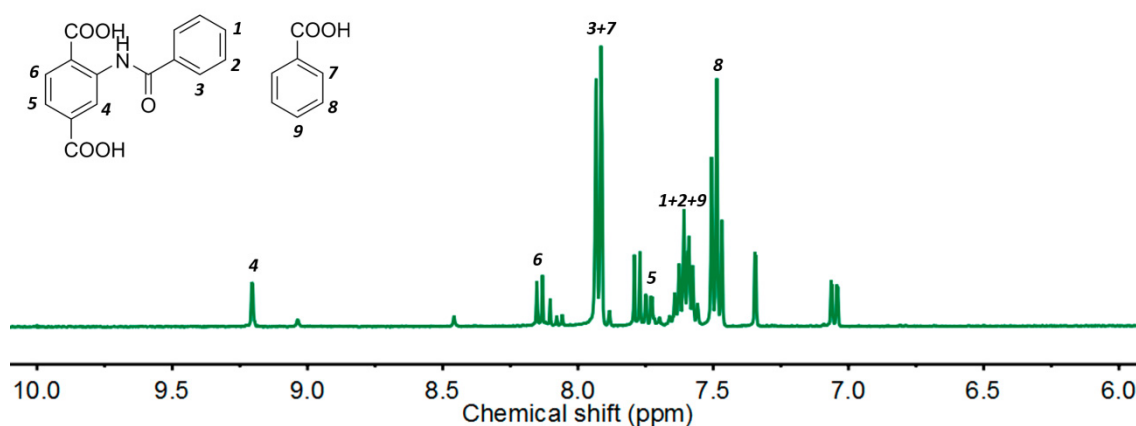
Figure 2.24. ^{1}H-NMR spectrum of digested (MIL-101-(Al)-BA)$_3$ upon irradiation at 500 mW·cm^{-2} (light guide-to-sample distance: 7 cm). NMR solvent: DMSO-d_6/HF.
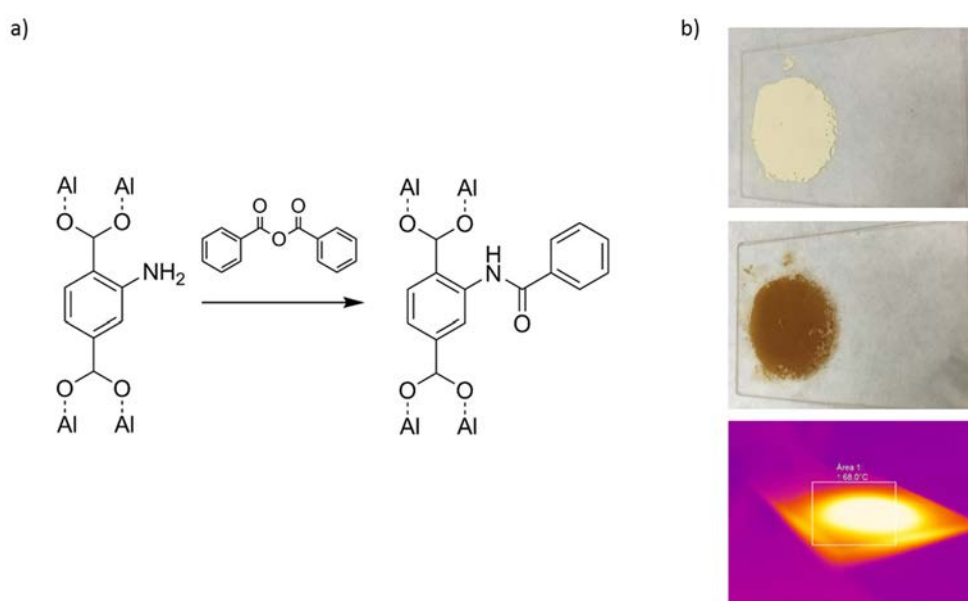
Figure 2.25. a) Scheme of the reaction between MIL-101-NH$_2$(Al) and benzoic anhydride. b) Photos of the formation of (MIL-101-(Al)-BA)$_3$ upon UV-Vis irradiation (265 mW·cm^{-2}) of MIL-101-NH$_2$(Al) and BA: before (top), after (middle) and infrared camera image during irradiation (down).
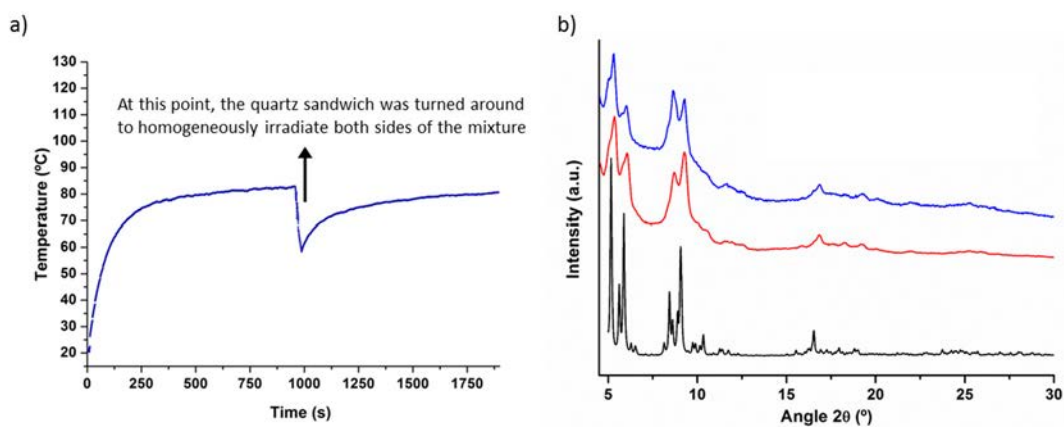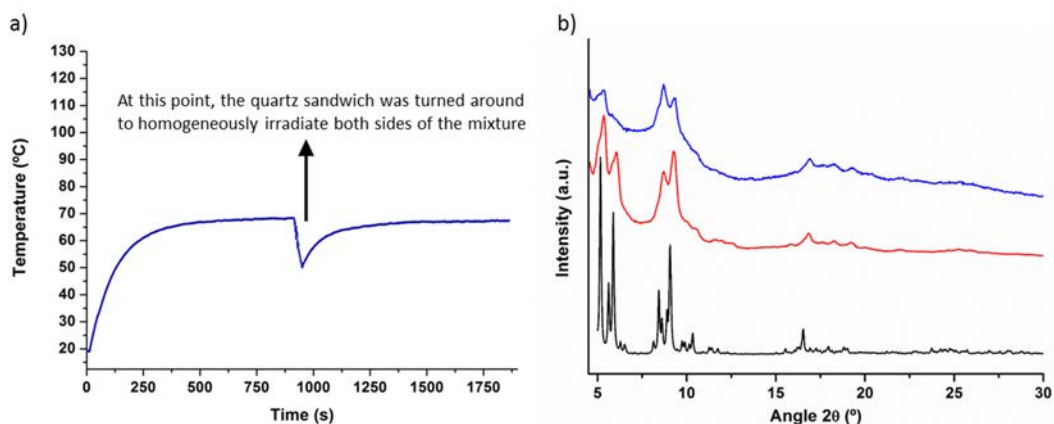

Figure 2.26. a) Photothermal plot of the formation of (MIL-101-(Al)-BA)$_3$ upon UV-Vis irradiation of MIL-101-NH$_2$(Al) and BA at 265 mW·cm^{-2}. b) XRPD patterns for synthesised (MIL-101-(Al)-BA)$_3$ irradiated at 265 mW·cm^{-2} (blue) as compared to those for activated MIL-101-NH$_2$(Al) (red) and simulated MIL-101-NH$_2$(Al) (black).

The post-functionalization of MIL-101-NH$_2$(Al) with BA was also characterized by XRPD, ^{1}H-NMR, ESI-MS and N$_2$ adsorption measurements. XRPD confirmed that (MIL-101-(Al)-BA)$_3$ retains the crystallinity of the parent MIL-101-NH$_2$(Al) (Figure 2.26b).^{1}H-NMR of the digested sample gave a conversion rate of 44.0 ± 2.5 % (Figure 2.27). ESI-MS confirmed the presence of the reacted molecule peak (m/z = 284.1 for [C$_{15}$H$_{10}$NO$_5$]$^-$) (Figure 2.28). In addition, the N$_2$ adsorption measurement of the irradiated sample presented an S$_{BET}$ value of 774 m^2·g^{-1}, much lower than the as-synthesised MIL-101-NH$_2$(Al) (2702 m^2·g^{-1}) (Figure 2.29). Table 2.2 summarizes the main values obtained from the CPSM experiments of this section.
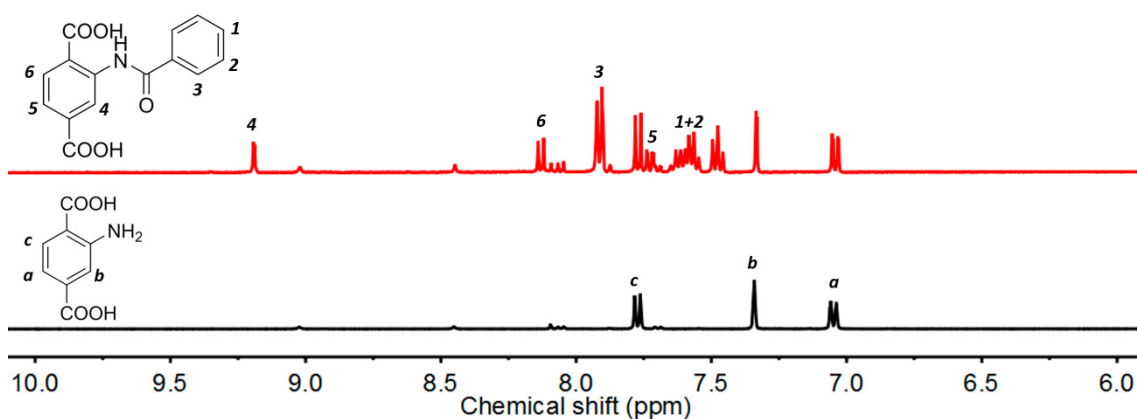
Figure 2.27. ^{1}H-NMR spectrum of digested (MIL-101-(Al)-BA)$_3$ (red) upon irradiation at 265 mW·cm^{-2} (light guide-to-sample distance: 9 cm), as compared to that of activated MIL-101-NH$_2$(Al) (black). NMR solvent: DMSO-d_6/HF.
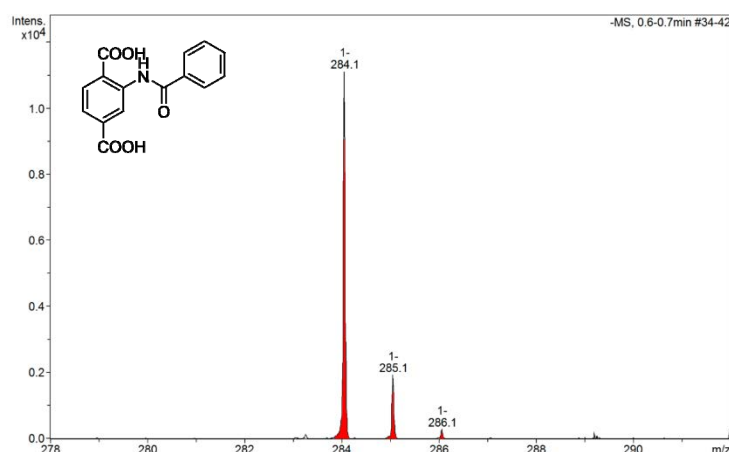
Figure 2.28. ESI-MS spectrum of digested (MIL-101-(Al)-BA)$_3$.
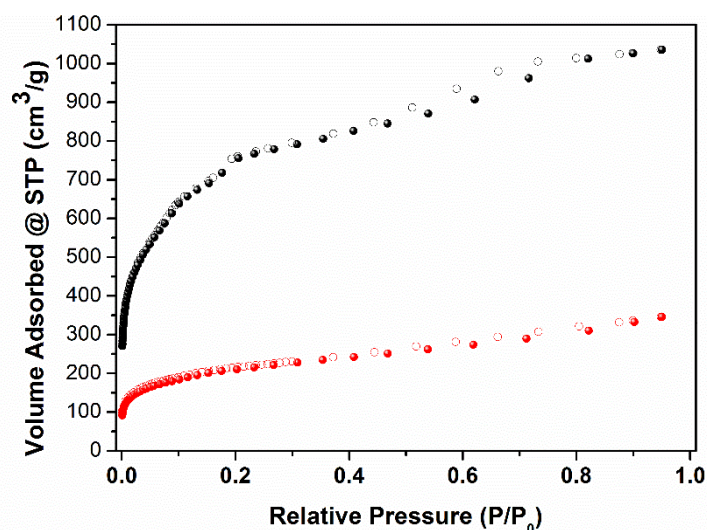
Figure 2.29. N_2 sorption isotherm of the photothermally activated MIL-101-NH_2(Al) (black) and (MIL-101-(Al)-BA)$_3$ (red).

Table 2.2. BET surface areas, pore volumes and conversion rates (%) for the synthesised and modified MOFs.

MOF	S_{BET} (m$^2 \cdot$g^{-1})	Pore volume (cm$^3 \cdot$g^{-1})[a]	Conversion (%)[b]
UiO-66-NH_2	936	0.4726	--
(UiO-66-NH_2-MA)$_3$	699	0.3375	85
(UiO-66-NH_2-BA)$_3$	621	0.3452	49
MIL-101-NH_2(Al)	2702	1.277	--
(MIL-101-(Al)-MA)$_3$	549	0.2662	79
(MIL-101-(Al)-BA)$_3$	774	0.3742	44

[a] Calculated at P/P$_0 \approx 0.4$. [b] Calculated from ^{1}H-NMR spectra of the digested samples.

From Table 2.2, it can be observed that, even though the conversion rate of (UiO-66-NH_2-MA)$_3$ (85 %) is higher than the one of (UiO-66-NH_2-BA)$_3$ (49 %), the S_{BET} values indicate higher N_2 blocking in the case of (UiO-66-NH_2-BA)$_3$. Contrarily, in the case of (MIL-101-(Al)-MA)$_3$ and (MIL-101-(Al)-BA)$_3$, the higher the conversion rate, the lower the S_{BET} values. From these observations, we attributed that the differences in the pore size of the studied MOFs play an important role during the gas sorption. In this sense, the pore channels of UiO-66-NH_2 (cages of 8 and 11 Å free diameters accessible through windows of 4-6 Å) are easily blocked by the phenyl substituents of BA. Thus, the reduction in the porosity is mainly due to the steric hindrance resulting from the introduction of more bulky groups from BA than from MA. In contrast, the reduction in the

porosity for MIL-101-NH$_2$(Al) is mainly related to the functionalization ratio than to the blocking of the windows, because the diffusion into the channels is easier due to the bigger pore size of MIL-101-NH$_2$(Al) (cages with 29 and 34 Å free diameter accessible through windows of 12-16 Å).

2.3. Photoinduced cascade CPSM reaction

Once the amide bond formation between different amino-tagged MOFs (UiO-66-NH$_2$ and MIL-101-NH$_2$(Al)) and anhydrides (MA and BA) was demonstrated, it was intended to explore other organic reactions. This section shows an unprecedented photoinduced cascade reaction that affords CPSM of MOFs using the light-induced method.

It is well know that condensation reactions between aldehydes with amines lead to formation of an imine group via water elimination. As recently proved by Maspoch and co-workers, this Schiff-base reaction can be performed using spray-drying methods in short times, both using amine- or aldehyde-tagged MOFs.[49] Thus, we looked forward to extend our CPSM to other reactions behind the already demonstrated involving the amino functionalized MOFs and anhydrides.

The goal was to assess the CPSM of UiO-66-NH$_2$ with a low melting point aldehyde such as 4-bromobenzaldehyde (BrBz-CHO) (m.p. = 55-58 °C). The experimental procedure was adapted from the previous experiments, using UV-Vis light irradiation (300-650 nm) at 500 mW·cm^{-2} for 30 minutes over a solid mixture of the MOF and the organic reagent. However, full characterization of the product resulting from this reaction did not show the expected ESI-MS peak of the imine moiety [C$_{15}$H$_9$BrNO$_4$]$^-$ (m/z = 346.0). Unexpectedly, we found a peak at m/z = 362.0 that matched with the molecular formula of the amide product [C$_{15}$H$_9$BrNO$_5$]$^-$ (m/z = 362.0) (Figure 2.30). It is well-known that the formation of an amide bond might occur when reacting an amino group with a carboxylic anhydride, an acyl chloride or a carboxylic acid (Figure 2.31). Therefore, to prove that one of these species was formed when irradiated the mixture, we studied the UV-Vis irradiation of the selected aldehyde (BrBz-CHO) alone. To this end, we systematically irradiated 47 mg of BrBz-CHO at 7 cm (500 mW·cm^{-2}) for 30 minutes, leading to a maximum temperature of 65-70 °C, high enough to melt it after exposure to light. The sample was let to cool down to room temperature and subsequent ^{1}H-NMR analysis was performed. The spectrum of the irradiated solid showed different chemical shifts (7.71 and 7.85 ppm) as compared with the commercial BrBz-CHO (7.79 ppm) (Figure 2.32). This spectrum was then compared with that of 4-bromobenzoic acid (BrBz-COOH), confirming that the new chemical

shifts observed after irradiation of BrBz-CHO were identical to the ones from BrBz-COOH (Figure 2.32). In addition, ESI-MS after irradiation of BrBz-CHO confirmed the presence of BrBz-COOH peak at m/z = 198.9, matching the expected $[C_7H_4BrO_2]^-$ (m/z=198.9) (Figure 2.33). Altogether, these results confirmed the formation of BrBz-COOH once BrBz-CHO was irradiated.
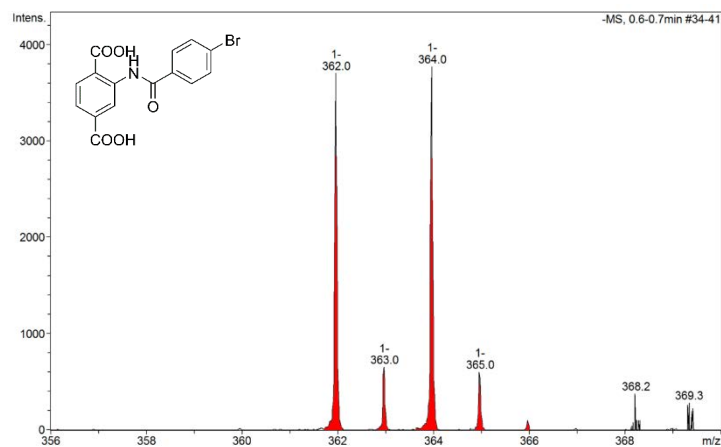
Figure 2.30. ESI-MS spectrum of digested (UiO-66-(BrBz-CHO))$_3$.
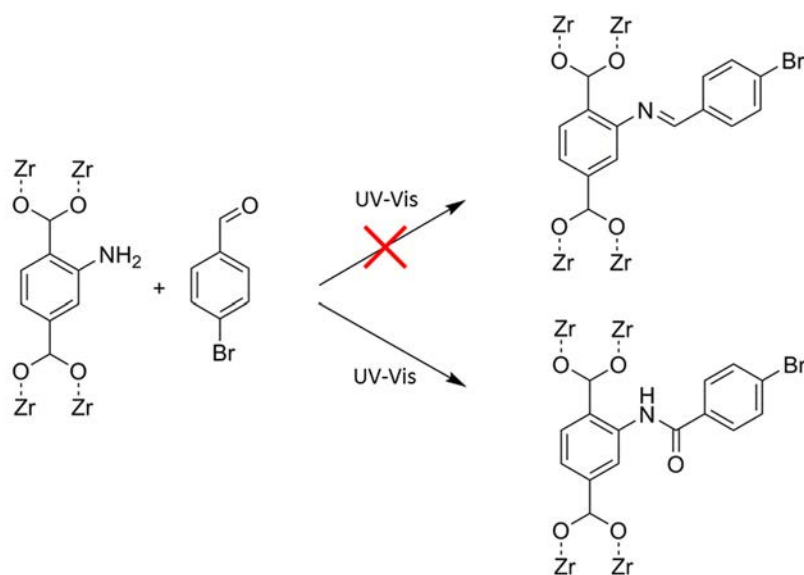
Figure 2.31. Reaction scheme between UiO-66-NH$_2$ and BrBz-CHO, which afforded the formation of an amide bond instead of the expected imine.
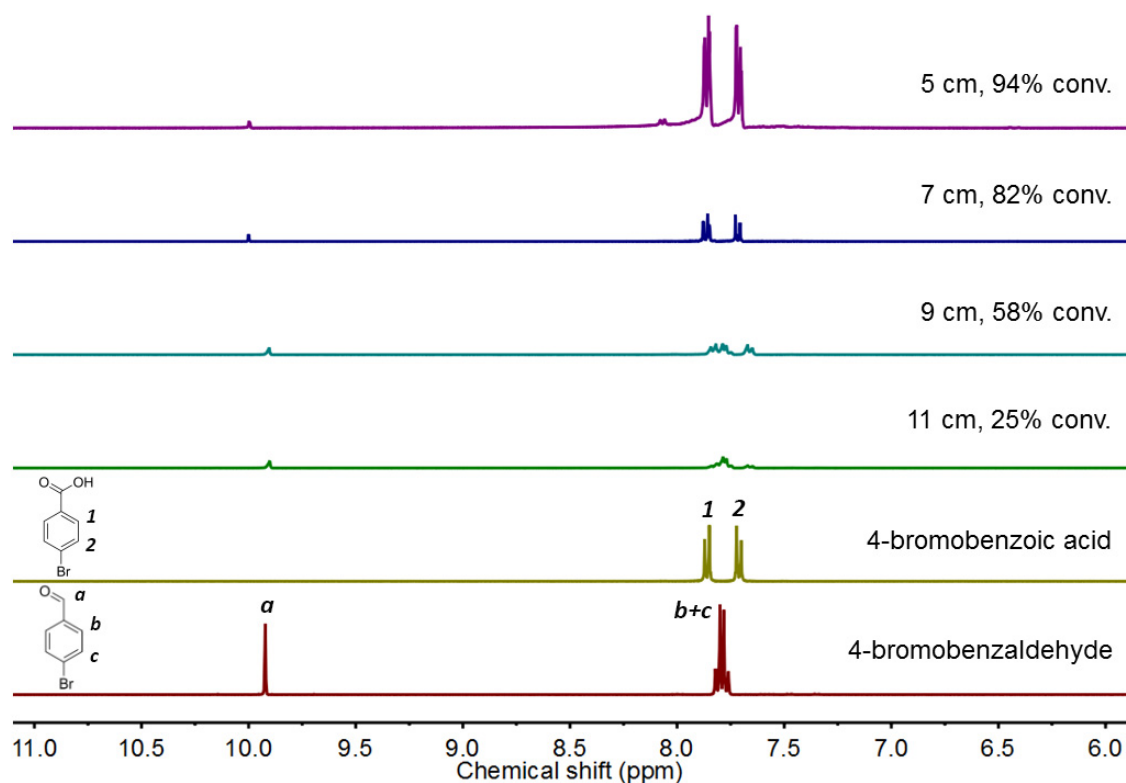
Figure 2.32. ^{1}H-NMR spectra of irradiated BrBz-CHO at different distances 5 (purple), 7 (navy), 9 (blue) and 11 (green) cm for 30 minutes, as compared to that of commercial BrBz-CHO (red) and BrBz-COOH (olive). NMR solvent: DMSO-d_6
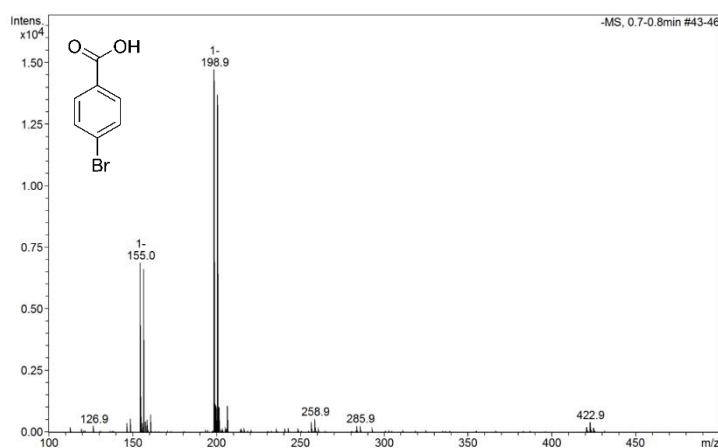
Figure 2.33. ESI-MS spectrum of the obtained BrBz-COOH.

The oxidation reaction from aldehyde to carboxylic acid under light irradiation has only been reported using a photosensitizer, which is able to convert the light into chemical energy.[55–57] Here, we describe the same reaction neither using any external photosensitizer nor requiring O_2 atmosphere and in very short times (30 minutes). In this sense, our hypothesised mechanism includes the formation of singlet oxygen ($^1O_2$), a well-known reactive oxygen species (ROS).[58] In

order to generate such species, the presence of a photosensitizer is required, as the direct transformation from $^1O_2$ to $^3O_2$ is forbidden. Once the photosensitizer is irradiated, electrons are promoted from the ground to an excited state, which is subsequently transformed to an excited triplet state. This excited state is able to transfer energy to surrounding $^3O_2$ molecules and convert them into $^1O_2$.(Figure 2.34).[59,60] In our studied system, the BrBz-CHO acts both as photosensitizer and reagent, by first absorbing UV-Vis light (Figure 2.35a) leading to the obtaining of $^1O_2$, which is able to oxidize *in situ* the aldehyde group of the photosensitizer and convert it into a carboxylic acid (Figure 2.35b).
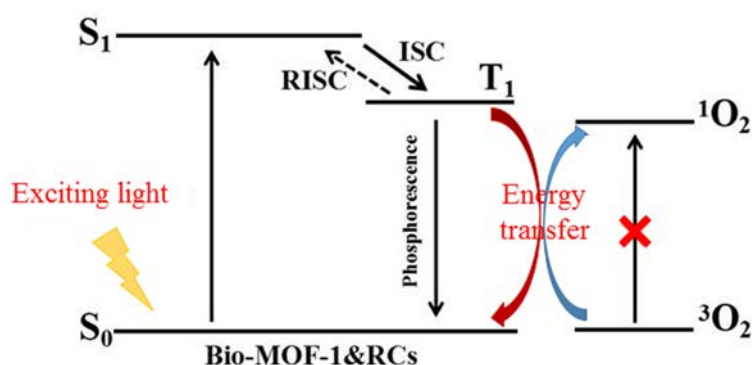
Figure 2.34. Energy level diagram for a photosensitizer and oxygen. The sensitizer in its ground state S_0 absorbs a photon of light and is excited to its first singlet state S_1. It spontaneously decays to its excited triplet state T_1 via intersystem crossing (ISC). From T_1, energy is transferred to ground state molecular oxygen $^3O_2$, creating reactive singlet oxygen $^1O_2$.[59,60]
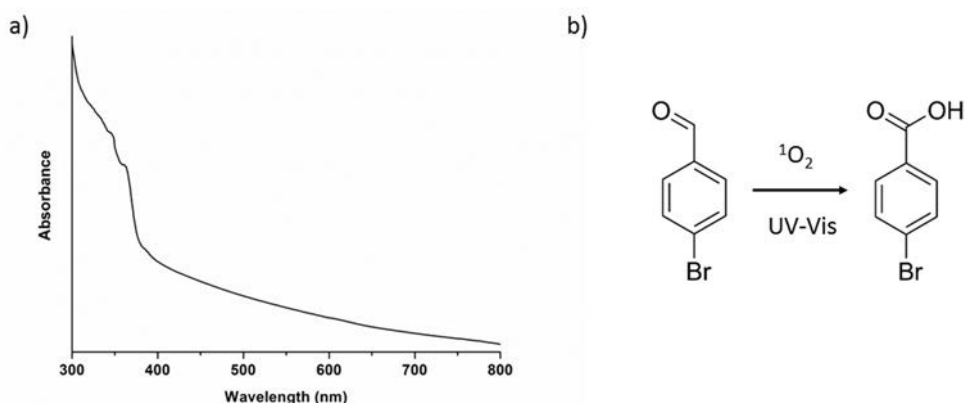
Figure 2.35. a) BrBz-CHO solid-state UV-Vis spectrum. b) Scheme of oxidation reaction during UV-Vis irradiation of BrBz-CHO.

The following step was to optimize the irradiation parameters for converting BrBz-CHO into BrBz-COOH. 47 mg of BrBz-CHO were UV-Vis irradiated at different irradiances by tuning the light guide-to-sample distance (5, 9 and 11 cm, corresponding to an irradiance of 900, 265 and 157 mW·cm^{-2}, respectively) for 30 minutes. The resulting solids were then analysed by ^{1}H-NMR

(Figure 2.32). The conversion percentage of BrBz-CHO to BrBz-COOH was calculated by comparing the integration of the carboxylic acid chemical shift (7.71 ppm) with the aldehyde one (7.79 ppm) (*vide infra*). In this systematic study, irradiation at 7 cm (500 mW·cm^{-2}) was selected as the most appropriate distance due to the high conversion rate (82 %). Longer light guide-to-sample distances did not allow high conversion rates (25-58 %), while shorter ones led to higher conversion rate (94 %) but also unidentified signals (8.07 ppm) appeared in the spectrum. Maintaining the light guide distance from the sample at 7 cm, we assessed the influence of UV-Vis light exposure by performing the same experiment at longer times (60 minutes). The reached conversion rate for this test was of 87 %, which was not significantly higher than when irradiating for 30 minutes (Figure 2.36).
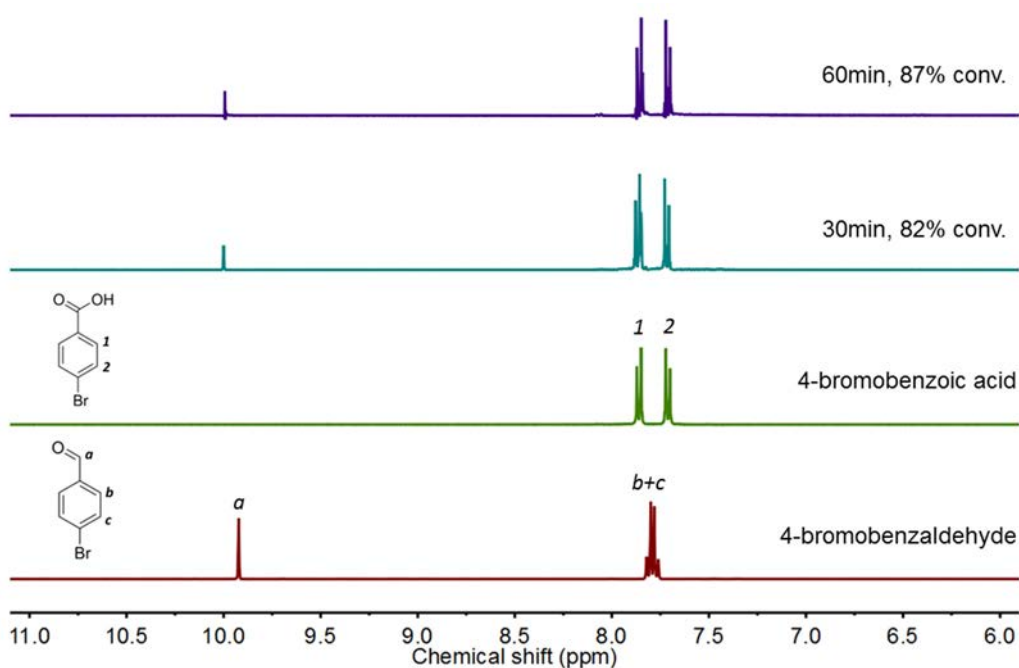
Figure 2.36. ^{1}H-NMR spectra of BrBz-CHO irradiated for different time: 60 (purple) and 30 (blue) minutes, as compared to that of commercial BrBz-CHO (red) and BrBz-COOH (green). NMR solvent: DMSO-d_6.

Table 2.3. Summary of the conversion rates from BrBz-CHO to BrBz-COOH under UV-Vis irradiation.

Irradiance (mW·cm^{-2})	Time (minutes)	Conversion (%)
157	30	25
265	30	58
500	30	82
900	30	94
500	60	87

Once the irradiation conditions for the oxidation reaction were selected (500 mW·cm^{-2} and 30 minutes), we continued with the optimization of the CPSM of UiO-66-NH$_2$ with BrBz-CHO. In this CPSM reaction, we should attribute the heating to both the MOF and the reagent, as the photothermal effect was proven for each compound separately. Therefore, we hypothesised a mechanism that consists on a first UV-Vis light absorption by the UiO-66-NH$_2$ and BrBz-CHO, leading to the melting of the aldehyde and oxidation to carboxylic acid. The formed species might then react with the amine moiety of the MOF affording the covalent binding through amide bonds (Figure 2.37).

The protocol of a typical experiment consisted on mixing 25 mg of activated UiO-66-NH$_2$ and x equivalents (x = 1, 3 or 6) of aldehyde (relative to the amino group of the unit cell) and grinding in a mortar for 5 minutes. The solid mixture was placed between two quartz slides forming a round pellet. UV-Vis light (300-650 nm) with an irradiance of 500 mW·cm^{-2} was applied for 15 minutes/side. The sample was then washed with 5 x 10 mL DMF and 5 x 10 mL acetone, air-dried and digested in 5 % HF and DMSO-d_6 (120 μL + 600 μL, respectively) and analysed by ^{1}H-NMR.
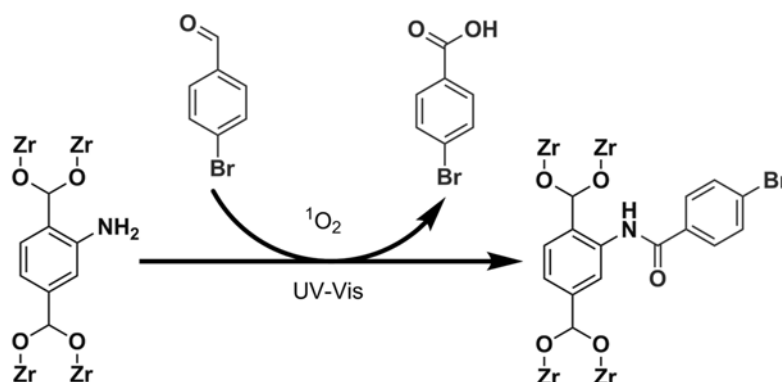
Figure 2.37. Hypothesised reaction scheme of the CPSM of UiO-66-NH$_2$ with BrBz-CHO under UV-Vis irradiation.

XRPD patterns of all the irradiated (UiO-66-(BrBz-CHO))$_x$ matched the one of the parental MOF (Figure 2.38b). ^{1}H-NMR allowed the conversion rate calculation by comparing the integration of the peak at 7.32 ppm corresponding to the NH$_2$-BDC molecules with the one at 9.11 ppm from the amide moiety. Increasing conversion rate was observed from 1 to 6 equivalents being 16.7, 44.4 and 54.8 % for (UiO-66-(BrBz-CHO))$_1$, (UiO-66-(BrBz-CHO))$_3$ and (UiO-66-(BrBz-CHO))$_6$, respectively (Figure 2.39). During UV-Vis irradiation of (UiO-66-(BrBz-CHO))$_6$, the maximum temperature reached by the sample was of 85-87 °C (Figure 2.38a), high enough to melt the aldehyde reagent.
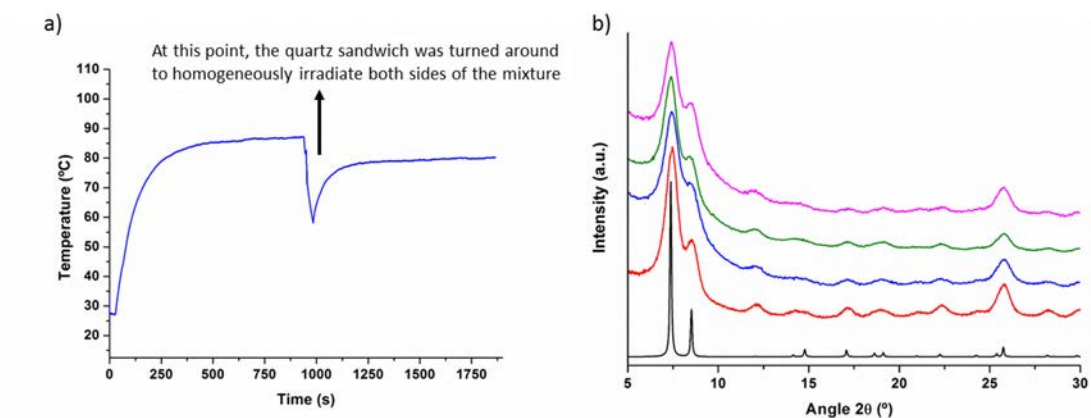
Figure 2.38. a) Photothermal plot of the formation of (UiO-66-(BrBz-CHO))$_6$ upon UV-Vis irradiation of UiO-66-NH$_2$ and BrBz-CHO at 500 mW·cm^{-2}. b) XRPD patterns for synthesised (UiO-66-(BrBz-CHO))$_1$ irradiated at 500 mW·cm^{-2} (blue), (UiO-66-(BrBz-CHO))$_3$ (green) and (UiO-66-(BrBz-CHO))$_6$ (magenta), as compared to those for activated UiO-66-NH$_2$ (red) and simulated UiO-66-NH$_2$ (black).
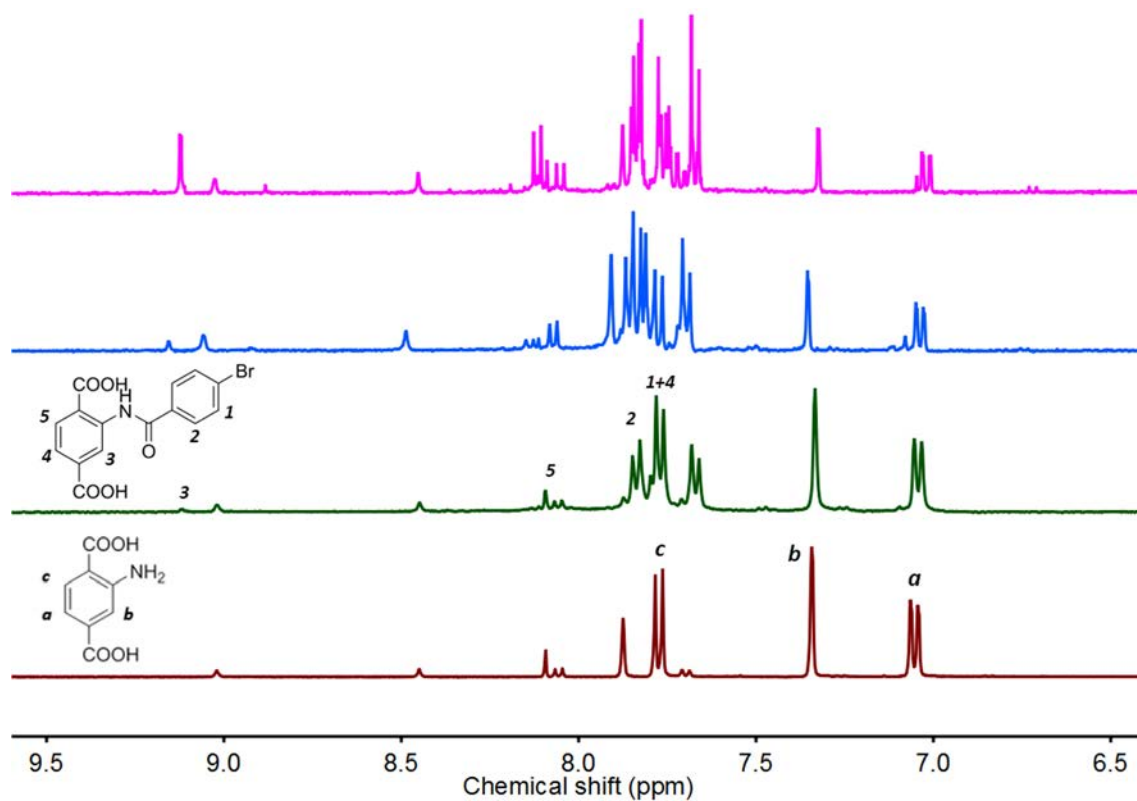
Figure 2.39. ^{1}H-NMR spectra of digested (UiO-66-(BrBz-CHO))$_1$ (green), (UiO-66-(BrBz-CHO))$_3$ (blue) and (UiO-66-(BrBz-CHO))$_6$ (magenta) irradiated at 500 mW·cm^{-2} for 30 minutes, as compared to the spectrum of activated UiO-66-NH$_2$ (red). NMR solvent: DMSO-d_6/HF.

3.   Experimental section

3.1. Synthetic procedures

Synthesis of UiO-66-NH$_2$

In a typical synthesis,[54] 16.10 g (50.00 mmol) of ZrOCl$_2$·8H$_2$O was dissolved in 125 mL of DMF at room temperature under stirring for 15 minutes. In a separate flask, 2-aminoterephtalic acid (NH$_2$-BDC) (8.30 g, 45.82 mmol) was dissolved in 125 mL of DMF at room temperature under stirring for 15 minutes. The yellow NH$_2$-BDC solution obtained was added to the ZrOCl$_2$·8H$_2$O solution, followed by addition of 3 mL of HCl 37% under stirring. The resulting mixture was heated at 120 °C under stirring for 4 hours. The obtained solid was collected by centrifugation at 9000 rpm for 5 minutes, washed twice with 100 mL of DMF for 12 hours and twice with 100 mL of absolute ethanol for 12 hours. Finally, the resulting powder was dried at 85 °C overnight.

Synthesis of MIL-101-NH$_2$(Al)

In a typical synthesis,[52] 0.51 g (2.13 mmol) of AlCl$_3$·6H$_2$O was dissolved in 15 mL of DMF. In a separate flask, 0.56 g (3.11 mmol) of NH$_2$-BDC was dissolved in 15 mL of DMF at room temperature. The yellow NH$_2$-BDC solution obtained was added to the AlCl$_3$·6H$_2$O solution under stirring. The resulting mixture was heated for 72 hours at 130 °C in an oven. The resulting solid was collected by centrifugation at 9000 rpm for 5 minutes and washed absolute ethanol (2 x 200 mL) at 80 °C. Finally, the resulting powder was dried at 85 °C overnight.

3.2. Conversion rate calculation

Conversion rates of the different CPSM were determined by ^{1}H-NMR analysis of the digested MOF crystals. The digestion step consisted on mixing 10 mg of sample with 120 µL of 5% HF in D$_2$O and 500 µL of DMSO-d_6, and further sonication was applied for 10 minutes.

In both cases, UiO-66-NH$_2$ and MIL-101-NH$_2$(Al), the chemical shift of NH$_2$-BDC ligand at 7.34 ppm was used as a reference, which counts per one proton and integration value was set to 1. For the reaction with MA, the shift at 6.58 ppm that corresponds to a single proton of the C-C double bond formed in the amide moiety was chosen. Both protons (7.34 and 6.58 ppm) could be easily identified and isolated in the spectra, leading to an accurate integration.

In the reactions with BA, the signal used for conversion calculation was the one at 8.14 ppm, identified as a single proton of the BDC ring in the reacted molecule. This peak was selected because a mixture and overlapping of signals were found at the region 7.4-8 ppm.

For the experiments using BrBz-CHO, we selected the signal at 9.11 ppm in order to quantify the reacted species that formed the amide moiety.

Equation 1 was employed to quantify the extension of the CPSM in each MOF:

$$Conversion \ (\%) = \frac{Int \ (a)}{Int \ (a) + Int \ (b)} x100 \qquad (1)$$

, where *Int (a)* is the integration value of the amide moiety signal (6.58, 8.14 or 9.11 ppm) and *Int (b)* the integration value of the NH_2-BDC (7.34 ppm) (always set to 1).

4. Conclusions

In this chapter, we used the photothermal effect of MOFs to perform CPSMs on them. Two different organic reactions were assessed, the amide condensation between UiO-66-NH$_2$ or MIL-101-NH$_2$(Al)) and MA or BA, and the cascade reaction leading to amide bond formation between UiO-66-NH$_2$ and BrBz-CHO.

In the first example, the local heat generated upon UV-Vis irradiation of the MOF allowed melting the reagent in the solid mixture. Once in the liquid state, the anhydride is able to react with the amino pendant arms forming an amide moiety thanks to the thermal energy released by the MOF. This approach converted the MOFs as "heaters", where the heat is efficiently used in the organic reaction. Remarkably, by using this CPSM method, the need for solvents was suppressed, making it a greener strategy. In this sense, we should note that it is only useful when the melting point of the reagent is lower than the maximum temperature reached by the MOF during the UV-Vis irradiation. Noteworthy, a great advantage of this method is the short time required to perform CPSM of MOFs (only 30 minutes) with quite high conversion rates: 85 % for (UiO-66-MA)$_3$ and 79 % for (MIL-101-(Al)-MA)$_3$.

The second example, based on the reaction between the amino tag of UiO-66-NH$_2$ and BrBz-CHO, takes advantage of the photothermal heating of both, the MOF and the aldehyde. We demonstrated the mechanism of a photoinduced cascade reaction that allowed the *in situ* oxidation of the aldehyde to carboxylic acid followed by the CPSM step. Such mechanism allowed the formation of amide moieties instead of the expected imine bonds and conversion rates up to 55 % for (UiO-66-(BrBz-CHO))$_6$.

As demonstrated in this chapter, the recently reported photothermal effect in MOFs opens a number of new possibilities, such as the presented activation and post-synthetic modification, where the irradiated light monitors the temperature of the MOF crystals. This performance might be useful in other functions like confining reactions inside the channels or crystal surface, or increasing the efficiency of MOFs as catalysts.

5. References

1. Eddaoudi, M., Kim, J., Rosi, N., Vodak, D., Wachter, J., O'Keeffe, M. & Yaghi, O. M. Systematic Design of Pore Size and Functionality in Isoreticular MOFs and Their Application in Methane Storage. *Science* **295,** 469–472 (2002).

2. Maspoch, D., Ruiz-Molina, D., Wurst, K., Domingo, N., Cavallini, M., Biscarini, F., Tejada, J., Rovira, C. & Veciana, J. A Nanoporous Molecular Magnet with Reversible Solvent-Induced Mechanical and Magnetic Properties. *Nat. Mater.* **2,** 190–195 (2003).

3. Devic, T., Horcajada, P., Serre, C., Salles, F., Maurin, G., Moulin, B., Heurtaux, D., Clet, G., Vimont, A., Grenèche, J.-M., Ouay, B. Le, Moreau, F., Magnier, E., Filinchuk, Y., Marrot, J., Lavalley, J.-C., Daturi, M. & Férey, G. Functionalization in Flexible Porous Solids: Effects on the Pore Opening and the Host–Guest Interactions. *J. Am. Chem. Soc.* **132,** 1127–1136 (2010).

4. Kandiah, M., Nilsen, M. H., Usseglio, S., Jakobsen, S., Olsbye, U., Tilset, M., Larabi, C., Quadrelli, E. A., Bonino, F. & Lillerud, K. P. Synthesis and Stability of Tagged UiO-66 Zr-MOFs. *Chem. Mater.* **22,** 6632–6640 (2010).

5. Banerjee, R., Furukawa, H., Britt, D., Knobler, C., O'Keeffe, M. & Yaghi, O. M. Control of Pore Size and Functionality in Isoreticular Zeolitic Imidazolate Frameworks and their Carbon Dioxide Selective Capture Properties. *J. Am. Chem. Soc.* **131,** 3875–3877 (2009).

6. Wang, Z. & Cohen, S. M. Postsynthetic Covalent Modification of a Neutral Metal–Organic Framework. *J. Am. Chem. Soc.* **129,** 12368–12369 (2007).

7. Wang, Z. & Cohen, S. M. Postsynthetic Modification of Metal-Organic Frameworks. *Chem. Soc. Rev.* **38,** 1315–1329 (2009).

8. Tanabe, K. K. & Cohen, S. M. Postsynthetic Modification of Metal-Organic Frameworks-a Progress Report. *Chem. Soc. Rev.* **40,** 498–519 (2011).

9. Cohen, S. M. Postsynthetic Methods for the Functionalization of Metal–Organic Frameworks. *Chem. Rev.* **112,** 970–1000 (2012).

10. Yaghi, O. M., Li, G. & Li, H. Selective Binding and Removal of Guests in a Microporous Metal–Organic Framework. *Nature* **378,** 703–706 (1995).

11. J. Kepert, C. & J. Rosseinsky, M. Zeolite-Like Crystal Structure of an Empty Microporous Molecular Framework. *Chem. Commun.* **0,** 375–376 (1999).

12. Liu, Y., Li, G., Li, X. & Cui, Y. Cation-Dependent Nonlinear Optical Behavior in an Octupolar 3D Anionic Metal–Organic Open Framework. *Angew. Chem. Int. Ed.* **119,** 6417–6420 (2007).

13. An, J. & Rosi, N. L. Tuning MOF CO_2 Adsorption Properties via Cation Exchange. *J. Am. Chem. Soc.* **132,** 5578–5579 (2010).

14. An, J., Shade, C. M., Chengelis-Czegan, D. A., Petoud, S. & Rosi, N. L. Zinc-Adeninate Metal–Organic Framework for Aqueous Encapsulation and Sensitization of Near-infrared and Visible Emitting Lanthanide Cations. *J. Am. Chem. Soc.* **133,** 1220–1223 (2011).

15. Chui, S. S.-Y., Lo, S. M.-F., Charmant, J. P. H., Orpen, A. G. & Williams, I. D. A Chemically Functionalizable Nanoporous Material $[Cu_3(TMA)_2(H_2O)_3]_n$. *Science* **283,** 1148–1150 (1999).

16. Deria, P., Mondloch, J. E., Tylianakis, E., Ghosh, P., Bury, W., Snurr, R. Q., Hupp, J. T. & Farha, O. K. Perfluoroalkane Functionalization of NU-1000 via Solvent-Assisted Ligand

Incorporation: Synthesis and CO_2 Adsorption Studies. *J. Am. Chem. Soc.* **135,** 16801–16804 (2013).

17. Evans, J. D., Sumby, C. J. & Doonan, C. J. Post-Synthetic Metalation of Metal-Organic Frameworks. *Chem. Soc. Rev.* **43,** 5933–5951 (2014).

18. Wu, C.-D., Hu, A., Zhang, L. & Lin, W. A Homochiral Porous Metal–Organic Framework for Highly Enantioselective Heterogeneous Asymmetric Catalysis. *J. Am. Chem. Soc.* **127,** 8940–8941 (2005).

19. Bloch, E. D., Britt, D., Lee, C., Doonan, C. J., Uribe-Romo, F. J., Furukawa, H., Long, J. R. & Yaghi, O. M. Metal Insertion in a Microporous Metal–Organic Framework Lined with 2,2'-Bipyridine. *J. Am. Chem. Soc.* **132,** 14382–14384 (2010).

20. Kaye, S. S. & Long, J. R. Matrix Isolation Chemistry in a Porous Metal–Organic Framework: Photochemical Substitutions of N_2 and H_2 in $Zn_4O[(\eta^6-1,4-Benzenedicarboxylate)Cr(CO)_3]_3$. *J. Am. Chem. Soc.* **130,** 806–807 (2008).

21. Karagiaridi, O., Bury, W., Mondloch, J. E., Hupp, J. T. & Farha, O. K. Solvent-Assisted Linker Exchange: An Alternative to the De Novo Synthesis of Unattainable Metal–Organic Frameworks. *Angew. Chem. Int. Ed.* **53,** 4530–4540 (2014).

22. Kim, M., Cahill, J. F., Su, Y., Prather, K. A. & Cohen, S. M. Postsynthetic Ligand Exchange as a Route to Functionalization of "Inert" Metal-Organic Frameworks. *Chem. Sci.* **3,** 126–130 (2012).

23. Das, S., Kim, H. & Kim, K. Metathesis in Single Crystal: Complete and Reversible Exchange of Metal Ions Constituting the Frameworks of Metal–Organic Frameworks. *J. Am. Chem. Soc.* **131,** 3814–3815 (2009).

24. Kiang, Y.-H., Gardner, G. B., Lee, S., Xu, Z. & Lobkovsky, E. B. Variable Pore Size, Variable Chemical Functionality, and an Example of Reactivity within Porous Phenylacetylene Silver Salts. *J. Am. Chem. Soc.* **121,** 8204–8215 (1999).

25. Seo, J. S., Whang, D., Lee, H., Jun, S. I., Oh, J., Jeon, Y. J. & Kim, K. A Homochiral Metal–Organic Porous Material for Enantioselective Separation and Catalysis. *Nature* **404,** 982–986 (2000).

26. Tanabe, K. K., Wang, Z. & Cohen, S. M. Systematic Functionalization of a Metal–Organic Framework via a Postsynthetic Modification Approach. *J. Am. Chem. Soc.* **130,** 8508–8517 (2008).

27. Garibay, S. J. & Cohen, S. M. Isoreticular Synthesis and Modification of Frameworks with the UiO-66 Topology. *Chem. Commun.* **46,** 7700–7702 (2010).

28. Kandiah, M., Usseglio, S., Svelle, S., Olsbye, U., Lillerud, K. P. & Tilset, M. Post-Synthetic Modification of the Metal-Organic Framework Compound UiO-66. *J. Mater. Chem.* **20,** 9848–9851 (2010).

29. Marshall, R. J. & Forgan, R. S. Postsynthetic Modification of Zirconium Metal-Organic Frameworks. *Eur. J. Inorg. Chem.* **2016,** 4310–4331 (2016).

30. Ahnfeldt, T., Gunzelmann, D., Loiseau, T., Hirsemann, D., Senker, J., Férey, G. & Stock, N. Synthesis and Modification of a Functionalized 3D Open-Framework Structure with MIL-53 Topology. *Inorg. Chem.* **48,** 3057–3064 (2009).

31. Hansen, T. V., Wu, P., Sharpless, W. D. & Lindberg, J. G. Just Click It: Undergraduate Procedures for the Copper(I)-Catalyzed Formation of 1,2,3-Triazoles from Azides and Terminal Acetylenes. *J. Chem. Educ.* **82,** 1833 (2005).

32. Goto, Y., Sato, H., Shinkai, S. & Sada, K. "Clickable" Metal–Organic Framework. *J. Am. Chem. Soc.* **130,** 14354–14355 (2008).

33. Tuci, G., Rossin, A., Xu, X., Ranocchiari, M., van Bokhoven, J. A., Luconi, L., Manet, I., Melucci, M. & Giambastiani, G. "Click" on MOFs: A Versatile Tool for the Multimodal Derivatization of N_3-Decorated Metal Organic Frameworks. *Chem. Mater.* **25,** 2297–2308 (2013).

34. Gadzikwa, T., Lu, G., Stern, C. L., Wilson, S. R., Hupp, J. T. & Nguyen, S. T. Covalent Surface Modification of a Metal-Organic Framework: Selective Surface Engineering via CuI-Catalyzed Huisgen Cycloaddition. *Chem. Commun.* **0,** 5493–5495 (2008).

35. Ingleson, M. J., Perez Barrio, J., Guilbaud, J.-B., Khimyak, Y. Z. & Rosseinsky, M. J. Framework Functionalisation Triggers Metal Complex Binding. *Chem. Commun.* **0,** 2680–2682 (2008).

36. Wang, Z., Tanabe, K. K. & Cohen, S. M. Accessing Postsynthetic Modification in a Series of Metal-Organic Frameworks and the Influence of Framework Topology on Reactivity. *Inorg. Chem.* **48,** 296–306 (2009).

37. Costa, J. S., Gamez, P., Black, C. A., Roubeau, O., Teat, S. J. & Reedijk, J. Chemical Modification of a Bridging Ligand Inside a Metal–Organic Framework while Maintaining the 3D Structure. *Eur. J. Inorg. Chem.* **2008,** 1551–1554 (2008).

38. Volkringer, C. & Cohen, S. M. Generating Reactive MILs: Isocyanate- and Isothiocyanate-Bearing MILs through Postsynthetic Modification. *Angew. Chem. Int. Ed.* **49,** 4644–4648 (2010).

39. Burrows, A. D., Frost, C. G., Mahon, M. F. & Richardson, C. Post-Synthetic Modification of Tagged Metal–Organic Frameworks. *Angew. Chem. Int. Ed.* **47,** 8482–8486 (2008).

40. Morris, W., Doonan, C. J., Furukawa, H., Banerjee, R. & Yaghi, O. M. Crystals as Molecules: Postsynthesis Covalent Functionalization of Zeolitic Imidazolate Frameworks. *J. Am. Chem. Soc.* **130,** 12626–12627 (2008).

41. Doonan, C. J., Morris, W., Furukawa, H. & Yaghi, O. M. Isoreticular Metalation of Metal–Organic Frameworks. *J. Am. Chem. Soc.* **131,** 9492–9493 (2009).

42. Canivet, J., Aguado, S., Daniel, C. & Farrusseng, D. Engineering the Environment of a Catalytic Metal–Organic Framework by Postsynthetic Hydrophobization. *ChemCatChem* **3,** 675–678 (2011).

43. Savonnet, M., Bazer-Bachi, D., Bats, N., Perez-Pellitero, J., Jeanneau, E., Lecocq, V., Pinel, C. & Farrusseng, D. Generic Postfunctionalization Route from Amino-Derived Metal–Organic Frameworks. *J. Am. Chem. Soc.* **132,** 4518–4519 (2010).

44. Li, B., Gui, B., Hu, G., Yuan, D. & Wang, C. Postsynthetic Modification of an Alkyne-Tagged Zirconium Metal–Organic Framework via a "Click" Reaction. *Inorg. Chem.* **54,** 5139–5141 (2015).

45. Gui, B., Hu, G., Zhou, T. & Wang, C. Pore Surface Engineering in a Zirconium Metal–Organic Framework via Thiol-Ene Reaction. *J. Solid State Chem.* **223,** 79–83 (2015).

46. von Zons, T., Brokmann, L., Lippke, J., Preuße, T., Hülsmann, M., Schaate, A., Behrens, P. & Godt, A. Postsynthetic Modification of Metal–Organic Frameworks through Nitrile Oxide–Alkyne Cycloaddition. *Inorg. Chem.* **57,** 3348–3359 (2018).

47. Jambovane, S. R., Nune, S. K., Kelly, R. T., McGrail, B. P., Wang, Z., Nandasiri, M. I., Katipamula, S., Trader, C. & Schaef, H. T. Continuous, One-pot Synthesis and Post-Synthetic Modification of NanoMOFs Using Droplet Nanoreactors. *Sci. Rep.* **6,** 36657

(2016).

48. Carné-Sánchez, A., Imaz, I., Cano-Sarabia, M. & Maspoch, D. A Spray-Drying Strategy for Synthesis of Nanoscale Metal–Organic Frameworks and Their Assembly into Hollow Superstructures. *Nat. Chem.* **5,** 203–211 (2013).

49. Garzón-Tovar, L., Rodríguez-Hermida, S., Imaz, I. & Maspoch, D. Spray Drying for Making Covalent Chemistry: Postsynthetic Modification of Metal–Organic Frameworks. *J. Am. Chem. Soc.* **139,** 897–903 (2017).

50. Deshpande, R. K., Minnaar, J. L. & Telfer, S. G. Thermolabile Groups in Metal–Organic Frameworks: Suppression of Network Interpenetration, Post-Synthetic Cavity Expansion, and Protection of Reactive Functional Groups. *Angew. Chem. Int. Ed.* **49,** 4598–4602 (2010).

51. Servalli, M., Ranocchiari, M. & Van Bokhoven, J. A. Fast and High Yield Post-Synthetic Modification of Metal-Organic Frameworks by Vapor Diffusion. *Chem. Commun.* **48,** 1904–1906 (2012).

52. Hintz, H. & Wuttke, S. Solvent-Free and Time Efficient Postsynthetic Modification of Amino-Tagged Metal–Organic Frameworks with Carboxylic Acid Derivatives. *Chem. Mater.* **26,** 6722–6728 (2014).

53. Ablott, T. A., Turzer, M., Telfer, S. G. & Richardson, C. High Temperature Postsynthetic Rearrangement of Dimethylthiocarbamate-Functionalized Metal–Organic Frameworks. *Cryst. Growth Des.* **16,** 7067–7073 (2016).

54. Ragon, F., Horcajada, P., Chevreau, H., Hwang, Y. K., Lee, U.-H., Miller, S. R., Devic, T., Chang, J.-S. & Serre, C. In Situ Energy-Dispersive X-ray Diffraction for the Synthesis Optimization and Scale-up of the Porous Zirconium Terephthalate UiO-66. *Inorg. Chem.* **53,** 2491–2500 (2014).

55. Hajimohammadi, M., Safari, N., Mofakham, H. & Shaabani, A. A New and Efficient Aerobic Oxidation of Aldehydes to Carboxylic Acids with Singlet Oxygen in the Presence of Porphyrin Sensitizers and Visible Light. *Tetrahedron Lett.* **51,** 4061–4065 (2010).

56. Iqbal, N., Choi, S., You, Y. & Cho, E. J. Aerobic Oxidation of Aldehydes by Visible Light Photocatalysis. *Tetrahedron Lett.* **54,** 6222–6225 (2013).

57. Hamami, Z. E., Vanoye, L., Fongarland, P., de Bellefon, C. & Favre-Reguillon, A. Metal-free, Visible Light-Promoted Aerobic Aldehydes Oxidation. *J. Flow Chem.* **6,** 206–210 (2016).

58. Plaetzer, K., Krammer, B., Berlanda, J., Berr, F. & Kiesslich, T. Photophysics and Photochemistry of Photodynamic Therapy: Fundamental Aspects. *Lasers Med. Sci.* **24,** 259–268 (2009).

59. Zhu, T. C. & Finlay, J. C. The Role of Photodynamic Therapy (PDT) Physics. *Med. Phys.* **35,** 3127–3136 (2008).

60. Zhang, W., Li, B., Ma, H., Zhang, L., Guan, Y., Zhang, Y., Zhang, X., Jing, P. & Yue, S. Combining Ruthenium(II) Complexes with Metal–Organic Frameworks to Realize Effective Two-Photon Absorption for Singlet Oxygen Generation. *ACS Appl. Mater. Interfaces* **8,** 21465–21471 (2016).

Chapter 5

Design, synthesis and characterization of photo-active CPs

This chapter introduces light-harvesting and photothermal complexes, their applications and, in some cases, the strategies to include them in CPs and MOFs. Moreover, we explore in detail the ligand design approach followed to prepare CPs in heterometallic two-step synthesis; firstly synthesising the metalloligand with light-harvesting properties and secondly using of the pendant coordinating groups to expand it with a secondary metal ion or cluster. Herein, we report our contribution working with two different light-harvesting cores; the 2,6-bis(1'-methylbenzimidazolyl)pyridine (MeBIP) and Ru^{2+}-terpyridine-based ligands. The photothermal effect of the extended CPs is assessed and compared with the reported for MOFs in Chapter 3.

1.   Photothermally active complexes

Behind the carbon-based materials with strong photothermal effect, introduced in Chapter 3, there are also complexes and coordination sites of supramolecular polymers with this property. The broad absorption bands in the UV-Vis and/or near-IR (NIR) regions of these organometallic species are the responsible of this light-to-heat conversion behaviour. Herein, we highlight some of the most remarkable works enclosing discrete or extended structures with significant photothermal effect and their applications.

In 2011, Rowan, Weder and co-workers reported an exceptional example of a supramolecular polymer with self-healing behaviour (Figure 1.1).[1] In order to attain this properties, the authors synthesised polymers containing poly(ethylene-co-butylene) cores, which gave the rubbery consistence to the material, with 2,6-bis(1'-methylbenzimidazolyl)pyridine (MeBIP) moieties capping the polymeric chains. The three amino groups in the MeBIP functionalities were subsequently coordinated to Zn^{2+} or La^{3+} leading to the formation of supramolecular polymers (Figure 1.1a). Thanks to this coordination environment, the material presents wide absorption bands in the UV range (Figure 1.1b). Thereafter, these supramolecular polymers exhibited strong photothermal effect when exposed to UV light (320-390 nm) at an irradiance of 950 mW·cm^{-2}. A local temperature increase up to 225 °C was observed after only 30 seconds of irradiation (Figure 1.1c). Having demonstrated the photothermal effect in the material, the authors used the generated heat to recover the initial shape of previously damaged polymeric films. In this sense, the rearrangement of the coordinative bonds in very short times allowed to fix the films.

Complexes containing nickel-bis(dithiolene) cores are also known to exhibit photothermal effect.[2,3] These complexes present strong absorption bands in the NIR region and high thermal- and photo-stability. In addition, the absorption maximum can be tuned depending on the dithiolene substituents. Noteworthy, nickel-bis(dithiolene) complexes are non-luminescent, thus, all the absorbed light is released as heat. In the work by Camerel and co-workers,[3] a water solution of complex 3 (Figure 1.2a) was irradiated using a laser at 940 nm. Considerable temperature increases were observed, being as high as +20 °C or +65 °C, when irradiating a sample of 500 μg·mL^{-1} at 1000 mW·cm^{-2} or 5000 mW·cm^{-2}, respectively. The strong photothermal effect shown by these nickel-bis(dithiolene)-based complexes allowed to evaluate them as photothermal therapy agents. The exposure of the complex (150 μg·mL^{-1}) to human renal carcinoma cells (786-0) and subsequent irradiation (5000 mW·cm^{-2} for 10 minutes), led to <20 % of cell viability, compared to a 70 % without light exposure.
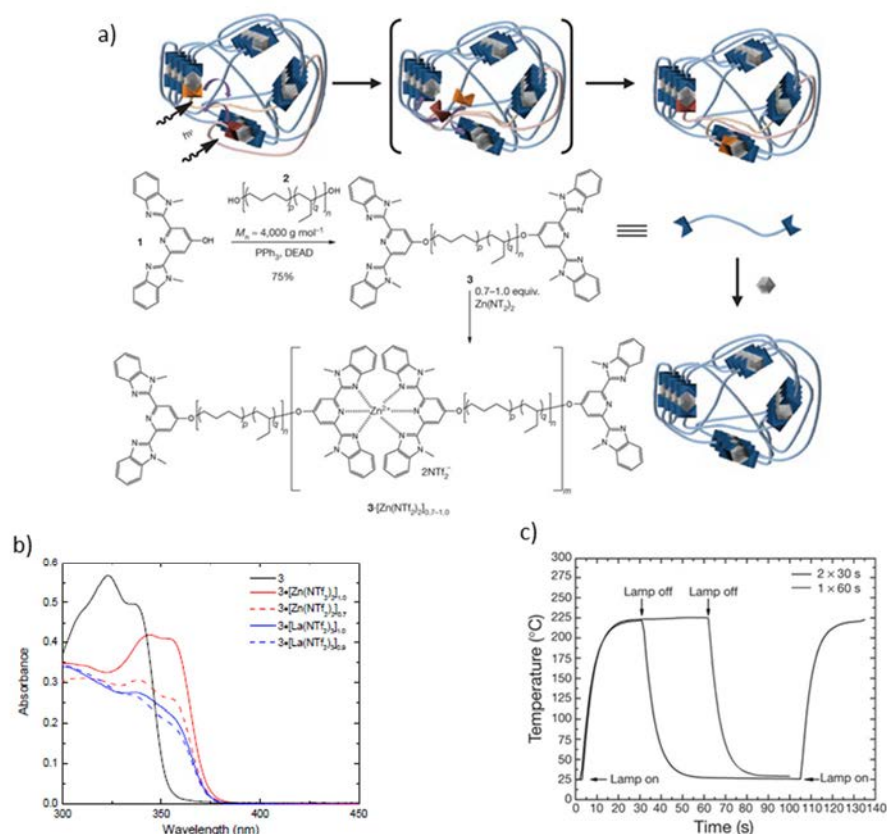
Figure 1.1. a) Scheme of the synthesis of the supramolecular polymer. b) UV-Vis spectra of 3 (Black solid), 3·[Zn(NTf2)2]1.0 (red solid), 3·[Zn(NTf$_2$)$_2$]$_{0.7}$ (red dash), 3·[La(NTf$_2$)$_3$]$_{1.0}$ (blue solid) and 3·[La(NTf$_2$)$_3$]$_{0.9}$ (blue dash) thin films (where 3 is the organic polymer) c) Temperature vs. time plot during irradiation of the Zn-based polymer at 950 mW·cm^{-2}.[1]
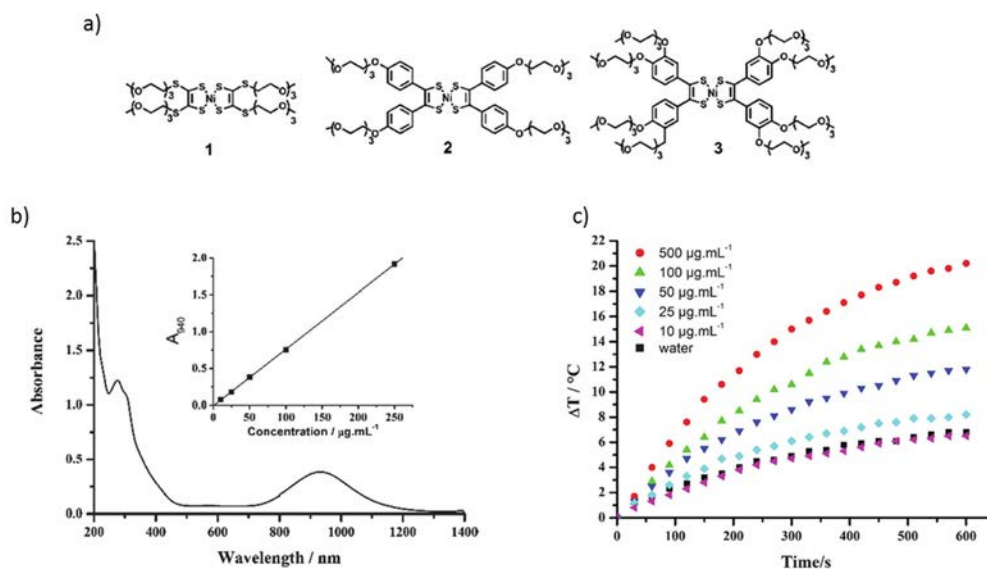
Figure 1.2. a) Synthesised nickel-bis(dithiolene)-based complexes. b) UV-Vis-NIR absorption spectrum of complex 3 dissolved in water. c) Temperature vs. time plot of complex 3 irradiated at 1000 mW·cm^{-2}.[3]

Metalla-aromatic complexes are a type of complexes where the metal centres are chelated by conjugated-carbon chains, also known as "carbolong complexes". A subfamily of these metallacyces contain osmium as the metal fragment. Some of these complexes have demonstrated to perform efficient light-to-heat conversion.[4–8] One of the early examples in this field was reported by Zhu and Xia in 2015.[4] In this work, they reported the stabilization of two antiaromatic moieties through coordination to an Os^{1+} core (Figure 1.3a). Moreover, the spectroscopic characterization of these complexes revealed absorption maxima in the UV, Vis and NIR regions (Figure 1.3b). In addition, subsequent irradiation of the dissolved complexes using a laser source (808 nm) at an irradiance of 1000 mW·cm^{-2} evidenced photothermal effect. The strongest temperature increase was shown by complex 2 at a concentration of 1 mg·mL^{-1}, which reached 56 °C (+24 °C increase) in 5 minutes (Figure 1.3c). Very recently, Chen and Xia synthesised a 12-carbon osmium carbolong complex.[7] In this work, they required 10-times less concentrated solution of complex (only 0.1 mg·mL^{-1}) to reach a temperature of 66 °C (+ 36 °C increase) under the same irradiation conditions.
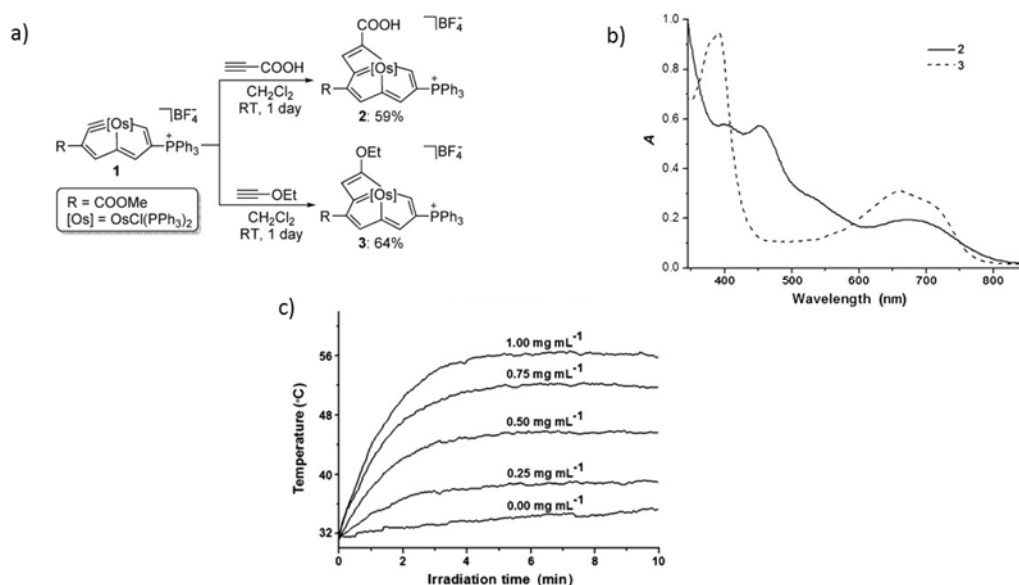
Figure 1.3. a) Synthesis scheme of Os complexes 2 and 3. b) UV-Vis absorption spectra of complexes 2 and 3 dissolved in dichloromethane. c) Temperature vs. time plot of complex 2 dissolved in DMSO under light irradiation (808 nm and 1000 mW·cm^{-2}).[4]

The light-harvesting properties of terpyridine-based complexes has been extensively studied.[9] These organometallic species have been used in multiple applications such as artificial photosynthesis, photodynamic therapy and photocatalysis. The main feature of these complexes is their broad light-absorption bands. Therefore, they are also potential candidates

for exhibiting photothermal effect. The following section encloses an overview of a subfamily of polypyridyl complexes and their applications. In addition, some bipyridine- and terpyridine-based compounds have been introduced in extended crystalline coordination polymers and metal-organic frameworks in order to transfer their unique properties to ordered materials.

2.   Ru^{2+} organometallic compounds

Metallic ruthenium (Z=44) is a rare element found in the Periodic Table located at the platinum-group metals, which is composed by Ru, Os, Rh, Ir, Pd, Pt (groups 8, 9 and 10 and periods 5 and 6). Ruthenium can be found in a number of oxidation states comprising -4, -2, 1, 2, 3, 4, 5, 6, 7 and 8. Noteworthy, oxidation states +2 or +3 can form soluble cations.[10] Ru^{2+} ion has an electronic configuration of $[Kr]4d^6$, which tends to generate organometallic complexes with **octahedral coordination geometries**. The most common coordination environments for Ru^{2+} are three bidentate N^N ligands like bipyridine or phenanthroline-based, or two tridentate N^N^N ligands such as terpyridine derivatives. The appealing features of this kind of organometallic compounds rely heavily on their ability to absorb light in the visible range, their relative long-lived excited states and the further emission in the red and near IR light. The combination of these properties with a remarkable chemical stability and redox features converted them in an attention focus for many research groups in the past decades, leading to the publication of a large number of derivatives.[11–13] A paradigmatic example of Ru^{2+}-polypyridyl complex is [Ru(bpy)$_3$]Cl$_2$, a compound that, although it was first synthesised in the 1930s, the report of its luminescent properties date from 1959.[14] Paris and Brandt proved experimentally the light absorption and luminescence of a solution of tris-2,2'-bipyridineruthenium^{2+} chloride and discussed the electronic transitions involved in the processes. This iconic example presents a maximum absorption band at *ca.* 452 nm and undergoes electron excitation upon photon absorption when irradiated with visible light. This process is rationalized as the excitation of one electron of the t_{2g} orbital of the metal center to the π^* orbital of the ligand, known as metal-to-ligand charge transfer (MLCT). The original photoexcited state consists on the singlet ^{1}[Ru(bpy)$_3$]$^{2+*}$ which has a short life and is rapidly transformed to the long-lived triplet state ^{3}[Ru(bpy)$_3$]$^{2+*}$ (microseconds). Such excited state is more oxidizing and reducing than the ground state, thus, leading to Ru(bpy)$_3^{3+}$ (1.29 V in MeCN) or Ru(bpy)$_3^+$ (-1.33 V in MeCN) when using an oxidative or a reductive quencher, respectively (Figure 2.1). This dual behaviour makes Ru^{2+}-polypyridyl complexes very attractive for photoredox reactions.

In addition, **Ru²⁺-based polypyridyl** complexes have emerged as designed compounds with **light-harvesting** properties in order to mimic natural chromophores in the photosynthesis.[15–24] The light-harvesting process is defined as the electronic energy transfer through the movement of electronic excitation energy.
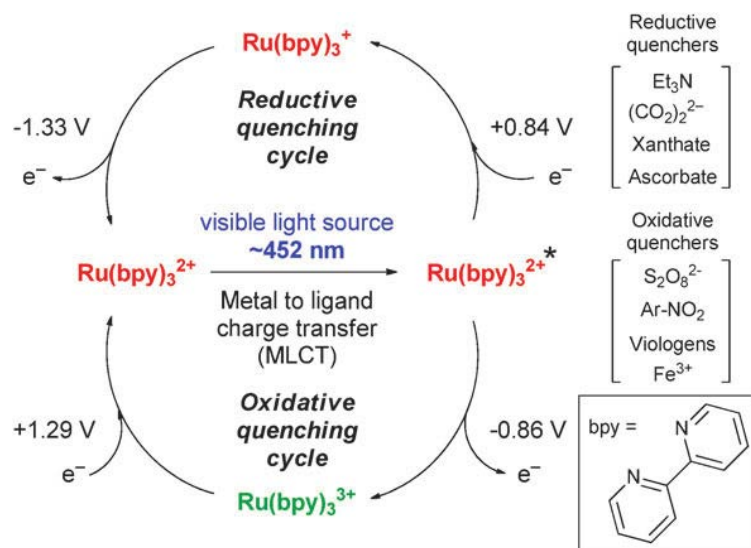
Figure 2.1. Scheme presenting the versatility of the Ru(bpy)₃²⁺ complex in both reductive and oxidative cycles upon visible light irradiation.[25]

2.1. Applications

The unique properties that these compounds exhibit have been proved useful in different fields of application such as solar cells,[26–30] sensing,[31–34] photocatalysis,[25,35–37] biomedicine,[38–42] among others. Some of the most representative examples are summarized below.

2.1.1. Dye-sensitized solar cells (DSSC)

In 1991, Grätzel and co-workers were the first to prepare an efficient DSSC.[26,27] This type of solar cells are structured as follows: a network of TiO_2 sintered nanoparticles is deposited over a transparent layer of conducting oxide, commonly fluorine doped tin oxide (FTO), coating a glass or plastic substrate. A monolayer of the Ru^{2+}-based dye [Ru(dcbpy)₂(NCS)₂] were dcbpy = 4,4'-dicarboxybipyridine and NCS is isothiocyanate, also known as "red dye", is attached to the mesoporous nanocrystalline film. This light-harvesting complex plays the role of charge transfer when it is photoexcited using sunlight, leaving it in the oxidized state (Ru^{3+}). The authors reported an ultrafast electron injection from the excited MLCT state of the photosensitizer to the TiO_2 conduction band. A solution of I^-/I_3^- redox system in an organic solvent covers the surface and restores the dye to its ground state. Once the photosensitizer is regenerated, the

formed I_3^- ions diffuse to the cathode coated with a Pt layer where the reduction to I^- species takes place completing the cycle (Figure 2.2).
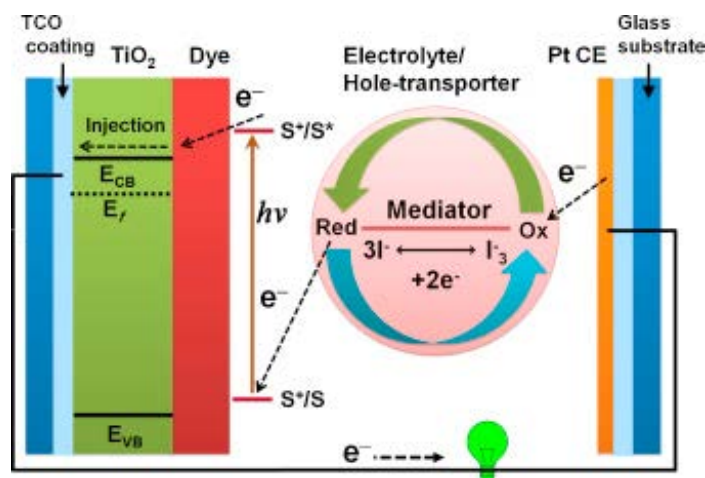
Figure 2.2. Schematic illustration of the structure and processes occurring in a DSSC.[43]

Although many derivatives have been synthesised with the aim to improve the efficiency of the parental example, only a Ru^{2+} complex based on terpyridine[9] has proven to be successful in DSSC. The "black dye", with formula $[Ru(tct)(NCS)_3]^-$, where tct is 4',4",4'''-tricarboxylic acid-tpy and tpy is 2,2':6',2"-terpyridine, presents extended light absorption until the near-IR region up to 920 nm (Figure 2.3).[30]
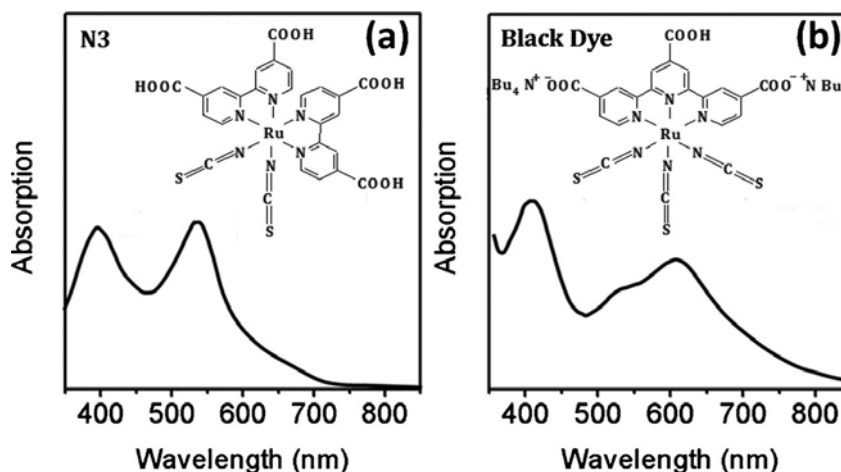
Figure 2.3. UV-Vis absorption spectra and structures of a) red dye and b) black dye.[44]

2.1.2. Photothermal effect

The ability to absorb light by Ru^{2+} complexes has also been exploited to enhance the photothermal effect in Au nanoparticles. Chao and co-workers grafted a Ru^{2+} complex with Au

nanorods and nanostars, which conferred a higher absorbance in the Vis-NIR range to the nanoparticles (Figure 2.4).[45] The wider absorption band permitted to increase the generated heat of the composite. While the Au nanoparticles alone led to a temperature rise of 20 °C, the Ru@Au composite reached an increase of *ca*. 40 °C. Such high photothermal effect was applied as hyperthermia therapy *in vitro* using HeLa cell line and *in vivo* in tumour-bearing mice, leading to efficient destruction of cancer cells.
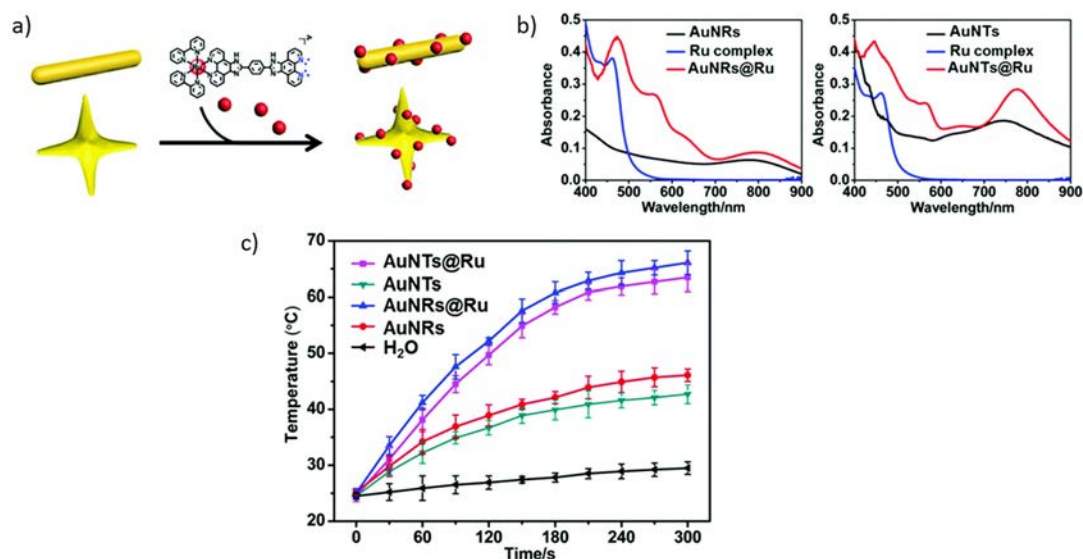
Figure 2.4. a) Grafting scheme between Au nanoparticles and the Ru[2+] complex. B) Vis-NIR spectra of the precursors and the final composite. c) Temperature vs. time plot upon irradiation using a laser at 808 nm under 0.25 W·cm^{-2}.

2.1.3. Biomedical applications

Ru[2+]-polypyridyl complexes have been extensively studied in the biomedical field following several approaches. For instance, they can be used as luminescence probes for diagnosis and imaging, as therapeutic agents or conjugated with biomolecules.[41,42] These complexes usually absorb light around 400-500 nm (visible), which are wavelengths suitable for *in vitro* assessments but too energetic for *in vivo* applications, as tissue penetration demands the use of wavelengths ranging from 650-900 nm (near-IR). One smart strategy to overcome such limitation was to perform a two-photon absorption, consisting on the simultaneous absorption of two photons of the half energy required to excite a Ru[2+] complex from the ground to the excited state.[46]

Light induced therapeutic treatments, such as photodynamic therapies, result very appealing thanks to the spatial and temporal control that this stimuli provides. Ru[2+]-polypyridyl complexes

have proved useful in this kind of therapies thanks to their ability to transfer electrons and energy in order to obtain reactive oxygen species (Figure 2.5).[41,47] The generation of reactive oxygen species upon irradiation are able to trigger cell damage to leading to apoptosis or necrosis of a malicious tumour.
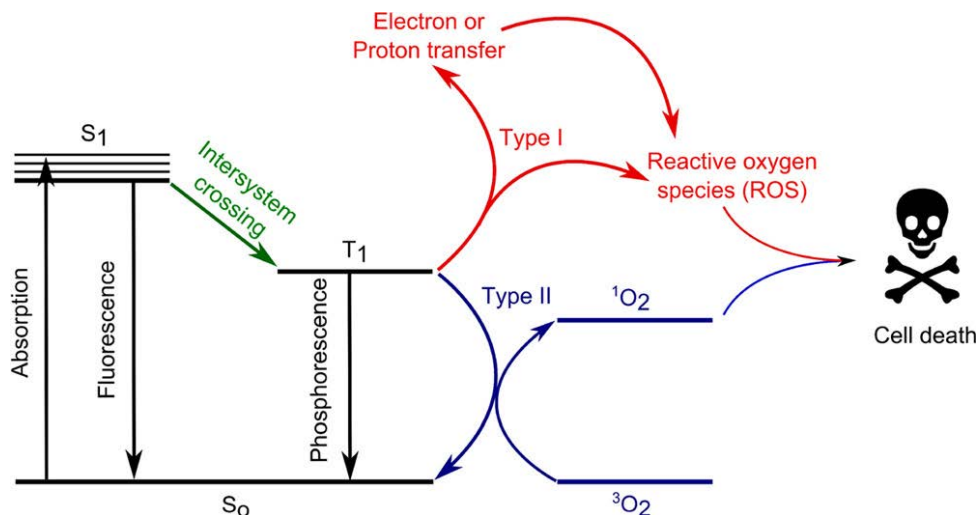
Figure 2 5. Scheme of the different routes followed by light-harvesting compounds with the goal to generate toxic species for photodynamic therapies.[47]

Gunnlaugsson, Williams and co-workers designed and synthesised the complex [Ru(TAP)$_2$pdppz]·2PF$_6$, being TAP=tetraazaphenanthrene and pdppz=[2,3-*h*]dipyrido[3,2-*a*:2',3'-*c*]phenazine, where the lipophilic aromatic group pdppz allowed cell incorporation and the TAP group displays the photo-active role (Figure 2.6).[40] This complex did not show high activity against HeLa cells under dark conditions (IC$_{50}$>100 µM). However, when irradiated with visible light (λ>400 nm and 18 J·cm^{-2}), it provided strong cytotoxicity (IC$_{50}$=8.8 µM) due to the generation of reactive oxygen species.
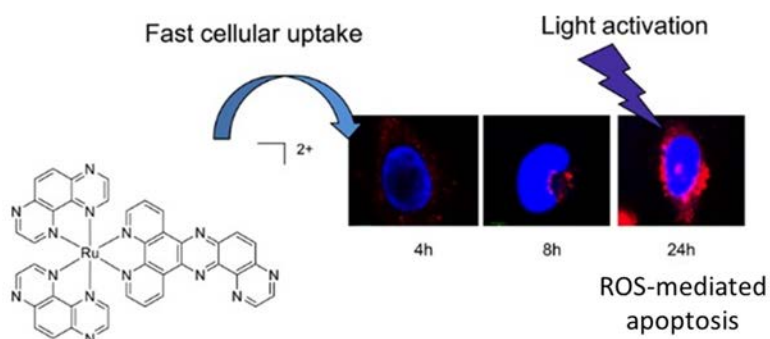
Figure 2.6. Ru^{2+}-polypyridyl complex that combined a fast cellular uptake and effective photoexcitation for photodynamic therapies.[40]

2.1.4. Photocatalysis

Thanks to the ease of synthesis, the stability at RT and the excellent photoredox properties, Ru^{2+}-polypyridine complexes have been proposed as candidates for photocatalysis in a number of reactions, including organic synthesis, water oxidation, reduction and splitting and CO_2 reduction. The number of reviews on this topic reveals the importance and the advantages that many researchers have found in this kind of organometallic compounds.[25,37,48–52]

As illustrative example, the oxidation of water to O_2 was achieved by Scandola, Satorel and co-workers using the well-standardized $Ru(bpy)_3^{2+}$ complex, as the light-harvesting moiety, and a Co^{2+} organometallic complex as the catalyst for oxygen evolution.[53] The reported catalytic process starts with the photon capture by the Ru^{2+} antenna, which leads to a photoexcited state able to transfer an electron to persulfate ($S_2O_8^{2-}$) that acts as a sacrificial electron acceptor. Such electron transfer promotes the formation of $SO_4^{..}$ radicals involved in the oxidation of Ru^{2+} to Ru^{3+}. Thereafter, the Ru^{3+}-polypyridyl species are ready to oxidise the Co^{2+} catalyst to a hypothesized Co^{+4}-oxo intermediate generating an O-O bond (Figure 2.7).
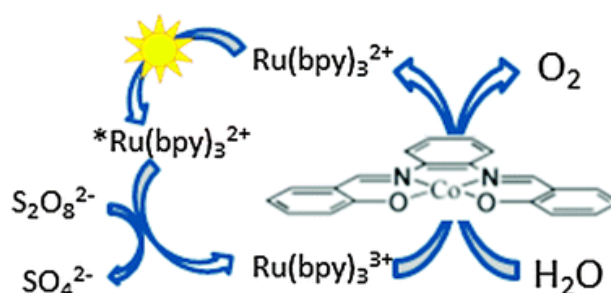
Figure 2.7. Schematic representation of the photocatalytic cycle for water oxidation mediated by $Ru(bpy)_3^{2+}$ and a Co^{2+} salophen catalyst.[53]

2.2. Ru-based coordination polymers and metal-organic frameworks

An optimal disposition and distance is required to have an efficient electron transfer between the Ru^{2+} light-harvesting organometallic complex and the electron acceptor. In some cases, these processes might show lowered efficiency due to aggregation-induced quenching or long-range distances between both the donor and acceptor species. For this reason, self-assembly of such entities through coordination chemistry has emerged as an engaging strategy to favour a close and periodic arrangement avoiding this type of problems.

To date, several approaches have been explored for including Ru^{2+}-complexes in CPs and MOFs. These approaches can be classified into three main groups depending on how the

functional building unit is added to the final architecture: post-synthetic modification (PSM), encapsulation, doping and **heterometallic two-step synthesis.**

Cohen and co-workers reported the inclusion of Ru^{2+} photocatalyst complexes into UiO-67 frameworks via PSM. Two different approaches were employed in order to achieve the desired incorporation. On one hand, pre-synthesized UiO-67, using H_2dcbpy (where H_2dcbpy is [2,2'-bipyridine]-5,5'- dicarboxylic acid) as a bridging ligand, was reacted with $Ru(bpy)_2Cl_2$ in order to carry out a post-synthetic metalation with Ru loadings from 2-15 % (Figure 2.8). The complex was integrated into the final structure by substituting the labile Cl atoms for the N donor atoms located in $dcbpy^{2-}$ ligands. On the other hand, a post-synthetic ligand exchange (PSE) approach was employed to substitute the whole linker by dicarboxylate containing Ru^{2+} complexes leading to a Ru loading of 1 % (Figure 2.8).[54]
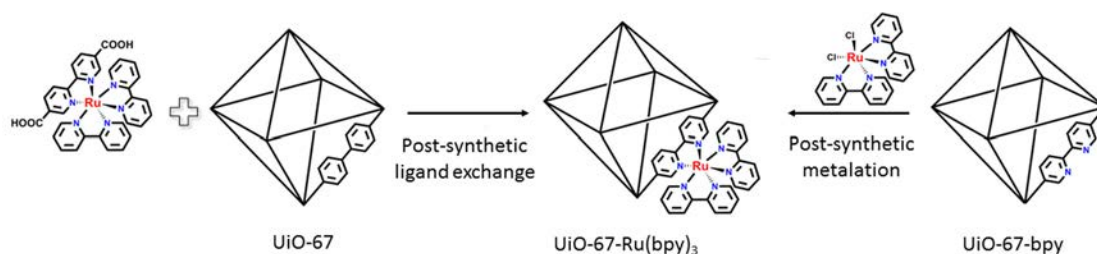
Figure 2.8. Scheme of the post-synthetic ligand exchange and the metalation approaches to obtain a UiO-67-Ru(bpy)₃ MOF.

Occluding Ru^{2+} complexes in the cavities of MOFs has also been proved as a useful strategy. Despite the large size that these complexes might present, the tunability of the MOF pore size allows their inclusion as it has been reported in several examples.[55–59] The work published by Grzybowski and co-workers shows the encapsulation of $Ru(bpy)_3Cl_2$ (1.15 nm diameter) inside a cyclodextrin MOF (1.7 nm pore diameter).[55] By using this approach, a maximum loading of 40 % of occupied cavities was achieved. Light irradiation of the samples permitted light-harvesting by the Ru^{2+} species and subsequent reduction of metal salts to nanoparticles. These cavities provided the photosensitizer with electron donors (OH⁻ ions) closing the catalytic cycle (Figure 2.9).
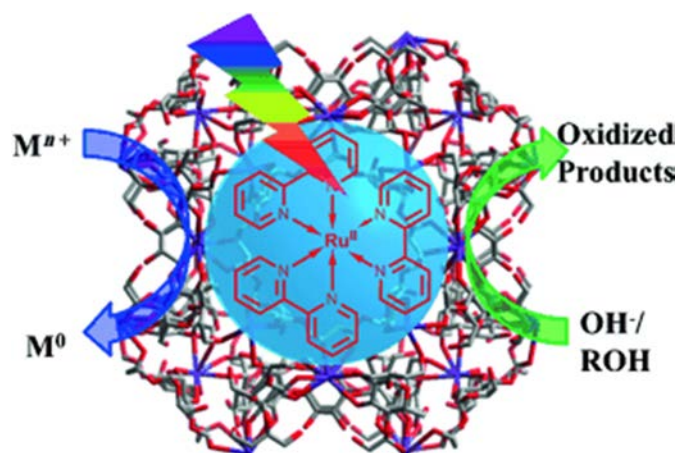
Figure 2.9. Scheme of the encapsulation of Ru^{2+} in a CD-MOF approach.[55]

The well-known mixed ligand or doping strategy was used in several examples aiming for the introduction of a photosensitizer in the MOF scaffold.[60–63] For instance, Lin and co-workers selected two building blocks as spacers between the Zr-clusters; one metalloligand moiety containing Ru^{2+}, $[Ru(bpy)_2(dcbpy)]Cl_2$, where dcbpy = 2,2'-bipyridine 4,4'-dicarboxylic acid, and bpdc, 4,4'-biphenyldicarboxylic acid, as pure organic linker (Figure 2.10).[60] Both spacers are ditopic carboxylic donors with identical length, avoiding structural strain and, therefore, they both participate in the construction of the UiO like framework. A doping percentage of a 5.9 wt % of the complex was achieved and further oxygen sensing experiments were carried out.

However, among all these strategies, the two-step synthesis based on purely metalloligands is a useful tool in order achieve a higher degree of inclusion of Ru^{2+} centres in comparison to PSM, encapsulation and doping methods, where the conversion rate is usually moderate to low. This synthesis requires the use of a building block known as **metalloligand**. A metalloligand can be described as a discrete coordination compound that contains a primary coordinated metal centre and appended donor sites able to coordinate a further metallic centre.[64] Following this approach, some examples of structures purely based on Ru^{2+}-bipyridine as metalloligands combined with additional metallic ions, acting as nodes or clusters, have been reported.[65–68]

Two illustrating structures are the ones synthesised by Lin and co-workers, who designed a couple of Ru^{2+}-polypyridyl complexes tagged with carboxylic groups leading to $[Ru(dcbpy)_2bpy]^{2+}$ and $Ru(dcbpy)_2(CN)_2$, where dcbpy is 4,4'-dicarboxybipyridine (Figure 2.11).[65,66] These compounds were extended using Zn^{2+} under solvothermal conditions forming 2D MOFs. The goal of this work was to obtain doped structures by mixing different amounts of the equivalent Os^{2+}

complex during the MOF synthesis in order to assess the energy transfer from the excited MLCT of the Ru^{2+} moiety (chromophore) to the Os^{2+} centre (quencher).
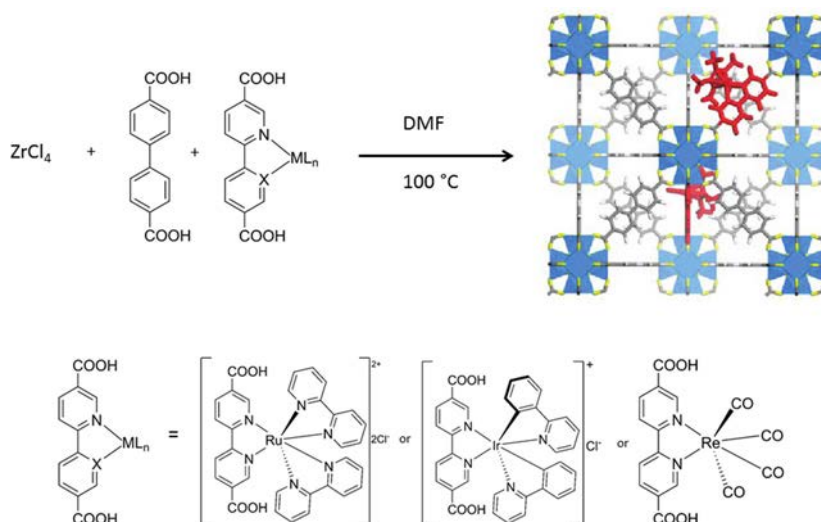
Figure 2.10. Reaction scheme of the doping strategy to include organometallic complexes in MOF structures.[60]
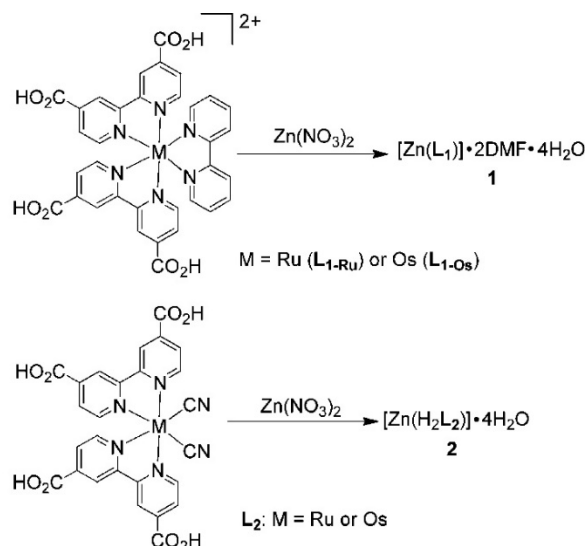
Figure 2.11. Synthetic routes employed to obtain two MOFs using Ru^{2+} bipyridine as metalloligands.[65,66]

Luo and co-workers contributed with the synthesis of a highly symmetric MOF built up from the assembly of the light-harvesting complex $Ru(dcbpy)_3\cdot2Cl^-$ and In^{3+} (Figure 2.12).[67] Photoluminescence characterization of this MOF confirmed a wide absorption in the UV-Vis range and fluorescence emission with a maximum centred at 657 nm. These properties, which where conferred to the MOF thanks to the inclusion of the Ru^{2+} complex, allowed using it for the photodecomposition of methyl orange and for detecting explosives. Light-driven dye decomposition was hypothesised to occur due to hydroxyl radical generation during visible light

irradiation. On the other hand, the detection ability was related to the fluorescence quenching when interacting with electron deficient analytes.
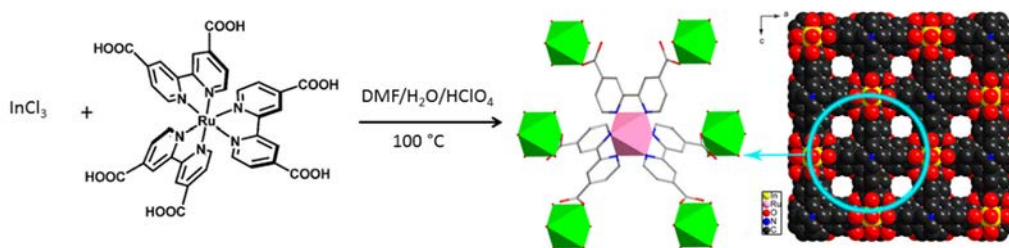
Figure 2.12. Synthesis scheme of the MOF based on the complex Ru(dcbpy)$_3$.[67]

Further research on the heterometallic two-step synthetic routes has been developed focusing the interest on integrating terpyridinic Ru^{2+}-containing complexes (Figure 2.13). These compounds based on terpyridine are good candidates for dye sensitized solar cells (*vide supra*).

To the best of our knowledge, few examples of extended structures containing Ru^{2+} terpyridine metalloligands have been reported. Toyao and co-workers synthesised a Ti-based photocatalyst CP using the carboxylic donor Ru(cptpy)$_2$$^{2+}$ (where cptpy is 4'-(4-carboxyphenyl)-2,2':6,2''-terpyridine) as building block. This MOF was used for H$_2$ production.[69] However, single crystals were impossible to obtain and consequently, full structural information was not reported. Other N-donor Ru^{2+}-terpyridinic complexes have also been used for the construction of CPs (Figure 2.13). Moreover, two-dimensional CPs were also obtained by Constable, Housecroft and co-workers combining Ru^{2+} pyrimidinyl-terminated terpyridine complexes with Cu^{2+} ions.[70]
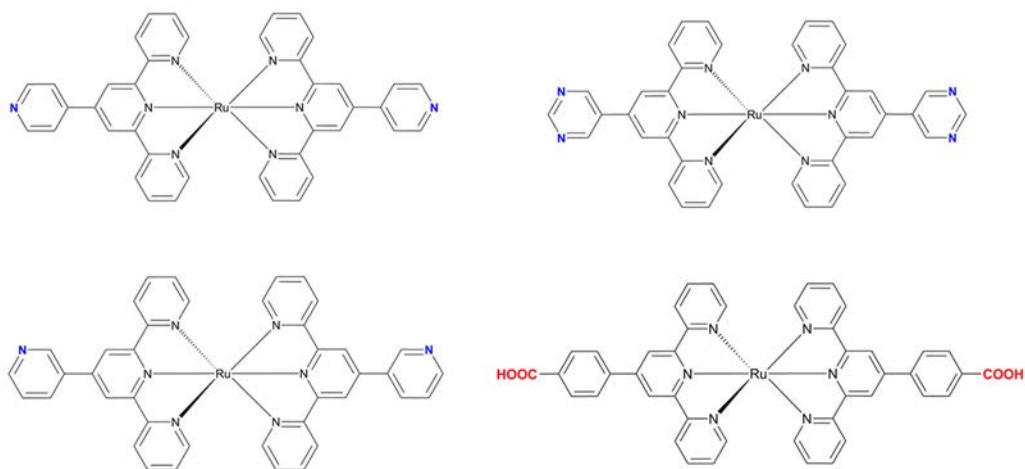
Figure 2.13. Ru^{2+}-terpyridinic ligands used to construct CPs.

3.   Results and discussion

As summarized in Chapter 2, the main goal of this project was to transfer the light harvesting ability 2,6-bis(1'-methylbenzimidazolyl)pyridine (MeBIP) and Ru^{2+}-terpyridine-based complexes to extended ordered crystalline structures. In these sense, metal-organic frameworks or coordination polymers with the properties of the original building blocks might be obtained.

3.1. Synthesis of organic MeBIP-based ligands and metalloligands

With the aim for constructing photo-responsive MOFs, we synthesised organic ligands with the 2,6-bis(1'-methylbenzimidazolyl)pyridine (MeBIP) core. This organic moiety was proved to be responsible of strong photothermal effect when introduced in a supramolecular polymer.[1] Therefore, we first attempted to attach a pendant carboxylic group to the photo-active molecule.

The reported procedure[71] allowed us to synthesise the hydroxy-substituted MeBIP, namely **HOBIP**. This ligand was synthesised *via* Phillips condensation. The reaction consists on the condensation between *ortho* phenylenediamines (*N*-methyl-1,2-phenylenediamine) and organic acids (chelidamic acid) using mineral acids (H$_3$PO$_4$) leading to the formation of benzimidazole moieties. A final precipitation in methanol allowed to obtain the expected product as proved by EA, ESI-MS and ^{1}H-NMR analyses (Figure 3.1).
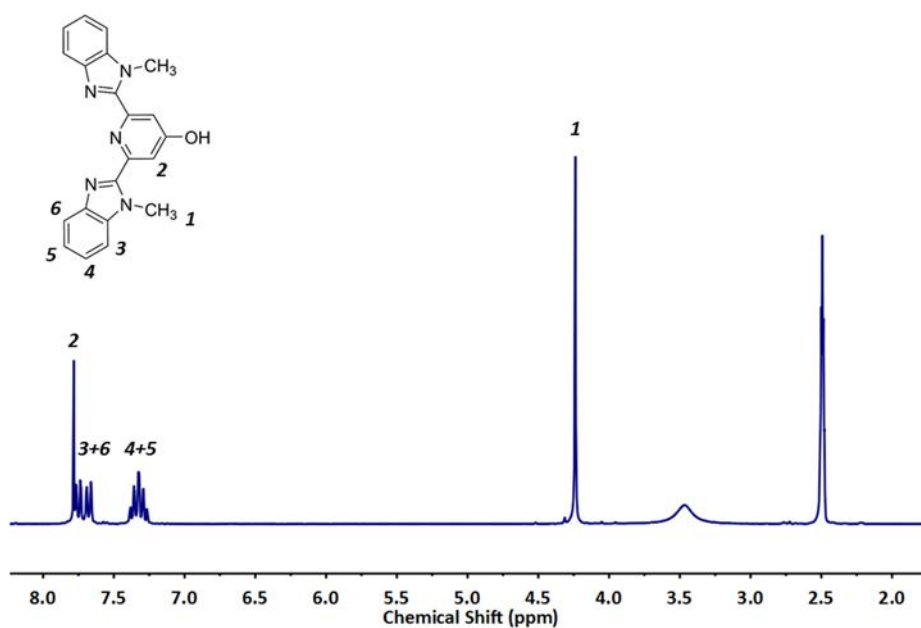
Figure 3.1. ^{1}H-NMR spectrum of HOBIP in DMSO-d_6.

The synthesis of **HAcOBIP** was reported in the literature.[72] Nucleophilic substitution of the OH group using benzyl bromoacetate gave rise to the desired ligand. This step led an ether bond and a pendant carboxylic group. ^{1}H-NMR spectrum confirmed the presence of the protons 1-6 observed in the **HOBIP** molecule and the new shift at 4.36 ppm was attributed to proton 7 (Figure 3.2).
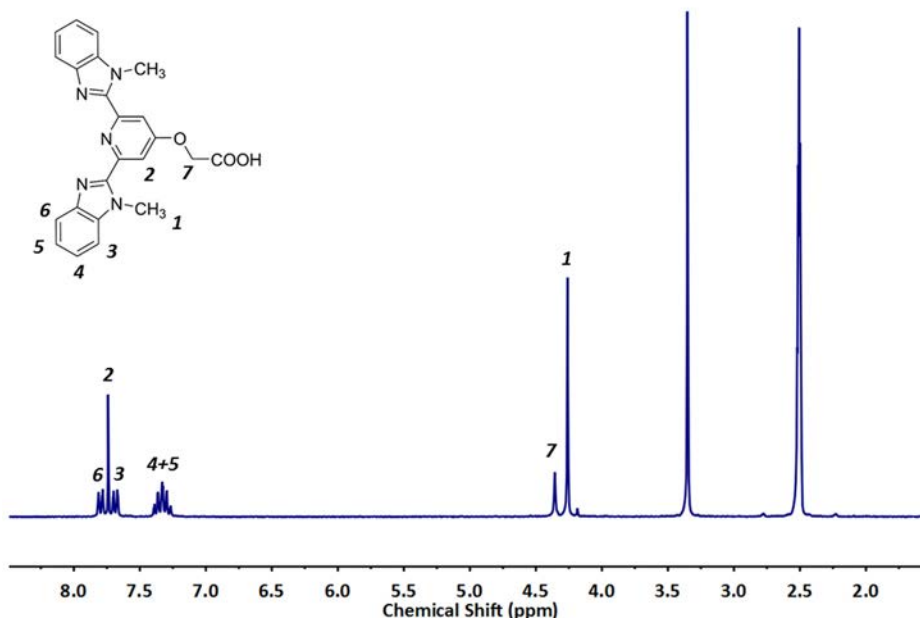
Figure 3.2. ^{1}H-NMR spectrum of HAcOBIP in DMSO-d_6.

A more detailed explanation of the synthesis of the organic ligands is given below.

3.1.1. Synthesis of HOBIP

The synthesis of **HOBIP** was adapted from the literature (Figure 3.3).[71] $H_3PO_{4(aq)}$ 85 % (25 mL) was poured in a 100 mL round-bottom flask. Then, chelidamic acid (6.75 g, 36.86 mmol) was added to the acidic solution and stirred using a glass rod in order to break solid aggregates. N-methyl-1,2-phenylenediamine (8.4 mL, 73.91 mmol) was added dropwise to the mixture under magnet stirring. Afterwards, the flask was heated gradually up to 220 °C using a heating mantle without capping the flask (colour change from pink to dark blue). The mixture was left at 220 °C for 10 hours under stirring. The viscous mixture was let to cool down to around 100°C and it was poured to 600 mL of deionized water. The aqueous solution was stirred with a glass rod to break aggregates until a light blue suspension was formed. The solid was collected by filtration and subsequently added to 1L of K_2CO_3 10 % (dark red/pink suspension formed). This mixture was filtered using a Büchner funnel and the obtained solid added to 1 L f hot MeOH (ca. 50 °C) under vigorous stirring. Finally, HCl 1M was added dropwise to the methanolic solution until it changed

from dark pink to dark blue (*ca*. pH 5) and let cool down overnight. The solid was collected and washed three times with 10 mL H_2O. Final weight: 8.20 g (Yield: 71 %); Elemental Analysis (%): Found: C 71.49; H 4.51; N 19.94; $C_{21}H_{17}N_5O$ requires C 70.97; H 4.82; N 19.71; ^{1}H-NMR (250 MHz, DMSO-*d₆*): δ_H (ppm) = 7.78 (2H, s), 7.75 (2H, dd), 7.68 (2H, dd), 7.32 (4H, m), 4.24 (6H, s); *m/z* (ESI-MS) calculated for $[C_{21}H_{17}N_5O]^+$: 356.15 ; Found 356.15 $[M]^+$.
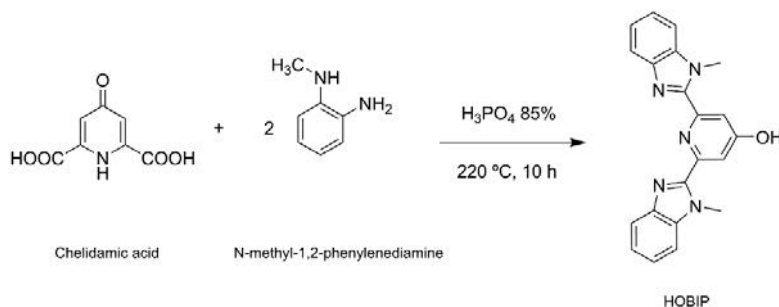
Figure 3.3. Scheme of the synthesis of HOBIP intermediate.

3.1.2. Synthesis of HAcOBIP

HAcOBIP ligand was synthesised using a reported protocol (Figure 3.4).[72] K_2CO_3 (1.5 g, 10.85 mmol) and absolute EtOH (45 mL) were mixed in a 100 mL round-bottom flask. Then, **HOBIP** (1.5 g, 4.22 mmol) was added and the mixture was subsequently heated up to 50 °C until it was all dissolved and a red solution was formed. Once the set temperature was reached, benzyl bromoacetate (1 mL, 6.31 mmol) was added dropwise. The solution was heated to reflux (*ca.* 90 °C) for 18 hours. Afterwards, the mixture was let to cool down and the solid was collected using a Büchner funnel. The pink/brownish solid was washed once with 5 mL EtOH and five times with 5 mL H_2O. Final weight: 0.95 g (Yield: 55 %); Elemental Analysis (%): Found: C 67.30; H 4.71; N 16.85; $C_{23}H_{19}N_5O_3$ requires C 66.82; H 4.63; N 16.94; ^{1}H-NMR (250 MHz, DMSO-*d₆*): δ_H (ppm) = 7.80 (2H, dd), 7.74 (2H, s), 7.69 (2H, dd), 7.33 (4H, m), 4.36 (2H, s), 4.26 (6H, s); *m/z* (ESI-MS) calculated for $[C_{23}H_{19}N_5O_3]^-$: 412.14 ; Found 412.14 $[M]^-$.

Two strategies were followed in order to extend **HAcOBIP**. On one hand, a two step synthesis approach, where an organometallic complex is first isolated and subsequently reacted with a second metal. On the other hand, a one-pot synthesis, mixing two metals with different affinities for amino or carboxylate coordination.
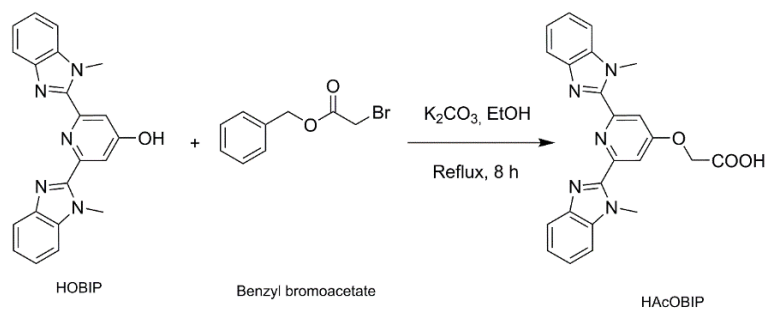
Figure 3.4. Scheme of the synthesis of HAcOBIP

3.1.3. Synthesis of HAcOBIP complexes

The ligand **HAcOBIP** was reacted with metal ions that coordinate preferably in an octahedral environment. The six amino groups from two ligands might promote this disposition when coordinating to a central metal ion. Therefore, the two carboxylic groups remain uncoordinated and might be available to extend the structure.

3.1.3.1. Synthesis of Ni(HAcOBIP)$_2$

HAcOBIP (10 mg, 0.024 mmol) was dissolved in 2 mL of EtOH (pink solution). Then, Ni(AcO)$_2$·4H$_2$O (6 mg, 0.024 mmol) was dissolved in 2 mL of H$_2$O and added to the ligand solution. The pale pink mixture was let stand 24 hours at room temperature. Gray/pink crystals were formed. The crystalline structure was solved using SCXRD (Figure 3.5).
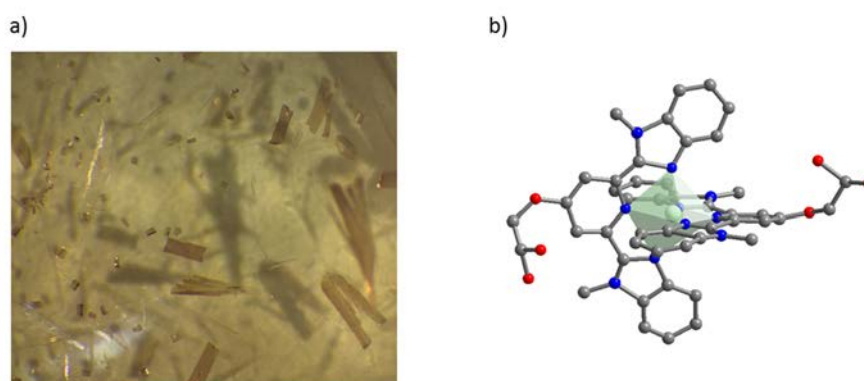
Figure 3.5. Photograph (a) and structure of Ni(HAcOBIP)$_2$ crystals.

3.1.3.2. Synthesis of Co(HAcOBIP)$_2$

The synthesis was the same as for Ni(HAcOBIP)$_2$ but using a Co^{2+} salt. **HAcOBIP** (10 mg, 0.024 mmol) was dissolved in 2 mL of EtOH and a solution of Co(AcO)$_2$·4H$_2$O (6 mg, 0.024 mmol) in 2

mL of H_2O was added to the ligand mixture. The solution colour changed immediately from pink to yellow. After leaving the vial for 24 hours at room temperature yellow crystals were obtained (Figure 3.6). The XRPD pattern of the crystals matched the one of $Ni(HAcOBIP)_2$, thus, we can conclude that the same structure was obtained (Figure 3.7).
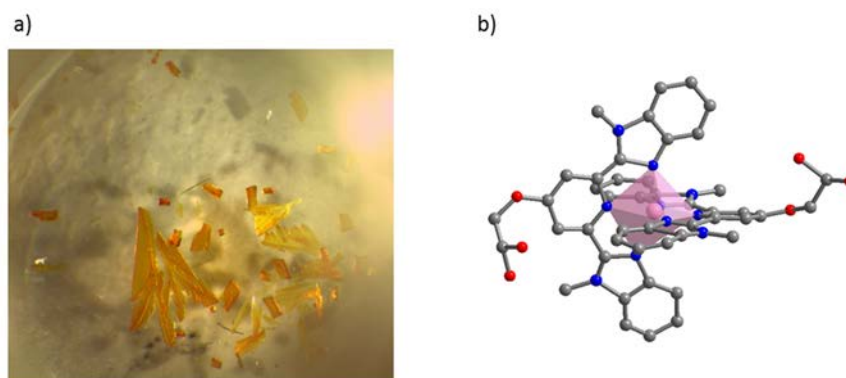
Figure 3.6. Photograph (a) and structure of $Co(HAcOBIP)_2$ crystals.
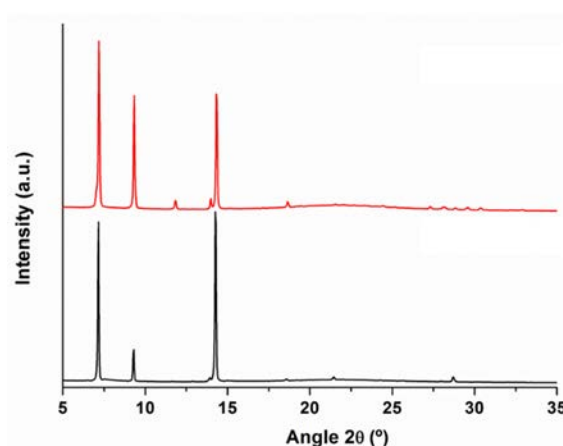
Figure 3.7. XRPD of $Ni(HAcOBIP)_2$ (black) and $Co(HAcOBIP)_2$ (red)

3.1.3.3. Synthesis of $Fe_2(HAcOBIP)_2Cl_4$

Using a similar procedure as for the Ni^{2+} and Co^{2+} complexes, an organometallic complex with Fe^{3+} was obtained. **HAcOBIP** (10 mg, 0.024 mmol) was dissolved in 2 mL of EtOH (pink solution). A solution of $FeCl_3 \cdot 6H_2O$ (6.5 mg, 0.024 mmol) in 2 mL H_2O was added to the ligand solution. The solution colour changed immediately from pink to orange. The final mixture was let to stand for 24 hours at room temperature. Final orange/yellow crystalline plates were obtained. SCXRD allowed solving the crystalline structure (Figure 3.8). However, XRPD was amorphous due to structural collapse once dried.
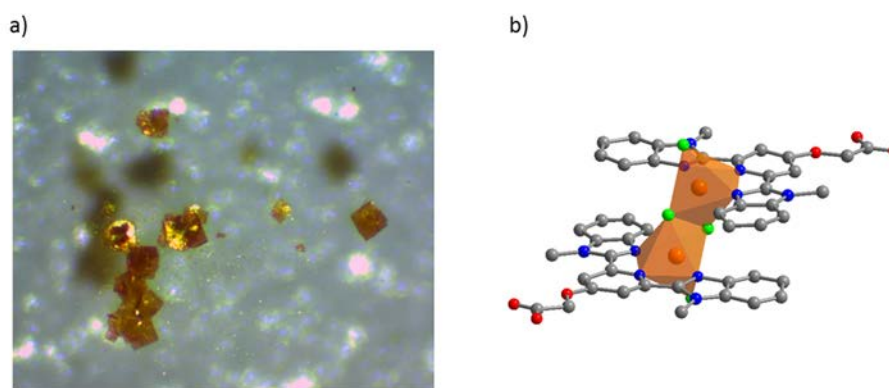
Figure 3.8. Photograph (a) and structure of $Fe_2(HAcOBIP)_2Cl_4$.crystals.

Unfortunately, the yield of these reactions was very low and full characterization could not be performed. Although few reactions with a second metal salt could be performed, none of these complexes led to extended crystalline structures. In some cases, amorphous solids were obtained. We hypothesised that the flexibility of the carboxylic arms, altogether with the bulkiness of the MeBIP cores, might hinder the formation of coordination polymers or metal-organic frameworks.

3.1.4. One-pot synthesis using HAcOBIP

The following strategy consisted on mixing two different metal salts with the ligand in one step. In this sense, the formation of the organometallic core and the extension of the structure might occur in the same reaction vial. We designed reactions taking into consideration the hard-soft acid-base theory of coordination chemistry. One of the metal ions should favour octahedral coordination with the amines core and the other should be oxophilic to coordinate the pendant carboxylates. Despite the large number of combinations, only one led to a crystalline product, containing Fe^{3+} and Zn^{2+} ions.

3.1.4.1. Synthesis of $Fe_2Zn_2(HAcOBIP)_4$

HAcOBIP (11 mg, 0.027 mmol) was dissolved in 2 mL of DMF in a scintillation vial. Then, $FeCl_3 \cdot 6H_2O$ (14.38 mg, 0.053 mmol) and $Zn(AcO)_2 \cdot 2H_2O$ (11.4 mg, 0.052 mol) were dissolved in 2 mL of DMF, respectively. Add the Fe^{3+} solution to the ligand vial and then add the Zn^{2+} solution to the mixture. Place the vial in the oven and heat it up using a temperature ramp (2 hours up to 120 °C, 48 hours at 120 °C and cool down for 12hours). Wash the black crystals twice with 2 mL of DMF. The crystalline structure was solved by SCXRD (Figure 3.9).
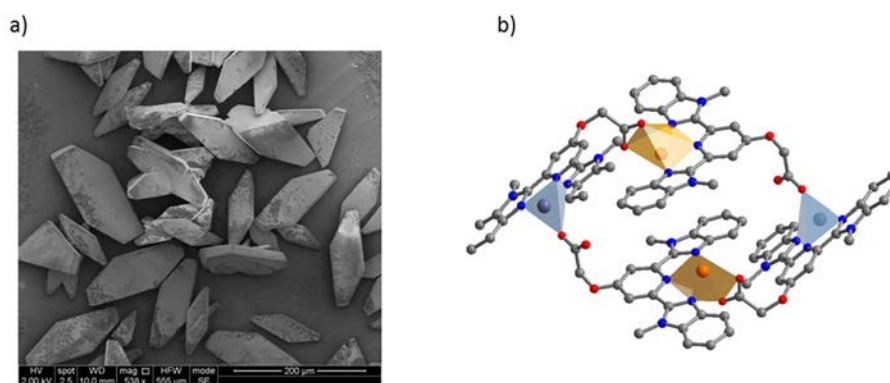
Figure 3.9. a) SEM imatge of the $Fe_2Zn_2(HAcOBIP)_4$ crystals. b) Crystalline structure of $Fe_2Zn_2(HAcOBIP)_4$.

The crystal structure consisted on organometallic discrete cages built up from 4 **HAcOBIP** ligands, 2 Fe^{3+} ions and 2 Zn^{2+} ions. Two different coordination environments were observed. Fe^{3+} was pentacoordinated to three amino groups from one **HAcOBIP** ligand and two oxygen from the carboxylic acid group of the neighbouring moiety. However, Zn^{2+} was tetracoordinated to three amino groups from one **HAcOBIP** ligand and only one oxygen from the carboxylic acid group of the neighbouring moiety.

The crystallographic tables of the structures **Ni(HAcOBIP)₂** , **Fe₂(HAcOBIP)₂Cl₄** and **Fe₂Zn₂(HAcOBIP)₄** are included in the Appendix. Refinement of **Ni(HAcOBIP)₂** and **Fe₂(HAcOBIP)₂Cl₄** led to high R1 indices due to the degree of symmetry and disorder. However, the organic ligands and central metal ions could be clearly identified. In these cases, distance and angle values are not calculated.

Despite the number of reactions tested with the two-step heterometallic synthesis and the one-pot strategy, any of the obtained solids resulted in extended coordination polymers or metal-organic frameworks. In order to continue pursuing the formation of extended structures containing photo-active building blocks, we considered to focus on a family of Ru^{2+}-terpyridinic complexes.

3.2. Synthesis of the organic terpyridine-based ligands and Ru-metalloligands

To construct the Ru^{2+}-based coordination polymers, the first step consisted on the synthesis of the organic moieties, which were later used to synthesise the metalloligands. The key feature

of these ditopic ligands is the fact that they contain both a terpyridine and a carboxylic group capable to coordinate to metal ions

Following previous reports,[73,74] **L₁** and **L₂** were prepared by the reaction of 2-acetylpyridne and the corresponding aldehyde. Then, these two organic ditopic ligands were utilized in order to synthesize dicarboxylic metalloligands **1** and **2**. While metalloligand **2** was easily synthesized in one-step reaction, **1** required two steps, complexation and oxidation, to obtain the final Ru^{2+}-complex. Both the ligands and the metalloligands required further purifications before being reacted in the next step. The organic precursors and Ru^{2+}-metalloligands were characterized by EA, ESI-MS and ¹H-NMR. In **1,** the carboxylic groups are protonated, so in order to balance the charge of the Ru^{2+} ions, two PF_6^- molecules are present. Contrarily, the carboxylic groups of **2** are deprotonated, affording to a neutral metalloligand.

¹H-NMR spectra of both families of compounds were measured in order to verify that the synthetic process was successful. Figure 3.10 shows the ¹H-NMR spectra of **L₁₋Furyl** and **1**. It is possible to observe that the signals corresponding to the furfural moiety (δ_H (ppm) = 8.04 (1), 6.75 (2) and 7.54 (3)) disappear because of the oxidative step. On the other hand, the coordination to Ru^{2+} ion causes shift (to downfield and upfield) in the terpyridinic protons, except for proton 8.
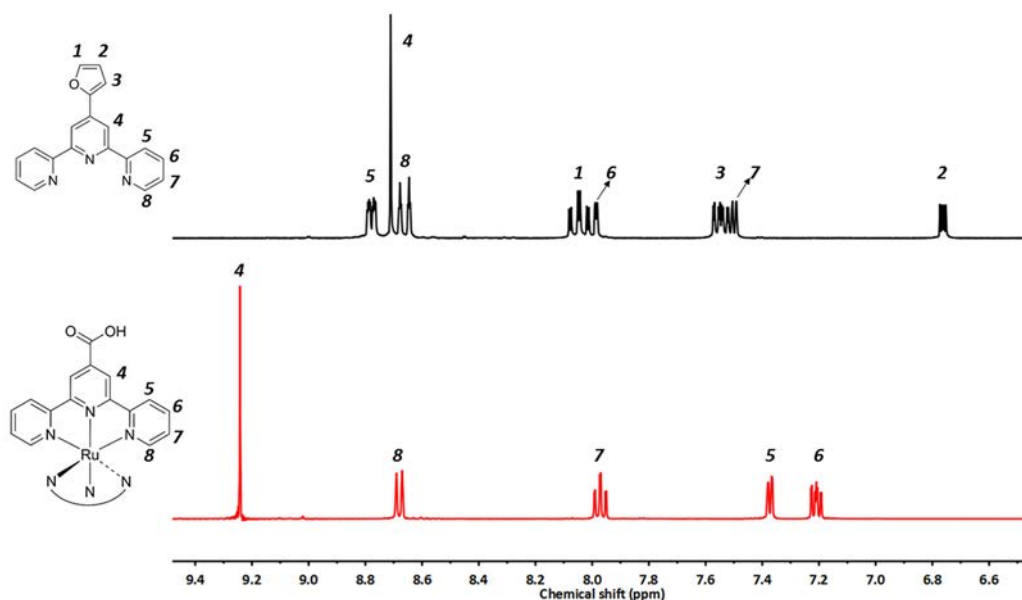
Figure 3.10. ¹H-NMR spectra of L₁₋Furyl and 1.

Figure 3.11 shows ¹H-NMR spectra of **L₂** and **2**. In this case, the number of signals is the same in both spectra but, once again, the presence of the coordination bond affects to the chemical shift of the peaks, specially, to the terpyridinc protons (from 3 to 7).
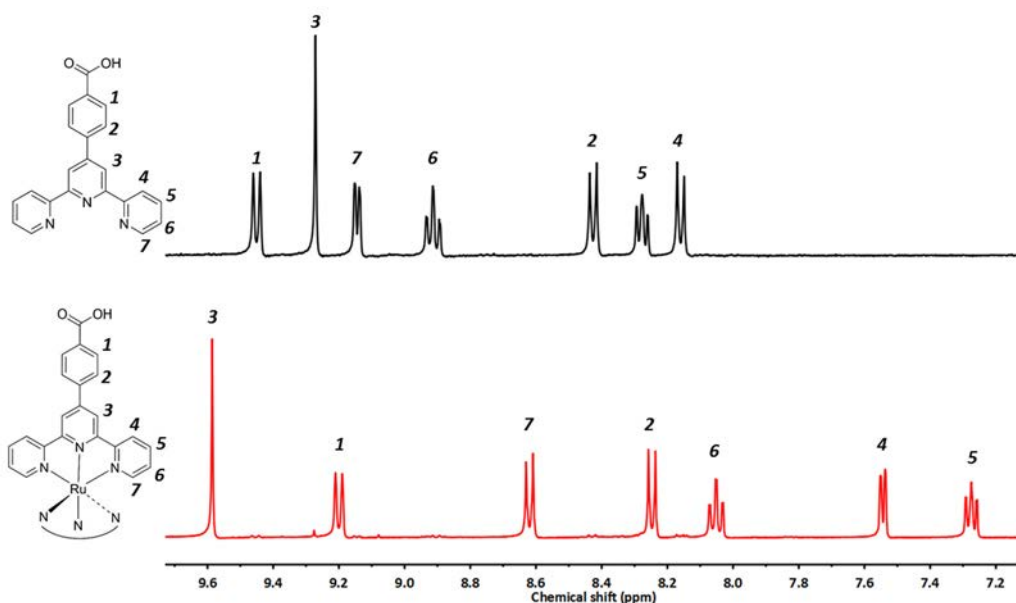
Figure 3.11. ^{1}H-NMR spectra of L$_2$ and 2.

A more detailed explanation of the synthesis of the organic ligands and corresponding metalloligands with Ru^{2+} is given below.

3.2.1. Synthesis of L$_{1\text{-Furyl}}$ (4'-(furan-2-yl)-2,2':6',2"-terpyridine)

The synthesis of **L$_{1\text{-Furyl}}$**, in which the carboxylic group is protected with a furyl group, is reported in the literature (Figure 3.12).[73] 2-acetylpyridine (40 mmol, 4.84 g) was dissolved in EtOH (100 mL) and furfuraldehyde (20 mmol, 1.92 g) was added to this solution. Then, KOH pellets (54.89 mmol, 3.08 g) and NH$_{3(aq)}$ 25% (v/v) (58 mL) were added to the reaction vessel. The resulting dark yellow-brown solution was vigorously stirred open to the air for 24 hours. The yellow-white solid obtained was filtered under vacuum with a sintered glass funnel and washed with ice-cold EtOH:H$_2$O 50% (v/v) until washings were colourless. The white-yellow solid obtained was dried under vacuum, characterized and stored protecting it from light. Note that it could be stored at room temperature without noticeable decomposition for several months. Final weight: 2.16 g (Yield: 36 %); Elemental Analysis (%): Found: C 76.29; H 4.31; N 13.96; C$_{19}$H$_{13}$N$_3$O requires C 76.24; H 4.38; N 14.04; ^{1}H-NMR (250 MHz, DMSO-d_6): δ_H (ppm) = 8.77 (2H, m), 8.7 (2H, s), 8.65 (2H, dt), 8.04 (2H, td), 7.98 (1H, dd), 7.54 (2H, dd), 7.49 (1H, dd), 6.75 (1H, dd); m/z (ESI-MS) calculated for [C$_{19}$H$_{13}$N$_3$O+Na]$^+$: 322.10 ; Found 322.09 [M+Na]$^+$.
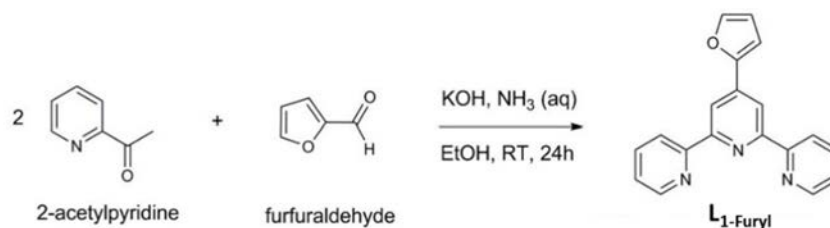
Figure 3.12. Schematic illustration of the synthesis of L$_{1\text{-Furyl}}$.

3.2.2. Synthesis of L$_2$ (4'-(4-Carboxyphenyl)-2,2':6',2"-terpyridine)

L$_2$ was also synthesised following a reported procedure (Figure 3.13).[70] In this case, the organic ligand contains one extra phenyl ring between the terpyridine moiety and the carboxylic group. 2-acetylpyridine (12.2 mmol, 1.93 g) was dissolved in EtOH (25 mL), and 4-methoxycarbonylbenzaldehyde (6.1 mmol, 1.0 g) was added to this solution. Then, 1 mL of NH$_{3\text{(aq)}}$ 30% (w/v) and NaOH (12.2 mmol, 0.488 g), dissolved in the minimum amount of water, were added to this solution. The resulting yellow solution was vigorously stirred at room temperature in a flask opened to the air for 17 hours, obtaining a yellow precipitate. Water (50 mL) and HCl$_{conc}$ were added until pH was around 6 and the solution was stirred overnight. After that, a yellow solid was collected by filtration and washed with water and, in order to obtain a further purification, it was refluxed in EtOH (50 mL) for 1 hour. A white solid was collected by filtration, dried under vacuum and characterized. Final weight: 757.5 mg (Yield: 35 %); Elemental Analysis (%): Found: C 76.29; H 4.31; N 13.96; C$_{22}$H$_{15}$N$_3$O$_2$ requires C 74.78; H 4.28; N 11.89; ^{1}H-NMR (400 MHz, DMSO-d_6/DCl): δ_H (ppm) = 9.45 (1H, d), 9.27 (1H, s), 9.14 (1H, d), 8.91 (1H, td), 8.43 (1H, d), 8.28 (1H, t), 8.16 (1H, d); m/z (ESI-MS) calculated for [C$_{22}$H$_{15}$N$_3$O$_2$+Na]$^+$: 376.12; Found 376.12 [M+Na]$^+$.

Figure 3.13. Schematic illustration of the synthesis of L$_2$.

3.2.3. Synthesis of 1 ([Ru(L$_{1-COOH}$)$_2$][PF$_6$]$_2$)

Synthesis of **1** was adapted from reported procedures (Figure 3.14).[74] **L$_{1-Furyl}$** (2.92 mmol, 873 mg) was dispersed in EtOH (40 mL) by sonication and then, RuCl$_3$·3H$_2$O (1.46 mmol, 381 mg) and N-ethylmorpholine (140 μL) were added to the reaction flask. The suspension was heated to reflux for 24 hours. After that, the bright red suspension obtained was evaporated under vacuum, and the resulting red solid was suspended in a KMnO$_{4(aq)}$ (2.85 mmol, 450 mg) solution (50 mL) to oxidize the furan group to the carboxylic group. The reaction was monitored using TCL analysis (SiO$_2$, MeCN-KNO$_{3(aq)}$ saturated solution-H$_2$O 7:1:0.5). After stirring 3 hours, significant amount of [Ru(**L$_{1-Furyl}$**)$_2$] was still present in the mixture (R$_f$ = 0.53). For this reason, further portions of KMnO$_4$ (9.81 mmol, 1550 mg) were stepwised added stirring the solution overnight. After this period, TCL analysis did not show the presence of [Ru(**L$_{1-Furyl}$**)$_2$] but two new red spots appeared, which were associated to [Ru(**L$_{1-Furyl}$**)(**L$_{1-COOH}$**)]$^+$ (R$_f$ = 0.21) and [Ru(**L$_{1-COOH}$**)$_2$]$^{2+}$ (R$_f$ = 0.06). Then, KMnO$_4$ (9.74 mmol, 1.54 g) was added over a period of 2 hours and the solution was stirred for 7 hours. After that, the solution was filtered and washed with water. The solid was extracted using H$_2$SO$_4$ (5 M) stirring overnight at room temperature. Then, in order to obtain a dark red precipitate, NH$_4$PF$_{6(aq)}$ (0.4 M, 10 mL) was added. After stirring overnight, the suspension was filtered under vacuum with a sintered glass funnel over Celite and washed with NH$_4$PF$_{6(aq)}$ (0.02 M) and water. The Cellite pellet was liophilized under vacuum overnight and the complex was extracted with acetonitrile. Finally, solvent was evaporated leading to a red solid (**1**). Final weight: 528.04 mg (Yield: 38 %); Elemental Analysis (%): Found C 39.02; H 2.61; N 8.74; C$_{32}$H$_{22}$F$_{12}$N$_6$O$_4$P$_2$Ru requires C 40.65; H 2.35; N 8.89; ^{1}H-NMR (400 MHz, MeCN-d_3): δ$_H$ (ppm) = 9.24 (s, 4H), 8.68 (d, 4H), 7.97 (td, 4H), 7.37 (d, 4H), 7.21 (m, 4H); *m/z* (ESI-MS) calculated for [C$_{32}$H$_{22}$F$_{12}$N$_6$O$_4$P$_2$Ru −PF$_6$]$^+$: 801.04, [C$_{32}$H$_{22}$F$_{12}$N$_6$O$_4$P$_2$Ru −2PF$_6$]$^{2+}$: 328.00; Found 801.04 [M−PF$_6$]$^+$, 328.01 [M−2PF$_6$]$^{2+}$.
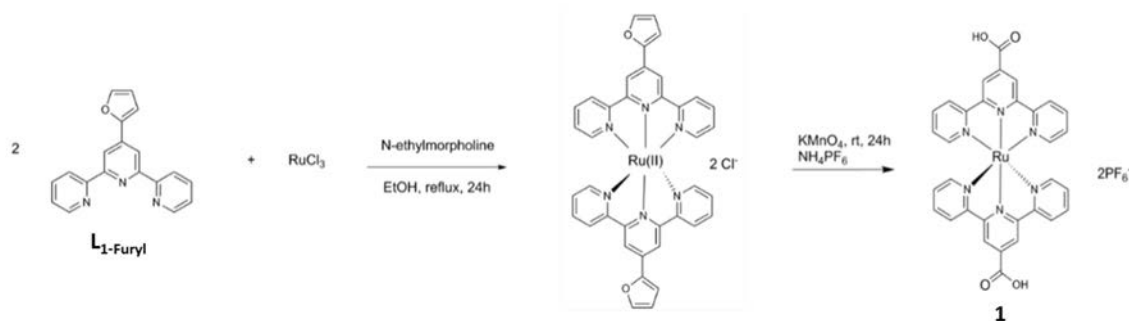
Figure 3.14. Schematic illustration of the synthesis of **1**.

3.2.4. Synthesis of 2 ([Ru(L₂)₂])

Synthesis of **2** was adapted from reported procedures (Figure 3.15).[74] **L₂** (0.97 mmol, 342 mg) and $RuCl_3 \cdot 3H_2O$ (0.48 mmol, 126.5 mg) were suspended in EtOH (3 mL). Then, triethylamine was added (2.2 mmol, 0.3 mL) and the mixture was placed in a Teflon high pressure vessel al 150 °C for 18 hours. The vessel was slowly cooled down to room temperature, and the red precipitate formed was filtered under vacuum onto a glass sintered funnel over Celite. The Celite pellet was washed with EtOH (5 mL), water containing 10 drops of NaOH (2M) (10 mL) and water (10 mL). After 24 hours of liophilizing, the complex was extracted with boiling MeOH and a bright red solid was obtained after evaporating the solvent (**2**). Final weight: 254 mg (Yield: 65 %); Elemental Analysis (%): Found: C 66.91; H 4.25; N 10.60; $C_{44}H_{28}N_6O_4Ru$ requires C 65.58; H 4.28; N 10.43; ^{1}H-NMR (400 MHz, DMSO-d_6/DCl): δ_H (ppm) = 9.59 (s, 4H), 9.2 (d, 4H), 8.62 (d, 4H), 8.24 (d, 4H), 8.05 (td, 4H), 7.54 (d, 4H), 7.27 (t, 4H); m/z (ESI) calculated for $[C_{44}H_{28}N_6O_4Ru+H]^+$: 807.13; Found 807.13 $[M+H]^+$.
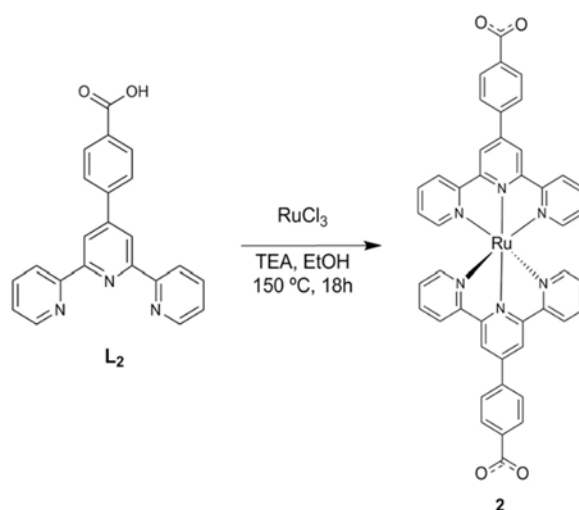
Figure 3.15. Schematic illustration of the synthesis of **2.**

3.3. Synthesis of coordination polymers

Metalloligands **1** and **2** were reacted with different Co^{2+} and Zr^{4+} salts under solvothermal conditions, from which dark-red single crystals of **Co-1**, **Co-2** and **Zr-2** could be obtained in good yields. Attempts to obtain a CP build by **1** and Zr^{4+} metal ion were unsuccessful. **Co-1**, **Co-2** and **Zr-2** crystals were washed with MeCN, acetone and DMF, respectively. Structures were unequivocally elucidated by single crystal X-ray diffraction (SCXRD). The simulated, derived from the single crystal structures, and experimental powder X-ray diffraction (XRPD) patterns were consistent, confirming the phase purity of these samples (Figure 3.16). Furthermore, **Co-1**, **Co-2**

and **Zr-2** were fully characterized by standard spectroscopic and analytical techniques. The molecular formula of these coordination polymers is [Co(**1**)](PF$_6$)$_2$·solv **(Co-1)**, [Co$_2$(**2**)(Cl$_4$)] **(Co-2)**, [Zr(**2**)(HCOO)$_4$] **(Zr-2)**, where different secondary anionic ligands complete the coordination sphere of Co^{2+} and Zr^{4+} ions. A detailed synthetic procedure of these coordination polymers is given below.
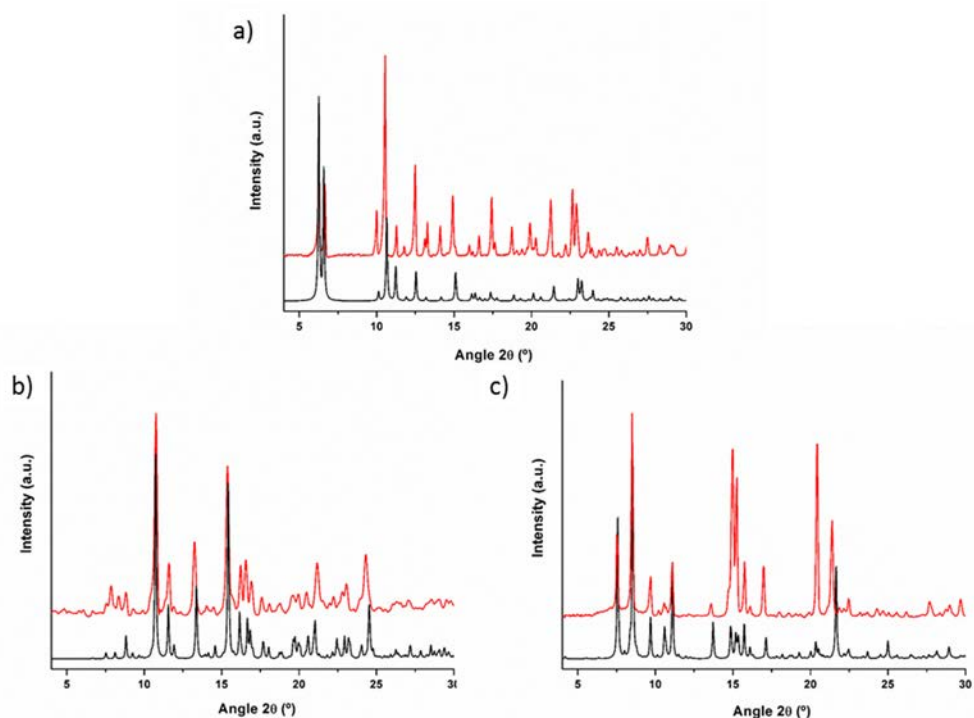
Figure 3.16. Comparison of the simulated (black) and experimental (red) powder patterns of **Co-1** (a), **Co-2** (b) and **Zr-2** (c).

3.3.1. Synthesis of Co-1 ([Co(1)](PF$_6$)$_2$·solv])

A solution of Co(NO$_3$)$_2$·6H$_2$O (0.021 mmol, 6.2 mg) in DMF (1 mL) was added to a solution of **1** (0.012 mmol, 10 mg) in DMF (1 mL). Then, triethylamine (0.22 mmol, 30 µL) was added to the final solution and an inhomogeneous suspension was formed. The final mixture was placed in the oven at 120 °C for 5 days, obtaining dark red cubic crystals. Final weight: 7.12 mg (Yield: 55 %); Elemental Analysis (%): Found: C 41.02; H 3.67; N 11.01; C$_{32}$H$_{22}$F$_{12}$N$_6$O$_4$P$_2$Ru·(C$_3$H$_7$NO)$_4$ requires C 40.75; H 3.89; N 10.8; ICP (ratio Ru:Co): Found: 0.97; Required: 1.00.

3.3.2. Synthesis of Co-2 ([Co$_2$(2)(Cl$_4$)]])

2 (0.012 mmol, 10 mg) was suspended in DMF (2 mL) and HNO$_{3(conc.)}$ (4 µL) was added to the suspension in order to acquire a dark red solution. Separately, CoCl$_2$·6H$_2$O (0.025 mmol, 6 mg) was dissolved in DMF (2 mL) and this solution was added to the metalloligand solution. The final

mixture was placed in the oven at 120 °C for 5 days, from which dark red crystals with prism shape were obtained. Final weight: 6.67 mg (Yield: 50 %); Elemental Analysis (%): Found: C 48.58; H 3.06; N 8.59; $C_{44}H_{28}N_6O_4RuCo_2Cl_4 \cdot C_3H_7NO$ requires C 49.49; H 3.27; N 8.60; ICP (ratio Ru:Co): Found: 0.48; Required: 0.50.

3.3.3. Synthesis of Zr-2 ([Zr(2)(HCOO)$_4$])

A solution of $ZrOCl_2 \cdot 8H_2O$ (0.025 mmol, 8 mg) and formic acid (6.35 mmol, 0.5 mL) in DMF (2 mL) was added to a suspension of **2** (0.012 mmol, 10 mg) in DMF (2 mL). After sonicating, a dark red solution was obtained and placed in the oven at 120 °C for 5 days. After that, dark red crystals with prism shape were collected. Final weight: 10.63 mg (Yield: 79 %); Elemental Analysis (%): Found: C 50.05; H 3.05; N 7.73; $C_{44}H_{28}N_6O_4RuZr(HCOO)_4$ requires C 53.42; H 3.19; N 7.79; ICP (ratio Ru:Zr): Found: 1.00; Required: 1.00.

3.4. Single crystal structures

3.4.1. Co-1 ([Co(1)](PF$_6$)$_2$·DMF$_2$)

Co-1 crystallizes in the monoclinic *P2an* space group, forming an extended two-dimensional structure. As expected, **Co-1** is formed by the macro-complex **1** bridged by Co^{2+} ions through their carboxylate groups. **1** can be considered a metalloligand formed by two terpyridinic organic ligands that contain available carboxylic groups and one chelated Ru^{2+} ion bonded to the terpyridinic moieties. Therefore, Ru^{2+} ion is coordinated through six pyridinic N atoms showing a {N$_6$}-hexacoordinated environment in *mer-* conformation forming four 5-membered chelate rings. The geometry around the Ru^{2+} metal centre can be described as an almost perfect octahedron. This slight distortion is caused by the arrangement of the terpyridine planes (89.62°) (Figure 3.17a).
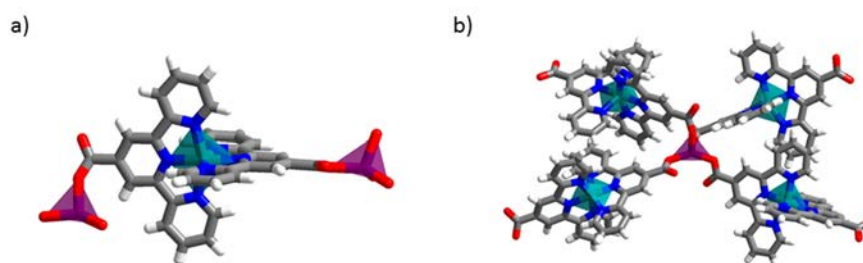
Figure 3.17. a) Coordination environment around the Ru^{2+} ion in **1**. b) Co^{2+} ions are coordinated to four different **1** units through the carboxylate groups.

In this structure, Co^{2+} ions are coordinated to four different metalloligands **1** forming a two-dimensional layer that is extended along the *ab* plane describing a square lattice (sql) network (Figures 3.17b and 3.18a). Co^{2+} is $\{O_4\}$-tetracoordinated to the carboxylate groups in a monodentate fashion, showing a strongly distorted tetrahedral environment. The angles formed between carboxylate O atoms coming from different **1** and the Co^{2+} ion varies from 143.12° to 93.24°. These angle values are deviated from the expected angle in an ideal tetrahedron (109.5°). The sql network described in the *ab* plane does not present perfect squares in its lattice because the angles formed between Ru^{2+} and Co^{2+} ions (Ru-Co-Ru) are 63° and 127° (Figure 3.18b). The association of different layers is established through supramolecular interactions along the *c* axis. The external pyridinic rings of the terpyridine moieties are able to establish two different types of π interactions: π···π [d(centroid(1)···centroid(2)) = 3.72 Å] and C-H···π [d(C-H···centroid(3)) = 3.59 Å] interactions between an aromatic ring of one layer and two different rings of a neighbour layer (Figure 3.18c). C-H···π interaction is possibly weaker than an ordinary because the C-H donor ring is slightly rotated with respect to the electron density donor ring.

Co-1 crystallized with guest DMF molecules that are located in the interlayer space contributing to the global stability and the supramolecular packing of **Co-1**. DMF establishes H-bond interactions showing either donor and acceptor character. Its $-CH_3$ groups interact with the nearest non-coordinated carboxylate O atom of the terpyridinic groups, and the carbonyl O atom interacts with aromatic -CH groups of different terpyridines. Due to all these supramolecular interactions explained above, layers are perfectly packed and one dimensional oval channels are generated. These channels are filled with two PF_6^- anions (needed as counteranions to balance the charge of **Co-1**) that probably establish C-H···F H-bond interactions with the framework. Unfortunately, the localization of these anions could not be rigorously established by SCXRD (Figure 3.18d).
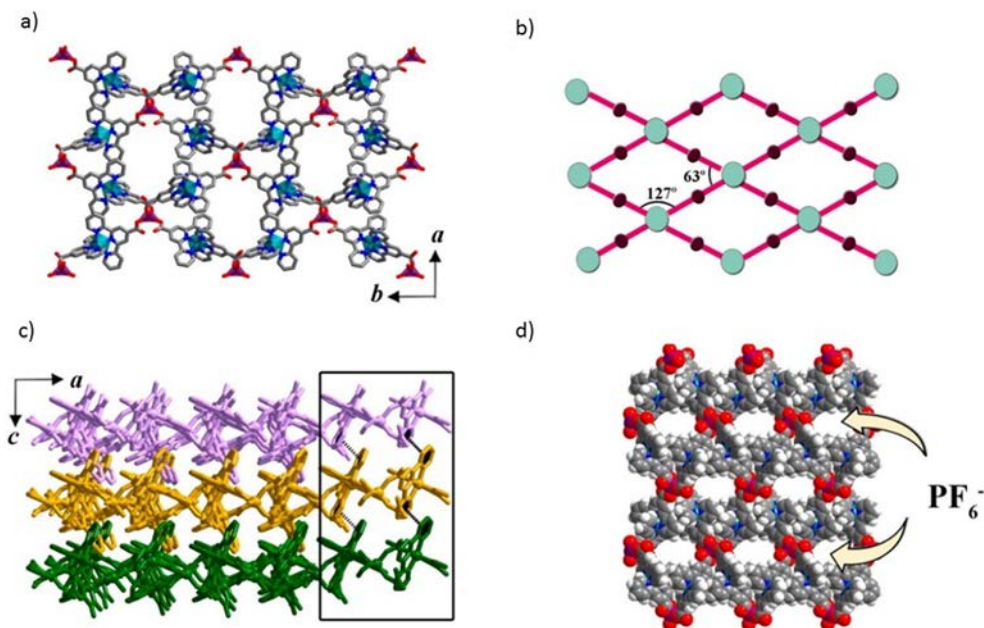
Figure 3.18. a) 2D layers of **Co-1** are extending along the *ab* plane showing 1D channels that are filled with the PF$_6^-$ counteranions. PF$_6^-$ counteranions are not represented for clarity. b) Representation of the square lattice network and the (Ru-Co-Ru) angles. c) Packing of 2D layers through π···π interactions. d) Porous cavities without PF$_6^-$ counteranions.

3.4.2. Co-2 ([Co$_2$(2)(Cl$_4$)])

Metalloligand **2** was designed under the reticular chemistry principles: one benzene carboxylic group was added in *para-* position of the central ring of the terpyridinic moiety in order to increase the distance between the carboxylic groups. This distance is increased from 12.47 Å in **1** to 20.88 Å in **2** (Figure 3.19). However, **Co-2**, which crystallized in the monoclinic *P2/a* space group, only showed the formation of a one-dimensional coordination polymer (Figure 3.20a). **Co-2** is formed by **2** and dinuclear Co^{2+} units coordinated to the available carboxylate groups (Figure 3.20b). The geometry around the Ru^{2+} metal centre can be described as a distorted octahedron with an angle value between the terpyridine planes of 88.51°. The extra benzene carboxylate groups are differently rotated with respect to its terpyridinic plane (32.30° and 51.96°). Consequently, these two different angle rotations cause an alternation of phenyl rings disposition in the chains forming an angle of 26° between them (Figure 3.20c).
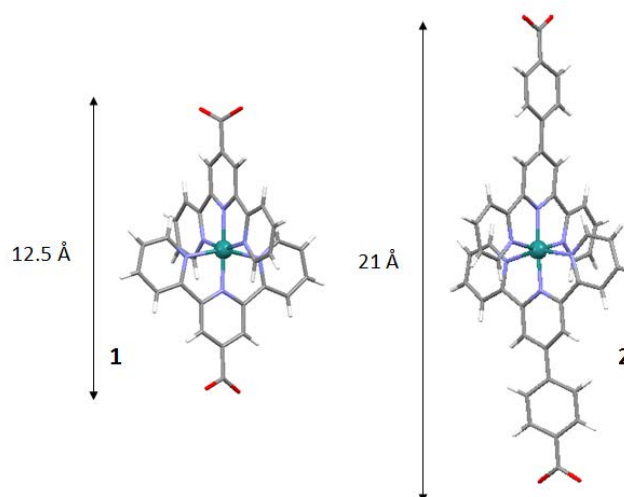
Figure 3.19. Comparative lengths of 1 and 2.

2 is linked to four Co^{2+} ions exhibiting the same distorted tetrahedral coordination environment. Co^{2+} ions are coordinated to two Cl ions and two carboxylate O atoms in a bridge bidentate fashion coming from two different metalloligands. Angles vary depending on the binding atom specie giving rise to a distorted tetrahedral with angles values between 96.78° and 124.60°. The structure of **Co-2** is constructed by the alternation of Ru^{2+} and Co^{2+} centres forming a one-dimensional strand extended along the *c* axis.
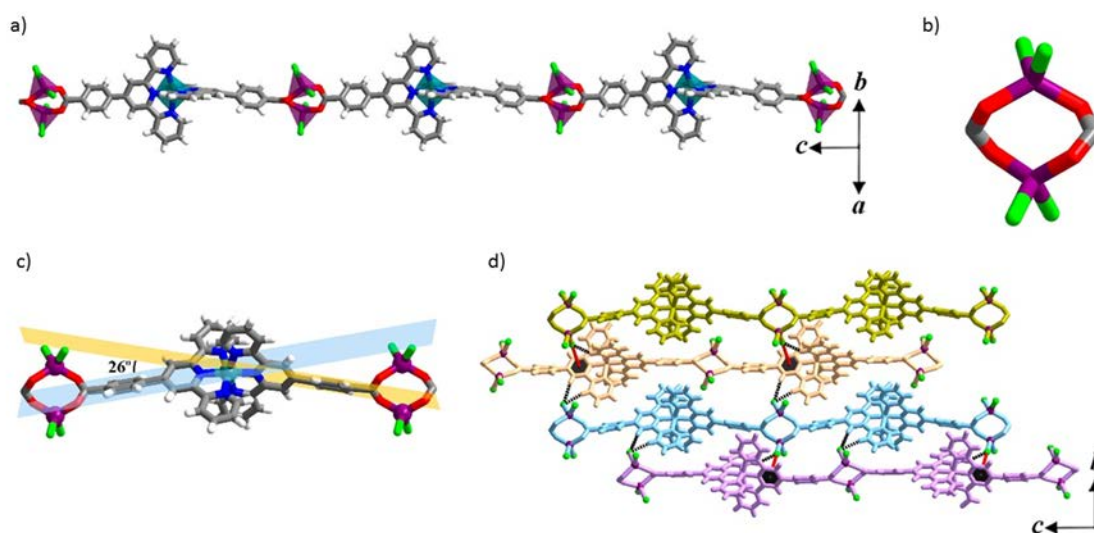
Figure 3.20. a) 1D chain of alternating Ru-Co-Ru are running along the *c* axis. b) Coordination environment around Co^{2+} ions. c) Angle between the two terminal phenyl rings. d) C-H···Cl (black lines) and Cl··· π (red lines) interactions are established between neighboring chains.

The one-dimensional chains are then inter-connected through different types of weak interactions. Cl atoms establish two different supramolecular interactions. They act as acceptors

of several C-H⋯Cl H-bond interactions established with terpyridinic -CH groups. In addition, they also establish Cl⋯π interactions, which can be also classified in two separate groups: Cl(1)⋯π interaction [d(Cl(1)⋯centroid(1)) = 3.43 Å] can be observed with the external ring of the terpyrinic moiety, whereas Cl(2)⋯π interactions are established with the central pyridinic ring [d(Cl(2)⋯centroid(2)) = 3.52 Å] (Figure 14d). O atoms in the dinuclear Co^{2+} unit are able to form a H-bond with a terpyridinc -CH group [d(-CH⋯O) = 2.66 Å]. Moreover, π⋯π stacking between external pyridinic rings and the *para* benzoic ring is established [d(centroid(3)⋯centroid(4)) = 4.22 Å].

3.4.3. Zr-2 ([Zr(2)(HCOO)₄])

Zr-2 crystallises in the monoclinic *C2/c* space group forming a one-dimensional CP (Figure 3.21a). The structure is very similar to that of **Co-2,** but metalloligand **2** is now binding to Zr^{4+} ions. Ru^{2+} is {N_6}-hexacoordinated with two terpyridinic moieties in *mer-* conformation which dihedral angle is 76.12°. Likewise in **Co-2**, **Zr-2** also shows an alternation of phenyl rings rotation. Carboxylate benzoic groups are differently rotated with respect to its terpyridinic group (26.85° and 4.80°) and consequently, the dihedral angle between these two benzoic rings is 68°(Figure 3.21b).

In this structure, Zr^{4+} ions show an {O_8}-octacoordinated environment formed by four carboxylate O atoms of two different metalloligands and four formates (Figure 3.21c). The shortest Zr-O bonding distance corresponds to the terminal formate ligand, which is around 2.1 Å. The angle formed by these ligands and the Zr^{4+} ion varies between 95.86° and 90.96°. The carboxylate groups show a bidentate chelate fashion, forming 4-membered chelate rings with Zr^{4+} ions. They are arranged in two almost perpendicular planes (84.87°) showing an angle of 56.68° between the carboxylic O located in the same plane. The structure of **Zr-2** is constructed by the connection of Ru-based metalloligands through the octacoordinated Zr^{4+} clusters described above forming a 1D strand that extends in the *a* axis.
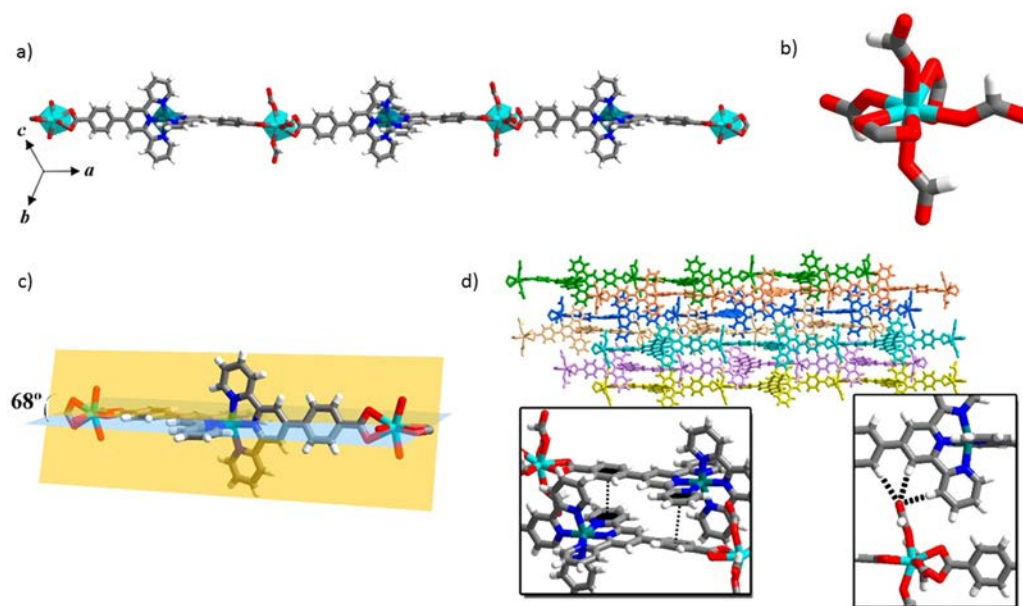
Figure 3.21. a) 1D chains of **Zr-2** are extended along the *a* axis. b) Coordination environment of Zr⁴⁺ ions. c) Angle between the two terminal phenyl rings. d) π···π and C-H···O supramolecular interactions of the final 3D-arrangement.

The association of different one-dimensional entities is established through supramolecular interactions giving rise to a very compact structure. The most relevant and abundant weak interaction established in this structure is the H-bond where O atoms are the acceptors. As it has been described above, each Zr⁴⁺ chain shows four coordinated formates, which have four terminal O atoms. These O atoms are able to form C-H···O bonds with the aromatic –C-H groups of the terpyridinic and the benzoic moieties. O atoms can establish many H-bonds interactions with O···H distances between 2.3 Å and 2.7 Å. As a consequence, each chain is surrounded by six more one-dimensional chains thanks to the huge amount of aromatic –C-H groups present in **2**. Interestingly, O atoms interact with more than one –C-H groups, showing 5 and 7-membered H-bond rings. Moreover, π···π staking is established between external terpyridinic rings and carboxylic benzoic rings [d(centroid(1)···centroid(2))= 3.48 Å]. Two types of C-H···π interactions between the rings mentioned above are also present in **Zr-2** and their distances are 3.85 Å and 2.78 Å (Figure 3.21d)

The crystallographic tables of the structures **Co-1**, **Co-2** and **Zr-2** are included in the Appendix.

3.5. Stability of the coordination polymers

3.5.1. Solvent Stability

Solvent stability assessment was carried out to determine in which solvents the structure of the synthesised coordination polymers is maintained, modified or collapsed. This study is very important to define which solvents can be used to prove the catalytical activity of these compounds in heterogenous catalysis. To this end, **Co-1**, **Co-2** and **Zr-2** were immersed at room temperature for 12 hours in different solvents. After that, XRPD patterns were collected and compared to the initial ones (Figures 3.22 and 3.23). The selected solvents were (in ascending order of polarity using the polarity parameter $E_T(30)$): toluene, ether, THF, dichloromethane, acetone, DMF, DMSO, MeCN, EtOH and water.[75]

Co-1 and **Co-2** showed similar solvent stability. When **Co-1** was immersed in EtOH, water and DMSO and **Co-2** in dichloromethane, DMSO and water, clear solutions were obtained. In the case of **Co-1**, amorphous materials were obtained when it was immersed in toluene, dichloromethane and DMF. When it was immersed in EtOH, toluene, DMF and THF, **Co-2** resulted in amorphous powders. These low stabilities may be attributed to the low Co-O bond strength, meaning that these solvents can attack the metal center and labilize the metalloligand-Co bond. However, the crystal structures of both **Co-1** and **Co-2** were maintained after being immersed in MeCN, acetone, ether and THF (this lately only for **Co-1**), showing chemical stability in these solvents (Figure 3.22).
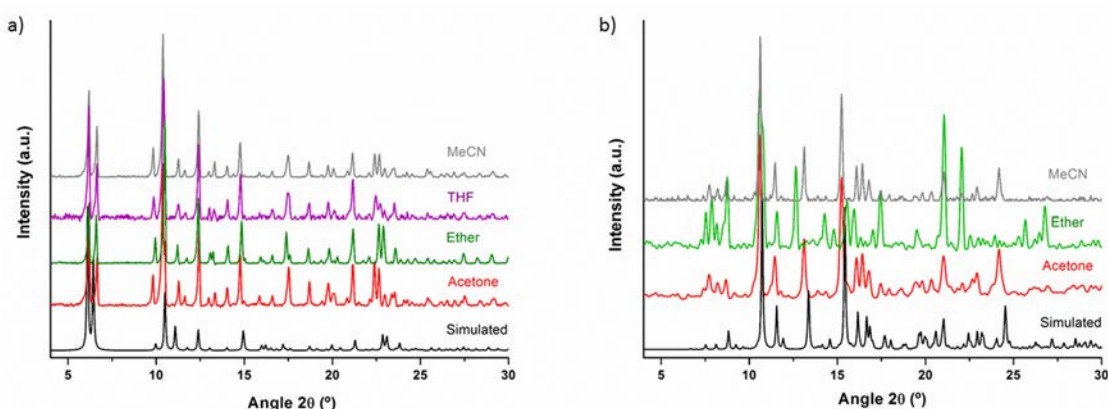
Figure 3.22. Comparison of the simulated (black) XRPD patterns and the experimental ones collected after immersing **Co-1** (a) and **Co-2** (b) in different solvents.

Zr-2 solvent stability experiments give rise to totally different results. Figure 3.23 shows that crystalline structure was completely maintained after exposition to all tested solvents, independently of their polarity or molecular structure. In this crystalline structure, **2** is extended

through Zr^{4+} with an {O_8}-octacoordinated environment. So, it is possible to attribute this behavior to the exceptional strength of the Zr-O bond since Group IV elements are known for interacting strongly with O atoms.[76]
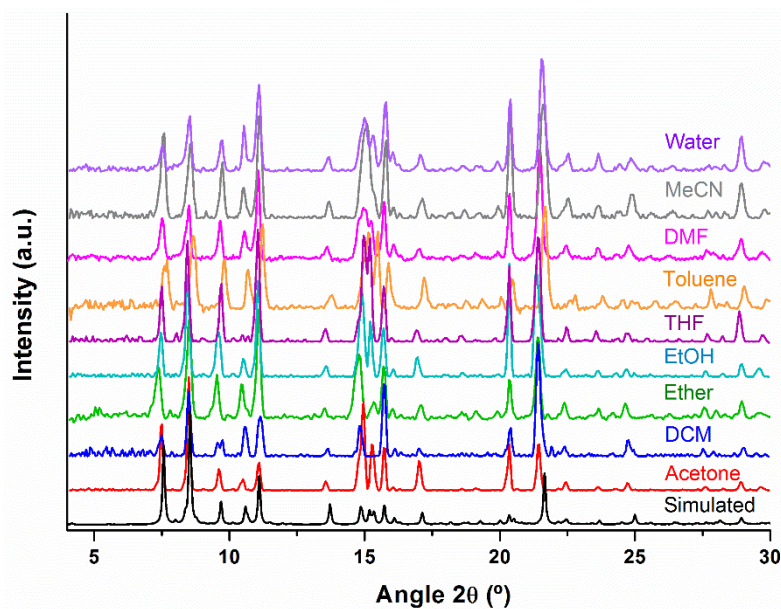
Figure 3.23. Comparison of the simulated (black) XRPD pattern of **Zr-2** and the experimental ones after immersing it in different solvents.

3.5.2. Thermal stability

Figures 3.24, 3.25 and 3.26 show the thermogravimetric (TGA) diagrams of **Co-1**, **Co-2** and **Zr-2**. **Co-1** diagram shows a gradual loss of mass from room temperature to 200 °C, which can be attributed to the removal of the solvent molecules stored in the crystalline structure. Indeed, this first mass loss, 15 %, can be attributed to four DMF molecules which theoretically represent the 13 % of the total mass. After that, **Co-1** starts to decompose at around 275 °C.
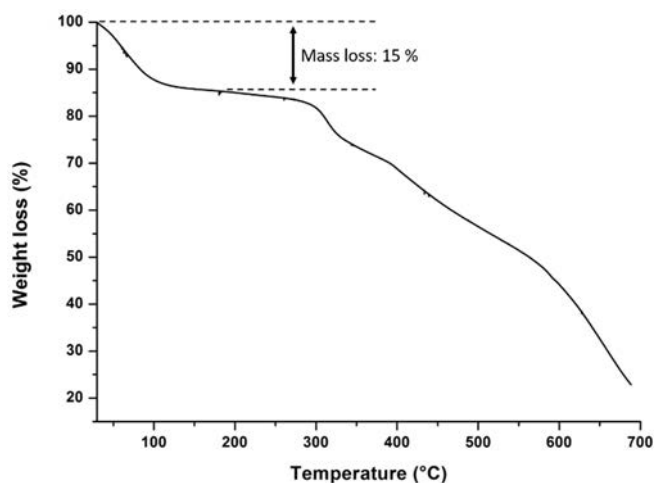
Figure 3.24. TGA diagram of Co-1.

In the thermogravimetric curve of **Co-2**, it is possible to observe a 7 % of mass loss, which may be associated to one DMF molecule. It theoretically represents a 6% of the total mass. In this case, **Co-2** framework starts to decompose at around 400 °C, higher than the temperature of decomposition of **Co-1** and **Zr-2** (*vide infra*).
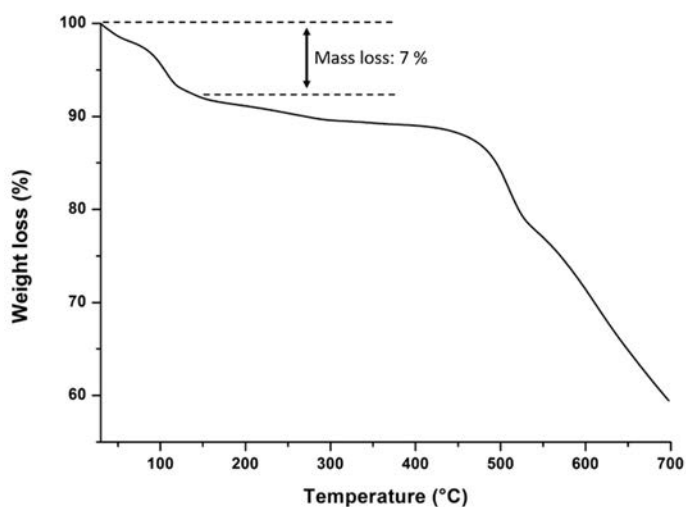
Figure 3.25. TGA diagram of Co-2.

Finally, **Zr-2** diagram shows a gradual mass loss of 5 % from room temperature to 150 °C, which is attributed to DMF solvent molecules, and of 17 % from 150 °C to 350 °C, which tentatively associated to the loss of the formate anions coordinating the Zr^{4+} centre. After this temperature, the network starts to decompose gradually.
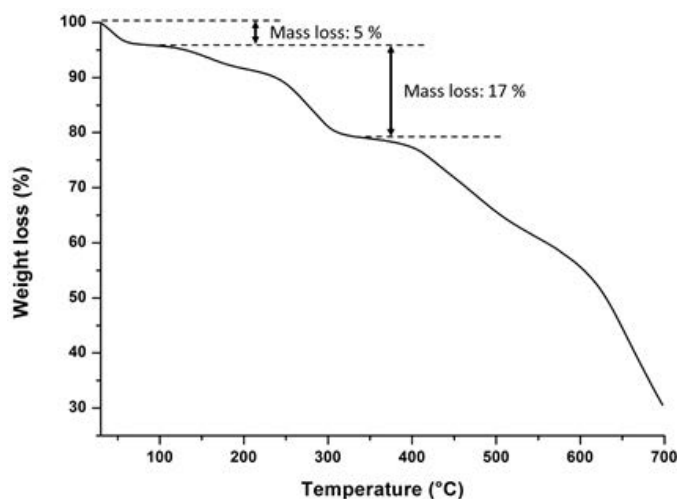
Figure 3.26. TGA diagram of Zr-2.

3.6. Fourier Transform-Infrared Spectroscopy

FT-IR spectra of **1**, **2**, **Co-1**, **Co-2** and **Zr-2** are shown in Figures 3.27 and 3.28. There, terpyridine moiety can be clearly identified in the spectrum of **2** thanks to the presence of its distinctive peaks at 1329 cm^{-1} and 1241 cm^{-1}, which are associated with the stretching vibration of C=C and C=N bonds, respectively. Moreover, the peak observed at 780 cm^{-1} can be assigned to the bending vibration of the C-N-C bond (Figure 3.27).[77] Remarkably, these peaks are also present in **Co-2** and **Zr-2** spectra confirming the incorporation of the metalloligand to the extended structure. In the case of **1** and **Co-1**, the vibration modes of the C=C and C=N functional groups could not be rigorously assigned due to the complexity of the spectra and the high number of overlapped peaks. However, a peak at 780 cm^{-1}, attributable to C-N-C bending vibration, was observed confirming the presence of the metalloligand **1** in **Co-1**. In addition, in both spectra, a sharp and intense peak at 850 cm^{-1} was identified and assigned to the PF$_6^-$ anions.
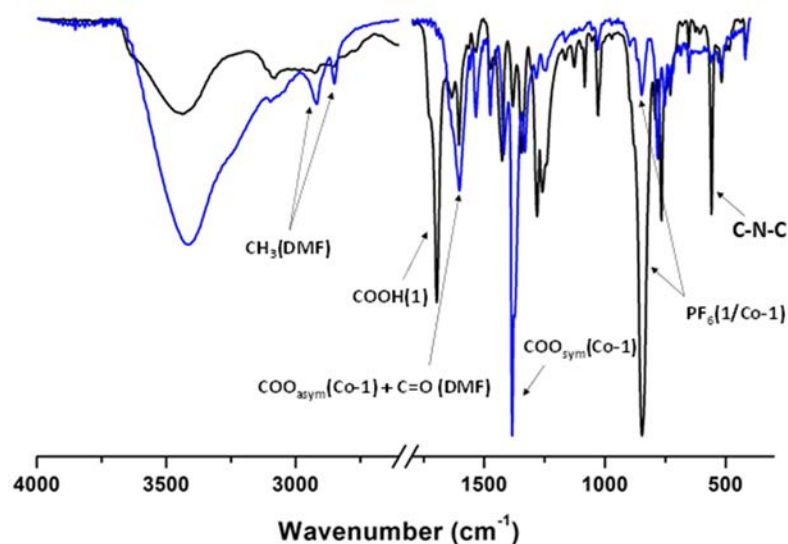
Figure 3.27. IR spectra of 1 (black) and Co-1 (blue).

Previous studies in the FT-IR field have demonstrated that the wavenumber difference between the asymmetric and the symmetric vibrations of the carboxylate group (Δ(OCO) = ν_{asym} (OCO) - ν_{sym} (OCO)) depends on how they are bonded to metals. Generally, it is possible to find that ionic behaviour shows a Δ(OCO) = 170 cm^{-1}, covalent chelates imply a Δ(OCO) < 170 cm^{-1}, and a Δ(OCO) > 170 cm^{-1} suggests vibrational modes associated to covalent monodentated coordination. Unfortunately, exceptions to these rules can be found because of the existence of extremely asymmetric vibrational modes or pseudo-monodentated coordination, which causes variations in the coordination environment and, as a result, expected Δ(OCO) are not obtained.[78]

In our compounds, carboxylate symmetric and asymmetric stretching vibrations were also analyzed in order to corroborate their coordination to metal ions. The carboxylate coordination bond should be represented by a shift in their assigned vibrational peaks caused by the charge displacement produced by the metal presence. By comparing **1** and **Co-1** spectra it is possible to determine that the peak associated with the asymmetric vibration of the free carboxylic group in **1,** assigned at 1694 cm^{-1}, appears at 1604 cm^{-1} in **Co-1** confirming the behaviour explained above. Furthermore, the coordination around Co^{2+} ions was also analysed comparing the distance between the carboxylic asymmetric and symmetric bands. **Co-1** spectrum shows two peaks at 1604 cm^{-1} and 1380 cm^{-1} that can be attributed to these asymmetric and symmetric vibrations, respectively. Consequently, the Δ(OCO) is 224 cm^{-1} that is consistent with the monodentate coordination obtained in the crystallographic data (Figure 3.27). The presence of some other molecules, such as DMF, in **Co-1** can also be confirmed by using FT-IR. DMF shows three distinctive peaks: 2916 cm^{-1} and 2849 cm^{-1}, which can be associated to the -CH$_3$ stretching

vibration, and 1604 cm^{-1}, which corresponds to the C=O$_{DMF}$ vibration. This peak is especially broad probably because C=O$_{DMF}$ and COO$_{Co-1}$ signals are too close to be distinguishable (Figure 3.27).

Figure 3.28 shows an IR comparison between **2**, **Co-2** and **Zr-2**. In these spectra, it is possible to observe a displacement of the peak associated with the asymmetric vibrational mode of the free carboxylic group in **2** (1673 cm^{-1}) to lower energies in **Co-2** (1653 cm^{-1}) and **Zr-2** (1628 cm^{-1}). This shift indicates that the carboxylic groups are coordinated to Co^{2+} and Zr^{4+} ions. It is interesting to point out that the displacement shown in **Zr-2** spectrum is more pronounced. It can be attributed to the higher strength of the Zr-O bond. A deeper study of the coordination modes of the carboxylate groups in **Co-2** and **Zr-2** could not be possible to perform due to the high number of overlapped peaks in the area of the symmetric vibrational modes.
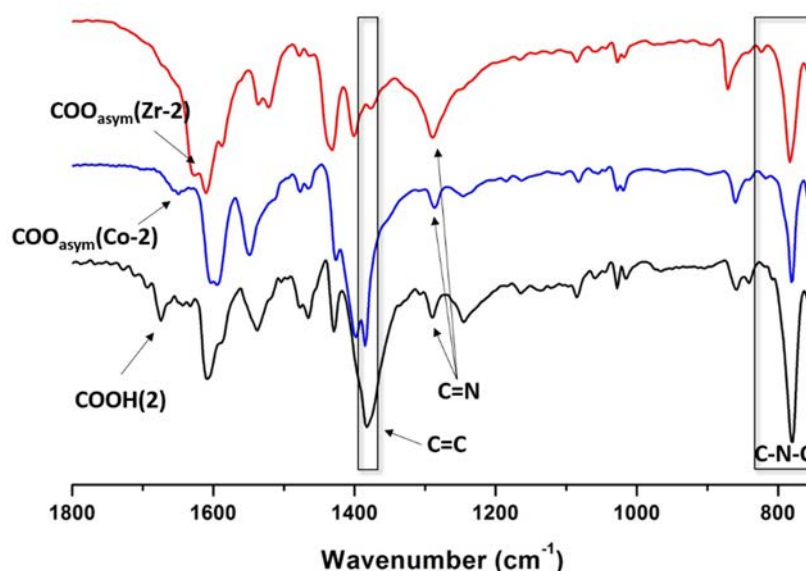
Figure 3.28. IR spectra of 2 (black), Co-2 (blue) and Zr-2 (red).

3.7. UV-Vis spectroscopy

UV-Vis spectra of **1**, **2**, **Co-1**, **Co-2** and **Zr-2** are shown in Figure 3.29. These spectra show two absorption bands located in the UV region: at around 275 nm and 325 nm for **Co-1,** and one band at around 350 nm for **Co-2** and **Zr-2**. These very intense bands correspond to the ligand-centered π-π* transitions of the terpyridine moieties. In addition, an absorption band in the visible region and centered approximately at 510 nm was observed for **Co-1**, **Co-2** and **Zr-2**. This relatively intense and broad absorption band is ascribed to the spin-allowed d-π metal-to-ligand charge transfer which is responsible for the deep red colour of these compounds.[79,80]
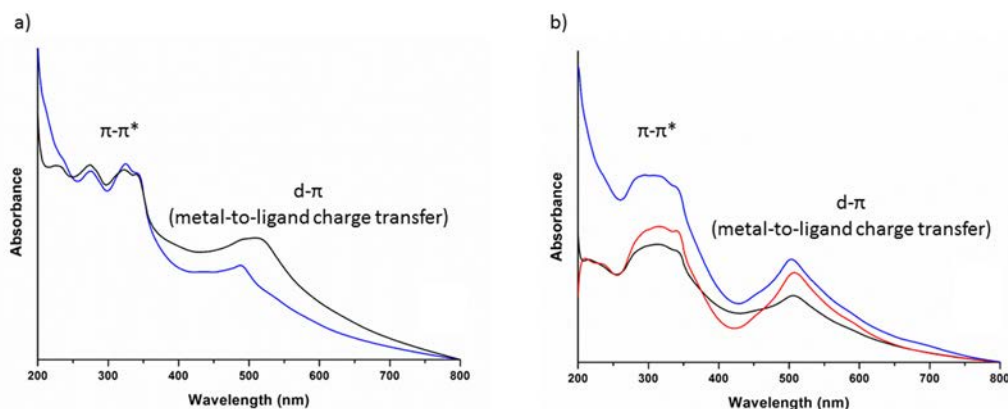
Figure 3.29. UV-Vis spectra of a) **1** (black) and **Co-1** (blue) and b) **2** (black) and **Co-2** (blue) **Zr-2** (red).

3.8. Photothermal characterization of the Ru-based coordination polymers

The photothermal behaviour of the three new coordination polymers (**Co-1**, **Co-2** and **Zr-2**) was assessed following the same protocol as per the MOFs in Chapter 3. However, in this case we employed 20 mg of sample instead of 100 mg, due to the low yield attained in their syntheses. These 20 mg were spread over a quartz slide and the light guide was placed at a distance of 7 cm (irradiance = 500 mW·cm^{-2}). The samples were then irradiated for 30 minutes (Figure 3.30).

Although **Co-2** exhibited a temperature increase of +48.5 °C, reaching a maximum of 77 °C, is the coordination polymer with the lower photothermal effect. **Zr-2**, which is built using the same Ru complex but Co nodes are replaced by Zr, showed a maximum temperature of 82 °C (+53.6 °C). However, the strongest photothermal effect is shown by **Co-1**, reaching 88 °C (+59.1 °C). All the maximum temperatures were reached after 5 minutes of irradiation, then, a plateau at this temperature is registered for the next 25 minutes. In order to compare the photothermal results attained with the Ru-based coordination polymers with the previously studied MOFs, we irradiated 20 mg of HKUST-1 and UiO-66-NH$_2$. The selected MOFs are known to be two of the MOFs with strongest photothermal effect. In this case, we could observe that HKUST-1 reached a maximum temperature of 75.4 °C (+46.4 °C) and UiO-66-NH$_2$ showed a maximum temperature of 97.6 °C (+69.1 °C). With these results we can conclude that the Ru coordination polymers exhibit stronger photothermal effect than HKUST-1. However, the temperature attained by UiO-66-NH$_2$ is higher than the synthesised coordination polymers.
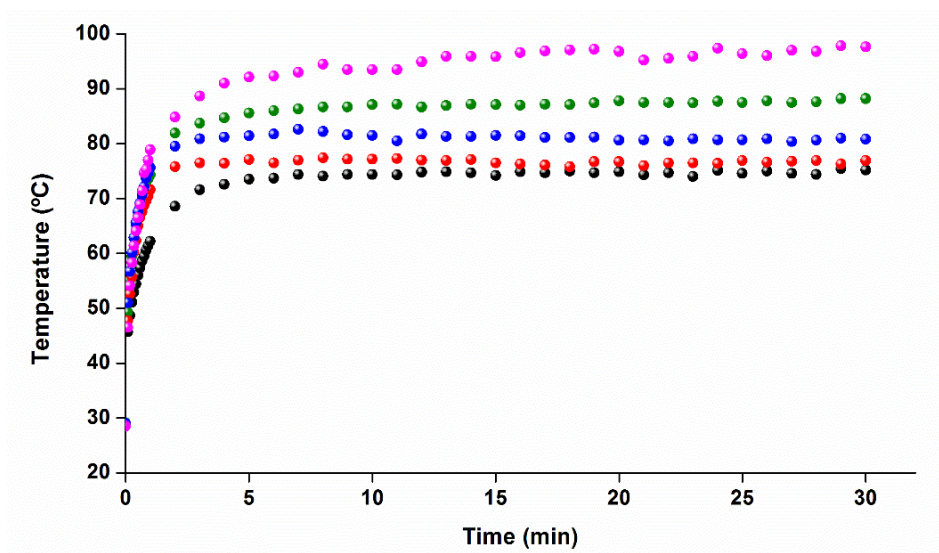
Figure 3.30. Temperature vs. time plot of the Ru coordination polymers 1-Co (green), 2-Co (red) and 2-Zr (blue) compared with HKUST-1 (Black) and UiO-66-NH$_2$ (pink).

XRPD patterns of the coordination polymers after irradiation experiments show that crystallinity was mostly retained (Figure 3.31). **Co-1** suffered from some crystallinity loss (Figure 3.31a). as it is known to be the less robust coordination polymer.
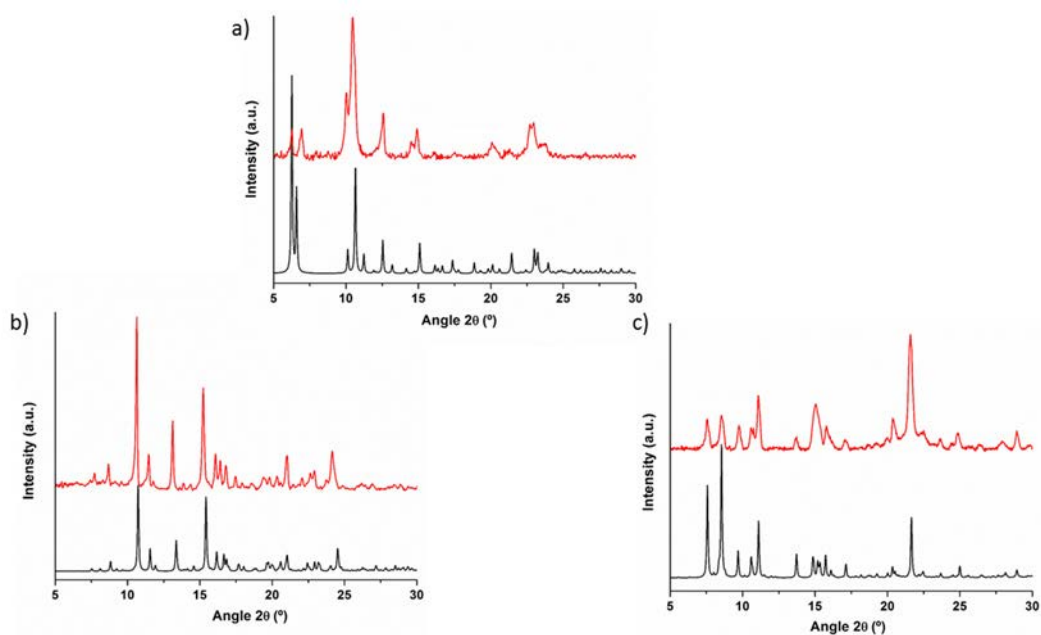
Figure 3.31. Comparison of the simulated (Black) and experimental (red) poder paterns after UV-Vis exposure for 30 min at 500 mW·cm^{-2} of **Co-1** (a), **Co-2** (b) and **Zr-2** (c).

4. Perspectives

The future work about this project might follow different directions. The previously shown coordination polymers (**1-Co**, **2-Co** and **2-Zr**) require external anions (PF$_6^-$) or coordinated ions (Cl$^-$ and HCOO$^-$) to balance the charge of the Ru core and/or the metal extending the structure. Therefore, a route that should be followed would be the synthesis of new Ru^{2+} complexes with an overall neutral or negative charge. A manner to reach this objective is by attaching more carboxylic groups to the terpyridinic moiety. For instance, Figure 4.1 shows two potential Ru^{2+} complexes that consists on hexacarboxylic and tetracarboxylic metalloligands. These complexes might use two of their pendant carboxylic groups to balance the charge of the central metal ion (Ru^{2+}) and use the remaining carboxylic groups to coordinate other metal ions for extending the structure.
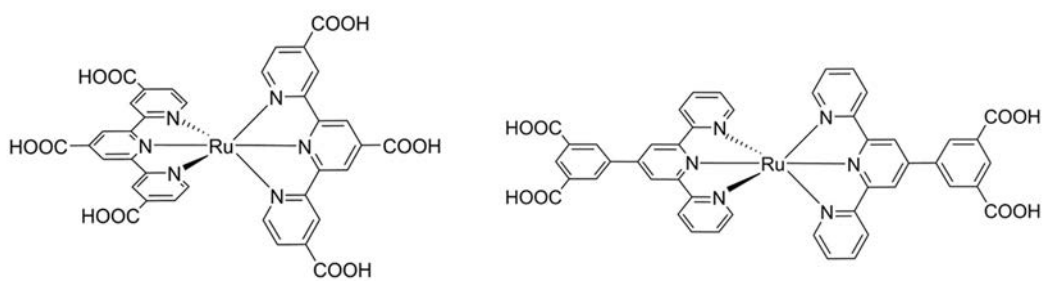
Figure 4.1. Scheme of the proposed Ru complex.

On the applications point of view, the periodic arrangement of Ru^{2+} complexes with catalytic ions, such as Co^{2+}, in a crystalline structure might be useful in photocatalysis. The close disposition of both building blocks should favour the light-harvesting of the Ru moiety and the subsequent energy transfer to the catalytic ions, converting the coordination polymer into a heterogeneous catalyst. For instance, water stable coordination polymers could be tested in water oxidation photocatalyisis reactions.

5.   Conclusions

This chapter introduced the ligand-design approach strategy to incorporate photo-active building blocks in metal-organic frameworks. Extension of the MeBIP-based ligand was attempted using both, one-pot synthesis and two-step heterometallic synthesis. However, none of these strategies was useful for obtaining coordination polymers or metal-organic frameworks.

Contrarily, novel coordination polymers based on photo-responsive Ru^{2+}-terpyridinic metalloligands. Following a two-step heterometallic synthesis, heterometallic coordination polymers namely **Co-1**, **Co-2** and **Zr-2** could be constructed.

when we These coordination polymers were built up from the assembly of the complexes **1** ($Ru(ctpy)_2^{2+}$) and **2** ($Ru(cptpy)_2^{2+}$), where ctpy is 2,2':6',2''-terpyridine-4'-carboxylic acid and cptpy is 4'-(4-carboxyphenyl)-2,2':6,2''-terpyridine, with Co^{2+} and Zr^{4+}. One- and two-dimensional CPs have been obtained depending on the length of the used metalloligand. While in **Co-2** and **Zr-2**, chains are arranged in a packed supramolecular structure, the square lattice network of **Co-1** shows potential porosity. However, PF_6^- counteranions completely fill the available voids. Anionic exchange with smaller ions might increase the accessible surface area yielding to a porous material. **Zr-2** exhibits an extraordinary structural stability towards different solvents with an extensive range of polarities. This finding reveals the potential of Zr^{4+} ions as metallic centres to construct stable coordination polymers.

Moreover, the photothermal effect of these coordination polymers was assessed, confirming their strong light-to-heat conversion. This effect is comparable to two of the MOFs with higher thermal emission (HKUST-1 and UiO-66-NH$_2$) under the same irradiation conditions.

Future work on this project should include the synthesis of Ru^{2+}-terpyridine complexes with an overall neutral or negative charge, in order to favour extension of the metalloligands in three dimensions affording MOFs. In addition, photocatalysis studies might be performed using the obtained CPs.

6. References

1. Burnworth, M., Tang, L., Kumpfer, J. R., Duncan, A. J., Beyer, F. L., Fiore, G. L., Rowan, S. J. & Weder, C. Optically Healable Supramolecular Polymers. *Nature* **472,** 334–337 (2011).

2. Mebrouk, K., Debnath, S., Fourmigué, M. & Camerel, F. Photothermal Control of the Gelation Properties of Nickel Bis(dithiolene) Metallogelators under Near-Infrared Irradiation. *Langmuir* **30,** 8592–8597 (2014).

3. Mebrouk, K., Chotard, F., Goff-Gaillard, C. Le, Arlot-Bonnemains, Y., Fourmigué, M. & Camerel, F. Water-Soluble Nickel-Bis(dithiolene) Complexes as Photothermal Agents. *Chem. Commun.* **51,** 5268–5270 (2015).

4. Zhu, C., Yang, Y., Luo, M., Yang, C., Wu, J., Chen, L., Liu, G., Wen, T., Zhu, J. & Xia, H. Stabilizing Two Classical Antiaromatic Frameworks: Demonstration of Photoacoustic Imaging and the Photothermal Effect in Metalla-aromatics. *Angew. Chem. Int. Ed.* **54,** 6181–6185 (2015).

5. Zhu, C., Yang, C., Wang, Y., Lin, G., Yang, Y., Wang, X., Zhu, J., Chen, X., Lu, X., Liu, G. & Xia, H. CCCCC Pentadentate Chelates with Planar Möbius Aromaticity and Unique Properties. *Sci. Adv.* **2,** (2016).

6. He, X., He, X., Li, S., Zhuo, K., Qin, W., Dong, S., Chen, J., Ren, L., Liu, G. & Xia, H. Amphipathic Metal-Containing Macromolecules with Photothermal Properties. *Polym. Chem.* **8,** 3674–3678 (2017).

7. Lin, Q., Li, S., Lin, J., Chen, M., Lu, Z., Tang, C., Chen, Z., He, X., Chen, J. & Xia, H. Synthesis and Characterization of Photothermal Osmium Carbolong Complexes. *Chem. – Eur. J.* **24,** 8375–8381 (2018).

8. Yang, C., Lin, G., Zhu, C., Pang, X., Zhang, Y., Wang, X., Li, X., Wang, B., Xia, H. & Liu, G. Metalla-Aromatic Loaded Magnetic Nanoparticles for MRI/Photoacoustic Imaging-Guided Cancer Phototherapy. *J. Mater. Chem. B* **6,** 2528–2535 (2018).

9. Hofmeier, H. & Schubert, U. S. Recent Developments in the Supramolecular Chemistry of Terpyridine-Metal Complexes. *Chem. Soc. Rev.* **33,** 373–399 (2004).

10. Rayner-Canham, G. & Overton, T. *Descriptive Inorganic Chemistry*. (WH Freeman, 2013).

11. Kalyanasundaram, K. Photophysics, Photochemistry and Solar Energy Conversion with Tris(bipyridyl)Ruthenium(II) and its Analogues. *Coord. Chem. Rev.* **46,** 159–244 (1982).

12. Balzani, V., Juris, A., Venturi, M., Campagna, S. & Serroni, S. Luminescent and Redox-Active Polynuclear Transition Metal Complexes. *Chem. Rev.* **96,** 759–834 (1996).

13. Juris, A., Balzani, V., Barigelletti, F., Campagna, S., Belser, P. & von Zelewsky, A. Ru(II) Polypyridine Complexes: Photophysics, Photochemistry, Eletrochemistry, and Chemiluminescence. *Coord. Chem. Rev.* **84,** 85–277 (1988).

14. Paris, J. P. & Brandt, W. W. Charge Transfer Lunimescense of a Ruthenium(II) Chelate. *J. Am. Chem. Soc.* **81,** 5001–5002 (1959).

15. Giarikos, D. G. in *Natural and Artificial Photosynthesis: Solar Power as an Energy Source* (ed. Razeghifard, R.) (John Wiley & Sons, Ltd., 2013).

16. Barber, J. Photosynthetic Energy Conversion: Natural and Artificial. *Chem. Soc. Rev.* **38,** 185–196 (2009).

17. Tachibana, Y., Vayssieres, L. & Durrant, J. R. Artificial Photosynthesis for Solar Water-Splitting. *Nat. Photonics* **6,** 511–518 (2012).

18.   Alstrum-Acevedo, J. H., Brennaman, M. K. & Meyer, T. J. Chemical Approaches to Artificial Photosynthesis. 2. *Inorg. Chem.* **44,** 6802–6827 (2005).

19.   Sun, L., Hammarstrom, L., Akermark, B. & Styring, S. Towards Artificial Photosynthesis: Ruthenium-Manganese Chemistry for Energy Production. *Chem. Soc. Rev.* **30,** 36–49 (2001).

20.   Gust, D., Moore, T. A. & Moore, A. L. Mimicking Photosynthetic Solar Energy Transduction. *Acc. Chem. Res.* **34,** 40–48 (2001).

21.   Lubitz, W., Reijerse, E. J. & Messinger, J. Solar Water-Splitting into H_2 and O_2: Design Principles of Photosystem II and Hydrogenases. *Energy Environ. Sci.* **1,** 15–31 (2008).

22.   McConnell, I., Li, G. & Brudvig, G. W. Energy Conversion in Natural and Artificial Photosynthesis. *Chem. Biol.* **17,** 434–447 (2010).

23.   Benniston, A. C. & Harriman, A. Artificial Photosynthesis. *Mater. Today* **11,** 26–34 (2008).

24.   Su, J. & Vayssieres, L. A Place in the Sun for Artificial Photosynthesis? *ACS Energy Lett.* **1,** 121–135 (2016).

25.   Narayanam, J. M. R. & Stephenson, C. R. J. Visible Light Photoredox Catalysis: Applications in Organic Synthesis. *Chem. Soc. Rev.* **40,** 102–113 (2011).

26.   O'Regan, B. & Grätzel, M. A Low-Cost, High-Efficiency Solar Cell based on Dye-Sensitized Colloidal TiO_2 Films. *Nature* **353,** 737–740 (1991).

27.   Hagfeldt, A. & Grätzel, M. Molecular Photovoltaics. *Acc. Chem. Res.* **33,** 269–277 (2000).

28.   Hagfeldt, A., Boschloo, G., Sun, L., Kloo, L. & Pettersson, H. Dye-Sensitized Solar Cells. *Chem. Rev.* **110,** 6595–6663 (2010).

29.   Islam, A., Sugihara, H. & Arakawa, H. Molecular Design of Ruthenium(II) Polypyridyl Photosensitizers for Efficient Nanocrystalline TiO_2 Solar Cells. *J. Photochem. Photobiol. A Chem.* **158,** 131–138 (2003).

30.   K. Nazeeruddin, M., Pechy, P. & Gratzel, M. Efficient Panchromatic Sensitization of Nanocrystalline TiO_2 Films by a Black Dye based on a Trithiocyanato-Ruthenium Complex. *Chem. Commun.* **0,** 1705–1706 (1997).

31.   Amao, Y. & Okura, I. Optical Oxygen Sensing Materials: Chemisorption Film of Ruthenium(II) Polypyridyl Complexes Attached to Anionic Polymer. *Sens. Actuators, B.* **88,** 162–167 (2003).

32.   Elmes, R. B. P. & Gunnlaugsson, T. Luminescence Anion Sensing via Modulation of MLCT Emission from a Naphthalimide–Ru(II)–Polypyridyl Complex. *Tetrahedron Lett.* **51,** 4082–4087 (2010).

33.   Ocakoglu, K. & Okur, S. Humidity Sensing Properties of Novel Ruthenium Polypyridyl Complex. *Sens. Actuators, B.* **151,** 223–228 (2010).

34.   Kitchen, J. A., Boyle, E. M. & Gunnlaugsson, T. Synthesis, Structural Characterisation and Luminescent Anion Sensing Studies of a Ru(II)polypyridyl Complex Featuring an Aryl Urea Derivatised 2,2'-bpy Auxiliary Ligand. *Inorg. Chim. Acta* **381,** 236–242 (2012).

35.   Gersten, S. W., Samuels, G. J. & Meyer, T. J. Catalytic Oxidation of Water by an Oxo-Bridged Ruthenium Dimer. *J. Am. Chem. Soc.* **104,** 4029–4030 (1982).

36.   Kärkäs, M. D., Johnston, E. V., Karlsson, E. A., Lee, B., Åkermark, T., Shariatgorji, M., Ilag, L., Hansson, Ö., Bäckvall, J. & Åkermark, B. Light-Induced Water Oxidation by a Ru complex Containing a Bio-Inspired Ligand. *Chem. – Eur. J.* **17,** 7953–7959 (2011).

37. Limburg, B., Bouwman, E. & Bonnet, S. Rate and Stability of Photocatalytic Water Oxidation using [Ru(bpy)$_3$]$^{2+}$ as Photosensitizer. *ACS Catal.* **6,** 5273–5284 (2016).

38. Meng, X., Leyva, M. L., Jenny, M., Gross, I., Benosman, S., Fricker, B., Harlepp, S., Hébraud, P., Boos, A., Wlosik, P., Bischoff, P., Sirlin, C., Pfeffer, M., Loeffler, J.-P. & Gaiddon, C. A Ruthenium-Containing Organometallic Compound Reduces Tumor Growth through Induction of the Endoplasmic Reticulum Stress Gene CHOP. *Cancer Res.* **69,** 5458–5466 (2009).

39. Baggaley, E., Gill, M. R., Green, N. H., Turton, D., Sazanovich, I. V., Botchway, S. W., Smythe, C., Haycock, J. W., Weinstein, J. A. & Thomas, J. A. Dinuclear Ruthenium(II) Complexes as Two-Photon, Time-Resolved Emission Microscopy Probes for Cellular DNA. *Angew. Chem. Int. Ed.* **53,** 3367–3371 (2014).

40. Cloonan, S. M., Elmes, R. B. P., Erby, M., Bright, S. A., Poynton, F. E., Nolan, D. E., Quinn, S. J., Gunnlaugsson, T. & Williams, D. C. Detailed Biological Profiling of a Photoactivated and Apoptosis Inducing pdppz Ruthenium(II) Polypyridyl Complex in Cancer Cells. *J. Med. Chem.* **58,** 4494–4505 (2015).

41. Poynton, F. E., Bright, S. A., Blasco, S., Williams, D. C., Kelly, J. M. & Gunnlaugsson, T. The Development of Ruthenium(II) Polypyridyl Complexes and Conjugates for In Vitro Cellular and In Vivo Applications. *Chem. Soc. Rev.* **46,** 7706–7756 (2017).

42. Mital, M. & Ziora, Z. Biological Applications of Ru(II) Polypyridyl Complexes. *Coord. Chem. Rev.* (2018). doi:https://doi.org/10.1016/j.ccr.2018.02.013

43. Yun, S., Freitas, J. N., Nogueira, A. F., Wang, Y., Ahmad, S. & Wang, Z.-S. Dye-Sensitized Solar Cells Employing Polymers. *Prog. Polym. Sci.* **59,** 1–40 (2016).

44. Nafiseh, S., Fariba, T. & Nima, T. Recent Developments in Dye-Sensitized Solar Cells. *ChemPhysChem* **15,** 3902–3927 (2014).

45. Zhang, P., Wang, J., Huang, H., Qiu, K., Huang, J., Ji, L. & Chao, H. Enhancing the Photothermal Stability and Photothermal Efficacy of AuNRs and AuNTs by Grafting with Ru(II) Complexes. *J. Mater. Chem. B* **5,** 671–678 (2017).

46. Helmchen, F. & Denk, W. Deep Tissue Two-Photon Microscopy. *Nat. Methods* **2,** 932–940 (2005).

47. Heinemann, F., Karges, J. & Gasser, G. Critical Overview of the Use of Ru(II) Polypyridyl Complexes as Photosensitizers in One-Photon and Two-Photon Photodynamic Therapy. *Acc. Chem. Res.* **50,** 2727–2736 (2017).

48. Kirsten, Z. Photoredox Catalysis with Visible Light. *Angew. Chem. Int. Ed.* **48,** 9785–9789 (2009).

49. Yoon, T. P., Ischay, M. A. & Du, J. Visible Light Photocatalysis as a Greener Approach to Photochemical Synthesis. *Nat. Chem.* **2,** 527–532 (2010).

50. Sala, X., Romero, I., Rodríguez, M., Escriche, L. & Llobet, A. Molecular Catalysts that Oxidize Water to Dioxygen. *Angew. Chem. Int. Ed.* **48,** 2842–2852 (2009).

51. Kärkäs, M. D., Verho, O., Johnston, E. V & Åkermark, B. Artificial Photosynthesis: Molecular Systems for Catalytic Water Oxidation. *Chem. Rev.* **114,** 11863–12001 (2014).

52. Blakemore, J. D., Crabtree, R. H. & Brudvig, G. W. Molecular Catalysts for Water Oxidation. *Chem. Rev.* **115,** 12974–13005 (2015).

53. Pizzolato, E., Natali, M., Posocco, B., Montellano Lopez, A., Bazzan, I., Di Valentin, M., Galloni, P., Conte, V., Bonchio, M., Scandola, F. & Sartorel, A. Light Driven Water

Oxidation by a Single Site Cobalt Salophen Catalyst. *Chem. Commun.* **49,** 9941–9943 (2013).

54. Yu, X. & Cohen, S. M. Photocatalytic Metal-Organic Frameworks for the Aerobic Oxidation of Arylboronic Acids. *Chem. Commun.* **51,** 9880–9883 (2015).

55. Han, S., Wei, Y. & Grzybowski, B. A. A Metal–Organic Framework Stabilizes an Occluded Photocatalyst. *Chem. – Eur. J.* **19,** 11194–11198 (2013).

56. Whittington, C. L., Wojtas, L. & Larsen, R. W. Ruthenium(II) Tris(2,2'-bipyridine)-Templated Zinc(II) 1,3,5-Tris(4-carboxyphenyl)benzene Metal Organic Frameworks: Structural Characterization and Photophysical Properties. *Inorg. Chem.* **53,** 160–166 (2014).

57. Tang, Y., He, W., Lu, Y., Fielden, J., Xiang, X. & Yan, D. Assembly of Ruthenium-Based Complex into Metal–Organic Framework with Tunable Area-Selected Luminescence and Enhanced Photon-to-Electron Conversion Efficiency. *J. Phys. Chem. C* **118,** 25365–25373 (2014).

58. Chen, R., Zhang, J., Chelora, J., Xiong, Y., Kershaw, S. V, Li, K. F., Lo, P.-K., Cheah, K. W., Rogach, A. L., Zapien, J. A. & Lee, C.-S. Ruthenium(II) Complex Incorporated UiO-67 Metal–Organic Framework Nanoparticles for Enhanced Two-Photon Fluorescence Imaging and Photodynamic Cancer Therapy. *ACS Appl. Mater. Interfaces* **9,** 5699–5708 (2017).

59. Zhang, W., Li, B., Ma, H., Zhang, L., Guan, Y., Zhang, Y., Zhang, X., Jing, P. & Yue, S. Combining Ruthenium(II) Complexes with Metal–Organic Frameworks to Realize Effective Two-Photon Absorption for Singlet Oxygen Generation. *ACS Appl. Mater. Interfaces* **8,** 21465–21471 (2016).

60. Wang, C., Xie, Z., deKrafft, K. E. & Lin, W. Doping Metal–Organic Frameworks for Water Oxidation, Carbon Dioxide Reduction, and Organic Photocatalysis. *J. Am. Chem. Soc.* **133,** 13445–13454 (2011).

61. Barrett, S. M., Wang, C. & Lin, W. Oxygen Sensing via Phosphorescence Quenching of Doped Metal-Organic Frameworks. *J. Mater. Chem.* **22,** 10329–10334 (2012).

62. Zhu, J., Maza, W. A. & Morris, A. J. Light-Harvesting and Energy Transfer in Ruthenium(II)-Polypyridyl Doped Zirconium(IV) Metal-Organic Frameworks: A Look Toward Solar Cell Applications. *J. Photochem. Photobiol. A Chem.* **344,** 64–77 (2017).

63. Maza, W. A. & Morris, A. J. Photophysical Characterization of a Ruthenium(II) Tris(2,2'-bipyridine)-Doped Zirconium UiO-67 Metal–Organic Framework. *J. Phys. Chem. C* **118,** 8803–8817 (2014).

64. Kumar, G. & Gupta, R. Molecularly Designed Architectures - the Metalloligand Way. *Chem. Soc. Rev.* **42,** 9403–9453 (2013).

65. Kent, C. A., Mehl, B. P., Ma, L., Papanikolas, J. M., Meyer, T. J. & Lin, W. Energy Transfer Dynamics in Metal–Organic Frameworks. *J. Am. Chem. Soc.* **132,** 12767–12769 (2010).

66. Kent, C. A., Liu, D., Ma, L., Papanikolas, J. M., Meyer, T. J. & Lin, W. Light Harvesting in Microscale Metal–Organic Frameworks by Energy Migration and Interfacial Electron Transfer Quenching. *J. Am. Chem. Soc.* **133,** 12940–12943 (2011).

67. Zhang, S., Han, L., Li, L., Cheng, J., Yuan, D. & Luo, J. A Highly Symmetric Metal–Organic Framework Based on a Propeller-Like Ru-Organic Metalloligand for Photocatalysis and Explosives Detection. *Cryst. Growth Des.* **13,** 5466–5472 (2013).

68. Kobayashi, A., Ohba, T., Saitoh, E., Suzuki, Y., Noro, S., Chang, H.-C. & Kato, M. Flexible

Coordination Polymers Composed of Luminescent Ruthenium(II) Metalloligands: Importance of the Position of the Coordination Site in Metalloligands. *Inorg. Chem.* **53,** 2910–2921 (2014).

69. Toyao, T., Saito, M., Dohshi, S., Mochizuki, K., Iwata, M., Higashimura, H., Horiuchi, Y. & Matsuoka, M. Development of a Ru Complex-Incorporated MOF Photocatalyst for Hydrogen Production under Visible-Light Irradiation. *Chem. Commun.* **50,** 6779–6781 (2014).

70. Beves, J. E., Constable, E. C., Decurtins, S., Dunphy, E. L., Housecroft, C. E., Keene, T. D., Neuburger, M. & Schaffner, S. Homoleptic metal complexes of 4'-(5-pyrimidinyl)-2,2':6',2''-terpyridine: tetrafurcated expanded ligands. *CrystEngComm* **10,** 986 (2008).

71. Rowan, S. J. & Beck, J. B. Metal–Ligand Induced Supramolecular Polymerization: A Route to Responsive Materials. *Faraday Discuss.* **128,** 43–53 (2005).

72. Beck, J. B., Ineman, J. M. & Rowan, S. J. Metal/Ligand-Induced Formation of Metallo-Supramolecular Polymers. *Macromolecules* **38,** 5060–5068 (2005).

73. Husson, J., Dehaudt, J. & Guyard, L. Preparation of Carboxylate Derivatives of Terpyridine via the Furan Pathway. *Nat. Protoc.* **9,** 21–26 (2014).

74. Constable, E. C., Dunphy, E. L., Housecroft, C. E., Neuburger, M., Schaffner, S., Schaper, F. & Batten, S. R. Expanded Ligands: Bis(2,2':6',2''-Terpyridine Carboxylic Acid)Ruthenium(II) Complexes as Metallosupramolecular Analogues of Dicarboxylic Acids. *Dalton Trans.* **0,** 4323–4332 (2007).

75. Reichardt, C. Solvatochromic Dyes as Solvent Polarity Indicators. *Chem. Rev.* **94,** 2319–2358 (1994).

76. Cavka, J. H., Jakobsen, S., Olsbye, U., Guillou, N., Lamberti, C., Bordiga, S. & Lillerud, K. P. A New Zirconium Inorganic Building Brick Forming Metal Organic Frameworks with Exceptional Stability. *J. Am. Chem. Soc.* **130,** 13850–13851 (2008).

77. Zhou, D., Cheng, Q.-Y., Cui, Y., Wang, T., Li, X. & Han, B.-H. Graphene–Terpyridine Complex Hybrid Porous Material for Carbon Dioxide Adsorption. *Carbon N. Y.* **66,** 592–598 (2014).

78. Lago Blanco, A. B. Diseño, Síntesis y Caracterización de Polímeros de Coordinación. (2008).

79. Sauvage, J.-P., Collin, J.-P., Chambron, J.-C., Guillerez, S., Coudret, C., Baltani, V., Barigelletti, F., De Cola, L. & Flamigni, L. Ruthenium(II) and Osmium(II) Bis(terpyridine) Complexes in Covalently-Linked Multicomponent Systems: Synthesis, Electrochemical Behavior, Absorption Spectra, and Photochemical and Photophysical Properties. *Chem. Rev.* **94,** 993–1019 (1994).

80. Ng, W. Y., Gong, X. & Chan, W. K. Electronic and Light-Emitting Properties of Some Polyimides Based on Bis(2,2':6',2''-terpyridine) Ruthenium(II) Complex. *Chem. Mater.* **11,** 1165–1170 (1999).

Conclusions

This Thesis has been focused on assessing **light interaction with metal-organic frameworks and coordination polymers** following two different approaches: 1) the evaluation of the photothermal effect in pure MOFs upon UV-Vis light irradiation and subsequent application in activation and CPSM fields, and 2) the synthesis of CPs through a ligand design approach, which afforded the introduction of the light-harvesting Ru^{2+}-terpyridyl complexes in extended structures.

The first part of this Thesis consisted on the study of the light-to-heat conversion in reported MOFs upon UV-Vis irradiation, as explained in Chapter 3. It should be noted that the assessment of the **photothermal effect** in pure MOFs was accomplished for the first time. We observed that MOFs with absorption maxima in the emitting wavelength range (300-650 nm) exhibited temperature increases up to 120-250 °C after 5 minutes of irradiation. The localized high temperatures allowed us to test the viability to **activate MOFs** by only applying UV-Vis light. Upon optimization of the setup and the experimental conditions, we concluded that the MOFs presenting strong photothermal effect can be activated in only 30 minutes of irradiation and without the need for previous solvent exchange steps. The S_{BET} values for HKUST-1, UiO-66-NH$_2$, ZIF-67, IRMOF-3, MIL-101-NH$_2$(Fe) and CPO-27-M (M = Zn, Ni, Mg) were comparable to the reported ones using conventional activation methods. In addition, this activation method was also proved useful for a covalent organic framework.

In order to exploit the described photothermal effect, **covalent post-synthetic modification of MOFs** was also attained by using the local heat generated in the crystalline samples. Chapter 4 describes the development of a novel CPSM approach based on the performance of MOF crystals as "heaters". In this sense, we could promote solvent-free organic reactions between pendant functional groups of the MOFs and organic reagents. The conditions that should be met to achieve this goal are the following: 1) the used MOF should present strong photothermal effect, 2) the MOF has contain free functional groups in the organic ligand and 3) the organic reagent must have a lower meting point than the temperature reached by the MOF. In this sense, amide coupling between UiO-66-NH$_2$ and MIL-101-NH$_2$(Al), and maleic or benzoic anhydride were achieved. Moreover, a photoinduced cascade reaction was demonstrated between UiO-66-NH$_2$ and an aldehyde, which, upon UV-Vis irradiation afforded the formation of the intermediate carboxylic acid and yielded the synthesis of an amide moiety instead of the expected imine bond.

The second strategy was detailed in Chapter 5 and summarized the ligand-design approach in order to introduce **photo-active ligands and metalloligands** into metal-organic frameworks.

The ligand containing the 2,6-bis(1'-methylbenzimidazolyl)pyridine (MeBIP) core was complexed using Co^{2+}, Ni^{2+} and Fe^{3+}. However, neither two-step nor one-pot syntheses allowed the formation of extended structures.

Ru^{2+}-terpyridyl metalloligands with carboxylic functionalities were successfully synthesised. In this case, the **heterometallic two-step synthesis** in combination with Co^{2+} and Zr^{4+} afforded the synthesis of three CPs, **Co-1, Co-2** and **Zr-2.** Full characterization of all the CPs was performed, and it was demonstrated that their photothermal effect is comparable to the MOFs with strongest heat conversion. Moreover, future work might follow two directions: 1) the synthesis of new Ru^{2+} complexes with neat neutral or negative charge, and 2) assess the CPs in photocatalytic reactions in order to benefit from the periodic arrangement of both building blocks, the antenna Ru^{2+} complex and the Co^{2+} catalytic ion.

Appendix

1. Materials and instrumentation

1.1. Reagents

Starting materials and solvents were purchased and used without further purification from commercial suppliers (Sigma-Aldrich (σ), TCI (*), Acros Organics (+), Fisher (φ), Alfa Aesar (α) and Eurisotop (ε)). Deionized water was obtained using a Milli-Q system (18.2 MΩ cm).

Specific reagents used in Chapter 3	
$Cu(NO_3)_2 \cdot 2.5H_2O$ (σ)	$Ni(OAc)_2 \cdot 4H_2O$ (σ)
1,3,5-benzenetricarboxylic acid (σ)	$Mg(OAc)_2$ (σ)
$ZrCl_4$ (σ)	$FeCl_3 \cdot 6H_2O$ (σ)
benzene-1,4-dicarboxylic acid (σ)	$Zn(NO_3)_2 \cdot 6H_2O$ (σ)
2-aminoterephthalic acid (σ)	1,3,5-benzenetricarbaldehyde (σ)
$Zn(OAc)_2 \cdot 2H_2O$ (+)	1,3,5-tris-(4-aminophenyl)benzene (*)
2-methylimidazole (σ)	Acetic acid 99.7 % (σ)
$Co(OAc)_2 \cdot 4H_2O$ (σ)	Mesitylene (σ)
2,5-dihydroxyterephthalic acid (σ)	1,4-dioxane (σ)
NaOH (σ)	

Specific reagents used in Chapter 4	
$ZrOCl_2 \cdot 8H_2O$ (σ)	Benzoic anhydride (σ)
2-aminoterephthalic acid (σ)	Maleic anhydride (σ)
$AlCl_3 \cdot 6H_2O$ (α)	4-bromobenzaldehyde (σ)
HCl 97 % (σ)	4-bromobenzoic acid (*)

Specific reagents used in Chapter 5	
Chelidamic acid (σ)	N-methyl-1,2-phenylenediamine (σ)
Benzyl bromoacetate (σ)	K_2CO_3 (σ)
H_3PO_4 85 % (σ)	HCl 97 % (σ)
2-acetylpyridine (σ)	$RuCl_3 \cdot 3H_2O$ (σ)
Furfuraldehyde (σ)	$Co(NO_3)_2 \cdot 6H_2O$ (σ)
4-methoxycarbonylbenzaldehyde (*)	$CoCl_2 \cdot 6H_2O$ (σ)
N-ethylmorpholine (σ)	$ZrOCl_2 \cdot 8H_2O$ (σ)
NaOH (σ)	HNO_3 (σ)
KOH (σ)	KNO_3 (σ)
Triethylamine (σ)	H_2SO_4 (σ)
NH_3 (σ)	Formic acid (σ)
$KMnO_4$ (σ)	HCl 97 % (σ)
NH_4PF_6 (+)	

General solvents	
EtOH absolute (φ)	Acetone (φ)
DMF (φ)	DMSO (φ)
MeCN (φ)	MeOH (φ)
Toluene (φ)	MeCN-d_3 (ε)
Diethyl ether (φ)	DMSO-d_6 (ε)
THF (φ)	DCl (ε)
DCM (φ)	Chloroform (φ)

1.2. Characterization techniques

Nuclear Magnetic Resonance (NMR)

Spectra were collected in deuterated solvents (DMSO-d_6, DMSO-d_6/DCl and MeCN-d_3) in a *Bruker Avance DRX-250* and a *Bruker Avance III-400SB* spectrometers depending on the solubility of the samples.

X-Ray Diffraction (XRD)

Powder X-ray diffraction (XRPD) patterns were collected on a PANalytical *X'PERT PRO Multi-purpose Diffratometer* (MPD) (45 kV; 40 mA) using CuKα radiation (λ = 1.5419 Å).

Crystallographic data for single crystals was collected at 100 K at XALOC beamline at ALBA synchrotron. Simulated patterns derived from the single crystal were obtained using Mercury utility.

Thermogravimetric analysis (TGA)

TGA was performed on a *Pyris 8000* thermogravimetrical analyser at a heat rate of 10 °C/min from 30 °C to 700 °C under a nitrogen flow of 20 mL/min.

Fourier-transform infrared spectroscopy (FT-IR)

FT-IR spectra were obtained using a *Tensor 27 FTIR spectrometer* in the frequency range 400-4000 cm^{-1}. 1-2% of sample was mixed with KBr to obtain a pellet disk in order to minimize the background signals. Blank KBr pellets were measured before any analysis. OPUS software was employed for data treatment.

Ultraviolet–visible spectroscopy (UV-vis)

Absorbance spectra were recorded with a *Cary 4000 UV-Vis-NIR spectrometer* (Agilent Technologies) in the wavelength range 200-800 nm previously preparing KBr pellets of the samples. Blank KBr pellets were measured before any analysis. Cary WinUV software was employed for data treatment.

Nitrogen adsorption isotherms

Nitrogen adsorption measurements were carried out at 77 K using an *Autosorb-IQ-AG analyser* (Quantachrome Instruments).

Photothermal assessment setup

The UV-Vis high-intensity spot lamp without filter (300-650 nm) was a *Bluepoint 4 Ecocure* (Hönle UV Technology), and the infrared camera was a *PI 450* (Optris), working in a temperature range of 0-250 °C. Data were obtained and treated using the PI Connect software.

2.   Supplementary Information for Chapter 3

2.1. ^{1}H-NMR spectroscopy characterization
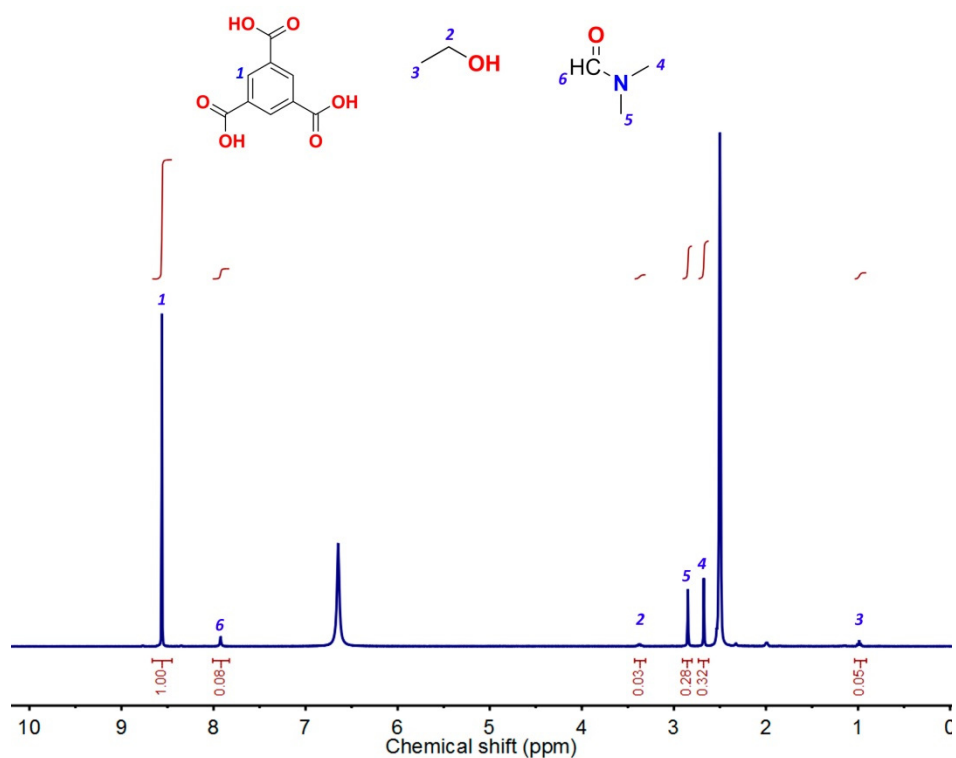
Figure 2.1. ^{1}H NMR spectrum of the photothermally activated HKUST-1 once digested in DCl/DMSO-d_6.
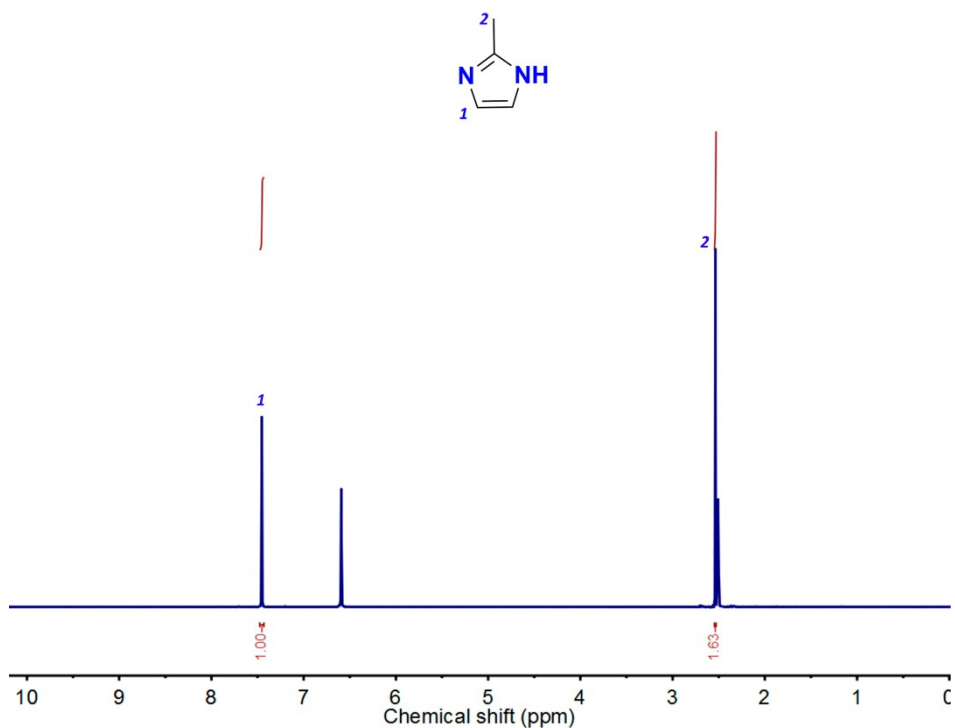
Figure 2.2. ^{1}H NMR spectrum of the photothermally activated ZIF-8 once digested in DCl/DMSO-d_6.
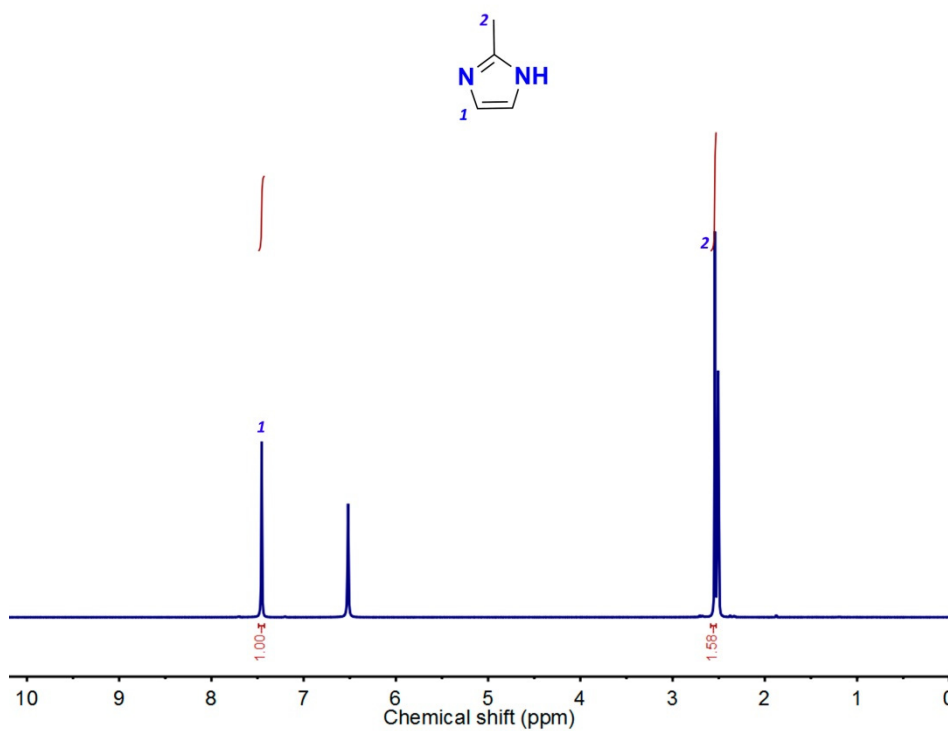
Figure 2.3. ^{1}H NMR spectrum of the photothermally activated ZIF-67 once digested in DCl/DMSO-d_6.
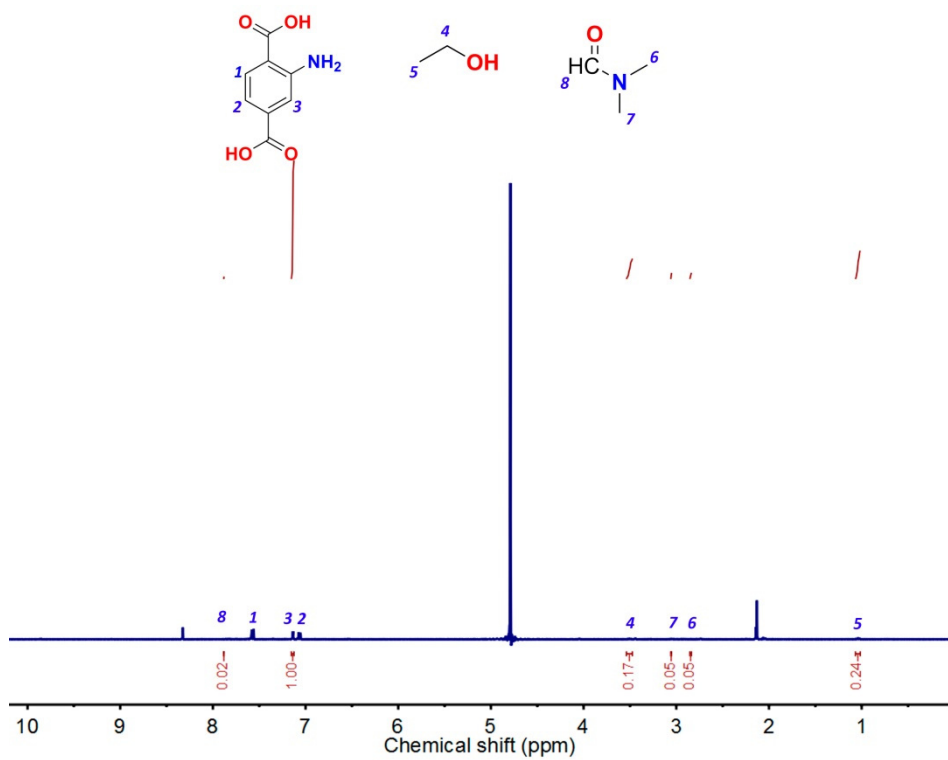
Figure 2.4. ^{1}H NMR spectrum of the photothermally activated MIL-101-NH$_2$(Fe) once digested in NaOD/D$_2$O.
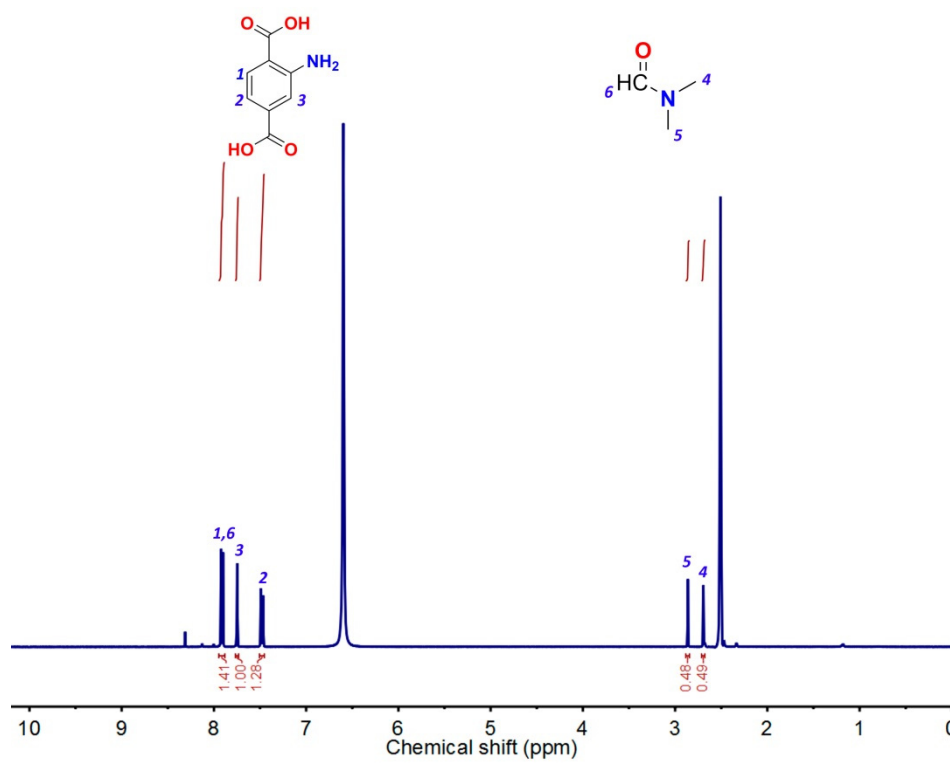
Figure 2.5. ^{1}H NMR spectrum of the photothermally activated IRMOF-3 once digested in DCl/DMSO-d_6.
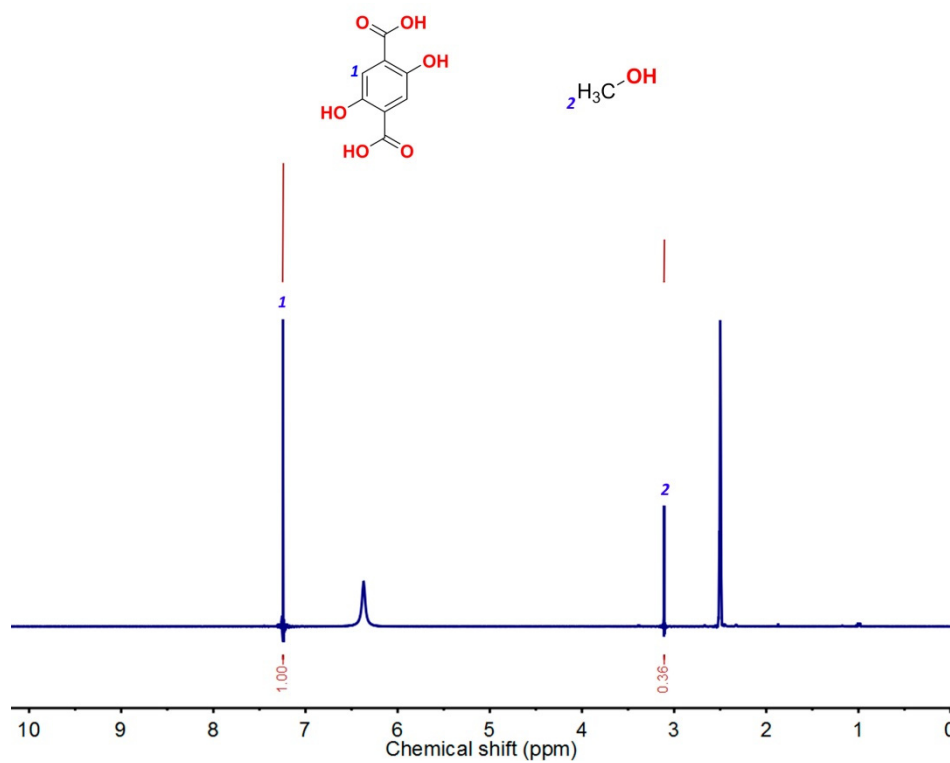
Figure 2.6. ^{1}H NMR spectrum of the photothermally activated CPO-27-Zn once digested in DCl/DMSO-d_6.
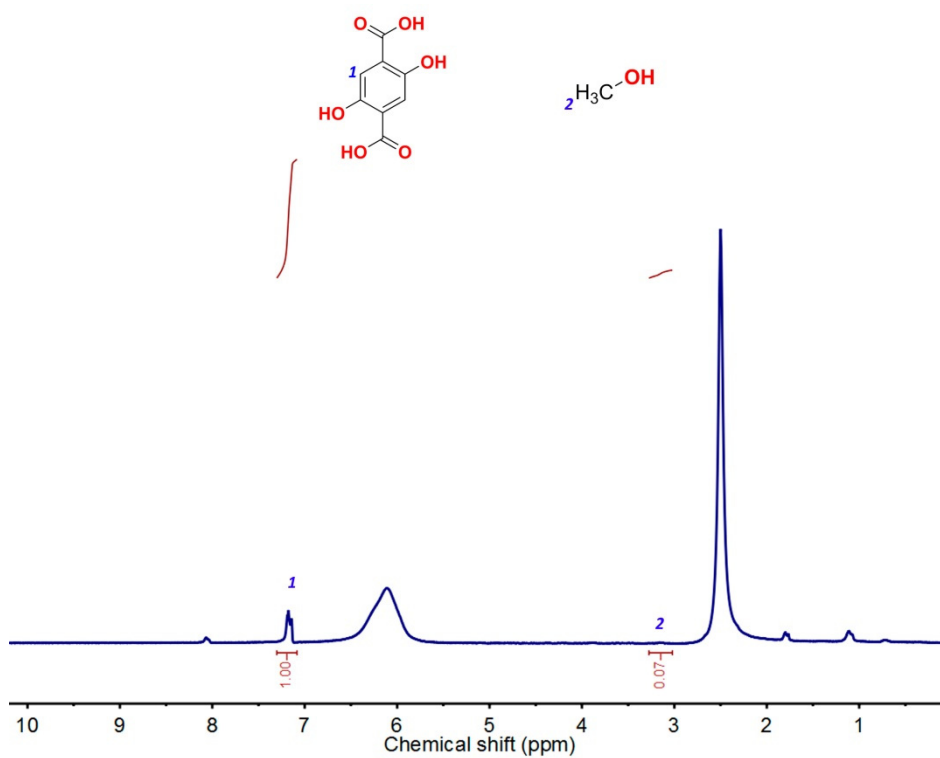
Figure 2.7. ^{1}H NMR spectrum of the photothermally activated CPO-27-Ni once digested in DCl/DMSO-d_6.
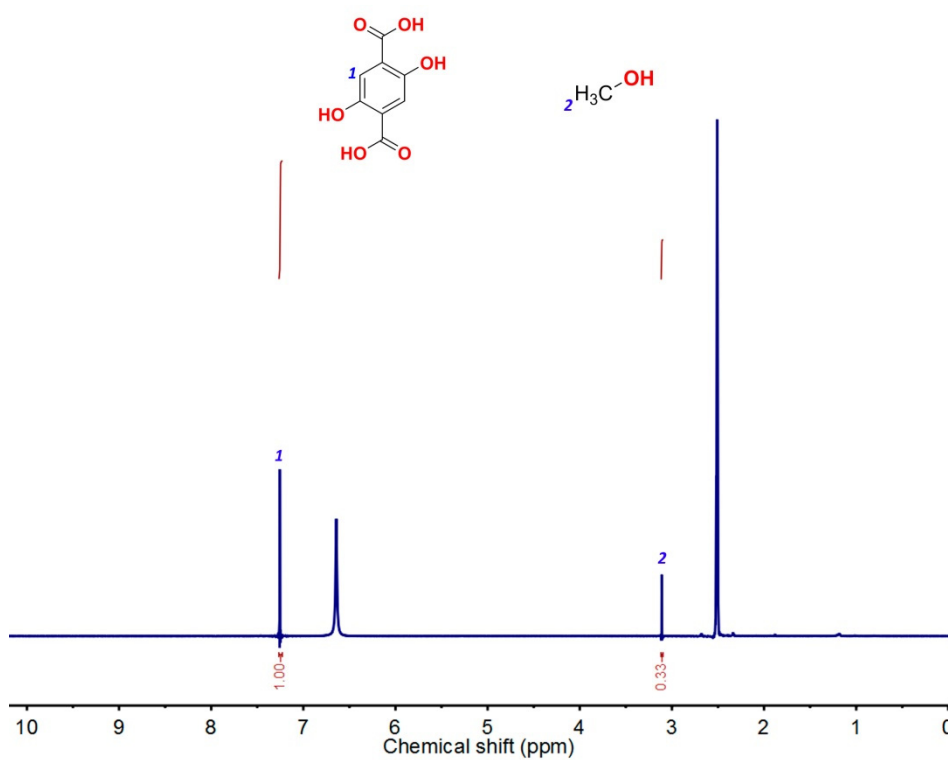
Figure 2.8. ^{1}H NMR spectrum of the photothermally activated CPO-27-Mg once digested in DCl/DMSO-d_6.
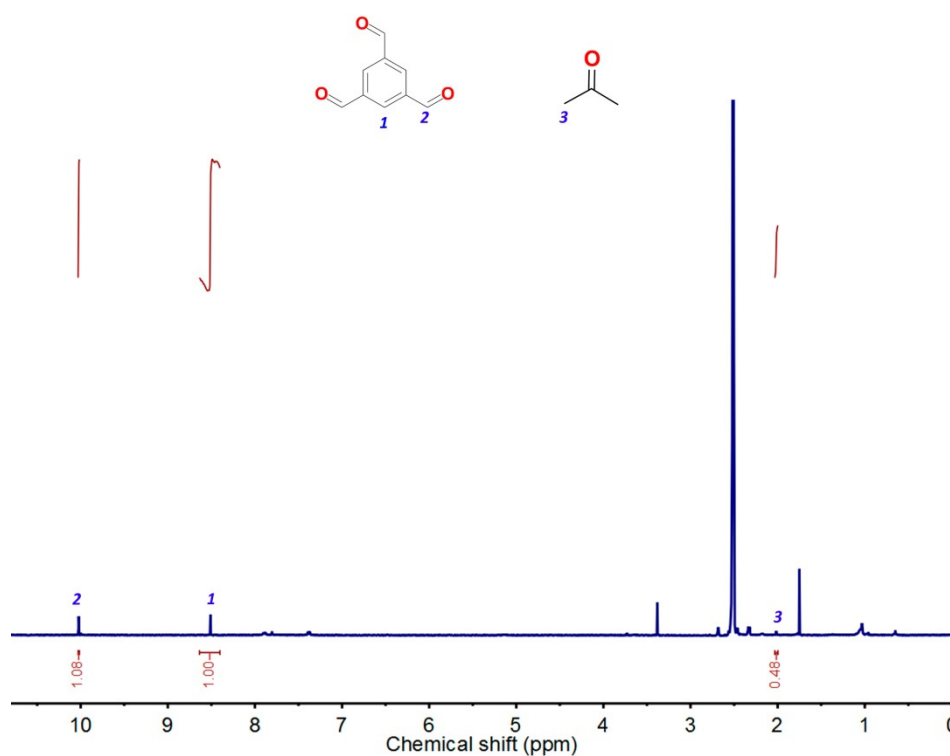
Figure 2.9. ^{1}H NMR spectrum of the photothermally activated COF-TAPB-BTCA once digested in D_2SO_4/DMSO-d_6.

2.2. N_2 adsorption fitting
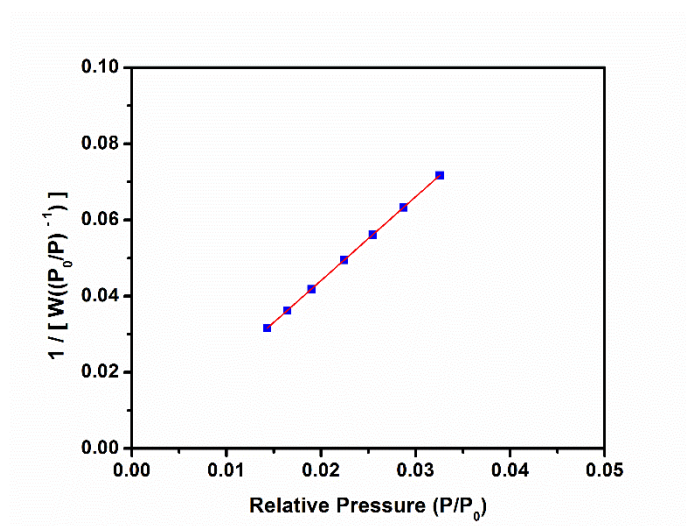
Figure 2.10. Linear fit of HKUST-1 upon photothermal activation for 30 minutes at a light guide-to-sample distance of 7cm.
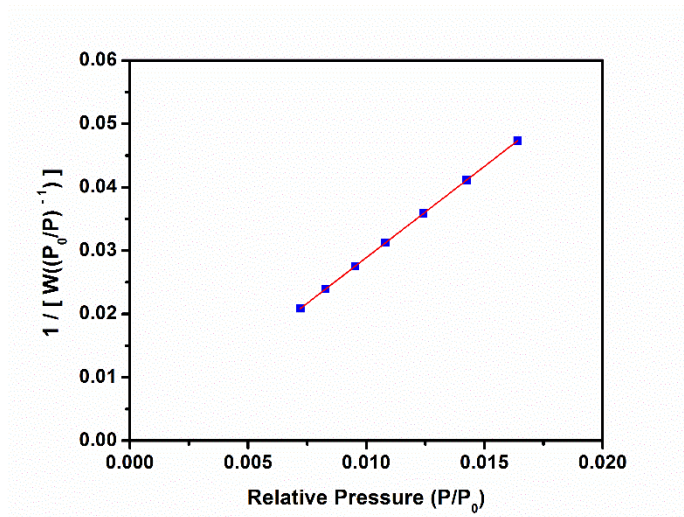
Figure 2.11. Linear fit of HKUST-1 upon photothermal activation for 5 minutes at a light guide-to-sample distance of 7cm.
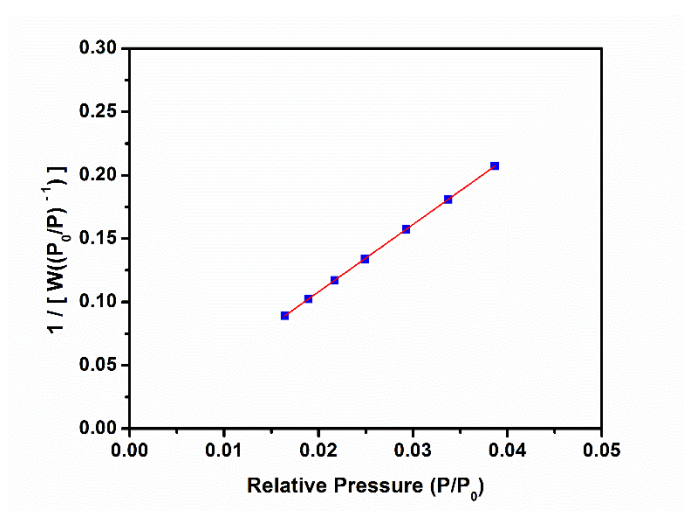
Figure 2.12. Linear fit of HKUST-1 upon thermal activation for 30 minutes.
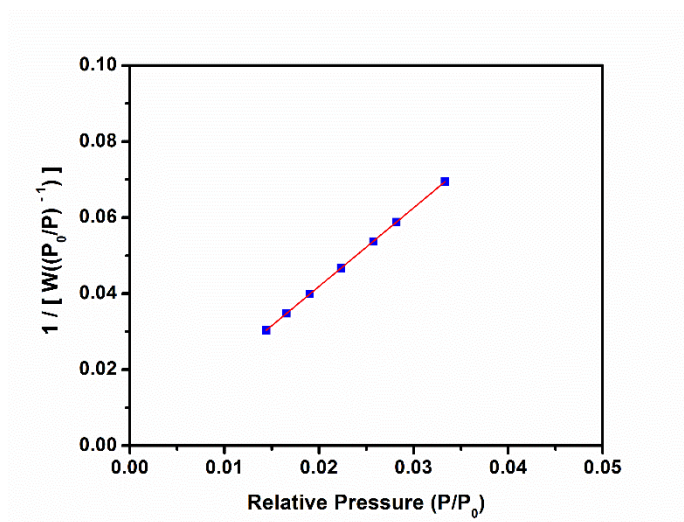
Figure 2.13. Linear fit of HKUST-1 upon photothermal activation for 30 minutes at a light guide-to-sample distance of 5cm.
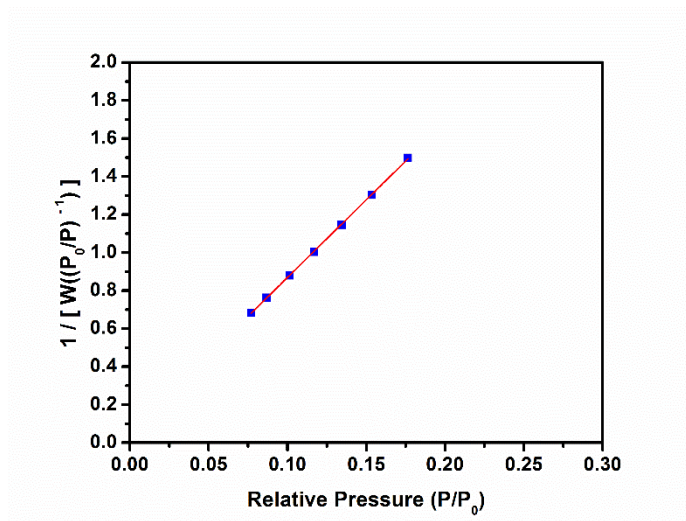
Figure 2.14. Linear fit of UiO-66 upon photothermal activation for 30 minutes at a light guide-to-sample distance of 7cm.
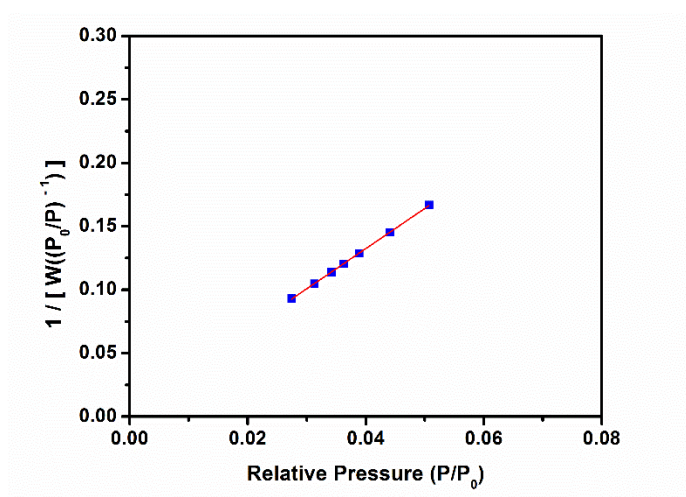
Figure 2.15. Linear fit of UiO-66-NH$_2$ upon photothermal activation for 30 minutes at a light guide-to-sample distance of 7cm.
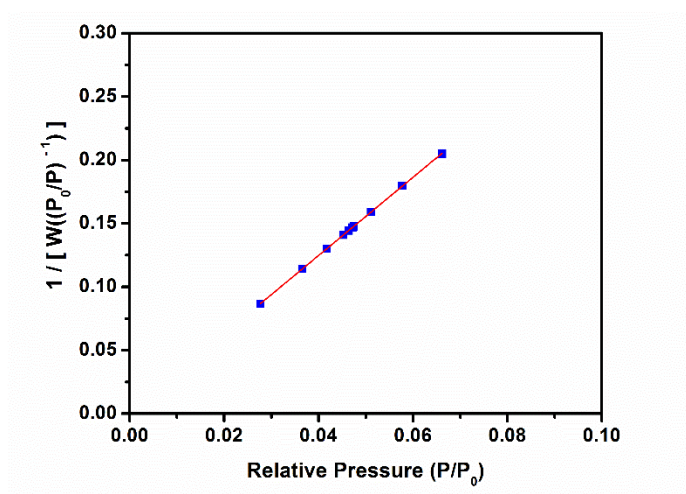
Figure 2.16. Linear fit of ZIF-8 upon photothermal activation for 30 minutes at a light guide-to-sample distance of 7cm.
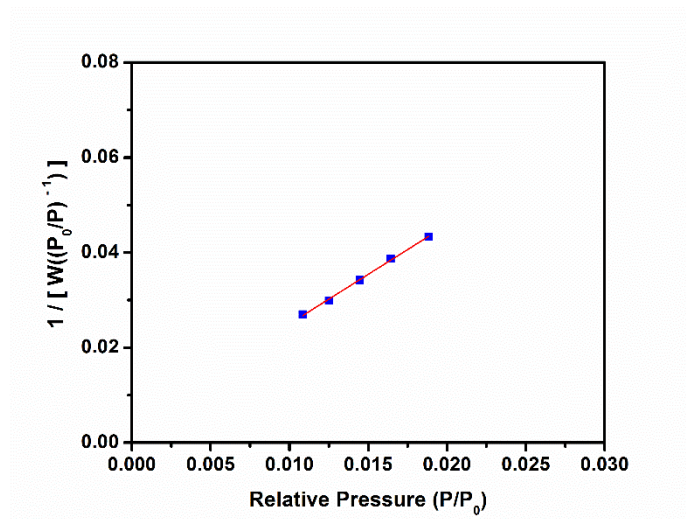
Figure 2.17. Linear fit of ZIF-67 upon photothermal activation for 30 minutes at a light guide-to-sample distance of 7cm.
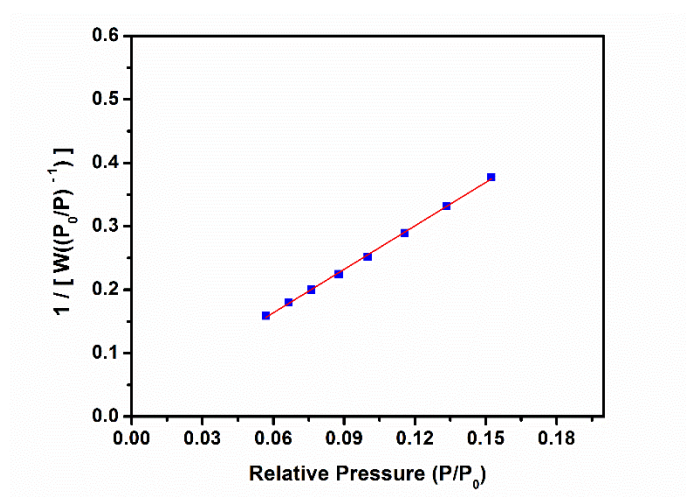
Figure 2.18. Linear fit of MIL-101-NH$_2$(Fe) upon photothermal activation for 30 minutes at a light guide-to-sample distance of 7cm.
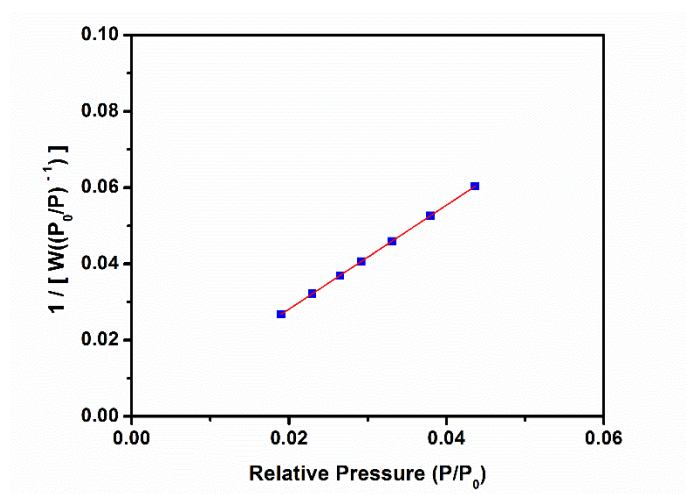
Figure 2.19. Linear fit of IRMOF-3 upon photothermal activation for 30 minutes at a light guide-to-sample distance of 7cm.
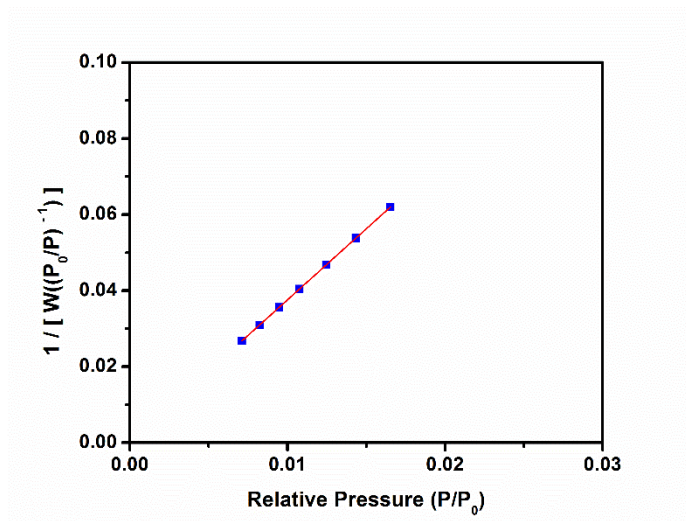
Figure 2.20. Linear fit of CPO-27-Zn upon photothermal activation for 30 minutes at a light guide-to-sample distance of 7cm.
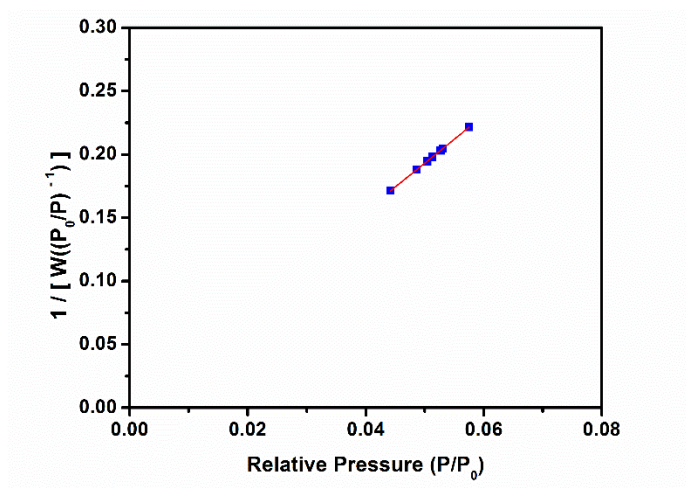
Figure 2.21. Linear fit of CPO-27-Ni upon photothermal activation for 30 minutes at a light guide-to-sample distance of 7cm.
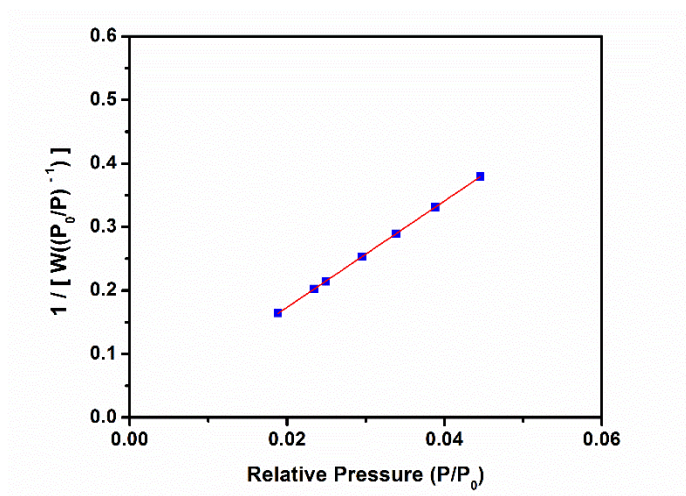
Figure 2.22. Linear fit of CPO-27-Mg upon photothermal activation for 30 minutes at a light guide-to-sample distance of 7cm.
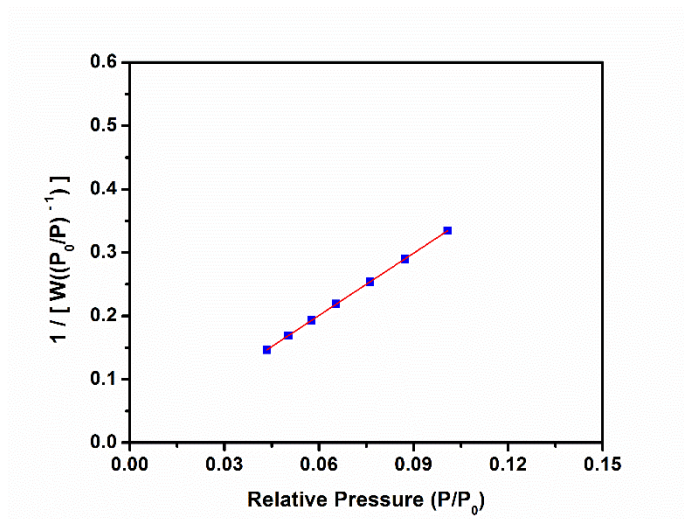
Figure 2.23. Linear fit of CPO-27-Mg upon photothermal activation for 30 minutes at a light guide-to-sample distance of 5cm.
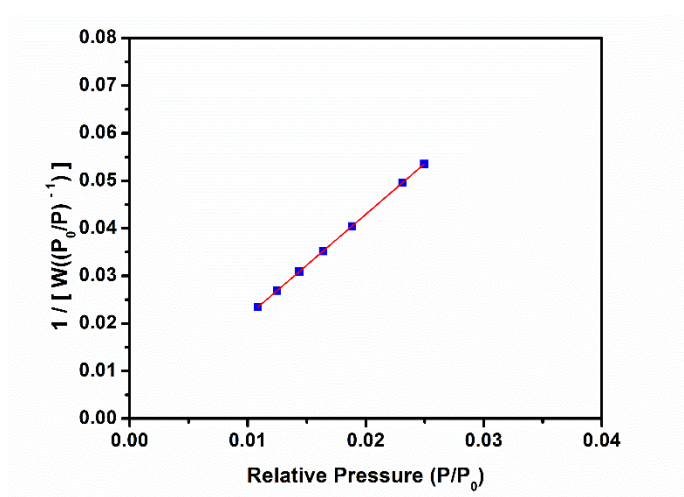
Figure 2.24. Linear fit of CPO-27-Mg upon photothermal activation for 30 minutes at a light guide-to-sample distance of 3cm.
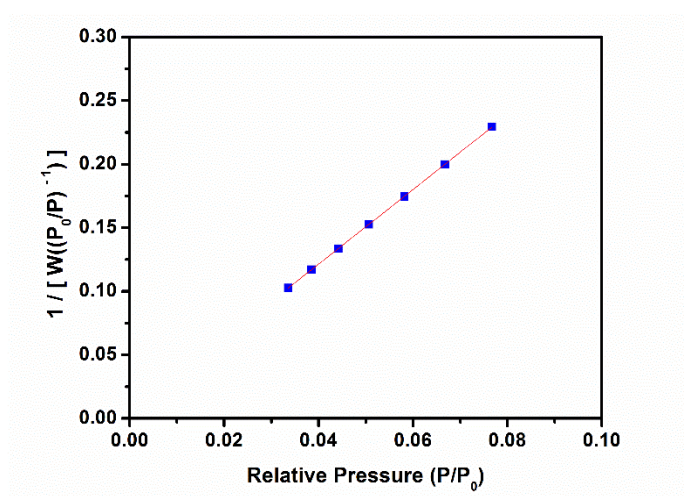
Figure 2.25. Linear fit of COF-TAPB-BTCA upon photothermal activation for 30 minutes at a light guide-to-sample distance of 7cm.

3.   Supplementary Information for Chapter 4

3.1.   N$_2$ adsorption fitting
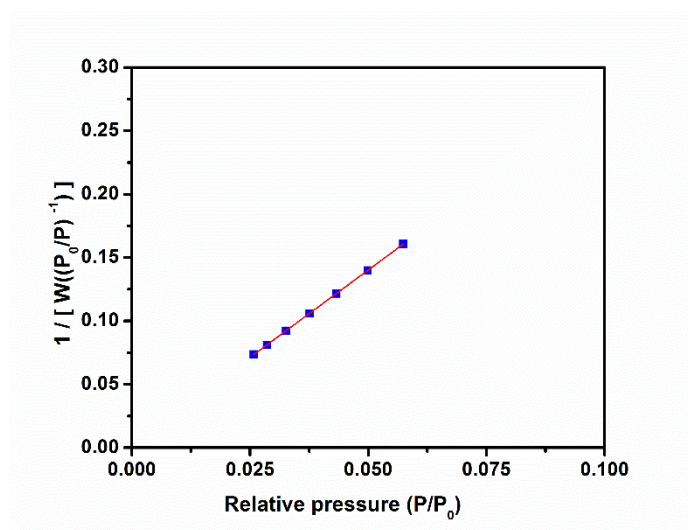
Figure 3.1. Linear fit of UiO-66-NH$_2$ upon photothermal activation.
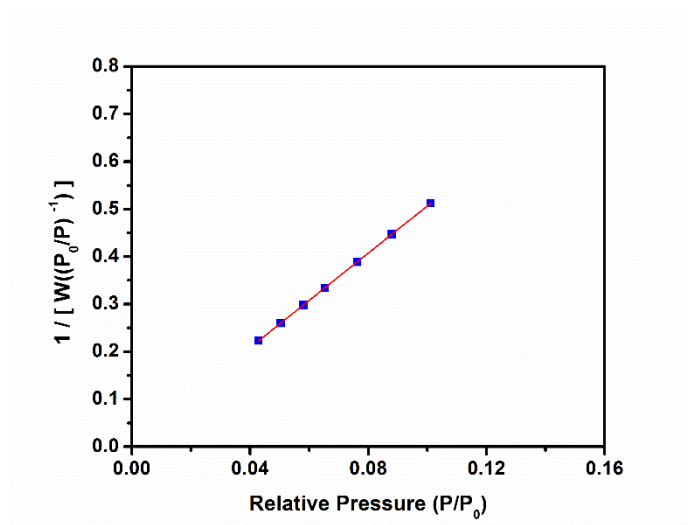
Figure 3.2. Linear fit of (UiO-66-MA)$_3$.
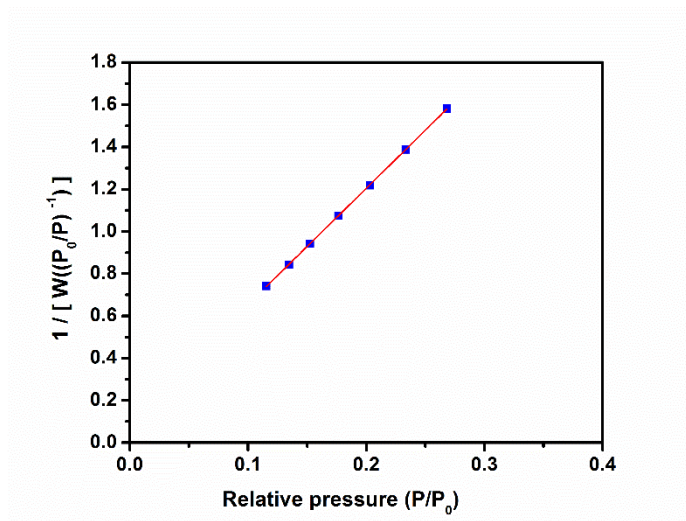
Figure 3.3. Linear fit of (UiO-66-BA)$_3$.
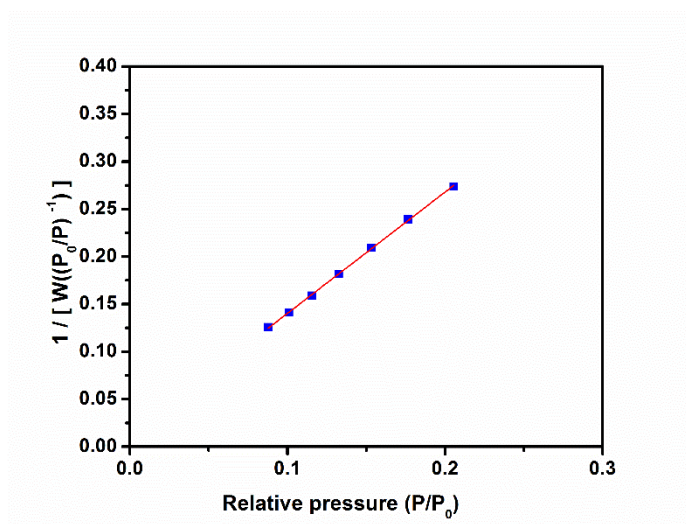
Figure 3.4. Linear fit of MIL-101-NH$_2$(Al) upon photothermal activation.
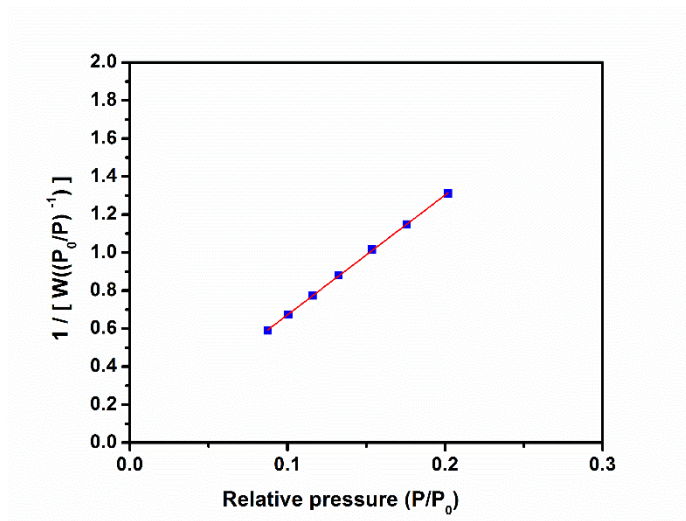
Figure 3.5. Linear fit of (MIL-101-MA)$_3$.
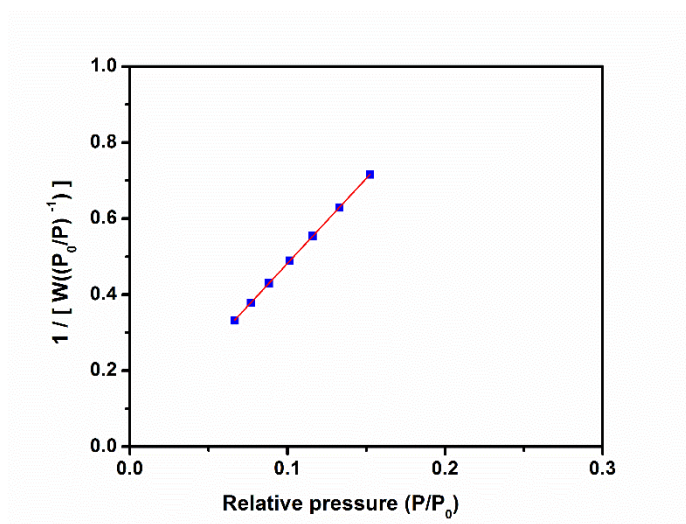
Figure 3.6. Linear fit of (MIL-101-BA)$_3$.

4. Supplementary Information for Chapter 5

4.1. Crystallographic Tables

Table 4.1. Crystal and structure refinement data of **Ni(HAcOBIP)$_2$** , **Fe$_2$(HAcOBIP)$_2$Cl$_4$** and **Fe$_2$Zn$_2$(HAcOBIP)$_4$**.

Compound	Ni(HAcOBIP)$_2$	Fe$_2$(HAcOBIP)$_2$Cl$_4$	Fe$_2$Zn$_2$(HAcOBIP)$_4$
Emp. formula	C$_{50}$H$_{42}$N$_6$OP$_2$Ni$_{12}$	C$_{50}$H$_{42}$N$_6$O$_6$Cl$_4$Fe$_2$	C$_{100}$H$_{82}$Fe$_2$N$_{12}$O$_{12}$Zn$_2$
Formula weight	880.25	1076.41	1886.28
Crystal system	Monoclinic	Monoclinic	Triclinic
Space group	*P21/c*	*C2/c*	*P-1*
Unit cell dimensions			
a (Å)	15.220	15.540	8.800
b (Å)	38.083	15.800	13.190
c (Å)	9.990	24.370	20.450
α (deg)			94.45
β (deg)	94.36	98.20	98.88
γ (deg)			86.71
V (Å^3)	5774.0	5922.44	2335.7
Z	2	4	1
F (000)	422	2912	1106
θ range (°)	1.444-28.317	2.109-26.372	1.010- 28.543
Ind. Refln. (R$_{int}$)	13262 (0.0897)	6029 (0.1051)	8951 (0.0432)
Goodness-of-fit on F^2	2.032	2.070	1.065
Final R indices [I > 2σ(I)]	R1 = 0.2415 wR2 = 0.5688	R1 = 0.1978 wR2 = 0.5243	R1 = 0.0957 wR2 = 0.2892

Table 4.2. Selected bond distances (Å) and angles (°) in **Fe$_2$Zn$_2$(HAcOBIP)$_4$**.[a]

Fe(1)-N(1)	2.183(4)	Zn(1)-N(6)	2.132(5)
Fe(1)-N(3)	2.175(4)	Zn(1)-N(8)	2.157(6)
Fe(1)-N(4)	2.158(4)	Zn(1)-N(9)	2.143(5)
Fe(1)-O(5)	2.097(4)	Zn(1)-O(3)	1.992(4)
N(1)-Fe(1)-N(3)	73.24(15)	N(6)-Zn(1)-N(8)	79.45(17)
N(3)-Fe(1)-N(4)	72.88(15)	N(8)-Zn(1)-N(9)	72.3(2)
N(1)-Fe(1)-N(4)	143.89(16)	N(6)-Zn(1)-N(9)	143.1(2)
N(3)-Fe(1)-O(5)	153.05(16)	N(6)-Zn(1)-O(3)	108.05(18)
N(4)-Fe(1)-O(5)	110.23(17)	N(8)-Zn(1)-O(3)	105.73(18)

[a] Symmetry equivalence: #1 1-x, 1-y, 1-z

Table 4.3. Crystal and structure refinement data of **Co-1**, **Co-2** and **Zr-2**.

Compound	Co-1	Co-2	Zr-2
Emp. formula	$C_{73}H_{61}N_{15}O_{11}P_2F_{12}Ru_2Co$	$C_{44}H_{28}N_6O_4Ru_2Co_2$	$C_{144}H_{96}N_{18}O_{36}Ru_3Zr_3$
Formula weight	1875.37	1065.45	3231.25
Crystal system	Orthorhombic	Monoclinic	Monoclinic
Space group	P2an	P2/a	C2/c
Unit cell dimensions			
a (Å)	16.583(4)	19.110(3)	52.540(10)
b (Å)	26.828(3)	13.240(3)	23.070(2)
c (Å)	8.730(10)	25.310(4)	23.420(2)
β (deg)	90	90.380(15)	95.115(4)
V (Å³)	3884(5)	6404(2)	28274(3)
Z	2	6	8
F (000)	1890	3192	13008
θ range (°)	1.679-34.086	0.936-33.896	0.905-33.879
Ind. Refln. (R_{int})	8739 (0.0675)	14307 (0.0416)	31973 (0.0543)
Goodness-of-fit on F^2	1.086	1.030	1.164
Final R indices	R1 = 0.0398	R1 = 0.0898	R1 = 0.0953
[I > 2σ(I)]	wR2 = 0.1068	wR2 = 0.2813	wR2 = 0.3339

Table 4.4. Selected bond distances (Å) and angles (°) in **Co-1**.[a]

Ru(1)-N(1)	2.067(4)	Ru(1)-N(4)	2.069(4)
Ru(1)-N(2)	1.980(3)	Ru(1)-N(5)	1.970(3)
Ru(1)-N(3)	2.064(4)	Ru(1)-N(6)	2.077(4)
Co(1)-O(1)	1.970(4)	Co(1)-O(4)#1	
N(1)-Ru(1)-N(2)	78.89(16)	N(2)-Ru(1)-N(3)	79.45(17)	N(3)-Ru(1)-N(5)	102.00(15)
N(1)-Ru(1)-N(3)	158.29(16)	N(2)-Ru(1)-N(4)	1012.37(15)	N(3)-Ru(1)-N(6)	91.65(15)
N(1)-Ru(1)-N(4)	91.59(14)	N(2)-Ru(1)-N(5)	177.96(16)	N(4)-Ru(1)-N(5)	79.08(14)
N(1)-Ru(1)-N(5)	99.69(15)	N(2)-Ru(1)-N(6)	99.62(16)	N(4)-Ru(1)-N(6)	157.99(14)
N(1)-Ru(1)-N(6)	93.40(15)	N(3)-Ru(1)-N(4)	91.60(15)	N(5)-Ru(1)-N(6)	78.96(14)
O(1)-Co(1)-O(1)#1	143.1(2)			O(1)-Co(1)-O(4)#3	109.32(18)
O(1)-Co(1)-O(4)#2	93.26(18)			O(4)#2-Co(1)-O(4)#3	104.5(2)

[a] Symmetry equivalence: #1 x, 1-y, 1-z; #2 1/2+x, 1/2+y, 1-z; #3 1/2+x, 1/2-y, z.

Table 4.5. Selected bond distances (Å) and angles (°) in **Co-2**.[a]

Ru(1)-N(1)	2.078(6)			Co(3)-O(4)	1.972(6)
Ru(1)-N(2)	1.976(6)			Co(3)-O(6)	1.967(5)
Ru(1)-N(3)	2.056(6)	Co(1)-O(2)	2.030(9)	Co(3)-Cl(3)	2.252(2)
Ru(2)-N(4)	2.052(7)	Co(1)-Cl(1)	2.257(5)	Co(3)-Cl(4)	2.267(3)
Ru(2)-N(5)	1.974(5)	Co(2)-O(1)	1.999(7)	Co(4)-O(3)	1.960(5)
Ru(2)-N(6)	2.063(6)	Co(2)-Cl(2)	2.181(5)	Co(4)-O(5)	1.974(6)
Ru(2)-N(7)	2.076(6)			Co(4)-Cl(5)	2.260(3)
Ru(2)-N(8)	1.976(5)			Co(5)-Cl(6)	2.261(3)
Ru(2)-N(9)	2.054(6)				
N(1)-Ru(1)-N(3)	157.8(2)	N(4)-Ru(2)-N(5)	79.2(2)	O(2)-Co(1)-O(2)[#2]	122.0(5)
N(1)-Ru(1)-N(2)	78.6(2)	N(4)-Ru(2)-N(6)	158.5(2)	O(2)-Co(1)-Cl(1)	105.1(3)
N(2)-Ru(1)-N(3)	79.2(2)	N(4)-Ru(2)-N(7)	90.8(3)	O(2)-Co(1)-Cl(1)[#2]	104.6(3)
N(1)-Ru(1)-N(1)[#1]	92.1(3)	N(4)-Ru(2)-N(8)	98.9(2)	Cl(1)-Co(1)-Cl(1)[#2]	116.3(3)
N(1)-Ru(1)-N(2)[#1]	105.1(3)	N(4)-Ru(2)-N(9)	92.1(3)	O(1)-Co(1)-O(1)[#2]	124.6(4)
N(1)-Ru(1)-N(3)[#1]	92.9(2)	N(5)-Ru(2)-N(6)	79.4(2)	O(1)-Co(1)-Cl(2)	116.6(2)
N(2)-Ru(1)-N(1)[#1]	105.1(3)	N(5)-Ru(2)-N(7)	103.2(2)	O(1)-Co(1)-Cl(2)[#2]	98.2(2)
N(2)-Ru(1)-N(2)[#1]	174.8(3)	N(5)-Ru(2)-N(8)	177.2(3)	Cl(2)-Co(1)-Cl(2)[#2]	101.2(4)
N(2)-Ru(1)-N(3)[#1]	97.1(3)	N(5)-Ru(2)-N(9)	98.5(2)	O(6)-Co(3)-O(4)	113.4(3)
N(3)-Ru(1)-N(1)[#1]	92.9(2)	N(6)-Ru(2)-N(7)	92.5(2)	O(6)-Co(3)-Cl(3)	115.2(2)
N(3)-Ru(1)-N(2)[#1]	97.1(2)	N(6)-Ru(2)-N(8)	102.6(2)	O(4)-Co(3)-Cl(3)	103.5(2)
N(3)-Ru(1)-N(3)[#1]	90.5(3)	N(6)-Ru(2)-N(9)	92.6(2)	O(6)-Co(3)-Cl(4)	104.3(2)
		N(7)-Ru(2)-N(8)	78.8(2)	O(4)-Co(3)-Cl(4)	112.8(2)
		N(7)-Ru(2)-N(9)	158.3(2)	Cl(3)-Co(3)-Cl(4)	107.63(13)
		N(8)-Ru(2)-N(9)	79.4(2)	O(3)-Co(4)-O(5)	121.2(3)
				O(3)-Co(4)-Cl(5)	102.8(2)
				O(5)-Co(4)-Cl(5)	111.6(2)
				O(3)-Co(4)-Cl(6)	109.1(2)
				O(5)-Co(4)-Cl(6)	96.78(19)

[a] Symmetry equivalence: #1 3/2-x, y, 1-z; #2 3/2-x, y, 2-z

Table 4.6. Selected bond distances (Å) and angles (°) in **Zr-2**.

Ru(1)-N(1)	2.063(8)	Ru(3)-N(7)	2.070(6)	Ru(4)-N(10)	2.061(6)
Ru(1)-N(2)	1.985(5)	Ru(3)-N(8)	1.968(5)	Ru(4)-N(11)	1.971(4)
Ru(1)-N(3)	2.070(8)	Ru(3)-N(9)	2.052(6)	Ru(4)-N(12)	2.048(5)
Ru(2)-N(4)	2.050(7)	Ru(3)-N(16)	2.067(7)	Ru(4)-N(13)	2.051(5)
Ru(2)-N(5)	1.980(5)	Ru(3)-N(17)	1.970(5)	Ru(4)-N(14)	1.976(4)
Ru(2)-N(6)	2.048(6)	Ru(3)-N(18)	2.047(6)	Ru(4)-N(15)	2.072(6)
Zr(1)-O(1)	2.385(4)	Zr(2)-O(5)	2.311(5)	Zr(3)-O(10)	2.315(5)
Zr(1)-O(2)	2.250(4)	Zr(2)-O(6)	2.248(5)	Zr(3)-O(11)	2.259(5)
Zr(1)-O(3)	2.294(4)	Zr(2)-O(7)	2.326(5)	Zr(3)-O(12)	2.284(5)
Zr(1)-O(4)	2.332(4)	Zr(2)-O(9)	2.266(5)	Zr(3)-O(13)	2.306(5)
Zr(1)-O(1f)	2.104(6)	Zr(2)-O(9f)	2.079(7)	Zr(3)-O(17f)	2.108(8)
Zr(1)-O(3f)	2.091(5)	Zr(2)-O(11f)	2.088(13)	Zr(3)-O(19f)	2.126(7)
Zr(1)-O(5f)	2.109(5)	Zr(2)-O(13f)	2.090(6)	Zr(3)-O(21f)	2.073(8)
Zr(1)-O(7f)	2.077(6)	Zr(2)-O(15f)	2.127(10)	Zr(3)-O(23f)	2.103(8)

Table 4.7. H-bond, π⋯π and C-H⋯π interactions (Å/°) in **Co-1**.[a]

D-H⋯A	d (D-H)	d (H⋯A)	d (D⋯A)	< (DHA)
C(14)-H(14)⋯O(1s)	0.95	2.30	3.001(8)	129.8
C(15)-H(15)⋯O(1s)	0.95	2.66	3.181(7)	115.4
C(17)-H(17)⋯O(1s)[#1]	0.95	2.36	3.206(7)	147.5
C(20)-H(20)⋯O(3)[#2]	0.95	2.47	3.322(7)	148.7
C(23)-H(23)⋯O(3)[#2]	0.95	2.29	3.098(8)	142.8
C(12s)-H(12a)⋯O(2)[#3]	0.98	2.61	3.129(10)	113.1
	Cg⋯Cg	**α**	**β**	**γ**
Cg(1)[b]⋯Cg(2)[b]	3.726(5)	3.2(2)	23.0	22.5
Cg(3)[b]⋯Cg(4)[b]	3.714(5)	3.5(2)	21.8	20.5
C-H⋯Cg		**H⋯Cg**	**C⋯Cg**	**<(CHCg)**
C(1)-H(1)⋯Cg(5)[b]		2.90	3.248(6)	103
C(4)-H(4)⋯Cg(6)[b]		2.75	3.585(7)	148
C(19)-H(19)⋯Cg(7)[b]		3.00	3.667(7)	129

[a] Symmetry code: #1 x+1/2, -y+1/2, z; #2 x, -y, -z; #3 x-1/2, y-1/2, -z. [b] Cg(1): N(1)-C(1)-C(2)-C(3)-C(4)-C(5), Cg(2): N(3)-C(11)-C(12)-C(13)-C(14)-C(15), Cg(3): N(4)-C(17)-C(18)-C(19)-C(20)-C(21), Cg(4): N(6)-C(27)-C(28)-C(29)-C(30)-C(31), Cg(5): Ru(1)-N(4)-N(5)-C(21)-C(22), Cg(6): N(6)-C(27)-C(28)-C(29)-C(30)-C(31), Cg(7): N(1)-C(1)-C(2)-C(3)-C(4)-C(5).

Table 4.8. H-bond, π···π and Co-Cl-π interactions (Å/°) in **Co-2**.[a,b]

D-H···A	d (D-H)	d (H···A)	d (D···A)	< (DHA)
C(1)-H(1)···Cl(6)[#1]	0.95	2.84	3.504(8)	127.5
C(2)-H(2)···Cl(6)[#1]	0.95	2.88	3.507(9)	124.4
C(9)-H(9)···Cl(3)[#2]	0.95	2.71	6.648(8)	170.6
C(12)-H(12)···Cl(3)[#2]	0.95	2.63	3.557(8)	164.4
C(15)-H(15)···Cl(4)[#3]	0.95	2.81	3.573(8)	138.4
C(26)-H(26)···Cl(1)[#4]	0.95	2.62	3.547(9)	164.0
C(29)-H(29)···Cl(1)[#4]	0.95	2.92	3.849(9)	167.6
C(34)-H(34)···Cl(2)[#5]	0.95	2.92	3.545(9)	124.1
C(45)-H(45)···Cl(2)[#6]	0.95	2.67	3.520(8)	148.9
C(53)-H(53)···Cl(6)[#7]	0.95	2.79	3.574(8)	140.0
C(56)-H(56)···Cl(6)[#7]	0.95	2.59	3.335(8)	135.7
C(59)-H(59)···Cl(1)[#8]	0.95	2.71	3.432(8)	133.4
		Cl···Cg		**<(CoClCg)**
Co(2)-Cl(2)...Cg(1)[b]		3.484(6)		167.1(2)
	Cg···Cg	**α**	**β**	**γ**
Cg(2)[b]-Cg(3)[b]	4.073(5)	23.5(4)	17.1	39.7

[a] Symmetry code: #1 −x+1/2, y+1, -z; #2 x+1, y, z+1; #3 −x+1, -y+1, -z; #4 x-1, y-1, z-1; #5 x-1/2, -y+1, z-1; #6 -x+1/2, y, -z+1; #7 −x, -y, -z; #8 −x+1, -y+1, -z+1. [b] Cg(1): N(5)-C(28)-C(29)-C(30)-C(31)-C(32), Cg(2): C(16)-C(17)-C(18)-C(19)-C(20)-C(21), Cg(3): N(9)-C(55)-C(56)-C(57)-C(58)-C(59).

Table 4.9. H-bond, π···π and C-H-π interactions (Å/°) in **Zr-2**.[a,b]

D-H···A	d (D-H)	d (H···A)	d (D···A)	< (DHA)
C(1)-H(1)···O(12f)[#1]	0.95	2.21	3.138(8)	164.5
C(4)-H(4)···O(24f)[#2]	0.95	2.42	3.341(10)	162.3
C(9)-H(9)···O(18f)[#3]	0.95	2.43	3.338(12)	160.5
C(12)-H(12)···O(18f)[#3]	0.95	2.30	3.241(10)	169.5
C(14)-H(14)···O(22f)[#4]	0.95	2.63	3.286(10)	126.2
C(27)-H(27)···O(10f)[#5]	0.95	2.25	3.186(10)	168.6
C(30)-H(30)···O(10f)[#5]	0.95	2.41	3.339(10)	167.4
C(32)-H(32)···O(14f)[#6]	0.95	2.56	3.488(9)	164.1
C(35)-H(35)···O(14f)[#6]	0.95	2.39	3.279(8)	155.9
C(38)-H(38)···O(20f)[#7]	0.95	2.18	3.040(8)	149.8
C(46)-H(46)···O(18f)[#8]	0.95	2.31	3.165(8)	148.8
C(49)-H(49)···O(4f)[#9]	0.95	2.31	3.161(7)	148.0
C(52)-H(52)···O(4f)[#9]	0.95	2.56	3.354(10)	141.3
C(54)-H(54)···O(2f)[#10]	0.95	2.43	3.337(9)	158.9
C(57)-H(57)···O(2f)[#10]	0.95	2.34	3.257(9)	161.2
C(60)-H(60)···O(14f)[#11]	0.95	2.58	3.310(8)	134.3
C(68)-H(68)···O(4f)[#12]	0.95	2.20	3.030(7)	145.0
C(71)-H(71)···O(16f)[#8]	0.95	2.46	3.400(9)	168.0
C(77)-H(77)···O(20f)[#13]	0.95	2.61	3.503(10)	157.1
C(80)-H(80)···O(20f)[#13]	0.95	2.28	3.196(8)	160.6
C(83)-H(83)···O(6f)[#2]	0.95	2.37	3.134(7)	137.5
C(91)-H(91)···O(24f)[#13]	0.95	2.44	3.211(8)	138.1
C(94)-H(94)···O(6f)[#14]	0.95	2.26	3.209(7)	176.3
C(97)-H(97)···O(6f)[#14]	0.95	2.54	3.470(9)	165.2
C(102)-(H102)···O(8f)[#2]	0.95	2.43	3.347(8)	161.7
C(105)-H(105)···O(10f)[#8]	0.95	2.36	3.154(8)	140.4
C(113)-H(113)···O(2f)[#9]	0.95	2.39	3.150(9)	137.3
C(116)-H(116)···O(12f)[#11]	0.95	2.34	3.258(9)	162.1
C(119)-H(119)···O(12f)[#13]	0.95	2.64	3.519(16)	154.9
C(121)-H(121)···O(22f)[#15]	0.95	2.63	3.550(14)	164.2
C(124)-H(124)···O(22f)[#15]	0.95	2.40	3.334(9)	166.1
C(127)-H(127)···O(8f)[#16]	0.95	2.33	3.173(8)	147.1

[a] Symmetry code: #1 x, y, z-1; #2 -x+3/2, -y+1/2, -z+1; #3 −x+3/2, y+1/2, -z+3/2; #4 x-1/2, -y+1/2, z-1/2; #5 x+1/2, y+1/2, z-1; #6 x+1/2, -y+1/2, z-1/2; #7 −x+2, y, -z+3/2; #8 −x+1, -y, -z+2; #9 x-1/2, -y+1/2, z+1/2; #10 −x+1, y, -z+3/2; #11 −x+1/2, -y+1/2, -z+2; #12 −x+3/2, y-1/2, -z+3/2; #13 −x+3/2, -y+1/2, -z+2; #14 x, y, z+1; #15 −x+2, -y, -z+2; #16 x-1/2, y-1/2, z+1.

	Cg···Cg	α	β	γ
Cg(9)[b]-Cg(23)[b]	3.6866	12	25.0	14.1
Cg(11)-Cg(21)	3.544	12	23.6	12.8
Cg(14)-Cg(40)	3.6052	7	18.0	12.9
Cg(15)-Cg(23)	3.8827	7	21.1	23.4
Cg(17)-Cg(21)	3.4817	4	20.5	19.6
Cg(18)-Cg(39)	3.6445	6	21.9	25.1
Cg(22)-Cg(36)	3.8094	14	8.0	19.8
Cg(24)-Cg(33)	3.8205	13	10.8	2.7

C-H···Cg	H···Cg	C···Cg	<(CHCg)
C(20)-H(20)···Cg(9)	2.93	3.8357	160
C(36)-H(36)···Cg(24)	2.76	3.5308	138
C(42)-H(42)···Cg(17)	2.65	3.5475	158
C(64)-H(64)···Cg(12)	2.66	3.6440	162
C(65)-H(65)···Cg(18)	2.78	3.6731	158
C(70)-H(70)···Cg(40)	2.78	3.6748	158
C(109)-H(109)···Cg(14)	2.77	3.6930	163
C(125)-H(125)···Cg(39)	2.72	3.4612	135
C(132)-H(132)···Cg(35)	2.83	3.5941	138

List of Publications

Publications related to this Thesis

1) Espín, J., Garzón-Tovar, L., Carné-Sánchez, A., Imaz, I., Maspoch, D.
Photothermal activation of metal–organic frameworks using a UV–Vis light source
ACS Appl. Mater. Interfaces **2018**, 10, 9555-9562.

2) Espín, J., Garzón-Tovar, L., Boix i Soler, G., Imaz, I., Maspoch, D.
The photothermal effect in MOFs: covalent post-synthetic modification of MOFs mediated by UV-Vis light under solvent-free conditions
Chem. Commun. **2018**, 54, 4184-4187.

Non-related publications

3) Espín, J., Zarzuela, R., Statuto, N., Juanhuix, J., Maspoch, D., Imaz, I., Chudnovsky, E.M., Tejada, J.
Narrowing the zero-field tunneling resonance by decreasing the crystal symmetry of Mn$_{12}$ acetate
J. Am. Chem. Soc. **2016**, 138, 9065-9068.

4) Tejada, J., Zarzuela, R., García-Santiago, A., Imaz, I., Espín, J., Maspoch, D., Chudnovsky, E.M.
Enhanced spin tunneling in a molecular magnet mixed with a superconductor
J. Supercond. Nov. Magn. **2016**, 29, 1133-1137.

5) Espín, J., Ruyra, À., Yazdi, A., Carné-Sánchez, A., Roher, N., Lorenzo, J., Imaz, I., Maspoch, D.
Synthesis, culture medium stability, and *in vitro* and *in vivo* Zebrafish embryo toxicity of metal–organic framework nanoparticles
Chem. - Eur. J. **2015**, 21, 2508-2518.

6) Lendínez, S., Zarzuela, R., Tejada, J., Terban, M. W., Billinge, S. J. L., Espín, J., Imaz, I., Maspoch, D., Chudnovsky, E. M.
Resonant spin tunneling in randomly oriented nanospheres of Mn12 acetate
Phys. Rev. B **2015**, 91, 024404.

Photothermal Activation of Metal−Organic Frameworks Using a UV−Vis Light Source

Jordi Espín,[†] Luis Garzón-Tovar,[†] Arnau Carné-Sánchez,[†] Inhar Imaz,*,[†] and Daniel Maspoch*,[†,‡]

[†]Catalan Institute of Nanoscience and Nanotechnology (ICN2), CSIC and The Barcelona Institute of Science and Technology, Campus UAB, Bellaterra, 08193 Barcelona, Spain
[‡]ICREA, Pg. Lluís Companys 23, 08010 Barcelona, Spain

Ⓢ Supporting Information

ABSTRACT: Metal−organic frameworks (MOFs) usually require meticulous removal of the solvent molecules to unlock their potential porosity. Herein, we report a novel one-step method for activating MOFs based on the photothermal effect induced by directly irradiating them with a UV−vis lamp. The localized light-to-heat conversion produced in the MOF crystals upon irradiation enables a very fast solvent removal, thereby significantly reducing the activation time to as low as 30 min and suppressing the need for time-consuming solvent-exchange procedures and vacuum conditions. This approach is successful for a broad range of MOFs, including HKUST-1, UiO-66−NH$_2$, ZIF-67, CPO-27−M (M = Zn, Ni, and Mg), Fe−MIL-101−NH$_2$, and IRMOF-3, all of which exhibit absorption bands in the light emission range. In addition, we anticipate that this photothermal activation can also be used to activate covalent organic frameworks (COFs).

KEYWORDS: metal−organic framework, photothermal effect, activation, UV−vis light, permanent porosity
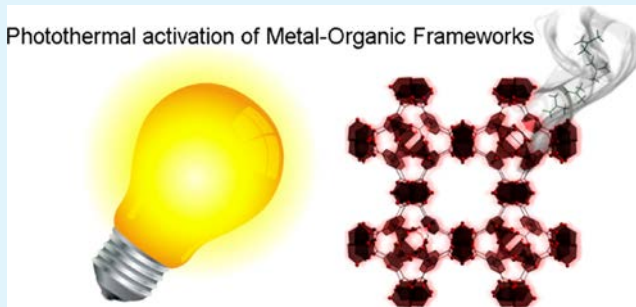
INTRODUCTION

Metal−organic frameworks (MOFs) are a class of porous crystalline materials built from the coordination of organic linkers and metal ions or clusters.[1−3] One of the main features of these materials is their high and tuneable porosity, which makes them good candidates for multiple applications, including gas storage and separation,[4,5] catalysis,[6] sensing,[7] and drug delivery,[8] among many others. However, a prerequisite before using MOFs in any of these applications is their activation or, in other words, the removal of all guest molecules located in their pores. These molecules can be either bound to the metal ions or residual from the synthesis solvent. The most common activation process currently entails a first step of solvent exchange, in which the solvents employed in the MOF synthesis and located in the pores are replaced by more volatile ones, followed by thermal evacuation of the solvent molecules by applying heat and/or vacuum. In other cases, in which this process damages the crystalline integrity of MOFs, milder alternative processes such as supercritical CO$_2$ drying, freeze-drying, and chemical treatment have proved useful.[9] However, most of these activation methods consist of multiple steps, require expensive equipment, and/or suffer from extensive use of solvents and time. Thus, although many efforts have been devoted to optimize MOF syntheses in terms of cost, safety, and environmental criteria, there is a lack of alternative one-step activation protocols that can be applied to as-synthesized MOFs.

Light-to-heat conversion (also known as the photothermal effect) has significant potential in evaporation processes because of the local nature of the heat generated, thereby minimizing heat diffusion and energy loss. This principle has already been employed in water evaporation devices by using inorganic nanoparticles,[10−12] polymers,[13] and carbon-based materials[14] as light-induced heaters. In MOFs, light has been exploited to trigger gas release[15−18] and in catalytic processes.[19−21] Herein, we report that this principle can be applied to activate as-synthesized MOFs in a single-step—suppressing any solvent-exchange procedure—by showing that, when irradiated with high-intensity UV−vis light, MOFs exhibiting absorption bands in the range 300−650 nm (light emission range) reach high temperatures (above 120 °C) within minutes and that this localized heat can efficiently remove the trapped and coordinated solvent molecules from the MOF structure, thereby generating activated MOFs in unprecedentedly short times at atmospheric pressure (Figure 1a). We have demonstrated this concept by activating several MOFs covering the most representative subfamilies, including HKUST-1, UiO-66, UiO-66−NH$_2$, ZIF-8, ZIF-67, CPO-27−M (M = Zn, Ni, and Mg), Fe−MIL-101−NH$_2$, and IRMOF-3. In all cases, the activated MOFs retain their crystallinity and show Brunauer−Emmett−Teller (BET) surface areas (S_{BET}) com-
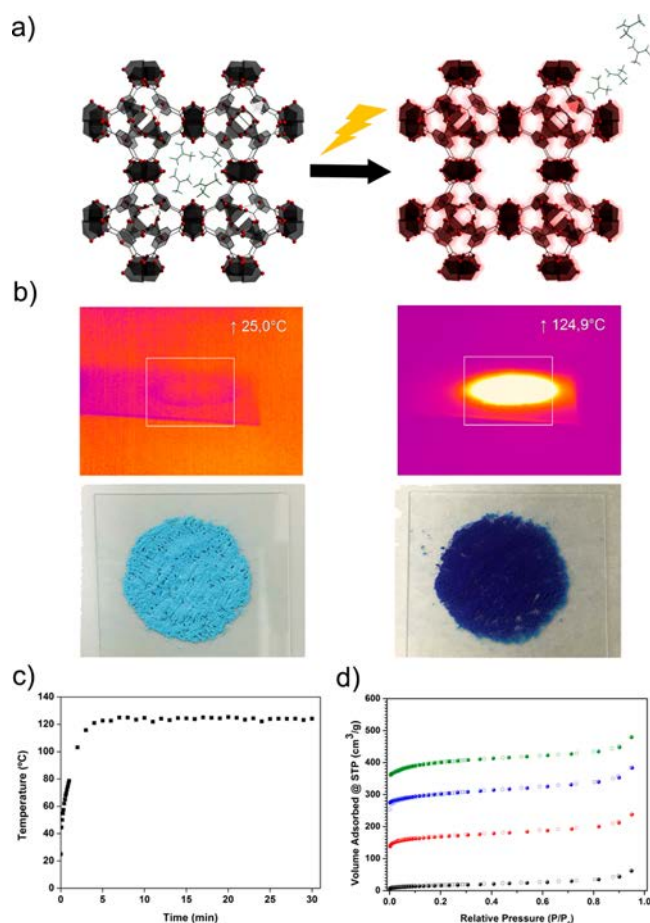
Figure 1. (a) Schematic representation of the photothermal activation of MOFs. (b) IR camera pictures (top) of HKUST-1 before (left) and during UV−vis irradiation (right). Photographs of HKUST-1 powder (bottom) before (left) and after (right) irradiation. (c) Temperature evolution as a function of time for HKUST-1 irradiated at a distance of 7 cm. (d) N_2 adsorption isotherms for HKUST-1 after 30 min of heat treatment (red) and after photothermal activation for 5 min (blue) and 30 min (green), in comparison to the as-synthesized sample (black).

parable to the highest reported values. Moreover, a covalent organic framework (COF TAPB−BTCA) was activated using this method, suggesting that this concept could be extended to other COFs.

■ EXPERIMENTAL SECTION

Materials and Instrumentation. Reagents and solvents were purchased from Sigma-Aldrich and Fisher Scientific, respectively, and used without further purification. Deionized (DI) water was obtained using a Milli-Q system (18.2 MΩ cm). X-ray powder diffraction (XRPD) patterns were collected using an X'Pert PRO MPDP analytical diffractometer (PANalytical) at 45 kV and 40 mA with a Cu Kα radiation source (λ = 1.5419 Å). Nitrogen adsorption measurements were carried out at 77 K using an Autosorb-iQ-AG analyzer (Quantachrome Instruments). Solid-state UV−vis spectra were recorded using a Cary 4000 spectrophotometer (Agilent Technologies) in the wavelength range 200−800 nm, previously preparing KBr pellets of the samples. The UV−vis high-intensity spot lamp without a filter (300−650 nm) was a bluepoint 4 ecocure (Hönle UV Technology), and the infrared camera was a PI 450 (Optris), working in a temperature range of 0−250 °C. Data were obtained using the PI Connect software.

Synthetic Procedures. *Synthesis of HKUST-1.* In a typical synthesis,[22] a solution of 2 g (8.5 mmol) of $Cu(NO_3)_2 \cdot 2.5H_2O$ and 1.20 g (5.5 mmol) of 1,3,5-benzenetricarboxylic acid (BTC) in 50 mL of a mixture of dimethylformamide (DMF), ethanol, and water (1:1:1) was spray-dried in a B-290 mini-spray dryer (BÜCHI Labortechnik) at a feed rate of 4.5 mL·min⁻¹, a flow rate of 336 mL·min⁻¹, and an inlet temperature of 180 °C, using a spray cap with a 0.5 mm diameter hole. After 12 min, 2.13 g of blue powder was collected. This powder was washed several times with 40 mL of methanol and recovered by centrifugation. The final product was air-dried.

Synthesis of UiO-66. In a typical synthesis,[23] 0.68 g (2.9 mmol) of $ZrCl_4$ in 15 mL of a mixture of DMF and water (5.48:1 v/v) was added to a solution of 0.48 g (2.9 mmol) of benzene-1,4-dicarboxylic acid (BDC) in 15 mL of DMF. The resulting mixture was heated at 120 °C under stirring for 2 h. The solid obtained was collected by centrifugation, washed twice with 20 mL of DMF and twice with 20 mL of absolute ethanol, and finally air-dried overnight.

Synthesis of UiO-66−NH₂. In a typical synthesis,[23] 3.5 mL of 37% HCl was added to a solution of 1.17 g (5 mmol) of $ZrCl_4$ and 0.91 g (5 mmol) of 2-aminoterephthalic acid (NH_2−BDC) in 50 mL of DMF. The resulting mixture was heated at 120 °C under stirring for 2 h. The solid obtained was collected by centrifugation, washed twice with 20 mL of DMF and twice with 20 mL of absolute ethanol, and finally air-dried overnight.

Synthesis of ZIF-8. In a typical synthesis,[24] a solution of 0.30 g (1.4 mmol) of $Zn(OAc)_2 \cdot 2H_2O$ in 5 mL of DI water was added to a solution of 1.12 g (13.6 mmol) of 2-methylimidazole (2-MIM) in 5 mL of DI water. The resulting mixture was homogenized by stirring for a few seconds, and then the mixture was left to stand at room temperature for 6 h. White crystals were recovered by centrifugation, washed three times with 20 mL of methanol, and finally air-dried.

Synthesis of ZIF-67. In a typical synthesis,[24] a solution of 0.60 g (2.4 mmol) of $Co(OAc)_2 \cdot 4H_2O$ in 5 mL of DI water was added to a solution of 2.24 g (27.3 mmol) of 2-MIM in 5 mL of DI water. The resulting mixture was homogenized by stirring for a few seconds, and then the mixture was left to stand for 2 h at room temperature. Purple crystals were collected by centrifugation, washed three times with 20 mL of methanol, and finally air-dried.

Synthesis of CPO-27−Zn. In a typical synthesis,[25] a solution of 0.36 g (1.8 mmol) of 2,5-dihydroxyterephthalic acid (DHTA) and sodium hydroxide (0.29 g, 7.3 mmol) in 5.0 mL of DI water was added to a solution of 0.79 g (3.6 mmol) of $Zn(OAc)_2 \cdot 2H_2O$ in 5.0 mL of DI water. The resulting yellow suspension was stirred for 60 min at room temperature. The product was collected by centrifugation, washed twice with DI water (30 mL) and twice with 30 mL of methanol, and finally air-dried overnight.

Synthesis of CPO-27−Ni. In a typical synthesis,[25] a solution of 0.09 g (0.5 mmol) of DHTA and sodium hydroxide (0.07 g, 1.8 mmol) in 10.0 mL of DI water was added to a solution of 0.22 g (0.88 mmol) of $Ni(OAc)_2 \cdot 4H_2O$ in 10.0 mL of DI water. The resulting green solution was stirred at room temperature for 24 h. The product was collected by centrifugation, washed three times with 30 mL of DI water and three times with 30 mL of methanol, and finally air-dried overnight.

Synthesis of CPO-27−Mg. In a typical synthesis,[25] a solution of 0.18 g (0.9 mmol) of DHTA and sodium hydroxide (0.15 g, 3.8 mmol) in 5.0 mL of DI water was added to a solution of 0.48 g (2.2 mmol) of $Mg(OAc)_2 \cdot 4H_2O$ in 5.0 mL of DI water. The resulting green suspension was stirred for 6 h at room temperature. The product was collected by centrifugation, washed three times with 30 mL of DI water and three times with 30 mL of methanol, and finally air-dried overnight.

Synthesis of Fe−MIL-101−NH₂. The synthesis was adapted from reported procedures.[26] Thus, 0.68 g (2.5 mmol) of $FeCl_3 \cdot 6H_2O$ in 7.5 mL of DMF was added to a solution of 0.225 g (1.2 mmol) of NH_2−BDC in 7.5 mL of DMF, and the resulting mixture was heated at 120 °C for 24 h. The solid obtained was collected by centrifugation and then washed three times with 20 mL of DMF and twice with 20 mL of absolute ethanol. The resulting powder was air-dried overnight. To eliminate most of the free NH_2−BDC, the product was dispersed in

DMF at 110 °C under stirring for 8 h and precipitated by centrifugation. This process was repeated three times.

Synthesis of IRMOF-3. The synthesis was adapted from reported procedures.[27] Thus, 1.20 g (4.0 mmol) of $Zn(NO_3)_2 \cdot 6H_2O$ and 0.30 g (1.6 mmol) of NH_2-BDC were dissolved in 40 mL of DMF. The solution was divided into eight scintillation vials and heated at 100 °C for 24 h in an oven. Crystals were harvested from the bottom of these vials and then washed twice with 10 mL of DMF and 10 mL of chloroform. Dried crystals were kept under an argon atmosphere.

Synthesis of COF TAPB−BTCA. The COF TAPB−BTCA was synthesized following a previously reported method.[28] In a typical synthesis, 0.03 g (0.2 mmol) of 1,3,5-benzenetricarbaldehyde (BTCA) in 12.5 mL of acetone and 2.5 mL of acetic acid was added to a solution of 0.06 g (0.2 mmol) of 1,3,5-tris(4-aminophenyl)benzene (TAPB) in 12.5 mL of acetone. The resulting mixture was stirring for 1 h. The obtained yellow solid was collected by centrifugation and washed two times with 20 mL of acetone and two times with 20 mL of THF. After that, the solid was dispersed in a mixture of 1,4-dioxane and mesitylene (9:1 v/v), adding 1.75 mL of water and 2.6 mL of acetic acid under continuous stirring at room temperature. The resulting mixture was heated at 80 °C under stirring for 8 days. The obtained solid was collected by centrifugation at 9000 rpm for 4 min, washed three times with 10 mL of toluene, and finally air-dried.

Light Guide-to-Sample Distance Effect. It is known that the irradiance of a lamp changes depending on the proximity of the irradiated body. To assess the light intensity received per surface unit of MOF in our activation experiments, the detector of a power meter (Newport 1918-C) was systematically placed at different distances (3, 4, 5, 6, 7, 8, and 9 cm), the UV−vis lamp was turned on at 100% power, and the irradiance was measured for each distance. Figure S1 shows the irradiance ($mW \cdot cm^{-2}$) as a function of inverse-squared distance (cm^{-2}), which follows the inverse-square law ($I \propto 1/r^2$).[29,30]

Photothermal Effect Characterization. One hundred milligrams of each MOF was spread on a quartz slide to form a thin round layer with the largest possible surface area (diameter of between 2 and 3.5 cm) at a distance of 7 cm from the light guide, which corresponds to an irradiance of 500 $mW \cdot cm^{-2}$. The infrared camera was placed next to the irradiation setup focusing on the MOF sample, and video recording was started just before the UV−vis lamp was set to 100% intensity. The recorded video allowed the temperature change to be plotted against time. The blank experiment involved irradiating the quartz slide holder alone and proved that there was no change in temperature.

UV−Vis Activation Procedure. In a typical UV−vis activation experiment, 100 mg of each MOF was first placed in a three-neck round-bottom flask. The light guide was then introduced via the central neck and placed at a distance of 7 cm from the MOF sample. In some cases, the separation between the MOF and the light guide was reduced to 5 and 3 cm, corresponding to irradiances of 900 and 2650 $mW \cdot cm^{-2}$, respectively. The neck was then wrapped with Parafilm. Both side necks were capped with a septum and a needle. One of these necks was used as the gas inlet attached to the argon tube, whereas the other served as the gas purge. Once the argon flow had been adjusted [8 normal liter per minute ($NL \cdot min^{-1}$)], the UV−vis lamp was turned on, irradiating the MOF sample for the desired time at 100% intensity (Figure S2). When the exposure time was finished, the light guide was removed from the flask, which was rapidly capped with a septum, kept under argon, and subsequently introduced into a glovebox, where the powder was weighed in the gas sorption cell under an argon atmosphere. The MOF sample was then transferred from the glovebox to the gas sorption equipment, where the N_2 isotherm was measured for further BET surface area (S_{BET}) calculation.

■ RESULTS AND DISCUSSION

Photothermal Activation of HKUST-1. HKUST-1 was chosen to benchmark the UV−vis activation protocol because of its well-standardized activation process. Indeed, HKUST-1 is usually activated using several solvent-exchange steps (e.g., with dichloromethane or methanol), followed by a thermal treat-

ment (from 80 to 170 °C) under vacuum, thus resulting in S_{BET} values ranging from 1450 to 1800 $m^2 \cdot g^{-1}$ when fully activated.[31,32]

Our experiment started with an evaluation of the photothermal effect on a sample of as-synthesized HKUST-1 by monitoring the temperature change with irradiation time (Figure 1). It was found that HKUST-1 was immediately heated when exposed to UV−vis light, reaching a plateau at 120 °C after irradiation for 4−5 min (Figure 1b,c and Video S1). The strong photothermal effect could be rationalized by analyzing the solid-state UV−vis spectrum of HKUST-1, which showed a broad absorption band centered at 720 nm attributed to the d−d transitions of the Cu(II) in the paddle wheel,[33] which falls within the wavelength used in the irradiation experiments (Figures S3−S5). The contribution of this absorption band was further studied by irradiating HKUST-1 in wavelength ranges of 320−390 nm (UV) and of 390−500 nm (visible). As expected, in both cases, lower temperatures (40 and 60 °C, respectively) were reached, demonstrating that light of wavelengths close to the maximum absorption band in the visible range mainly contributes to the photothermal effect (Figure S6). It is noteworthy that the color of the HKUST-1 powder changed from sky blue to deep purple after the irradiation experiments (Figure 1b). This color change was a first clear evidence of the removal of the solvent molecules coordinated to the Cu(II) paddle wheel clusters.

To assess the efficiency of the photothermal activation, we then measured the XRPD and S_{BET} for HKUST-1 samples irradiated for 5 and 30 min without any further treatment (Figure 1d). XRPD indicated that both irradiated samples retain the crystallinity of the initial HKUST-1 MOF (Figure S7). Remarkably, HKUST-1 irradiated for only 5 min showed an S_{BET} of 1209 $m^2 \cdot g^{-1}$ (Figure S8), and increasing the irradiation time increased this value further. Indeed, after irradiation for 30 min, the S_{BET} value had increased to 1583 $m^2 \cdot g^{-1}$ (Figure S9). These results confirm that the photothermal effect in HKUST-1 is sufficiently intense to evacuate both trapped and coordinated solvent molecules from the framework. We hypothesize that the high efficiency of the photothermal activation method to evacuate solvent molecules is due to the localized heat generation, which minimizes heat loss. To further confirm this hypothesis, HKUST-1 was heated to 120 °C for 30 min but using an external heating source such as a heating mantle. In this case, S_{BET} of the thermally treated sample was significantly lower ($S_{BET} = 655$ $m^2 \cdot g^{-1}$, Figure S10), thus highlighting the benefits of UV−vis-induced localized heating on solvent removal from the HKUST-1 framework.

An important factor that can influence the photothermal activation of MOFs is the MOF-to-light guide distance. To evaluate this parameter, we studied the photothermal activation of HKUST-1 by reducing this distance to 5 and 3 cm, thus meaning that the irradiance increased to 900 and 2650 $mW \cdot cm^{-2}$, respectively. As expected, shorter distances meant that HKUST-1 reached a higher temperature (Figure S11). When irradiated for 5 min, HKUST-1 reached a maximum of 187 °C (distance = 5 cm) and above 250 °C (distance = 3 cm). These different heating conditions were critical for HKUST-1 activation. Indeed, whereas HKUST-1 irradiated at 3 cm was found to be amorphous and nonporous, the sample irradiated at 5 cm retained its crystallinity and showed an S_{BET} of 1819 $m^2 \cdot g^{-1}$ (Figures S12 and S13). This result is remarkable because it demonstrates that HKUST-1 can be activated in only 5 min and that the MOF-to-light guide distance is a parameter
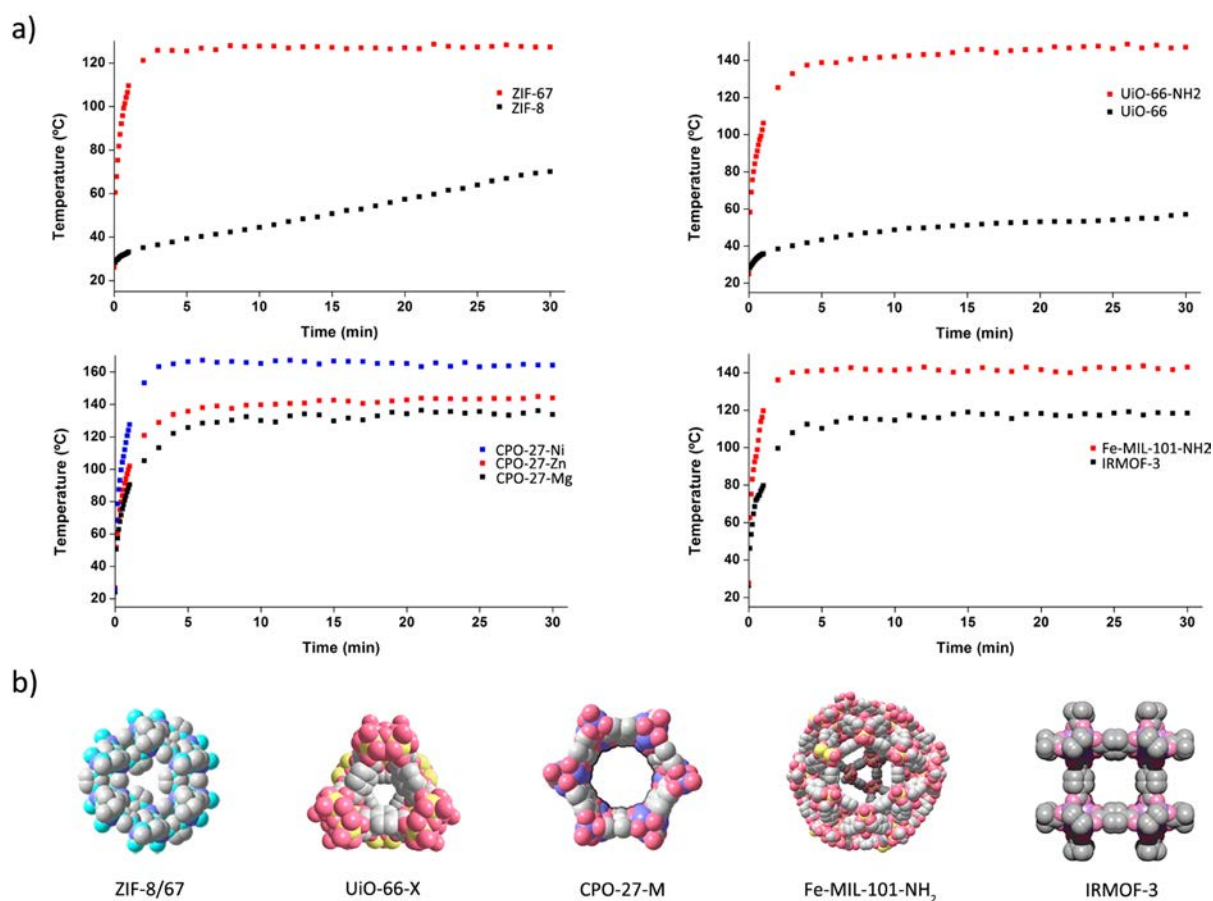
Figure 2. (a) Temperature evolution as a function of time for all studied MOFs when irradiated at a distance of 7 cm. (b) Representation of the crystalline structure of the studied MOFs.

that can be tuned to optimize the photothermal activation of MOFs (vide infra).

Versatility of the Photothermal Activation Method. To demonstrate the scope of this activation method beyond HKUST-1, we used it to study the activation of a series of MOFs representing the major subfamilies of porous MOFs. The MOFs studied comprised UiO-66, UiO-66−NH$_2$, ZIF-8, ZIF-67, CPO-27−M (where M is Zn(II), Ni(II), and Mg(II)), Fe−MIL-101−NH$_2$, and IRMOF-3. Figure 2 shows the photothermal response of each of these MOFs as a function of time. Two different behaviors can be seen from this figure. Thus, MOFs that do not exhibit an absorption band in the range 300−650 nm (light emission range; Figures S17 and S27) showed a mild temperature increase after irradiation for 30 min. For example, UiO-66 and ZIF-8 were heated to 57 and 70 °C, respectively. In contrast, MOFs that show absorption bands in this range exhibited a much higher photothermal effect (Figures S18, S28, S36, S41, and S48). The temperatures reached for each of these MOFs irradiated for 30 min were as follows: IRMOF-3 (119 °C), ZIF-67 (127 °C), CPO-27−Mg (136 °C), Fe−MIL-101−NH$_2$ (143 °C), CPO-27−Zn (145 °C), UiO-66−NH$_2$ (149 °C), and CPO-27−Ni (167 °C). Moreover, as in HKUST-1, each of these latter MOFs reached their maximum temperature after irradiation for only 4−5 min.

Once the photothermal effect of the selected MOFs had been assessed, we studied their activation using the UV−vis light source. The photothermal activations of UiO-66 and UiO-66−NH$_2$ were initially compared because of the differences in their photothermal behaviors but similarities in their structures.

In addition, it is known that the activation of UiO-66 analogues is quite challenging because of the presence of DMF molecules in the pores, which cannot be completely removed unless a long solvent-exchange process is carried out. Accordingly, both MOFs were irradiated for 30 min, with no further treatment, and their XRPD patterns and S_{BET} were subsequently measured. Again, XRPD indicated that both irradiated samples retained the crystallinity of the initial UiO-66-type MOFs (Figures S19 and S20). However, the N$_2$ adsorption isotherms showed a clear difference in their activation (Figure 3a). Thus, whereas the irradiated UiO-66−NH$_2$ showed an S_{BET} of 1098 m^2·g^{-1} (close to the highest reported value;[34,35] Figure S22), the irradiated UiO-66 showed a much lower S_{BET} of 424 m^2·g^{-1}, in accordance with its weaker photothermal effect (Figures 2 and S21). This difference was further studied by first digesting the as-synthesized and irradiated UiO-66 and UiO-66−NH$_2$ samples and then analyzing the resulting solutions by ^{1}H NMR spectroscopy (Figures 3b,c, S23, and S24). We then calculated the percentage of DMF molecules removed from both frameworks during the activation process by comparison of the integration of one peak at 7.90 ppm corresponding to DMF and those at 8.02 and 7.78 ppm corresponding to BDC and NH$_2$−BDC, respectively. From these data, it was clear that photothermal activation was more efficient at evacuating the DMF molecules from the UiO-66−NH$_2$ framework (94% of the initial DMF molecules were evacuated) than from the UiO-66 framework (only 55% were evacuated). This fact correlates well with the higher temperature and photothermal trans-duction efficiency (η) reached by UiO-66−NH$_2$ (149 °C and

Figure 3. (a) N_2 adsorption isotherms for UiO-66 (black) and UiO-66−NH$_2$ (red) after photothermal activation. (b) ^{1}H NMR spectra of as-synthesized UiO-66 (red) and after photothermal activation (blue). (c) ^{1}H NMR spectra of as-synthesized UiO-66−NH$_2$ (red) and after photothermal activation (blue). DMF peaks are highlighted with an asterisk (*).
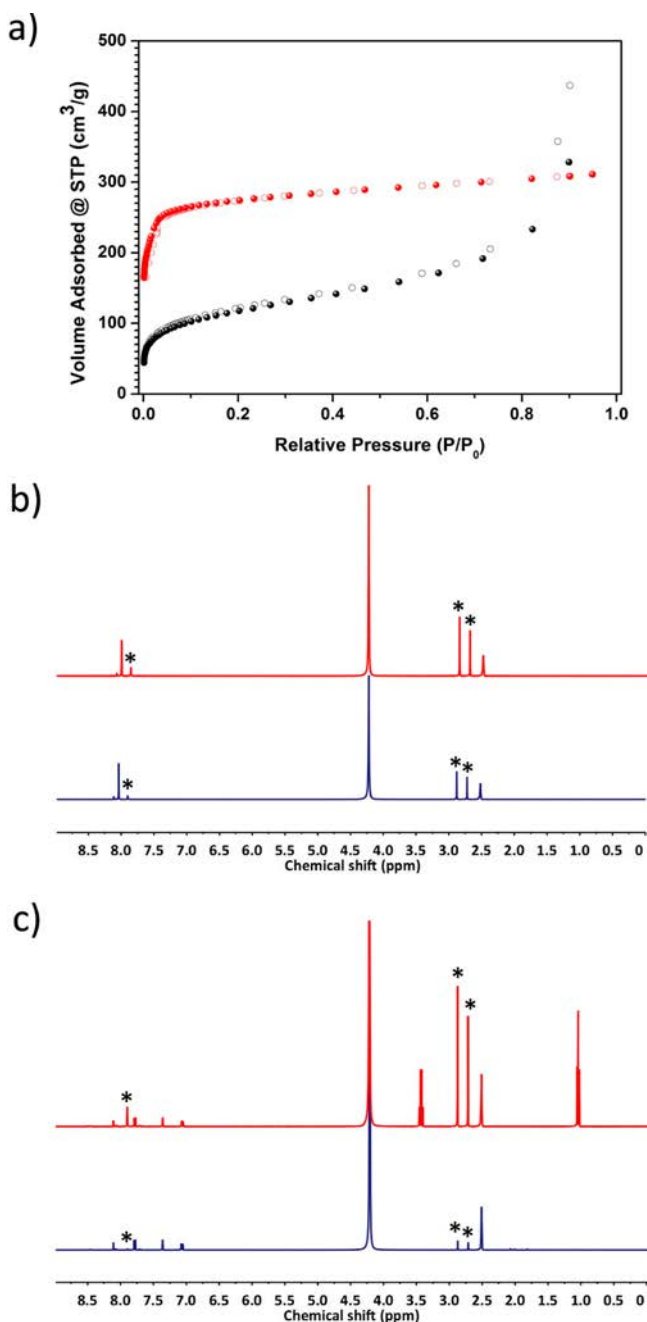
59.3%) in comparison to those reached by UiO-66 (57 °C and 5.0%) when irradiated for 30 min (Table 1 and section S10).

A similar but less pronounced trend was also found when both ZIF-8 and ZIF-67 were irradiated. S_{BET} for the irradiated ZIF-8 was 1130 m^2·g^{-1} (calculated from the second step of the isotherm between 0.01 and 0.2P/P_0; Figure S31), which is lower than typical reported values ($S_{BET} \approx 1400-1500$ m^2·g^{-1}).[36,37] In contrast, the photothermally activated ZIF-67 exhibited an S_{BET} of 1666 m^2·g^{-1} (calculated from the second step of the isotherm between 0.01 and 0.2P/P_0; Figure S32), which is comparable to the highest reported values.[38] In this

case, however, ZIF-8 showed a significant degree of activation despite its mild photothermal effect (Figure 2). We attribute this effect to the efficiency of the localized heat together with the lack of open metal sites in the structure and the nonhigh-boiling point solvents used in the synthesis (water) and washing (methanol) steps, which significantly reduces the energy required to remove occluded solvent molecules (Figures S33 and S34).

The efficient photothermal activation was further proven for Fe−MIL-101−NH$_2$ and IRMOF-3 (Figures S35−S44). In both cases, the irradiated MOFs exhibited good S_{BET} values of 1506 and 2556 m^2·g^{-1}, respectively.[39,40] It is important to highlight here that IRMOF-3 has been reported to require supercritical CO$_2$ activation to achieve an optimum S_{BET} value (2850 m^2·g^{-1}).[40] Therefore, our activation method seems to respect less robust MOFs, most likely because of the localized and homogeneous heating produced and the lack of high vacuum conditions.

In accordance with this observation, we also tested our activation method with some CPO-27 analogues as activation of this MOF family is quite difficult because of the presence of open metal sites that strongly coordinate with water molecules.[25] Activation of these MOFs generally entails a long solvent-exchange process (from 6 to 12 days) with methanol followed by high-temperature thermal treatments (above 180 °C) under vacuum. Consequently, three members of this MOF family were activated by UV−vis light irradiation for 30 min. In all cases, irradiated CPO-27−Zn/CPO-27−Ni/CPO-27−Mg retained their initial crystallinity (Figures S49−S51) and showed a change in color, which was a first indication of the removal of solvent molecules coordinated to the respective metal centers (Figures S45−S47). In fact, the successful photothermal activation of CPO-27−Zn and CPO-27−Ni was accomplished with only 30 min of UV−vis irradiation, as demonstrated by the measured S_{BET} values of 932 m^2·g^{-1} for CPO-27−Zn and 922 m^2·g^{-1} for CPO-27−Ni (Figures 4a, S52, and S53).[25]

However, these activation conditions were not found to be optimum to efficiently activate CPO-27−Mg (S_{BET} = 416 m^2·g^{-1}, Figure S54). In this case, photothermal activation was optimized by reducing the MOF-to-light guide distance down to 5 cm (irradiance = 900 mW·cm^{-2}) and 3 cm (irradiance = 2650 mW·cm^{-2}; Figure S1). Under these new conditions, CPO-27−Mg reached temperatures of 184 and 250 °C, respectively, when irradiated for 30 min. In both cases, XRPD showed that the crystallinity was maintained (Figure S55). In addition, the measured S_{BET} values confirmed a better activation process, with values of 1062 and 1630 m^2·g^{-1} (the latter being comparable to the highest reported values; Figure 4b)[25] when exposed to light powers of 900 and 2650 mW·cm^{-2}, respectively.

Finally, we opened up the possibility of using this photothermal activation method in covalent organic frameworks (COFs). To this end, a two-dimensional COF (COF TAPB−BTCA) assembled from two trigonal building blocks, BTCA and TAPB (Figure S61), was irradiated at a distance of 7 cm (irradiance = 500 mW·cm^{-2}) for 30 min, obtaining an S_{BET} value of 1185 m^2·g^{-1}, which is comparable to that reported in the literature (Figure S66).[28] Similar to the MOFs, this COF also reached a temperature of 136 °C after irradiation for 4−5 min.

Table 1. Summary of the Main Parameters of the Photothermally Activated Materials

material	photothermal temperature (°C)	η (%)[a]	S_{BET} (m²·g⁻¹)		residual solvent (%)[b]
			this work	reported	
HKUST-1	125	33.6	1583	1740[31]	5.1[a]
UiO-66	57	5.0	424	1580[35]	11.2[b]
UiO-66−NH₂	149	59.3	1098	1200[35]	3.4[b]
ZIF-8	60	0.3	1130	1079[36]	[c]
ZIF-67	127	50.0	1666	1319[38]	[c]
CPO-27−Zn	145	23.8	932	1154[25]	1.7[d]
CPO-27−Ni	167	93.6	922	1351[25]	0.4[d]
CPO-27−Mg	136	21.6	1630	1603[25]	2.0[d]
Fe−MIL-101−NH₂	143	86.6	1506	2436[39]	1.8[a]
IRMOF-3	119	25.8	2556	2850[40]	3.6[b]
COF TAPB−BTCA	136	55.4	1185	1120[28]	3.0[e]

[a]Calculated as explained in the Supporting Information. [b]Calculated from the residual [a]DMF and EtOH, [b]DMF, [d]MeOH, and [e]acetone. [c]Note that H₂O could not be determined by NMR.
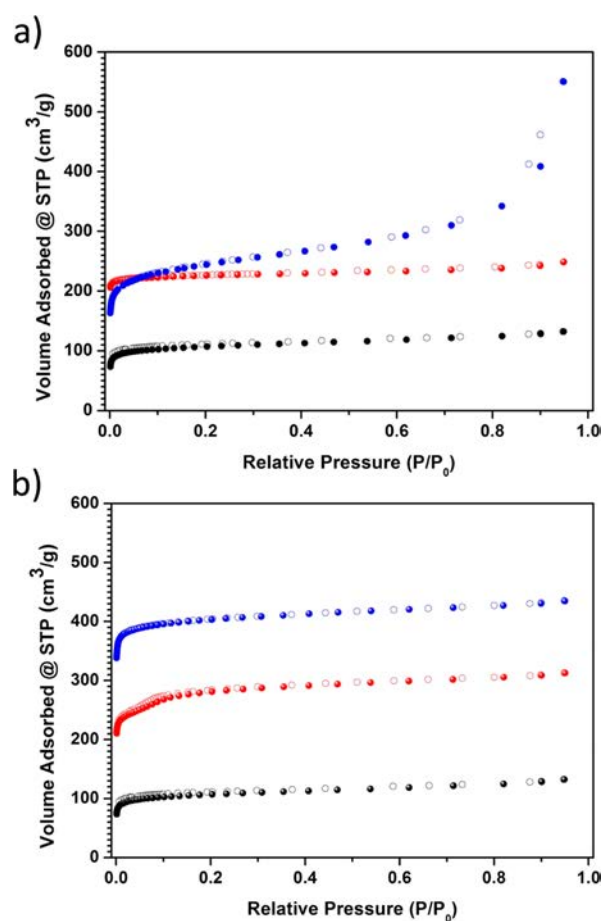
Figure 4. (a) N₂ adsorption isotherms of CPO-27−Mg (black), CPO-27−Zn (red), and CPO-27−Ni (blue) after irradiated at 500 mW·cm⁻². (b) N₂ adsorption isotherms of CPO-27−Mg after irradiated at 500 (black), 900 (red), and 2650 mW·cm⁻² (blue).

CONCLUSIONS

In summary, we have reported that a UV−vis lamp can be used to activate as-synthesized MOFs in a single step. MOFs with absorptions in the UV−vis wavelength range emitted by this lamp undergo a significant heating (120−220 °C) in 4−5 min. This localized light-to-heat conversion in the MOF crystals when irradiated enables a very fast solvent removal, thereby significantly reducing the activation time down to 30 min and

suppressing the need for time-consuming solvent-exchange procedures and vacuum conditions. We have found that the S_{BET} values obtained after photothermal activation for only 30 min are comparable to the highest reported values for conventionally activated HKUST-1, ZIF-67, UiO-66−NH₂, Fe−MIL-101−NH₂, IRMOF-3, and CPO-27−M (M = Ni, Zn, and Mg). Moreover, we have demonstrated that this activation method could be extended to COFs. Our findings should facilitate the integration of an activation step in processes in which MOFs/COFs are manufactured in a continuous way as well as the use of this photothermal effect in applications in which the triggered desorption of volatile species (e.g., water) is desired.

ASSOCIATED CONTENT

ⓢ Supporting Information

The Supporting Information is available free of charge on the ACS Publications website at DOI: 10.1021/acsami.8b00557.

> Lamp irradiance calibration, setup description, photographs and infrared camera pictures before and after irradiation, solid-state UV−vis spectra, XRPD patterns, N₂ adsorption isotherms, photothermal plots, NMR spectra, and photothermal transduction efficiency calculations (PDF)
>
> Infrared camera video showing the temperature change against time (AVI)

AUTHOR INFORMATION

Corresponding Authors

*E-mail: inhar.imaz@icn2.cat (I.I.).
*E-mail: daniel.maspoch@icn2.cat (D.M.).

ORCID

Luis Garzón-Tovar: 0000-0003-0253-4041
Inhar Imaz: 0000-0002-0278-1141
Daniel Maspoch: 0000-0003-1325-9161

Author Contributions

The manuscript was written through contributions of all authors. All authors have given approval to the final version of the manuscript.

Notes

The authors declare no competing financial interest.

■ ABBREVIATIONS

XRPD, X-ray powder diffraction; UV−vis, ultraviolet−visible; DI, deionized; MOF, metal−organic framework; COF, covalent organic framework; DMF, dimethylformamide; NMR, nuclear magnetic resonance; PTE, photothermal transduction efficiency

■ REFERENCES

(1) Furukawa, H.; Ko, N.; Go, Y. B.; Aratani, N.; Choi, S. B.; Choi, E.; Yazaydin, A. Ö.; Snurr, R. Q.; O'Keeffe, M.; Kim, J.; Yaghi, O. M. Ultrahigh Porosity in Metal-Organic Frameworks. *Science* **2010**, *329*, 424−428.

(2) Kitagawa, S.; Kitaura, R.; Noro, S.-i. Functional Porous Coordination Polymers. *Angew. Chem., Int. Ed.* **2004**, *43*, 2334−2375.

(3) Zhou, H.-C.; Long, J. R.; Yaghi, O. M. Introduction to Metal−Organic Frameworks. *Chem. Rev.* **2012**, *112*, 673−674.

(4) Murray, L. J.; Dincă, M.; Long, J. R. Hydrogen Storage in Metal-Organic Frameworks. *Chem. Soc. Rev.* **2009**, *38*, 1294−1314.

(5) Makal, T. A.; Li, J.-R.; Lu, W.; Zhou, H.-C. Methane Storage in Advanced Porous Materials. *Chem. Soc. Rev.* **2012**, *41*, 7761−7779.

(6) (a) Lee, J.; Farha, O. K.; Roberts, J.; Scheidt, K. A.; Nguyen, S. T.; Hupp, J. T. Metal-Organic Framework Materials as Catalysts. *Chem. Soc. Rev.* **2009**, *38*, 1450−1459. (b) Jiao, L.; Wang, Y.; Jiang, H.-L.; Xu, Q. Metal−Organic Frameworks as Platforms for Catalytic Applications. *Adv. Mater.* **2017**, 1703663. (c) Yang, Q.; Xu, Q.; Jiang, H.-L. Metal−organic frameworks meet metal nanoparticles: synergistic effect for enhanced catalysis. *Chem. Soc. Rev.* **2017**, *46*, 4774−4808.

(7) Kreno, L. E.; Leong, K.; Farha, O. K.; Allendorf, M.; Van Duyne, R. P.; Hupp, J. T. Metal−Organic Framework Materials as Chemical Sensors. *Chem. Rev.* **2012**, *112*, 1105−1125.

(8) Horcajada, P.; Gref, R.; Baati, T.; Allan, P. K.; Maurin, G.; Couvreur, P.; Férey, G.; Morris, R. E.; Serre, C. Metal−Organic Frameworks in Biomedicine. *Chem. Rev.* **2012**, *112*, 1232−1268.

(9) Mondloch, J. E.; Karagiaridi, O.; Farha, O. K.; Hupp, J. T. Activation of Metal−Organic Framework Materials. *CrystEngComm* **2013**, *15*, 9258−9264.

(10) Neumann, O.; Urban, A. S.; Day, J.; Lal, S.; Nordlander, P.; Halas, N. J. Solar Vapor Generation Enabled by Nanoparticles. *ACS Nano* **2013**, *7*, 42−49.

(11) Wang, Z.; Liu, Y.; Tao, P.; Shen, Q.; Yi, N.; Zhang, F.; Liu, Q.; Song, C.; Zhang, D.; Shang, W.; Deng, T. Bio-Inspired Evaporation Through Plasmonic Film of Nanoparticles at the Air−Water Interface. *Small* **2014**, *10*, 3234−3239.

(12) Liu, Y.; Yu, S.; Feng, R.; Bernard, A.; Liu, Y.; Zhang, Y.; Duan, H.; Shang, W.; Tao, P.; Song, C.; Deng, T. A Bioinspired, Reusable, Paper-Based System for High-Performance Large-Scale Evaporation. *Adv. Mater.* **2015**, *27*, 2768−2774.

(13) Zhang, L.; Tang, B.; Wu, J.; Li, R.; Wang, P. Hydrophobic Light-to-Heat Conversion Membranes with Self-Healing Ability for Interfacial Solar Heating. *Adv. Mater.* **2015**, *27*, 4889−4894.

(14) Ghasemi, H.; Ni, G.; Marconnet, A. M.; Loomis, J.; Yerci, S.; Miljkovic, N.; Chen, G. Solar Steam Generation by Heat Localization. *Nat. Commun.* **2014**, *5*, 4449.

(15) Li, H.; Hill, M. R.; Doblin, C.; Lim, S.; Hill, A. J.; Falcaro, P. Visible Light Triggered CO_2 Liberation from Silver Nanocrystals Incorporated Metal−Organic Frameworks. *Adv. Funct. Mater.* **2016**, *26*, 4815−4821.

(16) Li, H.; Hill, M. R. Low-Energy CO_2 Release from Metal−Organic Frameworks Triggered by External Stimuli. *Acc. Chem. Res.* **2017**, *50*, 778−786.

(17) Khaletskaya, K.; Reboul, J.; Meilikhov, M.; Nakahama, M.; Diring, S.; Tsujimoto, M.; Isoda, S.; Kim, F.; Kamei, K.-i.; Fischer, R. A.; Kitagawa, S.; Furukawa, S. Integration of Porous Coordination Polymers and Gold Nanorods into Core−Shell Mesoscopic Composites toward Light-Induced Molecular Release. *J. Am. Chem. Soc.* **2013**, *135*, 10998−11005.

(18) Diring, S.; Carné-Sánchez, A.; Zhang, J.; Ikemura, S.; Kim, C.; Inaba, H.; Kitagawa, S.; Furukawa, S. Light Responsive Metal-Organic Frameworks as Controllable CO-Releasing Cell Culture Substrates. *Chem. Sci.* **2017**, *8*, 2381−2386.

(19) Yang, Q.; Xu, Q.; Yu, S.-H.; Jiang, H.-L. Pd Nanocubes@ZIF-8: Integration of Plasmon-Driven Photothermal Conversion with a Metal−Organic Framework for Efficient and Selective Catalysis. *Angew. Chem., Int. Ed.* **2016**, *55*, 3685−3689.

(20) Wang, F.; Huang, Y.; Chai, Z.; Zeng, M.; Li, Q.; Wang, Y.; Xu, D. Photothermal-enhanced Catalysis in Core-shell Plasmonic Hierarchical Cu_7S_4 Microsphere@Zeolitic Imidazole Framework-8. *Chem. Sci.* **2016**, *7*, 6887−6893.

(21) Chen, Y.-Z.; Wang, Z. U.; Wang, H.; Lu, J.; Yu, S.-H.; Jiang, H.-L. Singlet Oxygen-Engaged Selective Photo-Oxidation over Pt Nanocrystals/Porphyrinic MOF: The Roles of Photothermal Effect and Pt Electronic State. *J. Am. Chem. Soc.* **2017**, *139*, 2035−2044.

(22) Carné-Sánchez, A.; Imaz, I.; Cano-Sarabia, M.; Maspoch, D. A Spray-Drying Strategy for Synthesis of Nanoscale Metal−Organic Frameworks and their Assembly into Hollow Superstructures. *Nat. Chem.* **2013**, *5*, 203−211.

(23) Ragon, F.; Horcajada, P.; Chevreau, H.; Hwang, Y. K.; Lee, U.-H.; Miller, S. R.; Devic, T.; Chang, J.-S.; Serre, C. In Situ Energy-Dispersive X-ray Diffraction for the Synthesis Optimization and Scale-up of the Porous Zirconium Terephthalate UiO-66. *Inorg. Chem.* **2014**, *53*, 2491−2500.

(24) Avci, C.; Ariñez-Soriano, J.; Carné-Sánchez, A.; Guillerm, V.; Carbonell, C.; Imaz, I.; Maspoch, D. Post-Synthetic Anisotropic Wet-Chemical Etching of Colloidal Sodalite ZIF Crystals. *Angew. Chem., Int. Ed.* **2015**, *54*, 14417−14421.

(25) Garzón-Tovar, L.; Carné-Sánchez, A.; Carbonell, C.; Imaz, I.; Maspoch, D. Optimised Room Temperature, Water-Based Synthesis of CPO-27-M Metal-Organic Frameworks with High Space-Time Yields. *J. Mater. Chem. A* **2015**, *3*, 20819−20826.

(26) Bauer, S.; Serre, C.; Devic, T.; Horcajada, P.; Marrot, J.; Férey, G.; Stock, N. High-Throughput Assisted Rationalization of the Formation of Metal Organic Frameworks in the Iron(III) Amino-terephthalate Solvothermal System. *Inorg. Chem.* **2008**, *47*, 7568−7576.

(27) Tanabe, K. K.; Wang, Z.; Cohen, S. M. Systematic Functionalization of a Metal−Organic Framework via a Postsynthetic Modification Approach. *J. Am. Chem. Soc.* **2008**, *130*, 8508−8517.

(28) Rodríguez-San-Miguel, D.; Yazdi, A.; Guillerm, V.; Pérez-Carvajal, J.; Puntes, V.; Maspoch, D.; Zamora, F. Confining Functional Nanoparticles into Colloidal Imine-Based COF Spheres by a Sequential Encapsulation−Crystallization Method. *Chem.—Eur. J.* **2017**, *23*, 8623−8627.

(29) Born, M.; Wolf, E. *Principles of Optics: Electromagnetic Theory of Propagation, Interference and Diffraction of Light*; Cambridge University Press: Cambridge, 1999.

(30) McCluney, W. R. *Introduction to Radiometry and Photometry*, 2nd ed.; Artech House Publishers: Boston/London, 2014.

(31) Kim, H. K.; Yun, W. S.; Kim, M.-B.; Kim, J. Y.; Bae, Y.-S.; Lee, J.; Jeong, N. C. A Chemical Route to Activation of Open Metal Sites in the Copper-Based Metal−Organic Framework Materials HKUST-1 and Cu-MOF-2. *J. Am. Chem. Soc.* **2015**, *137*, 10009−10015.

(32) Song, X.; Jeong, S.; Kim, D.; Lah, M. S. Transmetalations in Two Metal-Organic Frameworks with Different Framework Flex-

ibilities: Kinetics and Core-Shell Heterostructure. *CrystEngComm* **2012**, *14*, 5753−5756.

(33) Prestipino, C.; Regli, L.; Vitillo, J. G.; Bonino, F.; Damin, A.; Lamberti, C.; Zecchina, A.; Solari, P. L.; Kongshaug, K. O.; Bordiga, S. Local Structure of Framework Cu(II) in HKUST-1 Metallorganic Framework: Spectroscopic Characterization upon Activation and Interaction with Adsorbates. *Chem. Mater.* **2006**, *18*, 1337−1346.

(34) Hu, Z.; Zhao, D. De facto Methodologies Toward the Synthesis and Scale-up Production of UiO-66-Type Metal-Organic Frameworks and Membrane Materials. *Dalton Trans.* **2015**, *44*, 19018−19040.

(35) Katz, M. J.; Brown, Z. J.; Colón, Y. J.; Siu, P. W.; Scheidt, K. A.; Snurr, R. Q.; Hupp, J. T.; Farha, O. K. A Facile Synthesis of UiO-66, UiO-67 and their Derivatives. *Chem. Commun.* **2013**, *49*, 9449−9451.

(36) Pan, Y.; Liu, Y.; Zeng, G.; Zhao, L.; Lai, Z. Rapid Synthesis of Zeolitic Imidazolate Framework-8 (ZIF-8) Nanocrystals in an Aqueous System. *Chem. Commun.* **2011**, *47*, 2071−2073.

(37) Lee, Y.-R.; Jang, M.-S.; Cho, H.-Y.; Kwon, H.-J.; Kim, S.; Ahn, W.-S. ZIF-8: A Comparison of Synthesis Methods. *Chem. Eng. J.* **2015**, *271*, 276−280.

(38) Shi, Q.; Chen, Z.; Song, Z.; Li, J.; Dong, J. Synthesis of ZIF-8 and ZIF-67 by Steam-Assisted Conversion and an Investigation of Their Tribological Behaviors. *Angew. Chem., Int. Ed.* **2011**, *50*, 672−675.

(39) Savonnet, M.; Kockrick, E.; Camarata, A.; Bazer-Bachi, D.; Bats, N.; Lecocq, V.; Pinel, C.; Farrusseng, D. Combinatorial Synthesis of Metal-Organic Frameworks Libraries by Click-Chemistry. *New J. Chem.* **2011**, *35*, 1892−1897.

(40) Nelson, A. P.; Farha, O. K.; Mulfort, K. L.; Hupp, J. T. Supercritical Processing as a Route to High Internal Surface Areas and Permanent Microporosity in Metal−Organic Framework Materials. *J. Am. Chem. Soc.* **2009**, *131*, 458−460.

Check for updates

The photothermal effect in MOFs: covalent post-synthetic modification of MOFs mediated by UV-Vis light under solvent-free conditions†

Jordi Espín, [‡][a] Luis Garzón-Tovar, [‡][a] Gerard Boix, [a] Inhar Imaz [*][a] and Daniel Maspoch [*][ab]

Here, we report the covalent post-synthetic modification (CPSM) of MOFs using the photothermal effect. Specifically, we subjected mixtures of a photothermally active MOF and another reagent to irradiation with a UV-Vis lamp. This caused the MOF to heat up, which in turn caused the other reagent to melt and subsequently react with the functional groups on the walls of the MOF pores. We have exploited this dual function of MOFs as both heater and host for CPSMs to achieve rapid formation of amides from the reaction of representative MOFs (UiO-66-NH$_2$ or MIL-101-NH$_2$-(Al)) with anhydrides under solvent-free conditions. In addition, this approach enables more complex CPSMs in MOFs such as the formation of amides in UiO-66-NH$_2$ by using an aldehyde through a cascade reaction.

Photo-irradiation of certain materials causes them to heat up. This is known as the photothermal effect. Ideally, one could exploit this conversion of light into heat to selectively increase the local temperature of a given material and its surroundings, while minimizing heat diffusion and energy loss. Photothermal materials have been harnassed for myriad applications such as cancer theranostics[1–7] and in water evaporation,[8–10] sterilisation[11] or desalination[12,13] devices. Such materials include organometallic complexes,[14] polymers,[1,2,15] carbon-based materials,[8,12,16] noble-metal and hybrid nanoparticles,[9–11,13,17] and semiconductors.[5–7,18]

Recently, we found that some porous metal–organic frameworks (MOFs) can exhibit a pronounced photothermal effect. After UV-Vis irradiation (300–650 nm), MOFs exhibiting absorption bands in this range can reach temperatures exceeding 120 °C within minutes. For example, 100 mg and 25 mg of the archetypical MOF UiO-66-NH$_2$ reaches a temperature of 140 °C and 78 °C, respectively, after only 5 minutes of irradiation (500 mW cm^{-2}) at a light guide-to-sample distance of 7 cm (Fig. S1, ESI†).

We demonstrated that this localised heat can be used to efficiently remove trapped and coordinated solvent molecules from within the MOF structure to generate activated MOFs at atmospheric pressure in unprecedented short times.[19]

Covalent post-synthetic modifications (CPSMs) are employed to derivatise MOFs with diverse functional groups, which enables tailoring of physicochemical properties (*e.g.* wettability[20,21]) and of functions (*e.g.* catalysis[22,23] and gas sorption).[24] These modifications are generally done by reacting MOF crystals with other reagents in solution for long periods of time (from hours to days).[25] However, alternative methods have recently been proposed to reduce the solvent volume and/or the reaction time. For example, our group has shown that Schiff-base condensation reactions between aldehydes and amines inside MOFs can be performed in mere seconds, by using spray-drying.[26] The first reported solvent-free method for the post-synthetic modification of MOFs was vapour diffusion. Thus, Ranocchiari, Bokhoven *et al.* described the CPSM of solid amino-tagged MOFs by exposing them to vapours produced by heating liquid aldehydes or anhydrides at 120 °C under vacuum for 16 h.[27] More recently, Wuttke *et al.* reported a second solvent-free CPSM strategy based on the direct heating of a solid mixture of an amino-terminated MOF and a carboxylic acid derivative (acid anhydride, acid chloride or carboxylic acid) at *ca.* 100 °C for minutes.[28] Similarly, Richardson *et al.* demonstrated that a Newman–Kwart rearrangement on a dimethylthiocarbamate-functionalized IRMOF-9 occurs by direct heating it at 285 °C.[29]

In the study reported here, we extended our previous work on localised photothermal activation of MOFs to perform CPSMs of MOFs under solvent-free conditions. We show that MOFs, once mixed with another reagent and irradiated by a UV-Vis lamp, can simultaneously act as both heater and host for CPSMs. The MOF crystals reach high temperatures, thereby heating their surroundings and melting the other reagent, which then reacts with the functional groups of the MOF. As a final step of this process, the mixture is washed with a solvent to remove the unreacted chemical reagent, and the post-modified MOF is collected by centrifugation and dried. Three conditions must

[a] Catalan Institute of Nanoscience and Nanotechnology (ICN2), CSIC and The Barcelona Institute of Science and Technology, Campus UAB, Bellaterra, 08193 Barcelona, Spain. E-mail: daniel.maspoch@icn2.cat

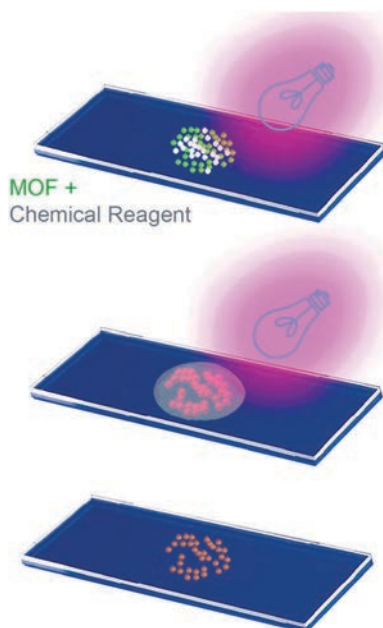*[b] ICREA, Pg. Lluís Companys 23, 08010 Barcelona, Spain*

† Electronic supplementary information (ESI) available. See DOI: 10.1039/c8cc01593g

‡ Both authors contributed equally.

be met in this CPSM approach. Firstly, the MOF must have functional groups available for reaction. Secondly, the MOF must be photothermally active. And finally, the chemical reagent must melt at a temperature below that of the previously heated MOF.

To demonstrate the feasibility of this solvent-free, photo-induced CPSM method, we chose UiO-66-NH$_2$ as a representative MOF, as it is strongly photothermal (*vide supra*) and contains free amino groups available for derivatization. As a model reaction, we reacted this MOF with anhydrides to form amides. Thus, UiO-66-NH$_2$ was synthesised and activated under previously reported conditions, and obtained as a pure phase as confirmed by X-ray powder diffraction (XRPD) and N$_2$ adsorption measurements (S_{BET} value: 936 m^2 g^{-1}; Fig. S2 and S3, ESI†).[30] Once synthesised, the activated UiO-66-NH$_2$ (25 mg) was mixed with maleic anhydride (MA) (melting point: 51–56 °C) at molar ratios (2-aminoterephthalate/MA) of 1:1, 1:3 and 1:6. Each solid mixture was placed between two quartz slides (Scheme 1). A light guide was fixed at a distance of 7 cm from the sample. Each pair of slides was then irradiated (irradiance: 500 mW cm^{-2}) for 30 min, causing the MOF to reach a temperature of 78–82 °C (Fig. S4 and S5, ESI†). To ensure homogeneous light exposure, each slide pair was turned around after 15 minutes. Note that, as a control experiment, a solid sample of MA alone was irradiated for 30 minutes; it did not exhibit any temperature increase. Finally, the resulting irradiated mixtures were washed with DMF and acetone and dried at room temperature. The different samples were named as (UiO-66-MA)$_x$, where x corresponds to the number of equivalents of anhydride.

Using XRPD, we confirmed that all three samples retained the crystallinity of the starting UiO-66-NH$_2$ (Fig. 1b and Fig. S6, ESI†).

To determine the degree of post-synthetic conversion, the digested powders (5% HF/DMSO-d_6) were analysed by ^{1}H-NMR spectroscopy. The conversion rates were then calculated by comparing the integration of the peak corresponding to unmodified 2-aminoterephthalic acid (7.34 ppm) to that of the peak corresponding to the alkenyl hydrogens of the newly formed amide moiety (6.58 ppm). The conversion rates were 69.9% ± 0.4% for (UiO-66-MA)$_1$, 85.1% ± 1.0% for (UiO-66-MA)$_3$ and 83.4% ± 0.3% for (UiO-66-MA)$_6$ (Fig. 1a and Fig. S7, ESI†). These values indicated that increasing the number of equivalents of MA from three to six did not provide a significant increase in product.

Having determined the optimal molar ratio of NH$_2$-bdc/MA to be 1:3, we then decided to study the effects of using a stronger irradiation intensity or a longer reaction time on a mixture of photo-activated UiO-66-NH$_2$ and MA. To assess the intensity, we used 900 mW cm^{-2} (instead of 500 mW cm^{-2}, as above), which we attained by setting the distance between the light-guide and the sample to 5 cm (instead of 7 cm, as above). To study the reaction time, we irradiated the mixture for 60 min (instead of 30 min, as above). As confirmed by XRPD, neither of these more aggressive conditions altered the structure of the parent UiO-66-NH$_2$ (Fig. S8 and S9, ESI†). In these reactions, the post-synthetic conversions were 78.5% ± 1.5% for the reaction done at a distance of 5 cm and 83.2% ± 4.9% for the reaction irradiation at 60 min (Fig. S10, ESI†). These values were similar (or even lower) to those obtained under the original (milder) conditions. Thus, for optimal reaction conditions, we chose a NH$_2$-bdc/MA molar ratio of 1:3; a light guide-to-sample distance of 7 cm (500 mW cm^{-2}); and an irradiation time of 30 min.

We found further evidence of amide formation by electrospray-ionisation mass spectrometry (ESI-MS) of the digested (UiO-66-MA)$_3$, which showed a peak at m/z = 278.0 that matched the molecular

Scheme 1 Illustration of the photo-mediated CPSM of MOFs. Once irradiated with a UV-Vis lamp (top), a photothermally active MOF, previously mixed with another reagent, will heat up, causing the other reagent to melt (middle). This in turn drives the reaction of the reagent with the functional groups on the pore walls of the MOF (below).
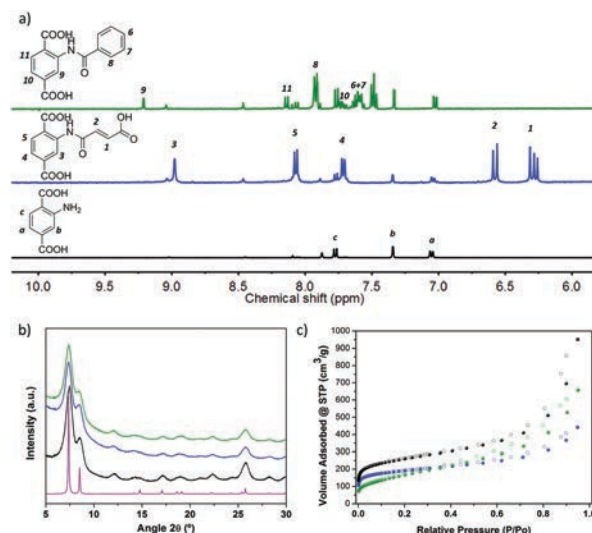

Fig. 1 (a) ^{1}H NMR spectra of the digested (UiO-66-MA)$_3$, (blue), (UiO-66-BA)$_3$ (green) and UiO-66-NH$_2$ (black) in HF/DMSO-d_6. (b) XRPD patterns for simulated UiO-66-NH$_2$ (purple), activated UiO-66-NH$_2$ (black), (UiO-66-MA)$_3$ (blue) and (UiO-66-BA)$_3$ (green). (c) N$_2$ sorption isotherms for UiO-66-NH$_2$ (black), (UiO-66-MA)$_3$ (blue) and (UiO-66-BA)$_3$ (green).

formula of the desired amide product $[C_{12}H_8NO_7]^-$ ($m/z = 278.0$) (Fig. S11, ESI†). Finally, the N_2 sorption isotherm of (UiO-66-MA)$_3$ measured at 77 K showed an S_{BET} value of 699 m^2 g^{-1}, confirming that the product MOF had a smaller surface area than the starting MOF, as expected for formation of amide groups, which are sterically bulkier than amino groups (Fig. 1c).[31]

We then applied our optimised conditions to the reaction of UiO-66-NH$_2$ with benzoic anhydride (BA) (melting point: 38–42 °C). Thus, a solid mixture of UiO-66-NH$_2$ (25 mg) and BA (NH$_2$-bdc : BA molar ratio of 1 : 3) was irradiated at 500 mW cm^{-2} for 30 min, reaching a temperature of 78–82 °C (Fig. S12 and S13, ESI†). The resulting (UiO-66-BA)$_3$ was first analysed by XRPD, which confirmed that it had retained the crystallinity of the parent MOF (Fig. 1b). As above, the formation of the expected amide group was corroborated by ESI-MS, in which the peak at $m/z = 284.1$ matched the molecular formula of the product $[C_{15}H_{10}NO_5]^-$ ($m/z = 284.1$) (Fig. S14, ESI†). Also, as above, the formation of these amide groups led to a smaller surface area in the final MOF (S_{BET}: 621 m^2 g^{-1}) (Fig. 1c).[28] In this case, comparing the integration of the ^{1}H-NMR peaks corresponding to unmodified 2-aminoterephtalic acid (7.34 ppm) and each amide moiety (8.14 ppm) revealed a conversion rate of 48.6% ± 1.0% (Fig. 1a). We attributed this lower conversion (relative to that for the reaction with MA) to the bulky phenyl substituents of BA, which may have slowed down diffusion of the reagent into the MOF pore channels.

To demonstrate the versatility of our CPSM method, we chose to study a second amino-tagged MOF: MIL-101-NH$_2$-(Al). This MOF is also photothermally active: when irradiated for 30 min at 265 mW cm^{-2} (light guide-to-sample distance of 9 cm), it reaches a temperature of 61 °C; and when irradiated at 500 mW cm^{-2}, reaches 72 °C (Fig. S15, ESI†). Thus, MIL-101-NH$_2$-(Al) was first synthesised under solvothermal conditions, which afforded it as a pure phase, as confirmed by XRPD and N_2 sorption measurements ($S_{BET} = 2702$ m^2 g^{-1}) (Fig. S16 and S17, ESI†).[28] Then, this MOF (25 mg) was reacted with either MA, under the optimised conditions for UiO-66-NH$_2$ (Fig. S18 and 19, ESI†), or BA, using the lower irradiance intensity of 265 mW cm^{-2} (Fig. S22 and S23, ESI†). A lower intensity was used for the BA reaction because in initial tests, the value of 500 mW cm^{-2} led to a decrease in the crystallinity of MIL-101-NH$_2$-(Al) due to a post-synthetic ligand exchange (62.9 ± 1.8%) between the NH$_2$-bdc ligands and benzoic acid molecules formed during the amide formation (Fig. S24 and S25, ESI†). The resulting (MIL-101-(Al)-MA)$_3$ and (MIL-101-(Al)-BA)$_3$ were analysed by XRPD and ESI-MS, which also confirmed that they each retained the crystallinity of the parent MOF (Fig. 2b) and exhibited the expected amide formation (Fig. S21 and S27, ESI†). The conversion rates were 79.1% ± 1.4% for (MIL-101-(Al)-MA)$_3$ and 44% ± 2.5% for (MIL-101-(Al)-BA)$_3$ (Fig. S20 and S26, ESI†). These results were consistent with the gradual decrease in surface area in each case, as indicated by the corresponding S_{BET} values (determined by the N_2-sorption isotherms at 77 K): 549 m^2 g^{-1} for (MIL-101-(Al)-MA)$_3$ and 774 m^2 g^{-1} for (MIL-101-(Al)-BA)$_3$ (Fig. 2b, Table 1).

The possibility to perform CPSMs under UV-Vis light allows one to incorporate photochemical reactions in these processes and therefore, provide researchers with novel reactions from
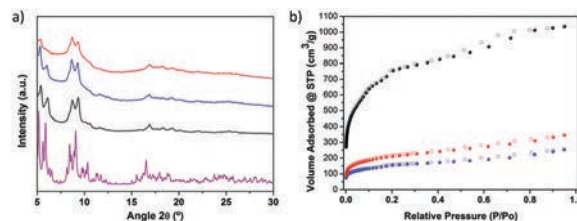
Fig. 2 (a) XRPD patterns for simulated MIL-101-NH$_2$-(Al) (purple), activated MIL-101-NH$_2$-(Al) (black), (MIL-101-(Al)-MA)$_3$ (blue) and (MIL-101-(Al)-BA)$_3$ (red). (b) N_2 sorption isotherms of MIL-101-NH$_2$-(Al) (black), (MIL-101-(Al)-MA)$_3$ (blue) and (MIL-101-(Al)-BA)$_3$ (red).

Table 1 BET areas, pore volumes and conversion rates (%) for the synthesised and modified MOFs

MOF	S_{BET} (m^2 g^{-1})	Pore vol.[a] (cm^3 g^{-1})	Conversion[b] (%)
UiO-66-NH$_2$	936	0.4726	—
(UiO-66-MA)$_3$	699	0.3375	85.1
(UiO-66-BA)$_3$	621	0.3452	48.6
MIL-101-NH$_2$-(Al)	2702	1.277	—
(MIL-101-(Al)-MA)$_3$	549	0.2662	79.1
(MIL-101-(Al)-BA)$_3$	774	0.3742	44.0

[a] Calculated at $P/P_0 \approx 0.4$. [b] Calculated from ^{1}H-NMR spectra of the digested samples.

which to introduce functionalities to MOFs. For example, our CPSM approach provides a simple route towards creating an amide (rather than the expected imine) starting from an aldehyde (in this case, 4-bromobenzaldehyde (BrBA)) through a cascade reaction (Scheme 2). This reaction first involves the generation of a singlet oxygen by UV-Vis light that reacts with BrBA to produce 4-bromobenzoic acid (Fig. S28 and S29, ESI†).[32] Then, this carboxylic acid reacts with the amino groups of the MOF to produce the amide. CPSM through this cascade reaction was done by irradiating a solid mixture of UiO-66-NH$_2$ (25 mg) and BrBA (NH$_2$-bdc : BrBA molar ratio of 1 : 6) at 500 mW cm^{-2} for 30 min. The resulting (UiO-66-BrBA)$_6$ was first analyzed by XRPD, which confirmed that it had retained the crystallinity of the parent MOF (Fig. S30, ESI†). Formation of the amide group was evidenced by ESI-MS, from which the peak at $m/z = 362.0$ matched with the molecular formula of the amide product $[C_{15}H_{10}BrNO_5]^-$ ($m/z = 362.0$) (Fig. S31, ESI†). The conversion rate of this photo-induced cascade reaction was of 54.7% ± 3.4% (Fig. S32, ESI†).
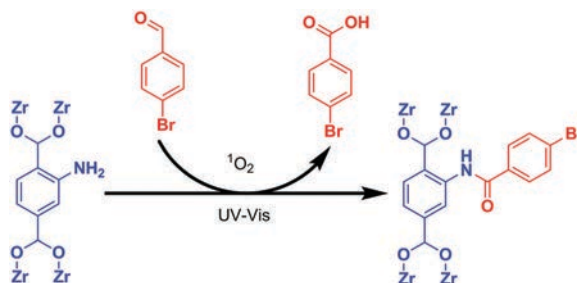
Scheme 2 Schematic representation of the CPSM reaction of UiO-66-NH$_2$ and BrBA forming an amide through a photoinduced cascade reaction.

In summary, we have shown that the photothermal effect in MOFs can be exploited for their CPSM in the solid state. Use of MOFs as photo-activated heaters should be amenable to performing other functions, such as triggering the release of species adsorbed in MOFs; confining reactions to the inside of MOF pores or to the crystal surfaces of MOFs; and increasing the efficiency of MOF catalysts.

Conflicts of interest

There are no conflicts to declare.

Notes and references

1 K. Yang, H. Xu, L. Cheng, C. Sun, J. Wang and Z. Liu, *Adv. Mater.*, 2012, **24**, 5586–5592.
2 L. Xu, L. Cheng, C. Wang, R. Peng and Z. Liu, *Polym. Chem.*, 2014, **5**, 1573–1580.
3 S. Li, X. Wang, R. Hu, H. Chen, M. Li, J. Wang, Y. Wang, L. Liu, F. Lv, X.-J. Liang and S. Wang, *Chem. Mater.*, 2016, **28**, 8669–8675.
4 C. Loo, A. Lowery, N. Halas, J. West and R. Drezek, *Nano Lett.*, 2005, **5**, 709–711.
5 X. Huang, W. Zhang, G. Guan, G. Song, R. Zou and J. Hu, *Acc. Chem. Res.*, 2017, **50**, 2529–2538.
6 C. M. Hessel, V. P. Pattani, M. Rasch, M. G. Panthani, B. Koo, J. W. Tunnell and B. A. Korgel, *Nano Lett.*, 2011, **11**, 2560–2566.
7 Q. Tian, F. Jiang, R. Zou, Q. Liu, Z. Chen, M. Zhu, S. Yang, J. Wang, J. Wang and J. Hu, *ACS Nano*, 2011, **5**, 9761–9771.
8 H. Ghasemi, G. Ni, A. M. Marconnet, J. Loomis, S. Yerci, N. Miljkovic and G. Chen, *Nat. Commun.*, 2014, **5**, 4449.
9 O. Neumann, A. S. Urban, J. Day, S. Lal, P. Nordlander and N. J. Halas, *ACS Nano*, 2013, **7**, 42–49.
10 Y. Liu, S. Yu, R. Feng, A. Bernard, Y. Liu, Y. Zhang, H. Duan, W. Shang, P. Tao, C. Song and T. Deng, *Adv. Mater.*, 2015, **27**, 2768–2774.
11 O. Neumann, C. Feronti, A. D. Neumann, A. Dong, K. Schell, B. Lu, E. Kim, M. Quinn, S. Thompson, N. Grady, P. Nordlander, M. Oden and N. J. Halas, *PNAS*, 2013, **110**, 11677–11681.
12 X. Li, W. Xu, M. Tang, L. Zhou, B. Zhu, S. Zhu and J. Zhu, *PNAS*, 2016, **113**, 13953–13958.
13 L. Zhou, Y. Tan, J. Wang, W. Xu, Y. Yuan, W. Cai, S. Zhu and J. Zhu, *Nat. Photonics*, 2016, **10**, 393.
14 X. He, X. He, S. Li, K. Zhuo, W. Qin, S. Dong, J. Chen, L. Ren, G. Liu and H. Xia, *Polym. Chem.*, 2017, **8**, 3674–3678.
15 I. H. El-Sayed, X. Huang and M. A. El-Sayed, *Cancer Lett.*, 2006, **239**, 129–135.
16 Y. Zeng, J. Yao, B. A. Horri, K. Wang, Y. Wu, D. Li and H. Wang, *Energy Environ. Sci.*, 2011, **4**, 4074–4078.
17 Z. Wang, Y. Liu, P. Tao, Q. Shen, N. Yi, F. Zhang, Q. Liu, C. Song, D. Zhang, W. Shang and T. Deng, *Small*, 2014, **10**, 3234–3239.
18 X. Bu, D. Zhou, J. Li, X. Zhang, K. Zhang, H. Zhang and B. Yang, *Langmuir*, 2014, **30**, 1416–1423.
19 J. Espín, L. Garzón-Tovar, A. Carné-Sánchez, I. Imaz and D. Maspoch, *ACS Appl. Mater. Interfaces*, 2018, **10**, 9555–9562.
20 H. N. Rubin and M. M. Reynolds, *Inorg. Chem.*, 2017, **56**, 5266–5274.
21 C. Liu, Q. Liu and A. Huang, *Chem. Commun.*, 2016, **52**, 3400–3402.
22 J. Wang, M. Yang, W. Dong, Z. Jin, J. Tang, S. Fan, Y. Lu and G. Wang, *Catal. Sci. Technol.*, 2016, **6**, 161–168.
23 C. J. Doonan, W. Morris, H. Furukawa and O. M. Yaghi, *J. Am. Chem. Soc.*, 2009, **131**, 9492–9493.
24 J. A. Thompson, N. A. Brunelli, R. P. Lively, J. R. Johnson, C. W. Jones and S. Nair, *J. Phys. Chem. C*, 2013, **117**, 8198–8207.
25 S. M. Cohen, *Chem. Rev.*, 2012, **112**, 970–1000.
26 L. Garzón-Tovar, S. Rodríguez-Hermida, I. Imaz and D. Maspoch, *J. Am. Chem. Soc.*, 2017, **139**, 897–903.
27 M. Servalli, M. Ranocchiari and J. A. Van Bokhoven, *Chem. Commun.*, 2012, **48**, 1904–1906.
28 H. Hintz and S. Wuttke, *Chem. Mater.*, 2014, **26**, 6722–6728.
29 T. A. Ablott, M. Turzer, S. G. Telfer and C. Richardson, *Cryst. Growth Des.*, 2016, **16**, 7067–7073.
30 F. Ragon, P. Horcajada, H. Chevreau, Y. K. Hwang, U. H. Lee, S. R. Miller, T. Devic, J.-S. Chang and C. Serre, *Inorg. Chem.*, 2014, **53**, 2491–2500.
31 S. J. Garibay and S. M. Cohen, *Chem. Commun.*, 2010, **46**, 7700–7702.
32 N. Iqbal, S. Choi, Y. You and E. J. Cho, *Tetrahedron Lett.*, 2013, **54**, 6222–6225.

Narrowing the Zero-Field Tunneling Resonance by Decreasing the Crystal Symmetry of Mn$_{12}$ Acetate

Jordi Espín,[†] Ricardo Zarzuela,[‡] Nahuel Statuto,[‡] Jordi Juanhuix,[§] Daniel Maspoch,[†,‖] Inhar Imaz,*[,†] Eugene Chudnovsky,[⊥] and Javier Tejada*[,‡]

[†]Catalan Institute of Nanoscience and Nanotechnology (ICN2), CSIC and The Barcelona Institute of Science and Technology, Campus UAB, Bellaterra, 08193 Barcelona, Spain

[‡]Departament de Física Fonamental, Facultat de Física, Universitat de Barcelona, Martí i Franquès 1, 08028 Barcelona, Spain

[§]Alba Synchrotron Light Facility, 08290 Cerdanyola del Vallés, Barcelona, Spain

[‖]ICREA, Pg Lluís Companys 23, 08100 Barcelona, Spain

[⊥]Physics Department, Lehman College, The City University of New York, 250 Bedford Park Boulevard West, Bronx, New York 10468-1589, United States

Ⓢ *Supporting Information*

ABSTRACT: We report the discovery of a less symmetric crystalline phase of Mn$_{12}$ acetate, a triclinic phase, resulting from recrystallizing the original tetragonal phase reported by Lis in acetonitrile and toluene. This new phase exhibits the same structure of Mn$_{12}$ acetate clusters and the same positions of tunneling resonances on the magnetic field as the conventional tetragonal phase. However, the width of the zero-field resonance is at least 1 order of magnitude smaller—can be as low as 50 Oe—indicating very small inhomogeneous broadening due to dipolar and nuclear fields.

Chemistry and physics of molecular magnets have been intensively studied in the last two decades[1] after it was found that they provide an ultimate limit of the miniaturization of a permanent magnet[2] and, on top of it, exhibit quantum tunneling of the magnetic moment.[3−6] Other fascinating quantum effects observed in molecular magnets include quantum topological Berry phase,[7] magnetic deflagration,[8,9] and Rabi oscillations.[10,11] Remarkably, recent experiments performed with individual magnetic molecules bridged between conducting leads and molecules grafted on carbon nanotubes have permitted the readout of quantum states of individual atomic nuclei.[12,13] Quantum superposition of spin states in magnetic molecules makes them candidates for qubits, elements of quantum computers.[14]

Among the most studied molecular magnets, Mn$_{12}$ acetate, which was first synthesized by Lis,[15] is a prototypical spin-10 molecular magnet that shows quantum magnetic hysteresis due to resonant spin tunneling.[3] Spin tunneling in a Mn$_{12}$ cluster is illustrated in Scheme 1. The resonances are achieved on changing the external magnetic field B. Their width is due to inhomogeneous dipolar and hyperfine broadening as well as due to D-strains and g-strains.[16] Typically, observed widths of the resonances are in the ballpark of 1 kOe. The zero-field resonance stands out because it is not subject to D-strains and g-strains. It also does not depend on whether one works with a single crystal or nonoriented microcrystals. For conventional

Scheme 1. Thermally Assisted Tunneling between Resonant Spin Levels in a Mn$_{12}$ Cluster of Spin $S = 10^a$
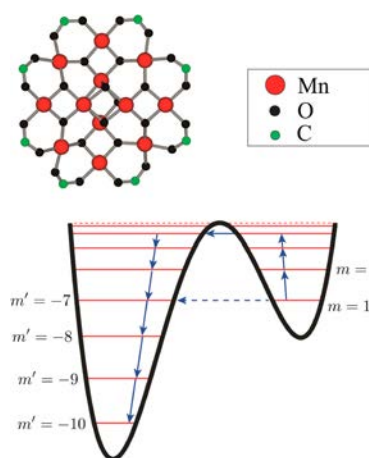
[a]The black solid curve shows the dependence of the classical magnetic anisotropy energy on the angle that the magnetic moment forms with the magnetic anisotropy axis. Red lines show energies of spin levels corresponding to magnetic quantum numbers m and m'. The dash line illustrates quantum tunneling from $m = 10$ to $m' = -7$.

Mn$_{12}$ acetate, the typical width of the zero-field resonance is in the ballpark of 300 Oe.[17] Inhomogeneous broadening of spin-tunneling resonances is one obstacle on the way to achieving terahertz lasing and superradiance effects in molecular magnets.[18,19] Herein we report the discovery of a less symmetric crystalline phase (triclinic phase) of Mn$_{12}$ acetate that exhibits surprisingly narrow width of the zero-field resonance, which, in some instances, can be as low as 50 Oe.

Recently, we reported spin-tunneling maxima in the field derivative of the magnetization of amorphous nonoriented Mn$_{12}$ acetate nanospheres.[20] This observation challenged the conventional wisdom that quantum resonances can only be
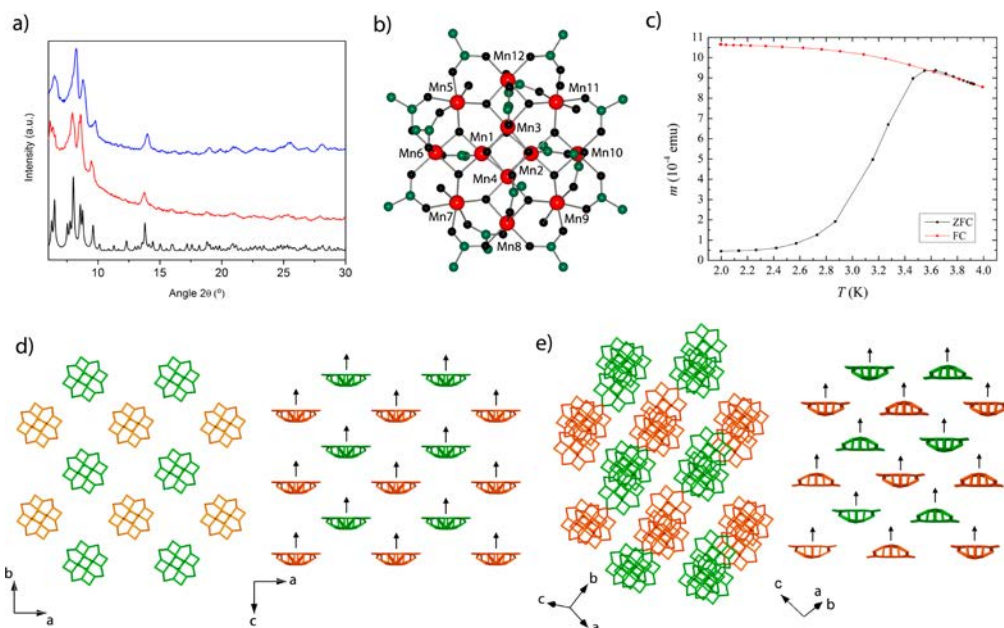
Figure 1. (a) XRPD of the $\mathbf{Mn_{12\_triclinic}}$ microribbons (blue) and the single crystals of $\mathbf{Mn_{12\_triclinic}}$ (red), as compared to the simulated powder pattern for the crystal structure of $\mathbf{Mn_{12\_triclinic}}$. (b) View of the Mn_{12} acetate cluster in $\overline{\mathbf{Mn}}_{12\_triclinic}$. (c) ZFC (black) and field-cooled (red) magnetization vs temperature for a sample of $\mathbf{Mn_{12\_triclinic}}$ at H = 100 Oe. A single peak indicates the absence of any second species of Mn_{12} clusters. (d,e) Comparison between the arrangement of Mn_{12} acetate clusters in the tetragonal (d) and triclinic (e) phases. Arrows (conceptual) show the directions of the easy magnetization axes of the clusters. Note that the Mn_{12} acetate clusters are aligned along their easy magnetization axes in the tetragonal phase, whereas they are not in the triclinic phase, and that acetate ligands and toluene and water molecules have been omitted for clarity.

observed in single crystals or in systems of oriented microcrystals. The amorphous Mn_{12} acetate spheres were prepared by initially dissolving single crystals of Mn_{12} acetate corresponding to the tetragonal phase reported by Lis[15] in acetonitrile.[21] Then, this solution was added into a toluene solution to provoke a fast precipitation of a brown solid. Finally, the resulting mixture was filtrated by conventional filtering paper, and the Mn_{12} acetate nanospheres were collected by centrifugation (8000 rpm during 4 min) of the filtrate. In this process, a surprising observation was that the initial collected brown solid was crystalline and that the X-ray powder diffraction showed a different pattern to that exhibited by the tetragonal Mn_{12} acetate crystals (see Figure S1).[15] Field-emission scanning electron microscope images of this brown crystalline powder revealed the formation of ribbon-like microcrystals (width: 0.8 ± 0.3 μm, length: 3.2 ± 1.9 μm; see Figure S2).

To identify this new crystalline phase, the reaction was slowed down by diffusing toluene vapors over a solution resulting from dissolving the tetragonal Mn_{12} acetate crystals in acetonitrile. After 3 days, small brown rectangular plate-like crystals suitable to perform single-crystal diffraction experiments using synchrotron radiation were obtained (see Figure S3). The new Mn_{12} phase (hereafter called $\mathbf{Mn_{12\_triclinic}}$) crystallizes in the $P\overline{1}$ space group; in contrast to the tetragonal $I\overline{4}$ space group of the original Mn_{12} acetate reported by Lis (Figure 1a; see Table S1).[15] In comparison to the initial tetragonal phase, the structure of the $Mn_{12}O_{12}(O_2CCH_3)_{16}(H_2O)_4$ cluster in this new crystalline phase is preserved (Figure 1b). The asymmetric unit contains 12 Mn atoms exhibiting octahedral coordination geometry. Two different environments for the Mn atoms can be observed. The four central Mn^{4+} (Mn1−Mn4) are situated in the core of the structure forming a cubic oxocluster $[Mn_4O_4]^{8+}$, where each

Mn^{4+} is coordinated to one oxygen atom from an acetate group and five bridging oxygen atoms. Surrounding the central Mn^{4+} oxocluster, there are eight more Mn^{3+} atoms (Mn5−Mn12) held within a nonplanar ring by eight oxygen atoms. Half of these Mn^{3+} atoms (Mn5, Mn7, Mn9, and Mn11) coordinate to three oxygen atoms from three different acetate groups, to one oxygen atom from a water molecule, and to two bridging oxygen atoms. The remaining four Mn^{3+} atoms (Mn6, Mn8, Mn10, and Mn12) coordinate to four oxygen atoms from four different acetate groups and to two bridging oxygen atoms. The 16 acetates are oriented in two different directions: in axial (four pointing up and four pointing down) and equatorial (eight acetates) directions.

The main difference between $\mathbf{Mn_{12\_triclinic}}$ and the tetragonal phase resides in the presence of intercalated toluene solvent molecules (Figure S4) as well as in the intermolecular packing of the Mn_{12} acetate clusters. Comparing both phases, the Mn_{12} acetate clusters in the more symmetric tetragonal phase show an overlap alignment along the a, b, and c axes. This latter corresponds to the alignment of the easy magnetization axes of the Mn_{12} acetate clusters (Figure 1d). However, this perfect alignment of the easy magnetization axes of the clusters is lost in $\mathbf{Mn_{12\_triclinic}}$ (Figure 1e). This phase only shows an overlap alignment of the clusters along the $\langle 1\overline{1}0 \rangle$ and $\langle \overline{1}10 \rangle$ directions.

To investigate the magnetic properties of $\mathbf{Mn_{12\_triclinic}}$, we first carried out low-temperature magnetic measurements on a compressed powdered sample inside a commercial rf-SQUID Quantum Design magnetometer. Figure 1c shows zero-field-cooled (ZFC) magnetization as a function of temperature. The maximum at about 3.5 K corresponds to the conventional blocking temperature of the Mn_{12} acetate cluster. Below this temperature, the clusters hold their magnetic moments, while above this temperature, they become superparamagnetic. The absence of any secondary maxima in the ZFC curve indicates

the presence of only one species of Mn_{12} acetate having fixed magnetic anisotropy energy of about 65 K. Hysteresis loops of the magnetization taken at different temperatures are shown in Figure 2a. The corresponding descending branches are
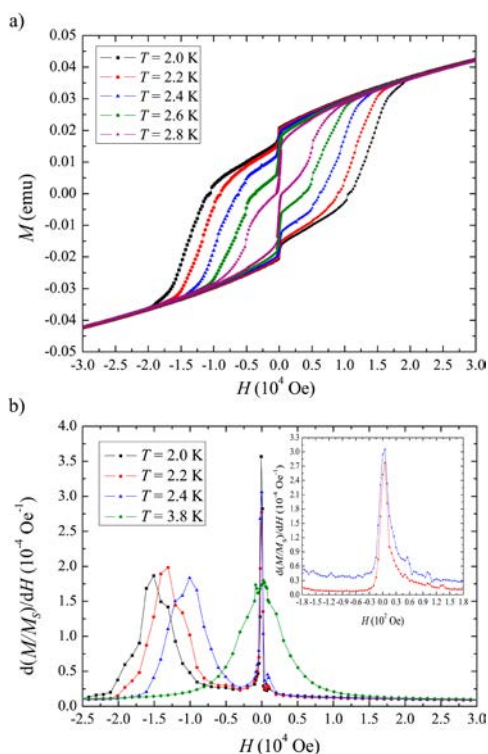

Figure 2. (a) Hysteresis loops of the magnetization of $Mn_{12\_triclinic}$ taken at different temperatures. The data along the descending branch are obtained by saturating the sample in a positive field and reducing and reversing the magnetic field. The curves show large jumps at zero field that have not been previously observed in Mn_{12} Lis phase. (b) $d(M/M_s)/dH$ along the descending branch of $Mn_{12\_triclinic}$ at different temperatures. Spin-tunneling maxima at zero and first resonant fields are clearly observed. Inset shows low-field structure of the zero-field maximum at 2.2 and 2.4 K in steps of 5 Oe.

obtained by first saturating $Mn_{12\_triclinic}$ in a positive magnetic field of up to 3 T and then reducing the magnetic field to zero, reversing it, and increasing the field in the opposite direction at a constant rate. Analogous protocol is carried out for the ascending branches. Striking feature of these magnetization curves is a very large narrow jump of the magnetization at zero field for both ascending and descending protocols. In the past, such jumps have only been seen in a large magnetic field due to the phenomenon of magnetic deflagration.[8,9] The latter is equivalent to chemical combustion: reversal of the magnetic moments of the molecules leads to the release of their Zeeman energy into heat that further enhances magnetic relaxation. However, at $B = 0$, there is no Zeeman energy to burn, so that the deflagration as an explanation to the jumps is ruled out. The derivative of the normalized magnetization, $d(M/M_s)/dH$, along the descending branch is shown at different temperatures in Figure 2b. It clearly indicates four tunneling maxima at the conventional resonant fields of Mn_{12} acetate, separated by about 0.46 T. Analogous behavior is observed for the ascending protocol. The presence of such maxima in $d(M/M_s)/dH$ of nonoriented amorphous particles of a molecular magnet has been explained in a previous study.[18] The new feature is an

extremely narrow width of the zero-field maximum. In some instances, it is below 50 Oe (Figure 2b, inset). Such a narrow spin tunneling resonance has never been observed in any molecular magnet.

In accordance with the narrow width of the zero-field resonance, one finds an unusually fast magnetic relaxation near-zero field (Figure 3). A single exponential provides a good fit to
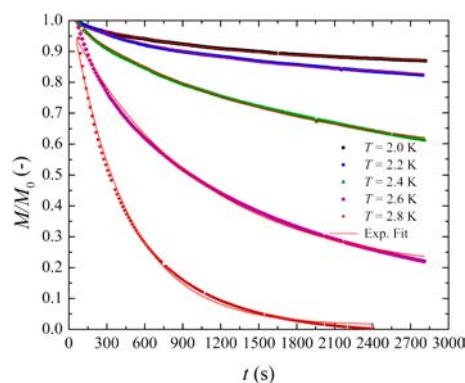

Figure 3. Exponential time relaxation of the normalized magnetization in a field of −20 Oe at different temperatures from 2.0 to 2.8 K in increments of 0.2 K.

the time dependence of the magnetic moment of the sample at all temperatures explored (2.0−2.8 K), with mean lifetimes ranging from ∼438 to 1530 s. This means that a single energy barrier contributes to the relaxation. It is determined by the distance from the ground-state level E_0 to the level E_m that dominates thermally assisted quantum tunneling (Scheme 1).

The jump in the magnetization due to resonant spin tunneling is determined by the incoherent Landau−Zener process.[22] The initial, M_i, and the final, M_f, magnetizations are connected through $M_i/M_f = \exp\{\pi\Delta_m^2 \exp[-(E_0 - E_m)/T]/(2v)\}$, where Δ_m is the tunnel splitting of the level m that dominates thermally assisted quantum tunneling, and $v = 2m\mu_B(dB/dt)$ is the rate at which Zeeman energy is changing due to the field sweep, μ_B being the Bohr magneton. The double exponential dependence on temperature provides a hint as to why the size of the magnetization jump in Figure 2a increases sharply with a relatively small increase of temperature. An additional proof of the Landau−Zener dynamics of the magnetization comes from the analysis of the experiment in which the field sweep near-zero field on a field reduction from saturation was conducted in equal field steps, with a sizable magnetization change after each step and a little change between the steps. For two consecutive steps, one has $(M_{i,n}/M_{f,n})$ $(M_{i,n+1}/M_{f,n+1}) = M_{i,n}/M_{f,n+1}$, where $M_{i,n+1} = M_{f,n}$ has been used. Writing $(dB/dt)_n$ as $\Delta B/\Delta t_n$, one obtains after N steps:

$$\frac{M_i}{M_f} = e^{(\pi\Delta_m^2 e^{-(E_0-E_m)/T}/4m\mu_B\Delta B)t}, \quad t = \Delta t_1 + \Delta t_2 + ... + \Delta t_N$$

resulting in $\ln(M_i/M_f) \propto t$. The linear time dependence of $\ln(M_i/M_f)$ observed in experiment is illustrated by Figure 4.

The width of the zero-field resonance is determined by the inhomogeneous broadening due to dipole−dipole interaction between magnetic moments of the Mn_{12} acetate clusters and due to hyperfine interactions that are rather strong in Mn_{12}. Strong dipolar broadening in conventional tetragonal crystals of Mn_{12} acetate is due to the tendency of the clusters to form ordered chains along the tetragonal c axis. This tendency should
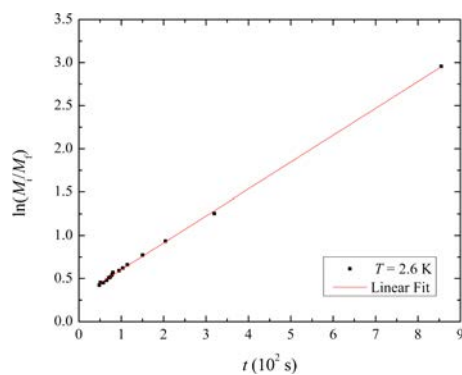
Figure 4. Linear time dependence of $\ln(M_i/M_f)$ during a stepwise field sweep at $T = 2.6$ K.

be greatly diminished in the triclinic structure. In the new crystal phase **Mn$_{12\_triclinic}$** reported here, the magnetic moments of the clusters do not perfectly overlap (Figure 1e). Still it appears unlikely that the dipolar broadening in **Mn$_{12\_triclinic}$** would fall below 50 Oe. Even if the dipolar broadening of the resonance is very low, the question would remain about the absence of the hyperfine broadening, which should be on the order of a few hundred Oe. One possible explanation to the data is provided by recent theoretical work that shows that the magnetization reversal in a molecular magnet may occur inside a front of quantum tunneling moving through the sample. This may happen either due to the formation of a domain wall with a zero dipolar bias inside the wall[23] or due to the formation of a self-organized front of quantum tunneling with zero bias between tunneling spin levels regardless of the nature of inhomogeneous broadening.[24] The latter effect presents the most interesting possibility. It is similar to the optical laser effect: The dipolar field in a system of magnetic dipoles self-organizes to provide the fastest relaxation to the minimum energy state. It has been demonstrated[24] that self-organization of dipolar field can provide the resonant condition in the presence of a very significant (up to 25%) broadening of the energy of spin levels. Further studies will reveal if self-organization is the reason for the observed narrow zero-field resonance. If it is, it may open the way to lasing with molecular magnets in the terahertz frequency range.

ASSOCIATED CONTENT

Supporting Information

The Supporting Information is available free of charge on the ACS Publications website at DOI: 10.1021/jacs.6b05380.

    Crystallographic data (CIF)
    Synthesis, XRPD, crystallographic table, SEM images. CCDC number is 1479959 (PDF)

AUTHOR INFORMATION

Corresponding Authors

*inhar.imaz@icn2.cat
*jtejada@ubxlab.com

Notes

The authors declare no competing financial interest.

ACKNOWLEDGMENTS

REFERENCES

(1) *Molecular Magnets — Physics and Applications*; Bartolomé, J., Luis, F., Fernández, J. F., Eds.; Springer: Heidelberg, 2014.
(2) Sessoli, R.; Gatteschi, D.; Caneschi, A.; Novak, M. A. *Nature* **1993**, *365*, 141.
(3) Friedman, J. R.; Sarachik, M. P.; Tejada, J.; Ziolo, R. *Phys. Rev. Lett.* **1996**, *76*, 3830.
(4) Hernandez, J. M.; Zhang, X. X.; Luis, F.; Bartolome, J.; Tejada, J.; Ziolo, R. *Europhys. Lett.* **1996**, *35*, 301.
(5) Thomas, L.; Lionti, F.; Ballou, R.; Gatteschi, D.; Sessoli, R.; Barbara, B. *Nature* **1996**, *383*, 145.
(6) Chudnovsky, E. M.; Tejada, J. *Macroscopic Quantum Tunneling of the Magnetic Moment*; Cambridge University Press: Cambridge, 1998.
(7) Wernsdorfer, W.; Sessoli, R. *Science* **1999**, *284*, 133.
(8) Suzuki; Sarachik, M. P.; Chudnovsky, E. M.; McHugh, S.; Gonzalez-Rubio, R.; Avraham, N.; Myasoedov, Y.; Zeldov, E.; Shtrikman; Chakov, N. E.; Christou, G. *Phys. Rev. Lett.* **2005**, *95*, 147201.
(9) Hernandez-Minguez, A.; Hernandez, J. M.; Macia, F.; Garcia-Santiago, A.; Tejada, J.; Santos, P. V. *Phys. Rev. Lett.* **2005**, *95*, 217205.
(10) Schlegel, C.; van Slageren, J.; Manoli, M.; Brechin, E. K.; Dressel, M. *Phys. Rev. Lett.* **2008**, *101*, 147203.
(11) Bertaina, S.; Gambarelli, S.; Mitra, T.; Tsukerblat, T.; Müller, A.; Barbara, B. *Nature* **2008**, *453*, 203; *Nature* **2010**, *466*, 1006.
(12) Ganzhorn, M.; Klyatskaya, S.; Ruben, M.; Wernsdorfer, W. *Nat. Nanotechnol.* **2013**, *8*, 165.
(13) Ganzhorn, M.; Klyatskaya, S.; Ruben, M.; Wernsdorfer, W. *ACS Nano* **2013**, *7*, 6225.
(14) Tejada, J.; Chudnovsky, E. M.; del Barco, E.; Hernandez, J. M.; Spiller, T. P. *Nanotechnology* **2001**, *12*, 181.
(15) Lis, T. *Acta Crystallogr., Sect. B: Struct. Crystallogr. Cryst. Chem.* **1980**, *36*, 2042.
(16) Park, K.; Novotny, M. A.; Dalal, N. S.; Hill, S.; Rikvold, P. A. *Phys. Rev. B: Condens. Matter Mater. Phys.* **2001**, *65*, 014426.
(17) Friedman, J. R.; Sarachik, M. P.; Ziolo, R. *Phys. Rev. B: Condens. Matter Mater. Phys.* **1998**, *58*, R14729.
(18) Chudnovsky, E. M.; Garanin, D. A. *Phys. Rev. Lett.* **2002**, *89*, 157201.
(19) Tejada, J.; Amigo, R.; Hernandez, J. M.; Chudnovsky, E. M. *Phys. Rev. B: Condens. Matter Mater. Phys.* **2003**, *68*, 014431.
(20) Lendínez, S.; Zarzuela, R.; Tejada, J.; Terban, M. W.; Billinge, S. J. L.; Espin, J.; Imaz, I.; Maspoch, D.; Chudnovsky, E. M. *Phys. Rev. B: Condens. Matter Mater. Phys.* **2015**, *91*, 024404.
(21) Imaz, I.; Luis, F.; Carbonera, C.; Ruiz-Molina, D.; Maspoch, D. *Chem. Commun.* **2008**, 1202.
(22) Garanin, D. A.; Chudnovsky, E. M. *Phys. Rev. B: Condens. Matter Mater. Phys.* **2002**, *65*, 094423.
(23) Garanin, D. A.; Chudnovsky, E. M. *Phys. Rev. B: Condens. Matter Mater. Phys.* **2008**, *78*, 174425.
(24) Garanin, D. A.; Chudnovsky, E. M. *Phys. Rev. Lett.* **2009**, *102*, 097206.

CrossMark

LETTER

Enhanced Spin Tunneling in a Molecular Magnet Mixed with a Superconductor

J. Tejada[1] · R. Zarzuela[1] (iD) · A. García-Santiago[1] · I. Imaz[2,3] · J. Espin[2,3] ·
D. Maspoch[2,3] · E. M. Chudnovsky[4]

Abstract We report characterization and magnetic studies of mixtures of micrometer-size ribbons of Mn_{12} acetate and micrometer-size particles of YBaCuO superconductor. Extremely narrow zero-field spin-tunneling resonance has been observed in the mixtures, pointing to the absence of the inhomogeneous dipolar broadening. It is attributed to the screening of the internal magnetic fields in the magnetic particles by Meissner currents flowing between superconducting grains surrounding the particles.

Keywords Spin tunneling · Molecular magnet · Superconductor

Molecular magnets have been at the forefront of research on quantum spin phenomena at the nanoscale [1]. They provide an ultimate limit of the miniaturization of magnetic memory and are promising candidates for qubits—elements of quantum computers [2]. Quantum effects observed in molecular magnets include quantum tunneling of the magnetic moment [3–6], topological Berry phase [7], quantum magnetic deflagration [8, 9], and Rabi oscillations [10, 11]. Most recently, it was demonstrated that measurement of the electric current through a magnetic molecule permits readout of quantum states of an individual atomic nucleus [12, 13].

Resonant spin tunneling in molecular magnets is strongly affected by the inhomogeneous broadening. It originates from dipolar and hyperfine interactions, as well as from D-strains and g-strains [14]. Typically observed widths of the resonances are in the ball park of 1 kOe. The zero-field resonance stands out because it is not subject to D-strains and g-strains and because it also shows the absence of hyperfine broadening [15], apparently due to the fast transitions between nuclear states on a time-scale of a typical field-sweep experiment. For conventional Mn_{12} acetate, the typical width of the zero-field resonance is in the ball park of 300 Oe.

In this paper, we report reduction of the width of the zero-field spin-tunneling resonance by mixing micron-size ribbons of Mn_{12} acetate with micron-size grains of YBaCuO. Mn_{12} ribbons with triclinic short-range crystal structure (see below) exhibit more narrow zero-field resonance than conventional Mn_{12} acetate [16]. Further reduction of the width of the resonance requires elimination of the dipolar broadening. Here, we explore the idea of screening the internal dipolar magnetic fields in Mn_{12} particles by superconducting currents in the YBaCuO grains surrounding the particles [17]. In accordance with our expectation, we observed a pronounced magnetic relaxation in the vicinity of zero field and the width of the zero-field resonance reduced to values as low as 25 Oe.

Ribbon-shaped Mn_{12}-acetate particles were prepared by re-precipitation [18] of Mn_{12}-acetate crystals of size

✉ R. Zarzuela
rzarzuela@ubxlab.com

[1] Departament de Física Fonamental, Facultat de Física, Universitat de Barcelona, Martí i Franquès 1, 08028 Barcelona, Spain

[2] Institut Català de Nanotecnologia, ICN2, Esfera Universitat Autònoma Barcelona (UAB), Campus UAB, 08193 Bellaterra, Spain

[3] Institució Catalana de Recerca i Estudis Avançats (ICREA), 08100 Barcelona, Spain

[4] Physics Department, Lehman College, The City University of New York, 250 Bedford Park Boulevard West, Bronx, New York, 10468-1589, USA

4.9 ± 1.0 μm that were synthesized as previously described by Lis [19]. We first dissolved 60-mg Mn_{12}-acetate crystals in 15 mL of acetonitrile, filtered the solution to avoid any solid trace, and mixed it with 30 mL of toluene under continuous stirring. After 1 h, a brown solid precipitate was collected by filtration. Its field-emission scanning electron microscopy (FE-SEM) revealed the formation of ribbon-shaped particles, Fig. 1a. The average ribbon size was
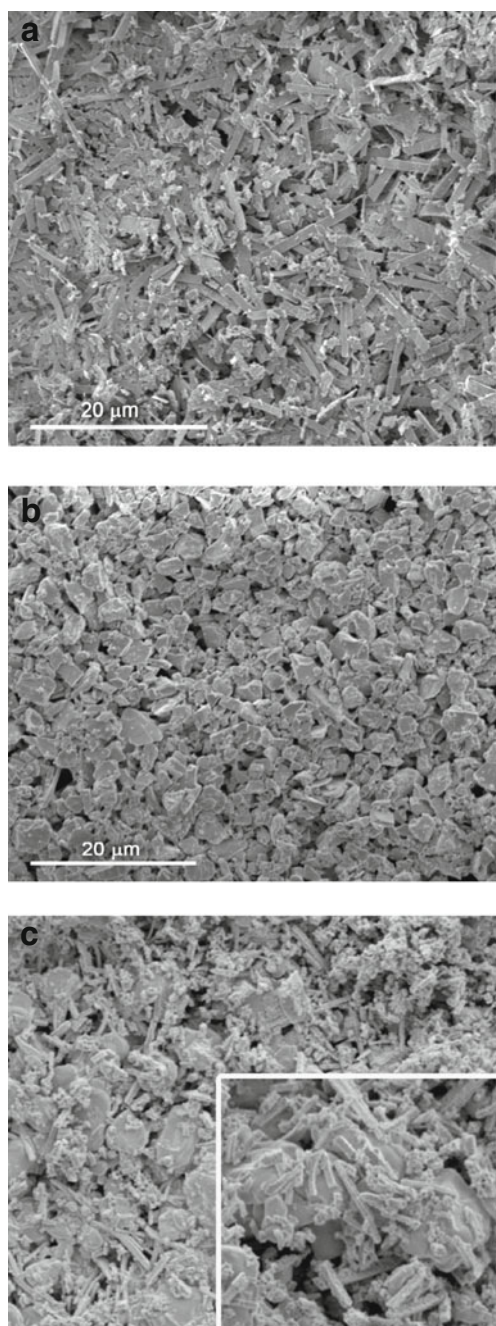
calculated statistically from FE-SEM images, measuring the length and the width of 150 particles of the same sample. The calculated average length was 3.2 ± 1.9 μm with the median of 2.8 μm, and the average width was 0.8 ± 0.3 μm with the median of 0.8 μm.

The X-ray powder diffraction pattern of the ribbons showed packing of Mn_{12} molecules that was different from the initial Mn_{12}-Ac crystals, Fig. 2. In order to grow single crystals of sufficient size to perform the single-crystal X-ray diffraction experiment, the synthesis procedure was further modified. The initial Mn_{12}-acetate crystals were dissolved in acetonitrile, filtered, and subjected to slow diffusion of toluene vapors. After a few days, we observed the formation of rectangular shaped crystals. Due to their small size, the single crystal X-ray diffraction experiment was performed under Synchrotron radiation in the XALOC beamline at the ALBA synchrotron. The powder pattern simulated from the resolution of the crystalline structure was in line with the powder diffractogram obtained from the ribbons, Fig 2. The intramolecular structure was identical to that in a conventional Mn_{12}-Ac crystal of tetragonal symmetry. However, the intermolecular packing corresponded to the triclinic space group.

Synthesis of the mixtures began with the preparation of a suspension of Mn_{12}-acetate particles in 3 mL of toluene and a suspension of YBaCuO particles in the same amount of toluene. The size of YBaCuO particles, 2.9 ± 1.3 μm, was calculated statistically from FE-SEM images, see Fig. 1b. They had composition $YBa_2Cu_3O_{6.93}$, orthorhombic crystal structure, and the critical temperature of 90 K. Mixtures with different weight ratio were prepared by mixing the two suspensions under continuous stirring for 15 min. The resulting mixtures were filtered and the collected granular solids were ground for 10 min to achieve an intimate mixing of Mn_{12}-acetate ribbons with YBaCuO particles.

Fig. 1 **a** FE-SEM image of Mn_{12}-acetate ribbons. **b** FE-SEM image of YBaCuO particles. **c** FE-SEM image of the mixture of Mn_{12}-acetate ribbons and YBaCuO particles (amplification is doubled in the inset)
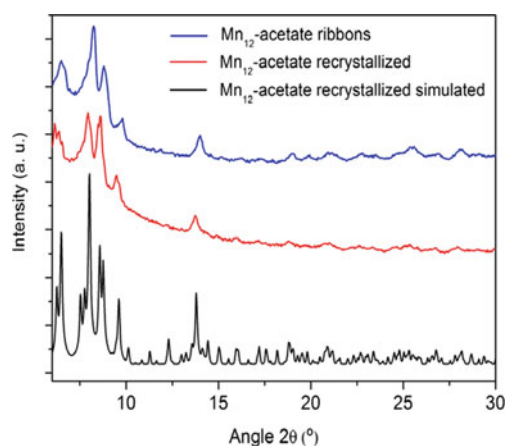

Fig. 2 Color online: X-ray data from M_{12} ribbons (*blue*), from triclinic crystal grown as described in the text (*red*), and simulated X-ray pattern from a triclinic crystal (*black*)

Field-emission scanning electron microscopy (FE-SEM) images demonstrated coexistence of both types of particles in the resulting mixtures, see Fig. 1c.

Magnetization data along the descending branch of the hysteresis loop for a sample consisting of compressed pure YBaCuO grains are presented in Fig. 3. Notice the negative dM/dH in the vicinity of zero field, the inset in Fig. 3a, that contrasts the positive dM/dH for the compressed pure sample of Mn_{12} ribbons shown in Fig. 4. The susceptibility of the compressed superconducting grains is very close to that of an ideal diamagnet, $-1/(4\pi)$, confirming the full Meissner effect in the absence of magnetic particles.

Earlier, we demonstrated [20] that neither single crystals nor oriented microcrystals were needed to observe resonant spin-tunneling in molecular magnets. The tunneling maxima can be convincingly detected by plotting the field derivative of the magnetization curve measured in non-oriented or even amorphous microcrystals if the structure of the magnetic core of the Mn_{12} molecules remains robust with respect to the local arrangement of molecules, which is the case for the ribbons. Figure 4 shows the field derivative of the magnetization curves along the descending branch of
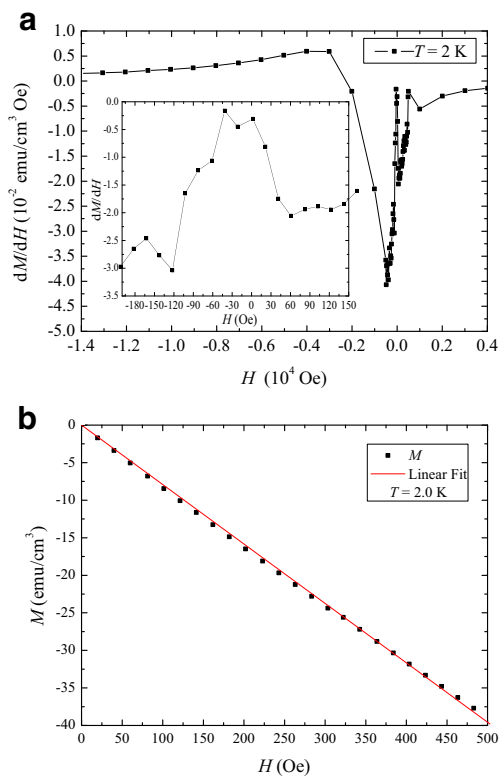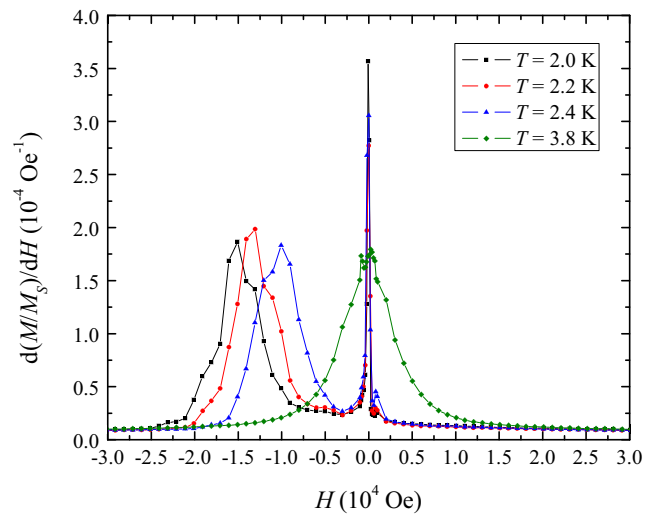

Fig. 4 Field derivative of the descending branch of the magnetization curves of the sample consisting of pure Mn_{12} ribbons at different temperatures. The presence of some of the conventional spin-tunneling maxima spaced by 0.46 T is manifested. The apparent absence of spin-tunneling peaks at the first resonant field $H_1 = -0.46$T is discussed in the text

Mn_{12}-acetate ribbons taken at different temperatures. These and other data taken at different temperatures and different field-sweep rates reveal all conventional spin-tunneling maxima in Mn_{12} spaced by 0.46 T. They clearly demonstrate that we deal with conventional Mn_{12} molecules. The strong thermal dependence of the resonant peaks in Mn_{12}-Ac molecules has been widely reported in the literature: for instance, spin-tunneling peaks at the first resonant field $H_1 = -0.46$ T are clearly seen only for temperatures above 2.4 K in the case of single crystals with the conventional tetragonal symmetry [4]. In the present case, the first resonant peaks in Fig. 4 are considerably smaller than the zero-field ones and superimpose to the next spin-tunneling maxima at all temperatures.

Zero-field-cooled magnetization of curve of the 1:1 (equal mass) mixture of Mn_{12}-acetate ribbons and YBaCuO particles is presented in Fig. 5a. It shows a pronounced conventional Mn_{12} blocking maximum at 3.5 K and the absence of any second species of molecules with a different spin or a different magnetic anisotropy barrier. The paramagnetic moment of the ribbons is superimposed on the negative diamagnetic moment of YBaCuO, which makes the total moment negative. Figure 5b shows a typical magnetic relaxation of the 1:1 mixture at low field. The sample was initially magnetized in a 3-T field at $T = 2$ K. The field was first taken down to 1 kOe and then rapidly reduced to zero and switched to −20 Oe, at which time the magnetization measurements were taken. The relaxation curve indicates an unusual for Mn_{12} acetate, very rapid, large decrease of the magnetization on the time scale of a few minutes.

Fig. 3 **a** Field derivative of the magnetization curve along the descending branch of the sample consisting of pure YBaCuO grains. **b** First magnetization curve $M(H)$ of the granular YBaCuO sample in the Meissner regime. The slope of the linear fit, $M/H = -0.0792$, is close to the magnetic susceptibility of an ideal diamagnet, $-1/(4\pi) = -0.0796$

a

b

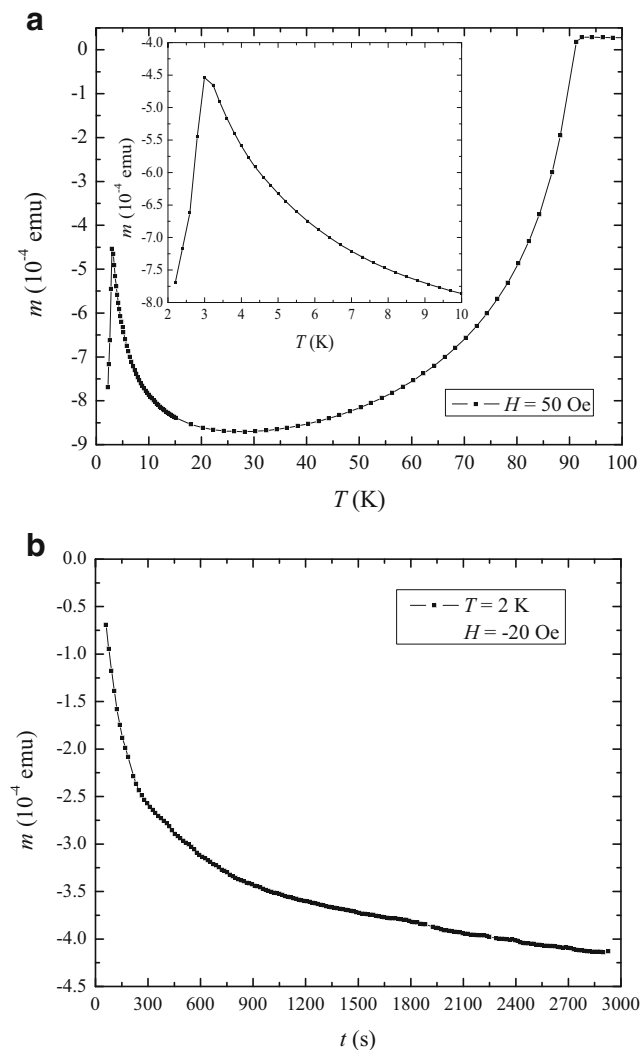**Fig. 5 a** Zero-field-cooled magnetization curve of the 1:1 (equal masses) mixture of Mn_{12}-Ac ribbons and YBaCuO particles at 50 Oe. The low-temperature paramagnetic peek (shown in the inset) is due to the ribbons. It is superimposed on the diamagnetic signal from the superconductor. **b** Magnetic relaxation from saturation to −20 Oe at 2.0 K

Low-field part of the descending branch of the magnetization curve of the sample consisting of pure Mn_{12}-Ac ribbons and of the 1:1 mixture of ribbons with the superconductor is shown in Fig. 6a. The 17 % jump for the mixture in a narrow field interval from 20 Oe to −20 Oe is more than two times the jump for pure ribbons that occurs in a much wider field interval. Such dramatic jumps have only been seen in molecular magnets under the conditions of magnetic deflagration—propagation of the front of combustion of the Zeeman energy which is similar to the combustion of a chemical substance [8, 9]. However, in a zero field, the Zeeman energy is zero and deflagration is not possible. Consequently, one has to assume that the jump is due to the unusually strong thermally-assisted quantum spin tunneling between matching spin levels.

a

b
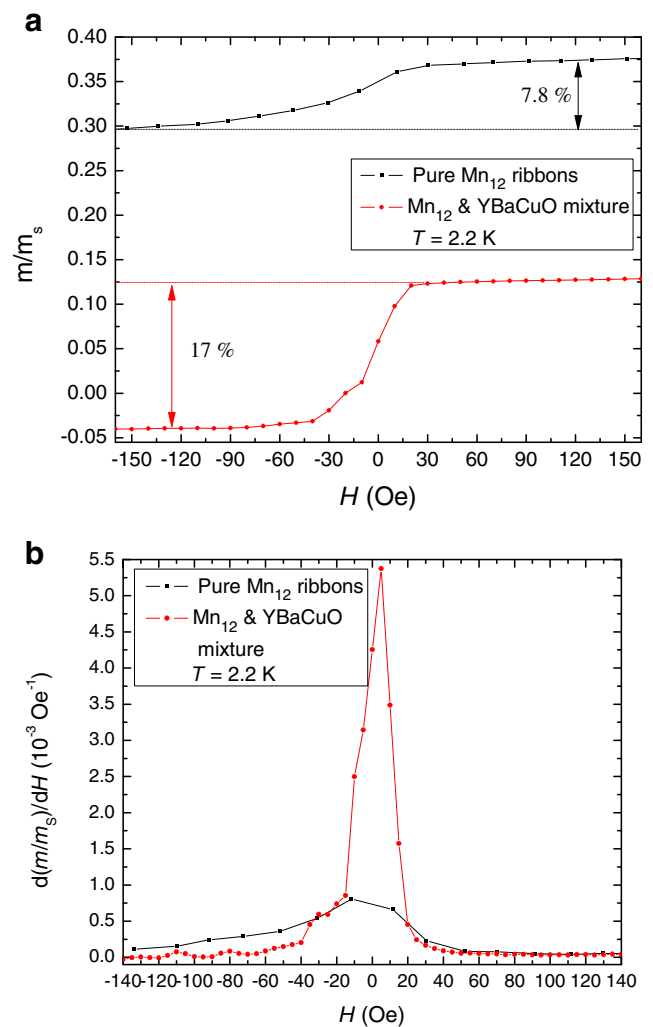
Fig. 6 a Low field part of the descending branch of the magnetization curve of pure Mn_{12}-Ac ribbons (*black*) and of the 1:1 (equal mass) mixture of the ribbons with YBaCuO particles (*red*). Percentage shows the relative change of the total magnetization. **b** Field derivative of the magnetization curves near the resonance

The derivatives of the magnetization curves depicted in Fig. 6b show that the width of the resonance at half-height is in the ball park of 25 Oe for the mixture compared to about 100 Oe for pure ribbons and 300 Oe for conventional Mn_{12} acetate. Note that the diamagnetic signal from pure YBaCuO has a negative minimum near zero-field (see Fig. 3a). This means that the paramagnetic signal due to the zero-field resonant spin tunneling in Mn_{12} ribbons mixed with the superconductor is even more dramatic than it appears.

We should emphasize that the above data represent a small cut of the data accumulated by us on mixtures of different composition, taken at different temperatures, under different field-sweep protocols. The conclusion about the narrow width of the zero-field spin-tunneling resonance is consistent throughout all data. We have checked that the

observed magnetic relaxation comes entirely from the Mn_{12} ribbons and not from the flux (if any) trapped in the superconducting grains. The sample prepared of YBaCuO grains alone showed no detectable relaxation at any temperature used in experiment.

The only reasonable explanation to these findings is the screening of the dipolar fields in Mn_{12} ribbons by superconducting currents. Note that the 1:1 sample is not a bulk superconductor but a mixture of microscopic superparamagnetic Mn_{12} ribbons and diamagnetic YBaCuO grains. The field of any strength penetrates into such a mixture. The critical field H_{c1} is of order 250 Oe in bulk YBaCuO and can be even higher in the micrograins. As long as the field is below H_{c1} of the grains, the dipolar fields of the ribbons can be screened by superconducting currents flowing between adjacent superconducting grains. This is no different from the screening of the field of a magnetic particle embedded in a bulk superconductor. While it is chemically impossible to embed Mn_{12} particles into a bulk YBaCuO superconductor, by making a microscopic mixture, we come as close to this as we possibly can. Based upon Fig. 6, the dipolar fields in the ribbons must be of order 100 Oe and, thus, they can be screened by the Meissner currents. The presence of closed superconducting circuits surrounding the ribbons is consistent with the FE-SEM images in Fig. 1 that show small ribbons fitting between larger superconducting grains touching each other. Large field penetrates into the grains, destroying superconducting currents, so that the paramagnetic signal from the ribbons is not significantly affected by the superconductor. As the field goes below H_{c1}, Meissner currents flowing between superconducting grains screen the internal dipolar fields of the ribbons. As a result, the dipolar broadening of the zero-field spin-tunneling resonance becomes suppressed. Resonances between spin energy levels with magnetic quantum numbers $\pm m$ are restored and thermally assisted quantum tunneling becomes greatly enhanced.

In conclusion, we have demonstrated that mixing of a molecular magnet with a superconductor results in a significant narrowing of spin tunneling resonances due to the screening of dipolar fields by superconducting currents. Besides fundamental interest, this effect may be of practical interest for generation of coherent electromagnetic radiation in the frequency range of a few hundred GHz which are difficult to obtain by other methods [21, 22]. Inhomogeneous broadening of the spin energy levels has been an impediment to observing superradiance and laser effects in molecular magnets [23]. Our findings indicate that mixing microcrystals of molecular magnets with a superconductor is one way to overcome this problem. In our work, we used a random mixture of magnetic and superconducting microparticles. Clever patterning of the mixture may produce better results and should be considered in the future.

References

1. See recent book: Molecular Magnets – Physics and Applications. In: Bartolomé, J., Luis., F., Fernández, J.F. (eds.) Springer, Heidelberg New York Dordrecht London (2014). doi:10.1007/978-3-642-40609-62014
2. Tejada, J., Chudnovsky, E.M., del Barco, E., Hernandez, J.M., Spiller, T.P.: Nanotech **12**, 181 (2001)
3. Friedman, J.R., Sarachik, M.P., Tejada, J., Ziolo, R.: Phys. Rev. Lett. **76**, 3830 (1996)
4. Hernandez, J.M., Zhang, X.X., Luis, F., Bartolome, J., Tejada, J., Ziolo, R.: Europhys. Lett. **35**, 301 (1996)
5. Thomas, L., Lionti, F.l., Ballou, R., Gatteschi, D., Sessoli, R., Barbara, B.: Nature (London) **383**, 145 (1996)
6. Chudnovsky, E.M., Tejada, J.: Macroscopic Quantum Tunneling of the Magnetic Moment. Cambridge University Press, Cambridge, England (1998)
7. Wernsdorfer, W., Sessoli, R.: Science **284**, 133 (1999)
8. Suzuki, Y., Sarachik, M.P., Chudnovsky, E.M., McHugh, S., Gonzalez-Rubio, R., Avraham, N., Myasoedov, Y., Zeldov, E., Shtrikman, H., Chakov, N.E., Christou, G.: Phys. Rev. Lett. **95**, 147201 (2005)
9. Hernandez-Minguez, A., Hernandez, J.M., Macia, F., Garcia-Santiago, A., Tejada, J., Santos, P.V.: Phys. Rev. Lett. **95**, 217205 (2005)
10. Schlegel, C., van Slageren, J., Manoli, M., Brechin, E.K., Dressel, M.: Phys. Rev. Lett. **101**, 147203 (2008)
11. Bertaina, S., Gambarelli, S., Mitra, T., Tsukerblat, B., Müller, A., Barbara, B.: Nature (London) **453**, 203 (2008); ibid **466**, 1006 (2010)
12. Ganzhorn, M., Klyatskaya, S., Ruben, M., Wernsdorfer, W.: Nat. Nano. **8**, 165 (2013)
13. Ganzhorn, M., Klyatskaya, S., Ruben, M., Wernsdorfer, W.: ACS Nano. **7**, 6225 (2013)
14. Park, K., Novotny, M.A., Dalal, N.S., Hill, S., Rikvold, P.A.: Phys. Rev. B **65**, 014426 (2001)
15. Friedman, J.R., Sarachik, M.P., Ziolo, R.: Phys. Rev. B **58**(R), 14729 (1998)
16. Imaz, I., Espin, J., Maspoch, D., Tejada, J., Zarzuela, R., Statuto, N., Chudnovsky, E.M.: arXiv:1510.08894 (2015)
17. Chudnovsky, E.M., Friedman, J.R.: Phys. Rev. Lett. **85**, 5206 (2000)
18. Imaz, I., Luis, F., Carbonera, C., Ruiz-Molina, D., Maspoch, D.: Chem. Commun. **2008**, 1202 (2008)
19. Lis, T.: Acta Crystallogr. B **36**, 2042 (1980)
20. Lendínez, S., Zarzuela, R., Tejada, J., Terban, M.W., Billinge, S.J.L., Espin, J., Imaz, I., Maspoch, D., Chudnovsky, E.M.: Phys. Rev. B **91**, 024404 (2015)
21. Chudnovsky, E.M., Garanin, D.A.: Phys. Rev. Lett. **89**, 157201 (2002)
22. Tejada, J., Amigo, R., Hernandez, J.M., Chudnovsky, E.M.: Phys. Rev. B **68**, 014431 (2003)
23. Bal, M., Friedman, J.R., Mertes, K., Chen, W., Rumberger, E.M., Hendrickson, D.N., Avraham, N., Myasoedov, Y., Shtrikman, H., Zeldov, E.: Phys. Rev. B **70**(R), 140403 (2004)

▌ **Metal–Organic Frameworks**

Synthesis, Culture Medium Stability, and In Vitro and In Vivo Zebrafish Embryo Toxicity of Metal–Organic Framework Nanoparticles

Àngels Ruyra,[a, b] Amirali Yazdi,[a] Jordi Espín,[a] Arnau Carné-Sánchez,[a] Nerea Roher,[b] Julia Lorenzo,[b, c] Inhar Imaz,[a] and Daniel Maspoch*[a, d]

Abstract: Metal–organic frameworks (MOFs) are among the most attractive porous materials available today. They have garnered much attention for their potential utility in many different areas such as gas storage, separation, catalysis, and biomedicine. However, very little is known about the possible health or environmental risks of these materials. Here, the results of toxicity studies on sixteen representative uncoated MOF nanoparticles (nanoMOFs), which were assessed for cytotoxicity to HepG2 and MCF7 cells in vitro, and for toxicity to zebrafish embryos in vivo, are reported. Interestingly, there is a strong correlation between their in vitro toxicity and their in vivo toxicity. NanoMOFs were ranked according to their respective in vivo toxicity (in terms of the amount and severity of phenotypic changes observed in the treated zebrafish embryos), which varied widely. Altogether these results show different levels of toxicity of these materials; however, leaching of solubilized metal ions plays a main role.

Introduction

Metal–organic frameworks (MOFs) are porous materials built from the controlled crystallization of metal ions or higher nuclearity metal clusters with multifunctional organic ligands.[1–3] When assembled at the nanoscale, they are called nanoMOFs. Analogously to other classes of nanoparticles, nanoMOFs show size-dependent properties (e.g., different adsorption kinetics or better dispersibility compared with their bulk analogues),[1] which can be exploited in numerous practical applications, including traditional storage[4] and catalysis,[5,6] and in newer areas such as sensors,[7] functional membranes and thin-films,[8,9] and in biomedical applications such as drug-delivery,[10–12] NO absorption,[13,14] and contrast agents.[15] The ever-increasing interest in nanoMOFs (and in their bulk analogues) should ultimately lead to their widespread production and use. However, little is known about the safety of these nanomaterials to humans and to the environment. Thus, before any nano-MOF can be adopted for practical use, its Environmental Health and Safety (EHS) profile must be determined.

Prior to the work we report here, other groups had already explored the in vitro toxicity of certain bare nanoMOFs in cells. In 2008, Lin et al. assayed the cytotoxicity of amorphous disuccinato-cisplatin/Tb[III] nanoparticles (size: ca. 60 nm) to HT-29 human colon adenocarcinoma cells, observing no appreciable cytotoxicity.[16] Starting in 2010, Horcajada, Gref, Serre et al. evaluated the in vitro toxicity of several Fe[III]-based nanoMOFs (e.g., nanoMIL-53, nanoMIL-88, nanoMIL-100, and nanoMIL-101; size: 90–200 nm) to various cell lines, including mouse macrophage J774.A1, human leukemia (CCRF-CEM), human multiple myeloma (RPMI-8226) and human cervical adenocarcinoma (HeLa) cells, and low cytotoxicities were generally found.[10,17–20] Roughly in parallel, Junior et al. assayed nanoZIF-8 (size: 200 nm) against three human cell lines (mucoepidermoid carcinoma of lung [NCI-H292], colorectal adenocarcinoma [HT-29], and promyelocytic leukemia [HL-60]), and found that at the highest tested concentration (109 μM), it was not cytotoxic to any of them.[11] However, Horcajada et al. recently observed cytotoxicity of nanoZIF-8 (size: 90 nm) to HeLa and J774 cell lines, reporting IC$_{50}$ values of 436 and 109 μM, respectively.[18] They also reported that Zr[IV]-based UiO-66 (size:

[a] Dr. À. Ruyra,+ A. Yazdi,+ J. Espín,+ Dr. A. Carné-Sánchez, Dr. I. Imaz, Prof. Dr. D. Maspoch
ICN2 (ICN-CSIC)
Institut Catala de Nanociencia i Nanotecnologia
Esfera UAB, 08193 Bellaterra, Barcelona (Spain)
E-mail: daniel.maspoch@icn.cat

[b] Dr. À. Ruyra,+ Dr. N. Roher, Dr. J. Lorenzo
Institut de Biotecnologia i de Biomedicina
Parc de Recerca UAB
Campus Universitat Autònoma de Barcelona
08193 Bellaterra, Barcelona (Spain)

[c] Dr. J. Lorenzo
Departament de Bioquímica i de Biologia Molecular
Campus Universitat Autònoma de Barcelona
08193 Bellaterra, Barcelona (Spain)

[d] Prof. Dr. D. Maspoch
Institució Catalana de Recerca
i Estudis Avançats (ICREA)
08100 Barcelona (Spain)

[+] These authors contributed equally.

💻 Supporting information for this article is available on the WWW under http://dx.doi.org/10.1002/chem.201405380.

100 nm) was more toxic, showing IC$_{50}$ values of 239 (HeLa) and 36 μM (J774).

The aforementioned results were obtained from in vitro studies only. Importantly, the only in vivo studies on nanoMOFs reported to date were done in Wistar female rats.[10,20] In these studies, the rats were given one of three Fe^{III}-based nanoMOFs (nanoMIL-88, nanoMIL-100, or nanoMIL-101) by intravenous injection, and subsequently analyzed for various parameters (e.g., serum, enzymatic, histological, etc.). The results revealed a lack of severe acute or sub-acute toxicity.

In this communication, we report combined in vitro (HepG2 and MCF7 cells) and in vivo (zebrafish embryos) studies on the toxicity of sixteen archetypical, uncoated nanoMOFs. As shown in Figure 1, the selected nanoMOFs comprise: MIL-100 [Fe$_3$O(H$_2$O)$_2$Cl(btc)$_2$] (**1**; btc: 1,3,5-benzenetricarboxylic acid);[21] MIL-101 [Fe$_3$Cl(H$_2$O)$_2$O(NH$_2$-bdc)$_3$] (**2**; NH$_2$-bdc: 2-aminobenzene-1,4-dicarboxylic acid);[22] MOF-5 [Zn$_4$O(bdc)$_3$] (**3**; bdc: 1,4-benzenedicarboxylic acid);[23] and MOF-74 (also called CPO-27 family) [M$_2$(dhbdc)] (**4–9**; M: Zn^{II}, Cu^{II}, Ni^{II}, Co^{II}, Mn^{II}, and Mg^{II}; dhbdc: 2,5-dihydroxy-1,4-benzenedicarboxylic acid);[24] ZIF-7 [Zn(Ph-im)$_2$] (**10**; Ph-im: benzylimidazole);[25] ZIF-8 [Zn(Me-im)$_2$] (**11**; Me-im: 2-methylimidazole);[25] UiO-66 [Zr$_6$O$_4$(OH)$_4$(bdc)$_6$] (**12**); UiO-66-NH$_2$ [Zr$_6$O$_4$(OH)$_4$(NH$_2$-bdc)$_6$] (**13**);[26] UiO-67 [Zr$_6$O$_4$(OH)$_4$(bpdc)$_6$] (**14**; bpdc: biphenyl-4,4′-dicarboxylic acid);[26] HKUST-1 [Cu$_3$(btc)$_2$] (**15**);[27] and NOTT-100 (also called MOF-505) [Cu$_2$(bptc)] (**16**; bptc: 3,3′,5,5′-biphenyl-tetracarboxylic acid).[28]

We screened the nanoMOFs for cytotoxicity to the two aforementioned cell lines (using standard in vitro methodologies), performed in vivo studies in zebrafish (as an in vivo model appropriate for comparative studies on mammalian biology), and finally the results from each study were compared. Zebrafish is recognized by the National Institute of Environmental Health Science (NIEHS, USA) and the Institute for Environment and Sustainability (IES, Europe) as an excellent system in which to study environmental toxicity,[29,30] and is accepted by the National Institutes of Health (NIH, USA) as an alternative model for exploring human diseases.[29–31] Furthermore, zebrafish embryo assays do not raise major ethical questions regarding vertebrate experimentation. Based on our results, we ranked the nanoMOFs according to their in vivo toxicity (in terms of the amount and severity of phenotypic changes in the treated zebrafish embryos). We found that this ranking parallels the in vitro toxicity rankings for both cell lines, and that the toxicity depends strongly on the solubility of the nanoMOFs and on their subsequent release of metal ions.

Results and Discussion

Synthesis and characterization of the nanoMOF library

We and other groups have previously reported several methods for synthesizing nanoMOFs.[1,32,33] By using solvo- and
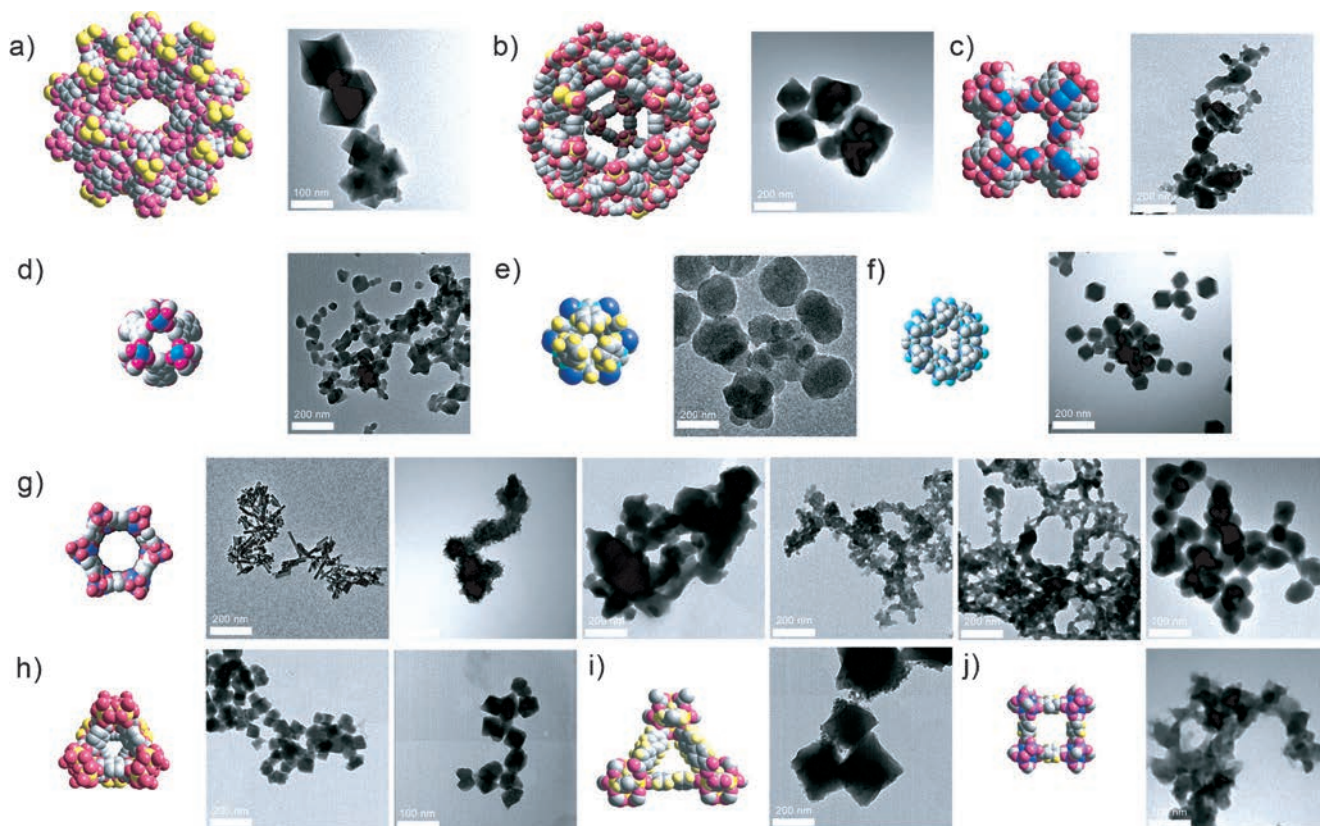

Figure 1. Representation of the crystal structures and corresponding TEM images of the synthesized nanoMOFs: a) nanoMIL-100; b) nanoMIL-101; c) nanoHKUST-1; d) nanoNOTT-100; e) nanoZIF-7; f) nanoZIF-8; g) the nanoM-MOF-74 family (from left to right, M = Co, Ni, Mg, Cu, Mn and Zn); h) nanoUiO-66 (left) and nanoUiO-66-NH$_2$ (right); i) nanoUiO-67; and j) nanoMOF-5.

hydro-thermal reactions reported previously, we prepared the following nanoMOFs: nanoMIL-100 (size: 143 ± 23 nm), nano-MIL-101 (size: 170 ± 50 nm), nanoM-MOF-74s ($M=Zn^{II}$; size: 35 ± 9 nm; $M=Cu^{II}$, size: 20 ± 8 nm; $M=Ni^{II}$, size: 111 ± 38 nm; $M=Co^{II}$, size: 112 ± 26 nm; $M=Mn^{II}$, size: 51 ± 18 nm; $M=Mg^{II}$, size: 122 ± 34 nm), nanoUiO-66 (size: 66 ± 34 nm), nanoUiO-66-NH$_2$ (size: 73 ± 32 nm), and nanoUiO-67 (size: 180 ± 30 nm). We employed fast precipitation to prepare nanoZIF-8 (size: 80 ± 15 nm) in water, nanoZIF-7 (size: 170 ± 20 nm) in N,N-dimethylformamide (DMF), and nanoMOF-5 (size: 85 ± 34 nm) in DMF; the latter, by slowly adding a base into the precursor solution. Finally, we used our recently developed spray-drying technique[34] to synthesize nanoHKUST-1 (size: 75 ± 28 nm) and nanoNOTT-100 (size: 45 ± 18 nm). Details on all the syntheses are provided in the Supporting Information.

Once synthesized, all the nanoMOFs were cleaned to remove any impurities (including trace amounts of toxic solvents from the syntheses), dried at 80 °C overnight, and finally redispersed in dimethyl sulfoxide (DMSO) to form stable colloids (concentrations: 25 to 100 mM) for the in vitro and in vivo toxicity studies. Transmission electron microscopy (TEM; Figure 1) and X-ray powder diffraction (XRPD) of the resulting colloids demonstrated that all selected nanoMOFs were obtained as homogeneous nanoscale crystals and that their XRPD patterns were fully coincident with the simulated patterns calculated from atomic coordinates (see Figure S1 in the Supporting Information). In addition, all colloidal dispersions were characterized by dynamic light scattering (DLS) studies to confirm the crystal size measured from the TEM images, as well as the homogeneity of each sample and the absence of any aggregation of the nanocrystals in solution (see Figures S2 and S3 in the Supporting Information).

Stability of the nanoMOFs in culture medium

The stability of all the nanoMOFs in the culture medium containing 10% fetal bovine serum (FBS) was studied. Each nanoMOF colloid was separately dispersed in the medium at a final concentration of 10 mM, and then incubated at 37 °C for 24 h. The resulting solids were then collected by centrifugation, dried, weighed, and finally characterized by XRPD.

The robustness of the crystal structure of each nanoMOF was evaluated by comparing the initial and final XRPD spectra (see Figure S4 in the Supporting Information). Furthermore, the XRPD spectra were used to check for any other crystalline species that might have formed in the event that the nanoMOFs had degraded. Each supernatant was also characterized by inductively coupled plasma-optical emission spectrometry (ICP-OES) to estimate the amount of metal ion that had leaked from the nanoMOF and dissolved into the culture medium. Table 1 shows all the values extracted from this study. These data clearly indicate that all the nanoMOFs were at least partially soluble in the culture medium, although the degree of solubility varied widely by structure. The data also reveal that some of the nanoMOFs had become amorphous in the culture medium, having undergone structural rearrangements and/or reactions that generated new inorganic species.

Table 1. NanoMOFs classified according to their degradation in the culture medium containing 10% fetal bovine serum (FBS).

nanoMOF	$[M_s]$ [μM][a]	Deg$_{min}$ [%][b]	XRPD analysis
UiO-67	215.6 ± 6.3	0.3 ± 0.0	amorphous
MIL-100	316.2 ± 46.1	1.1 ± 0.2	stable
MIL-101	310.4 ± 90.1	1.1 ± 0.3	amorphous
UiO-66	1099.8 ± 105.3	1.8 ± 0.2	stable
UiO-66-NH$_2$	1567.5 ± 183.1	2.6 ± 0.3	stable
ZIF-7	448.5 ± 23.4	4.5 ± 0.2	stable
MOF-5	3108.6 ± 634.1	7.8 ± 1.6	new crystalline species
Mn-MOF-74	2651.4 ± 73.6	13.3 ± 0.4	loss of crystallinity; new crystalline species (MnCO$_3$)
Co-MOF-74	3258.1 ± 58.8	16.2 ± 0.3	loss of crystallinity
ZIF-8	1916.2 ± 75.4	19.1 ± 0.8	stable
Zn-MOF-74	5442.6 ± 130.6	27.2 ± 0.5	stable
HKUST-1	9168.6 ± 137.5	30.3 ± 0.5	loss of crystallinity
Ni-MOF-74	7014.3 ± 174.9	35.1 ± 0.9	stable
NOTT-100	7967.5 ± 152.8	39.4 ± 0.8	loss of crystallinity
Cu-MOF-74	9556.8 ± 689.9	47.9 ± 3.4	loss of crystallinity
Mg-MOF-74	12573.7 ± 273.9	62.9 ± 1.4	loss of crystallinity

[a] The concentration of the corresponding metal ions solubilized after the incubation of each nanoMOF at 37 °C for 24 h was determined by ICP-OES. [b] The minimum percentage of degradation (deg$_{min}$(%)) was calculated as follows: deg_{min} (%) = ([M$_s$]·V·S)/n$_{MOF}$; where V is the volume of DMEM, S is the stoichiometric ratio of nanoMOF to metal ion, and n$_{MOF}$ is the number of moles of initial nanoMOF.

The most soluble nanoMOF in the culture medium was nanoMg-MOF-74 (12573 ± 274 μM Mg$^{II}_s$; which corresponds to 62.9% of its constituent Mg$^{II}_t$), and the least soluble, nanoUiO-67 (216 ± 6 μM Zr$^{IV}_s$; which corresponds to 0.3% of its constituent Zr$^{IV}_t$). Despite their vastly different levels of solubility, they each lost crystallinity and became amorphous upon contact with the culture medium.

NanoZIF-7 was poorly soluble in culture medium (449 ± 23 μM dissolved Zn$^{II}_s$ ions, corresponding to 4.5% of its constituent Zn$^{II}_t$), whereas nanoZIF-8 was more soluble, showing a leakage of 1916 ± 75 μM Zn$^{II}_s$ (19.1% of its constituent Zn$^{II}_t$). Interestingly, after incubation of each one in the culture medium, their respective crystal structures remained unaltered. NanoUiO-66 and nanoUiO-66-NH$_2$ were also very stable (see Figure S4), having released only 1100 ± 105 μM Zr$^{IV}_s$ (1.8% of the constituent Zr$^{IV}_t$) and 1568 ± 183 μM of Zr$^{IV}_s$ (2.6% of the constituent Zr$^{IV}_t$), respectively. In the case of nanoMIL-100 and nanoMIL-101, the concentrations of dissolved Fe^{III} ions were only 316 ± 46 μM Fe$^{III}_s$ (1.1% of the constituent Fe$^{III}_t$) and 310 ± 90 μM (1.1% of the constituent Fe$^{III}_t$), respectively. Although upon incubation both compounds became amorphous, upon subsequent exposure to ethanol, nanoMIL-100 recovered its crystallinity, which confirmed the robustness of its framework (see Figure S4).

The two Cu^{II}-based nanoMOFs (nanoHKUST-1 and nanoNOTT-100) were relatively soluble, releasing 9169 ± 138 μM Cu$^{II}_s$ (30.3% of its constituent Cu$^{II}_t$) and 7968 ± 153 μM Cu$^{II}_s$ (39.4% of its constituent Cu$^{II}_t$). This degradation was clearly accompanied by a loss of crystallinity, which, in the XRPD patterns, is evidenced by the disappearance of most of the char-

acteristic peaks. Similarly, the nanoM-MOF-74 family exhibited moderate to high solubility: nanoCu-MOF-74 released 9557 ± 690 μM Cu^{II}_s (47.9% of its constituent Cu^{II}_t); nanoNi-MOF-74, 7014 ± 175 μM Ni^{II}_s (35.1% of its constituent Ni^{II}_t); nanoZn-MOF-74, 5443 ± 131 μM Zn^{II}_s (27.2% of its constituent Zn^{II}_t); nanoCo-MOF-74, 3258 ± 59 μM Co^{II}_s (16.2% of its constituent Co^{II}_t); and nanoMn-MOF-74, 2651 ± 74 μM Mn^{II}_s (13.3% of its constituent Mn^{II}_t). Upon incubation in the culture medium, all of these nanoMOFs suffered a loss of crystallinity, with nanoCu-MOF-74, nanoCoMOF-74, and nanoMnMOF-74 exhibiting the greatest loss.

We would like to note that the proportion of metal ion (relative to the constituent amount of the tested nanoMOF) found in solution cannot always be directly related to the degradation of the nanoMOF. This is because degradation sometimes leads to formation of new, insoluble species. In our study, such species—provided that they were crystalline—were detectable by XPRD. Such was the case with nanoMn-MOF-74, the XPRD spectrum of which after incubation in culture medium indicated the formation of $MnCO_3$ (see Figure S5 in the Supporting Information). The formation of $MnCO_3$ was further studied by analyzing the powder resulting from the incubation, which confirmed the generation of new (rod-like) particles (see Figure S5). Electron-diffraction analysis (by TEM) of one of these particles revealed a diffraction that was pattern identical to that expected for $MnCO_3$ (see Figure S5). Formation of new species was also observed in the XRPD patterns for nanoCo-MOF-74, nanoMg-MOF-74, and nanoMOF-5. Unfortunately, in those cases, the new species could not be identified. Nano-MOF-5 released 3108 ± 634 μM Zn^{II}_s (7.8% of its constituent Zn^{II}_t), but its XRPD spectrum revealed the formation of a new, insoluble crystalline species, and lacked the characteristic peak of nanoMOF-5 itself (see Figure S4).

Given the above findings, we reasoned that the percentage of solubilized metal ions relative to the constituent amount of the tested nanoMOF represents the minimum percentage of degradation, because the ions might have further reacted to form insoluble species in the culture medium. Here, we would like to mention that four of the most structurally robust nano-MOFs (nanoMIL-100, nanoMIL-101, nanoUiO-66, and nanoUiO-66-NH$_2$) actually underwent greater degradation in culture medium than that detected by analyzing the solubilized metal ions. In these cases, the weight-loss values (calculated by comparing the post- and pre-weight values, and expressed as a percentage) were much higher than were the corresponding values for relative percentage of solubilized metal ions: 25.8 ± 2.5% for nanoMIL-100 (1.1%); 10.3 ± 4.1% for nanoMIL-101 (1.1%); 14.7 ± 0.3% for nanoUiO-66 (1.8%); and 10.1 ± 0.8% for nanoUiO-66-NH$_2$ (2.6%). We have tentatively attributed these differences to insoluble, amorphous metal-containing species resulting from the reaction of the released metal ions in the cell culture media. In fact, this phenomenon has previously been observed for Zn^{II} metal ions in cell culture media: for instance, ZnO nanoparticles have been reported to release Zn^{II} into cell culture media or serum, which then rapidly reacts to form a poorly soluble, amorphous nanostructured Zn^{II}-carbonate-phosphate precipitate.[35,36]

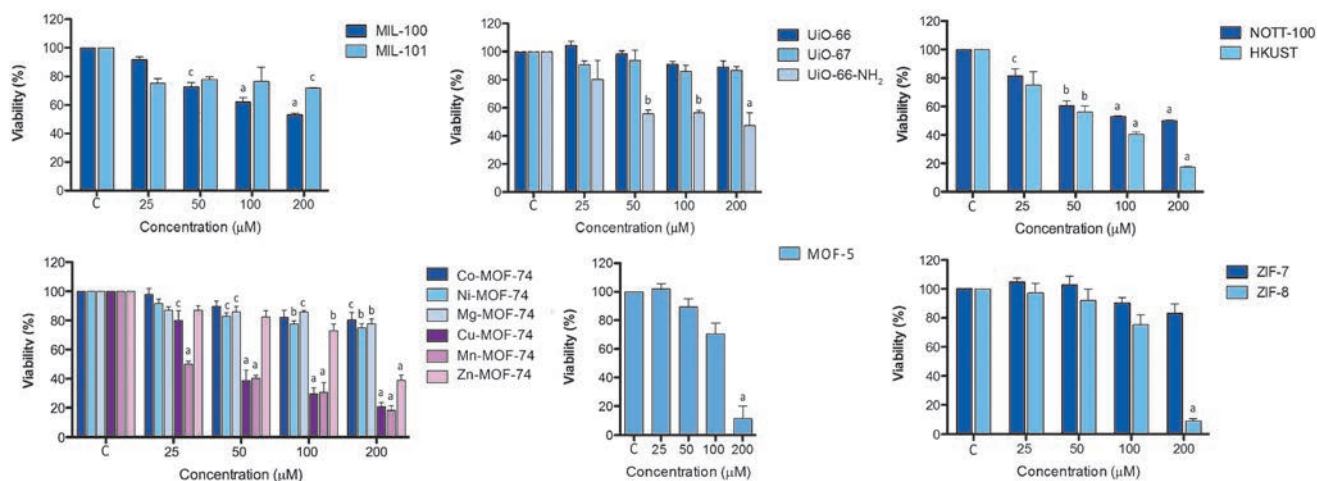## In vitro cytotoxicity of the nanoMOF components

The cytotoxicity of each organic ligand and each metal ion (as a chloride salt; except for MgSO$_4$) used to build the nanoMOFs was individually evaluated in HepG2 cells, using the XTT assay. The cells were exposed to a single organic ligand or metal salt at doses ranging from 1 to 200 μM for 24 h (see Figure S6 and S7). None of the organic ligands showed any significant cytotoxicity, even at the highest dose, nor did the Co^{II}, Ni^{II}, Zn^{II}, Zr^{IV} or Mg^{II} salts: cell viabilities were greater than 75% in all cases. In contrast, the Cu^{II} and Mn^{II} salts exhibited high cytotoxicity, even at low doses (5 to 10 μM); and Fe^{III} showed moderate to high cytotoxicity from 25 to 200 μM, respectively.

In vitro cytotoxicity of the nanoMOFs

The effect of each nanoMOF on cell viability was tested in HepG2 cells and in MCF7 cells using the XTT assay, at doses ranging from 25 to 200 μM, for 24 h and 72 h. Firstly, prior to the assay, the DMSO colloid of a given nanoMOF was mixed with the cell culture medium. We would like to mention that the formation and use of these colloids is an intermediate but necessary step for minimizing any possible aggregation of nanoMOFs in the cell-culture medium. However, despite this step, many of the nanoMOFs still gradually agglomerated in both media, forming soft agglomerates. Thus, under these conditions, we were unable to differentiate between toxicity arising from single nanocrystals of each nanoMOF and toxicity arising from their corresponding agglomerates.

For most of the nanoMOFs, their respective cytotoxicity depended on the cell type and on the concentration (see Figure 2 and Figure S8 in the Supporting Information). Interestingly, some of the nanoMOFs (Co-MOF-74, Mg-MOF-74, UiO-66, and UiO-67) showed little or no cytotoxicity, even at the highest dose (200 μM). Within the nanoMOF-74 family, the cytotoxicity of each member varied according to the metal component (Figure 2): those containing Co, Ni or Mg showed no marked cytotoxicity to either of the cell lines after 24 h of incubation, whereas those containing Cu, Mn or Zn showed high levels of cytotoxicity at the highest dose (200 μM). The viability levels observed in the cells exposed to the latter were 20.9 ± 2.7% (HepG2) and 38.2 ± 0.3% (MCF7) for nanoCu-MOF-74; 18.3 ± 3.0% (HepG2) and 32.4 ± 3.8% (MCF7) for nanoMn-MOF-74; and 38.8 ± 3.6% (HepG2) and 57.6 ± 0.6% (MCF7) for nanoZn-MOF-74. These results were generally consistent with those observed at 72 h (see Figure S8), although some differences were identified. For example, the cytotoxicity of nanoNi-MOF-74 to MCF7 cells was higher after 72 h, whereas that of nanoCu-MOF-74 to the same cells, and that of nanoZn-MOF-74 to HepG2 cells, were each lower after 72 h. NanoMIL-100 and -101 showed little or moderate toxicity to each cell line after 24 and 72 h. However, at its highest dose (200 μM) and 24 h incubation, nanoMIL-100 provoked a substantial decrease (53.2 ± 1.0%) in the viability of the HepG2 cells. After 72 h, nanoMIL-101 also led to a decrease in the viability (41.8 ± 7.3%) of HepG2 cells. None of the nanoUiO MOFs exhibited substantial cytotoxicity at either incubation time, except for
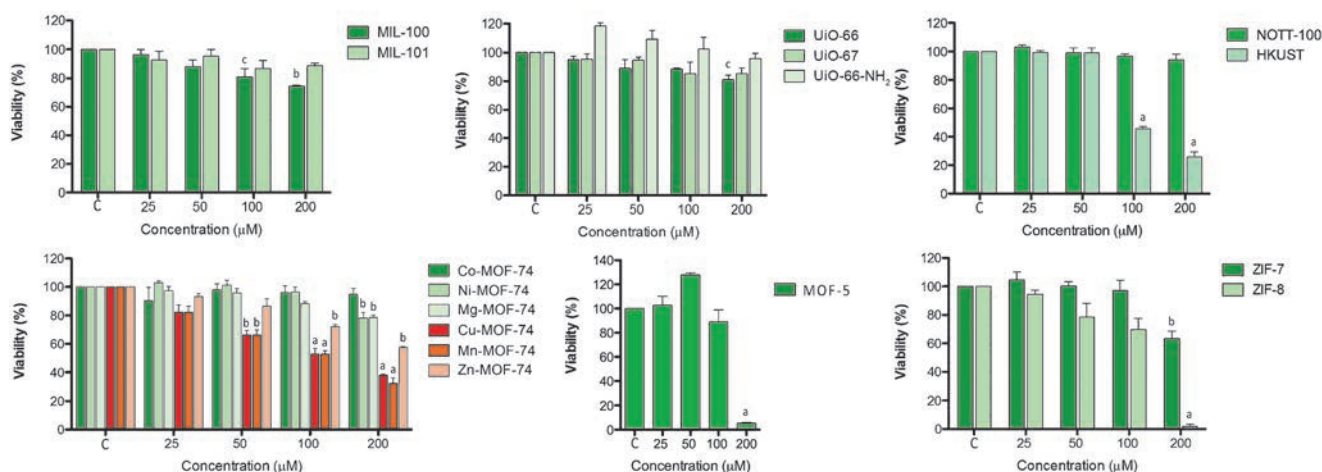
Figure 2. In vitro cytotoxicity of nanoMOFs to human cells. Cell viability of MCF7 or HepG2 cells after 24 h incubation with a single nanoMOF at one of various concentrations (25 to 200 μM). Untreated cells were used as controls (marked as C). Data represent the mean ±standard error of the mean (SEM) of three independent experiments. Significant differences from the control are marked accordingly ([c]$p < 0.05$, [b]$p < 0.01$, [a]$p < 0.005$).

nanoUiO-66-NH$_2$: at the highest dose (200 μM) and 24 h incubation, this material showed moderate cytotoxicity to HepG2 cells (47.2±9.4% viability). The results for the nanoZIF family of MOFs varied widely: nanoZIF-7 was not cytotoxic to the HepG2 cells and moderately cytotoxic to the MCF7 cells, whereas nanoZIF-8 was highly cytotoxic to both. Both nano-HKUST-1 and nanoNOTT-100 were highly cytotoxic to both cell lines at both incubation times: for example, at 200 μM and 24 h incubation, nanoHKUST-1 was highly toxic to HepG2 cells (17.4±0.5% viability). The only exception was nanoNOTT-100 at 200 μM after 24 h incubation in MCF7 cells (94.2±4.0% viability). Lastly, at 200 μM and 24 or 72 h incubation time, nano-MOF-5 was highly cytotoxic to both cell lines.

The toxicity of nanomaterials is widely accepted to derive from their chemical composition, through mechanisms such as dissolution and consequent release of toxic components (e.g., metal ions) or generation of reactive oxygen species, and/or to stress or stimuli caused by their surface reactivity, their size

and/or their shape.[37] Although distinguishing between these mechanisms is not trivial, our results indicate that the toxicity of nanoMOF crystals is at strongly related to their solubility and, therefore, to the release of solubilized (toxic) metal ions.

The solubility tests on the sixteen nanoMOFs confirmed that they are all at least partially soluble in cell culture media and show minimum percentage of degradation in solution, ranging from 0.3% (nanoUiO-67) to 62.9% (nanoMg-MOF-74). This degradation induces the release of their constituent metal ions and organic ligands into the media.

Given that free metal ions, rather than free organic ligands, have previously been imputed as the toxic agents in MOFs,[18] we focused our attention on the metal ions solubilized in the media. Indeed, we found that the most cytotoxic nanoMOFs in our assays were those that released sufficiently high amounts of soluble metal ions known to be moderately or highly cytotoxic in their free form (e.g., Cu^{II}, Mn^{II}, and Fe^{III}). For example, nanoCu-MOF-74, nanoHKUST-1, and nanoNOTT-100, all of

which are built from Cu^{II} ions, were highly soluble and toxic in our tests. We believe that this toxicity, similarly to that observed with other soluble nanomaterials,[36–40] might be attributed to the release and subsequent cellular uptake of Cu^{II} ions. For example, nanoCu-MOF-74 was highly cytotoxic and provoked a rapid toxic effect: at nanoCu-MOF-74 concentrations of 50 and 100 μm, and 24 h of incubation, the viability of treated HepG2 cells had decreased to approximately 40 and approximately 30%, respectively. This result is consistent with our cytotoxicity studies on free Cu^{II} ions (see Figure S6): for example, at a Cu$^{II}_s$ concentration of 50 μm and 24 h of incubation, the viability of treated HepG2 cells had dropped to 23.9%. Assuming a similar rate of release of Cu$^{II}_s$ over the entire range of concentrations, this viability value for Cu^{II} alone corresponds to approximately 50 μm of nanoCu-MOF-74 (47.9% of constituent Cu$^{II}_t$ lost; 38.7% cell viability for the same incubation time), approximately 55 μm of nanoHKUST-1 (30.3% of constituent Cu$^{II}_t$ lost; cell viability: < 60%) and approximately 63 μm of nano-NOTT-100 (39.4% of constituent Cu$^{II}_t$ lost; cell viability: < 60%) (see Figure 2). We observed a similar correlation between the cytotoxicity of free metal ions and the corresponding nanoMOFs in our studies on free Mn^{II} ions and on nanoMn-MOF-74. At the lowest concentration (25 μm) and 24 h of incubation, this nanoMOF caused the viability of HepG2 cells to decrease to 49.9%. At this concentration, a release of approximately 3 μm Mn$^{II}_s$ (13.3% of the constituent Mn$^{II}_t$) would be expected, which would correlated to cell viabilities of between 30 and 70%.

Unlike the aforementioned cases, the nanoMOFs that release significant amounts of soluble metal ions, but whose free constituent metal ion did not show cytotoxicity in the free form at the working concentrations [Co^{II}, Ni^{II}, or Mg^{II}], showed little or no toxicity. These include nanoMg-MOF-74, nanoCo-MOF-74, and nanoNi-MOF-74. Similarly, those nanoMOFs that do not release significant amounts of soluble metal ions showed low cytotoxicity. These include nanoMIL-100, nanoMIL-101, nanoUiO-66, nanoUiO-66-NH$_2$, nanoUiO-67, and nanoZIF-7. The only exceptions to this trend were three of the Zn^{II}-based nanoMOFs: nanoZn-MOF-74, nanoZIF-8, and nanoMOF-5. In all three cases, we expected the concentration of Zn$^{II}_s$ ions released from the nanoMOF to be lower than the maximum working concentration of 200 μm (at which free Zn^{II} ions did not show any significant cytotoxicity; in fact, the in vitro toxic concentration of Zn^{II} ions has been reported to be ca. 400 μm).[41] However, all three nanoMOFs caused high cytotoxicity at 200 μm. Interestingly, these results are consistent with recent studies on nanoIRMOF-3 that showed cytotoxicity to PC12 cells; in that study, cell viability was approximately 55% at 122 μm and < 20% at 488 μm.[42] They are also consistent with findings from studies on ZnO or Zn nanoparticles, the toxicity of which could not be imputed solely to their release of Zn^{II} ions into solution.[43] In fact, several authors have suggested that Zn nanoparticles might generate reactive oxygen species that induce oxidative stress[36,44–46] or that exhibit body burden or size effects; any of these factors might have contributed to the cytotoxicity that we observed in the Zn^{II}-based nanoMOFs.

In vivo toxicity in zebrafish embryos

We then evaluated the in vivo toxicity of nine of the sixteen nanoMOFs in zebrafish (*Danio rerio*) embryo, and subsequently compared the results to those corresponding to the in vitro assays. Zebrafish embryos have been used extensively to assay the in vivo toxicity of nanoparticles because they are comparable to mammalian systems and amenable to medium-to-high-throughput screening.[47–50] Zebrafish embryos exposed to different concentrations (1 to 200 μm) of a suspension of a single nanoMOF were assessed for several toxicity parameters every 24 h until 120 h post-fertilization (hpf): these include mortality, hatching rate, and appearance of abnormal phenotypes (e.g., low pigmentation, pericardial/yolk-sac edema, delayed development, bent spine, etc.).

We chose nine nanoMOFs for in vivo evaluation to represent a wide spectrum of cytotoxicity from the in vitro assays, including nontoxic or barely cytotoxic (nanoUiO-66, nanoUiO-67, and nanoCo-MOF-74, and nanoMg-MOF-74), moderately cytotoxic (nanoZIF-7, nanoMIL-100, and nanoMIL-101), and highly cytotoxic (nanoZIF-8 and nanoHKUST-1). To rule out any effects provoked by the 0.5% DMSO present in the three nanoMOF suspensions (1 μm, 20 μm and 200 μm), we also assessed its toxicity. At a final concentration of 0.5% in E3 medium, DMSO was found to have no visible effects on normal larvae development after 120 h exposure: no differences in survival rate, hatching rate, or phenotype were observed between the DMSO-treated group of larvae and the negative (untreated) control group.

Figure 3a shows the cumulative mortality of embryos from the assays. We found that at 120 h post fertilization (hpf), the vast majority of nanoMOFs had not altered embryo viability. Hence, the viabilities of the embryos exposed to nanoCo-MOF-74, nanoMg-MOF-74, nanoUiO-66, nanoUiO-67, nanoMIL-100, and nanoMIL-101 were not significantly different to those of the control (DMSO-treated) group. In contrast, nanoZIF-7, nanoZIF-8, and nanoHKUST-1 provoked significant decreases in embryo survival (Figure 3 and S9). NanoZIF-7 was slightly toxic at 200 μm (embryo viability at 120 hpf: 79.2%); nanoZIF-8 was more toxic at the same concentration (embryo viability at 120 hpf: 33.3%); and nanoHKUST-1 was extremely toxic at this concentration (viability: 0%); in fact, even at 20 μm nanoHKUST-1, none of the embryos treated with this nanoMOF had survived by 48 hpf (viability: 0%).

We quantified the hatching rate of the embryos in the nanoMOF-treated group and the control group. As shown in Figure 3b and c, some of the nanoMOF-treated group exhibited a significant concentration-dependent hatching delay. Many previous studies have reported that fish embryos exposed to nanoparticles exhibit delayed hatching,[40,47,51] although whether this delay is caused by the whole nanoparticles themselves or by their released constituent materials remains unknown.[52,53] Some researchers have proposed that the delay might be caused by interactions between the nanoparticles and the zebrafish hatching enzyme, which is crucial for digesting the inner layer of the chorion (the membrane surrounding the embryo).[52,54]
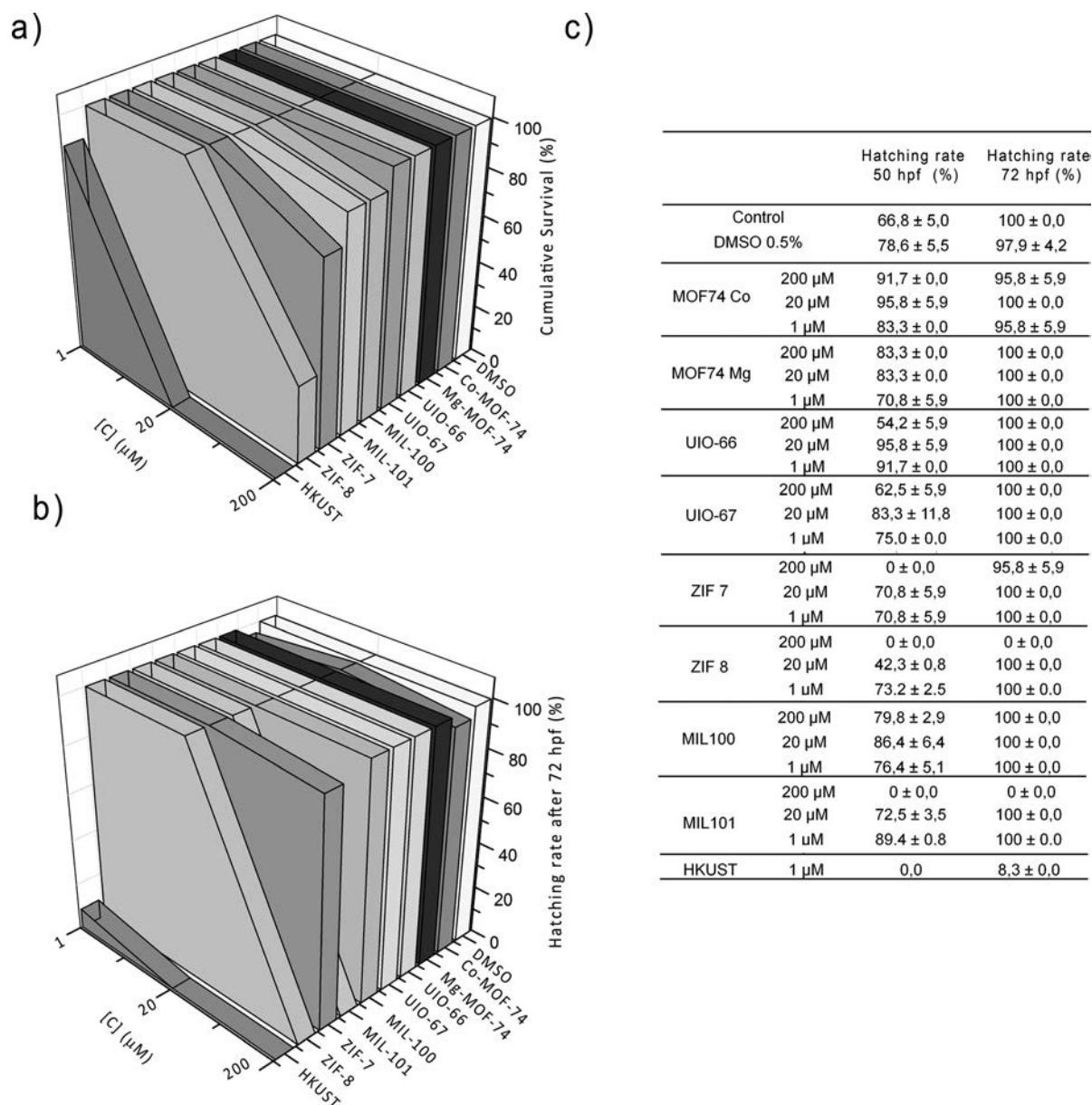
Figure 3. In vivo toxicity of nanoMOFs to zebrafish embryos. a) Cumulative survival of zebrafish larvae at 120 h post-fertilization (hpf) after exposure to a single nanoMOF at one of three concentrations (1, 20, or 200 μм). b) Concentration-dependent (1, 20, or 200 μм) effects of nanoMOFs on the hatching rates of zebrafish embryos at 120 hpf. c) Quantification of hatching rates (%) at 50 and 72 hpf.

When incubated under normal conditions, control embryos hatched from their chorion between 48 and 72 hpf (Figure 3 c), exhibiting slightly accelerated hatching, similar to an effect that has been previously reported.[55] However, the embryos incubated with nanoZIF-7 or nanoHKUST-1 hatched significantly later than did the control embryos (Figure 3 b and c, and Figure S10 in the Supporting Information), and of these two treated groups, only the nanoZIF-7 group reached 100% hatching rate. In the case of nanoHKUST-1, the hatching delay was only quantified at a nanoHKUST-1 dose of 1 μм, because no embryos survived at the higher doses. Interestingly, embryos exposed to the highest dose (200 μм) of nanoZIF-8 or nanoMIL-101 did not hatch at all by 120 hpf. It is important to mention here that nanoZIF-8 has an effect on the survival at this high-

est dose (200 μм). No significant hatching delay was observed in the groups exposed to nanoCo-MOF-74, nanoMg-MOF-74, nanoUiO-66, nanoUiO-67, or nanoMIL-100.

To further characterize the in vivo toxicity of nanoMOFs, we also quantified the morphological defects observed on the treated embryos after they had hatched (Figure 4 and Figure S11 in the Supporting Information). No significant malformations were found in the embryos that had been exposed to nanoMg-MOF-74; significant levels of yolk sac edema were found in the nanoCo-MOF-74, nanoUiO-66, nanoUiO-67, and nanoZIF-7 groups; concentration-dependent yolk sac edemas and significant pericardial edema was found in the nanoMIL-100 group. No further putative morphological defects could be detected in the groups exposed to 200 μм of nanoZIF-8 or
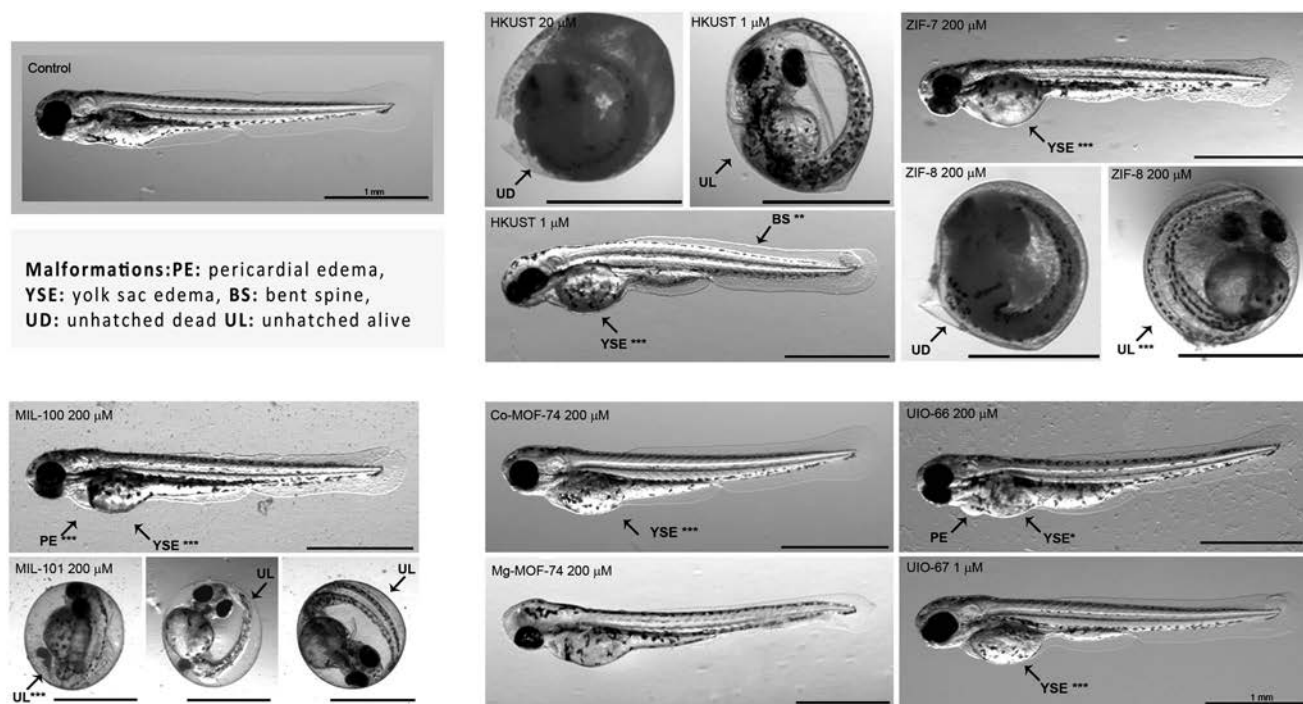
Figure 4. Malformations in zebrafish embryos that had been exposed to nanoMOFs. Representative images of embryos were taken after continuous exposure to nanoMOFs (72 hpf). The malformations were imaged and quantified. Significant differences from the control are marked accordingly (**p < 0.01, ***p < 0.005).

nanoMIL-101, due to their inability to hatch, although some morphological malformations were observed in the groups exposed to lower doses of nanoZIF-8 (pericardial edema, yolk-sac edema and bent spine) or nanoMIL-101 (yolk sac edema) (see Figure S11). Interestingly, significant levels of pericardial edema, yolk-sac edema, and bent spine were observed in the group that had been exposed to nanoHKUST-1 at the low dose of 1 μm; however, the malformations in the groups exposed to higher doses were not characterized because none of the embryos had survived.

Ranking of the in vivo toxicity of nanoMOFs

To compare the in vivo toxicity of the nine studied nanoMOFs, we quantified their in vivo effects on the zebrafish embryos using a scoring system that was first described by Peterson et al.[56,30] and subsequently modified by Nel et al.[47] Thus, we

scored the amount and severity of the phenotypic changes, on a scale from 0 to 4, whereby 0 = normal phenotype; 1 = a minor phenotypic change; 2 = multiple moderate alterations; 3 = severe embryo deformation; and 4 = no survival (see Table 2). The nanoMOFs scored as follows: 0 (nanoMg-MOF-74); 1 (nanoCo-MOF-74, nanoUiO-66, and nanoUiO-67); 2 (nanoMIL-100 and nanoZIF-7); 3 (nanoZIF-8 and nanoMIL-101); and 4 (nanoHKUST-1).

Comparison of the in vitro toxicity and the in vivo toxicity results for the nanoMOFs

We found a strong correlation between the in vitro toxicity results and the in vivo toxicity results for the nine nanoMOFs that were tested in both assays (Table 3). The only deviation from this trend was that observed for nanoMIL-101, which was

Table 2. Ranking of nanoMOFs by in vivo toxicity, according to a semiquantitative scoring system (adapted from Nel et al., 2011[47]; and Furgeson et al., 2009[30]).

Score	Attributes	nanoMOF	Morphological defects	Physiological defects
0	no morphological or physiological defects	nanoMg-MOF-74		
1	single morphological/physiological defect	nanoCo-MOF-74, nanoUiO-66 and nanoUiO-67	yolk sac edema	
2	multiple morphological and physiological defects	nanoMIL-100 and nanoZIF-7	pericardial and yolk sac edema, bent spine	mortality, reduced hatching rate
3	severe multiple morphological and physiological defects	nanoMIL-101 and nanoZIF-8	pericardial and yolk sac edema, bent spine	mortality, embryos failed to hatch
4	embryos do not survive	nanoHKUST-1	disintegrated embryo	

Table 3. Qualitative comparison between the in vitro and in vivo toxicity of the nanoMOFs studied in both assays.

Grade of toxicity	In vitro	In vivo
−	nanoMg-MOF-74, nanoCoMOF-74, nanoUiO-66 and nanoUiO-67	(0) nanoMg-MOF-74
+		(1) nanoCoMOF-74, nanoUiO-66 and nano-UiO-67
+ +	nanoMIL-100, nanoZIF-7 and nanoMIL-101	(2) nanoMIL-100 and nanoZIF-7
+ + +	nanoZIF-8	(3) nanoZIF-8 and nanoMIL-101
+ + + +	nanoHKUST-1	(4) nanoHKUST-1

more toxic to zebrafish embryos (adverse effect on hatching) than it was to HepG2 or MCF7 cells.

Conclusion

We have assessed the in vitro toxicity and in vivo toxicity of a series of representative, uncoated, nanoscale metal-organic frameworks (nanoMOFs). We first screened sixteen nanoMOFs against two human cell lines (HepG2 and MCF7), and then screened a diverse set of nine of these nanoMOFs in zebrafish embryos. We found a strong correlation between the in vitro toxicity results and the in vivo toxicity results, with nanoMg-MOF-74 being the least toxic in both assays. The only exception to this trend was nanoMIL-101, which was more toxic to embryos than to cell cultures. Our findings suggest that degradation of nanoMOFs in solution generates metal ions that strongly determine the toxicity of these nanomaterials. However, other factors might also influence the toxicity of nanoMOFs, including the formation of other species upon degradation, or certain crystal parameters (e.g., size, shape, charge, etc.). We affirm that more studies on the possible environmental and health risks of nanoMOFs must be performed before these new nanomaterials can be exploited for practical use.

Experimental Section

Materials

All reagents and solvents used in the nanoMOF syntheses were purchased from Sigma-Aldrich and Romil, respectively, and were used without any further purification.

NanoMOF synthesis

The nanoMOFs were prepared by using modified versions of reported methods.[1,32,33] The general procedures are detailed in the Supporting Information.

NanoMOF characterization

We characterized the synthesized nanoMOFs by XRPD, to determine their purity, and by transmission electron microscopy (TEM), field-emission scanning electron microscopy (FESEM) and dynamic light scattering (DLS), to determine their size distribution.

Stability studies

A carefully weighed sample of each nanoMOF was separately dispersed in 10 mL of DMEM medium with 10% FBS to achieve a final concentration of 10 mM. Each mixture was incubated at 37°C for 24 h with gentle stirring, and then centrifuged for 5 min at 10 000 rpm (Alegra 64R, Beckman Coulter). Each supernatant was characterized by ICP-OES with an Optima 4300DV unit (Perkin-Elmer) to determine the amount of solubilized metal ions. In parallel, each pellet was washed with 10 mL of deionized water to remove buffer salts, and then centrifuged. This process was repeated with methanol, and the resulting solids were dried in an oven at 90°C overnight, weighed and finally, characterized by XRPD. All the experiments were performed in triplicate.

Evaluation of the in vitro toxicity of the nanoMOFs and their constituent components to HepG2 and MCF7 cells

Human hepatocyte (HepG2) and breast cancer (MCF7) cell lines were separately incubated with a single nanoMOF, and then the effects of the nanoMOFs on cell viability were assessed by using the XTT (2,3-bis-(2-methoxy-4-nitro-5-sulfophenyl)-2H-tetrazolium-5-carboxanilide) cell viability assay[57] after 24 and 72 h incubation time. The cells were cultured in either DMEM (Dulbecco's modified Eagle's medium, Invitrogen; for HepG2 cells) or DMEM F12 (for MCF7 cells), containing GlutaMax 1 and supplemented with 10% (v/v) heat-inactivated fetal bovine serum (FBS) (Invitrogen) at 37°C, 5% CO_2 and 95% humidity. The cells were seeded into 96-well plates (cell density: 4.0×10^3 cells/well), incubated for 24 h, and then exposed to fresh medium containing a DMSO suspension of the desired nanoMOF (concentrations: 25 to 200 μM). At 24 and 72 h incubation, aliquots of 20 μL of XTT solution were added to each well, and the resulting color was quantified ($\lambda = 450$ nm) in a spectrophotometric plate-reader (PerkinElmer Victor3 V). Cell viability was expressed as a percentage of the control level. All the measurements were performed in triplicate, in three independent experiments. The same procedure was employed to separately evaluate the cytotoxicity of each nanoMOF component (metal salt or organic ligand) to HepG2 cells, except at a concentration range from 1 to 200 μM and at 24 h incubation time. Differences among the data were analyzed by using one-way ANOVA, followed by Tukey's post test ($p < 0.001$).

Exposure of zebrafish embryos to nanoMOFs

Adult zebrafish (*Danio rerio*) were maintained in tanks with recirculating water under a 14 h light/10 h dark cycle at 28°C. Male and female zebrafish were set up in pairs for breeding in breeding tanks. A grid insert in the tanks enabled the resulting embryos to fall to the bottom, avoiding parental predation. The embryos were collected in E3 medium (5 mM NaCl, 0.17 mM KCl, 0.33 mM $CaCl_2$, 0.33 mM $MgSO_4$ and 0.1% Methylene Blue), rinsed carefully to remove debris, and kept at 28°C in an incubator. The embryos were visually assessed with a microscope (Olympus, CKX31, Japan) for viability and developmental stage, and the selected healthy specimens were plated into 96-well plates at 1 embryo/well. Starting at 5 h post-fertilization, the embryos were exposed to 200 μL/well of a solution of a single nanoMOF at different concentrations

(1, 20, and 200 μm; final concentration of DMSO in E3 medium: 0.5%), or to a DMSO control solution (0.5% DMSO in E3 medium), or to E3 medium alone (negative control). The embryos were assessed for hatching rate, cumulative mortality and malformations at 24, 48, 72, 96, and 120 hpf. Screening for morphological defects included the assessment of abnormally developed eyes; lack of somite formation; delayed development; pericardial edema; yolk-sac edema; irregular pigmentation; tail malformation; and/or a bent spine. The most frequently found malformations (pericardial edema, yolk-sac edema, and bent spine), were quantified. Embryos with abnormal morphologies were anaesthetized with ethyl 3-aminobenzoate methanesulfonate (160 ppm MS-222, Sigma), transferred onto microscope slides, and then photographed in a Leica Stereomicroscope MZ FLIII. Each condition was tested in 24 individuals. All experimental procedures were submitted to the Ethical Committee of the Universitat Autònoma de Barcelona, and the procedures follow the International Guiding Principles for Research Involving Animals.

Acknowledgements

[1] A. Carné, C. Carbonell, I. Imaz, D. Maspoch, *Chem. Soc. Rev.* **2011**, *40*, 291–305.

[2] H. Furukawa, K. E. Cordova, M. O'Keeffe, O. M. Yaghi, *Science* **2013**, *341*, 974–980.

[3] W. Lin, W. J. Rieter, K. M. L. Taylor, *Angew. Chem. Int. Ed.* **2009**, *48*, 650–658; *Angew. Chem.* **2009**, *121*, 660–668.

[4] D. Tanaka, A. Henke, K. Albrecht, M. Moeller, K. Nakagawa, S. Kitagawa, J. Groll, *Nat. Chem.* **2010**, *2*, 410–418.

[5] K. H. Park, K. Jang, S. U. Son, D. A. Sweigart, *J. Am. Chem. Soc.* **2006**, *128*, 8740–8741.

[6] L. J. Zhang, F. L. Jiang, Y. F. Zhou, W. T. Xu, M. C. Hong, *Tetrahedron* **2013**, *69*, 9237–9244.

[7] W. J. Rieter, K. M. L. Taylor, W. Lin, *J. Am. Chem. Soc.* **2007**, *129*, 9852–9853.

[8] T. Rodenas, M. van Dalen, E. García-Pérez, P. Serra-Crespo, B. Zornoza, F. Kapteijn, J. Gascon, *Adv. Funct. Mater.* **2014**, *24*, 249–256.

[9] Y.-S. Li, H. Bux, A. Feldhoff, G.-L. Li, W.-S. Yang, J. Caro, *Adv. Mater.* **2010**, *22*, 3322–3326.

[10] a) P. Horcajada, T. Chalati, C. Serre, B. Gillet, C. Sebrie, T. Baati, J. F. Eubank, D. Heurtaux, P. Clayette, C. Kreuz, J. S. Chang, Y.-K. Hwang, V. Marsaud, P. N. Bories, L. Cynober, S. Gil, G. Ferey, P. Couvreur, R. Gref, *Nat. Mater.* **2010**, *9*, 172–178; b) W. Morris, W. E. Briley, E. Auyeung, M. D. Cabezas, C. A. Mirkin, *J. Am. Chem. Soc.* **2014**, *136*, 7261–7264.

[11] I. B. Vasconcelos, T. G. da Silva, G. C. G. Militao, T. A. Soares, N. A. Rodrigues, M. O. Rodrigues, N. B. da Costa Jr., R. O. Freire, S. A. Junior, *RSC Adv.* **2012**, *2*, 9437–9442.

[12] J. Zhuang, C.-H. Kuo, L.-Y. Chou, D.-Y. Liu, E. Weerapana, C.-K. Tsung, *ACS Nano* **2014**, *8*, 2812–2819.

[13] S. Diring, D. O. Wang, C. Kim, M. Kondo, Y. Chen, S. Kitagawa, K.-I. Kamei, S. Furukawa, *Nat. Commun.* **2013**, *4*, 2684.

[14] N. J. Hinks, A. C. McKinlay, B. Xiao, P. S. Wheatley, R. E. Morris, *Microporous Mesoporous Mater.* **2010**, *129*, 330–334.

[15] a) J. Della Rocca, W. Lin, *Eur. J. Inorg. Chem.* **2010**, 3725–3734; b) G. A. Pereira, J. A. Peters, F. A. Almeida Paz, J. Rocha, C. F. G. C. Geraldes, *Inorg. Chem.* **2010**, *49*, 2969–2974; c) A. Foucault-Collet, K. A. Gogick,

[16] W. J. Rieter, K. M. Pott, K. M. L. Taylor, W. Lin, *J. Am. Chem. Soc.* **2008**, *130*, 11584–11585.

[17] T. Baati, L. Njim, F. Neffati, A. Kerkeni, M. Bouttemi, R. Gref, M. F. Najjar, A. Zakhama, P. Couvreur, C. Serre, P. Horcajada, *Chem. Sci.* **2013**, *4*, 1597–1607.

[18] C. Tamames-Tabar, D. Cunha, E. Imbuluzqueta, F. Ragon, C. Serre, M. J. Blanco-Prieto, P. Horcajada, *J. Mater. Chem. B* **2014**, *2*, 262–271.

[19] T. Chalati, P. Horcajada, P. Couvreur, C. Serre, M. Ben Yahia, G. Maurin, R. Gref, *Nanomedicine* **2011**, *6*, 1683–1695.

[20] P. Horcajada, R. Gref, T. Baati, P. K. Allan, G. Maurin, P. Couvreur, G. Férey, R. Morris, C. Serre, *Chem. Rev.* **2012**, *112*, 1232–1268.

[21] P. Horcajada, S. Surble, C. Serre, D.-Y. Hong, Y.-K. Seo, J. S. Chang, J. M. Grenèche, *Chem. Commun.* **2007**, 2820–2822.

[22] S. Bauer, C. Serre, T. Devic, P. Horcajada, J. Marrot, G. Férey, N. Stock, *Inorg. Chem.* **2008**, *47*, 7568–7576.

[23] H. Li, M. Eddaoudi, M. O'Keeffe, O. M. Yaghi, *Nature* **1999**, *402*, 276–279.

[24] a) N. L. Rosi, J. Kim, M. Eddaoudi, B. Chen, M. O'Keeffe, O. M. Yaghi, *J. Am. Chem. Soc.* **2005**, *127*, 1504–1518; b) P. D. C. Dietzel, Y. Morita, R. Blom, H. Fjellvåg, *Angew. Chem. Int. Ed.* **2005**, *44*, 6354–6358; *Angew. Chem.* **2005**, *117*, 6512–6516.

[25] a) K. S. Park, Z. Ni, A. P. Côté, J. Y. Choi, R. Huang, F. J. Urbe-Romo, H. K. Chae, M. O'Keeffe, O. M. Yaghi, *Proc. Natl. Acad. Sci. USA* **2006**, *103*, 10186–10191; b) X.-C. Huang, Y.-Y. Lin, J.-P. Zhang, X.-M. Chen, *Angew. Chem. Int. Ed.* **2006**, *45*, 1557–1559; *Angew. Chem.* **2006**, *118*, 1587–1589.

[26] J. H. Cavka, S. Jakobsen, U. Olsbye, N. Guillou, C. Lamberti, S. Bordiga, K. P. Lillerud, *J. Am. Chem. Soc.* **2008**, *130*, 13850–13851.

[27] S. S.-Y. Chui, S. M.-F. Lo, J. P. H. Charmant, A. G. Orpen, I. D. Williams, *Science* **1999**, *283*, 1148–1150.

[28] B. Chen, N. W. Ockwig, A. R. Millward, D. S. Contreras, O. M. Yaghi, *Angew. Chem. Int. Ed.* **2005**, *44*, 4745–4749; *Angew. Chem.* **2005**, *117*, 4823–4827.

[29] C. Parng, *Curr. Opin. Drug Discov. Devel.* **2005**, *8*, 100–106.

[30] O. Bar-Ilan, R. M. Albrecht, V. E. Fako, D. Y. Furgeson, *Small* **2009**, *5*, 1897–1910.

[31] S. Lin, Y. Zhao, A. E. Nel, S. Lin, *Small* **2013**, *9*, 1608–1618.

[32] M. Sindoro, N. Yanai, A.-Y. Jee, S. Granick, *Acc. Chem. Res.* **2014**, *47*, 459–469.

[33] J. Della Rocca, D. Liu, W. Lin, *Acc. Chem. Res.* **2011**, *44*, 957–968.

[34] A. Carné-Sánchez, I. Imaz, M. Cano-Sarabia, D. Maspoch, *Nat. Chem.* **2013**, *5*, 203–211.

[35] T. W. Turney, M. B. Duriska, V. Jayaratne, A. Elbaz, S. J. O'Keefe, A. S. Hastings, T. J. Piva, P. F. A. Wright, B. N. Feltis, *Chem. Res. Toxicol.* **2012**, *25*, 2057–2066.

[36] C. Shen, S. A. James, M. D. de Jonge, T. W. Turney, P. F. A. Wright, B. N. Feltis, *Toxicol. Sci.* **2013**, *136*, 120–130.

[37] T. J. Brunner, P. Wick, P. Manser, P. Spohn, R. N. Grass, L. K. Limbach, A. Bruinink, W. J. Stark, *Environ. Sci. Technol.* **2006**, *40*, 4374–4381.

[38] Y.-N. Chang, M. Zhang, L. Xia, J. Zhang, G. Xing, *Materials* **2012**, *5*, 2850–2871.

[39] M. Ates, J. Daniels, Z. Arslan, I. O. Farah, H. F. Rivera, *Environ. Sci. Processes Impacts* **2013**, *15*, 225–233.

[40] W. Bai, Z. Zhang, W. Tian, X. He, Y. Ma, Y. Zhao, Z. Chai, *J. Nanopart. Res.* **2010**, *12*, 1645–1654.

[41] R. D. Palmiter, *Proc. Natl. Acad. Sci. USA* **2004**, *101*, 4918–4923.

[42] F. Ren, B. Yang, J. Cai, Y. Jiang, J. Xu, S. Wang, *J. Hazardous Mater.* **2014**, *271*, 283–291.

[43] V. Valdiglesias, C. Costa, G. Kiliç, S. Costa, E. Pásaro, B. Laffon, J. P. Teixeira, *Environ. Int.* **2013**, *55*, 92–100.

[44] A. Nel, T. Xia, L. Mädler, N. Li, *Science* **2006**, *311*, 622–627.

[45] T. Xia, M. Kovochich, J. Brant, M. Hotze, J. Sempf, T. Oberley, C. Sioutas, J. I. Yeh, M. R. Wiesner, A. E. Nel, *Nano Lett.* **2006**, *6*, 1794–1807.

[46] J. She, Z. Xiao, Y. Yang, S. Deng, J. Chen, G. Yang, N. Xu, *ACS Nano* **2008**, *2*, 2015–2022.

[47] S. George, T. Xia, R. Rallo, Y. Zhao, Z. Ji, S. Lin, X. Wang, H. Zhang, B. France, D. Schoenfeld, R. Damoiseaux, R. Liu, S. Lin, K. A. Bradley, Y. Cohen, A. Nel, *ACS Nano* **2011**, *5*, 1805–1817.

[48] X. Zhao, K. J. Ong, J. D. Ede, J. L. Stafford, K. W. Ng, G. G. Goss, S. C. J. Loo, *Small* **2013**, *9*, 1734–1741.

[49] B. J. Shaw, R. D. Handy, *Environ. Int.* **2011**, *37*, 1083–1097.

[50] S. Lin, X. Wang, Z. Ji, C. H. Chang, Y. Dong, H. Meng, Y.-P. Liao, M. Wang, T.-B. Song, S. Kohan, T. Xia, J. I. Zink, S. Lin, A. E. Nel, *ACS Nano* **2014**, *8*, 4450–4464.

[51] J. Cheng, E. Flahaut, S. H. Cheng, *Environ. Toxicol. Chem.* **2007**, *26*, 708–716.

[52] T. Xia, Y. Zhao, T. Sager, S. George, S. Pokhrel, N. Li, D. Schoenfeld, H. Meng, S. Lin, X. Wang, M. Wang, Z. Ji, J. I. Zink, L. Mädler, V. Castranova, S. Lin, A. E. Nel, *ACS Nano* **2011**, *5*, 1223–1235.

[53] X. Zhu, J. Wang, X. Zhang, Y. Chang, Y. Chen, *Nanotechnology* **2009**, *20*, 195103–195112.

[54] K. J. Ong, X. Zhao, M. E. Thistle, T. J. MacCormack, R. J. Clark, G. Ma, Y. Martinez-Rubi, B. Simard, J. S. C. Loo, J. G. C. Veinot, G. G. Goss, *Nanotoxicology* **2014**, *8*, 295–304.

[55] K. Fent, C. J. Weisbroda, A. Wirth-Heller, U. Pieles, *Aquat. Toxicol.* **2010**, *100*, 218–228.

[56] T. C. King Heiden, E. Dengler, W. J. Kao, W. Heideman, R. E. Peterson, *Toxicol. Appl. Pharmacol.* **2007**, *225*, 70–79.

[57] A. H. Cory, T. C. Owen, J. A. Barltrop, J. G. Cory, *Cancer Commun.* **1991**, *3*, 207–212.

Resonant spin tunneling in randomly oriented nanospheres of Mn$_{12}$ acetate

S. Lendínez, R. Zarzuela, and J. Tejada

Departament de Física Fonamental, Facultat de Física, Universitat de Barcelona, Martí i Franquès 1, 08028 Barcelona, Spain

M. W. Terban and S. J. L. Billinge[*]

Department of Applied Physics and Applied Mathematics, Columbia University, New York, New York 10027, USA

J. Espin, I. Imaz, and D. Maspoch[†]

Institut Català de Nanotecnologia, ICN2, Esfera Universitat Autònoma Barcelona (UAB), Campus UAB, 08193 Bellaterra, Spain

E. M. Chudnovsky

Physics Department, Lehman College, City University of New York, 250 Bedford Park Boulevard West, Bronx, New York 10468-1589, USA

We report measurements and theoretical analysis of resonant spin tunneling in randomly oriented nanospheres of a molecular magnet. Amorphous nanospheres of Mn$_{12}$ acetate have been fabricated and characterized by chemical, infrared, TEM, x-ray, and magnetic methods. Magnetic measurements have revealed sharp tunneling peaks in the field derivative of the magnetization that occur at the typical resonant field values for the Mn$_{12}$ acetate crystal in the field parallel to the easy axis. Theoretical analysis is provided that explains these observations. We argue that resonant spin tunneling in a molecular magnet can be established in a powder sample, without the need for a single crystal and without aligning the easy magnetization axes of the molecules. This is confirmed by reanalyzing the old data on a powdered sample of nonoriented micron-size crystals of Mn$_{12}$ acetate. Our findings can greatly simplify the selection of candidates for quantum spin tunneling among newly synthesized molecular magnets.

PACS number(s): 75.50.Xx, 81.07.−b, 75.50.Tt, 75.45.+j

I. INTRODUCTION

Spin tunneling in molecular magnets has been the subject of intensive research in the last 20 years [1,2]. These systems exhibit unique quantum features that show up in macroscopic experiments. Among them are stepwise quantum hysteresis due to resonant tunneling at discrete values of the magnetic field [3–5], topological Berry phase effects [6], magnetic deflagration [7,8], and Rabi oscillations [9,10]. Most recently, experiments with individual magnetic molecules bridged between conducting leads and molecules grafted on carbon nanotubes have been performed that permit readout of quantum states of individual atomic nuclei [11,12]. Quantum superposition of spin states in magnetic molecules makes them candidates for qubits—elements of quantum computers [13].

Beginning with the discovery of resonant spin tunneling in Mn$_{12}$ acetate [3] it has been generally believed that at the macroscopic level the effect can only be observed in a single crystal or in an array of microcrystallites whose crystallographic axes are aligned. The latter method was used in Refs. [3,4], and in a few subsequent publications by the same authors, before sufficiently large single crystals of molecular magnets had become available. Nowadays a large number of new molecular magnets are synthesized by chemists every year and subsequently tested by physicists for the presence

of spin tunneling. In many cases growing a sufficiently large single crystal is a challenging task as compared to growing microcrystals. At the same time the effectiveness of the room-temperature alignment of microscrystals by a high magnetic field in, e.g., an epoxy, strongly depends on the shape of the crystallites and may also be incompatible with their chemistry.

In this paper we show that neither macroscopic single crystals or the alignment of microcrystals are necessary to obtain solid evidence of spin tunneling in macroscopic magnetic measurements of molecular magnets. This can be done by simply measuring the magnetization curve, $M(H)$, and plotting the derivative of the magnetization on the magnetic field, dM/dH. To illustrate this point we use amorphous nanospheres of Mn$_{12}$ acetate [14,15]. Such nanospheres neither form crystals nor allow alignment of easy magnetization axes of Mn$_{12}$ molecules in a high magnetic field because of their isotropic magnetic susceptibility.

First magnetic measurements of similar Mn$_{12}$ nanoparticles were performed in Refs. [14,15] where peaks in dM/dH were observed and attributed to quantum tunneling. However, no explanation of such observation in a disordered sample has been provided. The zero-field-cooled magnetization curve of the measured sample revealed a large, up to 40%, fraction of fast-relaxing species of Mn$_{12}$ acetate. This resulted in a complicated pattern of displaced tunneling maxima as compared to typical resonances in a Mn$_{12}$ crystal, in the field parallel to the easy axis, that are separated by about 4.6 kOe.

Highly amorphous Mn$_{12}$ particles used in our experiments did not show any visible presence of the second species. Sharp tunneling maxima in dM/dH have been observed. Their location coincided with the position of tunneling maxima in a

---

Mn_{12} crystal. We provide theoretical analysis that explains observation of tunneling resonances in a fully disordered sample. The predicted postresonance field dependence of the peaks agrees with experiment. The practical value of this observation is that it can greatly reduce the preliminary work by chemists that is required to search for quantum spin tunneling in newly synthesized molecular magnets. As long as the magnetic molecules preserve their structure, the disordered sample of crystallites of any size is sufficient for that task. This was previously shown by studies of zero-field magnetic relaxation in Mn_{12} clusters frozen in solutions [16] and in highly disordered samples of Mn_{12} benzoate [17].

The paper is structured as follows. Fabrication and characterization of the samples by various techniques are discussed in Sec. II. Measurements of the field and temperature dependence of the magnetization, and of the ac susceptibility, are presented in Sec. III. They are analyzed and explained in Sec. IV. Section V summarizes our results and offers some final remarks.

II. FABRICATION AND CHARACTERIZATION OF Mn_{12} NANOSPHERES

To obtain spherical Mn_{12} acetate particles showing the highest degree of amorphous character, they were synthesized using a method adapted from the earlier publication [14]. In a typical experiment, 60 mg of Mn_{12} acetate was dissolved in 15 ml of acetonitrile. The solution was added to 30 ml of toluene under vigorous stirring. Precipitation of a brown solid was observed. One hour later the resulting dispersion was centrifuged ($4' \times 8000$ rpm) and the supernatant was collected. The pellet was redispersed with acetonitrile:toluene (1:2), centrifuged again, and the supernatant was collected again. Both supernatants were then mixed and dried under vacuum conditions. 5.8 mg of a brown solid (10% yield) was collected and stored in vacuum.

Scanning and transmission electron microscopy (SEM and TEM) images of the brown solid revealed the formation of uniform spherical particles; see Fig. 1. The size of the particles was calculated from FESEM images by averaging the diameter of at least 300 particles from different areas of the sample. An average size of 237 ± 69 nm and a median size of 238 nm were determined. This average size was further confirmed by dynamic light scattering (DLS). The chemical correspondence with bulk $[Mn_{12}O_{12}(CH_3COO)_{16}(H_2O)_4]$ crystals was confirmed by elemental analysis and by the positive matching between the IR spectra; see Fig. 2. As we shall see below, the additional evidence of the conventional structure of Mn_{12} molecules in the nanospheres follows from the magnetic measurements that reveal the resonant spin tunneling at the same values of the magnetic field as for the single crystals of Mn_{12} acetate.

To confirm the amorphous character of spherical Mn_{12} particles, x-ray studies have been conducted on the beamline X17A at the National Synchrotron Light Source at Brookhaven National Laboratory. Scattering intensity was measured from high-energy x rays at an energy of 67.419 keV using the rapid acquisition pair distribution function (RAPDF) technique [18,19]. A large-area 2-D Perkin Elmer detector with 2048×2048 pixels and $200 \times 200 \, \mu m$ pixel size was mounted
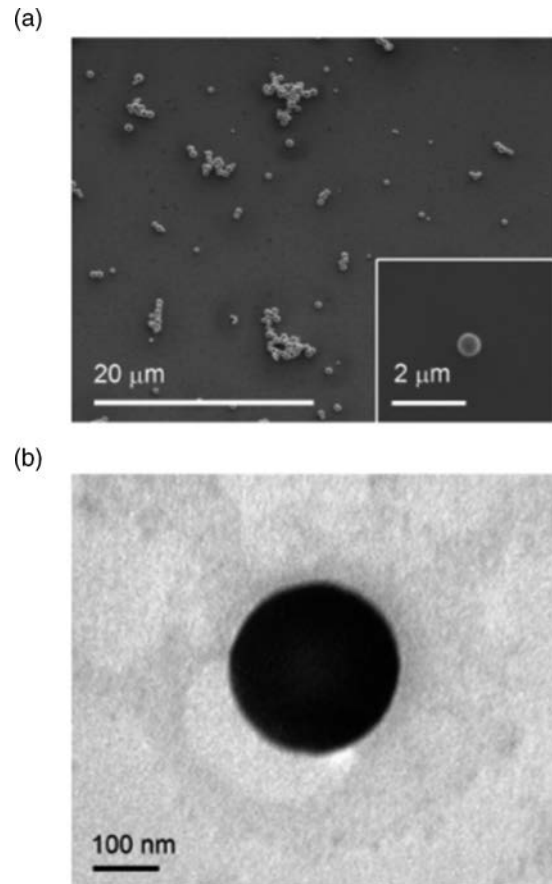

FIG. 1. (a) Representative SEM image of Mn_{12} acetate spherical particles. Inset: Individual particle. (b) TEM image of an individual Mn_{12} acetate nanosphere.

orthogonal to the beam path with a sample-to-detector distance of 206.1371 mm. Two samples have been measured for comparison: The sample of conventionally grown elongated micron-size crystallites of Mn_{12} acetate and the sample of Mn_{12} nanospheres described above.
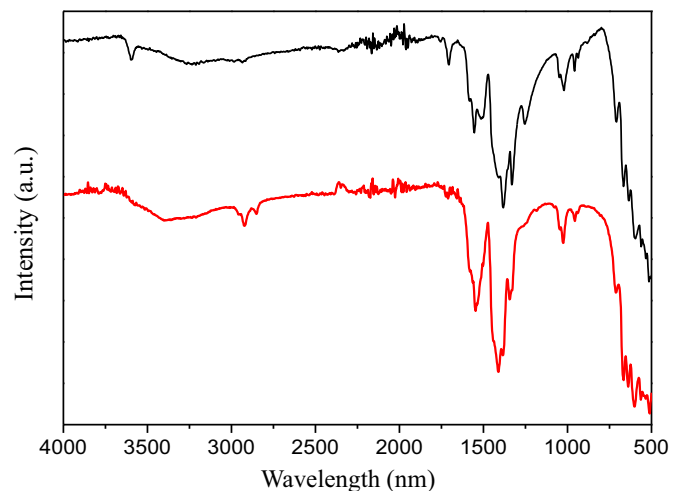

FIG. 2. (Color online) IR spectra of bulk Mn_{12} acetate crystals (black) and amorphous Mn_{12} acetate nanospheres (red).
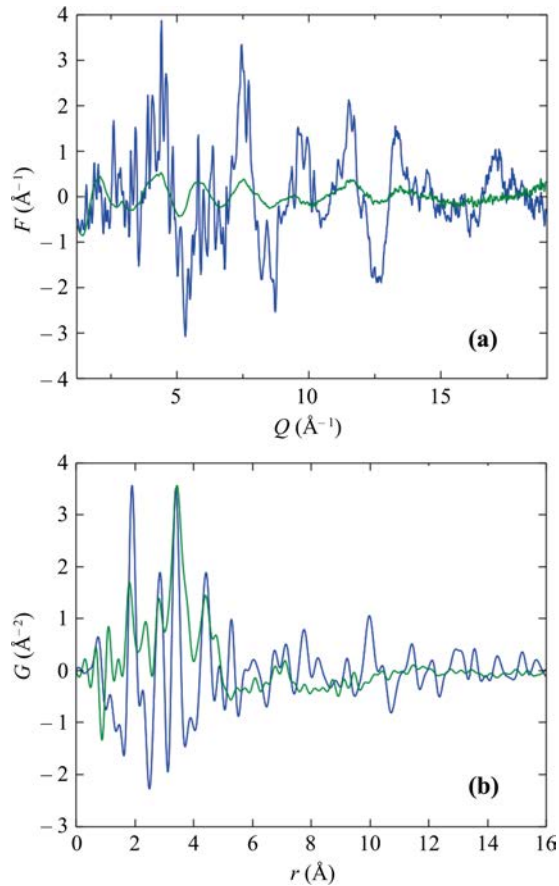
FIG. 3. (Color online) (a) Structure factors for microscrystals (blue) and nanospheres (green) of Mn_{12} acetate. (b) Superimposed pair distribution functions for microscrystals (blue) and nanospheres (green) of Mn_{12} acetate.

Structure factors and pair distribution functions for the two samples are shown in Fig. 3. While distinct Bragg picks of Mn_{12} acetate [20,21] are present in the microcrystalline sample, a very diffused intensity has been found in the nanospheres. Same differences have been observed in the RAPDF, indicating a high level of disorder in the nanospheres. They must be either extremely defected or amorphous. As we shall see from magnetic measurements, however, the Mn_{12} molecules are well preserved in the nanospheres despite the structural disorder.

Amorphous or highly disordered structure of Mn_{12} nanospheres raises the question of whether the easy axes of Mn_{12} molecules inside the spheres are aligned or disordered. One should notice in this connection that the direction of the easy axis is related to the orientation of the molecules while the Bragg peaks in the x-ray scattering are related to the translational order in a crystal. In an amorphous solid the orientation of local crystallographic axes is more robust than the translational order [22]. It may spread well beyond the amorphous structure factor. Evidence of the extended correlations in the orientation of local magnetic anisotropy axes has been previously reported in amorphous magnets [23].

In principle, spectroscopic studies of disordered samples, such as high-frequency electron spin resonance (HFESR) and frequency-domain magnetic-resonance
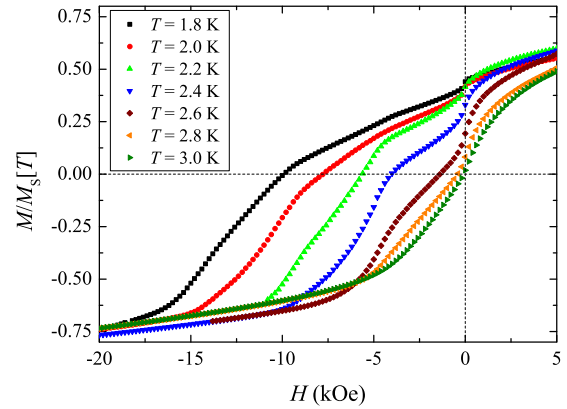

FIG. 4. (Color online) $H < 0$ branch of the hysteresis curves of the disordered powder of Mn_{12} nanospheres at different temperatures.

spectroscopy (FDMRS), combined with theoretical models that incorporate the effects of disorder and dipolar broadening on spin tunneling, may shed light on the structure of magnetic clusters and the orientation of easy axis, as has been demonstrated in Ref. [17] for nearly amorphous samples of Mn_{12} benzoate. Similar information has been obtained in Ref. [24] for a partially ordered sample of magnetic molecules deposited on surfaces by using synchrotron-based spectroscopic techniques combined with the study of angular dependence of the magnetic hysteresis and theoretical modeling. Such analysis is rather involved and depends on the model of disorder. For the conclusions made in this paper it does not matter whether the easy axes of the molecules are disordered at the level of individual nanospheres, or due to the random orientation of nanospheres, or both.

III. MAGNETIC MEASUREMENTS

Low-temperature magnetic measurements have been carried out on a compressed powdered sample inside a commercial rf-SQUID Quantum Design magnetometer. Before conducting the measurements, an attempt was made to orient the nanoparticles by a high magnetic field at room temperature in the epoxy, as has been done previously with micron-size microcrystals. Contrary to the latter case, the orienting procedure applied to the nanospheres rendered no difference in the magnetization data. This can be understood from the fact that micron-size crystallites of Mn_{12} acetate grow elongated along the easy magnetization axis. The resulting anisotropy of their magnetic susceptibility then enables the alignment of the crystallites by a high magnetic field in a Stycast, even though the molecules do not have magnetic moments at room temperature. This method, however, does not work for the Mn_{12} nanoparticles of spherical shape.

Negative branches of hysteresis curves are shown in Fig. 4. At the lowest temperature used, when thermal effects are weak, $M(0)$ is about one-half of the saturation value, M_S. This corresponds to the magnetic moments of Mn_{12} molecules looking randomly into a hemisphere, which follows from

$$\frac{M(0)}{M_S} = \frac{1}{4\pi} \int_0^{2\pi} d\phi \int_0^{\pi/2} \sin\theta \, d\theta = \frac{1}{2}. \qquad (1)$$
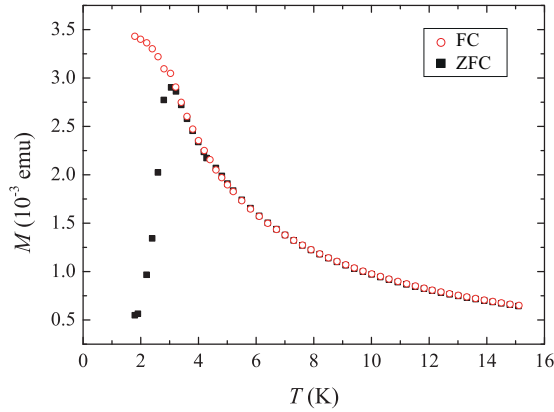
FIG. 5. (Color online) Field-cooled (FC) and zero-field-cooled (ZFC) magnetization vs temperature curves for a disordered powder of Mn_{12} nanospheres in the dc field of 100 Oe.

The latter is true regardless of whether the disorder in the orientation of easy magnetization axes occurs at the level of individual Mn_{12} molecules inside amorphous nanospheres or at the level of the nanospheres, each having a coherent orientation of the easy axes of the molecules.

Field-cooled (FC) and zero-field-cooled (ZFC) magnetization curves are shown in Fig. 5. High-temperature behavior is a $1/T$ Curie law. Figure 6 shows the ac susceptibility of the Mn_{12} nanospheres. The maximum in both families of curves occurs at the blocking temperature, T_B, determined by the magnetic moments that reverse their orientation on the time scale of the measurement, $t = t_0 \exp[U(H)/T_B]$, with t_0 being the attempt time and $U(H)$ being the energy barrier. In the ac measurements $t \sim 1/f$, so that T_B scales with the frequency of the ac field as $U(H)/\ln(1/t_0 f)$, which is in accordance with the data; see the inset in Fig. 6(b). The estimated values for the attempt time and the energy barrier at zero field are $t_0 = (5 \pm 1) \times 10^{-8}$ s and $U(0) = 69 \pm 2$ K, respectively.

The one-maximum structure of the curves shown in Figs. 5 and 6 contrasts with a pronounced two-maxima structure observed in Refs. [14,15], with the second, lower maximum occurring at a lower temperature. The latter, according to the authors of Refs. [14,15], where spherical nanoparticles of average size under 50 nm were studied, corresponded to the presence of 40% fast-relaxing species of Mn_{12} acetate. If such a species were present in our highly amorphous, larger spherical particles, it would have had a very low abundance. This simplifies the analysis of the data presented in the next section.

Figure 7 shows the derivative, dM/dH, along the negative branch of the hysteresis curve shown in Fig. 4, for two temperatures. The observed zero-field maximum has a width of about 1 kOe and is much more narrow than the zero-field maximum observed in Refs. [14,15]. There are clear maxima at $H_1 \approx 4.6$ kOe and $H_2 \approx 9.2$ kOe as in a Mn_{12} acetate crystal in the field parallel to the easy axis.

IV. ANALYSIS OF THE MAGNETIZATION DATA

At first glance, the presence of the maxima in the dM/dH plot, Fig. 7, that correlate with the typical tunneling maxima
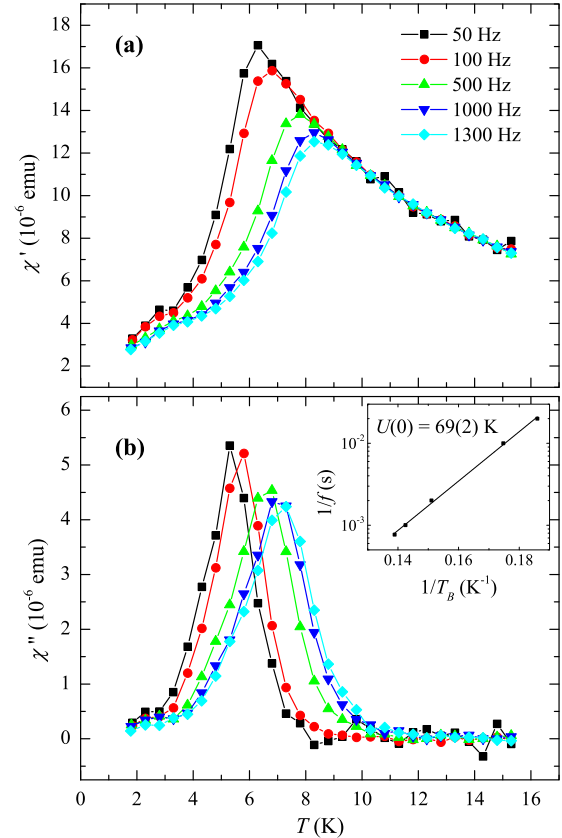

FIG. 6. (Color online) Real part (a) and imaginary part (b) of the ac susceptibility in the frequency range $f = 50$ Hz to 1.3 kHz in the presence of a 3 Oe ac field. The inset shows logarithmic dependence of the blocking temperature on $1/f$. The fitted value of the energy barrier in a zero field is $U(0) = 69 \pm 2$ K.

of Mn_{12} acetate in the field parallel to the easy axis, that occur at $H_n = nH_1$, with $H_1 \approx 4.6$ kOe, is surprising given the random orientation of the easy magnetization axes of the molecules. Simple analysis presented below shows however that the tunneling maxima can and should be observed in dM/dH obtained from a sample of randomly oriented magnetic molecules. Let us look closer at the magnetization curve in Fig. 4 that corresponds to the sweep from a positive to a negative field.

Thermally assisted spin tunneling illustrated by Fig. 8 takes place as the field becomes opposite to the magnetization, $H < 0$. If the easy axis of a particular molecule makes the angle θ with the negative direction of the field, then the condition of the nth resonance is

$$H = -\frac{H_n}{\cos\theta}, \quad 0 \leqslant \theta \leqslant \frac{\pi}{2}. \tag{2}$$

Thus, at any value of the field H the molecules that are on the nth resonance satisfy

$$\cos\theta = -\frac{H_n}{H}. \tag{3}$$

The zero-field maximum in dM/dH that has been observed in all cases has an obvious explanation. At $H = 0$ all molecules are close to the $n = 0$ resonance up to the detuning effect of local dipolar and hyperfine fields that provide the finite width
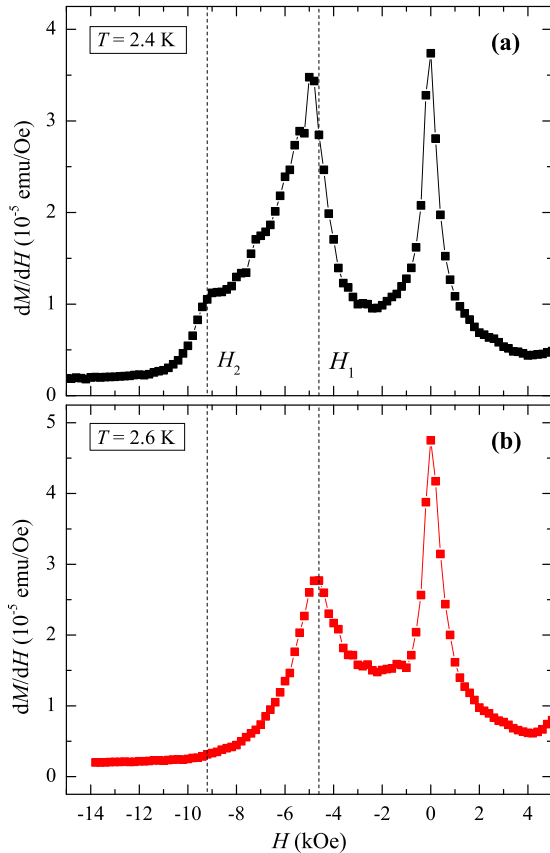
FIG. 7. (Color online) dM/dH for the $H < 0$ branch of the hysteresis curve of the disordered powder of Mn_{12} acetate nanospheres: (a) $T = 2.4$ K, (b) $T = 2.6$ K.

of the zero-field resonance. The latter is of the order of 1 kOe or below. Here we focus on the subsequent resonances $n = 1, 2, \ldots$ that have not been reported for disordered powders in the past.

Since the element of the spherical volume is proportional to $\sin\theta \, d\theta = -d\cos\theta$, the total number of molecules that enter
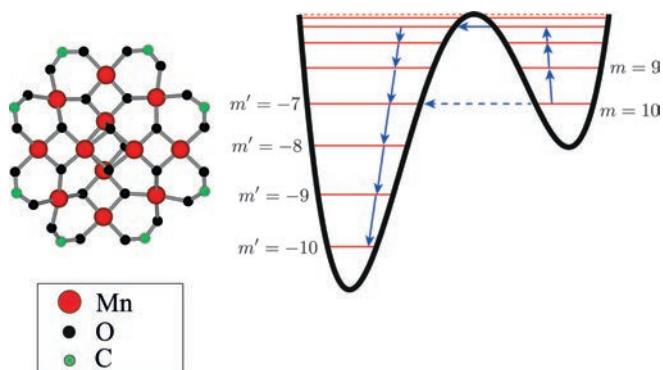

FIG. 8. (Color online) Thermally assisted tunneling between resonant spin levels in a Mn_{12} molecule. The black solid curve shows the dependence of the classical magnetic anisotropy energy on $\cos\theta$. Red lines show energies of spin levels corresponding to magnetic quantum numbers m and m'. The dashed line illustrates quantum tunneling from $m = 10$ to $m' = -7$ at $H = H_3$.

the resonance condition when the field increases in the negative direction by a small increment $dH < 0$ is

$$dN_{\text{res}} \propto -d\cos\theta \propto -\frac{dH}{H^2} \sum_{H_n \leqslant |H|} H_n > 0. \qquad (4)$$

At low temperature, when the field sweep is sufficiently slow, the change in the magnetization, dM, should be proportional to $-dN_{\text{res}}$,

$$dM \propto -dN_{\text{res}} \propto \frac{dH}{H^2} \sum_{H_n \leqslant |H|} H_n < 0. \qquad (5)$$

This gives

$$\frac{dM}{dH} \propto \frac{1}{H^2} \sum_{H_n \leqslant |H|} H_n > 0. \qquad (6)$$

The function on the right-hand side of this equation has a jumpwise behavior. At $H_1 \leqslant |H| < H_2 = 2H_1$ it behaves as H_1/H^2. At $H_2 \leqslant |H| < H_3 = 3H_1$ it behaves as $3H_1/H^2$. At $H_3 \leqslant |H| < H_4 = 4H_1$ it behaves as $6H_1/H^2$, and so on. Its value at $H = H_n$ equals

$$\frac{1}{H_n^2} \sum_{H_n \leqslant |H|} H_n = \frac{1}{n^2 H_1} \sum_{k=1}^{n} k = \frac{1}{2H_1}\left(1 + \frac{1}{n}\right). \qquad (7)$$

This analysis leads to the following conclusion. Spin tunneling resonances in a system of randomly oriented magnetic molecules can be seen as maxima in dM/dH. However, only the $H = 0$ maximum is a narrow tunneling resonance for all molecules within the dipolar/hyperfine window. Each subsequent nth "resonance" begins at $H = -H_n$ and extends to all $H < -H_n < 0$ due to different resonance conditions for differently oriented molecules. If one neglects broadening due to dipolar and hyperfine fields, these "resonances" begin with a vertical jump in dM/dH at $H = -H_n$, followed by the $1/H^2$ decrease of dM/dH. Dipolar and hyperfine fields must smear the initial vertical rise of the "resonance" by up to 1 kOe. However, the $1/H^2$ postresonance ($H < -H_n$) decrease of dM/dH over the 4.6 kOe range from $H = -H_n$ to $H = -H_{n+1}$ must be apparent. This is seen in Fig. 9 that shows the fit of the postresonance dM/dH by $1/H^2$ after crossing the first resonance. In the kelvin temperature range quantum effects become less pronounced at higher temperatures and higher n due to the exponential increase of thermal relaxation on temperature and on lowering the barrier by the field. This sensitivity to temperature and field must be especially strong as T approached the $H = 0$ dc blocking temperature of 3 K, which is seen in experiment.

Note that for the same reason as discussed above the evidence of spin tunneling in a disordered system can also be obtained by plotting the dependence of the blocking temperature on the dc magnetic field; see Fig. 10. The blocking temperature, T_B, is proportional to the energy barrier for the spin reversal, $U(H)$. At $H = 0$ the barrier is lowered due to thermally assisted quantum tunneling between resonant spin levels near the top of the barrier; see Fig. 8. The number of molecules on the zero-field resonance at a particular value of the field progressively drops as the field approaches the boundary of the dipolar/hyperfine window, which for Mn_{12} has a width of the order of 1 kOe. At that boundary T_B is
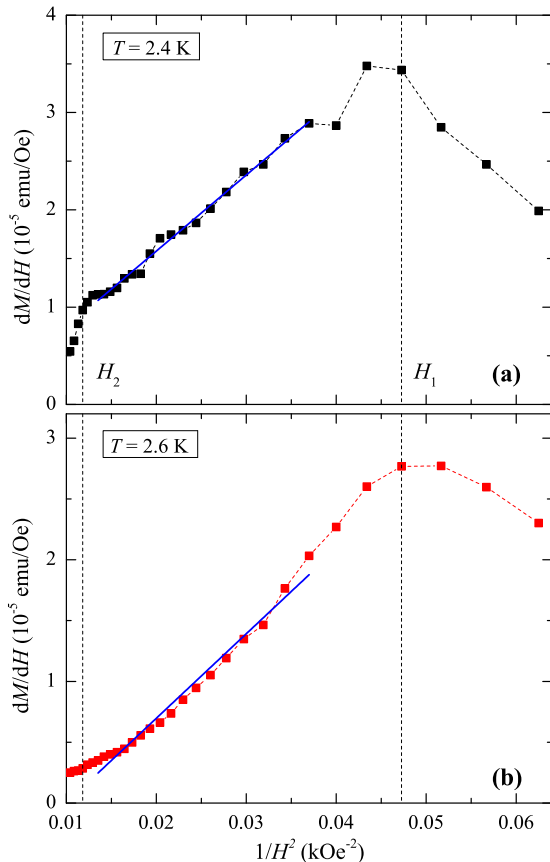
FIG. 9. (Color online) The $1/H^2$ fit (blue line) of dM/dH between first and second spin tunneling resonances for a disordered powder of Mn_{12} nanospheres: (a) $T = 2.4$ K, (b) $T = 2.6$ K.

approximately determined by the full 69 K classical energy barrier for the superparamagnetic spin flip. As the field continues to increase, the field dependence of the blocking temperature is dominated by the classical reduction of the energy barrier due to the growing Zeeman energy, which leads to the decrease of T_B on H. When the field reaches $H_1 \approx 4.6$ kOe, randomly oriented Mn_{12} molecules begin to
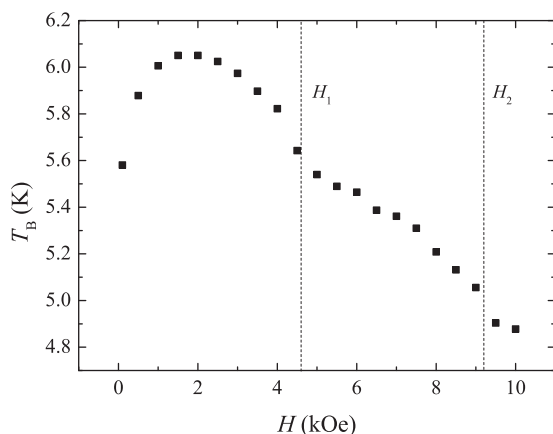

FIG. 10. Dependence of the blocking temperature on the dc field in the ac field of 100 Hz.

enter the first resonance. The evidence of that is clearly seen in Fig. 10 in the change of the derivative of T_B on H at $H = H_1$.

V. DISCUSSION

We have studied spin tunneling effects in amorphous nanospheres of Mn_{12} acetate. Samples have been characterized by chemical, infrared, TEM, x-ray, and magnetic methods. While the structure of Mn_{12} molecules appears to be the same as in a crystalline sample, their easy magnetization axes are completely disordered. Random orientation of the easy axes has been confirmed by magnetic measurements. It occurs either at the level of individual molecules inside the nanospheres, or at the level of randomly oriented nanospheres, or both. Isotropic magnetic susceptibility of the nanospheres at room temperature, when Mn_{12} molecules do not possess magnetic moments, excludes any possibility of aligning their easy axes in a high magnetic field as was done for the sample of Mn_{12} acetate consisting of elongated microcrystals [3].

Measurements of the FC and ZFC magnetization curves, and of the ac susceptibility, revealed the presence of only one magnetic species of Mn_{12} acetate, which is in contrast with previous measurements on nanospheres containing comparable amounts of slow and fast relaxing species [14,15]. The striking feature of the magnetization curve is the presence of well-defined sharp tunneling maxima in dM/dH in a sample with random orientation of easy magnetization axes of the molecules. The maxima occur at the conventional resonant fields for the Mn_{12} acetate crystal in the field parallel to the easy axis, $H_n = -nH_1$, with $H_1 \approx 4.6$ kOe.

Quantitative explanation to this observation is provided. At any value of the field H the molecules that are on the nth resonance have their easy axis at an angle θ with the field, satisfying $\cos\theta = -H_n/H$. Thus, as soon as the field enters the range $H \leqslant -H_n$ a new set of molecules that satisfy the nth resonance condition begins to reverse their magnetization. This results in the change of the slope of $M(H)$ every time when the field reaches the value $H_n = -nH_1$, and in the corresponding peaks in dM/dH. However, only the $n = 0$ peak is the same tunneling resonance as in a crystalline sample, when all molecules achieve the resonance condition inside the dipolar/hyperfine field window. As our analysis shows, all subsequent resonances are characterized by a steep jump of dM/dH at $H_n = -nH_1$ followed by a $1/H^2$ decrease. This conclusion agrees with the experimental data.

Inevitably, our findings raise the following question. Is the effort to grow a single crystal or the laborious procedure of aligning microcrystals, as was done in Ref. [3] that reported the discovery of the resonant spin tunneling in Mn_{12} acetate, really necessary to obtain the evidence of spin tunneling? As has been illustrated by this paper, the answer is apparently no. One can also make another useful statement: When a system of magnetic molecules exhibits tunneling maxima in dM/dH, it does not necessarily mean that the easy axes of the molecules are ordered. To further illustrate this point we conducted measurements of the nonoriented powder of micron-size crystals identical to the powder used in Ref. [3] where microcrystals were oriented in an epoxy prior to taking magnetic measurements. The dM/dH plot obtained from the
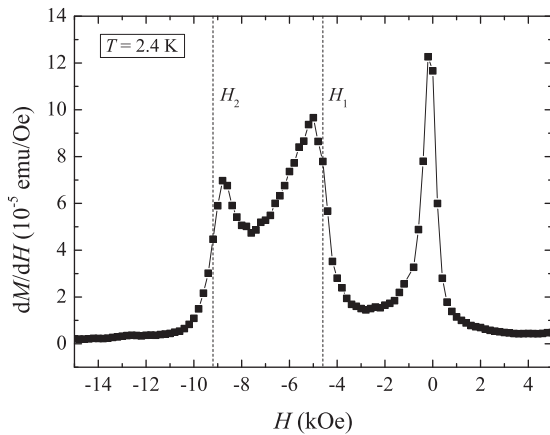
FIG. 11. Field derivative of the magnetization in a sample of randomly oriented micron-size crystallites of Mn_{12} acetate.

powder sample without any orientation effort is presented in Fig. 11. It clearly shows three tunneling maxima.

We, therefore, conclude that while single crystals are good for the in depth study of spin tunneling, the robust evidence of the effect can be obtained from the magnetization curve of any disordered microcrystalline sample as long as the magnetic molecules preserve their structure. This should greatly simplify the effort by chemists and physicists to track spin tunneling effects in newly synthesized molecular magnets.

ACKNOWLEDGMENTS

[1] E. M. Chudnovsky and J. Tejada, *Macroscopic Quantum Tunneling of the Magnetic Moment* (Cambridge University Press, Cambridge, 1998).

[2] *Molecular Magnets—Physics and Applications*, edited by J. Bartolomé, F. Luis, and J. F. Fernández (Springer, Heidelberg, 2014).

[3] J. R. Friedman, M. P. Sarachik, J. Tejada, and R. Ziolo, Phys. Rev. Lett. **76**, 3830 (1996).

[4] J. M. Hernandez, X. X. Zhang, F. Luis, J. Bartolome, J. Tejada, and R. Ziolo, Europhys. Lett. **35**, 301 (1996).

[5] L. Thomas, Fl. Lionti, R. Ballou, D. Gatteschi, R. Sessoli, and B. Barbara, Nature (London) **383**, 145 (1996).

[6] W. Wernsdorfer and R. Sessoli, Science **284**, 133 (1999).

[7] Y. Suzuki, M. P. Sarachik, E. M. Chudnovsky, S. McHugh, R. Gonzalez-Rubio, N. Avraham, Y. Myasoedov, E. Zeldov, H. Shtrikman, N. E. Chakov, and G. Christou, Phys. Rev. Lett. **95**, 147201 (2005).

[8] A. Hernandez-Minguez, J. M. Hernandez, F. Macia, A. Garcia-Santiago, J. Tejada, and P. V. Santos, Phys. Rev. Lett. **95**, 217205 (2005).

[9] C. Schlegel, J. van Slageren, M. Manoli, E. K. Brechin, and M. Dressel, Phys. Rev. Lett. **101**, 147203 (2008).

[10] S. Bertaina, S. Gambarelli, T. Mitra, B. Tsukerblat, A. Müller, and B. Barbara, Nature (London) **453**, 203 (2008); **466**, 1006 (2010).

[11] M. Ganzhorn, S. Klyatskaya, M. Ruben, and W. Wernsdorfer, Nat. Nanotechnol. **8**, 165 (2013).

[12] M. Ganzhorn, S. Klyatskaya, M. Ruben, and W. Wernsdorfer, ACS Nano **7**, 6225 (2013).

[13] J. Tejada, E. M. Chudnovsky, E. del Barco, J. M. Hernandez, and T. P. Spiller, Nanotechnology **12**, 181 (2001).

[14] I. Imaz, F. Luis, C. Carbonera, D. Ruiz-Molinac, and D. Maspoch, Chem. Commun. **2008**, 1202 (2008).

[15] C. Carbonera, I. Imaz, D. Maspoch, D. Ruiz-Molina, and F. Luis, Inorg. Chim. Acta **361**, 3951 (2008).

[16] F. El Hallak, J. van Slageren, J. Gómez-Segura, D. Ruiz-Molina, and M. Dressel, Phys. Rev. B **75**, 104403 (2007).

[17] C. Carbonera, F. Luis, J. Campo, J. Sánchez-Marcos, A. Camón, J. Chaboy, D. Ruiz-Molina, I. Imaz, J. van Slageren, S. Dengler, and M. González, Phys. Rev. B **81**, 014427 (2010).

[18] P. J. Chupas, X. Qiu, J. C. Hanson, P. L. Lee, C. P. Grey, and S. J. L. Billinge, J. Appl. Crystallogr. **36**, 1342 (2003).

[19] P. Juhas, T. Davis, C. L. Farrow, and S. J. L. Billinge, J. Appl. Crystallogr. **46**, 560 (2013).

[20] P. Langan, R. Robinson, P. J. Brown, D. Argyriou, D. Hendrickson, and G. Christou, Acta Crystallogr. C **57**, 909 (2001).

[21] A. Cornia, A. C. Fabretti, R. Sessoli, L. Sorace, D. Gatteschi, A.-L. Barra, C. Daiguebonne, and T. Roisnel, Acta Crystallogr. C **58**, m371 (2002).

[22] D. R. Nelson, J. Non-Cryst. Solids **61-62**, 475 (1984).

[23] E. M. Chudnovsky and J. Tejada, Europhys. Lett. **23**, 517 (1993).

[24] M. Mannini, F. Pineider, C. Danieli, F. Totti, L. Sorace, P. Sainctavit, M.-A. Arrio, E. Otero, L. Joly, J. C. Cezar, A. Cornia, and R. Sessoli, Nature (London) **468**, 417 (2010).